

Mechanistic Investigations of the Radical Transport Pathway in Fluorotyrosine-substituted Class Ia Ribonucleotide Reductases

by

Kanchana Ravichandran

B.S. Biochemistry, B.A. Neuroscience
Brandeis University, 2010

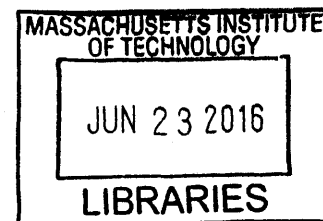
Submitted to the Department of Chemistry
in Partial Fulfillment of the Requirements for the Degree of

Doctor of Philosophy in Biological Chemistry

at the

MASSACHUSETTS INSTITUTE OF TECHNOLOGY

June 2016



ARCHIVES

© 2016 Massachusetts Institute of Technology. All rights reserved

Signature of Author: _____

Signature redacted

Department of Chemistry
May 16, 2016

Certified by: _____

Signature redacted

JoAnne Stubbe
Novartis Professor of Chemistry and Professor of Biology
Thesis Supervisor

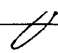
Accepted by: _____

Signature redacted

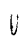
Robert W. Field
Haslam and Dewey Professor of Chemistry
Chairman, Departmental Committee on Graduate Studies

This Doctoral Thesis has been examined by a committee of the Departments of Chemistry and Biology as follows:


Signature redacted

 Elizabeth M. Nolan
Associate Professor of Chemistry
Thesis Chair

Signature redacted

 JoAnne Stubbe
Novartis Professor of Chemistry and Professor of Biology
Thesis Supervisor

Signature redacted

 Bradley L. Pentelute
Pfizer-Laubach Career Development Assistant Professor of Chemistry

To my family

ACKNOWLEDGMENTS

I would first like to thank my research advisor JoAnne Stubbe, whose passion and enthusiasm for RNR first attracted me to the project. Thank you for constantly challenging me and for teaching me how to be a good experimentalist and a critical thinker. I hope I've been able to provide some "science fixes" over the past 6 years! Thanks to my committee members, Liz and Brad, for their incredible support and guidance during my time at MIT.

I have been fortunate to have had several amazing collaborations that have truly enriched my grad school experience. Thanks to the Bennati lab at the Max Planck Institute (Marina, Thomas and Müge), the Britt lab at UC Davis (Dave, Paul and Troy), the Drennan lab at MIT (Cathy, Ed and Michael), the Nocera lab at Harvard (Dan, Pat, Arturo, Dave, Bryce, Bon Jun, Lisa and Brandon) and the Tommos lab at Penn (Cecilia and Li). These guys have exposed me to a range of techniques and have contributed both experimentally and intellectually to this thesis. A special thanks to Cecilia for my first lead author paper in grad school!

I am indebted to the members of the Stubbe lab without whom I could not have done any of this. Crystal, Ellen, Joey, Mimi and Rachael made me feel at home when I joined the lab. I'm so glad most of you stayed in Boston! Now, we only need to get Mimi and Joey back... Thanks especially to Ellen and Ken for training me during my first year in the lab, and for laying the foundation for the work described in this thesis. By my third year in grad school, this incredible group of people had moved on to be rock star scientists elsewhere, and Mac, Yifeng and Wankyu became my constant companions. Thank you guys for the last three years. I will never forget all the late nights in lab and the kitchen parties! Your scientific advice and friendship have been invaluable. Alex: I'm sad we didn't get to spend more time together in lab but I can't think of anyone better to take my spot in the PCET family. Good luck! I am confident that you and Wankyu will together figure out what is at the β/α interface! Denyce and Julia: I can't even explain how much I'm going to miss working with you. Wankyu will be able to attest to the fact that I complain when I haven't seen you guys in more than a couple of days. Thanks especially for your help with thesis editing. Thanks to our lab tech, Albert. You arrived at the perfect time during thesis writing and happily took on all of my lab responsibilities! Thanks to other Stubbe lab people that I have overlapped with during my time at MIT, my labmates: Leo, Henry, Xuling, Olga, Yan, Qinghui, Meng, and Yimon and undergrads/high school students that I've been fortunate enough to work with: Alice, Katarina, Camille and Simon.

Thanks to my fellow biological classmates, Ali, Megan, Amy, Haritha and Austin. Thanks especially to Ali, Megan and Amy for numerous coffee runs, dinners, movie nights, wine nights and more recently, skype sessions! You guys have kept me sane through it all.

I have been incredibly lucky to have some amazing friends in the Boston area. Thanks to my bffs, Jeremy, Emily and Alyssa, for countless lunches, TGIFs, Muddy trips, ice cream socials, BBQs and boat cruises. I am the type of person to veg out in front of the TV after a day in lab, and I am grateful that you guys force me to get out of the apartment and socialize. Thanks especially for making me celebrate my birthday this year! It ended up being kinda awesome. Thanks to my Brandeis friends, Rachel. W., Michelle and Rachel. H. We met during our first week at Brandeis because somebody out there decided we were going to live on the same floor in Usen Hall. I am

so grateful to that person because you guys have been my support network for the past 10 years. Thanks to my friends from home, Namrita, Soumya, Sushmita and Jyotsna. I've known some of these people since I was 10 years old and I'm so fortunate to still have them in my life. Thank you for being so understanding when I couldn't visit you guys. I'm excited about hanging out more often in the future than was possible in recent years.

Finally, this thesis would not be possible without my family. Appa, Amma, Krithika and Tom, I would not be here today without your love and support. Thank you for not complaining too much that I haven't visited you more in the last few years! Thanks to my sweet niece Rhea, whose happy and smiling face always cheers me up on bad days. Appa, Amma, Krithika, Tom and Rhea, this thesis is dedicated to you.

Mechanistic Investigations of the Radical Transport Pathway in Fluorotyrosine-substituted Class Ia Ribonucleotide Reductases

by

Kanchana Ravichandran

Submitted to the Department of Chemistry
On May 16, 2016 in Partial Fulfillment of the Requirements
for the Degree of Doctor of Philosophy in Biological Chemistry

ABSTRACT

Ribonucleotide reductase (RNR) catalyzes the reduction of nucleotides to 2'-deoxynucleotides, providing the monomeric precursors for DNA replication and repair. The focus of this thesis is on the *E. coli* class Ia RNR that is composed of two homodimeric subunits ($\alpha 2$ and $\beta 2$), which form an active $\alpha 2\beta 2$ complex. A stable diferric-tyrosyl radical ($Y_{122}\bullet$) in $\beta 2$ reversibly oxidizes an active site cysteine (C_{439}) in $\alpha 2$ via multiple proton-coupled electron transfer (PCET) steps through conserved aromatic amino acid residues: $Y_{122}\bullet \rightleftharpoons [W_{48}] \rightleftharpoons Y_{356}$ in $\beta 2$ to $Y_{731} \rightleftharpoons Y_{730} \rightleftharpoons C_{439}$ in $\alpha 2$. The transient $C_{439}\bullet$ is responsible for initiating nucleotide reduction. Long-range radical transport (RT) and nucleotide reduction are kinetically masked by rate-limiting protein conformational changes.

Herein, the stable $Y_{122}\bullet$ is site-specifically replaced with a 2,3,5-trifluorotyrosyl radical ($2,3,5-F_3Y\bullet$) that modulates the driving force for RT. This 2,3,5- F_3Y -substituted RNR perturbs PCET kinetics such that a radical intermediate ($Y_{356}\bullet$) can be observed and characterized. Rapid kinetic studies demonstrate that $Y_{356}\bullet$ is kinetically and chemically competent for nucleotide reduction, and provide the first evidence for a pathway $Y\bullet$ that can complete the RNR catalytic cycle. Temperature and pH dependent studies show equilibration of the stable 2,3,5- $F_3Y\bullet$ with the pathway radical intermediate, $Y_{356}\bullet$. These data are corroborated by similar experiments performed with 3,5-difluorotyrosine (3,5- F_2Y) in place of Y_{356} , which demonstrate equilibration of $Y_{122}\bullet$ with 3,5- $F_2Y\bullet$. These studies together provide insight into the thermodynamic landscape of the RT pathway. A model is proposed in which the RT pathway is thermodynamically uphill and driven forward by rapid irreversible water loss that occurs during nucleotide reduction.

The 3,5- F_2Y analog is further utilized to test the ability of E_{350} , a conserved $\beta 2$ C-terminal tail residue, to function as the proton acceptor for Y_{356} or Y_{731} . A model is put forth in which E_{350} does not participate in proton transfer, but is involved in $\alpha 2\beta 2$ subunit interaction and in controlling radical initiation. Finally, an X-ray crystal structure of the active $\alpha 2\beta 2$ complex has remained elusive. Herein, Ni-NTA pull-down assays are presented, demonstrating that injection of a single electron into the diferric cluster site generates a stable $\alpha 2\beta 2$ complex. These studies afford the opportunity to structurally characterize the $\alpha 2\beta 2$ complex with the goal of understanding PCET across the β/α interface.

Thesis Supervisor: JoAnne Stubbe

Title: Novartis Professor of Chemistry and Professor of Biology

TABLE OF CONTENTS

Dedication	5
Acknowledgments	7
Abstract	9
Table of Contents	11
List of Figures	16
List of Tables	19
List of Schemes	20
Abbreviations	21
CHAPTER 1. Introduction to the <i>Escherichia coli</i> class Ia ribonucleotide reductase	
1.1 GENERAL INTRODUCTION TO RIBONUCLEOTIDE REDUCTASE	24
1.1.1 Reaction catalyzed by RNR	24
1.1.2 The different classes of RNR	24
1.1.3 Mechanism of nucleotide reduction	26
1.2 INTRODUCTION TO THE CLASS IA RNR	30
1.2.1 Structure of the class Ia RNR	30
1.2.2 Radical transport pathway for oxidation of C ₄₃₉ by Y ₁₂₂ •	35
1.2.3 Mechanistic considerations for long-range RT	36
1.2.4 Conformationally governed RT in the <i>E. coli</i> class Ia RNR	39
1.2.5 Strategy to investigate RT and drawbacks	41
1.2.6 Radical distribution and half-sites reactivity	45
1.3 EVIDENCE FOR RADICAL INTERMEDIATES IN THE RT PATHWAY	48
1.4 PROTON MANAGEMENT IN THE RT PATHWAY	54
1.4.1 The pK _a s of all pathway Ys are minimally perturbed except for Y ₁₂₂	54
1.4.2 Orthogonal PCET through Y ₁₂₂	55
1.4.3 Orthogonal PCET through Y ₃₅₆	57
1.4.4 Collinear PCET in the $\alpha 2$ subunit	62
1.5 THERMODYNAMIC LANDSCAPE OF THE RT PATHWAY	70
1.5.1 Thermodynamic landscape of the pathway prior to the UAA work	70
1.5.2 Tolerance of the RT pathway to thermodynamic perturbations	71
1.5.3 Current thermodynamic landscape for the PCET pathway	77
1.6 CHAPTER PREVIEW	83

1.7 REFERENCES	87
CHAPTER 2. The formal reduction potential of 3,5-difluorotyrosine in a structured protein: insight into multistep radical transfer	
2.1 INTRODUCTION	96
2.2 MATERIALS AND METHODS	99
2.2.1 Purification of tyrosine phenol lyase (TPL)	99
2.2.2 Enzymatic synthesis of 3,5-F ₂ Y	99
2.2.3 Construction of α_3 TAG ₃₂ by site-directed mutagenesis	99
2.2.4 Expression of thioredoxin- $\alpha_3(3,5)$ F ₂ Y	100
2.2.5 Purification of $\alpha_3(3,5)$ F ₂ Y	100
2.2.6 Absorption spectroscopy	101
2.2.7 Circular dichroism (CD) spectroscopy	102
2.2.8 Square-wave voltammetry (SWV)	103
2.3 RESULTS	105
2.3.1 $\alpha_3(3,5)$ F ₂ Y expression and purification	105
2.3.2 Protein characterization	105
2.3.3 Preparation of SWV samples	110
2.3.4 SWV analysis of $\alpha_3(3,5)$ F ₂ Y	111
2.4 DISCUSSION	114
2.4.1 Measuring tyrosine reduction potentials	114
2.4.2 Using the α_3 X system as a guide to interpret mechanistic studies of <i>E. coli</i> RNR	116
2.4.3 Future perspectives	117
2.5 REFERENCES	119
CHAPTER 3. Reverse electron transfer completes the catalytic cycle in a 2,3,5-trifluorotyrosine-substituted ribonucleotide reductase	
3.1 INTRODUCTION	124
3.2 MATERIALS AND METHODS	128
3.2.1 Materials	128
3.2.2 Expression and purification of apo Y _{122(2,3,5)} F ₃ Y- β 2	128
3.2.3 Reconstitution of apo Y _{122(2,3,5)} F ₃ Y- β 2 to form the diferric-F ₃ Y• cofactor	129
3.2.4 Reaction of Y _{122(2,3,5)} F ₃ Y- β 2, wt- α 2, CDP and ATP monitored by RFQ-EPR spectroscopy	129

3.2.5 Reaction of $Y_{122}(2,3,5)F_3Y-\beta 2$, wt- $\alpha 2$, CDP and ATP monitored by the RCQ method	130
3.2.6 Reaction of $Y_{122}(2,3,5)F_3Y-\beta 2$, wt- $\alpha 2$, CDP, ATP, TR/TRR/NADPH monitored by hand-quench EPR spectroscopy	131
3.2.7 Reaction of $Y_{122}(2,3,5)F_3Y-\beta 2$, wt- $\alpha 2$, CDP, ATP and TR/TRR/NADPH monitored by the RCQ method	131
3.3 RESULTS	133
3.3.1 “Two or none” radical distribution and half-sites reactivity in $Y_{122}(2,3,5)F_3Y-\beta 2$	133
3.3.2 Kinetics in the absence of a reducing system: formation and disappearance of $Y_{356}\bullet$ at 25 °C	134
3.3.3 Kinetics in the absence of a reducing system: formation and disappearance of $Y_{356}\bullet$ at 5 °C	135
3.3.4 Kinetics of dCDP formation at 25 °C in the absence of a reducing system	137
3.3.5 Kinetics of dCDP formation at 5 °C in the absence of a reducing system	139
3.3.6 Kinetics in the presence of a reducing system: EPR analysis of $Y_{356}\bullet$ concentration during steady-state turnover	140
3.3.7 Kinetics of dCDP formation at 5 °C and 25 °C in the presence of a reducing system	141
3.4 DISCUSSION	144
3.5 REFERENCES	151
CHAPTER 4. The stable tyrosyl radical ($Y_{122}\bullet$) is in equilibrium with a pathway tyrosyl radical ($Y_{356}\bullet$) in the radical transport pathway of ribonucleotide reductase	
4.1 INTRODUCTION	156
4.2 MATERIALS AND METHODS	160
4.2.1 Materials	160
4.2.2 Hand-quench EPR analysis of $Y_{356}\bullet$ formation as a function of temperature	160
4.2.3 RFQ-EPR analysis of $Y_{356}\bullet$ formation as a function of temperature	161
4.2.4 Hand-quench EPR analysis of $Y_{356}\bullet$ formation as a function of pH	162
4.2.5 RFQ-EPR analysis of the reaction of $Y_{356}(3,5)F_2Y-\beta 2$, $Y_{731}F-\alpha 2$, CDP and ATP	162
4.3 RESULTS	163
4.3.1 Temperature dependent distribution of $F_3Y\bullet$ and $Y_{356}\bullet$: Equilibration of the two radical states	163
4.3.2 The pH can shift the equilibrium between $F_3Y\bullet$ and $Y_{356}\bullet$: Proton from Y_{356} is in rapid exchange with solvent	170
4.3.3 Equilibration of $Y_{122}\bullet$ and $F_2Y\bullet$ in the $Y_{356}(3,5)F_2Y-\beta 2$ system	173

4.4 DISCUSSION	179
4.4.1 Thermodynamic landscape of the RT pathway within the $\beta 2$ subunit	179
4.4.2 Relationship between the thermodynamic landscape and kinetics	184
4.4.3 Equilibration of $F_3 Y^\bullet$ and Y_{356}^\bullet as a function of pH: PCET across the β/α interface involves fast proton exchange between Y_{356} and solvent	187
4.4.4 Conclusions	189
4.5 REFERENCES	190
CHAPTER 5. A structural role for E_{350} in RNR function	
5.1 INTRODUCTION	195
5.2 MATERIALS AND METHODS	203
5.2.1 Materials	203
5.2.2 K_d for $\alpha 2/E_{350}X-\beta 2$ ($X = D$ or Q) interaction	203
5.2.3 Reaction of $E_{350}X-\beta 2$ ($X = D, Q$), wt- $\alpha 2$, N_3 UDP and TTP monitored by EPR spectroscopy	204
5.2.4 Specific activity of $E_{350}Q/Y_{356}(3,5)F_2 Y-\beta 2$ at pH 6.7 and pH 8.0	204
5.2.5 The pH rate profile of $E_{350}D-\beta 2/Y_{731}(3,5)F_2 Y-\alpha 2$	204
5.2.6 Specific activity of the triple mutant $E_{350}Q/Y_{356}(3,5)F_2 Y-\beta 2$ and $Y_{731}(3,5)F_2 Y-\alpha 2$ at pH 6.8 and pH 8.4	205
5.2.7 Construction of pBAD-nrdB ₁₂₂ TAG- $E_{350}D$	205
5.2.8 Expression, purification and reconstitution of $Y_{122}(2,3,5)F_3 Y/E_{350}D-\beta 2$	205
5.2.9 Reaction of $Y_{122}(2,3,5)F_3 Y/E_{350}D-\beta 2$, wt- $\alpha 2$, CDP and ATP monitored by RFQ-EPR spectroscopy	206
5.2.10 Expression and purification of $Y_{122}NO_2 Y/E_{350}D-\beta 2$	206
5.2.11 Chelation of iron from $Y_{122}NO_2 Y/E_{350}D-\beta 2$	207
5.2.12 Reaction of $Y_{122}NO_2 Y/E_{350}D-\beta 2$, wt- $\alpha 2$, CDP and ATP monitored by RFQ-EPR spectroscopy	207
5.3 RESULTS	208
5.3.1 K_d for $\alpha 2/E_{350}X-\beta 2$ ($X = D$ or Q) interaction	208
5.3.2 Amount of N^\bullet generated in the reaction of $E_{350}X-\beta 2/\alpha 2/N_3$ UDP/TTP is consistent with contaminating wt RNR	209
5.3.3 $E_{350}Q/Y_{356}(3,5)F_2 Y-\beta 2$ is not active for nucleotide reduction at pH 6.7 or pH 8.0	213
5.3.4 $E_{350}D-\beta 2/Y_{731}(3,5)F_2 Y-\alpha 2$ is not active for nucleotide reduction at any pH	214
5.3.5 $E_{350}Q/Y_{356}(3,5)F_2 Y-\beta 2$ cannot catalyze nucleotide reduction with $Y_{731}(3,5)F_2 Y-\alpha 2$ at any pH	215

5.3.6 Reaction of Y ₁₂₂ (2,3,5)F ₃ Y/E ₃₅₀ D-β ₂ , wt-α ₂ , CDP and ATP does not accumulate Y ₃₅₆ •	217
5.3.7 Reaction of Y ₁₂₂ NO ₂ Y/E ₃₅₀ D-β ₂ , wt-α ₂ , CDP and ATP does not accumulate Y ₃₅₆ • or W ⁺	219
5.4 DISCUSSION	221
5.5 REFERENCES	224
CHAPTER 6. Chemical steps required to generate a stable α₂β₂ complex	
6.1 INTRODUCTION	229
6.2 MATERIALS AND METHODS	234
6.2.1 Materials	234
6.2.2 Pull-down assay of Y ₁₂₂ NO ₂ Y-β ₂ by His ₆ -α ₂	234
6.2.3 Pull-down assay of wt-β ₂ by His ₆ -α ₂ in the presence of N ₃ CDP	235
6.2.4 Pull-down assay of Y ₁₂₂ NO ₂ Y-β ₂ by His ₆ -Y ₇₃₁ F-α ₂	235
6.2.5 Pull-down assay of DT/MV-β ₂ by His ₆ -Y ₇₃₁ F-α ₂	236
6.3 RESULTS	237
6.3.1 Multiple turnovers are not required for generation of a stable α ₂ β ₂ complex	237
6.3.2 CDP reduction is not required for formation of a stable α ₂ β ₂ complex	239
6.3.3 Radical injection into α ₂ is not required for generation of a stable α ₂ β ₂ complex	241
6.3.4 Injection of a single electron into the diferric cluster of wt-β ₂ is sufficient to form a stable α ₂ β ₂ complex	243
6.4 DISCUSSION	249
6.5 REFERENCES	254
APPENDIX 1. Supporting information for Chapter 1	258
APPENDIX 2. Expression and purification of α₃F_nY (n = 2, 3)	261
APPENDIX 3. Kinetics of cofactor assembly in Y₁₂₂F_nY-β₂	270
APPENDIX 4. Investigating the role of W₄₈ in long-range radical transport in RNR	287
APPENDIX 5. Supporting Figures for Chapter 3	314
APPENDIX 6. Supporting Figures for Chapter 4	320
APPENDIX 7. Supporting Figures for Chapter 6	324

LIST OF FIGURES

Figure 1.1 Reaction catalyzed by RNR	24
Figure 1.2 The different classes of RNR based on the metallocofactor used to generate C•	26
Figure 1.3 Mechanism of nucleotide reduction	27
Figure 1.4 Structural interconversions of RNR	31
Figure 1.5 Methods to characterize the diferric-Y• cofactor in $\beta 2$	32
Figure 1.6 Uhlin and Eklund's docking model for the <i>E. coli</i> active $\alpha 2\beta 2$ complex	33
Figure 1.7 Proposed residues on the RT pathway	36
Figure 1.8 Proposed PCET model for RT in the <i>E. coli</i> class Ia RNR	39
Figure 1.9 Kinetic model for wt RNR	41
Figure 1.10 UAAs that have been incorporated into <i>E. coli</i> class Ia RNR	44
Figure 1.11 Pourbaix diagrams for W, Y and its analogs	45
Figure 1.12 Two or none radical distribution model and half-sites reactivity in RNR	47
Figure 1.13 Distance determination by PELDOR spectroscopy	49
Figure 1.14 Experimental strategy for testing orthogonal PCET at Y ₁₂₂	56
Figure 1.15 A. Experimental strategy for testing orthogonal PCET at Y ₃₅₆	59
Figure 1.16 The pH rate profiles of EPL RNR and wt RNR	60
Figure 1.17 Absolute specific activities of Y ₃₅₆ F _n Y- $\beta 2$ generated by the EPL and nonsense codon suppression methods	62
Figure 1.18 Absolute specific activities of Y ₇₃₁ F _n Y- $\alpha 2$ and Y ₇₃₀ F _n Y- $\alpha 2$ as a function of pH	65
Figure 1.19 Normalized activities of Y ₃₅₆ F _n Y- $\beta 2$, Y ₇₃₁ F _n Y- $\alpha 2$ and Y ₇₃₀ F _n Y- $\alpha 2$ as a function of pH	68
Figure 1.20 Original thermodynamic landscape of the RT pathway	71
Figure 1.21 Perturbation of the thermodynamic landscape with UAAs	72
Figure 1.22 Relative activities of Y ₃₅₆ F _n Y- $\beta 2$ vs wt- $\beta 2$	74
Figure 1.23 Kinetic model for the reaction of Y ₁₂₂ NO ₂ Y- $\beta 2$, $\alpha 2$, CDP and ATP	78
Figure 1.24 Thermodynamic landscape of the RT pathway	80
Figure 1.25 X-band EPR spectra of F _n Y•	81
Figure 1.26 Overlay of the EPR spectra of Y ₃₅₆ • generated in each Y ₁₂₂ F _n Y- $\beta 2$ reaction compared to the Y ₃₅₆ • observed in the Y ₁₂₂ NO ₂ Y- $\beta 2$ reaction	82
Figure 2.1 SDS-PAGE analysis of $\alpha_3(3,5)F_2Y$ expression in <i>E. coli</i> BL21(DE3)	106
Figure 2.2 Analytical HPLC and mass spectrometry evaluation of purified $\alpha_3(3,5)F_2Y$	106

Figure 2.3 Characterization of $\alpha_3(3,5)F_2Y$ by UV-Vis absorption and CD spectroscopy	109
Figure 2.4 SWV analysis of the Y-O•/Y-OH redox system in $\alpha_3(3,5)F_2Y$	110
Figure 2.5 I_{net} of $\alpha_3(3,5)F_2Y$ and α_3Y recorded at identical experimental conditions	113
Figure 3.1 The proposed PCET pathway in <i>E. coli</i> class Ia RNR	126
Figure 3.2 Two or none radical distribution model and half-sites reactivity in RNR	134
Figure 3.3 Reaction of $Y_{122}(2,3,5)F_3Y-\beta_2$, wt- α_2 , CDP and ATP at 25 °C monitored by RFQ-EPR spectroscopy and the RCQ method	136
Figure 3.4 Reaction of $Y_{122}(2,3,5)F_3Y-\beta_2$, wt- α_2 , CDP and ATP at 5 °C monitored by RFQ-EPR spectroscopy and the RCQ method	136
Figure 3.5 Amount of dCDP generated in the absence of a reducing system	138
Figure 3.6 Kinetics of product formation in $Y_{122}(2,3,5)F_3Y-\beta_2$ in the presence of TR/TRR/NADPH at 25 °C and 5 °C	143
Figure 4.1 Proposed thermodynamic landscape of the PCET pathway at 25 °C and pH 7.6	157
Figure 4.2 Composite EPR spectra of the $Y_{122}(2,3,5)F_3Y-\beta_2/Y_{731}F-\alpha_2/CDP/ATP$ reaction as a function of temperature	164
Figure 4.3 Temperature dependence of $Y_{356}\bullet$ formation	169
Figure 4.4 Composite EPR spectra of the $Y_{122}(2,3,5)F_3Y-\beta_2/Y_{731}F-\alpha_2/CDP/ATP$ reaction as a function of pH	171
Figure 4.5 The pH dependence of $Y_{356}\bullet$ formation at 5 °C and 25 °C	173
Figure 4.6 Reaction of $Y_{356}(3,5)F_2Y-\beta_2$, $Y_{731}F-\alpha_2$, CDP and ATP monitored by RFQ-EPR spectroscopy	175
Figure 4.7A Reaction of $Y_{356}(3,5)F_2Y-\beta_2$, $Y_{731}F-\alpha_2$, CDP and ATP monitored by RFQ-EPR spectroscopy	178
Figure 4.7B Overlay of the EPR spectra of $F_2Y\bullet$ at different positions on pathway	178
Figure 4.8 Current thermodynamic landscape of the RT pathway at 25 °C and pH 7.6	187
Figure 5.1 EPR and SF analysis of the reaction of $E_{350}A/Y_{356}NH_2Y-\beta_2$, α_2 , CDP and ATP	198
Figure 5.2 Probes for investigating the role of E_{350} in RNR function	200
Figure 5.3 The pH rate profiles of $E_{350}X/Y_{356}(3,5)F_2Y-\beta_2$	201
Figure 5.4 K_d for $\alpha_2/E_{350}X-\beta_2$ (X = D or Q) interaction	209
Figure 5.5 Reaction of $E_{350}D-\beta_2$, wt- α_2 , N_3UDP and TTP monitored by EPR spectroscopy	212
Figure 5.6 Reaction of $E_{350}Q-\beta_2$, wt- α_2 , N_3UDP and TTP monitored by EPR spectroscopy	212
Figure 5.7 The pH rate profile of $E_{350}D-\beta_2/Y_{731}(3,5)F_2Y-\alpha_2$	214
Figure 5.8 Reaction of $Y_{122}(2,3,5)F_3Y/E_{350}D-\beta_2$, wt- α_2 , CDP and ATP monitored by RFQ-EPR spectroscopy	218

Figure 5.9 Reaction of Y ₁₂₂ NO ₂ Y/E ₃₅₀ D-β ₂ , wt-α ₂ , CDP and ATP monitored by RFQ-EPR spectroscopy	220
Figure 6.1 Conditions under which a stable α ₂ β ₂ complex can be generated	231
Figure 6.2 Pull-down assay of Y ₁₂₂ NO ₂ Y-β ₂ by His ₆ -α ₂	239
Figure 6.3 SDS-PAGE quantitation of the α ₂ :β ₂ ratio in the pull-downs assays	241
Figure 6.4 Pull-down assay of wt-β ₂ by His ₆ -α ₂ in the presence of N ₃ CDP	241
Figure 6.5 Pull-down assay of Y ₁₂₂ NO ₂ Y-β ₂ by His ₆ -Y ₇₃₁ F-α ₂	242
Figure 6.6 Reduction of the diferric-Y cofactor by DT/MV or HU	244
Figure 6.7 Pull-down assay of DT/MV treated-β ₂ by His ₆ -Y ₇₃₁ F-α ₂	246
Figure 6.8 Pull-down assay of Y ₁₂₂ NO ₂ Y-β ₂ by His ₆ -α ₂	248

LIST OF TABLES

Table 1.1 Summary of F_nY pH rate profiles	53
Table 1.2 pK_a s obtained by fitting the experimental pH rate profiles to a two-proton ionization model	68
Table 1.3 Reduction potential range within which RNR can produce deoxynucleotides	76
Table 2.1 Properties of Y , $3,5-F_2Y$, α_3Y and $\alpha_3(3,5)F_2Y$	112
Table 3.1 Amount of $Y_{356}\bullet$ and dCDP produced in the first turnover by $Y_{122}(2,3,5)F_3Y-\beta_2$	133
Table 3.2 DeoxyCDP formation kinetics in the absence and presence of TR/TRR/NADPH	139
Table 3.3 Amount of $Y_{356}\bullet$ generated during $Y_{122}(2,3,5)F_3Y-\beta_2$ turnover in the presence of TR/TRR/NADPH	141
Table 4.1 Temperature dependence of $Y_{356}\bullet$ formation: HQ vs RFQ-EPR	166
Table 4.2 The pH dependence of $Y_{356}\bullet$ formation	172
Table 4.3 Hyperfine values for $\beta-^1H$ and ^{19}F of $F_2Y\bullet$ at different positions on pathway	177
Table 5.1 Specific activities of $E_{350}X-\beta_2$	197
Table 5.2 K_d values for $E_{350}X-\beta_2/\alpha_2$	208
Table 5.3 Percentage of $N\bullet$ generated in the reaction of $E_{350}X-\beta_2/\alpha_2/N_3UDP/TTP$	211
Table 5.4 Specific activity of $E_{350}Q/Y_{356}(3,5)F_2Y-\beta_2$	213
Table 5.5 Specific activity of $E_{350}Q/Y_{356}(3,5)F_2Y-\beta_2$ with $Y_{731}(3,5)F_2Y-\alpha_2$	216
Table 6.1 Quantitation of $\alpha_2:\beta_2$ ratio in the pull-down assays	243

LIST OF SCHEMES

Scheme 2.1 Three-helix bundle scaffold	97
Scheme 3.1 Reaction catalyzed by RNR	125
Scheme 3.2 Cytosine release from the native substrate CDP in the presence of oxidized $\alpha 2$	140
Scheme 3.3 Kinetic model for wt RNR in the absence and presence of a reducing system	146
Scheme 3.4 Kinetic model for Y ₁₂₂ (2,3,5)F ₃ Y- $\beta 2$ in the absence and presence of a reducing system	146
Scheme 4.1 Proposed models for the fate of the Y ₃₅₆ proton	169

ABBREVIATIONS

$\alpha 2$	Class I RNR large subunit
Amp	Ampicillin
ATP	Adenosine 5'-triphosphate
$\beta 2$	Class I RNR small subunit
C•	Cysteine (thiyl) radical
CD	Circular dichroism
CDP	Cytidine 5'-diphosphate
Cm	Chloramphenicol
CV	Cyclic voltammetry
dATP	Deoxyadenosine 5'-triphosphate
dC	Deoxycytidine
dCDP	Deoxycytidine 5'-diphosphate
DOPA	3,4-Dihydroxyphenylalanine
DPV	Differential pulse voltammetry
DTT	Dithiothreitol
E	Effector
EDTA	Ethylenediaminetetraacetic acid
EM	Electron microscopy
ENDOR	Electron-nuclear double resonance
EPR	Electron paramagnetic resonance
ET	Electron transfer
F _n Y	Fluorotyrosines (n = 2, 3 or 4)
F _n Y•	Fluorotyrosyl radical
G•	Glycyl radical
GMML	Glycerol minimal medium with leucine
HEPES	4-(2-hydroxyethyl)-1-piperazineethanesulfonic acid
HU	Hydroxyurea
IPTG	Isopropyl-1-thio- β -galactopyranoside
Kan	Kanamycin
MBI	Mechanism-based inhibitor
met	Y•-reduced, diferric form of NrdB

MV	Methyl viologen
N•	Nitrogen-based radical that is generated upon incubation of $\alpha 2$, $\beta 2$, N ₃ NDP and E
NADPH	β -nicotinamide adenine dinucleotide phosphate, reduced form
N ₃ CDP	2'-azido-2'-deoxycytidine 5'-diphosphate
NH ₂ Y	3-Aminotyrosine
NH ₂ Y•	3-Aminotyrosyl radical
Ni-NTA	Nickel nitriloacetic acid
NO ₂ Y	3-Nitrotyrosine
NO ₂ Y•	3-Nitrotyrosyl radical
N ₃ UDP	2'-azido-2'-deoxyuridine 5'-diphosphate
PCET	Proton-coupled electron transfer
PELDOR	Pulsed electron-electron double resonance
PT	Proton transfer
RCQ	Rapid chemical-quench
RFQ	Rapid freeze-quench
RNR	Ribonucleotide reductase
RT	Radical transport
S	Substrate
SF	Stopped-flow
SWV	Square wave voltammetry
TR	Thioredoxin
Tris	Tris(hydroxymethyl)-aminoethane
TRR	Thioredoxin reductase
W•	Tryptophan radical
wt	Wild-type
Y•	Tyrosyl radical
UAA	Unnatural amino acid

Chapter 1

Introduction to the *E. coli* class Ia ribonucleotide reductase

1.1 GENERAL INTRODUCTION TO RIBONUCLEOTIDE REDUCTASE

1.1.1 Reaction catalyzed by RNR. Ribonucleotide reductase (RNR) catalyzes the formation of all four deoxynucleotides (dNDP or dNTP, N = A, U, C, G) from their corresponding ribonucleotides (NDP or NTP, Figure 1.1).^{1,2} RNR represents the only known source for the *de novo* biosynthesis of dNTPs and controls both the absolute amounts and the relative ratios of the dNTPs within the cell. Due to its central role in contributing to the fidelity of DNA replication, RNR is under strict allosteric regulation that in part ensures production of balanced dNTP pools.³ All RNRs share a structurally homologous active site for nucleotide reduction in a large subunit (α) wherein a transiently generated thiyl radical (C^\bullet) is directly responsible for initiating complex radical chemistry that produces the 2'-deoxynucleotides.^{4,5,6} The reaction requires reducing equivalents that are provided by oxidation of a pair of cysteines in the active site of α in almost all RNRs (Figure 1.1).⁷⁻¹⁰

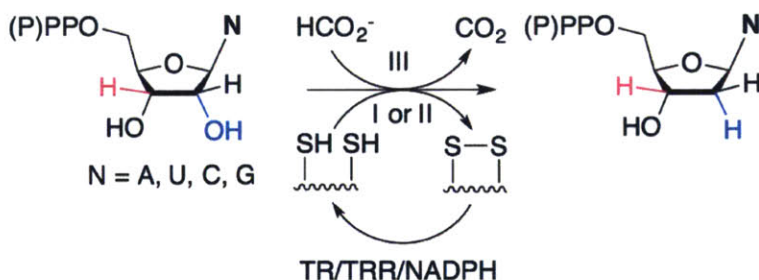


Figure 1.1 Reaction catalyzed by RNR. In all RNRs, the reaction is initiated by abstraction of the 3' H-atom by a transient C^\bullet . The reducing equivalents for the reaction are provided by a pair of cysteines in the active of the enzyme in class I, II and some class III RNRs.^{9,10} The class III RNRs can also use formate as a reductant.^{11,12}

1.1.2 The different classes of RNR. Whereas the mechanism of nucleotide reduction is conservedⁱ in all RNRs, the mechanism by which C^\bullet is formed in α is not. RNRs are subdivided into three classes (I, II and III, Figure 1.2) based on the metallocofactor used for C^\bullet generation.¹³

ⁱ An exception is the class III RNR that uses formate as a reductant.

The class I RNRs are found only in aerobic organisms and utilize dimetallocofactors located on a second subunit (β , NrdB or NrdF) to generate $C\bullet$.¹⁴ The class II RNRs are found in aerobic and anaerobic bacteria and archaea. This class utilizes adenosylcobalamin as a cofactor; the Co–C bond is homolytically cleaved to generate $5'$ -dA \bullet , which is directly responsible for oxidation of the active site C in the α subunit (NrdJ).⁶ The class III RNRs are found in obligate and facultative anaerobic bacteria and archaea and use a glycy radical ($G\bullet$) in α (NrdD) to reversibly oxidize the active site C. Generation of $G\bullet$ requires an activating enzyme (NrdG) that employs a reduced $[4Fe4S]^{1+}$ cluster and S-adenosylmethionine (SAM). Until recently, all characterized class III RNRs were shown to utilize formate as a reductant for nucleotide chemistry.¹¹ Through isolation of class III enzymes from different organisms (*Neisseria bacilliformis*, *Thermotoga maritima* and *Methanosarcina Barkeri*), our lab has further divided this class into three subgroups based on the nature of the reductant; NrdD1 couples nucleotide reduction to oxidation of formate,¹² NrdD2 uses the reducing equivalents provided by the thioredoxin (TR), thioredoxin reductase (TRR) and NADPH system,⁹ and NrdD3 utilizes a reducing system composed of a ferredoxin disulfide reductase and a thioredoxin-like protein (NrdH).¹⁰

The class I RNRs are further subdivided on the basis of the dimetallocofactor used to generate $C\bullet$. The most well studied class Ia RNRs, which are the focus of this thesis, use a stable diferric-tyrosyl radical ($Y\bullet$) in the β subunit to reversibly oxidize the C in α . This metallocofactor can be self-assembled *in vitro* by the addition of Fe^{2+} and O_2 to the apo protein.¹⁵ The class Ib RNRs use a flavoprotein NrdI to generate the active dimanganese(III)- $Y\bullet$ cofactor in NrdF, which can subsequently oxidize the C in α . In the case of the *Bacillus subtilis* NrdF, NrdI reacts with O_2 to produce $O_2^{\bullet-}$ that channels to Mn_2^{II} -NrdF to initiate cofactor assembly.¹⁶ McClarty and coworkers identified the class Ic RNR, which is unique in that $Y\bullet$ is replaced with a non redox active

phenylalanine (F).¹⁷ Bollinger and coworkers have recently proposed that the class Ic enzymes use a Mn^{IV}/Fe^{III} cofactor to oxidize the active site C.¹⁸ Until recently, all characterized class I RNRs fell into the three categories described above (Ia, Ib or Ic). However, recent bioinformatics analysis performed in our lab (Yifeng Wei) suggested the presence of a putative class Id RNR in the genome of certain flavobacteria, proteobacteria and halophilic archaea. This class of RNR maintains a Y in the cluster site; however, preliminary studies suggest that the class Id RNR does not use a Y• but a dimetallocofactor as the oxidant (Bollinger, Krebs and Boal labs).

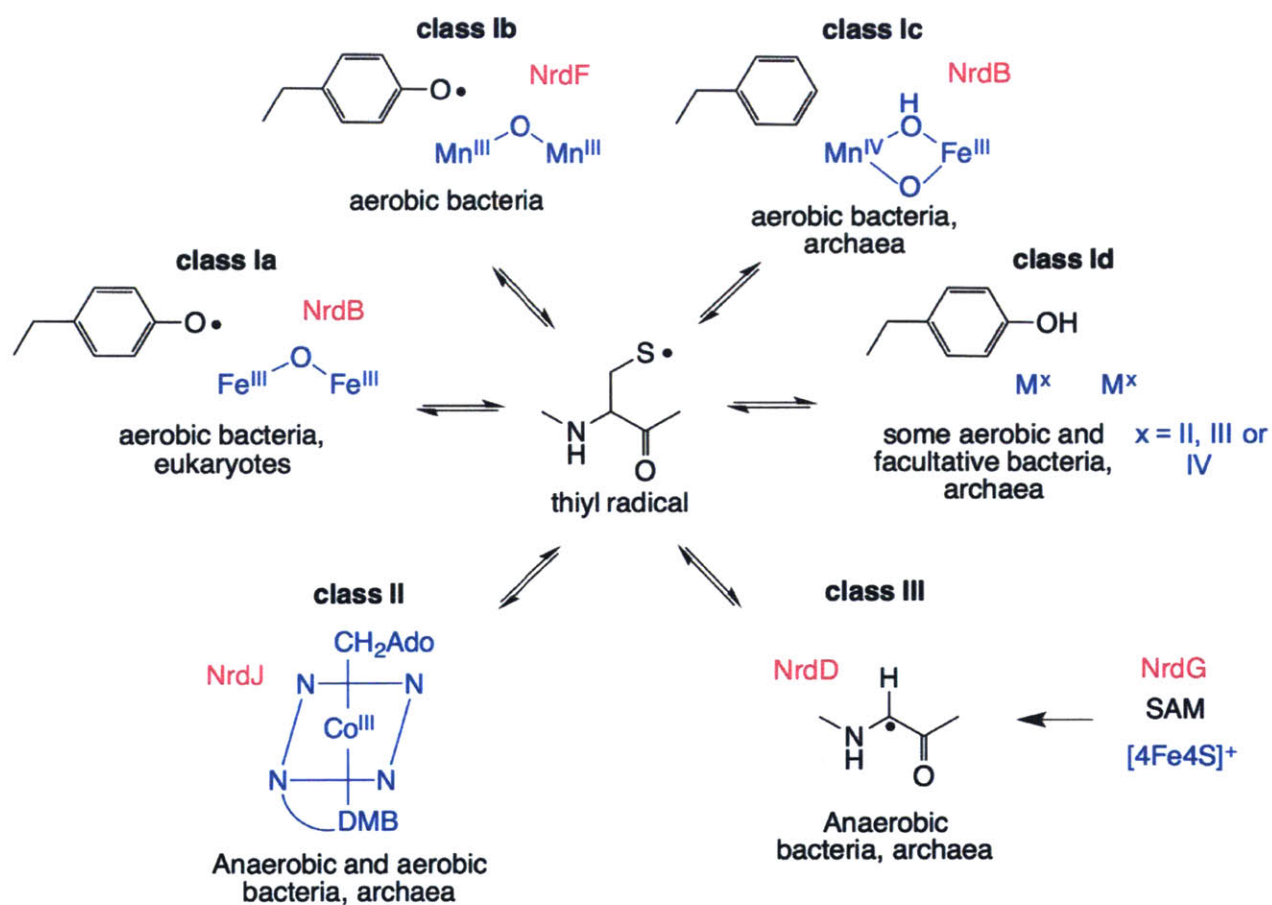


Figure 1.2 The different classes of RNR based on the metallocofactor used to generate C•.

1.1.3 Mechanism of nucleotide reduction. Despite the different mechanisms by which C• is generated in the active site of α , all RNRs catalyze nucleotide reduction by a similar mechanism with the formate-dependent class III RNR as the sole exception.¹² The nucleotide reduction

mechanism is shown in Figure 1.3 (top panel) and was assembled from extensive studies performed with isotopically labeled substrates (S),¹⁹ S analogs that acted as mechanism-based inhibitors (MBIs),²⁰⁻²² and mutant $\alpha 2s$ ^{7,23-26} where conserved active site residues were replaced with other canonical amino acids (Figure 1.3, bottom panel). The catalytic cycle is first outlined below, followed by the results from the MBI and mutant $\alpha 2$ studies.

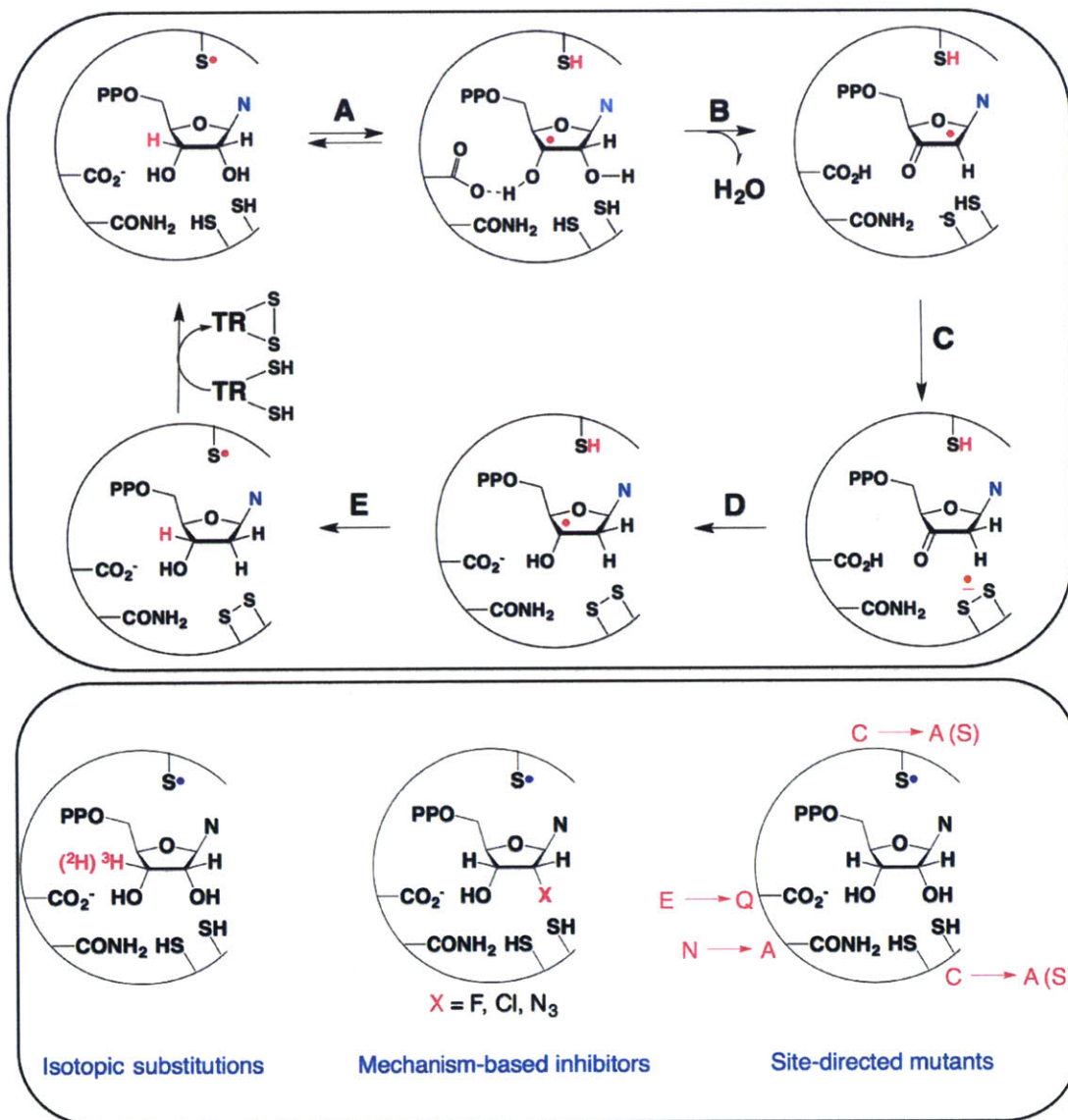


Figure 1.3 The top panel shows the proposed mechanism of nucleotide reduction in the active site of $\alpha 2$. Some of the probes that were utilized to construct this model are shown in the bottom panel.

Once generated, the active site C• (C₄₃₉ in *Escherichia coli* class Ia) initiates nucleotide reduction by abstraction of the 3' H-atom from the nucleotide (Figure 1.3, step **A**). This step is followed by rapid irreversible loss of water from the 2' position facilitated by C₂₂₅ on the bottom face of the sugar (step **B**). Steps **A** and **B** are also assisted by deprotonation of the 3'-OH by E₄₄₁. The resulting ketonucleotide-based radical is reduced by the two bottom face cysteines (C₂₂₅ and C₄₆₂) producing keto-deoxynucleotide and the disulfide radical anion (step **C**) between these cysteines. Proton-coupled electron transfer (PCET) results in formation of the product-based radical and a disulfide between C₂₂₅ and C₄₆₂ (step **D**). In the final step, the H-atom that was initially abstracted by C₄₃₉• is returned back to the 3' position in the product (step **E**). Subsequent turnover is only possible upon re-reduction of the active site disulfide, and in the case of the *E. coli* class Ia RNR, the TR/TRR/NADPH system is utilized *in vitro*.

The mechanistic model shown in Figure 1.3 was constructed from extensive studies performed with isotopically labeled S,¹⁹ MBIs²⁰⁻²² and site-directed mutants of α S.^{7,23-26} Experiments with [²H]- and [³H]-NDP provided the first evidence for cleavage of the 3' C-H bond (step **A**) and for return of the abstracted H atom back to the 3' position (step **E**). Incubation of RNR with MBIs such as FNDP, CINDP or N₃NDP (S analogs with F, Cl or N₃ at the 2' position) provides support for steps **A-C** in the nucleotide reduction mechanism. In all three cases, chemistry is initiated by abstraction of the 3' H-atom (Figure 1.3, step **A**); subsequently, the reaction partitions between turnover and inactivation. During inactivation, rapid loss of F⁻, Cl⁻ or N₂ is followed by reduction of the ketonucleotide-based radical by the top face cysteine (C₄₃₉). This reduction produces 3'-keto-deoxynucleotide which subsequently dissociates from the active site and decomposes to release the base, PP_i and 2-methylene-3(2H)-furanone. Evidence for steps **A-C** have also been provided by site-directed mutagenesis of the residues in the active site of α 2.

Mutation of C₄₃₉ to A abolishes catalytic activity,^{27,28} whereas mutation of either of the bottom face cysteines^{7,23} results in destruction of S, similar to that observed with the MBIs.

A key piece of the mechanistic puzzle was provided when the conserved glutamate in the active site of $\alpha 2$ (E₄₄₁) was mutated to Q.^{24,25} These studies presented the first evidence for formation of a disulfide radical anion during turnover, which accumulates due to removal of the essential proton for the proton-coupled electron transfer (PCET) step that generates the product-based radical (step **D**). Removal of E₄₄₁ also affects steps **A** and **B** (Figure 1.3) and thus, disulfide radical anion formation in E₄₄₁Q- $\alpha 2$ is slower ($\sim 0.8 \text{ s}^{-1}$) than steady-state turnover of the wt enzyme ($2\text{--}10 \text{ s}^{-1}$).^{25,29} This disulfide radical anion intermediate observed in E₄₄₁Q- $\alpha 2$ is not kinetically or chemically competent for deoxynucleotide formation. More recently, evidence for a chemically competent thiosulfuranyl radical was obtained in the *E. coli* class III RNR that utilizes formate as a reductant.¹² In the case of this enzyme (NrdD1), one of the bottom face cysteines (C₄₆₂) is replaced with a methionine. Wei et al have demonstrated that the reaction of NrdD1, CTP (S) and ATP (allosteric effector, E) in the absence of formate leads to the disappearance of G• concomitant with formation of a thiosulfuranyl radical (a thiyl radical stabilized by interaction with the methionine).¹² Subsequent addition of formate to the reaction leads to disappearance of the thiosulfuranyl radical and regeneration of G•. These studies on NrdD1 lend further support for the involvement of a disulfide radical anion in the class I, II and other class III RNRs (NrdD2, NrdD3).

1.2 INTRODUCTION TO THE CLASS IA RNR

1.2.1 Structure of the class Ia RNR. The class Ia is RNR from *E. coli* is composed of two homodimeric subunits, α_2 and β_2 . The active complex is proposed to be of the form $\alpha_2\beta_2$,³⁰ which can convert into an inactive $\alpha_4\beta_4$ complex in the presence of the negative allosteric effector dATP (Figure 1.4A).³¹ The α_2 subunit (172 kDa, 761 residues per monomer) contains the catalytic site where the four nucleotides (CDP, ADP, GDP, UDP) are reduced and two additional nucleotide binding sites: the specificity site (at the dimer interface) and the activity site (located at the N-terminus of α). Binding of ATP or dATP at the activity site controls the overall rate of nucleotide reduction.³²⁻³⁵ Saturation of this site with ATP stimulates activity by allowing formation of the active $\alpha_2\beta_2$ complex, while dATP binding to this site inhibits deoxynucleotide production via formation of the inactive $\alpha_4\beta_4$ species (Figure 1.4A).

Binding of allosteric effectors (ATP, dGTP, TTP, dATP) at the specificity site dictates which of the four nucleotides is reduced in the active site of α_2 (Figure 1.4B). Recent crystallographic studies performed by the Drennan lab provided the first insight into the molecular basis for allosteric specificity regulation in the *E. coli* class Ia RNR.³⁶ In these studies, a crystal form of the inactive $\alpha_4\beta_4$ was utilized to obtain the structures of all four S and specificity E pairs (CDP/dATP, UDP/dATP, ADP/dGTP and GDP/TTP) bound to α_2 . These studies demonstrate that loops 1 (residues 259–278) and 2 (residues 292–301) in α (Figure 1.4B, red) are directly responsible for reading the identity of the specificity E and communicating this information to the catalytic site. Within loop 2, R₂₉₈ and Q₂₉₄ were found to be the key residues that provide S specificity; mutation of these residues to A diminish nucleotide reduction activity.³⁶ These conformational changes that occur in α_2 upon S/E binding are key in controlling the long-range oxidation process during turnover and are further outlined in subsequent sections.

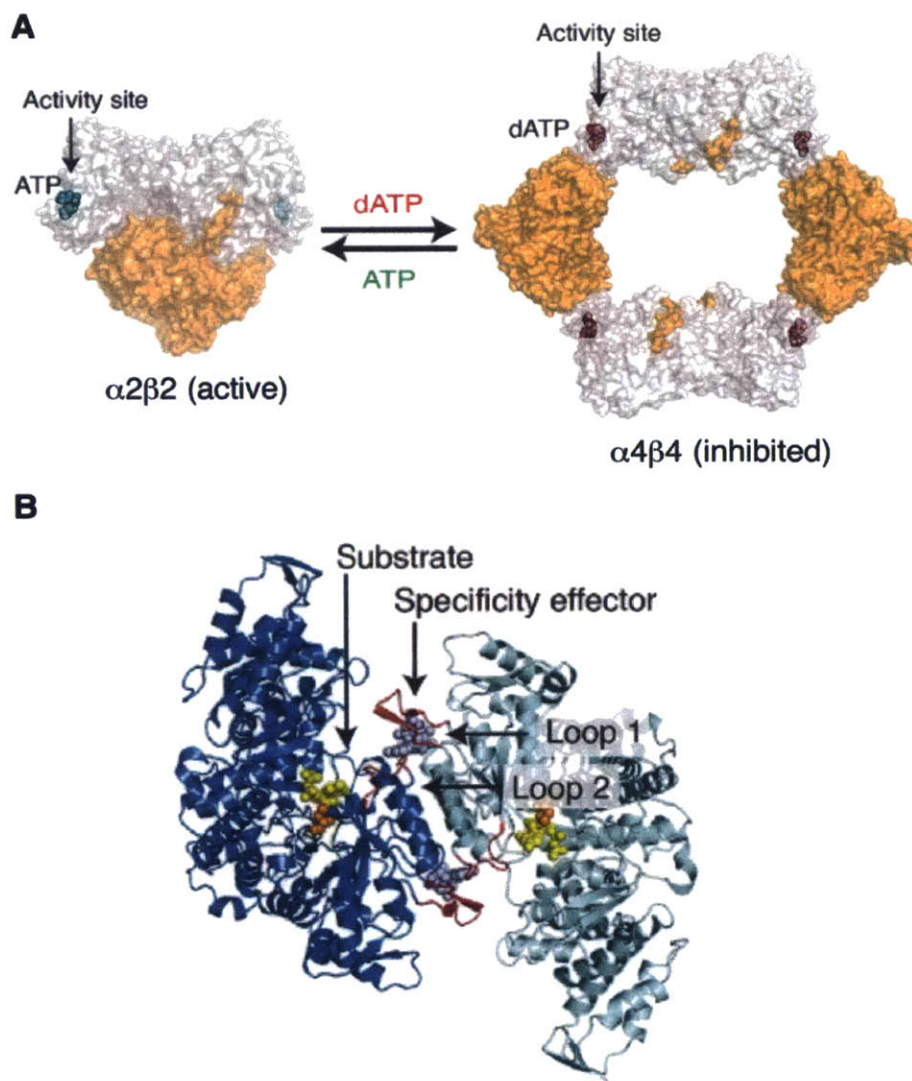


Figure 1.4 A. Structural interconversion between the active $\alpha 2\beta 2$ and inhibited $\alpha 4\beta 4$ states of the *E. coli* class Ia RNR. The $\alpha 2\beta 2$ model was generated from small angle X-ray scattering data³¹ to fit the individual crystal structures of $\alpha 2$ (PDB ID: 3R1R)³⁷ and $\beta 2$ (PDB ID: 1RIB)³⁸ together. $\alpha 2$ and $\beta 2$ are shown in gray and orange surface representations. B. Structure of $\alpha 2$ at a 90° angle from the representation shown in A. Each monomer is shown in blue and cyan, respectively. The yellow and purple spheres represent S (NDP) and E (dNTP). The catalytically essential C₄₃₉ is shown in orange spheres. Loops 1 and 2 (red) are responsible for substrate specificity. Figure reproduced from Ref. 36.

The small subunit of the *E. coli* class Ia RNR ($\beta 2$) is an obligate dimer (87 kDa, 375 residues per monomer) and contains the diferric-Y• (Y₁₂₂•) cofactor responsible for oxidizing C₄₃₉ in the active site of $\alpha 2$. This cofactor has two unique spectroscopic features that can be used to

monitor reactions: UV-vis spectroscopy shows a sharp feature (410 nm) and a shoulder (390 nm) that are associated with $Y\cdot$, and a characteristic doublet $Y\cdot$ spectrum associated with one of Y_{122} 's β -methylene protons and its 3,5 aromatic protons is observed by EPR spectroscopy (Figure 1.5). As-isolated β_2 typically contains $3.5 Fe^{3+}/\beta_2$ and $1.2 Y\cdot/\beta_2$. The distribution of $Y\cdot$ within β_2 has been a major focus of research in our lab. In this Chapter, we present several lines of evidence that suggest that the active form of β_2 contains a $Y\cdot$ in each monomer.³⁹⁻⁴¹ Further evidence for this “two or none” radical distribution model is also presented in Chapter 3.

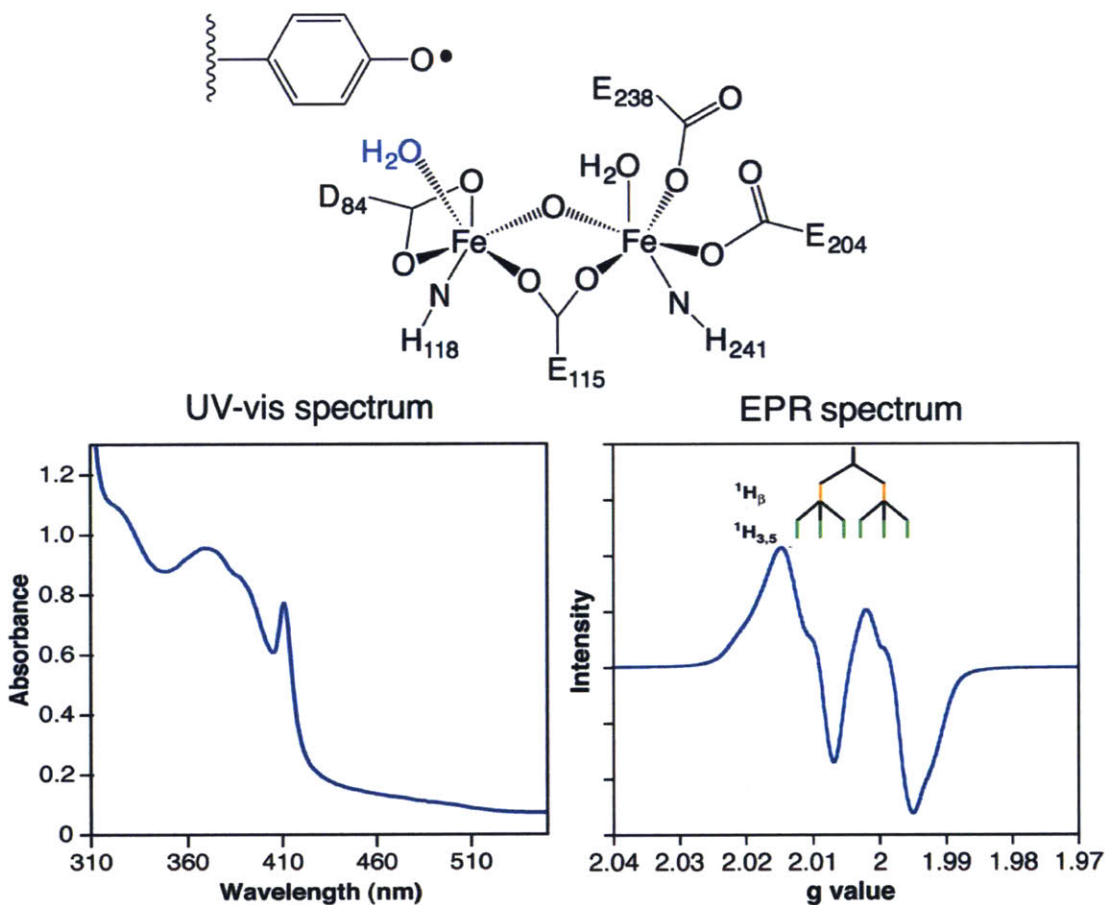


Figure 1.5 Methods to characterize the diferric- $Y\cdot$ cofactor in β_2 . The left panel shows a UV-vis spectrum of as-isolated β_2 . The features of the diferric cluster are observed at 325 nm and 365 nm respectively. The sharp peak at 410 nm represents $Y\cdot$. The right panel shows the doublet EPR spectrum that is characteristic of $Y\cdot$ in β_2 .

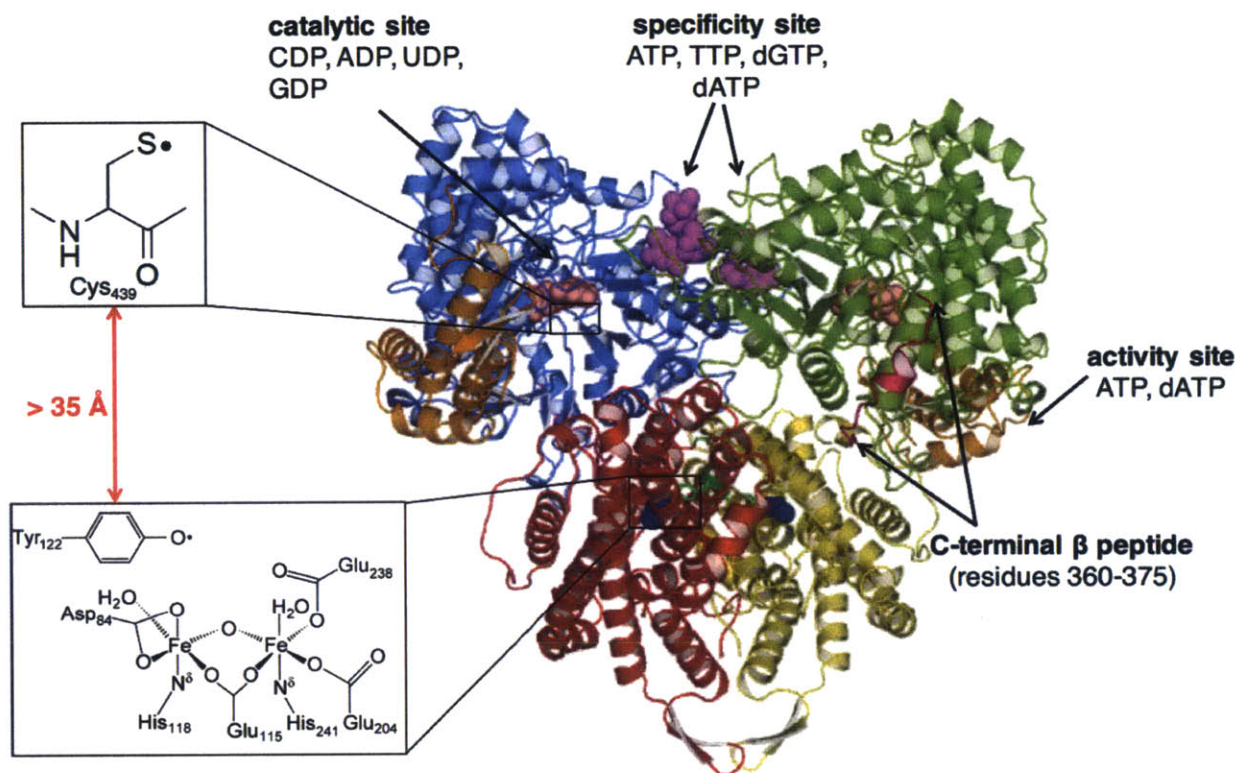


Figure 1.6 Uhlén and Eklund's docking model for the *E. coli* active $\alpha 2\beta 2$ complex. The monomers of $\alpha 2$ (PDB ID: 4R1R) and $\beta 2$ (PDB ID: 1RIB) are shown in blue and green, and red and yellow respectively. $\alpha 2$ was crystallized in the presence of GDP (salmon), TTP (purple) and a peptide corresponding to residues 360–375 of $\beta 2$ (pink). The ATP cone domain within which the activity site is located is shown in orange.

The *E. coli* class Ia RNR was originally proposed by Thelander to function as an $\alpha 2\beta 2$ complex,³⁰ although a crystal structure of the active complex has remained elusive primarily due to the weak affinity between the two subunits (K_d of 0.2 μM).⁴² The individual subunits of the *E. coli* class Ia RNR ($\alpha 2$ and $\beta 2$) have been well characterized by X-ray crystallography. The C-terminal tails of both subunits are structurally disordered. In the case of $\alpha 2$ (Figure 1.6, purple and green), residues 738–761 cannot be observed; this region houses the cysteine pair that is responsible for re-reduction of the active site disulfide after each turnover.²⁹ In the case of $\beta 2$ (Figure 1.6, red and yellow), residues 340–375 cannot be observed in most crystal structures reported to date. Work by Climent *et al.* has established that the primary mode of interaction

between $\alpha 2$ and $\beta 2$ is via the C-terminal tail of $\beta 2$ (residues 360–375).⁴² The authors demonstrate that synthetic peptides corresponding to different portions of the C-terminal tail of $\beta 2$ inhibit $\alpha 2\beta 2$ interaction (K_d of $\sim 18 \mu\text{M}$). Uhlin and Eklund co-crystallized $\alpha 2$ with this peptide (residues 355–375), providing molecular details about the interaction of $\alpha 2$ with residues 360–375 of $\beta 2$ (pink, Figure 1.6).⁴³ Based on the shape complementarity of $\alpha 2$ and $\beta 2$, Uhlin and Eklund created a docking model for the active complex from the individual crystal structures of $\beta 2$ and $\alpha 2$ (Figure 1.6).^{43,44} One of the most unexpected implications of this model is that the distance between Y_{122}^\bullet in $\beta 2$ and C_{439} in $\alpha 2$ is $\sim 35 \text{ \AA}$. As summarized below, extensive studies performed in collaboration with the Bennati^{39,45,46} and Drennan^{31,47} labs show that this prediction made by the docking model is an accurate representation of the distance in the active complex.

In the case of the *E. coli* class Ia RNR, active $\beta 2$ is proposed to contain a Y^\bullet in each monomer (section 1.2.6 and Chapter 3). Additionally, only one of the two Y^\bullet s is proposed to be active at a time, a phenomenon termed half-sites reactivity. As outlined in subsequent sections, the class Ia RNR uses several transient Y^\bullet intermediates during catalysis and several lines of evidence support that trapping one of these intermediates in one α/β pair (due to half-sites reactivity) increases subunit affinity (Ref. 47 and Chapter 6) and generates a stable complex. We have collaborated with the Drennan lab to perform small-angle X-ray scattering (SAXS) and electron microscopy (EM) studies on this stable complex.⁴⁷ These experiments show a compact $\alpha 2\beta 2$ complex that is similar to the docking model. The Bennati lab has also utilized pulsed electron-electron double resonance (PELDOR) spectroscopy, a technique that can measure distances (20–80 \AA) between two weakly coupled unpaired spins, to measure the distances between Y^\bullet intermediates in one α/β pair and the unreacted Y^\bullet in the second α/β pair in the stable

complex.^{39,45,46,48} These distances closely match those predicted by the docking model and support formation of an active $\alpha 2\beta 2$ complex.

1.2.2 Radical transport pathway for oxidation of C₄₃₉ by Y₁₂₂[•]. The docking model has been substantiated by a variety of biochemical and biophysical studies performed by our lab, in collaboration with the Drennan and Bennati labs. The long distance of 35 Å between Y₁₂₂[•] in β and C₄₃₉ in α requires the presence of intermediates to account for the turnover number of the *E. coli* class Ia RNR (2–10 s⁻¹).²⁹ Direct tunneling of the electron over 35 Å is predicted to occur at 10⁻⁴–10⁻⁹ s⁻¹;⁴⁹ thus, this model is not consistent with the observed turnover of the enzyme. This calculation combined with the shape complementarity between $\alpha 2$ and $\beta 2$ led Uhlin and Eklund to propose that aromatic amino acid radical intermediates (Y[•]s and W[•]s) must be involved during radical transport (RT).⁴³ A closer examination of the docking model and the amino acid sequences of the different class I RNRs showed the presence of four absolutely conserved amino acid residues (Figure 1.7, W₄₈ and Y₃₅₆ in $\beta 2$, and Y₇₃₁ and Y₇₃₀ in $\alpha 2$) located between Y₁₂₂[•] and C₄₃₉, which were proposed to participate in RT. Of these residues, Y₃₅₆ is located in the flexible region of $\beta 2$ (residues 340–360, dotted line in Figure 1.7) for which no structural information is available. This residue is a key player in mediating RT between $\beta 2$ and $\alpha 2$ and is an active focus of the research presented in Chapters 3 and 4. Site-directed mutagenesis of any of the proposed pathway residues greatly diminishesⁱⁱ nucleotide reduction activity.⁵⁰⁻⁵²

ⁱⁱ Site-directed mutagenesis of any essential residue in the *E. coli* class Ia RNR does not abolish activity. Low levels of activity (0.1–3%) are detected in these assays, which is ascribed to the small amounts of contaminating endogenous RNR that co-purifies with all mutants of this enzyme.²⁷

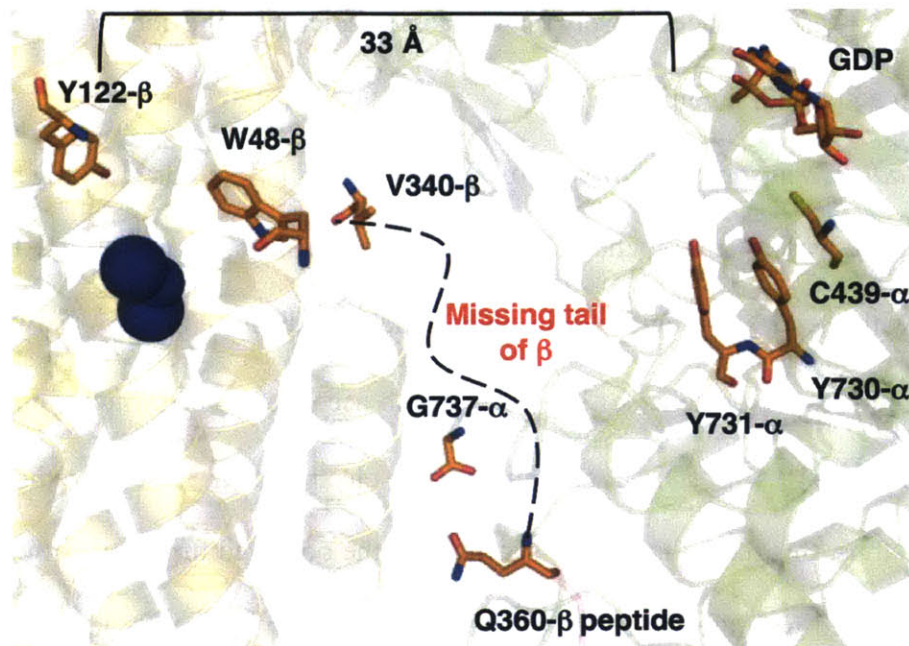


Figure 1.7 Proposed residues on the RT pathway. A rotated view of one α/β pair of the docking model (Figure 1.6). The α and β monomers are shown in green and yellow respectively. The μ -oxo diferric cluster is represented by the blue spheres. The proposed pathway residues are Y₁₂₂, W₄₈ and Y₃₅₆ (not shown) in β and Y₇₃₁, Y₇₃₀ and C₄₃₉ in α . V₃₄₀ is the last residue that is observed in the crystal structure of β (PDB ID: 1RIB). Q₃₆₀ of β is observed in the synthetic peptide that was co-crystallized with α 2. The last residue of α that is observed in the crystal structure (PDB ID: 4R1R) is G₇₃₇. From the docking model, a distance of 33 Å was measured between the phenolic oxygens of Y₁₂₂ and Y₇₃₁.

1.2.3 Mechanistic considerations for long-range RT. The RT pathway in the class I RNR is proposed to consist of three Ys (Y₃₅₆, Y₇₃₁ and Y₇₃₀) and a W (W₄₈). Oxidation of a Y at physiological pH requires the concerted movement of a proton and an electron⁵³ and thus, this pathway is proposed to be composed of several proton-coupled electron transfer (PCET) steps (Figure 1.8).⁴⁹ There are three main considerations for each of these PCET steps, which are critical in ensuring that RT occurs in a kinetically competent manner to support turnover of the enzyme (2–10 s⁻¹).²⁹ The first two factors are the pK_a and the reduction potential of each residue that is proposed to participate in this reaction; these two properties directly govern proton transfer (PT) and electron transfer (ET) kinetics, respectively. The protein environment can significantly perturb

both of these properties and it is essential that we define these perturbations within the context of the RNR protein environment. Our efforts to understand the pK_a and the reduction potential of each pathway residue are presented subsequently.

The third mechanistic consideration for RT is the distance over which PCET occurs. The distance between the donor (D) and acceptor (A) not only controls k_{ET} but also dictates the mechanism of PCET. The electron, as a lighter particle, can tunnel over large distances (10–15 Å) at very fast rates (10^8 s^{-1}), whereas the proton, as a heavier particle, is fundamentally limited to shorter distances ($\leq 1 \text{ Å}$).⁵³ When D and A are within H-bonding distance of each other, the proton and electron can move along the same path, a phenomenon termed collinear PCET. When the distances between D and A are longer, ET and PT must occur orthogonal to each other.

We have previously proposed that orthogonal PCET is functional within the $\beta 2$ subunit. In the first step of RT, ET from W_{48} to Y_{122}^\bullet is proposed to occur concomitant with PT from a water molecule on the diferric cluster (Fe1-H₂O) to Y_{122}^\bullet to generate the Y_{122} phenol (Figure 1.8).⁵⁴ D_{237} in $\beta 2$ is proposed to simultaneously deprotonate W_{48} to generate W_{48}^\bullet . Subsequently, ET from Y_{356} to W_{48}^\bullet occurs concomitant with PT from D_{237} to W_{48}^\bullet . Mutation of E_{350} , a conserved residue on the C-terminal tail of $\beta 2$ (Figure 1.8), greatly reduced nucleotide reduction activity leading to the proposal that this residue functions as the proton acceptor during oxidation of Y_{356} . In Chapters 4 and 5 of this thesis, we present extensive studies that address the mechanism of PCET through Y_{356} . These studies suggest that water clusters and not E_{350} , may play a role during oxidation of Y_{356} . Finally, the mechanism of PCET across the interface remains elusive. No amino acid residue that can function as a proton acceptor for Y_{731} is apparent in the immediate vicinity of this pathway residue. It has been proposed that either Y_{356} , or another residue within $\beta 2$ could function as the proton acceptor for Y_{731} .

The shorter distances observed between Y₇₃₁, Y₇₃₀ and C₄₃₉ in the crystal structure of $\alpha 2$ led to the proposal that collinear PCET occurs within this subunit (Figure 1.8). In subsequent sections, we provide evidence to support this model at physiological pH. However, RNR appears capable of switching from collinear to orthogonal PCET within the $\alpha 2$ subunit at high pH, suggesting the potential amphoteric role of water molecules during RT in this subunit. The crystal structure of $\alpha 2$ (PDB ID: 4R1R) that was used to construct the docking model demonstrates an unusual stacked conformation of Y₇₃₁ and Y₇₃₀ (Figure 1.7). In collaboration with the Nocera^{55,56} and Bennati^{57,58} labs, we have shown that this stacking is critical to maintaining the H-bonding network within $\alpha 2$ and can alter the reduction potentials of the two pathway Ys. However, Y₇₃₁ appears quite flexible; a flipped out conformation of Y₇₃₁ towards the subunit interface has been observed in some mutant *E. coli* class Ia RNRs either crystallographically⁵⁹ or using different EPR methods.^{48,58} This flipping motion would affect the distances between Y₃₅₆, Y₇₃₁ and Y₇₃₀ and consequentially, PCET kinetics. It is currently unknown if this structural rearrangement of Y₇₃₁ occurs during catalysis.

Since the initial proposal for long-range RT, we have successfully obtained evidence for radical intermediates at position Y₃₅₆, Y₇₃₁ and Y₇₃₀ (Section 1.3). However, we have not yet succeeded in establishing the role of W₄₈ in this process. This residue forms a H-bonding network with its putative proton acceptor D₂₃₇ and the Fe1 ligand H₁₁₈, which is remarkably similar to a H-bonding network found in cytochrome c peroxidase (CCP) from yeast.^{44,60} The cognate W residue in CCP is oxidized to a W⁺ during the reaction of CCP with peroxide,⁶¹ leading to the proposal that W₄₈ could be involved in RT. However, several lines of evidence support that W₄₈ may not participate in RT (Appendix 4). Similarly, it has been recently suggested that W₅₁, the W₄₈ equivalent in class Ic RNR, does not participate in RT in this class of RNR.⁶² Removal of W₄₈

from the RT pathway raises substantial issues regarding the distance over which the oxidant must traverse. A major unresolved question in the *E. coli* class Ia RNR is the location of Y₃₅₆ relative to Y₁₂₂ and Y₇₃₁ (Figures 1.7 and 1.8).

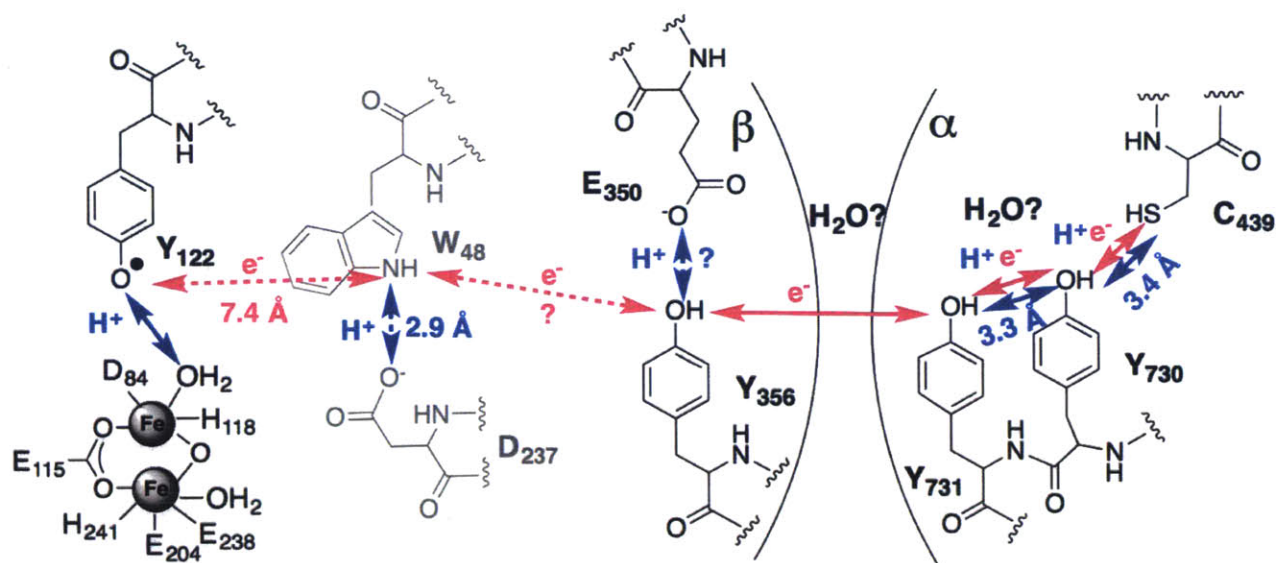


Figure 1.8 Proposed PCET model for RT in the *E. coli* class Ia RNR. The directions in which the electron and protons move are represented by the pink and blue arrows, respectively. Y₃₅₆ and its putative proton acceptor E₃₅₀ are located on the flexible C-terminal tail of β 2 (residues 340–375). W₄₈ and its proton acceptor D₂₃₇ are shown in gray as there is currently no evidence for their involvement in RT. The distance between W₄₈ in β 2 and Y₇₃₁ in α 2 is \sim 25 Å. All distances were measured edge-to-edge. The exact role of water at the subunit interface and within the α subunit remain unknown.

1.2.4 Conformationally governed RT in the E. coli class Ia RNR. A main hindrance to investigating the RT pathway in wt RNR is the rate-limiting protein conformational change(s) that occurs upon association of β 2, α 2, S and E.²⁹ The Y• in β 2 has two main spectroscopic features that can be used to monitor the progress of a reaction; the visible spectrum of β 2 shows a sharp feature at 410 nm that represents Y₁₂₂• and the EPR spectrum of Y₁₂₂• shows the characteristic doublet feature of a Y• associated with coupling to one of its β -methylene protons (Figure 1.5). When the reaction of β 2, α 2, CDP and ATP is monitored by stopped flow (SF) UV-vis

spectroscopy, no changes are detected in the concentration of Y_{122}^{\bullet} with time,²⁹ although chemistry requires the disappearance of Y_{122}^{\bullet} concomitant with formation of C_{439}^{\bullet} . This study immediately suggested that Y_{122}^{\bullet} is regenerated after every turnover. Pre-steady state rapid chemical-quench (RCQ) experiments showed that dCDP formation occurs at $2\text{--}10\text{ s}^{-1}$, identical to the steady-state turnover number of the enzyme at low protein concentrationsⁱⁱⁱ.²⁹ These data were interpreted to report on rate-limiting protein conformational changes that occur prior to RT. The kinetic model for wild-type (wt) RNR constructed from these studies is shown in Figure 1.9. The rate constants for several steps in catalysis have been modeled to account for the inability to see Y_{122}^{\bullet} disappear and reappear. Upon association of β_2 , α_2 , CDP and ATP, a rate-limiting protein conformational change (**A**, $2\text{--}10\text{ s}^{-1}$) sets the enzyme in the right orientation for chemistry. Subsequent steps including forward RT (**B**, $>200\text{ s}^{-1}$), nucleotide reduction chemistry (**C**, $>500\text{ s}^{-1}$) and reverse RT (**D**, $>10^3\text{ s}^{-1}$) have been modeled to occur fast, precluding the observation of Y_{122}^{\bullet} disappearance and reappearance. This kinetic model for wt RNR is further discussed in Chapter 3 where we present the first evidence for the disappearance and reappearance of an unnatural fluorotyrosyl radical at position 122.⁶³

ⁱⁱⁱ The protein conformational change(s) prior to RT is rate-limiting during steady-state only at low protein concentrations. Ge *et al.*²⁹ have shown that high protein concentrations can switch the rate-limiting step to re-reduction of α_2 by the TR/TRR/NADPH system.

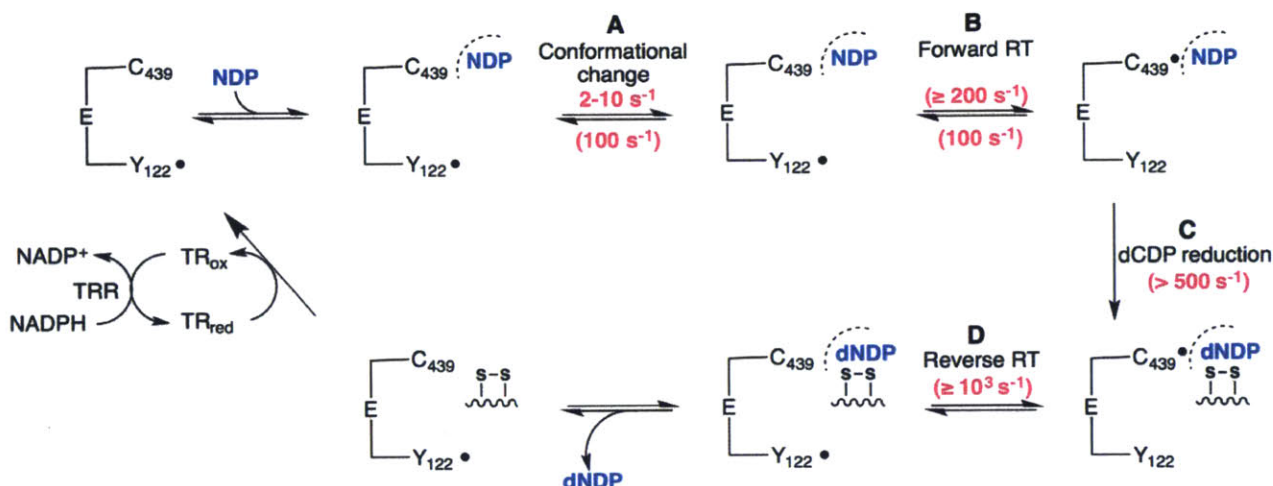


Figure 1.9 Kinetic model for wt RNR. The rate constants within the parentheses have been modeled to account for our inability to monitor Y₁₂₂• disappearance and reappearance during turnover. Model reproduced from Ref. 29.

1.2.5 Strategy to investigate RT and drawbacks. To unravel mechanistic details about the RT pathway, the strategy utilized by the Stubbe lab has been to change the rate-limiting step of the reaction from the conformational change(s) to one of the PCET steps. To do so, we have employed techniques where each of the pathway Ys are site-specifically replaced with unnatural Y analogs that have altered pK_as or reduction potentials relative to Y. The UAAs that were chosen for this purpose are shown in Figure 1.10. These UAAs were selected to function as radical traps (**2** and **3**), PT probes (**1**, **4–7**), pK_a perturbation probes (**8**) and driving force modulators (**4–8**). Each of these functions is expanded upon in subsequent sections.

Our earliest work utilized expressed protein ligation (EPL) to incorporate UAAs in place of Y₃₅₆ in the β₂ subunit (**1**, **2**, **4–8**, Figure 1.10).^{40,64-67} A chemically synthesized peptide corresponding to residues 354–375 of β₂ (native S₃₅₄ was mutated to C) was ligated to recombinantly expressed β₂ (residues 1–353, native V₃₅₃ was mutated to G) to generate the full-length protein containing the UAA of interest. The major drawback of this technology was its limitation to Y₃₅₆ due to the restrictions imposed by the length of the peptide that could be

chemically synthesized at the time.^{40,67} Additionally, EPL required two mutations on the C-terminal tail of $\beta 2$ ($V_{353}G$ and $S_{354}C$) to enable the ligation process.⁶⁴ These requirements introduced two major disadvantages to the EPL technique. First, the $Y_{122}\bullet$ radical content of EPL generated wt- $\beta 2$ decreased substantially compared to recombinantly expressed full-length wt- $\beta 2$ (0.3 $Y\bullet/\beta 2$ versus 1.2 $Y\bullet/\beta 2$). Second, the two mutations required for EPL ($V_{353}G$ and $S_{354}C$) lowered the activity of EPL- $\beta 2$ to 25% that of wt- $\beta 2$ (normalized for radical content).⁶⁷ These mutations that were introduced for EPL change the rate-limiting step during RNR turnover (sections 1.4 and 1.5).

Currently, we utilize the nonsense codon suppression method pioneered by Peter Schultz to incorporate UAAs into RNR.^{68,69} The main advantage of this technology is the ability to incorporate UAAs at any position in the protein. An orthogonal tRNA synthetase is mutated and screened for its ability to selectively charge an orthogonal tRNA with the UAA of interest. The mutated tRNA contains a suppressor anticodon and site-specifically incorporates the UAA in response to the amber stop codon (TAG) placed at the position of interest in the gene. This technique does not require any additional mutations, and allows assembly of higher amounts of the $Y\bullet$ cofactor (0.5–1.2 $Y\bullet/\beta 2$) compared to EPL (0.3 $Y\bullet/\beta 2$). However, this methodology also has certain drawbacks. The use of a stop codon for incorporation of the UAA results in competition between the mutant tRNA and the endogenous release factors. Consequentially, the UAA-containing protein is often contaminated with variable amounts of the truncated material. The ratio of full-length to truncated protein is position dependent and is also affected by the expression conditions. The concentration of UAA in the growth medium, the timing of its addition, and the timing of induction of the synthetase and the gene all affect the full-length to truncated ratio. Therefore, extensive optimization is required for each UAA at each position of interest. In the case

of RNR, it is also challenging to separate the full-length and truncated proteins. Using the nonsense codon suppression method, we have successfully incorporated analogs **3–8** (Figure 1.10) in place of Y₁₂₂ (all except **3**), Y₃₅₆, Y₇₃₁ and Y₇₃₀.⁷⁰⁻⁷³

Of particular importance to our mechanistic studies is an understanding of the perturbations introduced to RNR upon replacement of the native Ys with the UAAs. In this regard, we have determined the p*K*_as and the reduction potentials of all *N*-acetylated tyrosinamide derivatives by differential pulse voltammetry (DPV). One of the key issues with this methodology is that it can only provide solution peak potentials (*E*_p) for the analogs; rapid dimerization of Y• in solution gives rise to irreversible voltammograms. The Pourbaix diagrams obtained from the DPV experiments are shown in Figure 1.11. These studies provided a range for the p*K*_as (vary ~4 pH units from Y) and reduction potentials (-30 mV to +200 mV relative to Y) covered by these analogs.^{64,74} To overcome the issues associated with DPV, we recently initiated a collaboration with Cecilia Tommos at the University of Pennsylvania. The Tommos lab has designed a three alpha helix bundle protein (α_3) into which a single buried redox active amino acid can be introduced.⁷⁵ Square wave voltammetry (SWV) studies on this protein provided the first reversible voltammograms for Y⁷⁶ and W (Tommos unpublished results). In Chapter 2, we describe the successful incorporation of 3,5-F₂Y into α_3 , and similar SWV studies that provide the formal reduction potential of this UAA within a protein environment.⁷⁷ Although the p*K*_as and reduction potentials of Y and its analogs have been measured in solution or in α_3 , the RNR protein environment can significantly perturb these properties. Our attempts to quantitate these perturbations are presented in sections 1.4 and 1.5.

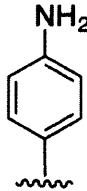
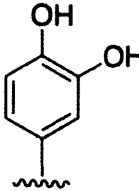
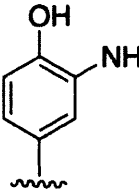
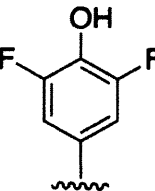
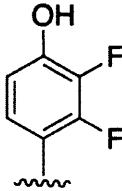
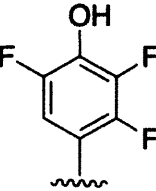
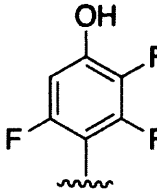
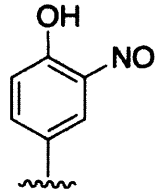
	PheNH₂	DOPA	NH₂Y	3,5-F₂Y
				
	1	2	3	4
pK_a	- ^a	9.7	10	7.2
ΔE(mV)	100	-260	-400 ^b	-30
	2,3-F₂Y	2,3,5-F₃Y	2,3,6-F₃Y	NO₂Y
				
	5	6	7	8
pK_a	7.8	6.4	7	7.1
ΔE(mV)	45	10	100	200

Figure 1.10 UAAs that have been incorporated into *E. coli* class Ia RNR. The ΔE_p values (pH dependent region) were obtained from DPV studies performed on the *N*-acetylated tyrosinamide derivatives. EPL was used to incorporate all analogs except **3** at position 356. Subsequently, all analogs except **1** and **2** were incorporated at positions 356, 731 and 730 using the nonsense codon suppression method. Recently, analogs **4–8** have also been incorporated at position 122 using the nonsense codon suppression method.

^a PheNH₂Y cannot be deprotonated in the biologically relevant pH regime (pK_a of 27).⁷⁸

^b A single DPV study reported a ΔE of ~190 mV between Y and NH₂Y.⁷⁹ However, in collaboration with the Nocera and Tommos labs we have performed DPV and CV studies that suggest that this difference is greater (~400 mV).

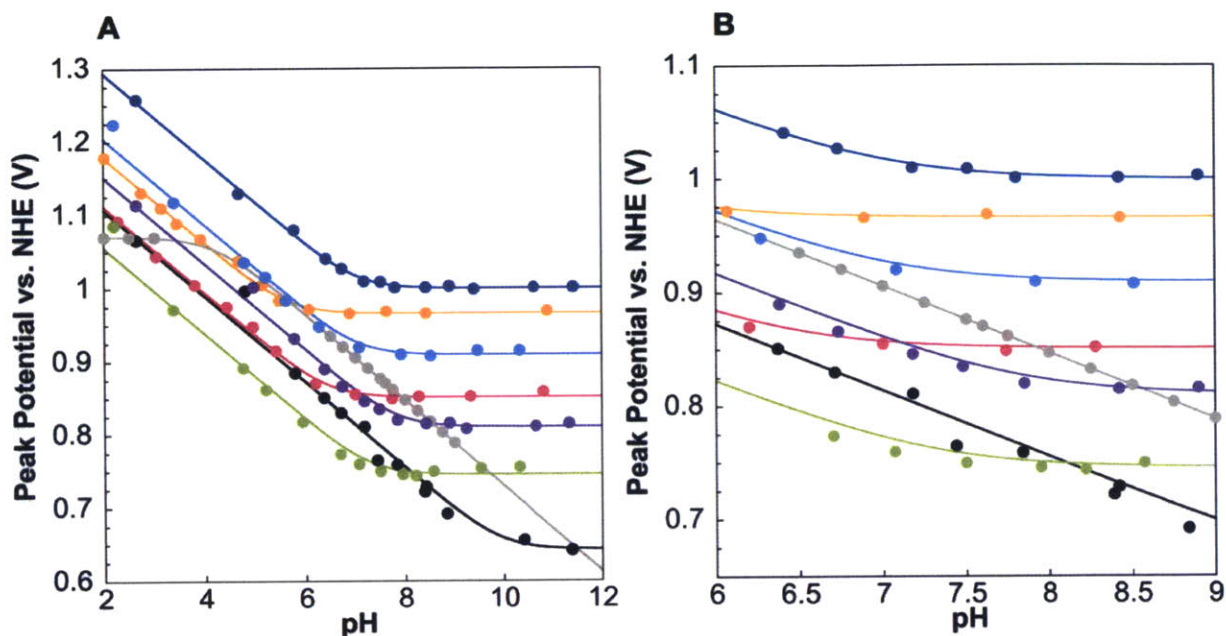


Figure 1.11 Pourbaix diagrams for W, Y and its analogs. DPV studies^{64,74} performed on the *N*-acetylated tyrosinamide derivatives were used to calculate E_p at each pH. The color code is as follows: Y (black), 3,5-F₂Y (green), 2,3,5-F₃Y (pink), 2,3-F₂Y (purple), 2,3,6-F₃Y (light blue), F₃Y (orange), W (gray) and NO₂Y (dark blue). Panel B shows an expanded view of the pH 6.0–9.0 regime where RNR activity is typically monitored.

1.2.6 Radical distribution and half-sites reactivity. Over the course of our work on the class Ia RNR we have identified two important features of the $\alpha_2\beta_2$ complex that complicate mechanistic studies on this system. The first feature relates to the distribution of $Y_{122}\bullet$ (1.2 $Y\bullet/\beta_2$) within the β monomers and the second feature is the apparent half-sites reactivity of the $\alpha_2\beta_2$ complex; each α/β pair in the complex is distinct despite the symmetrical appearance observed in the docking model (Figure 1.6). These properties of RNR were identified by the studies described in this thesis, but are presented here to lay the foundation for the data analysis and interpretation presented in subsequent sections.

The diferric- $Y\bullet$ cofactor in β_2 can be reconstituted in one of two ways. In one method, ferrous ammonium sulfate and sodium ascorbate are added to the cell-free extract prior to purification of β_2 . Alternatively, β_2 can be isolated in the apo form and subsequently treated with

ferrous ammonium sulfate and O₂ to self-assemble the cofactor. In both cases, the optimized protocol results in 3.6 Fe³⁺/β₂ and 1.2 Y•/β₂. Based on the results of the studies outlined herein^{39,41,45,46,63,80,81} and in Chapter 3, active β₂ is proposed to contain a Y• in each monomer (Figure 1.12A). This model would suggest that wt-β₂, which contains 1.2 Y•/β₂, is composed of 60% β₂ with a diferric-Y• in each monomer, and 40% β₂ with a diferric cluster in each monomer but no Y• (Figure 1.12A). This conclusion is supported by PELDOR experiments that measured the distance between the Y•s in each monomer of β (33 Å, Figure 1.13).⁸⁰ This distance is in accordance with that measured between the two Ys in the docking model (32 Å, Figure 1.6). In the case of the UAA-substituted β₂s, 0.4–1.0 Y•/β₂ are obtained by *in vitro* self-assembly of the diferric-Y• cofactor.^{40,41,59,63,67,71} The two or none radical distribution model suggests that only 20–50% of the β₂s are active in nucleotide reduction, impacting the signal to noise in our mechanistic studies. It is likely that a biosynthetic pathway exists *in vivo* for cofactor assembly that ensures complete loading (2 Y•/β₂).

The second important issue that complicates our mechanistic studies is that only one of the two Y•s reacts at a time (Figure 1.12B). A consequence of “half-sites” reactivity is that in a single turnover experiment only 0.5 dNDP/total radical is generated. Evidence for this model is also provided by PELDOR spectroscopy experiments. In the subsequent section, we describe the ability to accumulate pathway radical intermediates at Y₃₅₆, Y₇₃₁ or Y₇₃₀ by the site-specific incorporation of UAAs at these positions. Due to half-sites reactivity, only one Y• in the α₂β₂ complex generates the UAA-based radical. PELDOR spectroscopy was utilized to measure the distance between the UAA radical in one α/β pair and the unreacted Y• in the second α/β pair (Figure 1.13), providing further support for the docking model (Figure 1.6). The observation of half-sites reactivity suggests that the second α/β pair can only react upon completion of the catalytic cycle by the first α/β pair.

Although extensive evidence supports an active $\alpha 2\beta 2$ complex similar to the docking model (Figure 1.6), the symmetrical appearance of the complex in the docking model is not maintained during turnover.

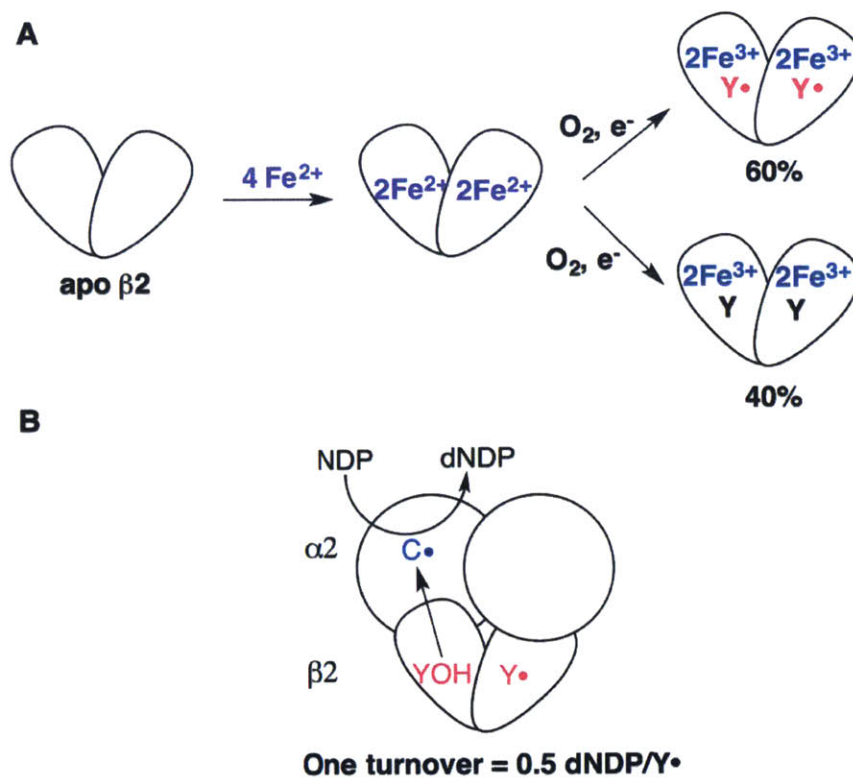


Figure 1.12 A. Two or none radical distribution in $\beta 2$. All preparations of wt- $\beta 2$ (1.2 $Y\bullet/\beta 2$) are proposed to contain 60% $\beta 2$ with 2 $Y\bullet$ and 40% $\beta 2$ with no $Y\bullet$. B. Half-sites reactivity in *E. coli* class Ia RNR. Only one of the two $Y\bullet$ s reacts at a time producing only 0.5 dNDPs in one turnover.

1.3 EVIDENCE FOR RADICAL INTERMEDIATES IN THE RT PATHWAY

Prior to our work with UAA-substituted RNRs, site-directed mutagenesis was used to investigate the importance of the proposed pathway residues (W₄₈,⁵² Y₃₅₆,⁵⁰ Y₇₃₁⁵¹ and Y₇₃₀⁵¹). These studies showed that mutation of any of these residues greatly diminished nucleotide reduction activity, precluding mechanistic insight into their involvement in RT. Thus, the initial question we focused on was whether there is a RT pathway during catalysis, in which amino acid radical intermediates are generated. As a first step to addressing this question, we proposed that lowering the reduction potential of the proposed pathway Ys with UAAs would create a radical trap due to their inability to oxidize the next Y on pathway. DOPA (**2**, Figure 1.10) was chosen for this study based on a single pulse radiolysis experiment that reported that this analog is ~260 mV easier to oxidize than Y at pH 7.0.⁸² However, this analog maintains the same pK_a as Y. At the time of this experiment, only the EPL method was available to incorporate UAAs and so DOPA was incorporated at position 356 in β2. Consistent with our prediction, the reaction of Y₃₅₆DOPA-β2, α2, CDP and ATP resulted in loss of Y₁₂₂• concomitant with formation of a new radical, assigned to DOPA• based on SF UV-vis and EPR spectroscopic methods.⁴⁰ DOPA• formation was dependent on the presence of α2, CDP and ATP. In fact, CDP binding was shown to be required for triggering the conformational changes associated with RT. The kinetics of the reaction were triphasic where two of the three phases (30–40 s⁻¹ and 2–7 s⁻¹) were kinetically competent (compared to wt turnover). Y₃₅₆DOPA-β2 itself was inactive in nucleotide reduction, supporting the proposal that DOPA₃₅₆• cannot oxidize Y₇₃₁. The slow third phase (0.5–0.7 s⁻¹) for DOPA• formation was ascribed to kinetic complexity arising from the two mutations (V₃₅₃G and S₃₅₄C) that were inserted to accommodate ligation.

The DOPA study provided the first insight into the reactivity of $Y_{122}\bullet$ in $\beta 2$; only 50% of $Y_{122}\bullet$ was converted into $DOPA_{356}\bullet$, an observation consistent with the two or none radical distribution model (Figure 1.12A) and half-sites reactivity in the class Ia RNR (Figure 1.12B). PELDOR spectroscopy was used to measure the distance between $DOPA_{356}\bullet$ in one α/β pair and the unreacted $Y_{122}\bullet$ in the second α/β pair providing the first structural constraint for $Y_{356}\bullet$ within the $\alpha 2\beta 2$ complex; $Y_{356}\bullet$ is located 30 Å away from $Y_{122}\bullet$ on the opposite α/β pair (Figure 1.13).

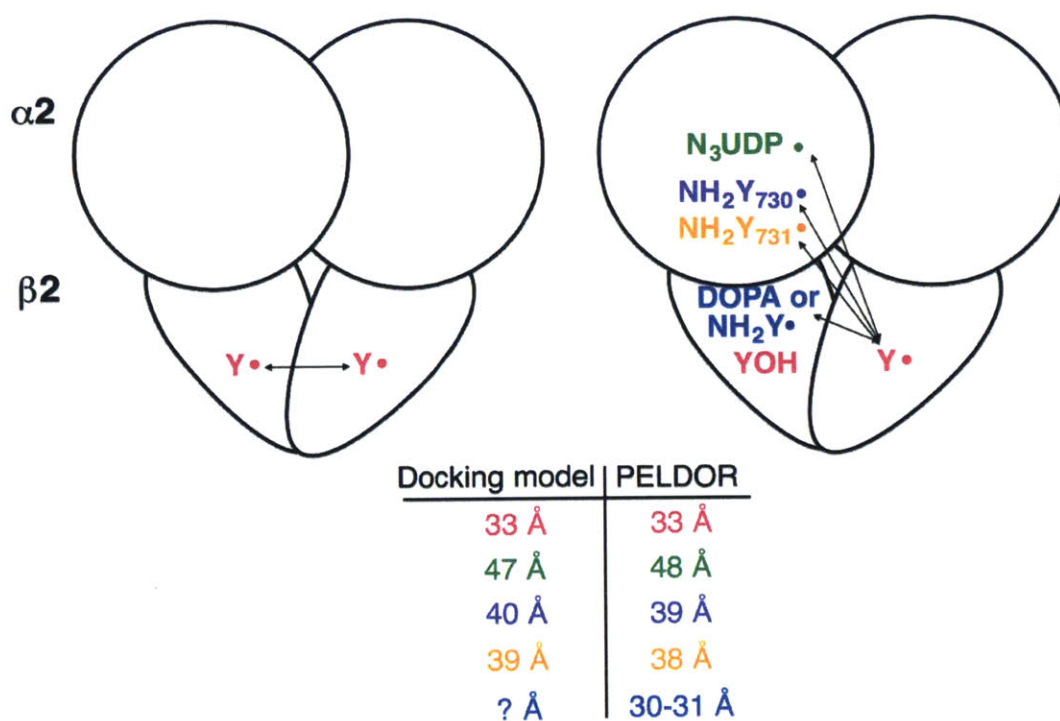


Figure 1.13 Distance determination by PELDOR spectroscopy. The *E. coli* class Ia RNR demonstrates half-sites reactivity where only one $Y_{122}\bullet$ reacts at a time. This feature allows for distance measurement between a pathway radical in one α/β pair and $Y_{122}\bullet$ in the second α/β pair. Distances have been measured between $Y_{122}\bullet$ – $DOPA_{356}\bullet$ (or $NH_2Y_{356}\bullet$) and $Y_{122}\bullet$ – $NH_2Y_{731}\bullet$ (or $NH_2Y_{730}\bullet$). Early studies performed with the MBI N_3UDP provided the distance constraint between $Y_{122}\bullet$ and an active site radical ($N\bullet$). Table A1.1 in Appendix 1 reports the errors associated with each distance measurement. The docking model measurements reflect the distances between the phenolic oxygens (for $Y\bullet$ – $Y\bullet$ distances) or between the phenolic oxygen and the 2' carbon atom of the substrate (for $Y\bullet$ – $N\bullet$ distance).

The DOPA study supported the role of Y₃₅₆ in RT. We next turned our attention to positions 730 and 731 in α 2. These positions are not amenable to the EPL methodology; thus, we explored the nonsense codon suppression method to site-specifically replace these pathway Ys with unnatural analogs. For the purpose of these studies, a tRNA synthetase/tRNA pair was evolved in collaboration with the Schultz lab to site-specifically incorporate 3-aminotyrosine (NH₂Y, **3**, Figure 1.10) into RNR.⁸³ This Y analog has the same pK_a as Y (10.0). At the time of these studies, there was only a single published reduction potential for NH₂Y, suggesting that this analog is ~190 mV easier to oxidize than Y.⁷⁹ More recently, we have initiated cyclic voltammetry (CV) studies on NH₂Y that suggest that this perturbation is greater (~400 mV) than originally predicted (Lee, Huynh, Tommos, Nocera and Stubbe unpublished results). Similar to DOPA, NH₂Y acts as a radical sink and the reaction of NH₂Y- α 2s with β 2, CDP and ATP produced NH₂Y• concomitant with Y₁₂₂• loss in a S dependent manner.⁸³ Formation of NH₂Y• was biphasic (12–40 s⁻¹, ~2 s⁻¹) with kinetics that were strikingly similar to the first two phases observed for DOPA• formation. These studies further supported that the third phase observed for DOPA• formation is associated with the EPL methodology. Finally, only 40% NH₂Y• was formed in contrast to the 50% anticipated from the half-sites reactivity model. The reason for this discrepancy remains unclear.

Generation of stable NH₂Y•s at position 356 in β and positions 731 and 730 in α provided distance measurements between Y₁₂₂• in one α/β pair and NH₂Y₃₅₆•, NH₂Y₇₃₁• or NH₂Y₇₃₀• in the second pair (Figure 1.12).^{45,73} These distances (~38–39 Å) are similar to those predicted by Uhlin and Eklund's docking model,⁴³ providing further support for an α 2 β 2 active complex. Interestingly, several lines of evidence suggest that the NH₂Y-RNRs are capable of producing deoxynucleotides,⁵⁹ even though oxidation of the next pathway Y by NH₂Y• could be as much as 400 mV uphill according to our recent numbers. The combined studies on DOPA-,⁴⁰ F_nY-⁶⁷ and

NO₂Y-substituted RNRs⁷⁰ suggest that turnover is abolished when the potential of a pathway Y is modulated by >200 mV (section 1.5.2). To account for the catalytic activity measured with NH₂Y-RNRs, we postulate that NH₂Y is conformationally perturbed in the RNR environment such that its reduction potential is brought closer to Y (Lee, Huynh, Tommos, Nocera and Stubbe unpublished results), thus facilitating oxidation of the next residue on pathway. If this interpretation holds true, it raises the possibility that RNR could perturb the reduction potentials of the other UAAs. Nonetheless, the combined experiments with DOPA- and NH₂Y-RNRs confirm that amino acid radical intermediates can be trapped at Y₃₅₆, Y₇₃₁ and Y₇₃₀, suggesting their role as intermediaries in long-range RT in the *E. coli* class Ia RNR.

At present, W₄₈ is the only proposed pathway residue for which there is no direct evidence for involvement in RT. This residue was originally proposed to be on the RT pathway due to the similarity in the H-bonding network formed by W₄₈, D₂₃₇ and H₁₁₈ to that observed in CCP.⁶⁰ In the case of CCP, a W^{•+} has been experimentally observed and characterized.⁶¹ Further support for the involvement of W₄₈ in RT was provided by cluster assembly studies that showed formation of W₄₈^{•+} during the reaction of apo β2 with 2.0–2.4 equiv. of Fe²⁺/β2 and O₂.⁸⁴ Efforts to replace W with unnatural W analogs have proven unsuccessful (Lee, Stubbe unpublished results). Several lines of evidence in our lab support that raising the driving force of RT by replacement of Y₁₂₂ with F_nYs or NO₂Y (Figure 1.10) results in accumulation of Y₃₅₆[•] (section 1.5.3 and Chapter 3).^{41,63,71,73} However, mutation of Y₃₅₆ to F fails to accumulate W₄₈[•] or W₄₈^{•+} (Appendix 4), suggesting that this residue is not involved in RT. These studies are further supported by recent work on the class Ic RNR, which utilizes a RT pathway similar to that proposed in class Ia RNR for the oxidation of C in α. During cluster assembly of the active Mn(IV)/Fe(III) cofactor, the class Ic RNR accesses a strongly oxidizing Mn(IV)/Fe(IV) state that, when reacted with α, S and E,

failed to accumulate $W_{51}\cdot$ (or $W_{51}^{+\cdot}$), the W_{48} equivalent in class Ic.⁶² As previously noted, elimination of this residue from the RT pathway results in a substantial increase in the distance over which PCET must occur. This issue of how the oxidant can potentially traverse long distances of 15–20 Å without a noticeable effect on turnover remains unresolved.

Table 1.1 Summary of F_nY pH rate profiles.

Position	UAA	pK _a ^a	ΔE _p ^b (mV) at pH 6.5	ΔE _p ^b (mV) at pH 9.0	SA at pH 6.5 vs wt (%)	SA at pH 9.0 vs wt (%)	SA at pH 9.0 as % max. activity ^c
356	EPL-PheNH ₂	- ^d	60	160	100	40	30
	EPL-3,5-F ₂ Y	7.6	-30	40	100 ^e	100 ^e	45
	EPL-2,3,5-F ₃ Y	6.8	41	146	100 ^e	^f	^f
	EPL-2,3-F ₂ Y	8.2	71	109	100 ^e	80 ^e	51
	EPL-2,3,6-F ₃ Y	7.4	123	204	20 ^e	^f	^f
	EPL-F ₄ Y	6.0	130	260	15 ^e	^f	^f
	3,5-F ₂ Y ^g	7.6	-30	40	86	26	20
	2,3,5-F ₃ Y ^g	6.8	41	146	15	5	30
	2,3-F ₂ Y ^g	8.2	71	109	40	27	40
731	3,5-F ₂ Y ^g	8.1	-60	5	60	23	25
	2,3,5-F ₃ Y ^g	7.3	15	110	20	5	15
	2,3-F ₂ Y ^g	8.7	70	75	25	8	25
730	3,5-F ₂ Y ^g	8.4	-55	-11	75	50	40
	2,3,5-F ₃ Y ^g	7.6	17	89	10	4	20
	2,3-F ₂ Y ^g	9.0	71	62	22	45	60
	2,3,6-F ₃ Y ^g	8.2	95	154	7	6	30

SA = specific activity.

At pH 6.5, the F_nYs are > 67% protonated. The highest pH where RNR activity is typically measured is pH 9.0. At this pH, the amount of deprotonated F_nY varies from 50–100% depending on the analog, the position and the pK_a perturbation. SAs for EPL-Y₃₅₆F_nY-β2 and Y₃₅₆F_nY-β2 are not scaled for radical content. All EPL proteins including EPL-Y contained 0.3 Y•/β2. All Y₃₅₆F_nY-β2s generated by the nonsense codon method contained 0.7–0.9 Y•/β2 compared to wt-β2 (1.2 Y•/β2). The radical content of each F_nY construct is shown in Table A1.2 (Appendix 1).

^a Predicted effective pK_{as} for each UAA based on the pK_a measurements made with NO₂Y-RNRs.⁷⁰ The solution pK_a is predicted to be perturbed by +0.4, +0.9 and +1.2 units at positions 356, 731 and 730 respectively.

^b The ΔE_{ps} were calculated from the solution DPV data^{64,74} collected on the *N*-acetylated tyrosinamide derivatives accounting for the pK_a perturbation at each position.

^c The absolute specific activity at pH 9.0 is calculated as a percent of the maximum activity observed for each F_nY. This normalization allows assessment of whether activity correlates with the pK_a of the F_nY.

^d PheNH₂Y cannot be deprotonated in the biologically relevant pH regime (pK_a of 27).⁶⁶

^e Specific activities are reported relative to EPL-Y. EPL-Y activity is decreased 75% compared to wt RNR.⁶⁷

^f Specific activities are below the detection limit.

^g The specific activities were measured by Ellen C. Minnihan.

1.4 PROTON MANAGEMENT IN THE RT PATHWAY

1.4.1 The pK_a s of all pathway Ys are minimally perturbed except for Y_{122} . An important question to address is whether the protein environment modulates the pK_a and the reduction potentials of each pathway Y. These two properties dictate the kinetics of PCET and it was hypothesized that RNR could alter them to facilitate efficient RT. Furthermore, any mechanistic interpretation of data collected with the UAA-substituted RNRs (Figure 1.10) requires an understanding of the magnitude to which the pK_a and the reduction potentials are perturbed. To estimate the pK_a perturbation at each pathway Y, we incorporated NO_2Y site-specifically at Y_{356} using the EPL methodology⁶⁴ and at Y_{122} , Y_{356} , Y_{731} and Y_{730} using the nonsense codon suppression method.⁷⁰ NO_2Y^- formation ($\lambda_{\text{max}} = 460 \text{ nm}$) was monitored as a function of pH (6.0–10.6). NO_2Y at physiologically pH is estimated to be $\sim 200 \text{ mV}$ harder to oxidize than Y, and incorporation of this analog at any position on pathway (except Y_{122}) abolishes activity.⁷⁰ The implications of this observation to the thermodynamic landscape of the RT pathway are discussed in section 1.5.2. Due to the absence of activity, the pK_a of NO_2Y at each pathway position could be determined in the $\alpha 2/\beta 2/\text{S}/\text{E}$ complex.

The pH titration experiments revealed that the pK_a of $\text{NO}_2\text{Y}_{356}$ was perturbed by +0.4 units and those of $\text{NO}_2\text{Y}_{731}$ and $\text{NO}_2\text{Y}_{730}$ were perturbed by $\sim +1$ unit relative to the solution pK_a of NO_2Y .⁷⁰ The greatest perturbation was observed at position 122 ($> +3$ units), consistent with the hydrophobic environment observed for Y_{122} in the crystal structure.^{38,70} The pK_a of $\text{NO}_2\text{Y}_{122}$ did not depend on the presence of the diferric cluster; similar pK_a s were recorded for the apo and holo proteins. However, only a lower limit was set for the pK_a perturbation at this position ($> +3$ units) due to the instability of $Y_{122}\text{NO}_2\text{Y}-\beta 2$ at $\text{pH} > 10.6$.

Surprisingly, these studies show that altering the H-bonding environment of the pathway Ys minimally affects the pK_a of NO_2Y . The crystal structure of S/E bound $\alpha 2$ reveals an unusual π - π stacking interaction between Y_{731} and Y_{730} .³⁷ Extensive studies performed in collaboration with the Bennati^{57,58,85} and Nocera^{55,56} labs suggest that this interaction is critical for maintaining the H-bonding network in $\alpha 2$ but also for controlling the reduction potential of these pathway Ys. However, the pK_a s of NO_2Y in $\text{NO}_2\text{Y}_{731}/\text{Y}_{730}\text{F}$ and $\text{Y}_{731}\text{F}/\text{NO}_2\text{Y}_{730}$ were minimally perturbed from the single mutant, suggesting that removal of this single H-bonding interaction does not affect the pK_a . In the following sections, we work on the assumption that the pK_a s of all UAAs are perturbed the same way as NO_2Y at each pathway position; specifically, that the pK_a is perturbed by +3, +0.4, +0.9 and +1.2 units at positions 122, 356, 731 and 730, respectively. Finally, an important observation that was made in the NO_2Y studies is that S is directly responsible for perturbing the pK_a of the pathway Ys. This result is in direct agreement with the DOPA- and NH_2Y studies, which show that S binding is predominantly responsible for triggering the conformational changes associated with RT.

1.4.2 Orthogonal PCET through Y_{122} . Oxidation of every Y on the RT pathway requires concomitant transfer of a proton and an electron. Thus, one of our primary goals is to define the mechanism of PCET at each step in the pathway including the nature of the proton acceptor/donor for each Y. It was previously proposed that the first step of RT involves PT from a water molecule on the diferric cluster ($\text{Fe1-H}_2\text{O}$) to $\text{Y}_{122}\bullet$ concomitant with ET from Y_{356} (or W_{48}).^{49,86} The crystal structure of met- $\beta 2$ (diferric-YOH state) provides a distance of ~ 4 Å between the phenolic oxygen and $\text{Fe1-H}_2\text{O}$.^{87,88} This distance is too long for PT, and it was hypothesized that S/E binding to $\alpha 2$ triggers conformational changes that bring $\text{Y}_{122}\bullet$ within H-bonding distance of $\text{Fe1-H}_2\text{O}$ such that the proton can be directly transferred. To provide evidence for this model, we took advantage of

the ability to trap radicals at different positions within the RT pathway and investigated the Mössbauer parameters of the diferric cluster.⁵⁴ In one set of experiments, ⁵⁷Fe-β2 was reacted with Y₇₃₁NH₂Y-α2, CDP and ATP to generate NH₂Y•⁸³ (Figure 1.14, I), whereas in a second set, ⁵⁷Fe-β2 was incubated with α2, N₃UDP (a MBI) and TTP to generate the active site radical abbreviated as N• (Figure 1.14, II).⁸⁹ The Mössbauer spectra of both reaction mixtures were compared to that of the diferric cluster in the reaction of ⁵⁷Fe-β2, α2 and E. The similarities in the isomer shifts of the three spectra but differences in the quadrupole splitting parameters associated with Fe1 between the reaction mixtures and the control were interpreted to report on deprotonation of Fe1-H₂O with no change in the oxidation state of Fe1. This Mössbauer study supports the model for orthogonal PCET at Y₁₂₂ and also provides the first evidence for involvement of the diferric cluster in catalysis. It additionally suggests that the conformational changes that occur upon S binding are in part related to this initial PT step.

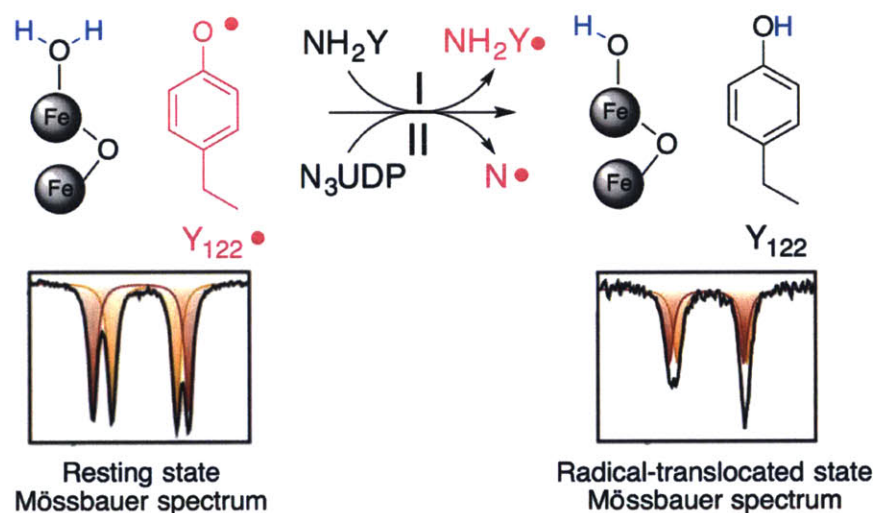


Figure 1.14 Experimental strategy for testing orthogonal PCET at Y₁₂₂. The first step in RT is proposed to involve PT from a water molecule on the diferric cluster to Y₁₂₂•. To test this model, ⁵⁷Fe-β2 was reacted with Y₇₃₁NH₂Y-α2/CDP/ATP (I) or α2/N₃UDP/TTP (II) to generate NH₂Y• or N• respectively. Extensive analysis of the resulting Mössbauer spectra showed perturbations that are consistent with deprotonation of Fe1-H₂O.⁵⁴

1.4.3 Orthogonal PCET through Y₃₅₆. Our current model for RT in the class Ia RNR proposes that orthogonal PCET is operative within the $\beta 2$ subunit. To oxidize Y₃₅₆, it was hypothesized that ET from Y₃₅₆ to Y₁₂₂[•] occurs concomitant with PT from Y₃₅₆ to E₃₅₀, a conserved residue on the C-terminal tail of $\beta 2$.^{49,50} To test this model, the experimental strategy shown in Figure 1.15A was followed and 2,3-F₂Y or PheNH₂ (Figure 1.10) were inserted at position 356 using EPL. DPV studies performed on the protected amino acids showed that these two analogs are 45 mV⁶⁵ and ~100 mV⁶⁶ harder to oxidize than Y at pH 7.0, respectively. Thus, it was anticipated that increasing the reduction potential of Y₃₅₆ might switch the rate-limiting step from the protein conformational change(s) to PCET through Y₃₅₆. The choice of 2,3-F₂Y and PheNH₂Y was additionally governed by the pK_as of these analogs. The 2,3-F₂Y has a pK_a of 7.8 allowing accessibility to the protonated and deprotonated states of this UAA in the pH regime where RNR is active (pH 6.0–9.0). PheNH₂ cannot be deprotonated in the biological pH regime prior to its oxidation (pK_a of 27).⁷⁸ The pK_a of the aniline cation radical is 8.5, more than 10 pK_a units higher than the corresponding tyrosyl cation radical which has a pK_a of -2 (Figure 1.15B). Replacement of Y₃₅₆ with PheNH₂ thus allows assessment of the sequence of the PT and ET steps; PheNH₂ would be capable of nucleotide reduction only if ET occurs before PT.

The activity of the two constructs were determined as a function of pH. In the case of 2,3-F₂Y, it was predicted that if orthogonal PCET is operative during Y₃₅₆ oxidation, then RT would not be dependent on the protonation state of 2,3-F₂Y; both protonated 2,3-F₂Y and deprotonated 2,3-F₂Y⁻ would be capable of nucleotide reduction. In the case of PheNH₂, if PT at position 356 occurred before ET, or if PT and ET occurred in a concerted manner, then PheNH₂ would be

inactive due to the inability to transfer a proton. Activity with this construct can only be measured if ET from PheNH₂ to Y₁₂₂[•] occurred before PT from Y₃₅₆ to the proposed proton acceptor, E₃₅₀.

Prior to introducing the results of these experiments, the pH rate profile of EPL-Y i.e. wt-β₂ generated by the EPL methodology and that of recombinantly expressed β₂ are presented. As shown in Figure 1.16A, the activity of EPL-Y demonstrates a pH dependence where activity increases from pH 6.5 to pH 8.0 and then subsequently decreases from pH 8.0 to pH 9.0. This pH rate profile was fit to a two proton ionization model providing p*K* values of 7.1 and 8.8. A similar pH dependence is also observed with recombinantly expressed wt-α₂ and wt-β₂ (Figure 1.16B), albeit with slightly different p*K* values (6.8 and 9.0). The ionizing species that produce the observed pH dependence of wt RNR remain unidentified. All pH rate profiles discussed subsequently were collected as described in Figure 1.16 for EPL-Y and wt-α₂ (or wt-β₂). The caveat to these data is that Y-containing RNR itself shows loss of ~30% (wt RNR) to 50% (EPL RNR) activity when the pH is increased from 8.0 to 9.0 (Figure 1.16).

The results of the 2,3-F₂Y and PheNH₂ experiments are summarized in Table 1.1. At pH 6.5, where 2,3-F₂Y is 98% protonated, the activity of EPL-2,3-F₂Y is identical to EPL-Y. At pH 9.0, where 2,3-F₂Y is ~86% deprotonated, 2,3-F₂Y maintains ~80% of the activity observed with EPL-Y.^{65,67} These studies immediately show that a proton can be removed from the RT pathway with little effect on nucleotide reduction and further suggest that the mechanism of RT can switch from PCET to ET upon deprotonation of 2,3-F₂Y.

The activity of EPL-PheNH₂ is identical to EPL-Y between pH 6.5–8.0 (Table 1.1 shows the activity at pH 6.5).⁶⁶ These observations support that PT is not required before ET for RT through Y₃₅₆. Interestingly, the activity of EPL-PheNH₂ decreases with increasing pH between 8.0 and 9.0 such that only 40% activity is observed relative to EPL-Y at pH 9.0 (Table 1.1).⁶⁶ These

results are interpreted to reflect a change in the rate-limiting step of the reaction from the conformational change to ET. The lowered activity of PheNH₂ compared to Y at pH 9.0 is ascribed to the increased potential difference between PheNH₂Y and Y at this pH value (160 mV, Table 1.1).⁶⁶

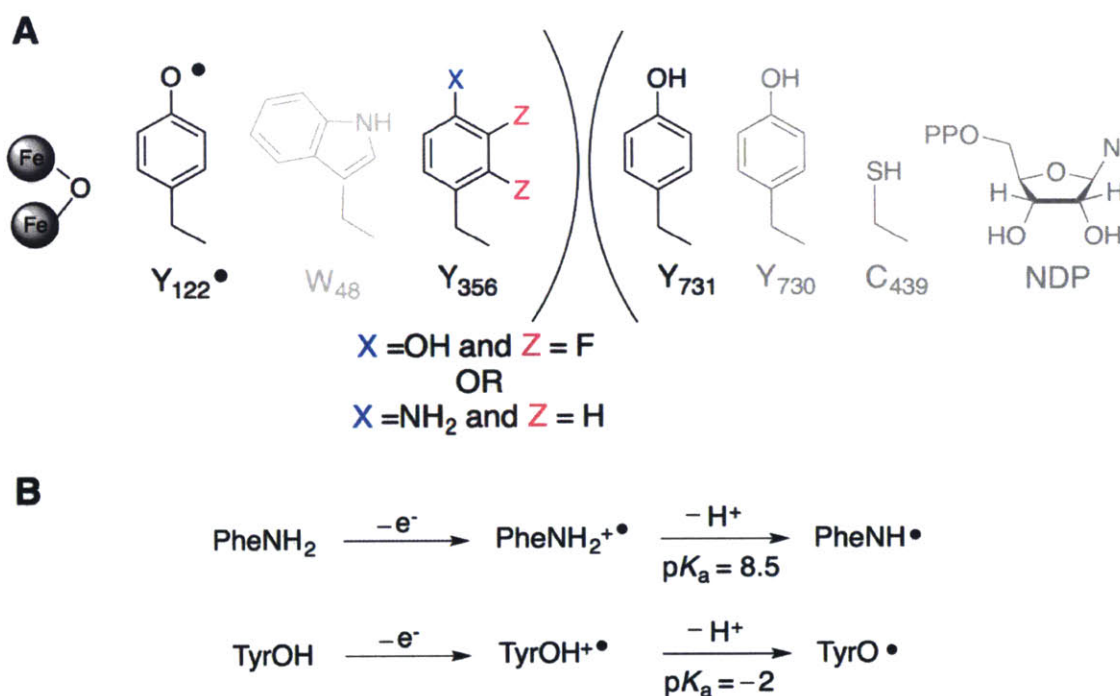


Figure 1.15 A. Experimental strategy for testing orthogonal PCET at Y₃₅₆. In the first set of experiments, 2,3-F₂Y (X = OH, Z = F) was inserted at position 356 and dCDP activity was monitored as a function of pH. In the second set of experiments, the pH rate profile of PheNH₂ at position 356 (X = NH₂, Z = F) was monitored. The two experiments confirmed that PT is not a requirement for turnover. B. pK_as of the Y and PheNH₂ cation radicals. PheNH₂ data is given for *p*-methylaniline. Reproduced from Ref. 66.

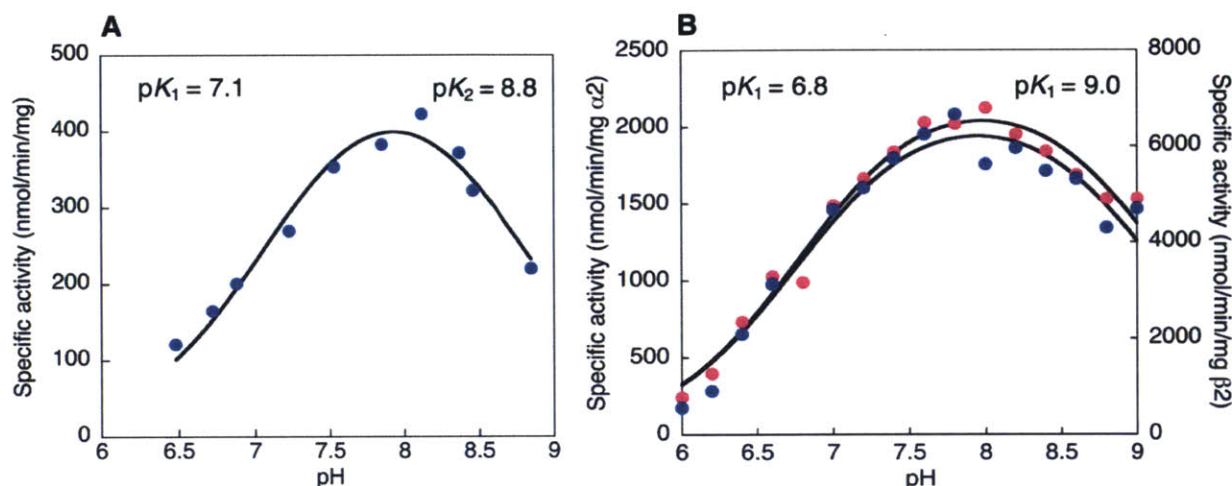


Figure 1.16 The pH rate profiles of EPL RNR (A) and wt RNR (B). A. The assays contained 3 μM each of EPL- $\beta 2$ ($V_{353}G$, $S_{354}C$, 0.3 $Y\bullet/\beta 2$) and wt- $\alpha 2$. B. The assays contained either 0.3 μM wt- $\alpha 2$ and 1.5 μM wt- $\beta 2$ (1.2 $Y\bullet/\beta 2$, pink) or 0.5 μM wt- $\beta 2$ and 2.5 μM wt- $\alpha 2$ (blue). Specific activity is reported per mg of $\alpha 2$ (pink) or $\beta 2$ (blue). The ~ 3 -fold difference in specific activity between $\alpha 2$ and $\beta 2$ has been recorded previously^{iv, 29}. The black lines represent fits to a two proton ionization model with the pK values shown in each panel. The identities of the ionizing species in EPL RNR and wt RNR remain unknown.

Since these preliminary studies on 2,3- F_2Y and PheNH₂, the pH rate profiles (pH 6.5–9.0) of all EPL generated $Y_{356}F_nY\text{-}\beta 2$ ($n = 2, 3, 4$) were collected.⁶⁷ Similar to the 2,3- F_2Y studies, no correlation is observed between activity and the protonation state of 3,5- F_2Y (Figure 1.17, Table 1.1). At pH 9.0, we estimate that $\sim 96\%$ of 3,5- F_2Y is deprotonated; however, EPL-3,5- F_2Y maintains the same activity as EPL-Y at this pH (Table 1.1). This observation suggests that the two constructs (EPL-3,5- F_2Y and EPL-Y) have the same pH rate profile; both proteins maintain 45% (EPL-3,5- F_2Y , Table 1.1) to 50% (EPL-Y, Figure 1.16A) of their maximum activity at pH 9.0. In contrast to the observations with EPL-2,3- F_2Y and EPL-3,5- F_2Y , loss of activity is

^{iv} Accounting for the MW differences between $\alpha 2$ (172 kDa) and $\beta 2$ (87 kDa), the turnover number of $\alpha 2$ ($5\text{--}7\text{ s}^{-1}$) is typically lower than that observed for $\beta 2$ ($9\text{--}12\text{ s}^{-1}$).²⁹ These differences are presumed to report on different rate-limiting steps in the two assays. When $\alpha 2$ concentration is limiting, turnover is governed by re-reduction of $\alpha 2$ by TR. When $\beta 2$ concentration is limiting, turnover is governed only by the protein conformational change(s) that occurs prior to RT.⁸¹

measured with 2,3,5-F₃Y, 2,3,6-F₃Y and F₄Y (Table 1.1) that is interpreted to report on the reduction potential difference between F_nY and Y. In the case of EPL-2,3,5-F₃Y, the activity measured at pH 6.5 is identical to EPL-Y, but no activity is detected at pH 9.0. The potential difference between 2,3,5-F₃Y and Y increases from ~40 mV to ~146 mV when the pH increases from 6.5 to 9.0 (Table 1.1). With 2,3,6-F₃Y and F₄Y, the potential difference between F_nY and Y is 120–260 mV over the entire pH regime (6.5–9.0). In accordance with this large potential difference, measured activities are in the range of 20–0% of wt activity (Table 1.1). This correlation between reduction potential and activity is discussed subsequently (section 1.5.2), but appears to be specific to the EPL generated proteins. A similar correlation is not observed when the nonsense codon suppression method is used to produce the UAA-substituted RNRs.

These studies taken together suggest that orthogonal PCET is operative through Y₃₅₆ and it was proposed that the Y₃₅₆ proton is transferred to solvent either via an amino acid residue or directly.⁶⁷ At the time of these studies, we favored PT to an amino acid residue and put forth E₃₅₀,^{49,50} a conserved residue on the structurally disordered tail of β2, as a potential proton acceptor candidate. In Chapters 4 and 5 of this thesis, we provide the first direct evidence for PT from Y₃₅₆ to solvent. We additionally show that PT may not be facilitated by E₃₅₀ but instead occur through water clusters.

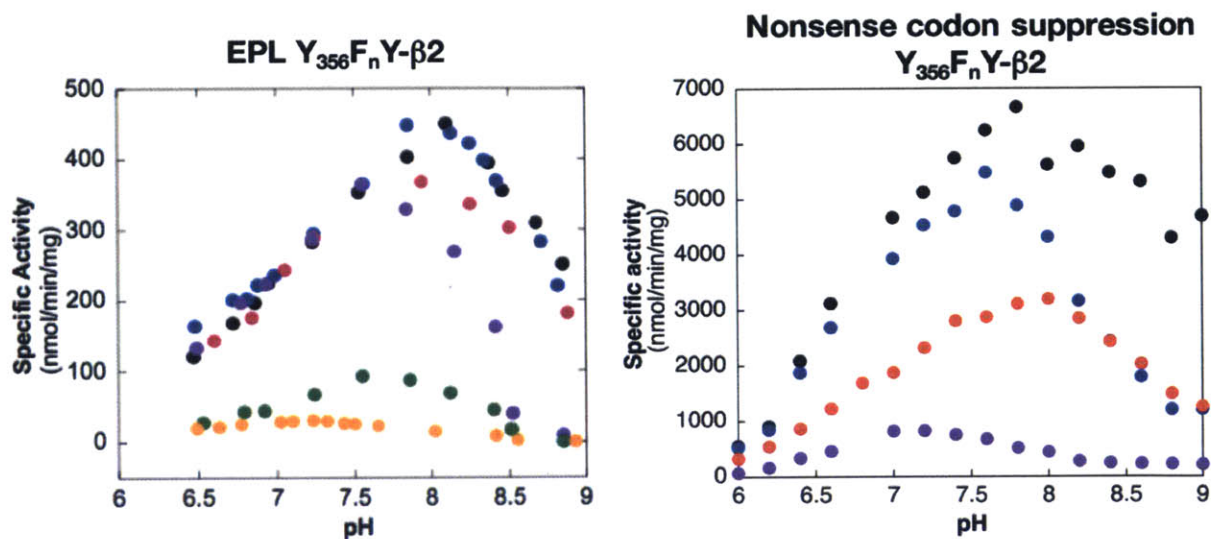


Figure 1.17 Absolute specific activities of Y₃₅₆F_nY-β2 generated by the EPL and nonsense codon suppression methods. The color code is as follows: Y (black), 3,5-F₂Y (blue), 2,3-F₂Y (red), 2,3,5-F₃Y (purple), 2,3,6-F₃Y (green) and F₄Y (orange). The pH rate profile of Y₃₅₆(2,3,6)F₃Y-β2 generated by the nonsense codon suppression method has not yet been collected. Attempts to incorporate F₄Y into RNR using the nonsense codon suppression method have proven unsuccessful. The proton dependence of the pH rate profiles of EPL-Y and wt-β2 are not understood. Panel A is reproduced from Ref. 67.

1.4.4 Collinear PCET in the α2 subunit. In contrast to the longer distances observed in β2, the pathway residues in α2 are within 3–4 Å of each other.⁴³ These distances led us to propose that collinear PCET is operative in the α2 subunit. Evidence for this model is obtained from high-field EPR and electron-nuclear double resonance (ENDOR) spectroscopy studies performed on NH₂Y₇₃₀• and NH₂Y₇₃₁• generated in the reaction of β2, NH₂Y-α2, CDP and ATP.^{57,85} High-field EPR studies (94 and 263 GHz) provide g_x values for these radicals that are considerably lower than the calculated value for free NH₂Y•, indicating a highly perturbed electrostatic environment.^{57,85,90} ENDOR spectroscopy in conjunction with structural information for α2⁵⁹ and DFT calculations allow assignment of the H-bonds to NH₂Y₇₃₀• and NH₂Y₇₃₁•.^{57,85} In the case of NH₂Y₇₃₀•, these studies reveal strong intramolecular H-bonds associated with the amino group, two moderately strong perpendicular H-bonding interactions ascribed to Y₇₃₁ and C₄₃₉ and a single

weaker H-bonding interaction that is assigned to an ordered water molecule. Mutation of C₄₃₉ to A results in loss of a moderate H-bonding interaction, consistent with one of the proposed assignments.⁵⁷ In the case of NH₂Y₇₃₁•, ENDOR studies show the presence of the strong intramolecular H-bonds from the amino group and a single moderately strong perpendicular H-bonding interaction ascribed to Y₇₃₀.⁵⁷ Mutation of Y₇₃₀ to F removes the moderate H-bonding interaction, consistent with the proposed assignment. Taken together these studies demonstrate a structured H-bonding network in $\alpha 2$ and support a collinear PCET mechanism for RT through Y₇₃₁, Y₇₃₀ and C₄₃₉.

To provide more direct evidence for collinear PCET in $\alpha 2$, we designed experiments similar to those described for Y₃₅₆; F_nYs (n = 2, 3) were incorporated at either position 731 or 730 using the nonsense codon suppression method and the pH rate profile of each construct was obtained and compared to wt RNR^y. We hypothesized that if collinear PCET is operative in $\alpha 2$, then nucleotide reduction activity would be measured when F_nY is protonated but reducing activity would be observed as F_nY gets deprotonated. We additionally collected the pH rate profiles of Y₃₅₆F_nY- $\beta 2$ to compare to our earlier work with EPL generated Y₃₅₆F_nY- $\beta 2$. Recall that the activities of the EPL-Y₃₅₆F_nY- $\beta 2$ s did not correlate with the pK_a of F_nY, leading us to propose that orthogonal PCET is operative at position 356.

The absolute specific activities of Y₃₅₆F_nY- $\beta 2$ s as a function of pH are shown in Figure 1.17B and compared to the pH rate profiles of EPL-Y₃₅₆F_nY- $\beta 2$ (Figure 1.17A).⁶⁷ It is immediately apparent that the two methods of protein production provide distinct results. The specific activities for EPL generated Y, 3,5-F₂Y, 2,3-F₂Y and 2,3,5-F₃Y are identical between pH 6.5–8.0 and

^y All pH rate profiles (Y₃₅₆F_nY- $\beta 2$, Y₇₃₁F_nY- $\alpha 2$ and Y₇₃₀F_nY- $\alpha 2$) discussed subsequently were collected and analyzed by Ellen C. Minnihan.

independent of ΔE_p between F_nY and Y , whereas loss in activity is observed at higher pH values. The latter data are proposed to report directly on ΔE_p between F_nY and Y (section 1.5.2).⁶⁷ In contrast, $Y_{356}F_nY$ - $\beta 2$ s generated by the nonsense codon suppression method show the following decreasing order in specific activity, $Y > 3,5-F_2Y > 2,3-F_2Y > 2,3,5-F_3Y$, over the entire pH regime (Figure 1.17, Table 1.1). A single exception to this trend is the activity of $Y_{356}(2,3)F_2Y$ - $\beta 2$ between pH 8.0 and 9.0, which is identical to that measured with $Y_{356}(3,5)F_2Y$ - $\beta 2$. Activity does not correlate with the reduction potential difference. For example, the activities of $Y_{356}(2,3,5)F_3Y$ - $\beta 2$ and $Y_{356}(2,3)F_2Y$ - $\beta 2$ are 15% and 40% of wt at pH 6.5, respectively (Table 1.1). However, 2,3,5- F_3Y is ~ 30 mV easier to oxidize than 2,3- F_2Y at this pH value. These observations are addressed in more detail in section 1.5.2. These data indicate that the activities observed by the two methods do not report on the same step(s) during turnover. It is likely that the additional mutations required for the EPL method ($V_{353}G$, $S_{354}C$) change the rate-limiting step of the reaction. Similar to the EPL studies, however, 20–40% of the maximum activity is retained even at pH 9.0, where 86–96% of the F_nY s are deprotonated (Table 1.1). Both studies confirm that ET through Y_{356} is not obligately coupled to PT.

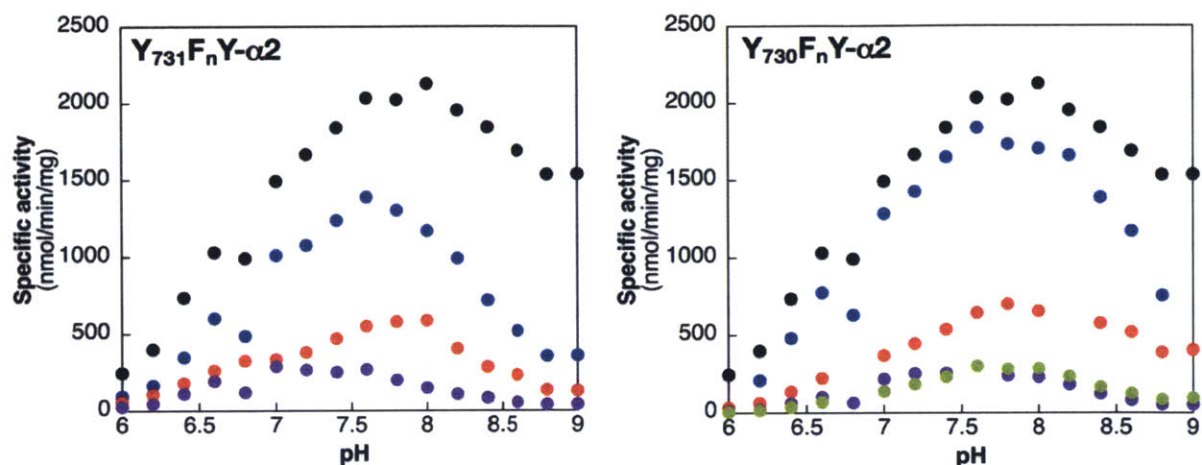


Figure 1.18 Absolute specific activities of $Y_{731}F_nY-\alpha 2$ and $Y_{730}F_nY-\alpha 2$ as a function of pH. The color code is as follows: Y (black), 3,5- F_2Y (blue), 2,3- F_2Y (red), 2,3,5- F_3Y (purple) and 2,3,6- F_3Y (green).

The absolute specific activities of $Y_{731}F_nY-\alpha 2$ and $Y_{730}F_nY-\alpha 2$ as a function of pH are shown in Figure 1.18. Similar to the observations for F_nY_{356} , activity decreases in the order $Y > 3,5-F_2Y > 2,3-F_2Y > 2,3,5-F_3Y \approx 2,3,6-F_3Y$ (only at position 730). These observations suggest that the observed activities at all three positions report on the same step(s) during turnover. Immediately apparent is the fact that $Y_{731}F_nY-\alpha 2$ and $Y_{730}F_nY-\alpha 2$ are active over the entire pH regime. That both UAAs at these positions are active is surprising, given our prediction of collinear PCET in the $\alpha 2$ subunit. Focusing on $Y_{730}(2,3,5)F_3Y-\alpha 2$ and $Y_{731}(2,3,5)F_3Y-\alpha 2$, 2,3,5- F_3Y is estimated to be 96–98% deprotonated at the two positions at pH 9.0. However, both mutants retain 15–20% of their maximum activity at this pH (Table 1.1). These data can be interpreted in one of two ways: either our model for collinear PCET through these positions is incorrect or a different mechanism for radical propagation is operative at high pH that facilitates nucleotide reduction. The ENDOR data collected on $NH_2Y_{730}\cdot$ and $NH_2Y_{731}\cdot$ provide strong support for collinear PCET.^{57,85} Thus, we favor the latter model where the mechanism of radical propagation changes at high pH. One way in which the mechanism could change is if C_{439} is deprotonated. A

deprotonated C₄₃₉ would rule out the need for a proton acceptor for this residue and also make oxidation of C₄₃₉ easier.^{91,92} However, deprotonation of C₄₃₉ alone is not sufficient to explain our observed results. For example, oxidation of the F_nY₇₃₀⁻ phenolate by Y₇₃₁• would require PT concomitant with ET to generate the Y₇₃₁ phenol. Similarly, oxidation of Y₇₃₀ by F_nY₇₃₁• at high pH would require transfer of the Y₇₃₀ proton to a residue that is not F_nY₇₃₁. To maintain activity at high pH (Table 1.1), the proton from Y₇₃₀ or Y₇₃₁ must be transferred to a residue that is not the adjacent Y on the pathway. The crystal structures of α2 show no proton acceptors in the immediate vicinity of the pathway Ys; the nearest Asp or Glu is located ~7–10 Å away from the pathway Ys. Thus, PT to a protein residue is not feasible unless the protein undergoes large conformational changes in the active complex. Alternatively, it is possible that RT could occur through a structured water network. Two separate groups have used DFT and QM/MM calculations to suggest that water could mediate PCET between Y₇₃₁, Y₇₃₀ and C₄₃₉.^{93,94} An ordered water molecule is present between Y₇₃₁ and Y₇₃₀ in some crystal structures of wt and mutant α2s.^{37,43,70} In fact, the previously presented ENDOR studies on NH₂Y₇₃₀• suggest the presence of a weak H-bonding interaction between NH₂Y₇₃₀• and this ordered water molecule. In Chapter 4, we present data suggesting that water clusters play a key role in PCET through Y₃₅₆. It is possible that this phenomenon is common to all pathway Ys and warrants further investigation. However, on the basis of the ENDOR data collected on NH₂Y₇₃₀• and NH₂Y₇₃₁•, collinear PCET is favored in α2 at pH 7.6, where RNR activity is typically monitored.

Although the F_nY-RNRs maintained 20–60% activity at pH 9.0 (Table 1.1), we wanted to examine if activity shows any correlation with the pK_a of the F_nY. The specific activities of the F_nY-RNRs were replotted as the percent maximum activity (Figure 1.19) and fit to a two proton ionization model with the pK_as shown in Table 1.2. At each position, the pH rate profiles of all

constructs (Y and F_nY) are similar between pH 6.0 and 7.5 and fits of the data to a two proton ionization model revealed pK₁ values between 6.8 and 7.0 (Table 1.2). In contrast to the behavior on the acidic side, activity on the basic side is affected by the pK_a of the F_nY. Table 1.2 shows the calculated pK_a for each F_nY at each position based on the pK_a perturbation measured with NO₂Y.⁷⁰ The pK_a increases in the order 2,3,5-F₃Y < 3,5-F₂Y < 2,3-F₂Y < Y and as seen in Figure 1.19, activity on the basic side drops off in an identical order (with the exception of Y₇₃₁(2,3)F₂Y-α2). However, we note that the calculated pK₂s do not exactly match the estimated pK_as for the F_nYs at the different positions (Table 1.2). It is possible that the switch in RT mechanism at high pH changes the observed pH rate profiles. Alternatively, the observed deprotonation events might report on the proton dependence of the conformational changes that gate RT. Finally, we compared the pH rate profiles of the F_nY-RNRs generated by the nonsense codon suppression method to the EPL proteins. All EPL pH rate profiles fit to an identical pK₁ (7.1) and pK₂ (8.7–8.8) and are not affected by the variations in the pK_as of the F_nYs. These data are consistent with the conclusion that the two mutations required for EPL (V₃₅₃G, S₃₅₄C) alter the rate-limiting step of the reaction.

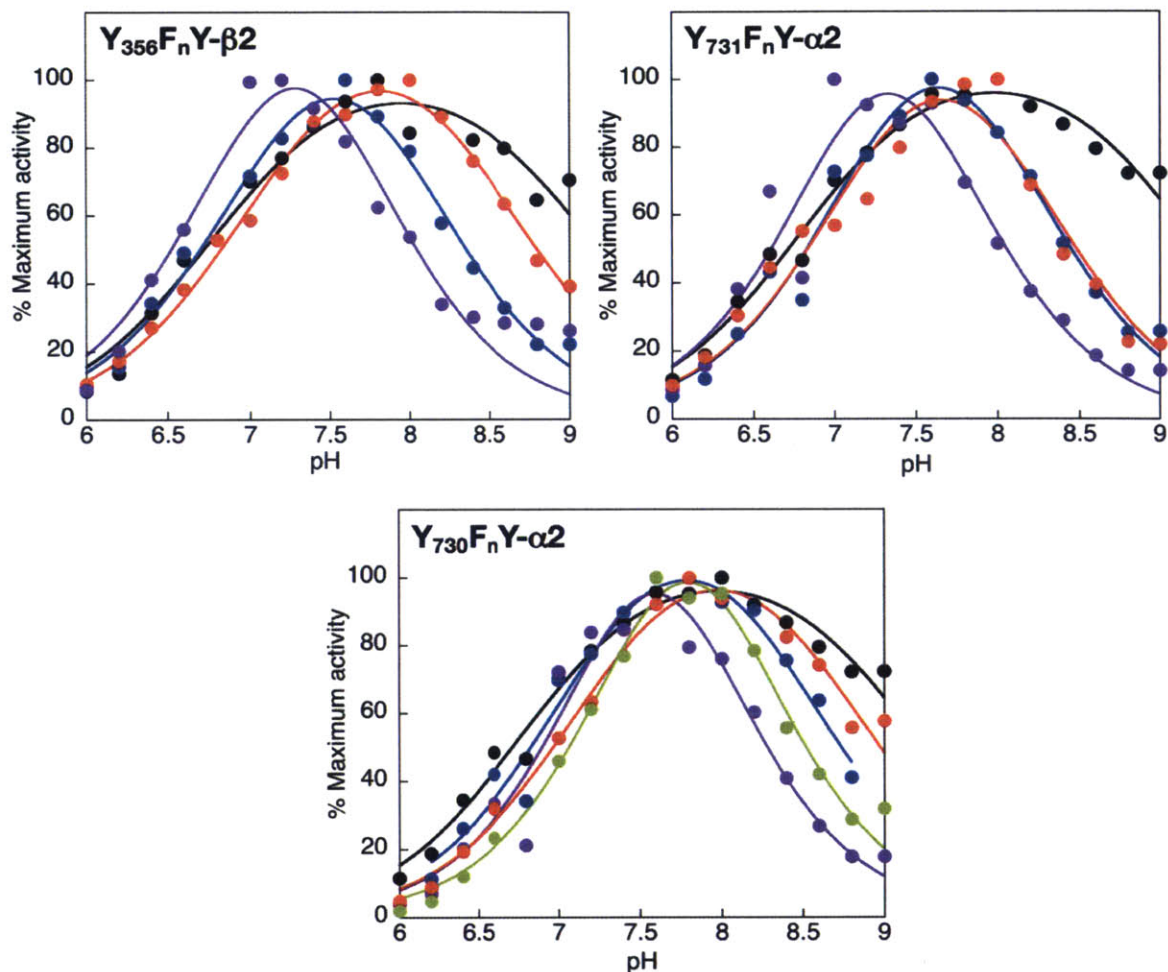


Figure 1.19 Normalized activities of $Y_{356}F_nY-\beta 2$, $Y_{731}F_nY-\alpha 2$ and $Y_{730}F_nY-\alpha 2$ as a function of pH. The specific activities shown in Figures 1.17 and 1.18 were replotted as the percent maximum activity. The color code is as follows: Y (black), 3,5- F_2Y (blue), 2,3- F_2Y (red), 2,3,5- F_3Y (purple) and 2,3,6- F_3Y (green). The black lines represent fits to a two proton ionization model with the pK_a values shown in Table 1.2.

Table 1.2 pK_a s obtained by fitting the experimental pH rate profiles to a two-proton ionization model.

Position	Y			2,3,5- F_3Y			2,3,6- F_3Y			3,5- F_2Y			2,3- F_2Y		
	pK_1	pK_2	pK_a^a	pK_1	pK_2	pK_a^a	pK_1	pK_2	pK_a^a	pK_1	pK_2	pK_a^a	pK_1	pK_2	pK_a^a
EPL	7.1	8.8	10.4	7.1	8.7	6.8	7.5	8.7	7.4	7.1	8.7	7.6	7.0	8.7	8.2
356	6.8	9.0	10.4	7.0	7.5	6.8	-	-	7.4	7.0	8.0	7.6	7.0	8.6	8.2
731	6.8	9.0	10.9	7.0	7.6	7.3	-	-	7.9	7.1	8.1	8.1	7.2	8.1	8.7
730	6.8	9.0	11.2	7.3	7.8	7.6	7.6	7.9	8.2	7.0	8.5	8.4	7.2	8.7	9.0

^a The pK_a s were obtained by adding +0.4, +0.9 and +1.2 units to the solution pK_a values for positions 356, 731 and 730 respectively.

With the combined results presented in this section we conclude that the pH rate profiles do not report on the mechanism of PCET at any position; the pH dependence of $Y_{356}F_nY-\beta_2$, $Y_{731}F_nY-\alpha_2$ and $Y_{730}F_nY-\alpha_2$ are remarkably similar although PT and ET are proposed to be orthogonal in β_2 and collinear in α_2 . It is likely that the change in mechanism that occurs upon deprotonation of the pathway Ys results in a rate constant for RT that is still faster than the conformational changes that govern turnover. The observed pH dependence likely reports on the proton dependence of these conformational changes.

A very important mechanistic insight is provided by the pH rate profiles discussed herein. The data strongly support the conclusion that turnover does not require PT through any of the pathway Ys. In fact, in Chapter 4 we present evidence that suggests that PT is not a requirement even at Y_{122} . Y oxidation at physiological pH requires the concerted loss of a proton and an electron. However, it appears that RNR can tolerate the removal of protons from the RT pathway by allowing nucleotide reduction to occur via ET.

1.5 THERMODYNAMIC LANDSCAPE OF THE RT PATHWAY

1.5.1 Thermodynamic landscape of the pathway prior to the UAA work. Thus far, we have described our efforts to understand PT during RT in the class Ia RNR and delineate the mechanism of PCET at each pathway residue. The second feature of RNR catalysis that governs kinetics is the ability of the protein environment to modulate the reduction potentials of the pathway Ys. Shown in Figure 1.20 is our original model for the thermodynamics of the RT pathway that was proposed in 2003.⁴⁹ Y₁₂₂• is placed as the minimum on the reaction landscape primarily due to the remarkable stability of this species ($t_{1/2}$ of 4 days¹⁵). The placement of W₄₈, the pathway Ys and C₄₃₉ is largely based on reduction potential measurements performed on the blocked amino acids.^{79,91,95} At the time we proposed this model, we noted that the protein environment could perturb the potentials of the pathway Ys but nonetheless suggested that oxidation of C₄₃₉ by Y₁₂₂• is thermodynamically uphill and driven forward by rapid irreversible loss of water during nucleotide reduction (10^6 – 10^8 s⁻¹).⁹⁶⁻⁹⁸ We now have experimental evidence supporting a thermodynamically uphill RT pathway (Ref. 41 and Chapter 4). The first part of this section focuses on thermodynamic perturbations that can be introduced to RNR, and the effects of these perturbations on turnover. These studies provide upper and lower limits for the reduction potential range within which RNR can operate. The second part of this section addresses our efforts to map the thermodynamic landscape of the RT pathway.

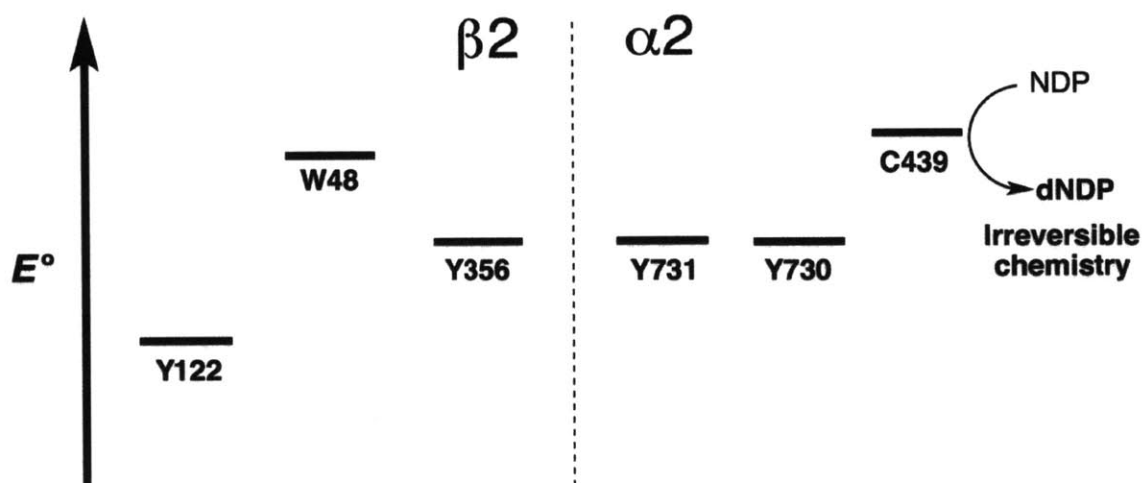


Figure 1.20 Original thermodynamic landscape of the RT pathway. This landscape is proposed in our 2003 review article based on the solution potentials of Y,⁹⁵ W^{79,95} and C⁹¹ available at the time. Y₁₂₂ is placed as the thermodynamic minimum on pathway due to its remarkable stability.

1.5.2 Tolerance of the RT pathway to thermodynamic perturbations. The UAAs that we have utilized in all our studies have been strategically chosen to perturb the reduction potentials of pathway Ys such that mechanistic details of RT can be elucidated. Our earliest work sought to obtain evidence that Y•s are involved in the long-range oxidation process and DOPA and NH₂Y were chosen to function as radical sinks. A single pulse radiolysis measurement estimates the reduction potential of DOPA as 260 mV lower than Y.⁸² The reduction potential of NH₂Y is still an active area of investigation with preliminary work suggesting that this analog is ~400 mV easier to oxidize than Y (Lee, Huynh, Tommos, Nocera and Stubbe unpublished results). As predicted, the reaction of DOPA- or NH₂Y-substituted RNRs with CDP and ATP generate a stable DOPA• or NH₂Y•.^{40,59,83} However, kinetic studies performed on the two systems suggest that whereas DOPA• is unable to catalyze nucleotide reduction,⁴⁰ NH₂Y• maintains 3–12% of the wt activity (Table 1.3, Figure 1.21).^{59,83} Whether NH₂Y• is indeed catalytically active, or whether the observed activity is associated with contaminating endogenous RNR,²⁷ is still an active area of focus in the lab. If the NH₂Y mutants are active, then the protein must be capable of

conformationally perturbing NH_2Y such that RT proceeds. Extensive kinetic studies performed on $\text{NH}_2\text{Y}\cdot$ suggest that there might be active and inactive populations of this radical.⁷³ Unfortunately, the active $\text{NH}_2\text{Y}\cdot$ appears to be the minor species, and the observed turnover is close to the detection limits of our assay methods.⁵⁹ Nonetheless, we conclude from these studies that lowering the reduction potential of a pathway Y by > 200 mV abolishes activity. This interpretation is bolstered by the results of our studies with NO_2Y in place of Y_{356} , Y_{731} or Y_{730} .⁷⁰ Based on the solution DPV data collected on the *N*-acetyl 3-nitro-*L*-tyrosinamide, NO_2Y is ~ 200 mV more oxidizing than Y at pH 7.0.⁶⁴ Accordingly, incorporation of NO_2Y at any pathway position eliminates all activity (Table 1.3, Figure 1.21).⁷⁰ These studies provide the upper and lower boundaries of the reduction potentials that allow RNR activity.

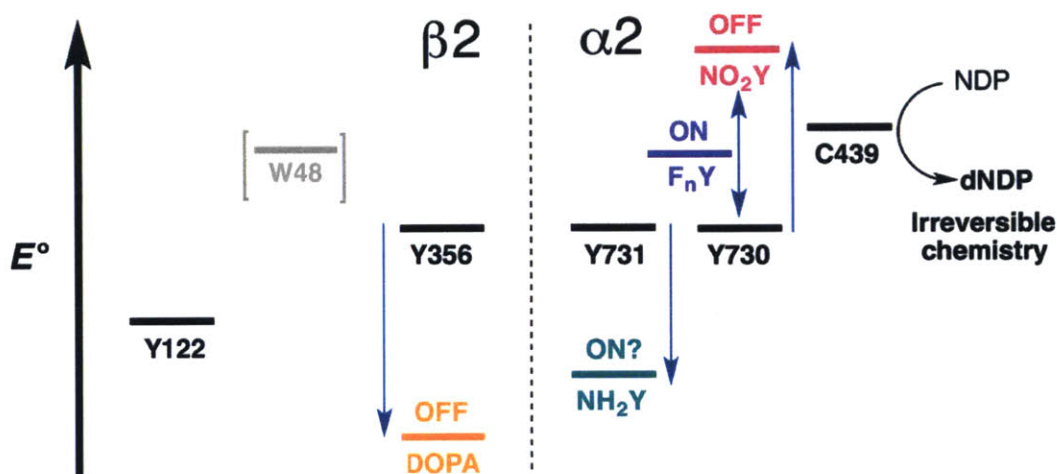


Figure 1.21 Perturbation of the thermodynamic landscape with UAAs. OFF indicates that the UAA mutant is incapable of turnover, whereas ON implies that catalysis is still possible albeit at lowered rates. UAAs that access the potential regime between DOPA and NO_2Y are ON. All activity measurements are reported at 25 °C and pH 7.6. DOPA has been site-specifically inserted via EPL at a single position on pathway (Y_{356}) located on the flexible C-terminal tail of $\beta 2$.⁴⁰ NH_2Y ,^{59,83} F_nY ^{72,73} and NO_2Y ⁷⁰ have been incorporated at Y_{356} , Y_{731} and Y_{730} using the nonsense codon suppression method. Each of these UAAs is shown at only one position for the sake of clarity.

Based on our observations with DOPA and NO₂Y, we hypothesized that perturbing the reduction potential of a pathway Y by < 200 mV could change the rate-limiting step of the reaction from the conformational change to ET. The solution DPV data presented in section 1.2.5 suggest that the F_nYs (-30 mV to +100 mV compared to Y) could span the desired reduction potential range. As noted earlier, our initial focus on replacement of Y₃₅₆ with F_nYs (n = 2, 3, 4), used the only available methodology, EPL.⁶⁷ The pH rate profiles of EPL-Y₃₅₆F_nY-β2 show no correlation between activity and the protonation state of F_nY (Figure 1.17A, Tables 1.1 and 1.2). The pH rate profiles of EPL-Y₃₅₆F_nY-β2 (3,5-F₂Y, 2,3,5-F₃Y and 2,3-F₂Y), although very similar that of EPL-Y between pH 6.5–7.5, decline in activity at pH > 7.5 in a fashion that appears to correlate with the reduction potential difference between each F_nY and Y (Table 1.1). This effect is apparent when the activity of each EPL-Y₃₅₆F_nY (vs EPL-Y) is replotted as a function of the reduction potential difference between F_nY and Y (Figure 1.20A). From the data shown in Figure 1.22A we conclude that activity falls into three regimes based on ΔE_p (F_nY–Y). When ΔE_p is < 80 mV (regime 1), EPL-Y₃₅₆F_nYs behave similarly to EPL-Y, with activities that range from 80–100% of EPL-Y. In regime 3, where ΔE_ps are > 200 mV, nucleotide reduction is completely shut down, an observation that is consistent with the data collected on NO₂Y-RNRs.^{64,70} In regime 2, 80 mV < ΔE_p < 200 mV, activity appears to directly correlate with ΔE_p and is independent of the nature of the Y analog at position 356. It is hypothesized that when ΔE_p is in regime 2, RT is modulated such that ET through Y₃₅₆ and not the conformational change(s), is rate-limiting for turnover. However, a reaction mixture of EPL-2,3,5-F₃Y, α2, CDP and ATP analyzed by SF UV-vis and RFQ-EPR spectroscopic methods at a pH where ΔE_p is within regime 2, do not exhibit any pathway radical intermediates, as evidenced by a lack of the characteristic 2,3,5-F₃Y• spectroscopic features (Figure 1.25).⁹⁹

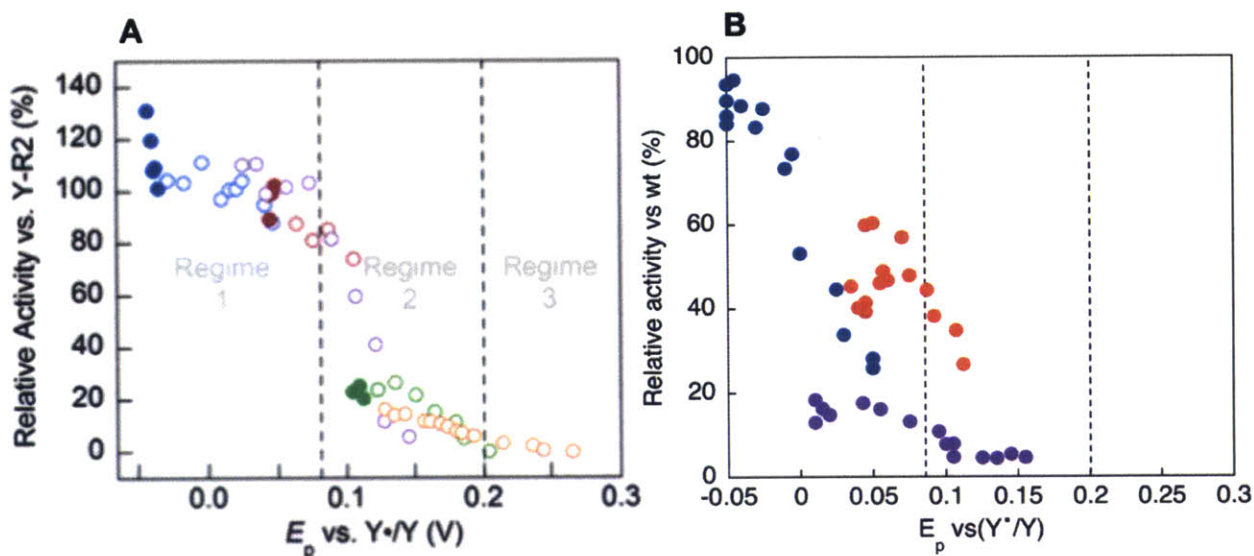


Figure 1.22 Relative activities of $Y_{356}F_nY$ - $\beta 2$ vs wt- $\beta 2$. A. $Y_{356}F_nY$ - $\beta 2$ s were generated by the EPL method. B. $Y_{356}F_nY$ - $\beta 2$ s were generated by the nonsense codon suppression method. The color code is as follows: 3,5- F_2Y (blue), 2,3- F_2Y (red), 2,3,5- F_3Y (purple), 2,3,6- F_3Y (green) and F_4Y (orange). The black dotted lines in panel B indicate the define the ΔE_p regimes that were identified from the EPL data. In panel A, the closed and open circles represent pH values where F_nY is protonated and deprotonated respectively. Panel A is reproduced from Ref. 67.

The low radical yields ($\sim 0.3 Y\cdot/\beta 2$, Table A1.2, Appendix 1) and reduced catalytic activity (25% compared to wt RNR) of EPL- $\beta 2$ hampered the detection of radical intermediates using current biophysical methods (SF-vis and RFQ-EPR). Thus, $Y_{356}F_nY$ - $\beta 2$ s were generated using nonsense codon suppression, a method that affords full-length proteins with greater radical content (0.7–0.9 $Y\cdot/\beta 2$, Table A1.2). The pH rate profiles of $Y_{356}F_nY$ - $\beta 2$ s were collected and the analysis presented above for the EPL proteins was repeated (Figure 1.22B). The pH rate profiles of $Y_{356}F_nY$ - $\beta 2$ generated by the nonsense codon suppression method are distinct from the EPL- $Y_{356}F_nY$ - $\beta 2$ pH rate profiles (Figures 1.17–19 and Table 1.2), with activities that reveal a dependence on the pK_a of F_nY (Table 1.2). Consistent with the distinct pH rate profiles, when relative activity (vs wt- $\beta 2$) is plotted as a function of ΔE_p (vs $Y\cdot/Y$), no correlation is observed (Figure 1.22B). In the case of EPL- $Y_{356}F_nY$, when ΔE_p is < 80 mV, EPL- $Y_{356}F_nY$ behaves similarly to EPL-Y with activities that range from 80% to 100%. In contrast to these observations, when

ΔE_p is < 80 mV (black dotted line in Figure 1.22B), $Y_{356}F_nY$ - $\beta 2$ activity is highly variable (15–100% of wt- $\beta 2$). Moving on to regime 2, the EPL data suggest that when ΔE_p lies between 80 and 200 mV, the rate-limiting step switches from the conformational change to ET. By contrast, $Y_{356}F_nY$ - $\beta 2$ demonstrates no correlation between activity and ΔE_p even in the predicted regime 2 (region between the two dotted lines, Figure 1.22B). These data suggest that we cannot access a regime where ET is rate-limiting by incorporating UAAs via the nonsense codon suppression method. Analysis of the $Y_{731}F_nY$ - $\alpha 2$ and $Y_{730}F_nY$ - $\alpha 2$ pH rate profiles provide results that are similar to $Y_{356}F_nY$ - $\beta 2$, and reveal a lack of correlation between activity and ΔE_p . Thus, the two mutations introduced into $\beta 2$ for EPL purposes ($V_{353}G$, $S_{354}C$) change the rate-limiting step of the reaction, allowing accessibility to a state where ET is slow and rate-limiting. The work of Ellen C. Minnihan on the F_nY -substituted RNRs support that the reduction potential of a pathway Y can be varied between -30 mV and +100 mV without a detrimental effect on turnover, consistent with our DOPA and NO_2Y studies predicting that a ΔE_p of >200 mV abolishes activity (Table 1.3).

Table 1.3 Reduction potential range within which RNR can produce deoxynucleotides.

Position	UAA	pK _a ^a	ΔE_p^b (mV) pH 7.6	Specific activity at pH 7.6 vs wt (%)
122	3,5-F ₂ Y	10.2	-30	85
	2,3,5-F ₃ Y	9.4	10	25
	2,3-F ₂ Y	10.8	45	6.5
	2,3,6-F ₃ Y	10.0	100	5
	NO ₂ Y	10.1	200	100 s ⁻¹ ^c
356	DOPA	10.1	-260	- ^e
	NH ₂ Y	10.4	-400 ^d	9–12
	3,5-F ₂ Y	7.6	-60	90
	2,3-F ₂ Y	8.2	35	46
	2,3,5-F ₃ Y	6.8	33	11
	NO ₂ Y	7.5	200	- ^e
731	NH ₂ Y	10.9	-400 ^d	5–10
	3,5-F ₂ Y	8.1	-60	70
	2,3-F ₂ Y	8.7	35	27
	2,3,5-F ₃ Y	7.1	10	13
	NO ₂ Y	8.0	200	- ^e
730	NH ₂ Y	11.2	-400 ^d	3–9
	3,5-F ₂ Y	8.4	-60	90
	2,3-F ₂ Y	9.0	40	32
	2,3,5-F ₃ Y	7.6	8	15
	2,3,6-F ₃ Y	8.2	90	15
	NO ₂ Y	8.3	191	- ^e

All proteins were generated by the nonsense codon suppression method. The activities of Y₁₂₂F_nY- β 2 (0.8–1.0 F_nY•/ β 2) and Y₃₅₆F_nY- β 2 (0.7–0.9 Y•/ β 2) are not scaled for radical content. The radical content of each F_nY construct is presented in Table A1.2 (Appendix 1).

^a Predicted effective pK_as for each UAA based on the pK_a measurements made with NO₂Y-RNRs.⁷⁰ The solution pK_a values are increased by +3, +0.4, +0.9 and +1.2 units for positions 122, 356, 731 and 730 respectively.

^b The ΔE_p s were calculated from the solution DPV data^{64,74} collected on the *N*-acetylated tyrosinamide derivatives accounting for the pK_a perturbation at each position.

^c Turnover occurs on one α /NO₂Y- β pair before enzyme inactivation.⁴¹ The first turnover occurs at ~100 s⁻¹, 10-fold faster than steady-state turnover in the wt enzyme.

^d Lee, Huynh, Tommos, Nocera, Stubbe unpublished results.

^e Measured specific activities are consistent with contaminating endogenous RNR.

1.5.3 Current thermodynamic landscape for the PCET pathway. The results described thus far have focused on the thermodynamic regime that is accessible to manipulation without detrimental effects on the nucleotide reduction activity of RNR. However, in our original thermodynamic model (Figure 1.20), we noted that the protein environment can have a significant impact on the reduction potentials of the pathway Ys. Particularly notable is the long half-life of $Y_{122}\bullet$ (4 days at 25 °C) compared to Y•s in solution (microseconds). The first experimental insight into the relative reduction potentials of the pathway Ys was obtained when the driving force of the reaction was increased by replacement of Y_{122} with NO_2Y . NO_2Y incorporation in place of Y_{356} , Y_{731} or Y_{730} shuts down nucleotide reduction due to the inability of Y• to oxidize NO_2Y . We speculated that $NO_2Y\bullet$ might be generated at position 122. In wt- $\beta 2$, the diferric-Y• cofactor can be self assembled *in vitro* by the addition of Fe^{2+} and O_2 to the apo protein.¹⁵ During this process, a highly oxidizing Fe(IV)/Fe(III) intermediate (**X**) is generated that is directly responsible for oxidation of Y_{122} . We predicted that **X** might be a sufficiently strong oxidant to generate $NO_2Y\bullet$. Indeed, incubation of apo $Y_{122}NO_2Y$ - $\beta 2$ with Fe^{2+} and O_2 rapidly (within 0.5 s) produces a short lived $NO_2Y\bullet$ ($t_{1/2}$ of 40 s at 25 °C).⁴¹ Excitingly, triple-mixing experiments where $NO_2Y\bullet$ is formed as described and immediately mixed with $\alpha 2$, CDP and ATP show rapid conversion of 0.5 equiv. $NO_2Y\bullet$ to NO_2Y^- (100–300 s^{-1}), rapid production of dCDP (0.5 equiv./ $NO_2Y\bullet$, 100 s^{-1}) and accumulation of 0.5 equiv. $Y_{356}\bullet$ at rate constants of 100–300 s^{-1} (Figure 1.23).⁴¹ These amounts of $Y_{356}\bullet$ and dCDP are consistent with our two or none radical distribution model and half-sites reactivity in RNR and suggest that $Y_{122}NO_2Y$ - $\beta 2$ performs only a single turnover prior to enzyme inactivation. Generation of NO_2Y^- instead of the anticipated phenol is surprising, given the pK_a perturbation predicted for this position ($>+3$ units). As noted in section 1.4.2, Mössbauer studies show that the first step in RT involves PT from the Fe1- H_2O to $Y_{122}\bullet$ and that the conformational

changes that trigger RT might be related to this step.⁵⁴ The observation of NO_2Y^- suggests that $\text{Fe1-H}_2\text{O}$ cannot protonate this Y analog and can be rationalized by the differences in the $\text{p}K_a$ of NO_2Y (7.1) and Y (10.0). This uncoupling of the PT and ET events allows $\text{Y}_{122}\text{NO}_2\text{Y-}\beta 2$ to partially overcome the conformational gate, and rate constants of $100\text{--}300\text{ s}^{-1}$ are measured for $\text{Y}_{356}\bullet$ formation and nucleotide reduction. Finally, $\text{Y}_{356}\bullet$ accumulates during reverse RT due to its inability to re-oxidize NO_2Y^- . On the basis of our observations for NO_2Y at positions 356, 731 and 730, we propose that this re-oxidation reaction could be $\geq 200\text{ mV}$ uphill.

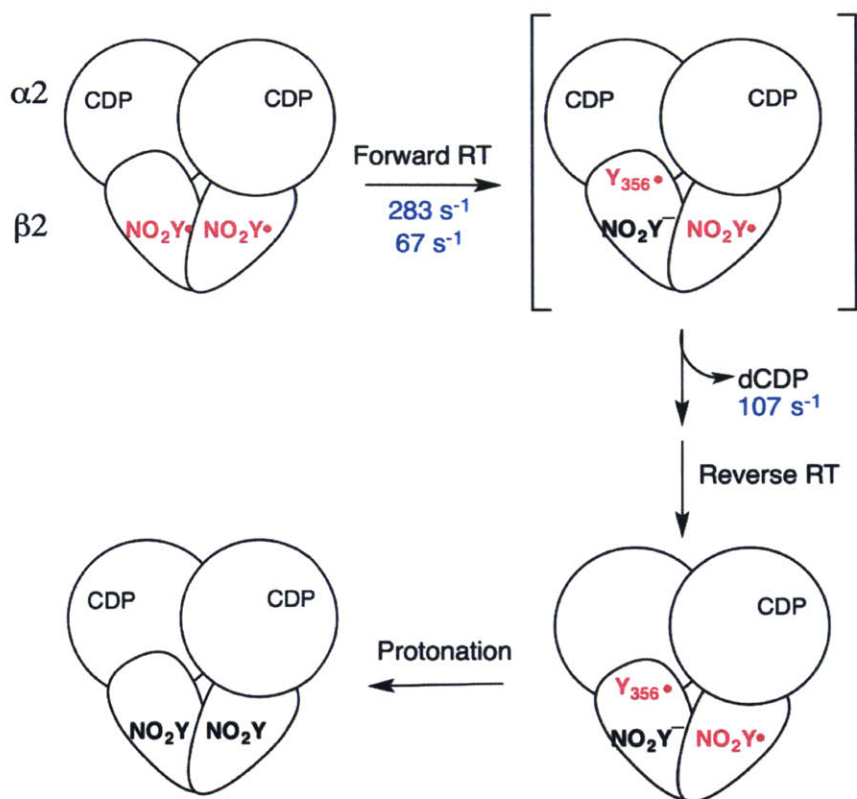


Figure 1.23 Kinetic model for the reaction of $\text{Y}_{122}\text{NO}_2\text{Y-}\beta 2$, $\alpha 2$, CDP and ATP. It is likely that the first fast phase for dCDP formation is small in amplitude and cannot be detected due to the detection limits of the RCQ method.

Assignment of the observed $\text{Y}\bullet$ as $\text{Y}_{356}\bullet$ is primarily based on PELDOR spectroscopy experiments that measured the $\text{NO}_2\text{Y}\bullet\text{--Y}\bullet$ distance. Surprisingly, two distance measurements are

recorded for this reaction mixture.⁴⁸ First, a 30 Å distance is observed that is proposed to reflect the NO₂Y•–Y₃₅₆• distance on the basis of our studies with Y₃₅₆DOPA-β²⁴⁵ and Y₃₅₆NH₂Y-β²⁷³ (Figure 1.13). Second, a small PELDOR signal is observed that corresponds to a distance of 38–39 Å. The latter distance is similar to that observed for Y₁₂₂•–NH₂Y₇₃₁• or Y₁₂₂•–NH₂Y₇₃₀•⁴⁵ and suggests electron delocalization over the pathway Ys. The PELDOR data provides the first evidence for equilibration of Y•s in the RT pathway and afforded the opportunity to assess the effect of protein environment on the reduction potentials of the Y. To quantitate the relative amounts of the different radicals, we installed 3,5-F₂Y at position 731 or 730. The substantial overlap in the EPR spectra of Y•s makes deconvolution of reaction mixtures containing multiple Y•s challenging. As outlined below and in Chapter 4, F_nY•s possess unique spectroscopic features in the high- and low-field sides of the spectrum that facilitate easy detection of small quantities of these radicals. Quantitation of Y₃₅₆• and 3,5-F₂Y₇₃₁• (or 3,5-F₂Y₇₃₀•) provide a Δ*E* of ~100 mV between the Ys in α2 and Y₃₅₆ (Figure 1.24). Finally, our current thermodynamic landscape places C₄₃₉ only slightly higher than Y₇₃₀. This placement is based on recent electrochemical measurements made on glutathione and tyrosine demonstrating that C and Y have approximately equal midpoint potentials at pH 7.0 (0.94 and 0.93 V, respectively).¹⁰⁰ However, recent DFT calculations have suggested that oxidation of C₄₃₉ by Y₇₃₀• could be as much as 120 mV uphill.⁸⁵ In addition to an uphill RT pathway, extensive studies on model systems have shown that abstraction of the 3' H-atom by C₄₃₉• is also uphill (3–6 kcal/mol).¹³ The implications of this overall uphill reaction landscape to turnover are discussed in Chapter 4.

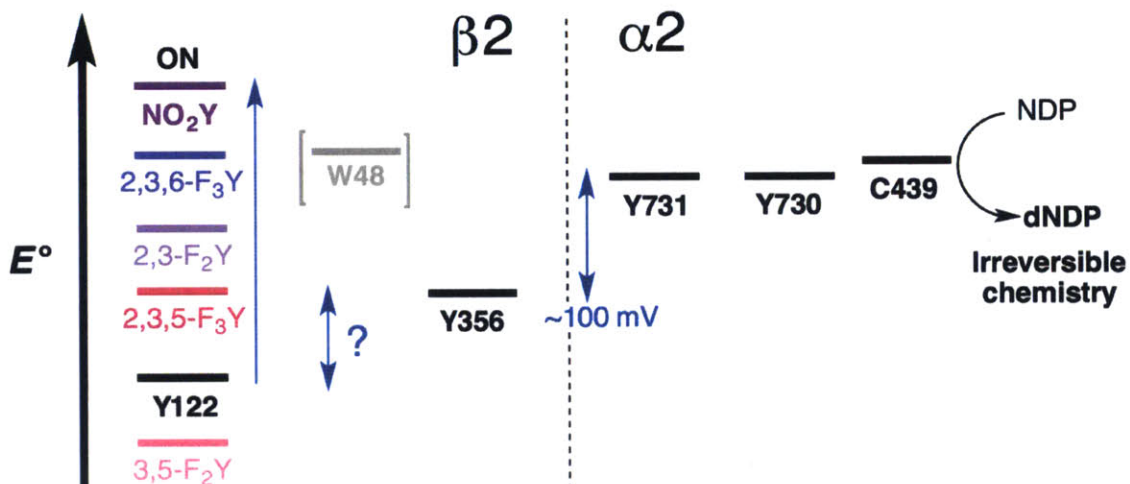


Figure 1.24 Thermodynamic landscape of the RT pathway prior to the work presented in this thesis.

Whereas $Y_{122}NO_2Y$ - $\beta 2$ was instrumental in mapping the thermodynamic landscape at the subunit interface and within $\alpha 2$, little information was available about the landscape within $\beta 2$. Mainly, equilibration between $NO_2Y\bullet$ and $Y_{356}\bullet$ could not be observed because oxidation of Y_{356} by $NO_2Y\bullet$ is irreversible. We postulated that lowering the driving force of RT might afford the opportunity to perform multiple turnovers while maintaining the ability to accumulate $Y_{356}\bullet$. With this goal in mind, we incorporated F_nY s ($n = 2, 3$) at position 122. Based on the solution DPV data collected on the *N*-acetyl tyrosinamide derivatives, we constructed the thermodynamic landscape shown in Figure 1.24 that demonstrates the predicted trend for the F_nY s. Incubation of apo $Y_{122}F_nY$ - $\beta 2$ s with Fe^{2+} and O_2 affords self-assembly of stable $F_nY\bullet$ s which have $t_{1/2}$ s of 30 min–several hours at 25 °C.⁷¹⁻⁷³ The X-band EPR spectra of all $F_nY\bullet$ s are shown in Figure 1.25. Readily apparent are the unique spectroscopic features on the high- and low-field sides of the spectra that are common to all $F_nY\bullet$ s but not present in $Y\bullet$. These features have been instrumental in mapping the thermodynamic landscape of the RT pathway (Ref. 48 and Chapter 4).

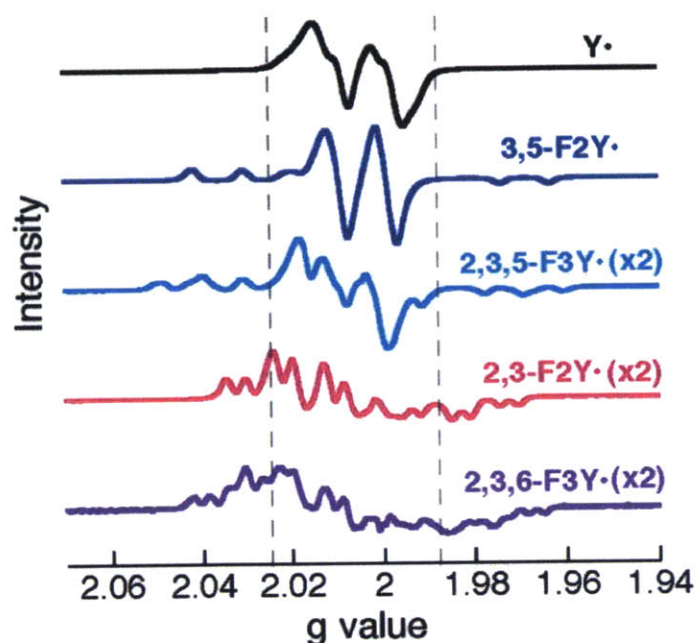


Figure 1.25 X-band EPR spectra of $F_n Y\bullet$. Figure reproduced from Ref. 72.

In contrast to $Y_{122}NO_2Y\text{-}\beta 2$, all $Y_{122}F_nY\text{-}\beta 2$ s can catalyze multiple turnovers with activities that are 5–85% of wt- $\beta 2$ (Table 1.3). Excitingly, with the exception of $Y_{122}(3,5)F_2Y\text{-}\beta 2$, the reaction of $Y_{122}F_nY\text{-}\beta 2$, $\alpha 2$, CDP and ATP accumulates $Y_{356}\bullet$ (Table 1.3).⁷³ The assignment of this radical is based on site-directed mutagenesis studies⁷³ and the similarity of the X-band EPR spectra of $Y_{356}\bullet$ observed in these reactions with that seen in $Y_{122}NO_2Y\text{-}\beta 2$ (Figure 1.24). In the case of $Y_{122}(2,3,5)F_3Y\text{-}\beta 2$ only, the Bennati lab has confirmed the identity of $Y_{356}\bullet$ by PELDOR spectroscopy.⁴⁶ The results observed with $Y_{122}F_nY\text{-}\beta 2$ are in direct agreement with the predicted thermodynamic landscape (Figure 1.22). $Y_{122}(3,5)F_2Y\text{-}\beta 2$ is predicted to be ~ 30 mV less oxidizing than Y .^{74,77} In accordance with this measurement, $Y_{122}(3,5)F_2Y\text{-}\beta 2$ behaves in an almost identical manner to wt- $\beta 2$. We propose that the ability to visualize $Y_{356}\bullet$ is related to partial unmasking of the conformational gate, allowing direct observation of driving force modulation on RT. At least in the case of $Y_{122}(2,3,5)F_3Y\text{-}\beta 2$, we demonstrate that the increased driving force slows down re-oxidation of 2,3,5- F_3Y by $Y_{356}\bullet$ (Chapter 3). This slow re-oxidation is rate-limiting during steady-

state turnover and is responsible for the ability to observe $Y_{356}\bullet$. Finally, the ability of $Y_{122}F_nY-\beta_2$ s to reversibly oxidize Y_{356} provides the first opportunity to investigate equilibration of $F_nY_{122}\bullet$ and $Y_{356}\bullet$. In Chapter 4, we present extensive EPR spectroscopic studies that monitor the equilibration of $2,3,5-F_3Y\bullet$ and $Y_{356}\bullet$ as a function of temperature and pH. These studies allow estimation of ΔE between F_3Y_{122} and Y_{356} , providing insight into the thermodynamic landscape of the RT pathway within β_2 .

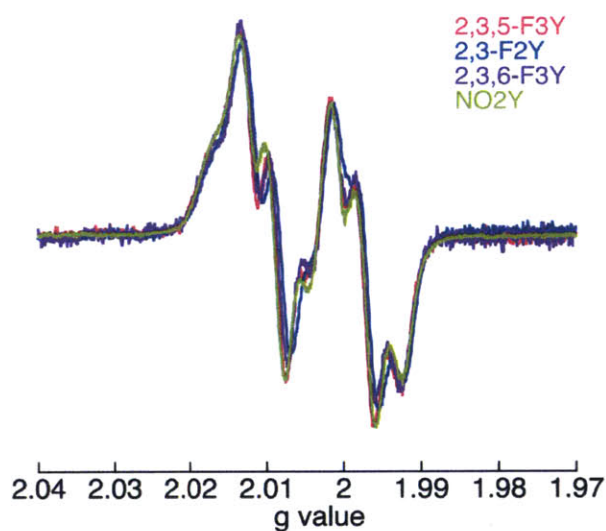


Figure 1.26 Overlay of the EPR spectra of $Y_{356}\bullet$ generated in each $Y_{122}F_nY-\beta_2$ reaction compared to the $Y_{356}\bullet$ observed in the $Y_{122}NO_2Y-\beta_2$ reaction.

1.6 CHAPTER PREVIEW

At the time the work described in this thesis was initiated, our lab had successfully incorporated a range of UAAs with different properties (Figure 1.10) that could probe different aspects of RNR catalysis. This thesis is focused on using these probes to unravel details of RT within the $\beta 2$ subunit and at the β/α interface. In **Chapter 2**, we describe the results of our fruitful collaboration with Cecilia Tommos that is focused on obtaining formal reduction potentials for F_nY within a structured protein environment. **Chapters 3** and **4** constitute the majority of this thesis and describe the results of our studies with $Y_{122}(2,3,5)F_3Y-\beta 2$. These studies allow construction of a detailed kinetic model for $Y_{122}(2,3,5)F_3Y-\beta 2$, provide insight into the thermodynamic landscape within the $\beta 2$ subunit, and present the first direct evidence for transfer of the Y_{356} proton to solvent upon oxidation of this pathway Y . In **Chapter 5**, we focus on identifying if PT at the subunit interface involves E_{350} , a conserved residue on the C-terminal tail of $\beta 2$. Our studies indicate that E_{350} is involved in subunit interaction and the protein conformational change(s) that initiate RT and provide no evidence for its involvement in PT. Finally, in **Chapter 6** we describe some of our efforts to stabilize the $\alpha 2\beta 2$ complex with the goal of obtaining a structure of the active complex that could provide insight into PCET across the β/α interface. A more detailed description of the individual chapters is presented below.

To assist in interpretation of our mechanistic studies on RNR, we have focused our attention on obtaining true reduction potentials for the F_nY s within a protein environment. For this purpose, we utilize a model three-alpha helix protein containing a single buried redox active Y (α_3Y). The reversible $Y-O\bullet/Y-OH$ redox properties of the α_3Y model protein enable access to the electrochemical and thermodynamic properties of F_nY . In Chapter 2, we describe the site-specific incorporation of 3,5- F_2Y at position 32, the dedicated radical site in α_3Y , by *in vivo* nonsense

codon suppression. Incorporation of 3,5-F₂Y gives rise to very minor structural changes in the protein scaffold at pH below the apparent p*K* (8.0 ± 0.1) of the unnatural residue. Square-wave voltammetry on α₃(3,5)F₂Y provides an *E*^o(Y-O•/Y-OH) of 1026 ± 4 mV versus the NHE (pH 5.70 ± 0.02) and shows that the fluoro-substitutions lower *E*^o by 30 ± 3 mV. These results provide the first measurement of the formal reduction potential of 3,5-F₂Y within a well-structured protein. Interestingly, the protein *E*^o' values differ significantly (+150 mV) from the peak potentials derived from irreversible voltammograms of Ac-3,5-F₂Y-NH₂. These studies provide insight into the effect of protein environment on the reduction potential of amino acid residues, and are discussed relative to the RT pathway in RNR.

Chapter 3 describes our detailed kinetic studies with Y₁₂₂(2,3,5)F₃Y-β₂. This mutant perturbs the driving force for radical propagation, while maintaining catalytic activity (1.7 s⁻¹). RFQ-EPR spectroscopy and RCQ analysis of the Y₁₂₂(2,3,5)F₃Y-β₂, α₂, CDP and ATP reaction show generation of 0.5 equiv. Y₃₅₆• and 0.5 equiv. dCDP, both at 30 s⁻¹. This amount of pathway radical (and product) is consistent with our two or none radical distribution model and half-sites reactivity in RNR (Figure 1.12). In the absence of an external reducing system, we demonstrate that Y₃₅₆• reduction occurs concomitant with 2,3,5-F₃Y re-oxidation (0.4 s⁻¹). These data provide the first evidence for the disappearance and reappearance of the stable radical at position 122. In the presence of the TR/TRR/NADPH reducing system, a burst of dCDP (0.4 equiv. at 22 s⁻¹) is observed prior to steady-state turnover (1.7 s⁻¹). Steady-state EPR experiments also demonstrate that the concentration of Y₃₅₆• does not change with time. Taken together, these data support that one turnover on one α/Y₁₂₂(2,3,5)F₃Y-β pair occurs prior to the rate-limiting step. With these studies we demonstrate for the first time the ability of a pathway radical in an active α₂β₂ complex

to complete the catalytic cycle and propose a model where reverse RT is rate-limiting during turnover.

Equilibration of $Y_{356}\bullet$, $Y_{731}\bullet$ and $Y_{730}\bullet$ was recently observed when the driving force for RT was increased with $NO_2Y\bullet$ (estimated as 200 mV more oxidizing than Y); however, it has never been detected between $Y_{122}\bullet$ and $Y_{356}\bullet$. In Chapter 4, we show equilibration of $2,3,5-F_3Y_{122}\bullet$ and $Y_{356}\bullet$ as a function of temperature and pH using EPR spectroscopy. Temperature dependent quantitation of the two radical states in the reaction of $Y_{122}(2,3,5)F_3Y-\beta 2$, $Y_{731}F-\alpha 2$, CDP and ATP reveals a break in the Van't Hoff plot at $\sim 13^\circ C$ and provides a $\Delta E^\circ (F_3Y\bullet - Y_{356}\bullet)$ of 16 ± 5 mV at $25^\circ C$. The pH dependence of the reaction (pH 6.8–8.4) reveals that the Y_{356} proton is in rapid exchange with solvent. To provide additional evidence for $Y_{122}\bullet/Y_{356}\bullet$ equilibration, we inserted $3,5-F_2Y$ at Y_{356} and monitored its reaction with $Y_{731}F-\alpha 2$, CDP and ATP at pH 8.2 and $25^\circ C$ by RFQ-EPR spectroscopy. This experiment provides evidence for equilibration between the native $Y_{122}\bullet$ and $3,5-F_2Y_{356}\bullet$. The amount of $3,5-F_2Y_{356}\bullet$ is quantitated as $\sim 3\%$ of the total spin in the reaction mixture, and is consistent with a $\Delta E^\circ (3,5-F_2Y\bullet - Y_{122}\bullet)$ of ~ 70 mV. Extrapolating this observation to wt RNR, we propose a model for the thermodynamic landscape where the RT pathway (Y_{122} to Y_{730}) is ~ 200 mV uphill. The implications of this landscape to turnover are discussed.

The pH dependent studies presented in Chapter 4 suggest that the Y_{356} proton is in rapid exchange with solvent with either an amino acid residue or water functioning as the initial proton acceptor. We and others have previously proposed that E_{350} , a conserved residue on the C-terminal tail of $\beta 2$ could function as the proton acceptor for Y_{356} . In Chapter 5, we attempt to address if E_{350} is involved in PT at the interface, either as a proton acceptor for Y_{356} or as a proton acceptor for Y_{731} . We have previously shown that PT is not obligately coupled to ET at any position on the RT

pathway; 3,5-F₂Y₃₅₆⁻, 3,5-F₂Y₇₃₁⁻ and 3,5-F₂Y₇₃₀⁻ can all catalyze multiple turnovers.⁷³ We hypothesized that if E₃₅₀ is the proton acceptor for Y₃₅₆ (or Y₇₃₁), then in the presence of E₃₅₀X (X = A, D or Q), 3,5-F₂Y₃₅₆ (or 3,5-F₂Y₇₃₁) would be inactive at pH values where the amino acid is protonated, but show activity when 3,5-F₂Y is deprotonated. Surprisingly, 3,5-F₂Y₃₅₆ (or 3,5-F₂Y₇₃₁) is inactive over the entire pH regime when E₃₅₀ is mutated to A, D or Q. These results suggest that the role of E₃₅₀ in RT is not limited to PT at the subunit interface. Competitive inhibition spectrophotometric assays demonstrate that E₃₅₀X (X = D or Q) increases the K_d for subunit interaction by ~10-fold. To address if E₃₅₀ is involved in the protein conformational change(s) that initiates RT, we monitored the reaction of Y₁₂₂(2,3,5)F₃Y-β2 (or Y₁₂₂NO₂Y-β2), α2, CDP and ATP by RFQ-EPR spectroscopy. The inability to detect Y₃₅₆[•] with these analogs supports that radical initiation and conformational gating is affected by E₃₅₀X (X = D or Q). The data together support a structural role for E₃₅₀ in RNR function that is not related to PT.

Whereas the individual subunits of RNR (β2 and α2) have been crystallographically characterized, a structure of the active complex remains elusive. Recently, we showed that formation of NH₂Y₇₃₀[•] produces a kinetically stable α2β2 complex (K_d of 7 nM compared to 0.2 μM for wt RNR).⁴⁷ In Chapter 6, we attempt to identify which chemical steps are required to generate this tight complex. A series of Ni-nitriloacetic acid (NTA) pull-down assays performed with different His₆-α2 (wt or Y₇₃₁F) and untagged β2 constructs (wt, Y₁₂₂NO₂Y-β2, and dithionite-treated β2) demonstrate that formation of a stable complex is a phenomenon common to any condition where a pathway radical intermediate is trapped. These studies also indicate that the lifetime of the tight α2β2 complex may be longer than that of the pathway radical intermediate. A model is put forth where injection of a single electron into the diferric cluster site is sufficient to generate a stable α2β2 complex. Additional experiments to validate this model are proposed.

1.7 REFERENCES

1. Stubbe, J.; van der Donk, W. A. Protein radicals in enzyme catalysis, *Chem Rev* **1998**, *98*, 705-62.
2. Jordon, A.; Reichard, P. Ribonucleotide reductases, *Annu. Rev. Biochem.* **1998**, *67*, 71-98.
3. Hofer, A.; Crona, M.; Logan, D. T.; Sjöberg, B. M. DNA building blocks: keeping control of manufacture, *Crit Rev Biochem Mol Biol* **2012**, *47*, 50-63.
4. Licht, S.; Gerfen, G. J.; Stubbe, J. Thiyl radicals in ribonucleotide reductases, *Science* **1996**, *271*, 477-81.
5. Stubbe, J.; Ackles, D. On the mechanism of ribonucleoside diphosphate reductase from *Escherichia coli*. Evidence for 3'-C-H bond cleavage, *J. Biol. Chem.* **1980**, *255*, 8027-30.
6. Licht, S.; Stubbe, J. Mechanistic investigations of ribonucleotide reductases, *Compr. Nat. Prod. Chem.* **1999**, *5*, 163-203.
7. Mao, S. S.; Holler, T. P.; Yu, G. X.; Bollinger, J. M., Jr.; Booker, S.; Johnston, M. I.; Stubbe, J. A model for the role of multiple cysteine residues involved in ribonucleotide reduction: amazing and still confusing, *Biochemistry* **1992**, *31*, 9733-43.
8. Booker, S.; Licht, S.; Broderick, J.; Stubbe, J. Coenzyme B12-dependent ribonucleotide reductase: evidence for the participation of five cysteine residues in ribonucleotide reduction, *Biochemistry* **1994**, *33*, 12676-85.
9. Wei, Y.; Funk, M. A.; Rosado, L. A.; Baek, J.; Drennan, C. L.; Stubbe, J. The class III ribonucleotide reductase from *Neisseria bacilliformis* can utilize thioredoxin as a reductant, *Proc. Natl. Acad. Sci. U S A* **2014**, *111*, E3756-65.
10. Wei, Y.; Prakash, D.; Ferry, J. G.; Elliot, S. J.; Stubbe, J. A ferredoxin disulfide reductase delivers electrons to the *Methanosarcina barkeri* class III ribonucleotide reductase, *Biochemistry* **2015**, *54*, 7019-28.
11. Mulliez, E.; Ollagnier, S.; Fontecave, M.; Eliasson, R.; Reichard, P. Formate is the hydrogen donor for the anaerobic ribonucleotide reductase from *Escherichia coli*, *Proc. Natl. Acad. Sci. U S A* **1995**, *92*, 8759-62.
12. Wei, Y.; Mathies, G.; Yokoyama, K.; Chen, J.; Griffin, R. G.; Stubbe, J. A chemically competent thiosulfuranyl radical on the *Escherichia coli* class III ribonucleotide reductase, *J Am Chem Soc* **2014**, *136*.
13. Stubbe, J.; van der Donk, W. A. Protein radicals in enzyme catalysis, *Chem. Rev.* **1998**, *98*, 705-62.
14. Cotruvo, J. A.; Stubbe, J. Class I ribonucleotide reductases: metallocofactor assembly and repair in vitro and in vivo, *Annu Rev Biochem* **2011**, *80*, 733-67.
15. Atkin, C. L.; Thelander, L.; Reichard, P.; Lang, G. Iron and free radical in ribonucleotide reductase. Exchange of iron and Mössbauer spectroscopy of the protein B2 subunit of the *Escherichia coli* enzyme, *J. Biol. Chem.* **1973**, *248*, 7464-72.

16. Cotruvo, J. A.; Stich, T. A.; Britt, R. D.; Stubbe, J. Mechanism of assembly of the dimanganese-tyrosyl radical cofactor of class Ib ribonucleotide reductase: enzymatic generation of superoxide is required for tyrosine oxidation via a Mn(III)Mn(IV) intermediate, *J Am Chem Soc* **2013**, *135*, 4027-39.
17. Roshick, C.; Iliffe-Lee, E. R.; McClarty, G. Cloning and characterization of ribonucleotide reductase from *Chlamydia trachomatis*, *J Biol Chem* **2000**, *275*, 38111-19.
18. Jiang, W., Yun, D., Saleh, L., Barr, E. W., Xing, G., Hoffart, L. M., Maslak, M. A., Krebs, C. & Bollinger, J. M., Jr. A manganese(IV)/iron(III) cofactor in *Chlamydia trachomatis* ribonucleotide reductase, *Science* **2007**, *316*, 1188-91.
19. Stubbe, J.; Ator, M. Mechanism of ribonucleoside diphosphate reductase from *Escherichia coli*. Evidence for 3' C-H bond cleavage, *J Biol Chem* **1983**, *258*, 1625-31.
20. Thelander, L.; Larsson, B. Active site of ribonucleoside diphosphate reductase from *Escherichia coli*. Inactivation of the enzyme by 2'-substituted ribonucleoside diphosphates, *J. Biol. Chem.* **1976**, *251*, 1398-405.
21. Stubbe, J.; Kozarich, J. W. Fluoride, pyrophosphate, and base release from 2'-deoxy-2'-fluoronucleoside 5'-diphosphates by ribonucleoside-diphosphate reductase, *J. Biol. Chem.* **1980**, *255*, 5511-13.
22. Salowe, S. P.; Ator, M. A.; Stubbe, J. Products of the inactivation of ribonucleoside diphosphate reductase from *Escherichia coli* with 2'-azido-2'-deoxyuridine 5'-diphosphate, *Biochemistry* **1987**, *26*, 3408-16.
23. Mao, S. S.; Johnston, M. I.; Bollinger, J. M. J.; Stubbe, J. Mechanism-based inhibition of a mutant *Escherichia coli* ribonucleotide reductase (cysteine-225- serine) by its substrate CDP, *Proc. Natl. Acad. Sci. U. S. A.* **1989**, *86*, 1485-1489.
24. Persson, A. L.; Eriksson, M.; Katterle, B.; Pötsch, S.; Sahlin, M.; Sjöberg, B. M. A new mechanism-based radical intermediate in a mutant R1 protein affecting the catalytically essential Glu441 in *Escherichia coli* ribonucleotide reductase, *J. Biol. Chem.* **1997**, *272*, 31533-41.
25. Lawrence, C. C., Bennati, M., Obias, H. V., Bar, G., Griffin, R. G. & Stubbe, J. High-field EPR detection of a disulfide radical anion in the reduction of cytidine 5'-diphosphate by the E₄₄₁Q-R1 mutant of *Escherichia coli* ribonucleotide reductase, *Proc. Natl. Acad. Sci. U. S. A* **1999**, *96*, 8979-84.
26. Kasrayan, A.; Persson, A. L.; Sahlin, M.; Sjöberg, B. M. The conserved active site asparagine in class I ribonucleotide reductase is essential for catalysis, *J. Biol. Chem.* **2002**, *277*, 5749-55.
27. Aberg, A.; Hahne, S.; Karlsson, M.; Larsson, A.; Ormö, M.; Ahgren, A.; Sjöberg, B. M. Evidence for two different classes of redox-active cysteines in ribonucleotide reductase of *Escherichia coli*, *J. Biol. Chem.* **1989**, *264*, 12249-52.
28. Mao, S. S.; Yu, G. X.; Chalfoun, D.; Stubbe, J. Characterization of C₄₃₉S-R1, a mutant of *Escherichia coli* ribonucleotide diphosphate reductase: evidence that C₄₃₉ is a residue essential for nucleotide reduction and C₄₃₉S-R1 is a protein possessing novel thioredoxin-like activity, *Biochemistry* **1992**, *31*, 9752-9.

29. Ge, J.; Yu, G.; Ator, M. A.; Stubbe, J. Pre-steady-state and steady-state kinetic analysis of *E. coli* class I ribonucleotide reductase, *Biochemistry* **2003**, *42*, 10071-83.
30. Thelander, L. Physicochemical characterization of ribonucleoside diphosphate reductase from *Escherichia coli*, *J. Biol. Chem.* **1973**, *248*, 4591-601.
31. Ando, N.; Brignole, E. J.; Zimanyi, C. M.; Funk, M. A.; Yokoyama, K.; Asturias, F. J.; Stubbe, J.; Drennan, C. L. Structural interconversions modulate activity of *Escherichia coli* ribonucleotide reductase, *Proc. Natl. Acad. Sci. U. S. A* **2011**, *108*, 21046-51.
32. Larsson, A.; Reichard, P. Enzymatic synthesis of deoxyribonucleotides. X. Reduction of purine ribonucleotides; allosteric behavior and substrate specificity of the enzyme system from *Escherichia coli* B, *J. Biol. Chem.* **1966**, *241*, 2540-9.
33. Brown, N. C.; Reichard, P. Ribonucleoside diphosphate reductase: Formation of active and inactive complexes of proteins B1 and B2, *J. Mol. Biol.* **1969**, *46*, 25-38.
34. Brown, N. C.; Reichard, P. Role of effector binding in allosteric control of ribonucleoside diphosphate reductase, *J. Mol. Biol.* **1969**, *46*, 39-55.
35. Larsson, K. M.; Jordan, A.; Eliasson, R.; Reichard, P.; Logan, D. T; Nordlund, P. Structural mechanism of allosteric substrate specificity regulation in a ribonucleotide reductase, *Nat. Struct. Mol. Biol.* **2004**, *11*, 1142-9.
36. Zimanyi, C. M.; Chen, P. Y.; Kang, G.; Funk, M. A.; Drennan, C. L. Molecular basis for allosteric specificity regulation in class Ia ribonucleotide reductase from *Escherichia coli*. *eLIFE* [Online Early Access]. DOI: 10.7554/eLife.07141. Published Online: 2016.
37. Eriksson, M.; Uhlin, U.; Ramaswamy, S.; Ekberg, M.; Regnstrom, K.; Sjöberg, B. M.; Eklund, H. Binding of allosteric effectors to ribonucleotide reductase protein R1: reduction of active-site cysteines promotes substrate binding, *Structure* **1997**, *5*, 1077-92.
38. Nordlund, P.; Eklund, H. Structure and function of the *Escherichia coli* ribonucleotide reductase protein R2., *J. Mol. Biol.* **1993**, *232*, 123-64.
39. Bennati, M.; Robblee, J. H.; Mugnaini, V.; Stubbe, J.; Freed, J. H.; Borbat, P. EPR distance measurements support a model for long-range radical initiation in *E. coli* ribonucleotide reductase, *J. Am. Chem. Soc.* **2005**, *127*, 15014-5.
40. Seyedsayamdost, M. R.; Stubbe, J. Site-specific replacement of Y₃₅₆ with 3,4-dihydroxyphenylalanine in the β 2 subunit of *E. coli* ribonucleotide reductase, *J. Am. Chem. Soc.* **2006**, *128*, 2522-3.
41. Yokoyama, K.; Uhlin, U.; Stubbe, J. A hot oxidant, 3-NO₂Y₁₂₂ radical, unmasks conformational gating in ribonucleotide reductase, *J. Am. Chem. Soc.* **2010**, *132*, 15368-79.
42. Climent, I.; Sjöberg, B. M.; Huang, C. Y. Carboxyl-terminal peptides as probes for *Escherichia coli* ribonucleotide reductase subunit interaction: kinetic analysis of inhibition studies, *Biochemistry* **1991**, *30*, 5164-71.
43. Uhlin, U.; Eklund, H. Structure of ribonucleotide reductase protein R1, *Nature* **1994**, *370*, 533-39.

44. Nordlund, P.; Sjöberg, B. M.; Eklund, H. Three-dimensional structure of the free radical protein of ribonucleotide reductase, *Nature* **1990**, *345*, 593-8.
45. Seyedsayamdost, M. R.; Chan, C. T.; Mugnaini, V.; Stubbe, J.; Bennati, M. PELDOR spectroscopy with DOPA- β 2 and NH₂Y- α 2s: distance measurements between residues involved in the radical propagation pathway of *E. coli* ribonucleotide reductase, *J. Am. Chem. Soc.* **2007**, *129*, 15748-9.
46. Nick, T. U. Hydrogen bonds and electrostatic environment of radical intermediates in ribonucleotide reductase Ia. Ph.D. Thesis, University of Göttingen, **2015**.
47. Minnihhan, E. C.; Ando, N.; Brignole, E. J.; Olshansky, L.; Chittuluru, J.; Asturias, F. J.; Drennan, C. L.; Nocera, D. G.; Stubbe, J. Generation of a stable, aminotyrosyl radical-induced α 2 β 2 complex of *Escherichia coli* class Ia ribonucleotide reductase, *Proc. Natl. Acad. Sci. U. S. A.* **2013**, *110*, 3835-40.
48. Yokoyama, K.; Smith, A. A.; Corzilius, B.; Griffin, R. G.; Stubbe, J. Equilibration of tyrosyl radicals (Y₃₅₆[•], Y₇₃₁[•], Y₇₃₀[•]) in the radical propagation pathway of the *Escherichia coli* class Ia ribonucleotide reductase, *J. Am. Chem. Soc.* **2011**, *133*, 18420-32.
49. Stubbe, J.; Nocera, D. G.; Yee, C. S.; Chang, M. C. Y. Radical initiation in the class I ribonucleotide reductase: long-range proton-coupled electron transfer?, *Chem. Rev.* **2003**, *103*, 2167-201.
50. Climent, I.; Sjöberg, B. M.; Huang, C. Y. Site-directed mutagenesis and deletion of the carboxyl terminus of *Escherichia coli* ribonucleotide reductase protein R2 - effects on catalytic activity and subunit interaction, *Biochemistry* **1992**, *31*, 4801-7.
51. Ekberg, M.; Sahlin, M.; Eriksson, M.; Sjöberg, B. M. Two conserved tyrosine residues in protein R1 participate in an intermolecular electron transfer in ribonucleotide reductase, *J. Biol. Chem.* **1996**, *271*, 20655-9.
52. Rova, U.; Goodtzova, K.; Ingemarson, R.; Behravan, G.; Gräslund, A.; Thelander, L. Evidence by site-directed mutagenesis supports long-range electron transfer in mouse ribonucleotide reductase, *Biochemistry* **1995**, *34*, 4267-75.
53. Reece, S. Y.; Hodgkiss, J. M.; Stubbe, J.; Nocera, D. G. Proton-coupled electron transfer: the mechanistic underpinning for radical transport and catalysis in biology, *Philos. Trans. R. Soc. Lond. B Biol. Sci.* **2006**, *361*, 1351-64.
54. Wörsdorfer, B.; Conner, D. A.; Yokoyama, K.; Livada, J.; Seyedsayamdost, M.; Jiang, W.; Silakov, A.; Stubbe, J.; Bollinger, J. M., Jr.; Krebs, C. Function of the diiron cluster of *Escherichia coli* class Ia ribonucleotide reductase in proton-coupled electron transfer, *J. Am. Chem. Soc.* **2013**, *135*, 8585-93.
55. Holder, P. G.; Pizano, A. A.; Anderson, B. L.; Stubbe, J.; Nocera, D. G. Deciphering radical transport in the large subunit of class I ribonucleotide reductase, *J. Am. Chem. Soc.* **2012**, *134*, 1172-80.
56. Koo, B. J.; Huynh, B. H.; Halbach, R. L.; Stubbe, J.; Nocera, D. G. Modulation of phenol oxidation in cofacial dyads, *J. Am. Chem. Soc.* **2015**, *137*, 11860-3.

57. Nick, T.; Lee, W.; Kossmann, S.; Neese, F.; Stubbe, J.; Bennati, M. Hydrogen bond network between amino acid radical intermediates on the proton-coupled electron transfer pathway of *E. coli* $\alpha 2$ ribonucleotide reductase, *J Am Chem Soc* **2015**, *137*, 289-98.
58. Kasanmascheff, M.; Lee, W.; Nick, T.; Stubbe, J.; Bennati, M. Radical transfer in *E. coli* ribonucleotide reductase: a NH₂Y₇₃₁/R₄₁₁- α mutant unmasks a new conformation of the pathway residue 731, *Chem. Sci.* **2016**, *7*, 2170-2178.
59. Minnihan, E. C.; Seyedsayamdost, M. R.; Uhlin, U.; Stubbe, J. Kinetics of radical intermediate formation and deoxynucleotide production in 3-aminotyrosine-substituted *Escherichia coli* ribonucleotide reductases, *J. Am. Chem. Soc.* **2011**, *133*, 9430-40.
60. Finzel, B. C.; Poulos, T. L.; Kraut, J. Crystal structure of yeast cytochrome *c* peroxidase refined at 1.7 Å resolution, *J. Biol. Chem.* **1984**, *259*, 13027-36.
61. Houseman, A. L. P.; Doan, P. E.; Goodwin, D. B.; Hoffman, B. M. Comprehensive explanation of the anomalous EPR spectra of wild-type and mutant cytochrome *c* peroxidase compound ES, *Biochemistry* **1993**, *32*, 4430-43.
62. Dassama, L. M.; Jiang, W.; Varano, P. T.; Pandelia, M. E.; Conner, D. A.; Xie, J.; Bollinger, J. M. J.; Krebs, C. Radical-translocation intermediates and hurdling of pathway defects in "super-oxidized" (Mn(IV)Fe(IV)) chlamydia trachomatis ribonucleotide reductase, *J. Am. Chem. Soc.* **2012**, *134*, 20498-506.
63. Ravichandran, K. R.; Minnihan, E. C.; Wei, Y.; Nocera, D. G.; Stubbe, J. Reverse electron transfer completes the catalytic cycle in a 2,3,5-trifluorotyrosine-substituted ribonucleotide reductase, *J. Am. Chem. Soc.* **2015**, *137*, 14387-95.
64. Yee, C. S.; Seyedsayamdost, M. R.; Chang, M. C. Y.; Nocera, D. G.; Stubbe, J. Generation of the R2 subunit of ribonucleotide reductase by intein chemistry: insertion of 3-nitrotyrosine at residue 356 as a probe of the radical initiation process, *Biochemistry* **2003**, *42*, 14541-52.
65. Yee, C. S.; Chang, M. C. Y.; Ge, J.; Nocera, D. G.; Stubbe, J. 2,3-difluorotyrosine at position 356 of ribonucleotide reductase R2: A probe of long-range proton-coupled electron transfer, *J. Am. Chem. Soc.* **2003**, *125*, 10506-7.
66. Chang, M. C.; Yee, C. S.; Nocera, D. G.; Stubbe, J. Site-specific replacement of a conserved tyrosine in ribonucleotide reductase with an aniline amino acid: a mechanistic probe for a redox-active tyrosine, *J Am Chem Soc* **2004**, *126*, 16702-3.
67. Seyedsayamdost, M. R.; Yee, C. S.; Reece, S. Y.; Nocera, D. G.; Stubbe, J. pH rate profiles of F_nY₃₅₆-R2s (n = 2, 3, 4) in *Escherichia coli* ribonucleotide reductase: evidence that Y₃₅₆ is a redox-active amino acid along the radical propagation pathway, *J. Am. Chem. Soc.* **2006**, *128*, 1562-8.
68. Wang, L.; Xie, J.; Schultz, P. G. Expanding the genetic code, *Annu. Rev. Biophys. Biomol. Struct.* **2006**, *35*, 225-49.
69. Liu, C. C.; Schultz, P. G. Adding new chemistries to the genetic code, *Annu. Rev. Biochem.* **2010**, *79*, 413-44.

70. Yokoyama, K.; Uhlin, U.; Stubbe, J. Site-specific incorporation of 3-nitrotyrosine as a probe of pK_a perturbation of redox-active tyrosines in ribonucleotide reductase, *J. Am. Chem. Soc.* **2010**, *132*, 8385-97.
71. Minnihan, E. C.; Young, D. D.; Schultz, P. G.; Stubbe, J. Incorporation of fluorotyrosines into ribonucleotide reductase using an evolved, polyspecific aminoacyl-tRNA synthetase, *J. Am. Chem. Soc.* **2011**, *133*, 15942-5.
72. Minnihan, E. C.; Nocera, D. G.; Stubbe, J. Reversible, Long-Range Radical Transfer in *E. coli* Class Ia Ribonucleotide Reductase, *Acc. Chem. Res.* **2013**, *46*, 2524-35.
73. Minnihan, E. C. Mechanistic studies of proton-coupled electron transfer in aminotyrosine- and fluorotyrosine-substituted class Ia ribonucleotide reductase. Ph.D. Thesis, Massachusetts Institute of Technology, **2012**.
74. Seyedsayamdost, M. R.; Reece, S. Y.; Nocera, D. G.; Stubbe, J. Mono-, di-, tri-, and tetra-substituted fluorotyrosines: new probes for enzymes that use tyrosyl radicals in catalysis, *J. Am. Chem. Soc.* **2006**, *128*, 1569-79.
75. Martínez-Rivera, M. C.; Berry, B. W.; Valentine, K. G.; Westerlund, K.; Hay, S.; Tommos, C. Electrochemical and structural properties of a protein system designed to generate tyrosine Pourbaix diagrams, *J. Am. Chem. Soc.* **2011**, *133*, 17786-17795.
76. Berry, B. W.; Martínez-Rivera, M. C.; Tommos, C. Reversible voltammograms and a Pourbaix diagram for a protein tyrosine radical, *Proc. Natl. Acad. Sci. U. S. A.* **2012**, *109*, 9739-43.
77. Ravichandran, K. R.; Liang, L.; Stubbe, J.; Tommos, C. Formal reduction potential of 3,5-difluorotyrosine in a structured protein: insight into multistep radical transfer, *Biochemistry* **2013**, *52*.
78. *CRC Handbook of Chemistry and Physics*, 75th ed.; Lide, D. R.; Frederikse, H. P. R., Eds.; CRC Press: Boca Raton, FL, 1994. Tyrosine pK_a : p 7-1. Aniline pK_a : p 8-49.
79. DeFilippis, M. R.; Murthy, C. P.; Broitman, F.; Weinraub, D.; Faraggi, M.; Klapper, M. H. Electrochemical properties of tyrosine phenoxy and tryptophan in indolyl radicals in peptides and amino acid analogs, *J. Phys. Chem.* **1991**, *95*, 3416-19.
80. Bennati, M.; Weber, A.; Antonic, J.; Perlstein, D. L.; Robblee, J. H.; Stubbe, J. Pulsed ELDOR spectroscopy measured the distance between the two tyrosyl radicals in the R2 subunit of the *E. coli* ribonucleotide reductase, *J. Am. Chem. Soc.* **2003**, *125*, 14988-9.
81. Olshansky, L. Kinetics and dynamics controlling proton-coupled electron transfer in ribonucleotide reductase. Ph.D. Thesis, Massachusetts Institute of Technology, **2015**.
82. Jovanovic, S. V.; Steenken, S.; Tosic, M.; Marjanovic, B.; Simic, M. G. Flavonoids as antioxidants, *J. Am. Chem. Soc.* **1994**, *116*, 4846-51.
83. Seyedsayamdost, M. R.; Xie, J.; Chan, C. T.; Schultz, P. G.; Stubbe, J. Site-specific insertion of 3-aminotyrosine into subunit α_2 of *E. coli* ribonucleotide reductase: direct evidence for involvement of Y730 and Y731 in radical propagation, *J. Am. Chem. Soc.* **2007**, *129*, 15060-71.

84. Bollinger, J. M., Jr.; Tong, W. H.; Ravi, N.; Huynh, B. H.; Edmondson, D. E. & Stubbe, J. Mechanism of assembly of the tyrosyl radical-diiron(II) cofactor of *Escherichia coli* ribonucleotide reductase 3. Kinetics of the limiting Fe²⁺ Reaction by optical, EPR, and Mössbauer spectroscopies, *J. Am. Chem. Soc.* **1994**, *116*, 8024-32.
85. Argirević, T.; Riplinger, C.; Stubbe, J.; Neese, F.; Bennati, M. ENDOR spectroscopy and DFT calculations: evidence for the hydrogen-bond network within $\alpha 2$ in the PCET of *E. coli* ribonucleotide reductase, *J. Am. Chem. Soc.* **2012**, *134*, 17661-70.
86. Siegbahn, P. E.; Eriksson, L. A.; Himø, F.; Pavlov, M. Hydrogen atom transfer in ribonucleotide reductase (RNR), *J. Phys. Chem. B.* **1998**, *102*, 10622-29.
87. Högbom, M.; Galander, M.; Andersson, M.; Kolberg, M.; Hofbauer, W.; Lassmann, G.; Nordlund, P.; Lenzian, F. Displacement of the tyrosyl radical cofactor in ribonucleotide reductase obtained by single-crystal high-field EPR and 1.4 Å X-ray data, *Proc. Natl. Acad. Sci. U S A* **2003**, *100*, 3209-14.
88. Oyala, P. H.; Ravichandran, K. R.; Funk, M. A.; Stucky, P.; Stich, T. A.; Drennan, C. L.; Britt, R. D.; Stubbe, J. Biophysical characterization of fluorotyrosine probes site-specifically incorporated into enzymes: *E. coli* ribonucleotide reductase as an example, *J. Am. Chem. Soc.* **2016**, *submitted*.
89. Ator, M.; Salowe, S.; Stubbe, J.; Emptage, M.; Robins, M. J. 2'-azido-2'-deoxynucleotide interaction with *E. coli* ribonucleotide reductase: generation of a new radical species, *J. Am. Chem. Soc.* **1984**, *106*, 1886-7.
90. Seyedsayamdost, M. R.; Argirević, T.; Minnihan, E. C.; Stubbe, J.; Bennati, M. Structural examination of the transient 3-aminotyrosyl radical on the PCET pathway of *E. coli* ribonucleotide reductase by multifrequency EPR spectroscopy, *J. Am. Chem. Soc.* **2009**, *131*, 15729-38.
91. Surdhar, P. S.; Armstrong, D. A. Reduction potentials and exchange reactions of thiy radicals and disulfide anion radicals, *J. Phys. Chem.* **1987**, *91*, 6532.
92. Armstrong, D. A. In *Sulfur-centered reactive intermediates in chemistry and biology*; Chatgililoglu, C.; ASmus, K. D.; Eds.; Plenum Press: New York, 1990; p 121.
93. Kaila, V. R. I.; Hummer, G. Energetics of direct and water-mediated proton-coupled electron transfer, *J. Am. Chem. Soc.* **2011**, *133*, 19040-43.
94. Chen, X.; Ma, G.; Sun, W.; Dai, H.; Xiao, D.; Zhang, Y.; Qin, X.; Liu, Y.; Bu, Y. Water promoting electron hole transport between tyrosine and cysteine in proteins via a special mechanism: double proton coupled electron transfer, *J. Am. Chem. Soc.* **2014**, *136*, 4515-24.
95. DeFilippis, M. R.; Murthy, C. P.; Faraggi, M.; Klapper, M. H. Pulse radiolytic measurement of redox potentials: the tyrosine and tryptophan radicals, *Biochemistry* **1989**, *28*, 4847-53.
96. Steenken, S.; Davies, M. J.; Gilbert, B. C. Pulse radiolysis and electron spin resonance studies of the dehydration of radicals from 1,2-diols and related compounds, *J. Chem. Soc. Perkin. Trans.2.* **1986**, 1003-1010.

97. Bansal, K. M.; Gratzel, M.; Henglein, A.; Janata, E. Polarographic and optical absorption studies of radicals produced in the pulse radiolysis of aqueous solutions of ethylene glycol, *J Phys Chem* **1973**, *77*, 16-19.
98. Lenz, R.; Giese, B. Studies on the mechanism of ribonucleotide reductases, *J. Am. Chem. Soc.* **1997**, *119*, 2784-2794.
99. Seyedsayamdost, M. R.; Yee, C. S.; Stubbe, J. Use of 2,3,5-F₃Y-β₂ and 3-NH₂Y-α₂ to study proton-coupled electron transfer in *Escherichia coli* ribonucleotide reductase, *Biochemistry* **2011**, *50*, 1403-11.
100. Madej, E.; Wardman, P. The oxidizing power of the glutathione thiyl radical as measured by its electrode potential at physiological pH, *Arch. Biochem. Biophys.* **2007**, *462*, 94-102.

Chapter 2

The formal reduction potential of 3,5-difluorotyrosine in a structured protein: insight into multistep radical transfer

Adapted with permission from Ravichandran, K.R.; Liang, L.; Stubbe, J.; Tommos C. Biochemistry, 2013, 52, 8907-15. Copyright 2013 American Chemistry Society

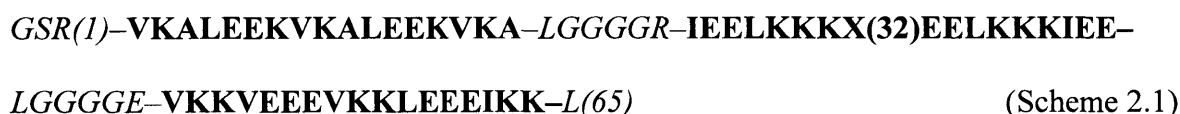
2.1 INTRODUCTION

The *E. coli* class Ia RNR utilizes a stable tyrosyl radical ($Y_{122}\bullet$) and three transient $Y\bullet$ s ($Y_{356}\bullet$, $Y_{731}\bullet$ and $Y_{730}\bullet$) to catalyze nucleotide reduction.¹ The rate-limiting step during turnover is a protein conformational change that occurs prior to radical transport (RT).² Forward RT, nucleotide reduction and reverse RT are much faster than the protein conformational change and thus, details of RT are kinetically masked in the wild-type (wt) system. To obtain evidence for $Y\bullet$ intermediates during catalysis we have employed a strategy of replacing the native Y s on pathway with unnatural Y analogs that perturb the pK_a and/or the reduction potential (E).³⁻⁶ To extrapolate the kinetic information obtained on these unnatural systems to wt RNR, we require knowledge on the exact perturbation to pK_a and E upon replacement of Y with the analogs. In this Chapter, we focus specifically on obtaining the E value for 3,5-difluorotyrosine (3,5- F_2Y). This amino acid has been site-specifically incorporated into a model three-alpha helix bundle⁷ ($\alpha_3(3,5)F_2Y$). Square-wave voltammetry (SWV) studies on $\alpha_3(3,5)F_2Y$ show that the fluorine substitutions decrease the reduction potential of Y by ~ 30 mV. The expression and purification of other α_3F_nY s with the goal of performing similar studies is described in Appendix 2.

Tyrosine serves as a one-electron redox cofactor in catalytic and multistep electron-transfer reactions.⁸⁻¹² It has been challenging to obtain precise and accurate thermodynamic information for this high-potential protein redox species. Electrochemical characterization of the natural systems has not been feasible due to their size, complexity and sensitivity to oxidative damage. Mechanistic studies on redox proteins employing $Y\bullet$ cofactors must thus partly rely on model systems to provide insights to the thermodynamics involved. Reduction potentials (E values) of aqueous Y and various analogs have been obtained by pulse radiolysis and voltammetry methods.¹³⁻¹⁸ Considerable uncertainty is associated with the reported values. This uncertainty is

in part due to varying experimental conditions, comparison of neutral and zwitterionic amino acids, and complicating issues such as solvent oxidation and the perturbation of solute/working electrode interactions. The most significant uncertainty, however, arises from the reactivity of the radical species themselves. Y•s generated in solution will rapidly dimerize ($\sim 10^8 \text{ M}^{-1} \text{ s}^{-1}$)¹⁹⁻²³ and give rise to quasi/irreversible voltammograms.^{24,25} Peak potentials (E_p) derived from such data reflect the electrode process (electrode driven oxidation-reduction of Y) as well as the thermodynamics and kinetics of the coupled side reactions (chemical reduction of Y•). The observed potentials may thus differ by 10s even 100s of millivolts from the formal (true) reduction potential (E°) of the Y redox system. Comparison between aqueous solution and protein Y redox chemistry is further complicated by the significant differences in the fundamental properties of these two media.^{26,27}

The $\alpha_3\text{X}$ family of well-structured proteins was developed to address these concerns.^{17,28} This model protein system yields thermodynamic information that is uncompromised by electrochemical irreversibility and radical side reactions.^{7,29,30} The $\alpha_3\text{X}$ proteins are based on a common *de novo* designed three-helix bundle scaffold:



Scheme 2.1 displays helical and loop regions in bold and italic, respectively. The N-terminal GS of the 67-residue sequence form part of a thrombin cleavage site and are labeled as -2 and -1 to keep the amino-acid numbering consistent between the chemically synthesized¹⁷ and recombinantly expressed^{31,32} $\alpha_3\text{X}$ proteins. The buried redox site (position 32 in the middle of the central helix) is occupied by a tryptophan (to form the $\alpha_3\text{W}$ protein), a tyrosine ($\alpha_3\text{Y}$), or a cysteine ($\alpha_3\text{C}$). C32 has been used to covalently attach phenol^{30,32} and quinone³³ molecules to the protein

scaffold. All of the α_3X proteins display very similar structural characteristics. They are stable and well-structured from pH \sim 4 to 10. Their single aromatic residue (W, Y, phenol or quinone) gives rise to UV-vis, fluorescence and NMR spectra that are highly sensitive to the microenvironment of the redox site. Protein voltammetry has shown that the α_3X system displays unique electrochemical properties. The protein scaffold is redox inert to at least +1.3 V vs. NHE.^{7,30,32} The system becomes redox active when a W,¹⁷ Y,^{7,29} phenol^{30,32} or quinone³³ is introduced at position 32. Fully reversible voltammograms and $E^{\circ'}$ values have thus far been reported for the Y and phenol-containing α_3X proteins.^{7,30}

In this study, we use the α_3X system in combination with the *in vivo* nonsense codon suppression method⁵ and square-wave voltammetry (SWV)^{24,34,35} to determine $E^{\circ'}$ for a protein 3,5-F₂Y residue. We report $\Delta E^{\circ'}$ between 3,5-F₂Y and Y residues obtained at highly comparable experimental conditions. The results are compared to published solution potentials and discussed relative to our recent mechanistic studies on the *E. coli* class Ia RNR site-specifically labeled with unnatural Y residues in an effort to understand the thermodynamic and kinetic landscape of the PCET pathway in this system.^{1,5,36}

2.2 MATERIALS AND METHODS

2.2.1 Purification of tyrosine phenol lyase (TPL). E. coli strain SVS370 harboring the plasmid pTZTPL was obtained as a gift from Dr. Robert Phillips (University of Georgia). pTZTPL encodes TPL under a constitutive promoter and the protein was expressed and purified^{37,38} using a slightly modified procedure. The elution fractions from the octyl-sepharose column were assayed using a coupled spectrophotometric assay where a small volume of the fraction was added to an assay mixture containing 2 mM L-tyrosine, 5 mM β -mercaptoethanol, 50 μ M pyridoxyl-5'-phosphate, 0.3 mg/mL lactate dehydrogenase (*Lactobacillus leichmannii* from Sigma-Aldrich) and 0.2 mM NADH in 50 mM potassium phosphate pH 8.0. The reaction was monitored at 340 nm for the disappearance of NADH. Fractions containing considerable activity were pooled and concentrated in an Amicon ultrafiltration cell with a YM 10 membrane and the protein was used with no additional purification steps. One unit (U) of activity is defined as 1 μ mol product/min. A total of 62 U/g cell paste was obtained, in excellent agreement with the previously reported yield.³⁷

2.2.2 Enzymatic synthesis of 3,5-F₂Y. TPL was used to enzymatically synthesize 3,5-F₂Y from the corresponding phenol. Briefly, a 2 L reaction mixture containing 10 mM fluorophenol, 30 mM ammonium acetate pH 8.0, 60 mM sodium pyruvate, 5 mM β -mercaptoethanol, 40 μ M pyridoxyl-5'-phosphate and 30 U of TPL at room temperature was stirred in the dark for a total of four days. The mixture was supplied with additional TPL, β -mercaptoethanol and pyridoxyl-5'-phosphate every other day. Once the reaction was complete (as assessed by TLC), the mixture was worked up as described.³⁸ The yields are typically > 85% for 3,5-F₂Y. The final products were characterized by ¹H and ¹⁹F NMR spectroscopy.^{18,39}

2.2.3 Construction of α_3 TAG₃₂ by site-directed mutagenesis. The amber stop codon (TAG) was introduced at position 32 of α_3 Y using a modified pET32b- α_3 Y plasmid^{7,31} as template and

forward primer 5'- GGC GGC CGT ATT GAA GAA CTG AAA AAA AAA TAG GAA GAA CTG AAA AAA AAA ATT GAA GAA CTG GGC GGC GGC-3' and reverse primer 5'- GCC GCC GCC CAG TTC TTC AAT TTT TTT TTT CAG TTC TTC CTA TTT TTT TTT CAG TTC TTC AAT ACG GCC GCC-3'. The mutation was performed using the Stratagene QuikChange kit and confirmed by sequencing at the MIT Biopolymers Laboratory.

2.2.4 Expression of thioredoxin- $\alpha_3(3,5)F_2Y$. pET32b- α_3TAG_{32} was co-transformed with a plasmid (pEVOL- F_nY -RS-E3) encoding the fluorotyrosine tRNA and aminoacyl-tRNA synthetase (F_nY -RS) genes⁵ into BL21(DE3) competent cells and grown on media containing ampicillin (Amp, 100 μ g/mL) and chloramphenicol (Cm, 35 μ g/mL) at 37 °C. Unnatural amino acid (UAA) concentration and protein expression were optimized on a small-scale resulting in the following protocol: 40 mL LB pre-cultures were started from single colonies, grown for ~ 16 h, and used to inoculate (50-fold dilution) 1 L 2XYT cultures containing 2.0 mM 3,5- F_2Y . The 3,5- F_2Y additions were made from stock solutions freshly prepared in water, NaOH solubilized and sterile filtered. The expression of F_nY -RS was induced at an OD₆₀₀ of 0.2–0.3 (L-arabinose, final concentration 0.05% (w/v)). The expression of $\alpha_3(3,5)F_2Y$ was induced at an OD₆₀₀ of 0.5 (IPTG, final concentration 1mM). Growth was continued for an additional 4 h and the cells were harvested by centrifugation (5000 x g, 15 min, 4 °C). Protein expression was monitored by SDS-PAGE. No toxicity was seen due to the UAA. A typical yield of 2.5 g cell paste/L media was obtained.

2.2.5 Purification of $\alpha_3(3,5)F_2Y$. Cell paste (~5–10 g) was resuspended (5 mL/g paste) in buffer A (20 mM Tris-HCl pH 7.9, 500 mM NaCl, 5 mM imidazole), treated with lysozyme (300 μ g/mL, 30 min, 30 °C) and lysed by sonication. The lysate was clarified by centrifugation (12000 x g, 20 min, 4 °C), passed over a nickel column (10 mL His•bind resin, EMD Millipore) equilibrated with buffer A, and the thioredoxin fusions eluted with a linear 0–40% buffer B (20

mM Tris-HCl, 500 mM NaCl, 1M imidazole, pH 7.9) gradient over 40 min (flow rate 1.5 mL/min). Fractions containing the thioredoxin fusions were identified by SDS-PAGE. Thrombin (T6634; Sigma-Aldrich) was added to the pooled fusion-protein fractions (thrombin/protein ratio 1:2000 (w/w)) and the resulting mixture dialyzed against 20 mM Tris-HCl, 500 mM NaCl, 2.5 mM CaCl₂, pH 8.0 at RT for >16 h. The thrombin digestion produces three major products: His-tagged thioredoxin, the truncated α_3 (residue 1–31) peptide (MW 3579 Da) and the full-length $\alpha_3(3,5)F_2Y$ protein (MW 7557 Da). A major fraction of the truncated α_3 (residue 1–31) product was removed during the overnight dialysis step (Spectra/Por tubing MWCO 3500 Da). The digestion/dialysis mixture (~30 mL) was passed over a nickel column (10 mL His•bind resin equilibrated with buffer A) to remove the His-tagged thioredoxin and any remaining undigested fusion products. $\alpha_3(3,5)F_2Y$ (sample injection volume 5–10 mL) was isolated by reversed-phase HPLC (218TP C18 column, particle size 10 μ m, column size 10 · 250 mm; Grace/VYDAC) using a linear water/acetonitrile/0.1% (w/v) trifluoroacetic acid gradient (30–60% acetonitrile over 45 min, flow rate 5 mL/min), and stored as lyophilized powder. The protein purification steps were monitored by SDS-PAGE. Purity was evaluated by reversed-phase HPLC (218TP C18 column, particle size 5 μ m, column size 4.6 · 250 mm; Grace/VYDAC) using a linear water/acetonitrile/0.1% (w/v) trifluoroacetic acid gradient (20–70% acetonitrile over 50 min, flow rate 1 mL/min). Molecular weights were verified by matrix-assisted desorption/ionization-time of flight (MALDI-TOF) mass spectrometry using a Bruker Microflex 3.1. An average yield of ~3 mg pure $\alpha_3(3,5)F_2Y/L$ culture was observed.

2.2.6 Absorption spectroscopy. Absorption spectra were recorded on a Varian Cary 50 Bio UV-vis spectrometer at room temperature. Protein concentrations were determined by the Bradford protein assay (Bio-Rad) with standard curves prepared using either bovine serum

albumin (for thioredoxin fusion samples) or α_3W^{17} (for α_3Y and $\alpha_3(3,5)F_2Y$ protein-characterization samples). An ϵ_{280} of $5690 \text{ M}^{-1} \text{ cm}^{-1}$ was used for $\alpha_3W^{17,40,41}$ when preparing the standard curves. The apparent tyrosinate/tyrosine pK_a (pK_{app}) of $(3,5)F_2Y_{32}$ was measured by dissolving lyophilized $\alpha_3(3,5)F_2Y$ in 3.0 mL 20 mM sodium acetate, 20 mM potassium phosphate, 20 mM sodium borate (APB buffer), pH 12 to give an absorption of 0.2 at 277 nm (10 mm path). The protein stock solution was added to 20 mM APB buffer generating two samples with pH ~ 5 and 12, respectively. The pH was pre-adjusted in the APB buffer samples to generate the final pH upon addition of the protein stock. The protein dilution was 2-fold providing a final 277 nm absorption of 0.1 (10 mm path; pH 12). Equal-volume (1.6 mL) titration was performed manually by removing a 100–400 μL portion from the cuvette containing the high-pH sample and then adding the same amount of low-pH sample per pH adjustment. The pK_{app} was obtained by fitting the pH-induced increase in the $(3,5)F_2Y_{32}\text{-O}^-$ absorption to a single pK_a .

2.2.7 Circular dichroism (CD) spectroscopy. CD spectra were collected on an Aviv 202 CD spectrometer at 25 °C. The instrument was equipped with an automated titration system. For the α -helical measurements, CD spectra were collected from α_3W , α_3Y and $\alpha_3(3,5)F_2Y$ dissolved in 20 mM sodium acetate, pH 5.6. Protein concentrations were determined by the Bradford assay and using α_3W as the standard. pH titrations were performed by dissolving lyophilized protein in 20 mM APB buffer, pH 4.8 to a 235 nm ellipticity of ~ -175 mdegrees (10 mm path). The protein stock solution was added to 20 mM APB buffer generating two samples with pH ~ 4 and 10, respectively. The pH was pre-adjusted in the APB buffer samples to generate the final pH upon addition of the protein stock. The protein dilution was 4-fold generating a final 222 nm ellipticity ~ -150 mdegrees (10 mm path; pH 4). Equal-volume (2.5 mL) titration was performed manually by removing a 40–1000 μL portion from the cuvette containing the high-pH sample and then

adding the same amount of low-pH sample per pH adjustment. Protein stability measurements were conducted by dissolving lyophilized protein in 20 mM sodium acetate, 20 mM potassium phosphate (AP buffer), pH 5.0 or 5.5 buffer to a 230 nm ellipticity of -75 to -140 mdegrees (1 mm path). The protein stock solution was added to 20 mM AP buffer containing 0 and 9.5 M urea, respectively. The pH was 5.0 or 5.5 in the protein/AP buffer and protein/AP buffer/urea solutions. The protein dilution was 18-fold generating a final 222 nm ellipticity in the -110 to -210 mdegrees range (10 mm path) at zero molar denaturant. The urea denaturation experiments were performed by automated equal-volume (2.0 mL) titration controlled from the Aviv software. Global stability values were determined by fitting the denaturation curves as described in Ref. 42.

2.2.8 Square-wave voltammetry (SWV). Voltammetry measurements^{24,34,35} were performed using an Autolab PGSTAT12 potentiostat equipped with a temperature-controlled, Faraday-cage protected three-electrode micro-cell (Princeton Applied Research). The Ag/AgCl reference electrode and the platinum wire counter electrode (Advanced Measurements Inc.) were stored dry and prepared by filling the former with a 3M KCl/saturated AgCl solution and the latter with sample buffer. All measurements were carried out using a 3 mm diameter pyrolytic graphite edge (PGE) working electrode (Bio-Logic, USA). The electrode surface was activated between measurements by manually polishing its surface for 60 s in a 1.0 μm diamond/water slurry on a diamond polishing pad (Bio-Logic, USA) followed by 60 s in a 0.05 μm alumina/water slurry on a microcloth pad (Bioanalytical systems Inc.). The electrode was rinsed with an excess of methanol followed by milli-Q water directed against the surface of the electrode. Measurements were performed immediately following the polishing procedures. Solution resistance was compensated for by using the positive feed-back iR compensation function of the Autolab system. Potentials are given *versus* the normal hydrogen electrode (NHE). All samples were prepared from ultra-pure

chemicals and the measurements performed under an argon atmosphere. Preparation of the voltammetry protein samples is described in the Results section. Protein concentration series were obtained by stepwise dilution of the protein samples in the electrochemical cell while keeping the sample volume constant at 2.5 mL. The pH was monitored directly in the electrochemical cell using a pH microelectrode (Microelectrodes Inc.) connected to a SevenMulti pH meter (Mettler Toledo). The pH electrode was disconnected from the pH meter during the active measurements to avoid the risk of introducing electric noise. Data processing and analyses were performed using the Autolab GPES software and PeakFit (Systat Software Inc.).

2.3 RESULTS

2.3.1 $\alpha_3(3,5)F_2Y$ expression and purification. 3,5-Difluorotyrosine was synthesized enzymatically^{37,38} as described in the Materials and Methods section. The amber stop codon (TAG) was introduced in place of the codon for residue 32 (Scheme 2.1) in a modified pET32b plasmid used for expression of the α_3X proteins.^{7,31} The α_3TAG variant was co-expressed with an evolved polyspecific fluorotyrosine aminoacyl-tRNA synthetase⁵ in *E. coli* BL21(DE3) cells. Protein expression was initially evaluated in 100 mL growth cultures by SDS-PAGE and mass spectrometry. Optimal expression was observed with 2.0 mM 3,5- F_2Y in 2XYT media (Figure 2.1). The growth cultures were scaled to 1 L to generate sufficient material for protein characterization and voltammetry studies. Protein expression and purification protocols are described in detail in Materials and Methods. The purity of the $\alpha_3(3,5)F_2Y$ preparations was evaluated by reversed-phase HPLC (Figure 2.2A) and the correct protein molecular weight was verified by mass spectrometry (Figure 2.2B). The average yield of pure $\alpha_3(3,5)F_2Y$ was ~ 3 mg/L culture, which represents a suppression efficiency of only $\sim 10\%$. Efforts to improve the suppression efficiency are described in Appendix 2.

2.3.2 Protein characterization. The aims of this study are to determine (i) the electrochemical reversibility of $\alpha_3(3,5)F_2Y$, (ii) $E^{\circ'}$ of $(3,5)F_2Y_{32}$, and (iii) $\Delta E^{\circ'}$ between $(3,5)F_2Y_{32}$ and Y_{32} when recorded at near identical conditions. Initially, we compared the structural properties of α_3Y and $\alpha_3(3,5)F_2Y$. α_3Y is highly helical and well-structured from pH 4.5 to 10.^{7,17} The apparent $Y-O^-/Y-OH$ pK_a (pK_{app}) of Y_{32} is 11.3 ± 0.1 (Table 2.1). Exchanging Y_{32} to $(3,5)F_2Y_{32}$ was not expected to significantly perturb the protein scaffold^{43,44} at pH conditions where the buried phenol side chain is uncharged. Experiments were carried out to determine a suitable pH range for

the SWV analysis, i.e., where (3,5) F_2Y_{32} remains protonated and the structural properties of $\alpha_3(3,5)F_2Y$ closely resemble those of α_3Y .

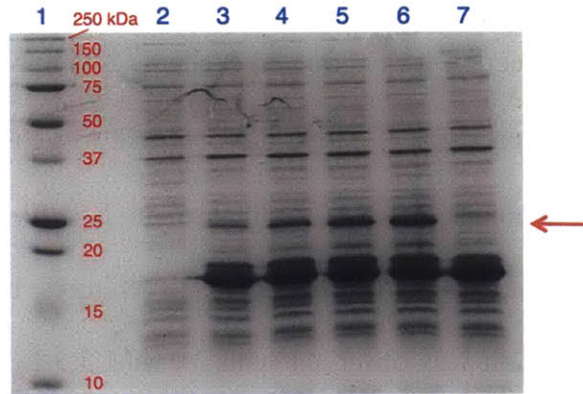


Figure 2.1 SDS-PAGE analysis of $\alpha_3(3,5)F_2Y$ expression in *E. coli* BL21(DE3). The SDS-PAGE (15%) gel displays in lane (1) molecular weight markers, lane (2) pre-induction sample, lane (7) post-induction sample of a culture to which no 3,5- F_2Y addition was made, and in lane (3–6) expression of $\alpha_3(3,5)F_2Y$ in cultures containing 0.5, 1.0, 1.5 and 2.0 mM 3,5- F_2Y respectively. The α_3X protein is expressed as a thioredoxin fusion. The calculated molecular weights of the truncated thioredoxin- α_3 (residue 1–31) and full-length thioredoxin- $\alpha_3(3,5)F_2Y$ fusions are 17370 Da and 21348 Da, respectively. The band consistent with full-length thioredoxin $\alpha_3(3,5)F_2Y$ fusion protein is indicated with an arrow.

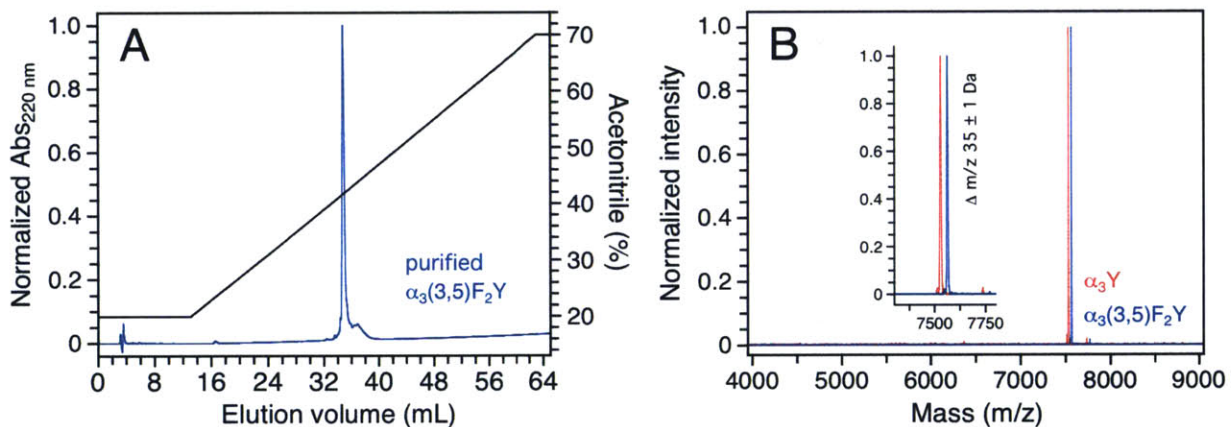


Figure 2.2 Analytical HPLC and mass spectrometry evaluation of purified $\alpha_3(3,5)F_2Y$. Panel A displays a typical analytical C18 reversed-phase chromatogram of purified $\alpha_3(3,5)F_2Y$. The freeze-dried protein was dissolved in 20 mM sodium acetate, pH 5.8, and eluted with a linear 20–70% acetonitrile gradient over 50 min. Panel B shows MALDI-TOF traces of purified $\alpha_3(3,5)F_2Y$ (blue) and α_3Y (red). Each trace displays a single major peak, whose maxima are separated by 35 ± 1 Da (inset). This is consistent with the exchange of Y_{32} to 3,5- F_2Y_{32} (calculated $\Delta m/z = 36$ Da).

Figure 2.3A displays absorption spectra of $\alpha_3(3,5)F_2Y$ collected over a pH 5.7 (gray) to 10.4 (purple) range. The $(3,5)F_2Y_{32-O^-}/(3,5)F_2Y_{32-OH}$ transition titrates with a pK_{app} of 8.0 ± 0.1 . The protein environment increases the pK_{app} by ~ 1 unit relative to aqueous 3,5- F_2Y (pK_a 7.0 ± 0.2 ; Table 2.1).^{18,39} The weak and blue shifted absorbance of aqueous 3,5- F_2Y-OH (ϵ_{263} $560 \text{ M}^{-1}\text{cm}^{-1}$) relative to unmodified Y-OH (ϵ_{275} $1490 \text{ M}^{-1}\text{cm}^{-1}$; Table 2.1) was expected to translate into a rather poorly defined absorption spectrum of $\alpha_3(3,5)F_2Y$. The blue shift increases the spectral overlap between the absorption of the aromatic side chain and the large absorption of the protein backbone (λ_{max} 190–220 nm) making $\alpha_3(3,5)F_2Y$ concentration measurements based on UV absorbance unreliable. Thus, the Bradford method was used to determine protein concentrations with standard curves prepared from α_3W . ϵ_{277} of 1500 ± 80 (pH 5.4) and ϵ_{294} of 2430 ± 130 (pH 13.4) $\text{M}^{-1}\text{cm}^{-1}$ were obtained for Y_{32-OH} and Y_{32-O^-} in α_3Y , respectively. The ϵ_{277} value is consistent with the average ϵ_{280} of $1490 \text{ M}^{-1}\text{cm}^{-1}$ typically used for protein Y-OH residues^{40,41} and close to the λ_{max} values of aqueous Y-OH (Table 2.1).¹⁸ We conclude that the Bradford assay determines the α_3X protein concentration with good accuracy.

CD spectroscopy was used to measure the absolute α -helical content, the pH sensitivity of this parameter, and the global stability of $\alpha_3(3,5)F_2Y$ relative to α_3Y (Table 2.1). Figure 2.3B displays far-UV CD spectra of $\alpha_3(3,5)F_2Y$ (blue) and α_3Y (red) collected at pH 5.6. The reference spectrum of the structurally characterized α_3W protein (green)^{17,31} is also shown. The protein concentration in the CD samples was determined by the Bradford method. The CD spectral line shapes are essentially identical and display the characteristic 208/222 nm double minima of a predominantly α -helical protein. The 222 nm mean residue molar ellipticity ($[\Theta]_{222}$) reflects the α -helical content, which was estimated to ~ 75 – 80% for $\alpha_3(3,5)F_2Y$ and α_3Y at pH 5.6 (Table 2.1).

This translates into 50 ± 1 residues with helical ψ and ϕ backbone angles in $\alpha_3(3,5)F_2Y$ and α_3Y . This degree of helicity has consistently been observed for structurally characterized α_3X proteins (α_3W PDB ID 1LQ7;³¹ 2-mercaptophenol- α_3C 2LXY³⁰). Figure 2.3C displays $[\Theta]_{222}$ and the corresponding % helix of $\alpha_3(3,5)F_2Y$ as a function of pH. The α -helical content of $\alpha_3(3,5)F_2Y$ decreases by only 2% from pH 4.7 to 6.7 and by 6% from pH 6.7 to 10. These small pH-induced changes in helical content are likely to be driven by the deprotonation of $(3,5)F_2Y_{32}$. The global stability of $\alpha_3(3,5)F_2Y$ and α_3Y was thus compared at acidic pH > two pH units below the pK_{app} of $(3,5)F_2Y_{32}$. The stability of the two proteins was found to be identical at pH 5.0 and differ by only 0.2 kcal mol⁻¹ at pH 5.5 (Table 2.1). The SWV analysis described below was conducted at low pH (5.6 ± 0.1) where the structural properties of $\alpha_3(3,5)F_2Y$ and α_3Y are very similar and their phenols are protonated.

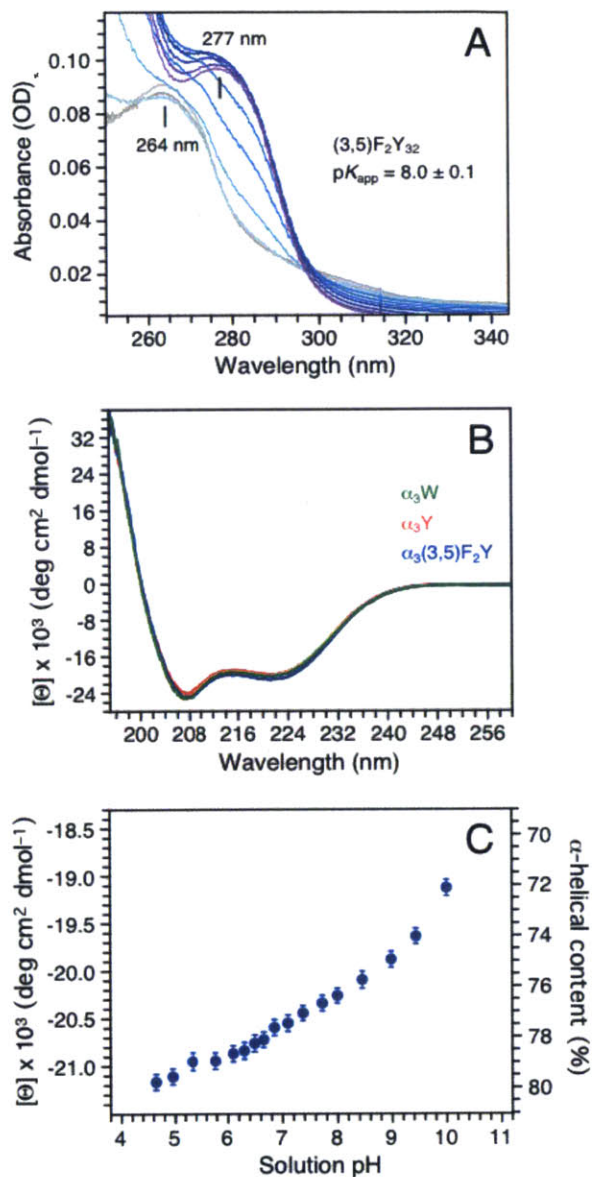


Figure 2.3 A. A pH titration of $\alpha_3(3,5)F_2Y$ monitored by UV-Vis absorption spectroscopy. Spectra were collected at pH 5.72 (gray), 6.38, 6.84, 7.49, 8.06, 8.53, 8.96, 9.31, 9.59, 10.02 and 10.42 (purple). B. Far-UV CD spectra of $\alpha_3(3,5)F_2Y$ (blue), α_3Y (red) and α_3W (green) in 20 mM sodium acetate, pH 5.62 ± 0.01 . The single aromatic residue in each protein is fully protonated at this pH. The CD spectra are displayed in units of mean residue molar ellipticity ($[\Theta]$) obtained by: $([\Theta]) = \theta_{obs}(10^6/Cln)$ where θ_{obs} is the observed ellipticity in mdegrees (spectrometer raw signal), C the protein concentration in μM , l the cuvette path length in mm, and n the number of amino-acid residues (65). $[\Theta]_{222}$ equals $-20.0 \pm 0.8 \times 10^3$ deg cm² dmol⁻¹ at pH 5.6 for $\alpha_3(3,5)F_2Y$ (Table 2.1). C. Changes in the mean residue molar ellipticity ($[\Theta]$) and the corresponding % α -helical content of $\alpha_3(3,5)F_2Y$ between pH 4.7 and 10.

2.3.3 Preparation of SWV samples. The protein concentration is a key parameter to control when investigating the protein/working electrode interactions and optimizing the Faradaic response.^{29,30} The high α -helical content of $\alpha_3(3,5)F_2Y$ makes CD spectroscopy a precise method to determine the protein concentration in a highly reproducible manner. Voltammetry samples were thus prepared by dissolving lyophilized protein in buffer until an appropriate θ_{222} and the protein concentration was calculated from the determined $[\Theta]_{222}$ value (see Figure 2.3 legend and Table 2.1). The supporting electrolyte, KCl, was added to the samples after the CD measurements to avoid UV absorption of the chloride ion.

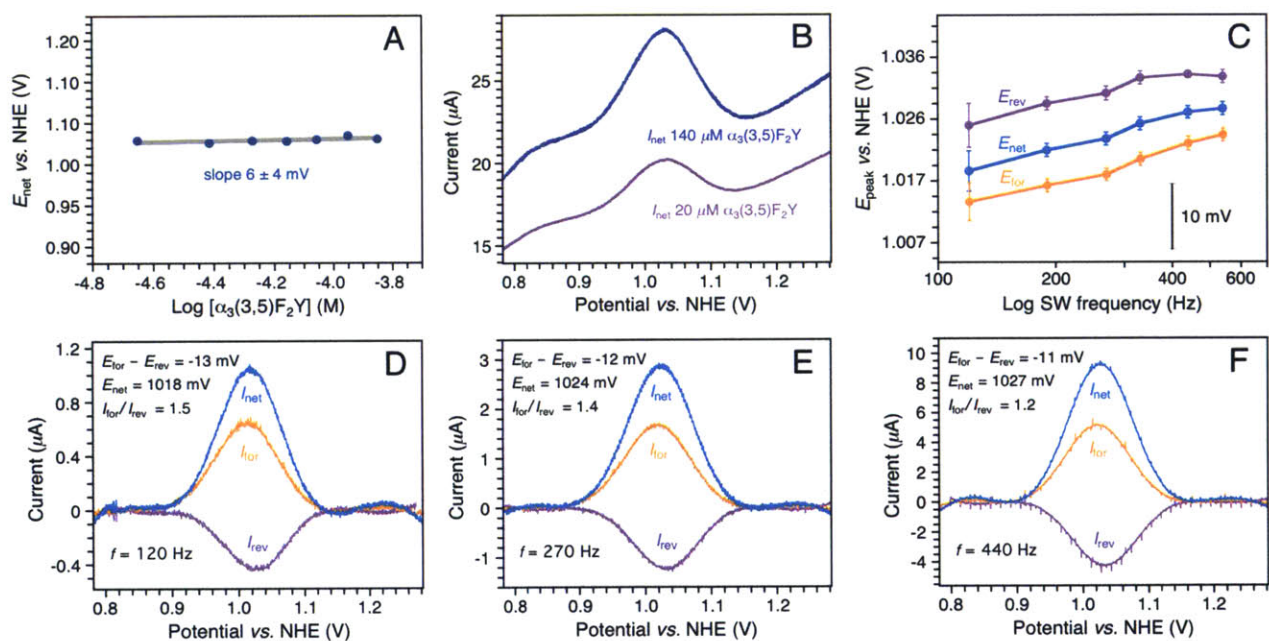


Figure 2.4 SWV analysis of the Y-O•/Y-OH redox system in $\alpha_3(3,5)F_2Y$. A. $E_{net}(270\text{ Hz})$ as a function of $[\alpha_3(3,5)F_2Y]$, pH 5.53 ± 0.11 . E_{net} is independent of the protein concentration, which is consistent with benign protein/working electrode interactions. B. Representative net voltammograms (I_{net}) collected at the upper (140 μM , purple) and lower (20 μM , magenta) limit of the $[\alpha_3(3,5)F_2Y]$ data series shown in panel A. The Faradaic response is optimal in this protein concentration range. C. Peak potential of the forward (E_{for}), reverse (E_{rev}) and net (E_{net}) $\alpha_3(3,5)F_2Y$ voltammograms as a function of the SW frequency (f), pH 5.70 ± 0.02 . D, E and F. Background-corrected voltammograms from the data series shown in panel C. SWV settings: 20 mM APB, 75 mM KCl, PGE working electrode, temperature 25 °C, step potential 0.15 mV, SW pulse amplitude 25 mV.

2.3.4 SWV analysis of $\alpha_3(3,5)F_2Y$. SWV voltammetry was conducted using a PGE working electrode. In SWV, the base potential (E_{step}) is changed incrementally in a series of forward and reverse pulses.^{24,34,35} The pulse height and length are set by the SW amplitude (E_{SW}) and frequency (f), respectively. The current is sampled at the end of each alternating pulse and traced out as a function of E_{step} . The pulse train generates a forward (I_{for}), a reverse (I_{rev}), and a net ($I_{\text{net}} = I_{\text{for}} - I_{\text{rev}}$) voltammogram. Previous studies using the PGE electrode have shown that $\sim 20\text{--}100\ \mu\text{M}$ α_3X in 20 mM APB buffer and 60–140 mM KCl yields Y and phenol voltammograms with optimal S/N at both acidic (5.5) and alkaline (8.5) pH.^{29,30} At these conditions, the system is governed by diffusion-controlled kinetics, the protein does not unfold on the electrode surface, and the observed potential is independent of functional groups present at the electrode surface. The $\alpha_3(3,5)F_2Y$ SWV measurements were consequently conducted using 20 mM APB and 75 mM KCl. Overall, $\alpha_3(3,5)F_2Y$ displays electrochemical properties very similar to those of α_3Y .²⁹ The Faradaic response is consistent with diffusion-controlled kinetics and benign $\alpha_3(3,5)F_2Y$ /working electrode interactions (Figures 2.4A and B). Figure 2.4C shows the change in the peak potential of the forward (I_{for}), reverse (I_{rev}) and net (I_{net}) currents as a function of the SW frequency. Background-corrected voltammograms from this data series are shown in Figures 2.4D-F. E_{for} , E_{rev} and E_{net} level off and come together as the SW frequency increases. This observation is consistent with a redox system that is shifting from the upper quasi-reversible region towards the fully reversible region as the SW frequency increases.^{34,35} E_{net} of 1026 ± 3 mV, E_{for} of 1021 ± 3 mV, and E_{rev} of 1032 ± 2 mV are observed for the 270–540 Hz range at pH 5.70 ± 0.02 . The observed frequency insensitivity and small separation in peak maxima mean that E_{net} closely approximates E° (i.e. within a few mV).^{29,30,35} With a pK_{app} of 8.0, we calculate $E^{\circ}(\text{pH } 7.0)$ to be 952 mV (Table 2.1). Comparing these results with the earlier reported α_3Y SWV study,²⁹ provides an ΔE° between Y_{32}

and (3,5)F₂Y₃₂ of $-28-33$ mV. This result was reproduced in a control experiment where $\alpha_3(3,5)F_2Y$ and α_3Y SW voltammograms were collected at identical experimental conditions, using the same electrode setup (Figure 2.5, $\Delta E_{\text{net}} -30 \pm 3$ mV). We conclude that E° of the Y32-O•/Y32-OH redox pair is lowered by 30 ± 3 mV upon fluoro-substitution at ring positions 3 and 5. We further note that the difference between E_{peak} of aqueous Y and E° of α_3Y is -150 mV, with the protein being the more oxidizing system (Table 2.1).

Table 2.1 Properties of Y, 3,5-F₂Y, α_3Y and $\alpha_3(3,5)F_2Y$

System	λ_{max} (nm) / ϵ (M ⁻¹ cm ⁻¹)	pK _a [pK _{app}]	Potential vs. NHE (mV) ^e	Ref.
Y(Ac/NH ₂) ^a	275/1400 (Y-OH) 293/2420 (Y-O ⁻)	10	E_{peak} 830 (pH 7.0)	18
3,5-F ₂ Y(Ac/NH ₂) ^a	263/560 (Y-OH) 275/1830 (Y-O ⁻)	7.0 ± 0.2	E_{peak} 770 (pH 7.0)	18
α_3Y	277/1500 (Y-OH, pH 5.4) 294/2430 (Y-O ⁻ , pH 13.4)	$[11.3 \pm 0.1]$	E° 1059 (pH 5.7) E° 980 (pH 7.0)	7, 17, 29 this work
$\alpha_3(3,5)F_2Y$	$\sim 264/\text{n.d.}$ (Y-OH) ^a $\sim 277/\text{n.d.}$ (Y-O ⁻) ^a	$[8.0 \pm 0.1]$	E° 1026 (pH 5.7) E° 952 (pH 7.0) ^f	this work
System	$[\Theta]_{222} \times 10^3$ (deg cm ² dmol ⁻¹)	Helix (%) ^b	ΔG (kcal mol ⁻¹)	Ref.
α_3Y	-20.0 ± 0.8 (pH 5.6)	75 ± 3 (pH 5.6) ^c 74 ± 1 (4.5–10) ^d	-3.7 ± 0.1 (pH 5.0) -3.9 ± 0.1 (pH 5.5)	7, 17 this work
$\alpha_3(3,5)F_2Y$	-20.9 ± 0.6 (pH 5.6)	79 ± 2 (pH 5.6) ^c	-3.7 ± 0.1 (pH 5.0) -3.7 ± 0.1 (pH 5.5)	this work

^a Acetyl-tyrosinamide (Ac/NH₂), ϵ was not determined (n.d.).

^b Scaled relative to the $[\Theta]_{222}$ of α_3W ($76 \pm 1\%$ α -helical, pH 4–10).^{17,31}

^c [Protein] determined by the Bradford assay.

^d [Protein] determined by UV absorption.^{7,17}

^e Anodic peak potentials from irreversible differential pulse voltammograms (E_p).^{17,18} The standard error in E° is $\leq \pm 4$ mV.

^f Extrapolated from the pH 5.7 value and assuming the same pH dependence as observed for α_3Y E° (pH 5.7) and E° (pH 7.0).²⁹

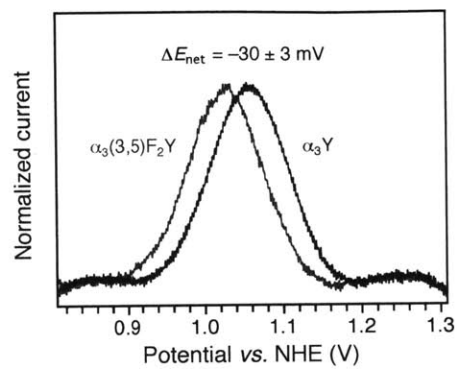


Figure 2.5 I_{net} of $\alpha_3(3,5)F_2Y$ (gray) and α_3Y (black) recorded at identical experimental conditions. SWV settings: 20 mM APB, 75 mM KCl, pH 5.62 ± 0.02 , PGE working electrode, temperature 25 °C, step potential 0.15 mV, SW frequency 190 Hz, SW pulse amplitude 25 mV.

2.4 DISCUSSION

2.4.1 Measuring tyrosine reduction potentials. There are three basic properties associated with Y that make electrochemical characterization a major challenge. The measurements must be carried out at highly oxidizing conditions ($\sim 1.0 \pm 0.3$ V vs. NHE), the Y• state is reactive¹⁹⁻²³ and both the reduced (ϵ_{280} 1490 M⁻¹ cm⁻¹)^{40,41} and oxidized (ϵ_{408} of 2750 M⁻¹ cm⁻¹)⁴⁵ states have weak extinction coefficients. The combination of these three properties rule out redox titration as a viable method to study the thermodynamics of Y redox cofactors. This is a significant problem since redox titration, using either chemical titrants and a redox cuvette or a potentiostat-controlled spectroelectrochemical cell, is the most common approach to measure reduction potentials of protein redox cofactors. The two former properties also make voltammetry a challenge. Measurements performed in the +1.0 V range will generate background currents arising from the working electrode and from the water solvent itself. These background currents will compromise data analysis unless the Faradaic current reflecting the Y redox cofactor is prominent. Moreover, uncontrolled oxidation of surface residues and general oxidative damage to the host protein are likely events. In addition to these concerns is the inherent issue associated with protein voltammetry, i.e., to identify conditions for which the folded protein exhibits direct and reversible electron transfer between the working electrode and the redox site of interest.⁴⁶⁻⁴⁸ These are the main reasons that a direct voltammetry approach on a complex radical enzyme such as *E. coli* RNR is not practical or even possible.

The α_3X system was developed to address these experimental barriers and allow rigorous electrochemical characterization of aromatic amino acids buried within a structured protein. In three recent studies,^{7,29,30} we have demonstrated that pulsed voltammetry methods (differential pulse voltammetry and SWV) generate reversible Y and phenol protein voltammograms of high

quality. Control studies have shown that the characteristics of the α_3X voltammograms are highly reproducible and that they uniquely reflect the aromatic residue at position 32 and its local environment. The more commonly used method of cyclic voltammetry²⁴ generates a poor Faradaic response from the α_3X proteins⁷ and this method was deemed too insensitive for this system. We note that the potential range probed in this study is very oxidizing for a protein system with measured E_{net} values well above +1.0 V. The high quality of the presented voltammograms is the result of combining the sensitivity provided by the pulsed SWV method (due to effective elimination of capacitive background currents) with carefully optimized protein/PGE working electrode conditions. The latter include electrode polishing procedures (described in the Materials and Methods sections), the sample composition (optimized for the α_3X /PGE system),^{29,30} and the protein concentration (Figure 2.4A). Importantly, the electrochemical reversibility observed for the α_3X proteins reflects the long halftimes (> 100s of ms) of the radicals generated in this system.^{29,30} Thus, the protein environment efficiently blocks the deleterious $Y\cdot$ side reactions that typically compromise electrochemical characterization of the solvated species.

In this study, the optimized α_3X radical system was combined with *in vivo* nonsense codon suppression⁵ to measure E^{oi} of a protein 3,5-F₂Y residue. The use of unnatural amino acids to study protein ET and PCET processes involving Y redox sites has emerged as an informative experimental approach.^{1,49,50} The Y analogs provide a means to introduce major changes in the pK_a of the reduced state and in the E^{oi} values of the Y-O \cdot /Y-OH and Y-O \cdot /Y-O⁻ redox couples. The pK_a of the oxidized state (-2 for aqueous Y-OH \cdot +) ⁵¹ is predicted to be non-accessible within the structural and catalytic pH ranges of proteins. Residue 32 resides in a structured, solvent-protected and low dielectric site typical of natural Y redox cofactors. The α_3X radical system will be used to generate a consistent set of ΔE^{oi} values to provide a guide for interpreting mutation-induced

changes in the free-energy profile of native ET/PCET chains involving aromatic amino-acid redox site(s). The availability of protein ΔE° values removes the uncertainty associated with using solution potentials to interpret protein redox events. Table 2.1 shows that there are considerable differences in protein potentials obtained under reversible conditions relative to solution potentials obtained under irreversible conditions. We find a difference between ΔE° (protein Y₃₂ and 3,5-F₂Y₃₂, -30 ± 3 mV) and ΔE_p (aqueous Y and 3,5-F₂Y, -60 mV) of 30 mV (Table 2.1). This difference most certainly arises from the irreversible characteristics of the small-molecule measurements. We also found that the absolute values of E° (protein Y₃₂ and 3,5-F₂Y₃₂) vs. E_p (aqueous Y and 3,5-F₂Y) is rather large (-150 - 180 mV). This observation suggests that the influence by the protein matrix on the absolute potentials of radical cofactors may be substantial. We conclude that site-specific incorporation of an unnatural amino acid into the electrochemically reversible α_3X redox system is a feasible and informative approach. It will be expanded to include other Y analogs in future studies, as described in more detail below.

2.4.2 Using the α_3X system as a guide to interpret mechanistic studies of *E. coli* RNR.

RNRs catalyze the formation of deoxynucleotides (dNDPs) from their corresponding nucleotides.^{1,8} *E. coli* class Ia RNR is composed of two homodimeric subunits, α_2 and β_2 . A stable diferric-Y₁₂₂[•] cofactor in β_2 generates a transient cysteine radical (C₄₃₉[•]) in the active site of α_2 located 35 Å away. The reversible long range radical-transfer process, triggered by substrate and effector binding to α_2 , is proposed to involve multiple PCET steps via a conserved pathway (Y₁₂₂ \Leftrightarrow [W₄₈] \Leftrightarrow Y₃₅₆ in β_2 to Y₇₃₁ \Leftrightarrow Y₇₃₀ \Leftrightarrow C₄₃₉ in α_2).¹ We have recently described the site-specific insertion of 3-nitrotyrosine (NO₂Y) in place of Y₁₂₂ in β_2 .⁶ The diferric-NO₂Y₁₂₂[•] cofactor was generated and studies with α_2 , substrate (CDP) and effector (ATP) allowed the first observation of a transient, kinetically competent Y[•] on pathway by EPR spectroscopy.⁶ Pulsed

electron-electron double resonance (PELDOR) spectroscopy was used to establish the primary location of the new radical as $Y_{356}\bullet$ - $\beta 2$ and suggested the formation of a small percentage of radical at either Y_{731} or Y_{730} in $\alpha 2$. To probe this further, the reaction of $Y_{122}NO_2Y$ - $\beta 2$ with $Y_{731}(3,5)F_2Y$ - $\alpha 2$ (or $Y_{730}(3,5)F_2Y$ - $\alpha 2$), CDP and ATP was performed. Analysis of the reactions by X-band EPR spectroscopy demonstrated an equilibrium between $Y_{356}\bullet$ in $\beta 2$ and $3,5-F_2Y_{731}\bullet$ or $3,5-F_2Y_{730}\bullet$ in $\alpha 2$ with 85–90% of the spin localized at Y_{356} and 15–10% distributed over F_2Y_{731}/F_2Y_{730} .³⁶ To extrapolate the equilibrium observed with $3,5-F_2Y$ to Y , the native pathway residue, requires a knowledge of E° values for $3,5-F_2Y$ and Y . To date, only solution E_p values derived from irreversible voltammograms have been available for the fluorotyrosines.^{1,18} The SWV measurements performed on α_3Y and $\alpha_3(3,5)F_2Y$ provide the first E° values representing the radical species in a well-defined protein environment. The small ΔE° of -30 ± 3 mV between Y_{32} and $3,5-F_2Y_{32}$ suggests that a thermodynamic landscape, formed by three transient tyrosyl radicals (Y_{356} , Y_{731} , Y_{730}) of similar energy with one (Y_{356}) being most prevalent, is a reasonable depiction of nature's design within this part of the pathway.

2.4.3 Future perspectives. We have shown that formal reduction potentials representing a reversible $Y-O\bullet/Y-OH$ redox system can be obtained for α_3Y ²⁹ and $\alpha_3(3,5)F_2Y$. Future studies are focused on obtaining a consistent set of E° values from other F_nY residues. One of our primary goals in the Stubbe lab is to understand the thermodynamic landscape of the RT pathway within the $\beta 2$ subunit. Toward that goal, we have successfully generated all diferric- $F_nY_{122}\bullet$ ($n = 2$ or 3) and demonstrated their ability to perform multiple turnovers (5–85% wt activity).^{5,52} With the exception of $Y_{122}(3,5)F_2Y$ - $\beta 2$, the reaction of $Y_{122}F_nY$ - $\beta 2$ with $\alpha 2$, CDP and ATP accumulates $Y_{356}\bullet$. In the case of $Y_{122}(2,3,5)F_3Y$ - $\beta 2$, the experiments described in Chapters 3 and 4 show that $Y_{356}\bullet$ is kinetically and chemically competent, and also that $2,3,5-F_3Y\bullet$ is in equilibrium with $Y_{356}\bullet$

(in the reaction with $Y_{731}F-\alpha 2$). Similarly, preliminary data collected in our lab suggests that 2,3- $F_2Y\bullet$ also equilibrates with $Y_{356}\bullet$ in the reaction of $Y_{122}(2,3)F_2Y-\beta 2$, $Y_{731}F-\alpha 2$, CDP and ATP (Taguchi, Stubbe unpublished results). Temperature-dependent quantitation of 2,3,5- $F_3Y\bullet$ (or 2,3- $F_2Y\bullet$) and $Y_{356}\bullet$ allows estimation of $\Delta E^\circ (F_nY\bullet - Y_{356}\bullet)$. Thus, protein E° values of F_nY relative to Y play an important role in extrapolating these numbers to the wt system. Finally, work to complement the α_3X protein E° data series with α_3W is also in progress. W is an important protein redox cofactor observed in a number of enzymes⁵³⁻⁵⁵ and engineered to study multistep electron tunneling in *Pseudomonas aeruginosa* azurin.⁵⁶ In the case of the *E. coli* class Ia RNR, no direct evidence yet exists for the participation of W_{48} in the RT pathway. Obtaining E° values for this residue would provide insight into whether oxidation of W_{48} by $Y_{122}\bullet$ is thermodynamically feasible.

2.5 REFERENCES

1. Minnihan, E. C.; Nocera, D. G.; Stubbe, J. Reversible, long-range radical transfer in *E. coli* class Ia ribonucleotide reductase, *Acc. Chem. Res.* **2013**, *46*, 2524-2535.
2. Ge, J.; Yu, G.; Ator, M. A.; Stubbe, J. Pre-steady-state and steady-state kinetic analysis of *E. coli* class I ribonucleotide reductase, *Biochemistry* **2003**, *42*, 10071-10083.
3. Seyedsayamdost, M. R.; Stubbe, J. Site-specific replacement of Y₃₅₆ with 3,4-dihydroxyphenylalanine in the β 2 subunit of *E. coli* ribonucleotide reductase, *J. Am. Chem. Soc.* **2006**, *128*, 2522-2523.
4. Seyedsayamdost, M. R.; Xie, J.; Chan, C. T.; Schultz, P. G.; Stubbe, J. Site-specific insertion of 3-aminotyrosine into subunit α 2 of *E. coli* ribonucleotide reductase: direct evidence for involvement of Y₇₃₀ and Y₇₃₁ in radical propagation, *J. Am. Chem. Soc.* **2007**, *129*, 15060-15071.
5. Minnihan, E. C.; Young, D. D.; Schultz, P. G.; Stubbe, J. Incorporation of fluorotyrosines into ribonucleotide reductase using an evolved, polyspecific aminoacyl-tRNA synthetase, *J. Am. Chem. Soc.* **2011**, *133*, 15942-15945.
6. Yokoyama, K.; Uhlin, U.; Stubbe, J. A hot oxidant, 3-NO₂Y₁₂₂ radical, unmasks conformational gating in ribonucleotide reductase, *J. Am. Chem. Soc.* **2010**, *132*, 15368-15379.
7. Martínez-Rivera, M. C.; Berry, B. W.; Valentine, K. G.; Westerlund, K.; Hay, S.; Tommos, C. Electrochemical and structural properties of a protein system designed to generate tyrosine Pourbaix diagrams, *J. Am. Chem. Soc.* **2011**, *133*, 17786-17795.
8. Stubbe, J.; van der Donk, W. A. Protein radicals in enzyme catalysis, *Chem. Rev.* **1998**, *98*, 705-762.
9. Tommos, C.; Babcock, G. T. Proton and hydrogen currents in photosynthetic water oxidation, *Biochim. Biophys. Acta.* **2000**, *1458*, 199-219.
10. Pesavento, R. P.; van der Donk, W. A. Tyrosyl radical cofactors, *Adv. Protein. Chem.* **2001**, *58*, 317-385.
11. Hoganson, C. W.; Tommos, C. The function and characteristics of tyrosyl radical cofactors, *Biochim. Biophys. Acta.* **2004**, *1655*, 116-122.
12. Warren, J. J.; Winkler, J. R.; Gray, H. B. Redox properties of tyrosine and related molecules, *FEBS Lett.* **2012**, *586*, 596-602.
13. Harriman, A. Further comments on the redox potentials of tryptophan and tyrosine, *J. Phys. Chem.* **1987**, *91*, 6102-6104.
14. DeFilippis, M. R.; Murthy, C. P.; Faraggi, M.; Klapper, M. H. Pulse radiolytic measurement of redox potentials: the tyrosine and tryptophan radicals, *Biochemistry* **1989**, *28*, 4847-4853.
15. Lind, J.; Shen, X.; Eriksen, T. E.; Merenyi, G. The one-electron reduction potential of 4-substituted phenoxyl radicals in water, *J. Am. Chem. Soc.* **1990**, *112*, 479-482.

16. DeFilippis, M. R.; Murthy, C. P.; Broitman, F.; Weinraub, D.; Faraggi, M.; Klapper, M. H. Electrochemical properties of tyrosine phenoxyl and tryptophan in indolyl radicals in peptides and amino acid analogs, *J. Phys. Chem.* **1991**, *95*, 3416-3419.
17. Tommos, C.; Skalicky, J. J.; Pilloud, D. L.; Wand, A. J.; Dutton, P. L. De novo proteins as models of radical enzymes, *Biochemistry* **1999**, *38*, 9495-9507.
18. Seyedsayamdost, M. R.; Reece, S. Y.; Nocera, D. G.; Stubbe, J. Mono-, di-, tri-, and tetra-substituted fluorotyrosines: new probes for enzymes that use tyrosyl radicals in catalysis, *J. Am. Chem. Soc.* **2006**, *128*, 1569-1579.
19. Gross, A. J.; Sizer, I. W. The oxidation of tyramine, tyrosine, and related compounds by peroxide, *J. Biol. Chem.* **1959**, *234*, 1611-1614.
20. Lehrer, S. S.; Fasman, G. D. Ultraviolet irradiation effects in poly-L-tyrosine and model compounds. Identification of bityrosine as a photoproduct, *Biochemistry* **1967**, *6*, 757-767.
21. Boguta, G.; Dancewicz, A. M. Radiation-induced dimerization of tyrosine and glycytyrosine in aqueous solutions, *Int. J. Radiat. Biol.* **1981**, *39*, 163-174.
22. Karam, L. R.; Dizdaroglu, M.; Simic, M. G. OH radical-induced products of tyrosine peptides, *Int. J. Radiat. Biol.* **1984**, *46*, 715-724.
23. Hawkins, C. L.; Davies, M. J. Generation and propagation of radical reactions on proteins, *Biochim. Biophys. Acta.* **2001**, *1504*, 93-109.
24. Bard, A. J.; Faulkner, L. R. *Electrochemical methods: Fundamentals and applications*, 2nd Ed., John Wiley & Sons, Inc., USA. **2001**.
25. Savéant, J. M. *Elements of molecular and biomolecular electrochemistry: An electrochemical approach to electron transfer chemistry*, John Wiley & Sons, Inc., USA. **2006**.
26. Warshel, A.; Sharma, P. K.; Kato, M.; Xiang, Y.; Liu, H.; Olsson, M. H. M. Electrostatic basis for enzyme catalysis, *Chem. Rev.* **2006**, *106*, 3210-3235.
27. Chandler, D. Interfaces and the driving force of hydrophobic assembly, *Nature* **2005**, *437*, 640-647.
28. Westerlund, K.; Berry, B. W.; Privett, H. K.; Tommos, C. Exploring amino acid radical chemistry: protein engineering and de novo design, *Biochim. Biophys. Acta.* **2005**, *1707*, 103-116.
29. Berry, B. W.; Martínez-Rivera, M. C.; Tommos, C. Reversible voltammograms and a Pourbaix diagram for a protein tyrosine radical, *Proc. Natl. Acad. Sci. U. S. A.* **2012**, *109*, 9739-9743.
30. Tommos, C.; Valentine, K. G.; Martínez-Rivera, M. C.; Liang, L.; Moorman, V. R. Reversible phenol oxidation and reduction in the structurally well-defined 2-mercaptophenol- α 3C protein, *Biochemistry* **2013**, *52*, 1409-1418.
31. Dai, Q. H.; Tommos, C.; Fuentes, E. J.; Blomberg, M. R. A.; Dutton, P. L.; Wand, A. J. Structure of a de novo designed model protein of radical systems, *J. Am. Chem. Soc.* **2002**, *124*, 10952-10953.

32. Hay, S.; Westerlund, K.; Tommos, C. Moving a phenol hydroxyl group from the surface to the interior of a protein: Effects on the phenol potential and pK_a , *Biochemistry* **2005**, *44*, 11891-11902.
33. Hay, S.; Westerlund, K.; Tommos, C. Redox characteristics of a de novo quinone protein, *J. Phys. Chem. B.* **2007**, *111*, 3488-3495.
34. Osteryoung, J.; O'Dea, J. J. Square-wave voltammetry. In Bard AJ (ed) *Electroanalytical chemistry* **1986**, *5*, 209-308.
35. Mirčeski, V.; Komorsky-Lovrić, Š.; Lovrić, M. Square-wave voltammetry: Theory and applications. In Scholtz F (ed), *Monographs in Electrochemistry*. **2007** (Springer-Verlag, Berlin, Germany).
36. Yokoyama, K.; Smith, A. A.; Corzilius, B.; Griffin, R. G.; Stubbe, J. Equilibration of tyrosyl radicals (Y_{356}^\bullet , Y_{731}^\bullet , Y_{730}^\bullet) in the radical propagation pathway of the *Escherichia coli* class Ia ribonucleotide reductase, *J. Am. Chem. Soc.* **2011**, *133*, 18420-18432.
37. Chen, H.; Gollnick, P.; Phillips, R. S. Site-directed mutagenesis of His343-->Ala in *Citrobacter freundii* tyrosine phenol-lyase. Effects on the kinetic mechanism and rate-determining step, *Eur. J. Biochem.* **1995**, *229*, 540-549.
38. Seyedsayamdost, M. R.; Yee, C. S.; Stubbe, J. Site-specific incorporation of fluorotyrosines into the R2 subunit of *E. coli* ribonucleotide reductase by expressed protein ligation, *Nat. Protoc.* **2007**, *2*, 1225-1235.
39. Kim, K.; Cole, P. A. Kinetic analysis of a protein tyrosine kinase reaction transition state in the forward and reverse directions, *J. Am. Chem. Soc.* **1998**, *120*, 6851-6858.
40. Edelhoch, H. Spectroscopic determination of tryptophan and tyrosine in proteins, *Biochemistry* **1967**, *6*, 1948-1954.
41. Pace, C. N.; Vajdos, F.; Fee, L.; Grimsley, G.; Gray, T. How to measure and predict the molar absorption coefficient of a protein, *Prot. Sci.* **1995**, *4*, 2411-2423.
42. Santoro, M. M.; Bolen, D. W. Unfolding free energy changes determined by the linear extrapolation method. 1. Unfolding of phenylmethanesulfonyl α -chymotrypsin using different denaturants, *Biochemistry* **1988**, *27*, 8063-8068.
43. Salwiczek, M.; Nyakatura, E. K.; Gerling, U. I. M.; Ye, S.; Koksche, B. Fluorinated amino acids: compatibility with native protein structures and effects on protein-protein interactions, *Chem. Soc. Rev.* **2012**, *41*, 2135-2171.
44. Buer, B. C.; Marsh, E. N. G. Fluorine: a new element in protein design, *Prot. Sci.* **2012**, *21*, 453-462.
45. Feitelson, J.; Hayon, E. Electron ejection and electron capture by phenolic compounds, *J. Phys. Chem.* **1973**, *77*, 10-15.
46. Rusling, J. F. Enzyme bioelectrochemistry in cast biomembrane-like films, *Acc. Chem. Res.* **1998**, *31*, 363-369.
47. Armstrong, F. A.; Wilson, G. S. Recent developments in faradaic bioelectrochemistry, *Electrochim. Acta.* **2000**, *45*, 2623-2645.

48. Armstrong, F. A. Recent developments in dynamic electrochemical studies of adsorbed enzymes and their active sites, *Curr. Opin. Chem. Biol.* **2005**, *9*, 110-117.
49. Rappaport, F.; Boussac, A.; Force, D. A.; Peloquin, J.; Brynda, M.; Sugiura, M.; Un, S.; Britt, R. D.; Diner, B. A. Probing the coupling between proton and electron transfer in photosystem II core complexes containing a 3-fluorotyrosine, *J. Am. Chem. Soc.* **2009**, *131*, 4425-4433.
50. Warren, J. J.; Herrera, N.; Hill, M. G.; Winkler, J. R.; Gray, H. B. Electron flow through nitrotyrosine in *Pseudomonas aeruginosa* azurin, *J. Am. Chem. Soc.* **2013**, *135*, 11151-11158.
51. Dixon, W. T.; Murphy, D. Determination of the acidity constants of some phenol radical cations by means of electron spin resonance, *J. Chem. Soc. Faraday. Trans. II* **1976**, *72*, 1221-1230.
52. Minnihan, E. C. Mechanistic studies of proton-coupled electron transfer in aminotyrosine- and fluorotyrosine-substituted class Ia ribonucleotide reductase. Ph.D. Thesis, Massachusetts Institute of Technology, **2012**.
53. Tsai, A. L.; Kulmacz, R. J. Prostaglandin H synthase: resolved and unresolved mechanistic issues, *Arch. Biochem. Biophys.* **2010**, *493*, 103-124.
54. Aubert, C.; Vos, M. H.; Mathis, P.; Eker, A. P.; Brettel, K. Intraprotein radical transfer during photoactivation of DNA photolyase, *Nature* **2000**, *405*, 586-590.
55. Tarboush, N. A.; Jensen, L. M. R.; Yukl, E. T.; Geng, J.; Liu, A.; Wilmot, C. M.; Davidson, V. L. Mutagenesis of tryptophan 199 suggests that hopping is required for MauG-dependent tryptophan tryptophylquinone biosynthesis, *Proc. Natl. Acad. Sci. U. S. A.* **2011**, *108*, 16956-16961.
56. Shih, C.; Museth, A. K.; Abrahamsson, M.; Blanco-Rodriguez, A. M.; Di Bilio, A. J.; Sudhamsu, J.; Crane, B. R.; Ronayne, K. L.; Towrie, M.; Vlcek, A. Jr.; Richards, J. H.; Winkler, J. R.; Gray, H. B. Tryptophan-accelerated electron flow through proteins, *Science* **2008**, *320*, 1760-1762.

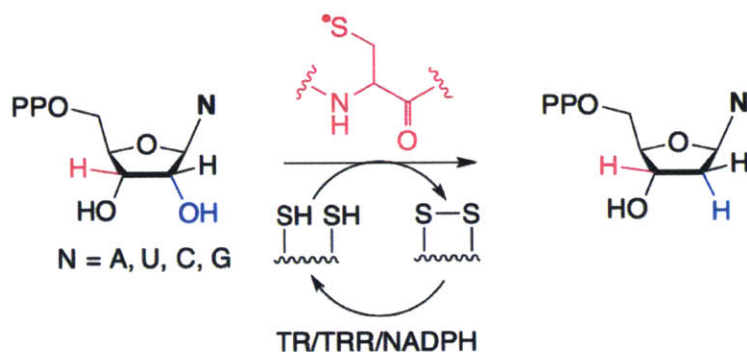
Chapter 3

Reverse electron transfer completes the catalytic cycle in a
2,3,5-trifluorotyrosine-substituted ribonucleotide reductase

Adapted with permission from Ravichandran, K.R.; Minnihan, E.C.; Wei, Y.; Nocera, D.G.; Stubbe, J. J. Am. Chem. Soc. 2015, 137, 14387-95. Copyright 2015 American Chemical Society

3.1 INTRODUCTION

Ribonucleotide reductases (RNRs) catalyze the formation of deoxynucleotides from their corresponding ribonucleotides (Scheme 3.1) in almost all organisms; allosteric regulation of substrate specificity and activity contributes to fidelity of both DNA replication and repair.^{1,2} The class Ia RNRs contain two homodimeric subunits, $\alpha 2$ and $\beta 2$, which form an active $\alpha 2\beta 2$ complex in the case of the *E. coli* enzyme.³ The $\beta 2$ subunit houses a diferric-tyrosyl radical ($Y_{122}\bullet$) cofactor that reversibly oxidizes C_{439} in the active site of $\alpha 2$ to a thiyl radical.^{4,5} The $C_{439}\bullet$ initiates nucleotide reduction by H-atom abstraction from the 3' position of the substrate (Scheme 3.1).^{6,7} Based on *in silico* docking of the individual X-ray structures of $\alpha 2$ and $\beta 2$,^{8,9} the distance between $Y_{122}\bullet$ and C_{439} is estimated to be >35 Å. This radical transport (RT) process occurs through a specific pathway that involves at least three transient aromatic amino acid radical intermediates (proton-coupled electron transfer or PCET through $Y_{122}\bullet \rightarrow [W_{48}] \rightarrow Y_{356}$ in $\beta 2$ to $Y_{731} \rightarrow Y_{730} \rightarrow C_{439}$ in $\alpha 2$, Figure 3.1).^{9,10} During turnover of wild-type (wt) RNR, only the resting state $Y_{122}\bullet$ is observed. In this Chapter, we describe the perturbation of PCET kinetics by site-specific incorporation of 2,3,5- F_3Y (or F_3Y) at position 122 in $\beta 2$ resulting in accumulation of a pathway tyrosyl radical intermediate ($Y_{356}\bullet$) that is kinetically and chemically competent to complete the catalytic cycle of RNR.



Scheme 3.1 Reaction catalyzed by RNR. Turnover requires reducing equivalents, which are provided by a pair of cysteines in the active site of the enzyme.

In wt RNR, PCET steps are preceded by a rate-limiting protein conformational change(s) ($5\text{-}10\text{ s}^{-1}$) that occur(s) upon association of $\alpha 2$, $\beta 2$, substrate (S, CDP) and allosteric effector (E, ATP).¹¹ Forward RT steps, active site chemistry and reverse RT steps occur on a much more rapid time scale than the protein conformational change(s), preventing observation of radical intermediates either during steady-state turnover or using rapid kinetic methods.¹¹ An approach adopted by our lab has been to change the rate-limiting step of the reaction by site-specifically incorporating tyrosine analogs with perturbed pK_a s and reduction potentials in an effort to accumulate and characterize the proposed radical intermediates (Figure 3.1). Previously, we described the insertion of 3-nitrotyrosine (NO_2Y) at residue 122 in $\beta 2$.¹² The reaction of $\text{Y}_{122}\text{NO}_2\text{Y-}\beta 2$, $\alpha 2$, CDP and ATP rapidly generates 0.5 equiv. of $\text{Y}_{356}\bullet$ and dCDP ($> 100\text{ s}^{-1}$). We have proposed that this stoichiometry is a consequence of half-sites reactivity in RNR where only 50% of $\text{Y}_{122}\bullet$ in the $\alpha 2\beta 2$ complex reacts at a time.¹³⁻¹⁷ We have recently shown that upon radical initiation in wt RNR, a proton is transferred from a water molecule on the diferric cluster to generate the corresponding Y_{122} phenol (Figure 3.1).¹⁸ In contrast, use of $\text{Y}_{122}\text{NO}_2\text{Y-}\beta 2$ to initiate RT uncouples this proton transfer (PT) and electron transfer (ET); the conjugate base NO_2Y^- is generated instead of the anticipated phenol NO_2Y . Furthermore, $\text{Y}_{356}\bullet$ generated during reverse RT is unable to re-oxidize NO_2Y^- and thus, this mutant could only perform a single turnover.¹²

This caveat prevented us from establishing the chemical competence of Y_{356}^{\bullet} to complete the catalytic cycle and determining if it is a true intermediate on the PCET pathway.

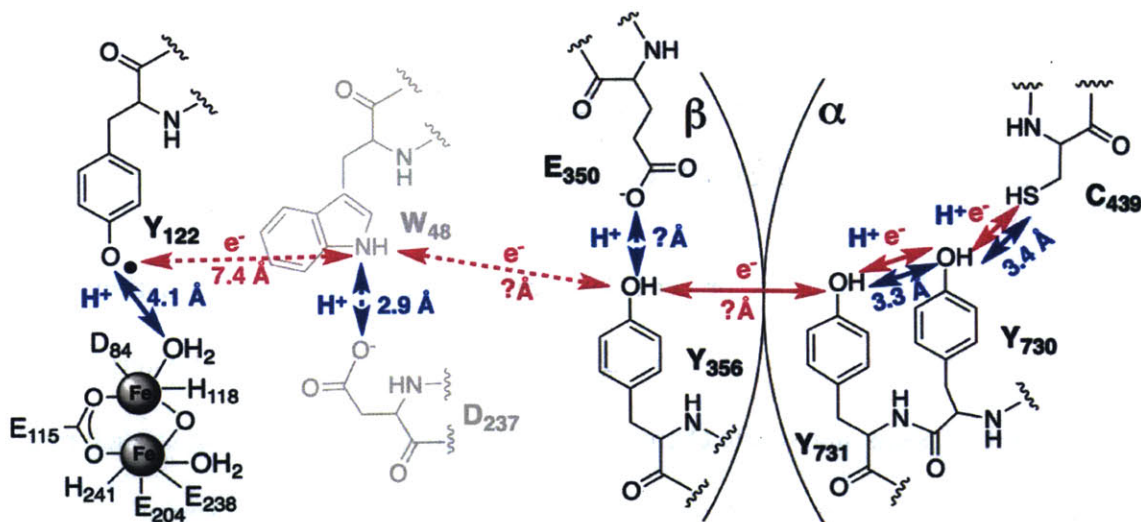


Figure 3.1 The proposed PCET pathway in *E. coli* class Ia RNR.¹⁰ The pink and blue arrows indicate the movement of electrons and protons through conserved aromatic amino acids (Y_{356} in $\beta 2$ and Y_{731} and Y_{730} in $\alpha 2$). W_{48} and its putative proton acceptor D_{237} are shown in gray, as there is no evidence for their participation in RT. The positions of Y_{356} and E_{350} are unknown, as these residues are disordered in all crystal structures of $\beta 2$.

In an attempt to engineer a smaller perturbation to the driving force, we inserted F_3Y at position 122 in $\beta 2$ and investigated the reaction of $Y_{122}(2,3,5)F_3Y$ - $\beta 2$, $\alpha 2$, CDP and ATP.¹⁹ Steady-state assays revealed that unlike the $Y_{122}NO_2Y$ - $\beta 2$ mutant, $Y_{122}(2,3,5)F_3Y$ - $\beta 2$ can catalyze multiple turnovers at 25% the steady-state wt activity. Hand-quench EPR experiments showed formation of a new tyrosyl radical, assigned to residue Y_{356} in $\beta 2$ based on multiple lines of evidence. First, the new radical is observed when the redox inert F is inserted at position 731 but not at position 356.¹⁹ Second, the 9 GHz EPR spectrum of the new radical is remarkably similar to that of the radical observed in the $Y_{122}NO_2Y$ - $\beta 2$ studies.^{12,19} In $Y_{122}NO_2Y$ - $\beta 2$, pulsed electron-electron double resonance (PELDOR) spectroscopy experiments measured a distance of 30 Å between the new radical in one α/β pair and NO_2Y^{\bullet} in the second α/β pair.²⁰ Similar experiments

with other unnatural amino acids inserted at position 356 (either 3,4-dihydroxyphenylalanine²¹ or 3-aminotyrosine²²) provide an identical distance measurement (30 Å). In preliminary PELDOR experiments, a similar distance is also observed between F_3Y^\bullet and the new radical.²³ These data together support that the radical observed in $Y_{122}(2,3,5)F_3Y$ - $\beta 2$ is located at position 356. Studies with $Y_{122}NO_2Y$ - $\beta 2$, however, have shown that while the predominant location of the radical is at position 356 (85–90%), Y_{356}^\bullet is in equilibrium with Y_{731}^\bullet and Y_{730}^\bullet in $\alpha 2$ (15–10%).²⁰ These initial studies laid the foundation for the work described herein and gave us an opportunity to investigate the importance of Y_{356}^\bullet and reverse RT in an active RNR complex.

In this work, we carry out thorough kinetic analyses of the reaction of $Y_{122}(2,3,5)F_3Y$ - $\beta 2$, $\alpha 2$, CDP and ATP in the absence and presence of an external reducing system composed of thioredoxin (TR), thioredoxin reductase (TRR) and NADPH. Rapid freeze-quench (RFQ) EPR spectroscopy and rapid chemical quench (RCQ) studies in the absence of a reducing system demonstrate that Y_{356}^\bullet is kinetically and chemically competent; similar amounts of Y_{356}^\bullet and dCDP are produced at similar rate constants. Furthermore, subsequent to complete oxidation of $\alpha 2$, Y_{356}^\bullet reduction occurs concomitant with F_3Y re-oxidation. RCQ analysis in the presence of a reducing system shows a burst of dCDP prior to steady-state turnover, suggesting that the rate-limiting step occurs after product formation. EPR studies detect no changes in Y_{356}^\bullet concentration during steady-state turnover. Together, the data support the conclusion that reverse RT within $\beta 2$ leading to regeneration of F_3Y^\bullet is rate-limiting during steady-state turnover of $Y_{122}(2,3,5)F_3Y$ - $\beta 2$.

3.2 MATERIALS AND METHODS

3.2.1 Materials. (His)₆ wt- α 2 (specific activity of 2500 nmol/min/mg) was expressed from pET28a-*nrdA* and purified using our standard protocol.²⁴ Wt- α 2 was pre-reduced by the addition of DTT and hydroxyurea prior to use.²⁵ Tyrosine phenol lyase (TPL) was expressed and purified as described.²⁶ F₃Y was enzymatically synthesized from the corresponding phenol using TPL (Chapter 2).²⁷ The pBAD-*nrdB*_{122TAG} and pBAD-*F_nYRS-E3* plasmids were generated and isolated as described.¹⁹ *E. coli* TR (40 U/mg) and TRR (1400 U/mg) were purified using established protocols.^{28,29} [³H] CDP was purchased from ViTrax (Placentia, CA). HEPES, MgSO₄, EDTA, 2XYT microbial medium, ampicillin (Amp), chloramphenicol (Cm), ATP, CDP and carrier deoxycytidine (dC) were obtained from Sigma Aldrich. Promega provided isopropyl β -D-1 thiogalactopyranoside (IPTG) and DTT. Calf alkaline phosphatase was purchased from Roche. Assay buffer consists of 50 mM HEPES pH 7.6, 15 mM MgSO₄ and 1 mM EDTA.

3.2.2 Expression and purification of apo Y_{122(2,3,5)}F₃Y- β 2. pBAD-*nrdB*_{122TAG} and pEVOL-*F_nYRS-E3* were co-transformed into *E. coli* TOP10 chemically competent cells and grown at 37 °C on LB-agar plates containing 100 μ g/mL Amp and 35 μ g/mL Cm. A starter culture (2 mL) supplemented with the antibiotics was inoculated with a single colony and grown until saturation (37 °C, 12 h). This starter culture was diluted 100-fold into fresh 2XYT medium containing Amp and Cm. After 16 h, the culture was diluted 100-fold into 4 x 2 L of 2XYT with antibiotics and 0.7 mM F₃Y (500 mM stock solution in water, NH₄OH solubilized). At an OD₆₀₀ of 0.5, 100 μ M *o*-phenanthroline (100 mM stock solution in 0.1 M HCl) was added to chelate iron. After 30 min, 0.05% (w/v) L-arabinose (10% w/v stock solution in water) was added to induce *F_nYRS* and *nrdB*. Growth was continued for an additional 5 h and the cells were harvested by centrifugation (3500 x g, 15 min). Y_{122(2,3,5)}F₃Y- β 2 was purified using anion-exchange

chromatography as previously described.³⁰ Typical yields of 10–15 mg pure protein/g cell paste were obtained.

3.2.3 Reconstitution of apo $Y_{122}(2,3,5)F_3Y\text{-}\beta 2$ to form the diferric- $F_3Y\bullet$ cofactor. Apo $Y_{122}(2,3,5)F_3Y\text{-}\beta 2$ was deoxygenated and taken into an anaerobic chamber maintained at 4 °C. $Fe^{II}(NH_4)_2(SO_4)_2$ (5 eq., 20 mM stock solution in 50 mM HEPES pH 7.6, 5% glycerol) was incubated with the protein for 15 min.¹² The sample was brought out of the chamber sealed, and 3.5 equiv. of O_2 in the form of O_2 -saturated 50 mM HEPES pH 7.6, 5% glycerol was added to reconstitute the cluster. $Y_{122}(2,3,5)F_3Y\text{-}\beta 2$ (250 μ L) was frozen in an EPR tube immediately after reconstitution to quantitate radical content. EPR spectroscopy was performed at the Department of Chemistry Instrumentation Facility at MIT using wt- $\beta 2$ (1.2 $Y\bullet/\beta 2$) as a standard. The concentration of $Y\bullet$ in the wt- $\beta 2$ standard was previously estimated using a $Cu(II)SO_4$ standard.³¹ EPR spectra were recorded at 77 K on a Bruker EMX X-band spectrometer with a quartz finger dewar containing liquid N_2 . The parameters were as follows: microwave frequency 9.45 GHz; power 30 μ W; modulation amplitude 1.50 G; modulation frequency 100 kHz; time constant 5.12 ms and scan time 41.93 s. Typical yields of 0.6–0.8 $F_3Y\bullet/\beta 2$ were obtained for the reconstituted protein. To assess the stability of $F_3Y\bullet$, the sample in the EPR tube was rapidly thawed in a 25 °C water bath, aged for varying periods of time on ice and quenched in liq. N_2 for re-analysis by EPR. The radical was stable on the order of several hours.

3.2.4 Reaction of $Y_{122}(2,3,5)F_3Y\text{-}\beta 2$, wt- $\alpha 2$, CDP and ATP monitored by RFQ-EPR spectroscopy. RFQ experiments were performed on an Update Instruments 1019 syringe ram unit and a model 715 Syringe Ram controller (ram speed 1.25–1.6 cm/s) equipped with a Lauda RM6 circulating water bath set at 5 °C or 25 °C. $Y_{122}(2,3,5)F_3Y\text{-}\beta 2$ (0.4–0.8 $F_3Y\bullet/\beta 2$, 80 μ M) and CDP (2 mM) in assay buffer was mixed on a rapid timescale (16 ms–15 s) with an equal volume of wt-

$\alpha 2$ (80 μM) and ATP (6 mM) in assay buffer. The reaction was quenched in liquid isopentane (-140 °C) and the crystals were packed into EPR tubes for analysis by EPR spectroscopy. A packing factor of 0.60 ± 0.02 was determined for wt- $\beta 2$. The reaction at 5 °C was additionally monitored on a longer time scale (20 s–2 min) by mixing all assay ingredients by hand (30 μM wt- $\alpha 2$, 30 μM $Y_{122}(2,3,5)F_3Y$ - $\beta 2$, 1 mM CDP and 3 mM ATP) and quenching in liquid isopentane. From each composite EPR spectrum, residual $F_3Y\bullet$ was subtracted by aligning the radical's distinct features on the high and low-field sides of the spectrum as previously reported.¹⁹ The subtracted spectrum was re-integrated to quantitate the percentage of any observed pathway radical. The complete data sets at 5 °C and 25 °C were fit to equation 3.1:

$$y = A_1(1 - e^{-k_1t}) + A_2(1 - e^{-k_2t}) \quad (3.1)$$

where A_1 and A_2 are the amplitudes of the two phases and k_1 and k_2 are the observed rate constants.

3.2.5 Reaction of $Y_{122}(2,3,5)F_3Y$ - $\beta 2$, wt- $\alpha 2$, CDP and ATP monitored by the RCQ method.

RCQ experiments were performed on a KinTek RQF-3 instrument equipped with a Lauda RM6 circulating water bath set at 5 °C or 25 °C. Syringe A containing 20 μM wt- $\alpha 2$ and 6 mM ATP in assay buffer was mixed with an equal volume from syringe B containing 20 μM $Y_{122}(2,3,5)F_3Y$ - $\beta 2$ (0.85 $F_3Y\bullet/\beta 2$) and 1 mM [^3H] CDP (22,000 cpm/nmol) in assay buffer. The reaction was aged for varying times (5 ms–100 s) and quenched with 2% HClO_4 in syringe C. The reaction was additionally monitored at >100 s by mixing the contents of the two syringes by hand, incubating the reaction mixture in a circulating water bath for the desired period of time and manually quenching the reaction with 2% HClO_4 . All samples were neutralized by the addition of 110–160 μL 0.5 M KOH and worked up as described.^{11,32} To measure radioactive background from [^3H] CDP, an equal volume of the contents of syringe B was mixed with assay buffer, followed by 2% HClO_4 and KOH. The reaction was also performed by hand (100 s at 5 °C or 25 °C) before and

after the entire RCQ time course to account for any air oxidation of wt- α 2. The 5 °C data set was fit to equation 3.1 and the 25 °C data set was fit to equation 3.2:

$$y = 0.50(1 - e^{-30t}) + A_2(1 - e^{-k_2t}) + k_3t \quad (3.2)$$

In equation 2, the first phase is fixed, A_2 and k_2 represent the amplitude and rate constant of the second phase and k_3 represents the rate constant for the third phase.

3.2.6 Reaction of $Y_{122}(2,3,5)F_3Y\text{-}\beta$ 2, wt- α 2, CDP, ATP, TR/TRR/NADPH monitored by hand-quench EPR spectroscopy. Reactions were performed in a total volume of 250 μ L containing 10 μ M wt- α 2, 10 μ M $Y_{122}(2,3,5)F_3Y\text{-}\beta$ 2 (0.6 $F_3Y\text{-}\beta$ 2), 1 mM CDP, 3 mM ATP, 40 μ M TR, 0.8 μ M TRR and 1 mM NADPH in assay buffer. Samples were incubated in a circulating water bath set at 5 °C and quenched for EPR analysis between 20 s and 90 s in liquid isopentane (-140 °C). The reactions were also performed at 25 °C in a final volume of 250 μ L containing 30 μ M wt- α 2, 10 μ M $Y_{122}(2,3,5)F_3Y\text{-}\beta$ 2 (0.6 $F_3Y\text{-}\beta$ 2), 2.5 mM CDP, 3 mM ATP, 80 μ M TR, 1.6 μ M TRR and 2.5 mM NADPH.

3.2.7 Reaction of $Y_{122}(2,3,5)F_3Y\text{-}\beta$ 2, wt- α 2, CDP, ATP and TR/TRR/NADPH monitored by the RCQ method. The reaction was performed in an identical fashion to that described in the absence of a reducing system with minor modifications. For data collected at 5 °C, syringe A contained 20 μ M wt- α 2, 6 mM ATP, 80 μ M TR and 1.6 μ M TRR in assay buffer, while syringe B contained 20 μ M $Y_{122}(2,3,5)F_3Y\text{-}\beta$ 2 (0.6 $F_3Y\text{-}\beta$ 2), 1 mM [3 H] CDP (20,000 cpm/nmol) and 2 mM NADPH. For the 25 °C reaction, the amount of [3 H] CDP in syringe B was increased to 2 mM. Samples were quenched and worked up as described earlier. The time courses of the reactions were fit to equation 3.3:

$$y = A(1 - e^{-k_1t}) + k_2t \quad (3.3)$$

where A and k_1 are the amplitude and rate constant for the burst phase respectively and k_2 is the rate constant for the linear phase.

3.3 RESULTS

3.3.1 “Two or none” radical distribution and half-sites reactivity in $Y_{122}(2,3,5)F_3Y\text{-}\beta 2$. The diferric- $F_3Y\bullet$ cofactor is self-assembled from apo $Y_{122}(2,3,5)F_3Y\text{-}\beta 2$ by the addition of Fe^{2+} and O_2 to produce $\sim 0.8 F_3Y\bullet/\beta 2$, lower than the $1.2 Y\bullet/\text{wt-}\beta 2$.³³ Although the radical distribution in $\beta 2$ has remained difficult to probe experimentally, evidence collected over the past few years supports that active $\beta 2$ contains one $Y\bullet$ in each monomer (“two or none”, Figure 3.2A), suggesting that only $\sim 40\%$ of $\beta 2$ is active in our $Y_{122}(2,3,5)F_3Y\text{-}\beta 2$ samples.^{12,13,21,22,34,35} To provide support for this conclusion, we monitored the effect of $F_3Y\bullet$ concentration on the amount of $Y_{356}\bullet$ that accumulates. RFQ-EPR experiments were performed at 25 °C with $Y_{122}(2,3,5)F_3Y\text{-}\beta 2$ containing 0.4 $F_3Y\bullet/\beta 2$ or 0.85 $F_3Y\bullet/\beta 2$, wt- $\alpha 2$, CDP and ATP. The kinetic analysis of these studies is discussed subsequently, but the amount of $Y_{356}\bullet$ is 0.43 and 0.5 equiv./ $F_3Y\bullet$ respectively (Table 3.1). This amount can be rationalized by the “two or none” radical distribution model (Figure 3.2A) as well as half-sites reactivity in RNR (Figure 3.2B); only one of the 2 $F_3Y\bullet$ reacts at a time to generate $Y_{356}\bullet$.²⁰⁻²³

Table 3.1 Amount of $Y_{356}\bullet$ and dCDP produced in the first turnover by $Y_{122}(2,3,5)F_3Y\text{-}\beta 2$ with varying radical content.

Radical content ($F_3Y\bullet/\beta 2$)	$[F_3Y\bullet]$ (μM)	$[Y_{356}\bullet]^b$ (μM)	$Y_{356}\bullet/F_3Y\bullet$	$[\text{dCDP}]^a$ (μM)	$\text{dCDP}/F_3Y\bullet$
0.4	$12^a\text{-}32^b$	15.7, 16.3	0.49, 0.51	6.1, 6.4	0.51, 0.53
0.65	6.5^a	-	-	2.8	0.43
0.85	34^b	14.6	0.43	-	-

All reactions were performed at 25 °C. Two independent trials are shown for $Y_{122}(2,3,5)F_3Y\text{-}\beta 2$ containing 0.4 $F_3Y\bullet/\beta 2$ whereas a single trial is shown for the other radical concentrations.

^a Concentrations under the experimental conditions utilized for RCQ. $[F_3Y\bullet]$ represents the total amount of radical prior to initiation of the reaction. $[\text{dCDP}]$ reported is the amount generated by ~ 100 ms, the time point where maximum $Y_{356}\bullet$ is observed.

^b Concentrations under the experimental conditions utilized for RFQ-EPR spectroscopy. $[F_3Y\bullet]$ represents the total amount of radical prior to initiation of the reaction. $[Y_{356}\bullet]$ reported is the maximum amount of pathway radical generated (within ~ 100 ms).

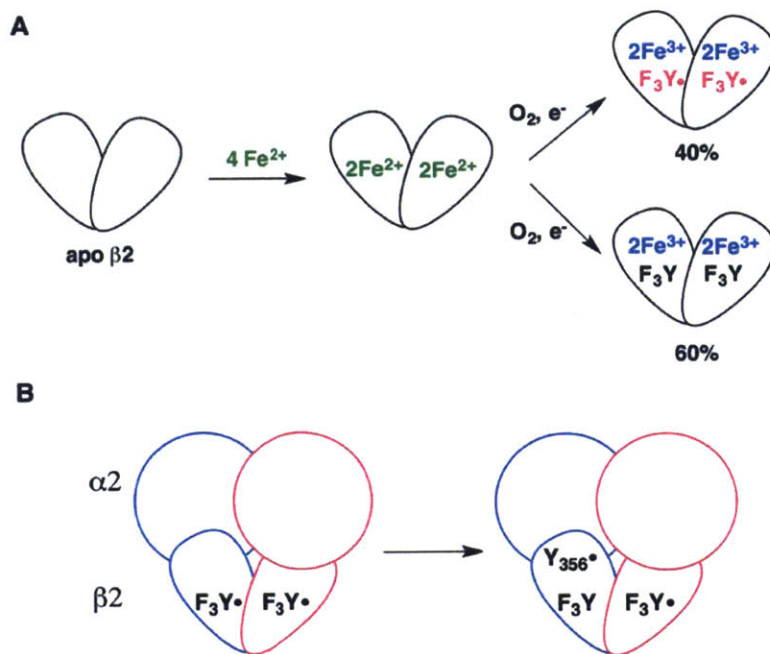


Figure 3.2 A. “Two or none” model for radical distribution in $\text{Y}_{122}(2,3,5)\text{F}_3\text{Y}-\beta 2$. The amounts of active (40%) and inactive $\beta 2$ (60%) are shown for a sample containing 0.8 $\text{F}_3\text{Y}\cdot$. The amount of radical in $\text{Y}_{122}(2,3,5)\text{F}_3\text{Y}-\beta 2$ is lower than that typically seen in wt- $\beta 2$ (1.2 $\text{Y}\cdot/\beta 2$).³³ B. Half-sites reactivity in $\text{Y}_{122}(2,3,5)\text{F}_3\text{Y}-\beta 2$. The total amount of $\text{Y}_{356}\cdot$ that can accumulate on one turnover is 0.5 equiv./ $\text{F}_3\text{Y}\cdot$.

3.3.2 Kinetics in the absence of a reducing system: formation and disappearance of $\text{Y}_{356}\cdot$

at 25 °C. To assess if $\text{Y}_{356}\cdot$ is formed faster than the turnover number of the enzyme (1.7 s^{-1} , Table 3.2), a RFQ-EPR experiment was performed in which wt- $\alpha 2$, $\text{Y}_{122}(2,3,5)\text{F}_3\text{Y}-\beta 2$, CDP and ATP were mixed rapidly (16 ms to 15 s). EPR analysis of each sample revealed a mixture of $\text{F}_3\text{Y}\cdot$ and $\text{Y}_{356}\cdot$ and spectral subtractions were performed to quantitate the relative fraction of each radical. The unique hyperfine interactions associated with the fluorine nuclei facilitated spectral deconvolution.¹⁹ The results of the experiment are shown in Figure 3.3A and the data were fit to a bi-exponential equation. Rapid loss of 0.51 ± 0.02 equiv. $\text{F}_3\text{Y}\cdot$ (not shown) concomitant with formation of identical amounts of $\text{Y}_{356}\cdot$ occurs at $30 \pm 5 \text{ s}^{-1}$. Subsequently, reduction of the pathway

radical with $k_{\text{app}} 0.4 \pm 0.1 \text{ s}^{-1}$ is accompanied by re-formation of $\text{F}_3\text{Y}\cdot$ with the same k_{app} (not shown). These data show for the first time, accumulation of a pathway radical ($\text{Y}_{356}\cdot$) in an active RNR complex that can regenerate the stable radical at position 122 ($\text{F}_3\text{Y}\cdot$). We note that between 0.1 s and 1 s, the concentration of $\text{Y}_{356}\cdot$ varies minimally. As shown subsequently, $\text{Y}_{122}(2,3,5)\text{F}_3\text{Y}\text{-}\beta 2$ can make multiple dCDPs in the absence of a reducing system and the reduction of $\text{Y}_{356}\cdot$ and re-oxidation of F_3Y is only visualized after the last turnover when all $\alpha 2\text{s}$ are oxidized. Finally, regeneration of $\text{F}_3\text{Y}\cdot$ is incomplete with only 0.25 equiv. of $\text{Y}_{356}\cdot$ re-oxidizing F_3Y within 10 s.

3.3.3 Kinetics in the absence of a reducing system: formation and disappearance of $\text{Y}_{356}\cdot$ at 5 °C. The rapid formation of $\text{Y}_{356}\cdot$ at 25 °C resulted in generation of 0.25 equiv. (50% of total $\text{Y}_{356}\cdot$) prior to the first data point (16 ms, Figure 3.3A) prompting us to switch to lower temperatures to slow down the reaction. RFQ-EPR experiments were set up at 5 °C as described for 25 °C and the results are shown in Figure 3.4A. A k_{app} of $3.8 \pm 0.5 \text{ s}^{-1}$ was measured for formation of $\text{Y}_{356}\cdot$ concomitant with loss of $\text{F}_3\text{Y}\cdot$ (not shown). In contrast to our observation at 25 °C, only 0.32 ± 0.02 equiv. of $\text{Y}_{356}\cdot$ is formed at 5 °C reflecting temperature dependent changes in the rates of formation and decay of the pathway radical. Similar to our observation at 25 °C, the concentration of $\text{Y}_{356}\cdot$ varies minimally between 0.8 s and 5 s supporting the proposal that $\text{Y}_{122}(2,3,5)\text{F}_3\text{Y}\text{-}\beta 2$ catalyzes multiple turnovers prior to visualization of reverse RT. Unlike in the 25 °C reaction, $\text{Y}_{356}\cdot$ reduction at 5 °C is accompanied by complete re-formation of $\text{F}_3\text{Y}\cdot$ (0.3 equiv., $0.06 \pm 0.01 \text{ s}^{-1}$) within ~40 s.

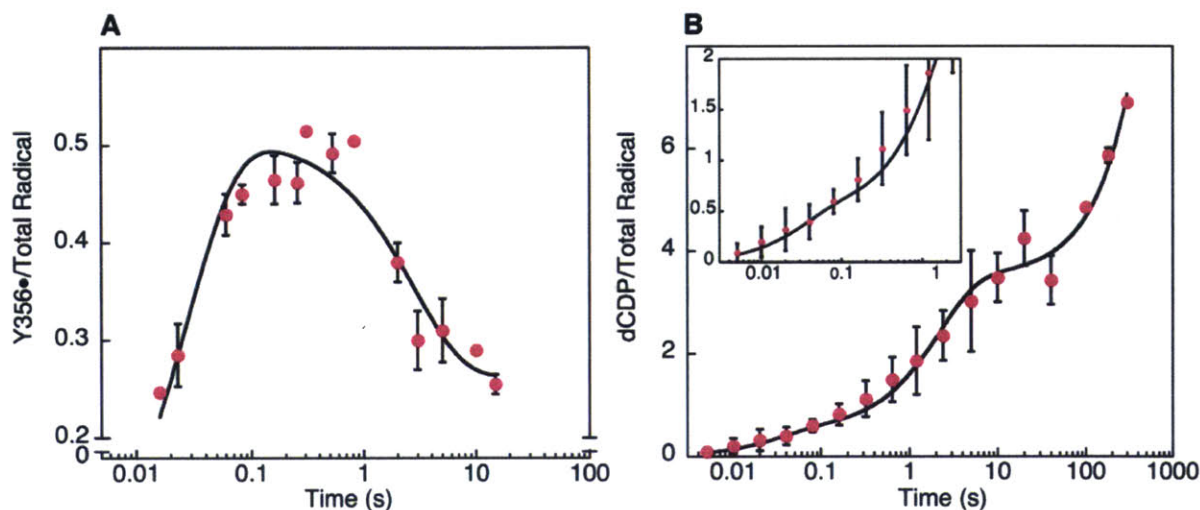


Figure 3.3 Reaction of $Y_{122}(2,3,5)F_3Y-\beta_2$, wt- α_2 , CDP and ATP at 25 °C monitored by RFQ-EPR spectroscopy (A) and the RCQ method (B). All data points represent the averages of two independent trials. Data were fit to a two (A) or three (B) phase model with the rate constants shown in Table 3.2. B. The inset shows dCDP formation during the first 2 s of the reaction. The rate constants measured for $Y_{356}\bullet$ formation and disappearance correlate with the fitted rate constants for dCDP formation in the first two phases.

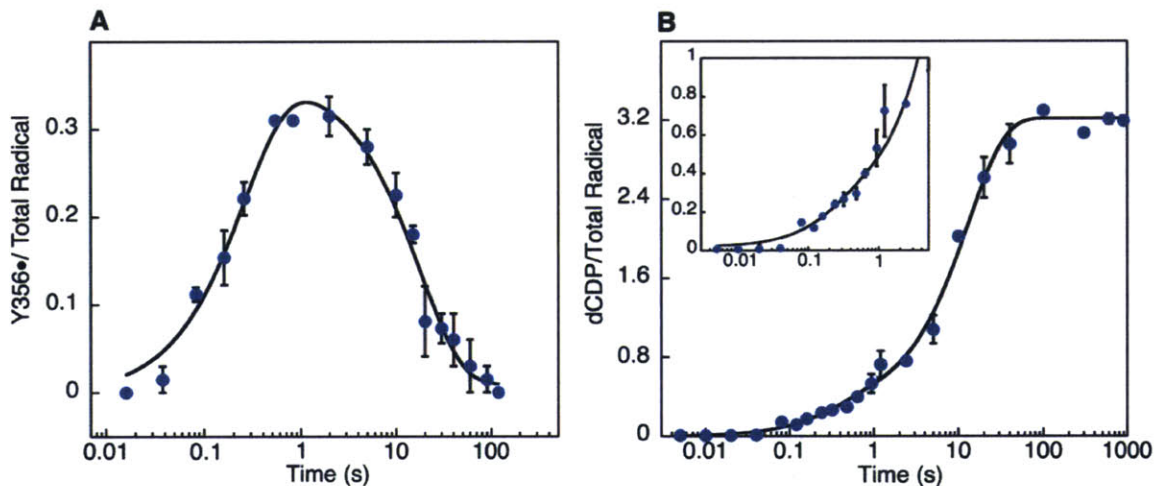


Figure 3.4 Reaction of $Y_{122}(2,3,5)F_3Y-\beta_2$, wt- α_2 , CDP and ATP at 5 °C monitored by RFQ-EPR spectroscopy (A) and the RCQ method (B). All data points represent the averages of two independent trials. Black lines represent bi-exponential fits to the data with the rate constants given in Table 3.2. B. The inset shows dCDP formation during the first 5 s of the reaction. The rate constants measured for $Y_{356}\bullet$ formation and disappearance are identical to the rate constants measured for dCDP formation.

3.3.4 Kinetics of dCDP formation at 25 °C in the absence of a reducing system. Each dCDP generated by RNR is accompanied by the formation of a disulfide bond in the active site of an α monomer (Scheme 3.1, Figure 3.5, step A). Re-reduction of the active site disulfide by a C-terminal cysteine pair on each monomer (step B) facilitates an additional turnover (step C),¹¹ giving a theoretical maximum of 4 dCDP/ α 2 in the absence of TR/TRR/NADPH. In practice, only 3 dCDP/ α 2 are routinely measured with wt RNR due to partial oxidation of α 2 (during purification and handling) and our inability to completely pre-reduce wt- α 2 before an experiment.¹¹ Our kinetic experiments with Y_{122(2,3,5)}F₃Y- β 2, contain 1:1 α 2:Y_{122(2,3,5)}F₃Y- β 2 with only 40% of active Y_{122(2,3,5)}F₃Y- β 2 (Figure 3.2A). However, 3 dCDP/ α 2 are generated in the absence of a reducing system (Table 3.2) requiring that each F₃Y• perform multiple turnovers (3.5 dCDP/F₃Y•, Table 3.2) to service all α 2s.

To assess if Y₃₅₆• is on-pathway, the kinetics of dCDP formation were determined. Wt- α 2, Y_{122(2,3,5)}F₃Y- β 2, [³H] CDP and ATP were mixed (5 ms to 300 s) and quenched rapidly with 2% HClO₄. CDP and dCDP were separated, analyzed by standard procedures^{11,32} and the results are shown in Figure 3.3B. The data are best described by equation 3.2 with a fixed first exponential phase, a variable second exponential phase and a very slow third linear phase. We initially attempted to fit the data with an exponential phase and a linear phase with poor results (Appendix 5, Figure A5.1A). To obtain the fit shown in Figure 3.3B (black line), we fixed the amplitude and rate constant (k_1) of the first phase at 0.5 dCDP/F₃Y• and 30 s⁻¹ respectively. Fixing this phase was required due to the scatter in the data at early time points. This scatter is a result of “two or none” and half-sites reactivity associated with RNR (Figure 3.2A-B). The [³H] dCDP measured between 5 ms and 100 ms is close to the background measured with [³H] CDP in the absence of α 2. The range of choices considered for the amplitude and k_1 of this phase were based on the amplitude

and rate constant measured for Y_{356}^{\bullet} formation by RFQ-EPR (Figure 3.3A) and the results obtained in the presence of the reducing system (presented in the next section). The detailed description of data fitting using different parameters for the first kinetic phase is presented in Appendix 5 (Figure A5.1). An additional experiment to justify the fixed first phase is also shown in Appendix 5 (Figure A5.2).

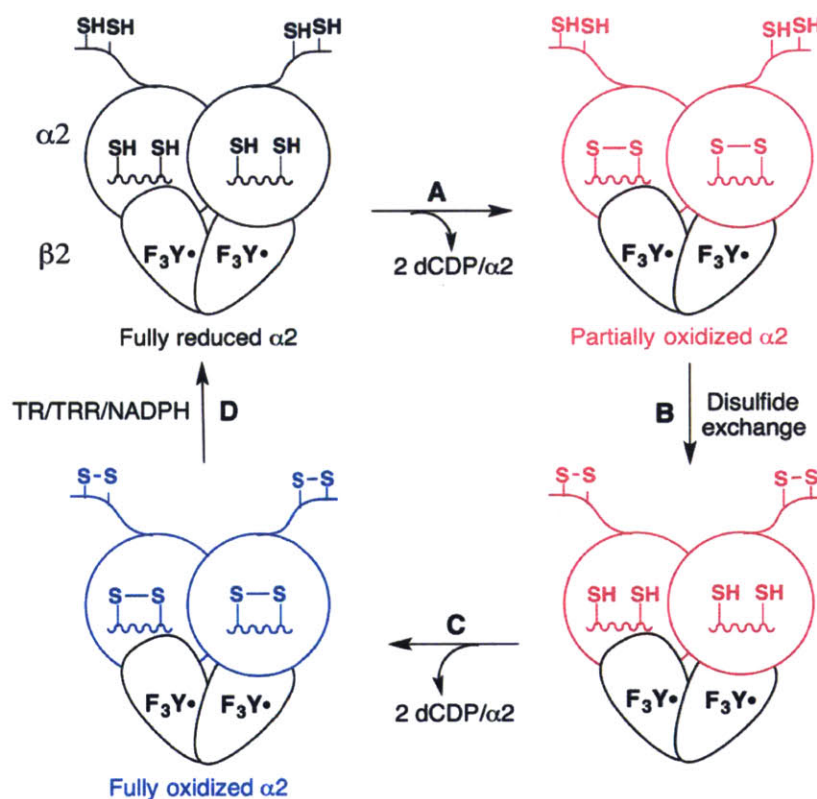


Figure 3.5 Amount of dCDP generated in the absence of a reducing system. A theoretical maximum of 4 dCDP/ α_2 can be produced; however, only 3 dCDP/ α_2 are routinely measured. The reaction mixture contains only 40% active $Y_{122}(2,3,5)F_3Y$ - β_2 (Figure 3.2A), supporting reorganization of active and inactive $\alpha_2/Y_{122}(2,3,5)F_3Y$ - β_2 complexes to oxidize all α_2 s.

Once the first phase was fixed using equation 3.2, we obtained an amplitude and rate constant (k_2) of 2.9 ± 0.1 dCDP/ F_3Y^{\bullet} and 0.5 ± 0.1 s^{-1} respectively for the second phase and a rate constant (k_3) of 0.012 ± 0.001 s^{-1} for the linear phase. This slow linear phase is associated with cytosine release and not dCDP formation. It occurs during the reaction of $Y_{122}(2,3,5)F_3Y$ - β_2 with

oxidized $\alpha 2$ as shown in Scheme 3.2.³⁶ The inability to monitor complete reverse RT at 25 °C (Figure 3.3A) is associated with re-oxidation of Y_{356} (0.25 equiv.) by $Y_{122}(2,3,5)F_3Y\text{-}\beta 2$ /oxidized $\alpha 2$ (data not shown).

The fit shown in Figure 3.3B suggests that the pathway radical is kinetically and chemically competent for nucleotide reduction at 25 °C. These data require that $Y_{356}\bullet$ accumulates during reverse RT. k_2 for product formation correlates well with k_{app} for $Y_{356}\bullet$ disappearance at this temperature (0.5 s^{-1} vs 0.4 s^{-1} , Figure 3.3A).

Table 3.2 DeoxyCDP formation kinetics in the absence and presence of TR/TRR/NADPH.

$\beta 2$	T (°C)	R	First phase		Second phase		Total dC	
			k_1 (s ⁻¹)	A/radical	k_2 (s ⁻¹)	A/radical	dC/ $\alpha 2$	dC/radical
F ₃ Y	25	N	30 ^a	0.5 ^a	0.5 (1)	2.9 (1)	2.8 (4) ^b	3.5 (3) ^b
F ₃ Y	25	Y	22 (9)	0.40 (5)	1.73 (4)	-	-	-
F ₃ Y	5	N	3 (1)	0.3 (1)	0.08 (1)	2.9 (1)	2.7 (1)	3.4 (1)
F ₃ Y	5	Y	6 (3)	0.26 (5)	0.20 (1)	-	-	-

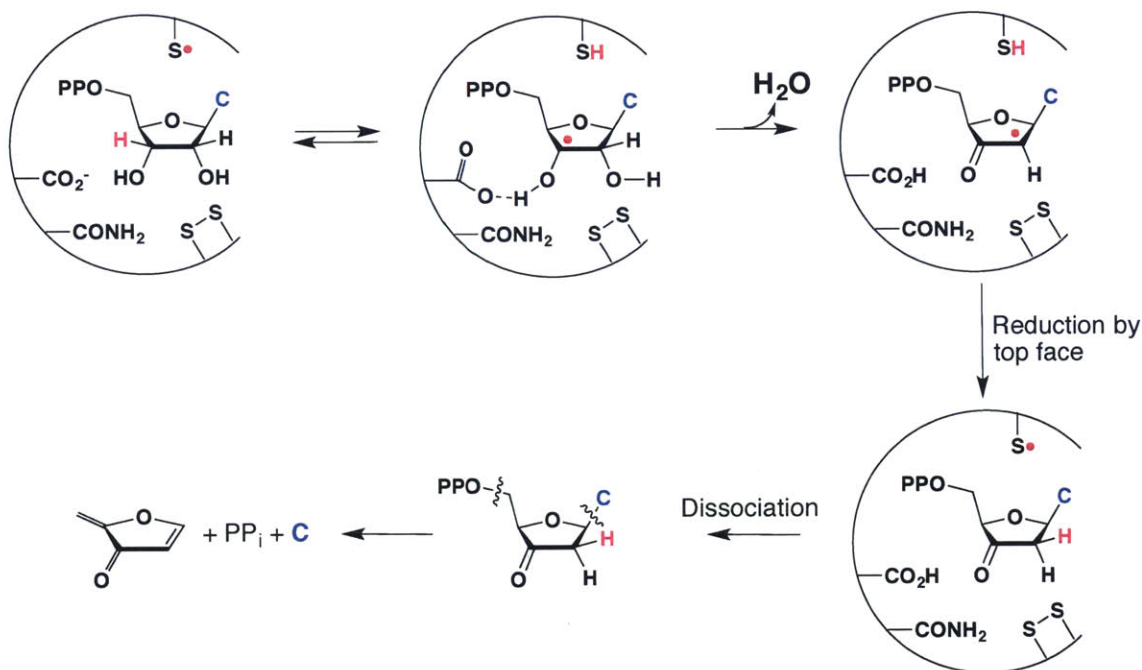
All experiments were performed with 10 μM wt- $\alpha 2$ and 10 μM $Y_{122}(2,3,5)F_3Y\text{-}\beta 2$. R notes the absence or presence of a reducing system. A represents the amplitude of each phase.

^a See description in text for more details regarding fitting.

^b Numbers reported reflect the total amount of dC generated within the first two phases. Product generated in the third phase is cytosine.

3.3.5 Kinetics of dCDP formation at 5 °C in the absence of a reducing system. The kinetics of dCDP formation were also measured at 5 °C and the results are shown in Figure 3.4B. The data were fit to a bi-exponential equation providing amplitudes of 0.3 ± 0.1 dCDP/ $F_3Y\bullet$ and 2.9 ± 0.1 dCDP/ $F_3Y\bullet$ with k_1 and k_2 of $3 \pm 1\text{ s}^{-1}$ and $0.08 \pm 0.01\text{ s}^{-1}$ respectively (Table 3.2). A_1 and k_1 for dCDP formation are very similar to the amplitude and rate constant measured for $Y_{356}\bullet$ formation by RFQ-EPR spectroscopy at the same temperature (Figure 3.4A). These data suggest that $Y_{356}\bullet$ is kinetically and chemically competent for dCDP formation and accumulates during reverse RT. Similar to our observations at 25 °C, k_2 of 0.08 s^{-1} for dCDP formation (Table 3.2) is similar to k_{app} of 0.06 s^{-1} for re-oxidation of F_3Y by $Y_{356}\bullet$ (Figure 3.4A).

The RCQ data were also analyzed relative to $\alpha 2$ to show that 2.7 ± 0.1 dCDPs/ $\alpha 2$ are generated. DeoxyCDP formation was monitored for a total of 20 min and in contrast to the 25 °C data, no third kinetic phase associated with cytosine was observed.



Scheme 3.2 Cytosine release from the native substrate CDP in the presence of oxidized $\alpha 2$. Radical initiation with oxidized $\alpha 2$ results in the formation of 3'-ketodeoxynucleotide from CDP, a species which subsequently decomposes to cytosine, pyrophosphate and 2-methylene-3(2H)-furanone.³⁶

3.3.6 Kinetics in the presence of a reducing system: EPR analysis of Y_{356}^{\bullet} concentration during steady-state turnover. The ability of $Y_{122}(2,3,5)F_3Y-\beta 2$ to perform multiple turnovers in the absence of a reducing system (3.5 dCDP/ F_3Y^{\bullet} , Table 3.2) and the observation of a plateau phase in the RFQ-EPR kinetic traces (Figures 3.3A and 3.4A) suggested that reverse RT is visualized subsequent to complete oxidation of $\alpha 2$. Thus, we predicted that the concentration of Y_{356}^{\bullet} would vary minimally in the presence of the reducing system, TR/TRR/NADPH, as oxidized $\alpha 2$ is re-reduced. To test this prediction, $Y_{122}(2,3,5)F_3Y-\beta 2$, wt- $\alpha 2$, CDP and ATP were combined in the presence of TR/TRR/NADPH and samples were quenched by hand in liquid isopentane between 20 s and 90 s. In accordance with our prediction, the amount of Y_{356}^{\bullet} does not change:

0.26 to 0.28 equiv./F₃Y• at 5 °C and 0.40 to 0.46 equiv./F₃Y• at 25 °C (Table 3.3). No reverse RT was visualized during the time frame of the reaction.

Table 3.3 Amount of Y₃₅₆• generated during Y₁₂₂(2,3,5)F₃Y-β2 turnover in the presence of TR/TRR/NADPH.

Time (s)	Y ₃₅₆ •/F ₃ Y•	Y ₃₅₆ •/F ₃ Y•
	5 °C	25 °C
20	0.27	0.46
30	0.28	-
45	0.27	-
90	0.26	0.40

3.3.7 Kinetics of dCDP formation at 5 °C and 25 °C in the presence of a reducing system.

The observation of Y₃₅₆• accumulation during reverse RT (Figures 3.3 and 3.4) in the absence of a reducing system and the lack of variation in [Y₃₅₆•] during steady-state turnover, suggest that the rate-limiting step occurs subsequent to dCDP formation and Y₃₅₆• re-formation during reverse RT. This model predicts that RCQ experiments in the presence of the reducing system would show a burst of dCDP representing the first turnover followed by a linear phase for steady-state turnover. Y₁₂₂(2,3,5)F₃Y-β2, wt-α2, [³H]CDP and ATP were mixed in the presence of TR/TRR/NADPH and the reaction was monitored from 5 ms to 100 s. The results of the Y₁₂₂(2,3,5)F₃Y-β2 experiments, at 5 °C and 25 °C are shown in Figure 3.6 and summarized in Table 3.2.

As predicted, a burst of dCDP formation is observed at both temperatures (0.26 ± 0.05 dCDP/F₃Y• at 6 ± 3 s⁻¹ at 5 °C and 0.40 ± 0.05 dCDP/F₃Y• at 22 ± 9 s⁻¹ at 25 °C) followed by a linear phase (0.20 ± 0.01 s⁻¹ at 5 °C and 1.73 ± 0.04 s⁻¹ at 25 °C). The large errors observed in these parameters are associated with low amounts of dCDP arising from the “two or none” model (Figure 3.2A) and half-sites reactivity (Figure 3.2B). Unfortunately, we are unable to increase protein concentration in these experiments as studies with wt RNR have revealed kinetic

complexities associated with the re-reduction process¹¹ and potentially quaternary structure interconversions.³⁷

The observed rate constant and amplitude for the burst phase are within error similar to the parameters observed for $Y_{356}\bullet$ formation (Figures 3.3A and 3.4A) and support our conclusion that $Y_{356}\bullet$ is on-pathway for dCDP formation. These data also correlate well with the kinetics of the first phase measured in the absence of TR/TRR/NADPH (0.3 dCDP/ $F_3Y\bullet$ at 3 s^{-1} at $5\text{ }^\circ\text{C}$ and 0.5 dCDP/ $F_3Y\bullet$ at 30 s^{-1} at $25\text{ }^\circ\text{C}$) supporting that k_1 in the absence of a reducing system and the burst phase in the presence of TR/TRR/NADPH report on the first turnover by one $\alpha/Y_{122}(2,3,5)F_3Y-\beta$ pair in the $\alpha 2/Y_{122}(2,3,5)F_3Y-\beta 2$ complex (Figure 3.2B). Subsequent to dCDP formation and $Y_{356}\bullet$ regeneration during reverse RT, re-oxidation of F_3Y and re-reduction of oxidized $\alpha 2$ facilitate further turnovers. We argue subsequently that the rate-limiting step in $Y_{122}(2,3,5)F_3Y-\beta 2$ is re-oxidation of F_3Y by $Y_{356}\bullet$.

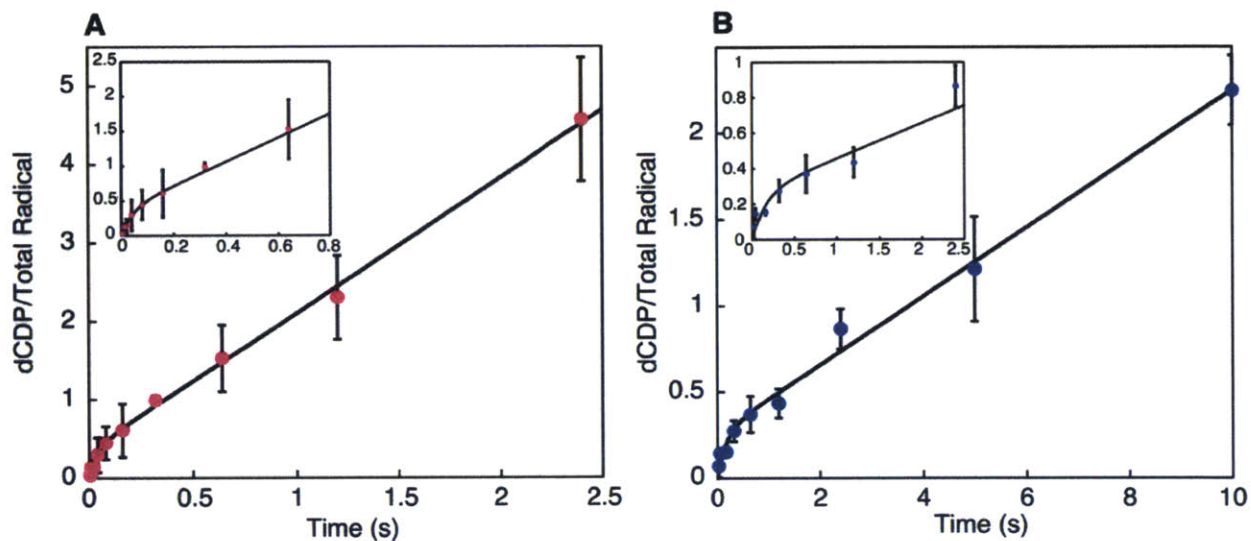


Figure 3.6 Kinetics of product formation in $Y_{122}(2,3,5)F_3Y-\beta 2$ in the presence of TR/TRR/NADPH at 25 °C (A) and 5 °C (B). The averages of 2–4 separate trials are shown. Data were fit to a two-phase model with the rate constants given in Table 3.2. The insets show dCDP formation during the first 0.8 s (A) and 2.5 s (B). The burst phase represents the very first turnover by an α/β pair. Reverse PCET regenerating $F_3Y\cdot$ is rate-limiting during steady-state turnover.

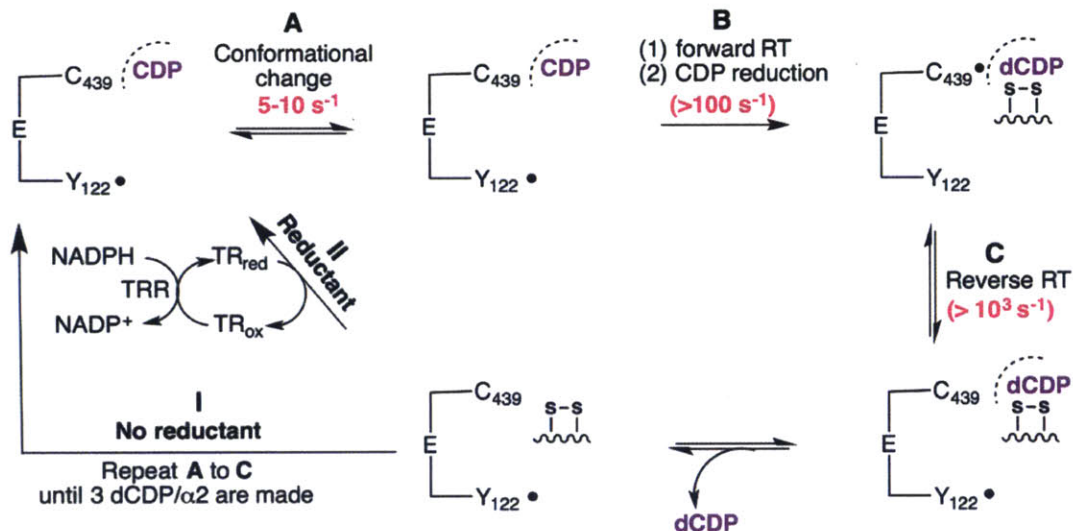
3.4 DISCUSSION

The rate-limiting protein conformational change(s) that gate(s) *E. coli* class Ia RNR turnover has precluded insight into the 35 Å forward RT, nucleotide reduction and reverse RT processes. Our current model for wt RNR based on studies similar to those described herein for Y₁₂₂(2,3,5)F₃Y-β₂ is shown in Scheme 3.3. Upon association of β₂/α₂/CDP/ATP, a conformational change(s) (5–10 s⁻¹, Scheme 3.3, step **A**) triggers rapid RT into α₂ and nucleotide reduction (>100 s⁻¹, step **B**).^{12,38} DeoxyCDP formation is rate-limited by the conformational change(s) and occurs at 5–10 s⁻¹ as measured by RCQ methods reported previously¹¹ and reproduced here under the same conditions utilized for the Y₁₂₂(2,3,5)F₃Y-β₂ studies (Figure A5.3, Appendix 5). Subsequent to dCDP formation, reverse RT to regenerate Y₁₂₂• is required to be downhill¹² and rapid (>10³ s⁻¹, step **C**) as modeled by Ge et al¹¹ to account for our inability to observe Y₁₂₂• disappear and reappear during turnover (± TR/TRR/NADPH). The physical steps in wt RNR preclude detection of intermediates in these processes. Thus, studying the chemistry has required engineering specific perturbations to the system initially through site-directed mutagenesis³⁹⁻⁴² and the use of mechanism-based inhibitors^{36,43,44} and more recently, with site-specific incorporation of unnatural amino acids.^{12,13,24,25} While with many of these approaches we were able to monitor the disappearance of Y₁₂₂• concomitant with formation of new radicals, in none of these cases was the catalytic cycle of RNR completed, and no insight was obtained into reverse RT.

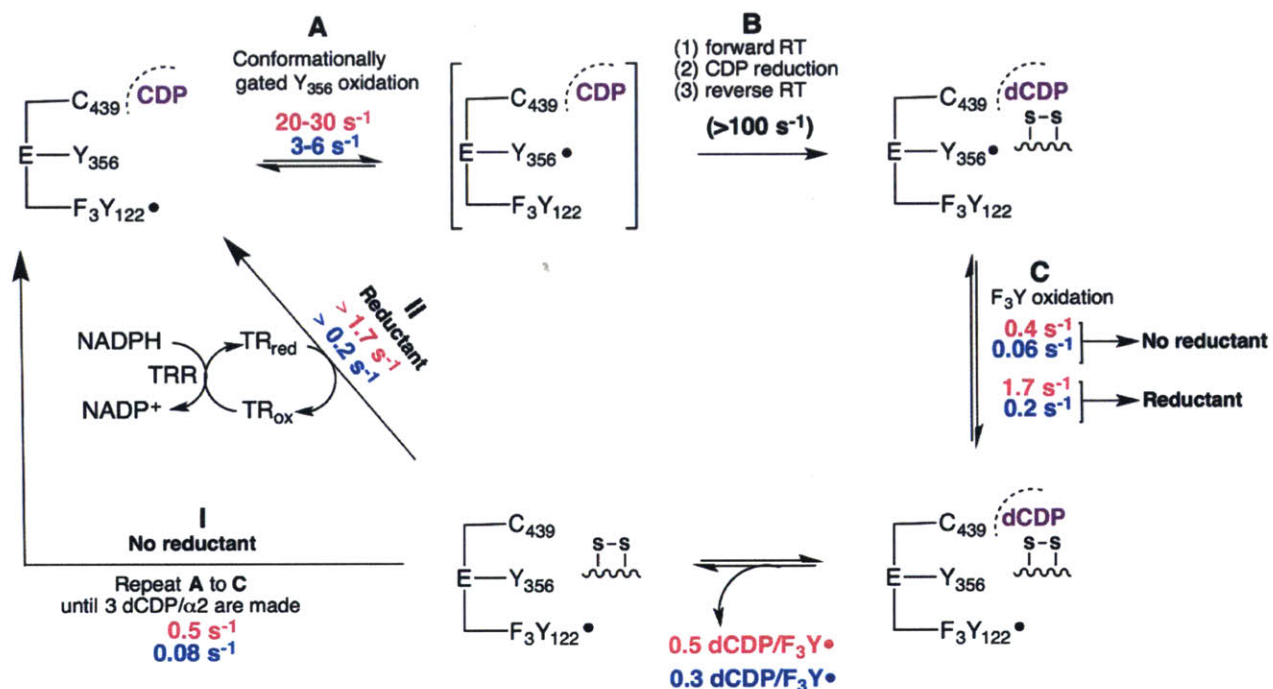
Our recent engineering of an orthogonal tRNA-synthetase tRNA pair that can incorporate di- and tri-fluorotyrosines (F_nY, n= 2, 3) with a range of reduction potentials and pK_as in RNR¹⁹ allowed us to introduce a tunable thermodynamic perturbation of PCET kinetics with minimal steric perturbations. F₃Y is predicted as ~ 10 mV harder to oxidize than Y,^{17,45} assuming that the

first step in forward RT involves PT from the water on the diferric cluster to F_3Y^\bullet concomitant with ET from Y_{356} to F_3Y^\bullet (Figure 3.1). $Y_{122}(2,3,5)F_3Y-\beta 2$ is capable of catalyzing multiple turnovers but allows detection of Y_{356}^\bullet (\pm TR/TRR/NADPH) due to perturbed reverse RT kinetics. Our current model for $Y_{122}(2,3,5)F_3Y-\beta 2$ turnover is shown in Scheme 3.4. The ability to accumulate Y_{356}^\bullet in $Y_{122}(2,3,5)F_3Y-\beta 2$ but not in wt RNR appears to be directly related to the differences in the rate-limiting step in the two systems.

In our model, the $Y_{122}(2,3,5)F_3Y-\beta 2$ /wt- $\alpha 2$ /CDP/ATP complex undergoes a conformational change prior to generation of Y_{356}^\bullet in one α/β pair (Scheme 3.4, step A). The RFQ-EPR data reported in Figures 3.3A and 3.4A provide the rate constants for this step and suggest that $Y_{122}(2,3,5)F_3Y-\beta 2$ perturbs the conformational gate relative to the wt enzyme ($20\text{--}30\text{ s}^{-1}$ vs $5\text{--}10\text{ s}^{-1}$). We expect that forward RT into α and dCDP production (step B in Schemes 3.3 and 3.4) occur with similar rate constants to wt RNR ($>100\text{ s}^{-1}$).^{12,38} DeoxyCDP formation is rate-limited by the slow, conformationally gated generation of Y_{356}^\bullet during forward RT as measured by the first phase in the absence of a reducing system (Figures 3.3B and 3.4B) or the burst phase in the presence of TR/TRR/NADPH (Figure 3.6) in the RCQ studies. Subsequent to product formation, we propose that reverse RT to regenerate Y_{356}^\bullet is fast¹² as modeled in wt RNR where reverse RT to regenerate Y_{122}^\bullet is 10^3 s^{-1} .¹¹ However, unlike in wt RNR, slow re-oxidation of F_3Y (step C) rate-limits subsequent turnovers.



Scheme 3.3 Kinetic model for wt RNR in the absence and presence of a reducing system. The figure shows only the key amino acids in the PCET pathway. Rate constants are shown for the reaction at 25 °C. Y₃₅₆• cannot be visualized in wt RNR due to the rate-limiting conformational change(s). Figure adapted from Ref. 11.



Scheme 3.4 Kinetic model for Y₁₂₂(2,3,5)F₃Y- β 2 in the absence and presence of a reducing system. The figure represents a reductionist view of key amino acids in the PCET pathway. The rate constants for each step are shown in pink (25 °C), blue (5 °C) and black (both temperatures). It is not known if the first RT step involves PCET to generate the phenol (F₃Y), as in wt RNR or ET to generate the phenolate (F₃Y⁻), as in Y₁₂₂NO₂Y- β 2. However, as described in Chapter 4, we favor F₃Y⁻ formation.

In the absence of a reducing system, the RFQ-EPR data (Figures 3.3A and 3.4A) provide the rate constants for step C. Upon regeneration of F_3Y^\bullet , $\beta 2$ rapidly dissociates from a partially oxidized $\alpha 2$, associates with a second reduced $\alpha 2$ and cycles through steps A to C until all $\alpha 2$ s are completely oxidized.⁴⁶ Y_{356}^\bullet concentration does not vary significantly during this time as visualized by the plateaus in the RFQ-EPR kinetic traces (Figures 3.3A and 3.4A). The second phase of the RCQ studies described in Figures 3.3B and 3.4B provide the rate constants for turnover in the absence of TR/TRR/NADPH (Scheme 3.4, branch I). Altered reverse RT kinetics in $Y_{122}(2,3,5)F_3Y$ - $\beta 2$ allow us to observe for the first time the disappearance and reappearance of the radical at position 122 subsequent to complete oxidation of $\alpha 2$. The molecular bases for our ability to observe reverse RT are not well understood but are likely related to the initiating step in the PCET process. In addition to perturbing the driving force for RT, the fluoro substitutions could alter the distance between the phenolic oxygen and the water on the diferric cluster, thus affecting PT between the two (Figure 3.1). F_3Y also perturbs the pK_a at position 122 compared to Y (solution pK_a 6.4 vs 10).⁴⁵ Depending on the pK_a of the water on the diferric cluster, the phenolate F_3Y^- could be generated instead of the anticipated phenol F_3Y . As detailed in Chapter 4, we favor F_3Y^- formation during RT.

Additional insight into the differences between wt and $Y_{122}(2,3,5)F_3Y$ - $\beta 2$ catalysis is obtained from the amplitudes for dCDP formation in the absence of a reducing system (Table 3.2 and Figure A5.3). In the $Y_{122}(2,3,5)F_3Y$ - $\beta 2$ system, the first phase (0.5 dCDP/ F_3Y^\bullet at 25 °C) reports on the very first turnover by an α/β pair (Figure 3.2B), whereas the second phase (2.9 dCDP/ F_3Y^\bullet) reports on consumption of all remaining reduced $\alpha 2$ s, rate-limited by reverse RT. This result is distinct from our previous¹¹ and current observations for wt RNR (Figure A5.3, Appendix 5) where two phases are also measured for dCDP formation. The first phase is presumed

to report on the conformationally gated generation of 2 dCDPs by all $\alpha 2$ s (the experimental observation is 1.3 ± 0.2 dCDP/ $\alpha 2$, 6 ± 1 s⁻¹) and the second phase is interpreted to report on the generation of 2 additional dCDPs subsequent to re-reduction of the active site disulfide (the experimental observation is 1.6 ± 0.2 dCDP/ $\alpha 2$, 0.5 ± 0.1 s⁻¹). The variation in the amplitudes of the two phases between wt and Y_{122(2,3,5)}F₃Y- $\beta 2$ is consistent with different rate-limiting steps in the two systems. However, in both cases, the total number of dCDPs generated is the same: 3 dCDP/ $\alpha 2$ (Schemes 3.3 and 3.4, branch I).

The EPR and RCQ data collected in the presence of a reducing system also lend support to Scheme 3.4. In Y_{122(2,3,5)}F₃Y- $\beta 2$, a burst of dCDP formation prior to steady-state turnover is observed. The amplitude of this phase (~ 0.5 dCDP/ F₃Y• at 25 °C) again reflects that turnover occurs only on one α/β pair prior to the rate-limiting step and is consistent with slow reverse RT. Upon regeneration of F₃Y• after one turnover (Scheme 3.4, step C) re-reduction of oxidized $\alpha 2$ by TR/TRR/NADPH resets the system for additional turnovers (branch II). Y₃₅₆• under these conditions behaves in a similar fashion to Y₁₂₂• in wt RNR, i.e no changes in its concentration are detected during steady-state (Table 3.3). Slow re-oxidation of F₃Y followed by rapid re-reduction, forward RT, nucleotide reduction and regeneration of Y₃₅₆• (Scheme 3.4, steps A to C) preclude observation of its disappearance and reappearance. We interpret the linear phases in Figures 3.6A and 3.6B as representative of the rate constants for reverse RT in the presence of a reducing system (Scheme 3.4, step C) and the rate constant limits for re-reduction of oxidized $\alpha 2$. Although we set a lower limit for re-reduction from our experiments, we note that the rate constant for this step must be relatively fast $> 5\text{--}10$ s⁻¹ to account for our inability to monitor changes in Y₃₅₆• concentration.

A comparison of the burst phase for $Y_{122}(2,3,5)F_3Y-\beta 2$ and that for wt RNR in the presence of TR/TRR/NADPH reveals distinct behavior in the two systems (Figure 3.6 and Figure A5.4 in Appendix 5).¹¹ Although the conformational change is rate-limiting for dCDP formation in wt RNR, we have previously noted that the rate-limiting step in the presence of a reducing system can switch to re-reduction of oxidized $\alpha 2$ at the high protein concentrations required for RCQ studies ($10 \mu M$).¹¹ In wt RNR, this results in a conformationally gated burst of 2 dCDPs by all $\alpha 2$ s (the experimental observation is $1.9 \pm 0.1, 9 \pm 2 s^{-1}$) prior to steady-state turnover (Figure A5.4).¹¹ The burst phase reflects oxidation of all $\alpha 2$ active sites despite the presence of only 60% active wt- $\beta 2$ ($1.2 Y\bullet/\beta 2$, Figure 3.2A) and does not represent a single turnover. In contrast to the wt system, we have isolated the very first turnover by an $\alpha 2\beta 2$ complex with $Y_{122}(2,3,5)F_3Y-\beta 2$ due to rate-limiting reverse RT.

As a final point, the rate constant measured for dCDP formation in the presence of a reducing system is 3-fold faster than that measured in its absence (Scheme 3.4, branch **I** vs **II**). A similar variation has been previously noted for dCDP formation in the wt system.¹¹ It is possible that re-reduction of the active site disulfide by the C-terminal tail (Figure 3.5, step **B**) is reversible and only driven to completion when the TR/TRR/NADPH system is included in the assays. However, we currently cannot rule out other modes by which TR accelerates re-reduction of the $\alpha 2$ active site.

At the onset of the work described herein, we had shown that the reaction of $Y_{122}(2,3,5)F_3Y-\beta 2$ with $\alpha 2$, CDP and ATP generates $Y_{356}\bullet$.¹⁹ The experiments presented in this Chapter support that $Y_{356}\bullet$ is kinetically and chemically competent for turnover and demonstrate for the very first time chemically competent reverse RT that completes the RNR catalytic cycle. Our studies additionally provide insight into radical stoichiometry within $\beta 2$ (two or none), half-

sites reactivity and the ability of $\beta 2$ to act catalytically during turnover. Finally, the reversible nature of Y_{356} oxidation by F_3Y^\bullet sets the stage to investigate the thermodynamic landscape of the RT pathway within the $\beta 2$ subunit. In the following Chapter, we vary temperature and pH to demonstrate the equilibration of F_3Y^\bullet and Y_{356}^\bullet . These studies coupled with similar experiments performed with $Y_{356}(3,5)F_2Y$ - $\beta 2$ support an unprecedented thermodynamic landscape for the RT pathway that is >200 mV uphill.

3.5 REFERENCES

1. Stubbe, J.; van der Donk, W. A. Protein radicals in enzyme catalysis. *Chem. Rev.* **1998**, *98*, 705-762.
2. Jordan, A.; Reichard, P. Ribonucleotide reductases. *Annu. Rev. Biochem.* **1998**, *67*, 71-98.
3. Brown, N. C.; Canellakis, Z. N.; Lundin, B.; Reichard, P.; Thelander, L. Ribonucleotide diphosphate reductase. Purification of the two subunits, proteins B1 and B2. *Eur. J. Biochem.* **1969**, *9*, 561-573.
4. Licht, S.; Gerfen, G. J.; Stubbe, J. Thiyl radicals in ribonucleotide reductases. *Science* **1996**, *271*, 477-481.
5. Stubbe, J. Ribonucleotide reductases in the twenty-first century. *Proc. Natl. Acad. Sci. U. S. A* **1998**, *95*, 2723-2724.
6. Licht, S.; Stubbe, J. Mechanistic investigations of ribonucleotide reductases. *Compr. Nat. Prod. Chem.* **1999**, *5*, 163-203.
7. Stubbe, J.; Ackles, D. On the mechanism of ribonucleoside diphosphate reductase from *Escherichia coli*. Evidence for 3'-C-H bond cleavage. *J. Biol. Chem.* **1980**, *255*, 8027-8030.
8. Nordlund, P.; Sjöberg, B. M.; Eklund, H. Three-dimensional structure of the free radical protein of ribonucleotide reductase. *Nature* **1990**, *345*, 593-598.
9. Uhlin, U.; Eklund, H. Structure of ribonucleotide reductase protein R1. *Nature* **1994**, *370*, 533-539.
10. Stubbe, J.; Nocera, D. G.; Yee, C. S.; Chang, M. C. Y. Radical initiation in the class I ribonucleotide reductase: long-range proton-coupled electron transfer? *Chem. Rev.* **2003**, *103*, 2167-2201.
11. Ge, J.; Yu, G.; Ator, M. A.; Stubbe, J. Pre-steady-state and steady-state kinetic analysis of *E. coli* class I ribonucleotide reductase. *Biochemistry* **2003**, *42*, 10071-10083.
12. Yokoyama, K.; Uhlin, U.; Stubbe, J. A hot oxidant, 3-NO₂Y₁₂₂ radical, unmasks conformational gating in ribonucleotide reductase. *J. Am. Chem. Soc.* **2010**, *132*, 15368-15379.
13. Seyedsayamdost, M. R.; Stubbe, J. Site-specific replacement of Y₃₅₆ with 3,4-dihydroxyphenylalanine in the β2 subunit of *E. coli* ribonucleotide reductase. *J. Am. Chem. Soc.* **2006**, *128*, 2522-2523.
14. Sjöberg, B. M.; Gräslund, A.; Eckstein, F. A substrate radical intermediate in the reaction between ribonucleotide reductase from *Escherichia coli* and 2'-azido-2'-deoxynucleoside diphosphates. *J. Biol. Chem.* **1983**, *258*, 8060-8067.
15. Salowe, S.; Bollinger, J. M., Jr.; Ator, M.; Stubbe, J.; McCracken, J.; Peisach, J.; Samano, M. C.; Robins, M. J. Alternative model for mechanism-based inhibition of *Escherichia coli* ribonucleotide reductase by 2'-azido-2'-deoxyuridine 5'-diphosphate. *Biochemistry* **1993**, *32*, 12749-12760.

16. Artin, E.; Wang, J.; Lohman, G. J.; Yokoyama, K.; Yu, G.; Griffin, R. G.; Bar, G.; Stubbe, J. Insight into the mechanism of inactivation of ribonucleotide reductase by gemcitabine 5'-diphosphate in the presence or absence of reductant. *Biochemistry* **2009**, *48*, 11622-11629.
17. Minnihan, E. C.; Nocera, D. G.; Stubbe, J. Reversible, long-range radical transfer in *E. coli* class Ia ribonucleotide reductase. *Acc. Chem. Res.* **2013**, *46*, 2524-2535.
18. Wörsdorfer, B.; Conner, D. A.; Yokoyama, K.; Livada, J.; Seyedsayamdost, M.; Jiang, W.; Silakov, A.; Stubbe, J.; Bollinger, J. M., Jr.; Krebs, C. Function of the diiron cluster of *Escherichia coli* class Ia ribonucleotide reductase in proton-coupled electron transfer. *J. Am. Chem. Soc.* **2013**, *135*, 8585-8593.
19. Minnihan, E. C.; Young, D. D.; Schultz, P. G.; Stubbe, J. Incorporation of fluorotyrosines into ribonucleotide reductase using an evolved, polyspecific aminoacyl-tRNA synthetase. *J. Am. Chem. Soc.* **2011**, *133*, 15942-15945.
20. Yokoyama, K.; Smith, A.A.; Corzilius, B.; Griffin R.G.; Stubbe, J. Equilibration of tyrosyl radical (Y₃₅₆[•], Y₇₃₁[•], Y₇₃₀[•]) in the radical propagation pathway of the *Escherichia coli* class Ia ribonucleotide reductase. *J. Am. Chem. Soc.* **2011**, *133*, 18420-18432.
21. Seyedsayamdost, M. R.; Chan, C. T.; Mugnaini, V.; Stubbe, J.; Bennati, M. PELDOR spectroscopy with DOPA-β2 and NH₂Y-α2: distance measurements between residues involved in the radical propagation pathway of *E. coli* ribonucleotide reductase. *J. Am. Chem. Soc.* **2007**, *129*, 15748-15749.
22. Minnihan, E. C. Mechanistic studies of proton-coupled electron transfer in aminotyrosine- and fluorotyrosine-substituted class Ia ribonucleotide reductases. Ph.D. Thesis, Massachusetts Institute of Technology, **2012**.
23. Nick, T. U. Hydrogen bonds and electrostatic environment of radical intermediates in ribonucleotide reductase Ia. Ph.D. Thesis. University of Göttingen. **2015**.
24. Minnihan, E. C.; Seyedsayamdost, M. R.; Uhlin, U.; Stubbe, J. Kinetics of radical intermediate formation and deoxynucleotide production in 3-aminotyrosine-substituted *Escherichia coli* ribonucleotide reductases. *J. Am. Chem. Soc.* **2011**, *133*, 9430-9440.
25. Seyedsayamdost, M. R.; Xie, J.; Chan, C. T.; Schultz, P. G.; Stubbe, J. Site-specific insertion of 3-aminotyrosine into subunit α2 of *E. coli* ribonucleotide reductase: direct evidence for involvement of Y₇₃₀ and Y₇₃₁ in radical propagation. *J. Am. Chem. Soc.* **2007**, *129*, 15060-15071.
26. Chen, H.; Gollnick, P.; Phillips, R. S. Site-directed mutagenesis of His343-->Ala in *Citrobacter freundii* tyrosine phenol-lyase. Effects on the kinetic mechanism and rate-determining step. *Eur. J. Biochem.* **1995**, *229*, 540-549.
27. Seyedsayamdost, M. R.; Yee, C. S.; Stubbe, J. Site-specific incorporation of fluorotyrosines into the R2 subunit of *E. coli* ribonucleotide reductase by expressed protein ligation. *Nat. Protoc.* **2007**, *2*, 1225-1235.
28. Chivers, P. T.; Prehoda, K. E.; Volkman, B. F.; Kim, B. M.; Markley, J. L.; Raines, R. T. Microscopic pK_a values of *Escherichia coli* thioredoxin. *Biochemistry* **1997**, *36*, 14985-14991.

29. Russel, M.; Model, P. Direct cloning of the *trxB* gene that encodes thioredoxin reductase. *Bacteriol.* **1985**, *163*, 238-242.
30. Yokoyama, K.; Uhlin, U.; Stubbe, J. Site-specific incorporation of 3-nitrotyrosine as a probe of pK_a perturbation of redox-active tyrosines in ribonucleotide reductase. *J. Am. Chem. Soc.* **2010**, *132*, 8385-8397.
31. Palmer, G. Electron paramagnetic resonance. *Methods. Enzymol.* **1967**, *10*, 594-610.
32. Steeper, J. R.; Steuart, C. D. A rapid assay for CDP reductase activity in mammalian cell extracts. *Anal. Biochem.* **1970**, *34*, 123-130.
33. Tong, W. H.; Chen, S.; Lloyd, S. G.; Edmondson, D. E.; Huynh, B. H.; Stubbe, J. Mechanism of assembly of the diferric cluster-tyrosyl radical cofactor of *Escherichia coli* ribonucleotide reductase from the diferrous form of the R2 subunit. *J. Am. Chem. Soc.* **1996**, *118*, 2107-2108.
34. Bennati, M.; Weber, A.; Antonic, J.; Perlstein, D. L.; Robblee, J. H.; Stubbe, J. Pulsed ELDOR spectroscopy measured the distance between the two tyrosyl radicals in the R2 subunit of the *E. coli* ribonucleotide reductase. *J. Am. Chem. Soc.* **2003**, *125*, 14988-14989.
35. Bennati, M.; Robblee, J. H.; Mugnaini, V.; Stubbe, J.; Freed, J. H.; Borbat, P. EPR distance measurements support a model for long-range radical initiation in *E. coli* ribonucleotide reductase. *J. Am. Chem. Soc.* **2005**, *127*, 15014-15015.
36. Ator, M. A.; Stubbe, J. Mechanism of inactivation of *Escherichia coli* ribonucleotide reductase by 2'-chloro-2'-deoxyuridine 5'-diphosphate: evidence for generation of a 2'-deoxy-3'-ketonucleotide via a net 1,2 hydrogen shift. *Biochemistry* **1985**, *24*, 7214-7221.
37. Ando, N.; Brignole, E. J.; Zimanyi, C. M.; Funk, M. A.; Yokoyama, K.; Asturias, F. J.; Stubbe, J.; Drennan, C. L. Structural interconversions modulate activity of *Escherichia coli* ribonucleotide reductase. *Proc. Natl. Acad. Sci. U. S. A.* **2011**, *108*, 21046-21051.
38. Olshansky, L.; Pizano, A. A.; Wei, Y.; Stubbe, J.; Nocera, D. G. Kinetics of hydrogen atom abstraction from substrate by an active site thiyl radical in ribonucleotide reductase. *J. Am. Chem. Soc.* **2014**, *136*, 16210-16216.
39. Lawrence, C. C., Bennati, M., Obias, H. V., Bar, G., Griffin, R. G. & Stubbe, J. High-field EPR detection of a disulfide radical anion in the reduction of cytidine 5'-diphosphate by the E₄₄₁Q-R1 mutant of *Escherichia coli* ribonucleotide reductase. *Proc. Natl. Acad. Sci. U. S. A.* **1999**, *96*, 8979-8984.
40. Mao, S. S.; Holler, T. P.; Yu, G. X.; Bollinger, J. M., Jr.; Booker, S.; Johnston, M. I.; Stubbe, J. A model for the role of multiple cysteine residues involved in ribonucleotide reduction: amazing and still confusing. *Biochemistry* **1992**, *31*, 9733-9743.
41. Persson, A. L.; Eriksson, M.; Katterle, B.; Pötsch, S.; Sahlin, M.; Sjöberg, B. M. A new mechanism-based radical intermediate in a mutant R1 protein affecting the catalytically essential Glu441 in *Escherichia coli* ribonucleotide reductase. *J. Biol. Chem.* **1997**, *272*, 31533-31541.
42. Kasrayan, A.; Persson, A. L.; Sahlin, M.; Sjöberg, B. M. The conserved active site asparagine in class I ribonucleotide reductase is essential for catalysis. *J. Biol. Chem.* **2002**, *277*, 5749-5755.

43. van der Donk, W. A.; Stubbe, J.; Gerfen, G. J.; Bellew, B. F.; Griffin, R. G. EPR investigations of the inactivation of *E. coli* ribonucleotide reductase with 2'-azido-2'-deoxyuridine-5'-diphosphate: evidence for the involvement of the thiyl radical of C₂₂₅-R1. *J. Am. Chem. Soc.* **1995**, *117*, 8908-8916.
44. van der Donk, W. A., Yu, G. X., Pérez, L., Sanchez, R. J., Stubbe, J., Samano, V. & Robins, M. J. Detection of a new substrate-derived radical during inactivation of ribonucleotide reductase from *Escherichia coli* by gemcitabine 5'-diphosphate. *Biochemistry* **1998**, *37*, 6419-6426.
45. Seyedsayamdost, M. R.; Reece, S. Y.; Nocera, D. G. Stubbe, J. Mono-, di-, tri- and tetra-substituted fluorotyrosines: new probes for enzymes that use tyrosyl radicals in catalysis. *J. Am. Chem. Soc.* **2006**, *128*, 1569-1579.
46. Olshansky, L. Kinetics and dynamics controlling proton-coupled electron transfer in ribonucleotide reductase. Ph.D. Thesis, Massachusetts Institute of Technology, **2015**.

Chapter 4

The stable tyrosyl radical ($Y_{122}\cdot$) is in equilibrium with a pathway tyrosyl radical ($Y_{356}\cdot$) in the radical transport pathway of fluorotyrosine-substituted ribonucleotide reductases

4.1 INTRODUCTION

The *E. coli* class Ia ribonucleotide reductase (RNR) contains two homodimeric subunits, $\alpha 2$ and $\beta 2$ and functions as an $\alpha 2\beta 2$ complex.^{1,2} The active cofactor in the class Ia RNR is a diferric-tyrosyl radical ($Y_{122}\bullet$) unit buried within $\beta 2$. This cofactor generates a transient thiyl radical ($C_{439}\bullet$) in $\alpha 2$ ³ which reduces the four nucleotides (CDP, GDP, ADP, UDP) to their corresponding 2'-deoxynucleotides (dNDP) as dictated by the allosteric effectors (ATP, TTP, dGTP, dATP).⁴⁻⁶ During each turnover, $Y_{122}\bullet$ reversibly oxidizes C_{439} via multiple PCET steps through the following aromatic amino acid residues: $Y_{122} \rightarrow [W_{48}] \rightarrow Y_{356}$ in $\beta 2$ to $Y_{731} \rightarrow Y_{730} \rightarrow C_{439}$ in $\alpha 2$ (no direct evidence yet exists for the involvement of W_{48} in RT, see Appendix 4).⁷⁻⁹ In the wild-type (wt) system, only $Y_{122}\bullet$ is observed with no detectable electron delocalization over the other pathway tyrosines.¹⁰ In this Chapter, we present the first insight into the thermodynamic landscape of this RT pathway within $\beta 2$. Site-specific replacement of either $Y_{122}\bullet$ or $Y_{356}\bullet$ with F_nY ($n = 2, 3$) in combination with X-band EPR spectroscopy¹¹ provides evidence for equilibration of $Y_{122}\bullet$ with $Y_{356}\bullet$ as a function of temperature and pH. These studies have allowed estimation of $\Delta E^\circ (Y_{122}\bullet - Y_{356}\bullet)$.

Detection of low concentrations of any pathway radical in the wt system is challenging due to the substantial overlap in the EPR spectra of the $Y\bullet$ s.¹² Initial attempts to address if $Y_{122}\bullet$ equilibrated with the pathway tyrosines (Y_{356} , Y_{731} and Y_{730}) utilized the ability to collapse the $Y\bullet$ doublet EPR spectrum into a singlet with β -methylene-deuterated Y s ($[\beta\text{-}^2\text{H}_2]$).^{10,12} $\beta 2$ containing globally incorporated $[\beta\text{-}^2\text{H}_2]Y$ s was reacted with $\alpha 2$ containing protonated Y s, dCDP and TTP.¹⁰ These conditions promote $\alpha 2\beta 2$ complex formation¹ but prevent turnover, thus potentially allowing equilibration of the pathway $Y\bullet$ s. Unfortunately, no protonated $Y\bullet$ signal could be detected; the EPR spectrum of $Y\bullet$ in the $\alpha 2\beta 2$ complex was identical to that in free $\beta 2$.¹⁰

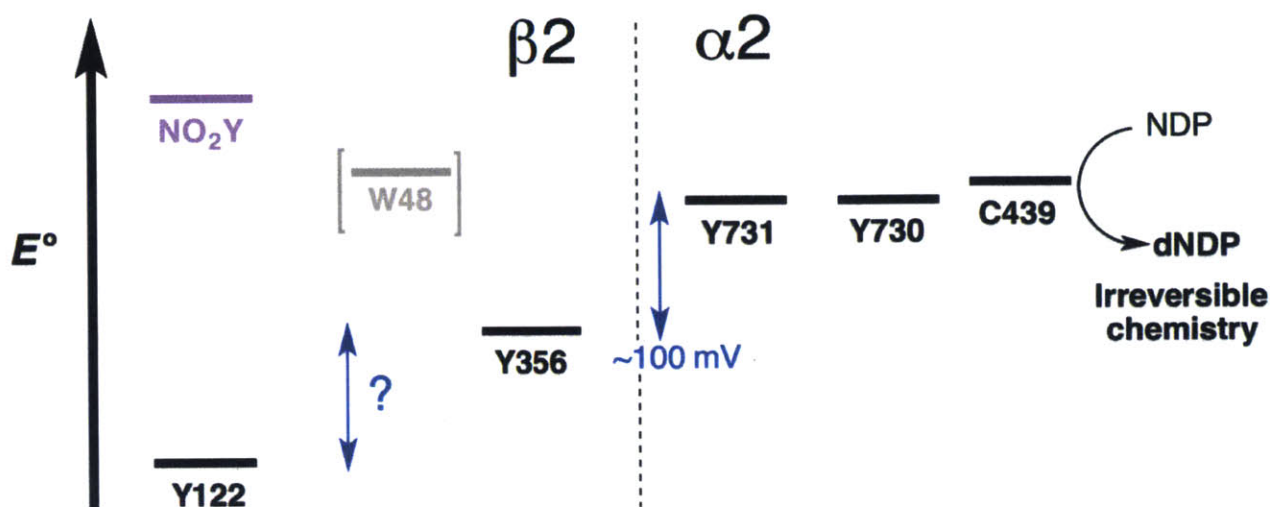


Figure 4.1 Proposed thermodynamic landscape of the PCET pathway at 25 °C and pH 7.6. The overall reaction is proposed to be thermodynamically uphill and driven forward by the rapid irreversible loss of water in the active site of $\alpha 2$. No direct evidence is available for the presence of a discrete W_{48} radical intermediate. Studies performed on $Y_{122}NO_2Y-\beta 2$ determined the relative reduction potentials of Y_{356} , Y_{731} and Y_{730} .¹²

More recently, we showed that the reaction of $Y_{122}NO_2Y-\beta 2$ (predicted to be 200 mV harder to oxidize than Y at pH 7.0)¹³ with $\alpha 2$, CDP and ATP generates a new $Y\bullet$, localized to Y_{356} .¹⁴ Using 3,5- F_2Y (or F_2Y) at Y_{731} (or Y_{730}) we demonstrated that $Y_{356}\bullet$ equilibrated with $F_2Y_{731}\bullet$ or $F_2Y_{730}\bullet$.¹² This analysis was facilitated by the unique EPR spectroscopic features of $F_2Y\bullet$ outside the envelope of the $Y\bullet$ spectrum, which arise from coupling of the unpaired electron to the fluorine nuclei.^{9,11} This exciting observation gave us the first opportunity to investigate the effect of protein environment on the reduction potentials of the pathway Ys; multifrequency EPR spectroscopy allowed estimation of a ΔE° of ~ 100 mV between the Ys in $\alpha 2$ and Y_{356} . The thermodynamic landscape of the RT pathway constructed from these studies is shown in Figure 4.1. We proposed that the overall RT pathway is thermodynamically uphill and driven forward by the nucleotide reduction process, specifically the rapid irreversible cleavage of the C2-OH bond¹⁵ of the substrate and loss of water (10^6-10^8 s⁻¹)¹⁶⁻¹⁸ in the active site of $\alpha 2$. Unfortunately, the

$Y_{122}NO_2Y-\beta 2$ system could not be used to monitor equilibration of $NO_2Y\bullet$ and $Y_{356}\bullet$ because oxidation of Y_{356} by $NO_2Y\bullet$ was irreversible.

In an attempt to obtain insight into the thermodynamic landscape within $\beta 2$, we take advantage of a recently engineered $\beta 2$ system containing 2,3,5- F_3Y (or F_3Y) at position 122 (Chapter 3).^{11,19} The reaction of $Y_{122}(2,3,5)F_3Y-\beta 2$, $\alpha 2$, CDP and ATP results in rapid formation of dCDP ($20-30\text{ s}^{-1}$) concomitant with accumulation of $Y_{356}\bullet$. In contrast to $Y_{122}NO_2Y-\beta 2$, we have demonstrated that $Y_{356}\bullet$ can re-oxidize F_3Y and that this re-oxidation process is rate-limiting for subsequent turnovers (Chapter 3).¹⁹ The reversible nature of Y_{356} oxidation in $Y_{122}(2,3,5)F_3Y-\beta 2$ led to the studies described herein and gave us the opportunity to investigate the relative reduction potentials of $F_3Y\bullet$ and $Y_{356}\bullet$.

In this work, temperature and pH dependent quantitation of $F_3Y\bullet$ and $Y_{356}\bullet$ in the reaction of $Y_{122}(2,3,5)F_3Y-\beta 2$, $Y_{731}F-\alpha 2$, CDP and ATP by EPR spectroscopy reveals equilibration of the two radical states. The Van't Hoff plot, relating the equilibrium constant for this reaction at pH 7.6 and temperature ($2-37^\circ\text{C}$), is described by two linear fits with the change in the mechanism of $Y_{356}\bullet$ formation occurring at $13 \pm 2^\circ\text{C}$. This change in mechanism results in an increase in the driving force of the reaction; $\Delta E^\circ (F_3Y\bullet - Y_{356}\bullet)$ is $-14 \pm 6\text{ mV}$ at 5°C but $16 \pm 5\text{ mV}$ at 25°C . The ability to equilibrate $F_3Y\bullet$ and $Y_{356}\bullet$ with $Y_{731}F-\alpha 2$ provided us the opportunity to investigate the fate of the Y_{356} proton upon oxidation of this pathway Y. The $\log([Y_{356}\bullet]/[F_3Y\bullet])$ between pH 6.8 and 8.4 provides a slope of 1.06 ± 0.05 (25°C) consistent with rapid release of the Y_{356} proton to solvent upon oxidation. Finally, we utilize the ability to perturb the equilibrium with temperature and pH to demonstrate equilibration of the native $Y_{122}\bullet$ with $F_2Y\bullet$ in $Y_{356}(3,5)F_2Y-\beta 2$. Rapid freeze-quench (RFQ)-EPR spectroscopy of the $Y_{356}(3,5)F_2Y-\beta 2$, $Y_{731}F-\alpha 2$, CDP and ATP reaction at pH 8.2 and 25°C shows that $F_2Y\bullet$ constitutes $3 \pm 1\%$ of the total radical amount. This allows

an estimation of 70 ± 5 mV for ΔE° ($F_2Y^\bullet - Y_{122}^\bullet$). Taken together, the data suggest an unprecedented thermodynamic landscape for the RT pathway in the *E. coli* class Ia RNR that is > 200 mV uphill.

4.2 MATERIALS AND METHODS

4.2.1 Materials. (His)₆ Y₇₃₁F- α 2 and wt- α 2 (specific activity of 2500 nmol/min/mg),²⁰ tyrosine phenol lyase,²¹ F₂Y²² and F₃Y²² were isolated as previously described. Apo Y₁₂₂(2,3,5)F₃Y- β 2 was expressed, isolated and reconstituted as reported in Chapter 3. Y₃₅₆(3,5)F₂Y- β 2 (0.7 Y•/ β 2) was available from an earlier study.²³ CDP and ATP were purchased from Sigma Aldrich. Assay buffer consists of 50 mM HEPES pH 7.6, 15 mM MgSO₄ and 1 mM EDTA unless otherwise specified.

4.2.2 Hand-quench EPR analysis of Y₃₅₆• formation as a function of temperature. Assay mixtures of final volume 250 μ L containing 25 μ M Y₇₃₁F- α 2, 1 mM CDP and 3 mM ATP in assay buffer were incubated in a Lauda RM6 circulating water bath set between 2 and 37 °C. Y₁₂₂(2,3,5)F₃Y- β 2 (0.8 F₃Y•/ β 2) was added to a final concentration of 25 μ M to initiate the reaction. Reaction mixtures were transferred to X-band EPR tubes that were also maintained in the water bath, frozen in liquid isopentane (-140 °C) at 20 s (or 1 min) and analyzed by X-band EPR spectroscopy. The EPR parameters were reported in Chapter 3.¹⁹ Residual F₃Y• was subtracted from the composite spectrum to quantitate the percentage of Y₃₅₆• in the following manner.

All $S = \frac{1}{2}$ radicals absorb equally well in a continuous wave (CW) EPR experiment, allowing for the equilibrium constant (K_{eq} , [Y₃₅₆•/F₃Y•]) between two such species to be determined from their relative integrated intensities. For the temperature-dependent spectra, the following procedure was applied to extract the K_{eq} 's and estimate their associated errors. The field (gauss) was converted into units of g value, in order to avoid any misalignment of the spectra caused by differences in the microwave frequency of the measurement. The baseline was subtracted with a linear fit to the regions of the spectrum lacking the Y• (or F₃Y•) signal. The spectra were then normalized in intensity to have the same area under the peak at $g = 2.038$

(associated with the ^{19}F and $\beta\text{-}^1\text{H}$ splittings). The remaining $^{19}\text{F}/\beta\text{-}^1\text{H}$ wing features were not included in this analysis due to their low S/N. The reference $\text{F}_3\text{Y}\cdot$ spectrum (i.e $\text{F}_3\text{Y}\cdot$ in free $\beta 2$) was subtracted from all of the traces, allowing for quantitation of the remaining $\text{Y}_{356}\cdot$ species by double integration. The K_{eq} was obtained by dividing this number by the $\text{F}_3\text{Y}\cdot$ area according to the half-sites reactivity model where only one $\text{F}_3\text{Y}\cdot$ in $\beta 2$ reacts at a time¹⁹ ($[\text{F}_3\text{Y}\cdot]_{\text{half-site}} = \frac{\text{The integrated area under the } \text{F}_3\text{Y}\cdot \text{ reference spectrum minus half of the total } [\text{F}_3\text{Y}\cdot + \text{Y}_{356}\cdot] \text{ integrated area}}{2}$).

The error in the calculated K_{eq} was estimated from the noise of the spectra. The standard deviation of 100 points selected from the noise was used to estimate the error per point in the CW EPR traces. This error was multiplied by the square root of the number of points used for the area calculations (to obtain the error of the peak area), and propagated through the calculation of the K_{eq} described above to generate the final errors. The data were analyzed using the Van't Hoff equation (Eq. 4.1):

$$\ln K_{\text{eq}} = -\frac{\Delta H^\circ}{RT} + \frac{\Delta S^\circ}{R} \quad (4.1)$$

where $K_{\text{eq}} = [\text{Y}_{356}\cdot]/[\text{F}_3\text{Y}\cdot]$, R is the ideal gas constant, T is the temperature (K) of the reaction and ΔH° and ΔS° represent the enthalpy and entropy changes for the reaction, respectively. These parameters were used to calculate the Gibbs free energy (ΔG°) for the reaction at 5 °C and 25 °C and hence, $\Delta E^\circ (\text{F}_3\text{Y}\cdot\text{--}\text{Y}_{356}\cdot)$.

4.2.3 RFQ-EPR analysis of $\text{Y}_{356}\cdot$ formation as a function of temperature. RFQ experiments were performed on an Update Instruments 1019 syringe ram unit and a model 715 syringe ram controller (ram speed 1.25 cm/s). Temperature was varied between 2 °C and 37 °C using an external Lauda RM6 circulating water bath. $\text{Y}_{122}(2,3,5)\text{F}_3\text{Y}\text{-}\beta 2$ (70 μM , 0.8 $\text{F}_3\text{Y}\cdot/\beta 2$) and CDP (2

mM) in assay buffer were mixed with Y₇₃₁F- α 2 (70 μ M) and ATP (6 mM). After an incubation period of either 4 s or 10 s, the reaction mixture was sprayed in a funnel containing liquid isopentane (-140 °C). The crystals were packed into EPR tubes for analysis by X-band EPR spectroscopy. Data analysis was performed as described above.

4.2.4 Hand-quench EPR analysis of Y₃₅₆• formation as a function of pH. Y₇₃₁F- α 2 (25 μ M), Y₁₂₂(2,3,5)F₃Y- β 2 (25 μ M, 0.6–0.8 F₃Y•/ β 2), CDP (1 mM) and ATP (3 mM) were combined in 50 mM MES (pH 6.8), HEPES (pH 7.0–8.0) or TAPS (pH 8.2 and 8.4), 15 mM MgSO₄ and 1 mM EDTA and incubated in a Lauda RM6 circulating water bath set at 5 °C or 25 °C. Reaction mixtures were transferred to X-band EPR tubes also maintained in the water bath and frozen in liquid isopentane (-140 °C) within 20 s (or 1 min) for analysis by X-band EPR spectroscopy. [Y₃₅₆•] and [F₃Y•] were quantitated as described earlier. The data were fit to Eq. 4.2 where $K = [Y_{356}\bullet]/[F_3Y\bullet]$.

$$\log K = pH - pK_a \quad (4.2)$$

4.2.5 RFQ-EPR analysis of the reaction of Y₃₅₆(3,5)F₂Y- β 2, Y₇₃₁F- α 2, CDP and ATP. Temperature was controlled with an external Lauda RM6 circulating water bath set at 25 °C. Y₇₃₁F- α 2 (80 μ M) and 6 mM ATP in 50 mM TAPS pH 8.2, 15 mM MgSO₄, 1 mM EDTA was mixed with an equal volume of Y₃₅₆(3,5)F₂Y- β 2 (80 μ M, 0.7 Y•/ β 2) and CDP (2 mM) in the same buffer. The reaction was aged for 10, 20 or 40 s and quenched for analysis by X-band EPR spectroscopy. The EPR parameters were as follows: microwave frequency 9.45 GHz; power 30 μ W; modulation amplitude 1.50 G; modulation frequency 100 kHz; time constant 163.8 ms and conversion time 20.48 ms. The number of scans were 100 (10 s sample), 600 (20 s sample, n = 100 for each separate scan) and 60 (40 s sample).

4.3 RESULTS

4.3.1 Temperature dependent distribution of F_3Y^\bullet and Y_{356}^\bullet : Equilibration of the two radical states. In Chapter 3, we showed that the reaction of $Y_{122}(2,3,5)F_3Y-\beta 2$, wt- $\alpha 2$, CDP and ATP generates a kinetically and chemically competent Y_{356}^\bullet that can re-oxidize F_3Y .¹⁹ We hypothesized that if F_3Y^\bullet and Y_{356}^\bullet are in equilibrium in the $Y_{122}(2,3,5)F_3Y-\beta 2$ system, then the amounts of the two radicals will vary with temperature as dictated by the relative redox potentials of the two states. $Y_{122}(2,3,5)F_3Y-\beta 2$, CDP and ATP were incubated with $Y_{731}F-\alpha 2$, a pathway mutant that blocks turnover,¹⁰ to ensure equilibration of F_3Y^\bullet and Y_{356}^\bullet . Studies performed on the $Y_{122}NO_2Y-\beta 2$ system have shown that Y_{356}^\bullet exists in equilibrium with Y_{731}^\bullet and Y_{730}^\bullet .¹² We decided to utilize $Y_{731}F-\alpha 2$ in all studies described in this Chapter, to remove this equilibration and simplify data analysis and interpretation. However, it has been shown that the electrostatic environment of Y_{356}^\bullet generated in the $Y_{731}F-\alpha 2$ reaction is distinct compared to that observed with wt- $\alpha 2$ and that the former radical species is potentially missing a H-bonding interaction.¹² The removal of this interaction could affect the equilibrium between F_3Y^\bullet and Y_{356}^\bullet ; thus, we performed a single experiment with $Y_{730}F-\alpha 2$ to ensure that placement of a F at the β/α interface did not dramatically perturb our equilibration studies (Taguchi, Stubbe unpublished results). The $Y_{731}F-\alpha 2$ data is discussed below, but almost identical results were observed with $Y_{730}F-\alpha 2$.

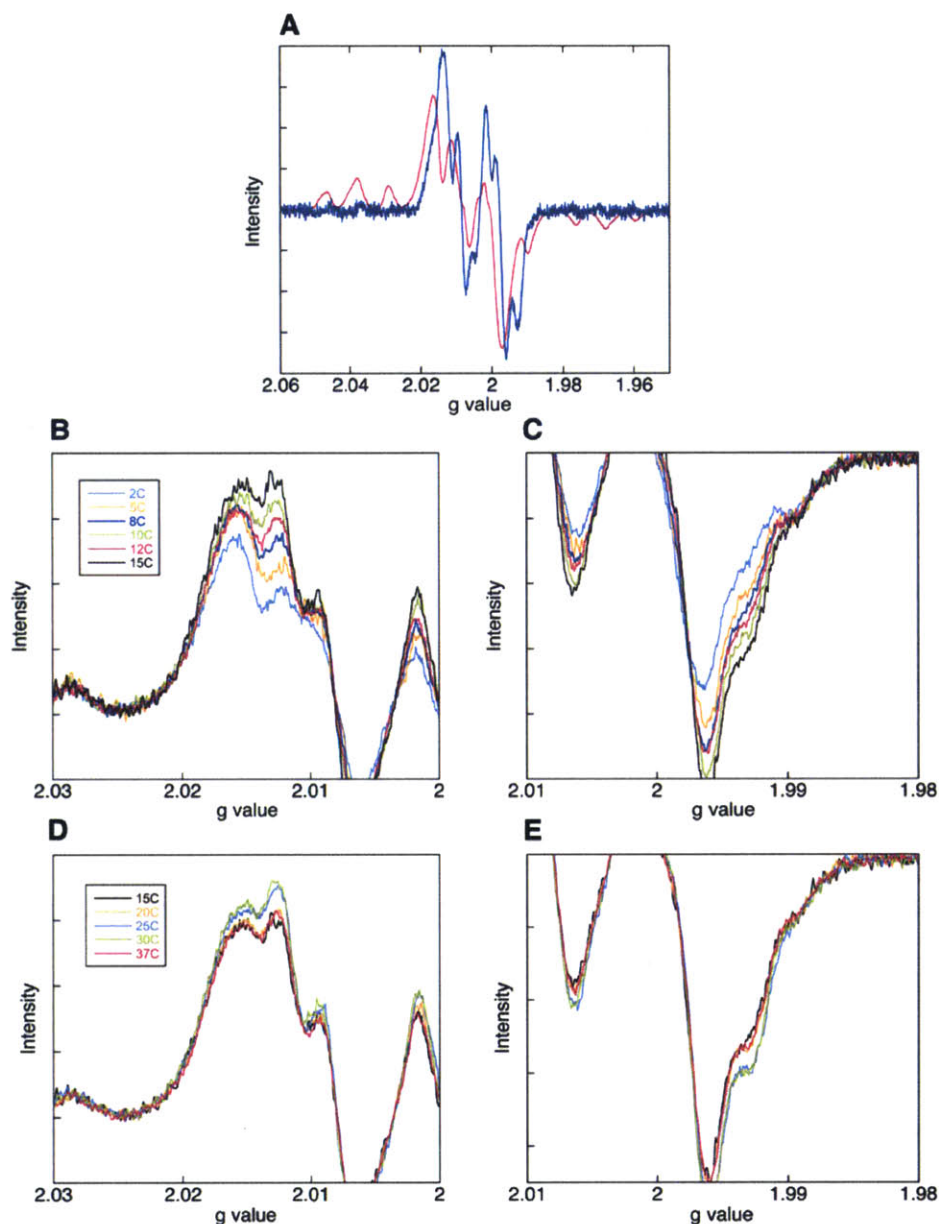


Figure 4.2 Composite EPR spectra of the $Y_{122}(2,3,5)F_3Y\text{-}\beta_2/Y_{731}F\text{-}\alpha_2/CDP/ATP$ reaction as a function of temperature. A. The X-band EPR spectra of $F_3Y\bullet$ (pink) and $Y_{356}\bullet$ (blue). The spectra shown in B-E are additive and contain different amounts of $F_3Y\bullet$ and $Y_{356}\bullet$. B and C show the low- and high-field regions of the spectra collected between 2 °C and 15 °C (color code as described in panel B). D and E show the low- and high-field regions of the spectra collected between 15 °C and 37 °C (color code as described in panel C). The composite spectrum at each temperature was acquired on three independently prepared samples. The expanded views for trials 2 and 3 are shown in Appendix 6 (Figures A6.1 and A6.2).

The $Y_{122}(2,3,5)F_3Y\text{-}\beta_2/Y_{731}F\text{-}\alpha_2/CDP/ATP$ reaction was performed by hand, aged at various temperatures in a circulating water bath and quenched in liquid isopentane (-140 °C) for analysis by X-band EPR spectroscopy. We initially decided to quench samples at two time points (20 s and 1 min) and looked at variability in $Y_{356}\bullet$ amounts and total radical content as indicators of whether the reaction was at equilibrium. The X-band EPR spectra of $F_3Y\bullet$ and $Y_{356}\bullet$ are shown in Figure 4.2A in pink and blue, respectively. We have previously shown that radical distribution in $Y_{122}(2,3,5)F_3Y\text{-}\beta_2$ can be described by a two or none model where active β_2 s contain a $F_3Y\bullet$ in each monomer (Figure 3.2, Chapter 3).¹⁹ $Y_{122}(2,3,5)F_3Y\text{-}\beta_2$ also demonstrates half-sites reactivity where only one of the two $F_3Y\bullet$ s (or one α/β pair) is active at a time.¹⁹ A consequence of this phenomenon is the presence of residual $F_3Y\bullet$ in all reaction mixtures; 50% of the total spin is in the form of unreacted $F_3Y\bullet$ in the second α/β pair. Thus, all spectra discussed subsequently are additive and contain different amounts of the two radicals. Figures 4.2B-C show expanded views of the EPR spectra of the reaction mixtures at 2, 5, 8, 10, 12 and 15 °C quenched at 20 s, prior to subtraction of $F_3Y\bullet$. At any given temperature, no variations in spin or spectral features were seen between the 20 s and 1 min samples (data not shown) suggesting that the reaction is at equilibrium. However, when the 20 s samples at different temperatures are compared (Figures 4.2B-C), changes are readily apparent in both the low- ($g = \sim 2.013$) and high-field ($g = \sim 1.994$) regions of the EPR spectra. The composite EPR spectra were collected on three independently prepared samples and the reproducibility of these spectral changes can be visualized in Figures 4.2B-C, A6.1A-B and A6.2A-B (Appendix 6). These changes directly correlate with increasing amounts of $Y_{356}\bullet$ from $14 \pm 4\%$ (average of three trials at 2 °C) to $30 \pm 2\%$ (average of three trials at 15 °C) as summarized in Table 4.1.

In contrast to the data collected between 2 °C and 15 °C, minimal changes are visualized in the composite EPR spectra recorded between 15 °C and 37 °C (Figures 4.2D-E). The lack of variability in the measurement of these small changes is apparent when the EPR data shown in Figures 4.2D-E are compared to those collected in two additional experiments (Figures A6.1C-D and A6.2C-D). The average Y_{356}^{\bullet} amounts in the three experiments subsequent to subtraction of F_3Y^{\bullet} are shown in Table 4.1 ($30 \pm 2\%$ at 15 °C and $33 \pm 3\%$ at 37 °C).

Table 4.1 Temperature dependence of Y_{356}^{\bullet} formation: hand-quench (HQ) vs rapid freeze-quench (RFQ).

Temperature (°C)	HQ (% Y_{356}^{\bullet} of total spin)	RFQ (% Y_{356}^{\bullet} of total spin)
2	14 ± 4	19
5	18 ± 1	30
8	22 ± 1	-
10	28 ± 4	36
12	27 ± 1	-
15	30 ± 2	37
20	33 ± 3	43
25	31 ± 5	41
30	34 ± 4	42
37	33 ± 3	40

The HQ data represents the average of three independent trials. The RFQ data represent a single trial.

We speculated that the variability observed in these EPR experiments might be associated with the HQ method prior to data acquisition. Previous studies have shown that this slow freezing process can shift the equilibrium.²⁴ Thus, an additional experiment was conducted to monitor the radical amounts by RFQ-EPR spectroscopy (Table 4.1). We initially investigated the reaction at 5 °C at 4 s and 10 s. The 4 s time point was chosen based on kinetic experiments performed with $Y_{122}(2,3,5)F_3Y-\beta 2$ and wt- $\alpha 2$ (Figure 3.4A, Chapter 3).¹⁹ We additionally chose a later time point (10 s) and probed for changes in total radical content and the amount of Y_{356}^{\bullet} to assess if the reaction was at equilibrium. No changes in spin quantitation were recorded and minimal changes

were observed in the EPR spectra between 4 s and 10 s. Subtraction of $F_3Y\bullet$ provided $Y_{356}\bullet$ amounts that were within 3% at the two time points. These results support the conclusion that the reaction is at equilibrium at both 4 s and 10 s. We repeated these reactions at one higher temperature (30 °C) and made similar observations regarding total spin and $Y_{356}\bullet$ amounts. Thus, the reactions at all other temperatures (2, 10, 15, 20, 25 °C) were performed at 10 s.

The composite spectra and the amounts of $Y_{356}\bullet$ at different temperatures are shown in Figure A6.3 and summarized in Table 4.1 respectively. The amount of $Y_{356}\bullet$ observed by RFQ is 5–10% higher than that recorded by the HQ method. Similar trends are observed between the RFQ-EPR and HQ samples; increasing amounts of $Y_{356}\bullet$ are recorded between 2 °C and 15 °C whereas, the spectra collected between 15 °C and 37 °C show almost no changes in the percentage of $Y_{356}\bullet$ (Figure A6.3, Table 4.1).

To calculate the reduction potential difference between $F_3Y\bullet$ and $Y_{356}\bullet$, we analyzed the HQ and RFQ-EPR data using Eq. 4.1 that relates $\ln K_{eq}$ ($[Y_{356}\bullet]/[F_3Y\bullet]$) and temperature. Figure 4.3A shows the Van't Hoff plot for the HQ data. The individual trials are shown in green, pink and orange, respectively while the blue squares represent the averages of the three independent experiments. The error bars shown on each trial were calculated based on the noise of the EPR spectra as described in the Materials and Methods. These error bars were found to not be overlapping in many cases, indicating that the predominant source of error in these experiments is systematic (variations in sample conditions on different days). As predicted by the observed EPR spectral changes (Figures 4.2, A6.1, A6.2), the reaction is described by two linear fits that intersect at 13 ± 2 °C. These results suggest that two mechanisms exist for $F_3Y\bullet/Y_{356}\bullet$ equilibration with the change in mechanism occurring at ~ 13 °C. The Van't Hoff plot in Figure 4.3A cannot be fit to a single ΔE° , but by considering the regions above and below 13 °C separately; the ΔE° ($F_3Y\bullet - Y_{356}\bullet$)

was calculated at 5 °C and 25 °C as -14 ± 6 mV and 16 ± 5 mV respectively. We did not estimate ΔE° from the RFQ-EPR data as only a single experiment was performed. However, Figure 4.3B shows the overlay between the Van't Hoff plots constructed from the RFQ-EPR and HQ-EPR data. As seen in the Figure, although the absolute amounts of F_3Y^\bullet and Y_{356}^\bullet change with the quench method, the RFQ points show a similar trend in which two temperature regimes exist for Y_{356}^\bullet formation. As mentioned earlier, we had also performed a single experiment with $Y_{730}F-\alpha 2$ to ensure that placement of a F at the interface did not perturb the reduction potential of Y_{356} (Taguchi, Stubbe unpublished results). The Van't Hoff plots from the $Y_{731}F-\alpha 2$ and $Y_{730}F-\alpha 2$ studies are within error of each other suggesting that $Y_{731}F-\alpha 2$ does not affect the equilibrium between F_3Y^\bullet and Y_{356}^\bullet . A strong temperature dependence on RNR turnover has been previously noted;²⁵ the Arrhenius plot for steady-state dC formation shows a break at ~ 12 °C. The sources of the break in the Van't Hoff and Arrhenius plots are currently unknown but likely relate to protein conformational changes.

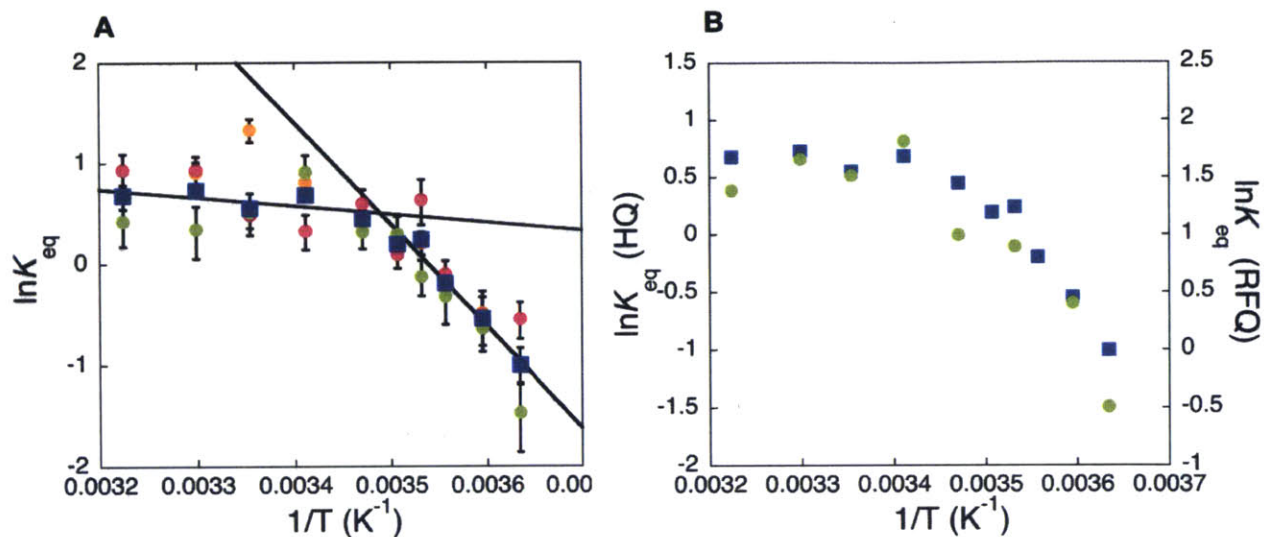
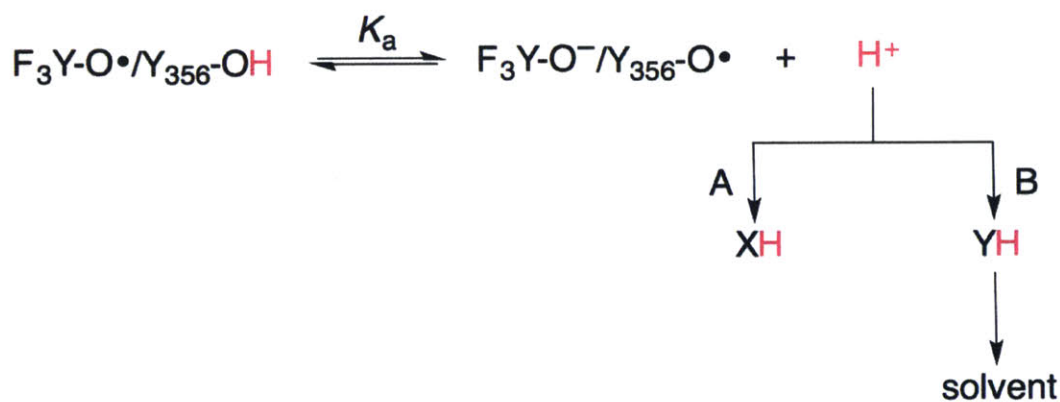


Figure 4.3 Temperature dependence (2–37 °C) of $Y_{356}\bullet$ formation. A. Van't Hoff plot for $Y_{356}\bullet$ formation as determined by HQ-EPR spectroscopy. The three independent trials are shown in green, pink and orange dots respectively while the averages of the three experiments are represented by the blue squares. The error bars for the individual trials are associated with the noise in the EPR spectra and were calculated as described in section 4.2.2. B. Van't Hoff plot for $Y_{356}\bullet$ formation as determined by HQ- and RFQ-EPR spectroscopic methods. The HQ data points (blue squares) represent the averages of three independent trials. The RFQ data points (green dots) represent a single trial.



Scheme 4.1 Proposed models for the fate of the Y_{356} proton. A. The proton released from Y_{356} is accepted by an amino acid residue (X) and is not solvent exchangeable. B. The proton is in fast exchange with solvent. The initial proton acceptor (Y) is either an amino acid residue or water. It is currently unknown if the proton from the water on the diferric cluster is transferred to $F_3Y\bullet$ upon RT.²⁶ However, as presented in the discussion we favor the model where the phenolate form of F_3Y is generated.

4.3.2 *The pH can shift the equilibrium between F_3Y^\bullet and Y_{356}^\bullet : Proton from Y_{356} is in rapid exchange with solvent.* Equilibration of F_3Y^\bullet and Y_{356}^\bullet in the $Y_{122}(2,3,5)F_3Y$ - $\beta 2$ system gave us the opportunity to investigate the fate of the proton released upon Y_{356} oxidation. Scheme 4.1 shows two scenarios for this proton transfer (PT) event. In scenario **A**, the proton from Y_{356} is accepted by an amino acid residue (X) and is not solvent exchangeable. In **B**, the proton from Y_{356} is in rapid exchange with solvent, and the initial proton acceptor (Y) is either an amino acid residue or a water cluster. If scenario **A** occurs in $Y_{122}(2,3,5)F_3Y$ - $\beta 2$, the amount of Y_{356}^\bullet should not vary with pH. Scenario **B** would result in a pH dependence and $\log([Y_{356}^\bullet]/[F_3Y^\bullet])$ would be directly proportional to the pH with a slope of 1. It has been previously proposed that E_{350} in $\beta 2$ could function as a proton acceptor for Y_{356}^\bullet .^{8,27} The location of E_{350} on the flexible C-terminal tail of $\beta 2$ and at the $\alpha 2/\beta 2$ interface is likely to make PT to this residue fall under scenario **B**.

$Y_{122}(2,3,5)F_3Y$ - $\beta 2$, $Y_{731}F$ - $\alpha 2$, CDP and ATP were combined in assay buffer (pH 6.8–8.4), incubated for 20 s or 1 min at 5 °C or 25 °C and hand-quenched in liquid isopentane for analysis by EPR spectroscopy. In the pH regime utilized for this experiment, RNR retains 50–100% of its maximum activity.²³ We predicted that if scenario **B** occurred then the data at the two temperatures would reflect two parallel lines with the same slope, but different pK_a s as Y_{356}^\bullet formation is favored more at 25 °C than at 5 °C (Figure 4.3).

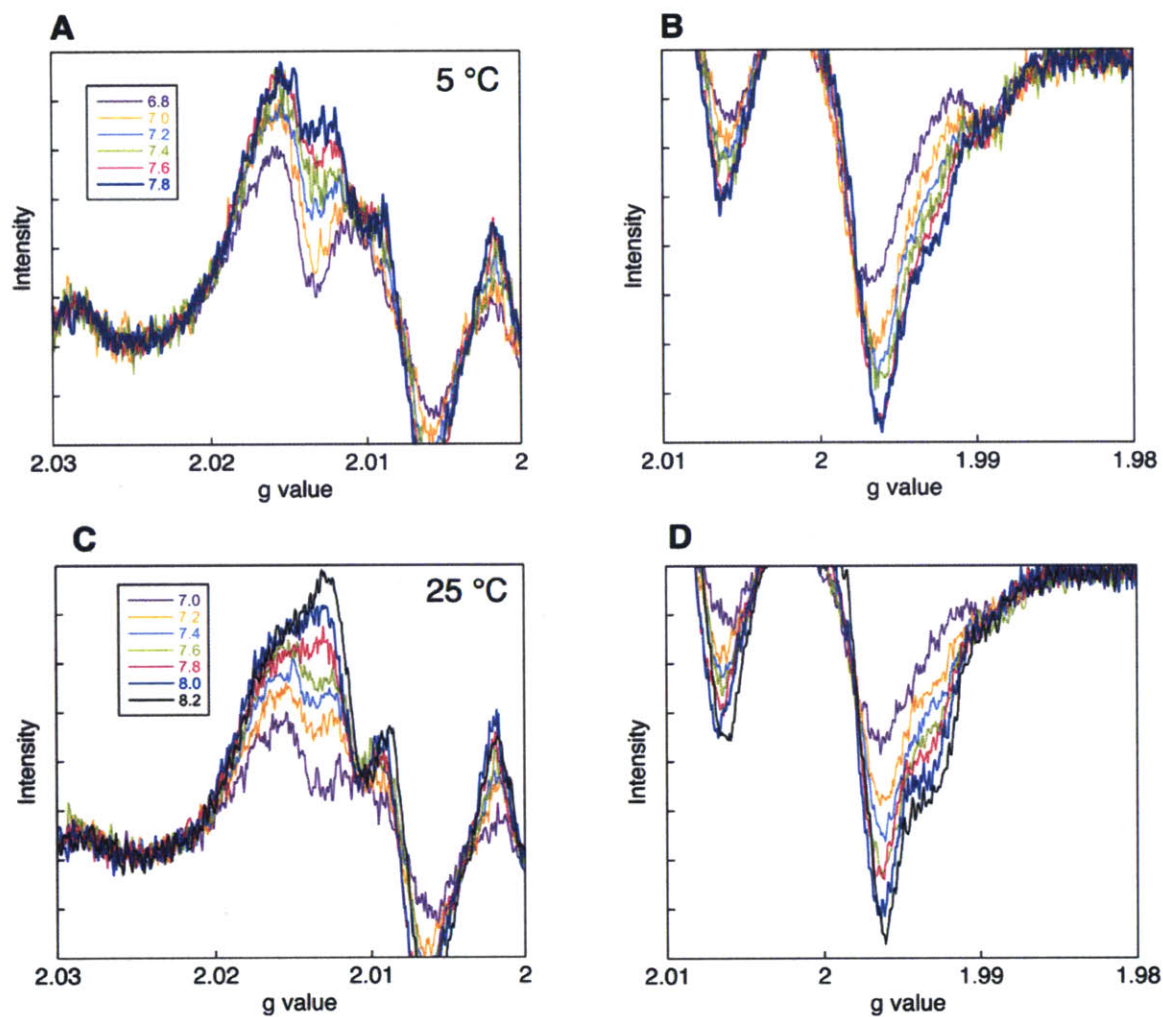


Figure 4.4 Composite EPR spectra of the $Y_{122}(2,3,5)F_3Y\text{-}\beta_2/Y_{731}F\text{-}\alpha_2/CDP/ATP$ reaction as a function of pH. A and B show the low- and high-field regions of the spectra collected at 5 °C. The colors represent different pH values as described in panel A. C and D show the low- and high-field regions of the spectra collected at 25 °C. The colors represent different pH values as described in panel C. The composite spectrum at each pH was acquired on two independently prepared samples. Expanded views for the second trial are shown in Appendix 6 (Figure A6.4).

Table 4.2 The pH dependence of $Y_{356}\bullet$ formation.

pH	5 °C	25 °C
	(% $Y_{356}\bullet$ of total spin)	(% $Y_{356}\bullet$ of total spin)
6.8	- ^a	- ^a
7.0	5.3 ± 0.3	12 ± 1
7.2	10 ± 2	19.4 ± 0.6
7.4	14 ± 4	25 ± 2
7.6	18 ^b	31 ^b
7.8	25 ± 2	35 ^b
8.0	26 ^c	38 ± 3
8.2	26 ^c	43 ^b
8.4	24 ^c	42 ^c

^aNo $Y_{356}\bullet$ could be detected. ^bThe two trials provided the same quantitation. ^cThese data points were collected once.

The EPR spectra of the reaction mixtures at 5 °C and 25 °C are shown in Figure 4.4. Each spectrum is a composite of different amounts of $F_3Y\bullet$ and $Y_{356}\bullet$ (see Figure 4.2A for the EPR spectra of the two radicals). At any given pH, no variations in spin or spectral features are observed between the 20 s and 1 min samples (data not shown) consistent with a reaction at equilibrium. Spectral changes are observed in the low- ($g \sim 2.013$) and high-field ($g \sim 1.994$) regions of the spectrum (Figure 4.4) with increasing pH and correlate with increasing amounts of $Y_{356}\bullet$. The composite spectra for a second trial are shown in Appendix 6 (Figure A6.4) and the average amounts of $Y_{356}\bullet$ from the two experiments are reported in Table 4.2. Figure 4.5 shows the data points for the pH range 7.0–7.8 (5 °C) or 7.0–8.2 (25 °C). The percentage of $Y_{356}\bullet$ at pH < 7.0 was below the detection limit (Table 4.2). The percentage of $Y_{356}\bullet$ above pH 7.8 (5 °C) or pH 8.2 (25 °C) does not change (~26% at 5 °C and ~43% at 25 °C, Table 4.2). We propose that these amounts reflect the equilibrium concentrations of $Y_{356}\bullet$ at each temperature.

The dependence of $\log([Y_{356}\bullet]/[F_3Y\bullet])$ on the pH of the reaction at 5 °C and 25 °C is shown in Figure 4.5. Slopes of 1.11 ± 0.13 and 1.06 ± 0.05 are measured at the two temperatures respectively supporting a model in which the proton from Y_{356} is in fast exchange with solvent

either through an amino acid residue or through water clusters (**B**, Scheme 4.1). Fitting the data shown in Figure 4.5 to Eq. 4.2 provides pK_a 's of 7.80 ± 0.02 and 7.43 ± 0.01 for the reaction at 5 °C and 25 °C respectively. These data support that $Y_{356}\bullet$ formation is favored more at 25 °C compared to 5 °C and are in accordance with our temperature dependent distribution between the two radical states (Figure 4.3).

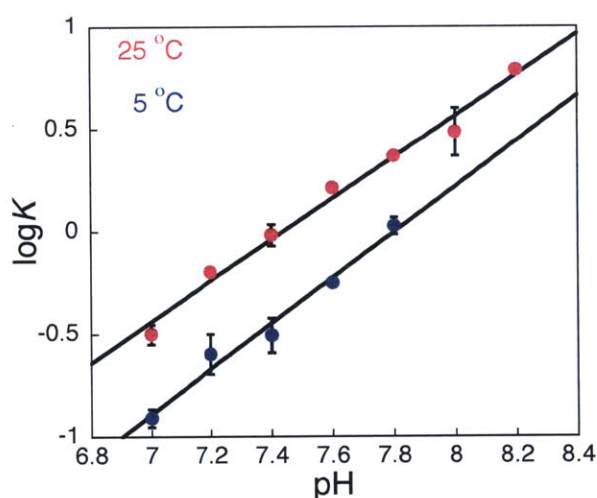


Figure 4.5 The pH dependence of $Y_{356}\bullet$ formation at 5 °C (blue dots) and 25 °C (pink dots). Data points represent the averages of two independent trials. The composite spectra for all trials are shown in Figures 4.4 and A6.4. The observed pH dependence of slope 1 supports that the $Y_{356}\bullet$ proton is in fast exchange with solvent.

4.3.3 Equilibration of $Y_{122}\bullet$ and $F_2Y\bullet$ in the $Y_{356}(3,5)F_2Y$ - $\beta 2$ system. As previously mentioned, equilibration of the tyrosyl radicals has never been observed in wt RNR.¹⁰ The studies with $Y_{122}(2,3,5)F_3Y$ - $\beta 2$ show that the stable radical at 122 ($F_3Y\bullet$) is in equilibrium with $Y_{356}\bullet$. Extrapolation of ΔE° ($F_3Y\bullet$ - $Y_{356}\bullet$) to wt RNR is challenging in many ways, each of which are outlined in the Discussion. Thus, we attempted to detect equilibration of the native $Y_{122}\bullet$ with $Y_{356}\bullet$. For this purpose, we chose to incorporate F_2Y into Y_{356} in $\beta 2$. This amino acid minimally perturbs the reduction potential of Y_{356} (≤ 30 mV as dictated by the pH)^{28,29} and maintains the same activity

as wt RNR at pH 7.6, the standard pH where RNR activity is measured.²³ But most importantly, this construct allows detection of small quantities of $F_2Y\cdot$ ($\geq 5\%$ at the concentrations typically utilized in the EPR experiments) in reaction mixtures containing multiple $Y\cdot$ s.^{9,11} $Y_{356}(3,5)F_2Y\text{-}\beta 2$, $Y_{731}F\text{-}\alpha 2$, CDP and ATP were reacted at pH 8.2, aged for varying periods of time (10, 20 or 40 s), and quenched in liquid isopentane for EPR analysis. The reaction was performed with the RFQ instrument to avoid potential shifting of the equilibrium with slow quenching.²⁴ The other reaction conditions (temperature and pH) were chosen to maximize the amounts of $F_2Y\cdot$ based on the results of our $Y_{122}(2,3,5)F_3Y\text{-}\beta 2$ studies. As seen in Figure 4.3, minimal changes are observed in the amount of $Y_{356}\cdot$ when the temperature is varied between 15 and 37 °C. Thus, we performed the experiment at 25 °C. To determine the optimal pH for the reaction, we considered the differences in the pK_a 's of F_2Y and Y . The pK_a of F_2Y is ~ 3 units lower than Y (solution pK_a 7.2 compared to 10.0)²⁹ and previous studies performed on NO_2Y site-specifically inserted at different positions on pathway have shown that the pK_a at position 356 is perturbed by +0.4 units (i.e 7.6 for F_2Y_{356}). We wanted to perform the $Y_{356}(3,5)F_2Y\text{-}\beta 2/Y_{731}F\text{-}\alpha 2$ reactions under conditions where F_2Y was either mostly protonated or mostly deprotonated. However, as seen in Figure 4.5, rapid proton exchange between Y_{356} and solvent results in lower amounts of $Y_{356}\cdot$ at lower pH values. Due to these reasons, we chose to perform the reaction at pH 8.2, where F_2Y is $\sim 80\%$ deprotonated. At this pH value, $Y_{356}(3,5)F_2Y\text{-}\beta 2$ maintains 60% of its maximum activity.²³

The RFQ-EPR data for the reaction at 10 s, 20 s and 40 s are shown in Figure 4.6A. An expanded view of these spectra (Figure 4.6B) reveals small features on the low- and high-field sides (indicated by the black arrows) that suggested the presence of $F_2Y\cdot$. Due to the extremely low intensities of these features we chose to focus on one sample (20 s) and collected additional EPR spectra for signal averaging. The 20 s sample was subject to 600 total scans using the EPR

parameters described in the methods section and the averaged EPR spectrum is shown in Figure 4.7A. An expanded view of this spectrum (inset) clearly reveals the presence of the wing features that are characteristic of $F_2Y\cdot$.¹¹

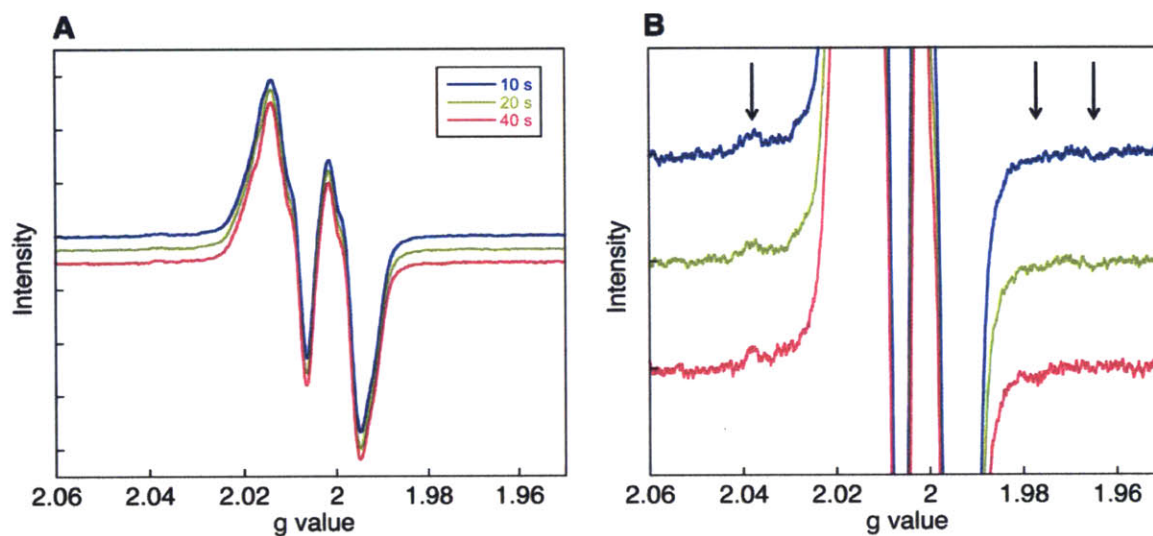


Figure 4.6 Reaction of $Y_{356}(3,5)F_2Y\text{-}\beta 2$, $Y_{731}F\text{-}\alpha 2$, CDP and ATP monitored by RFQ-EPR spectroscopy. A. The composite EPR spectra recorded at the indicated time points. B. An expanded view of the spectra shows wing features (indicated by the black arrows) that are assigned to $F_2Y\cdot$. The 20 s sample was chosen for further data collection. The average of 600 scans of this spectrum is shown in Figure 4.7A. Data were collected with Alexander T. Taguchi.

The well-resolved hyperfine splittings from ^{19}F and $\beta\text{-}^1H$ of $F_2Y_{356}\cdot$ were simulated with the “pepper” module of EasySpin v5.0.18 in Matlab R2015b. These wing features manifest as two symmetrically located pairs of peaks, where only on the high-field side of the spectrum (at $g = 1.98$ and 1.96) is the doublet well-resolved from the intensive $Y_{122}\cdot$ signal (Figure 4.7A, inset). The splitting between these two peaks is due to the $\beta\text{-}^1H$ coupling, whereas the larger inter-doublet splitting is caused by strong hyperfine interactions with the 3- and 5-position fluorines.

The g -values (2.0073, 2.0044, 2.0022) and $\beta\text{-}^1H$ hyperfine tensor (54, 52, 54 MHz) were fixed in the simulations based on previously reported values for $Y_{356}\cdot$ in the reaction of $Y_{122}NO_2Y\text{-}\beta 2$ with $Y_{731}F\text{-}\alpha 2$.¹² From initial simulations it was immediately recognized that the $\beta\text{-}^1H$

hyperfine parameters matched the doublet splitting on the high-field side of the spectrum, thus confirming the identity of this radical species as $F_2Y_{356}\bullet$. The inter-doublet splitting was reproduced with two ^{19}F couplings having an A_{zz} of 147 MHz. The simulation parameters, alongside previous determinations for $F_2Y\bullet$ at positions Y_{122} , Y_{731} and Y_{730} are listed in Table 4.3 with their corresponding spectra shown in Figure 4.7B.

The amount of $F_2Y\bullet$ was approximated from the simulated spectrum by matching the signal intensities of the wing features in the experimental and simulated spectra and comparing the double integral of the two. The greatest source of error in this analysis comes from the intrinsic line broadening factor (17 ± 4 MHz) used in all $F_2Y\bullet$ simulations.¹² The amount of $F_2Y_{356}\bullet$ in the 20 s sample was quantitated as $3 \pm 1\%$ of total spin. This amount of radical reflects an ΔE° ($F_2Y_{356}\bullet$ – $Y_{122}\bullet$) of 70 ± 5 mV.

Table 4.3 Hyperfine values (MHz) for β - ^1H and ^{19}F of $\text{F}_2\text{Y}\cdot$ at different positions on pathway.

Position	Nucleus	A_{xx}	A_{yy}	A_{zz}
$\text{F}_2\text{Y}_{122}\cdot^a$	β - ^1H	52	50	56
	^{19}F	9	16	157
$\text{F}_2\text{Y}_{730}\cdot^{b,c}$	β - ^1H	63	63	63
	^{19}F	-15	-3	151
$\text{F}_2\text{Y}_{731}\cdot^{b,c}$	β - ^1H	40	40	40
	^{19}F	-15	-3	157
$\text{F}_2\text{Y}_{356}\cdot^{b,d}$	β - ^1H	54	52	54
	^{19}F	-15	-3	147

^a Ref. 11.

^b The intrinsic EPR linewidth of 17 MHz was used. The hyperfine values for 2,6- ^1H and one of the two β - ^1H are significantly smaller than the EPR linewidth and were not implemented into the simulations.

^c g values of 2.0063, 2.0044 and 2.0022 were used. The simulation parameters were taken from Ref. 12.

^d g values of 2.0073, 2.0044 and 2.0022 were used.¹² Simulation was performed by Alexander T. Taguchi.

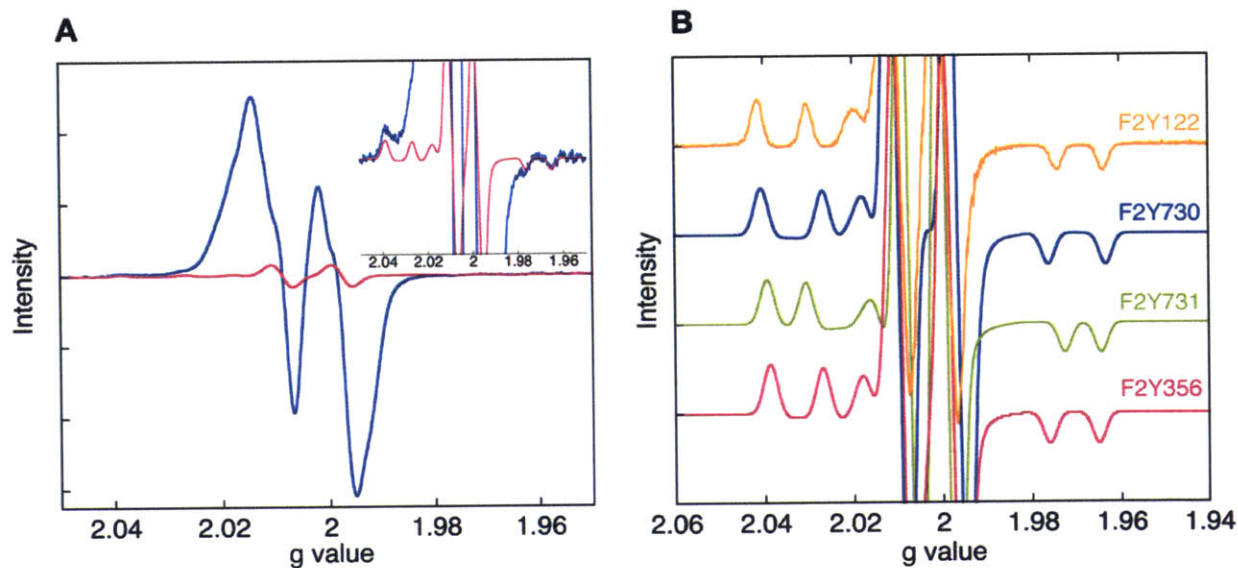


Figure 4.7 A. Reaction of $Y_{356}(3,5)F_2Y\text{-}\beta 2$, $Y_{731}F\text{-}\alpha 2$, CDP and ATP monitored by RFQ-EPR spectroscopy. Overlay of the EPR spectrum of the reaction mixture quenched at 20 s (blue) with the simulated spectrum of $F_2Y_{356}\bullet$ (pink). The inset shows an expanded view of the spectra and highlights the presence of $F_2Y_{356}\bullet$ in the reaction mixture. B. Overlay of the EPR spectra of $F_2Y\bullet$ at different positions on pathway. All spectra were simulated using the parameters shown in the Table 4.3 except $F_2Y_{122}\bullet$, which represents an experimental spectrum. At position 122, a stable $F_2Y_{122}\bullet$ can be self-assembled from apo $F_2Y\text{-}\beta 2$, Fe^{2+} and O_2 .¹¹

4.4 DISCUSSION

RNRs are divided into three classes based on the metallo-cofactor used for thiyl radical formation.⁵ All classes of RNR initiate nucleotide reduction by thiyl radical mediated 3'-H-atom abstraction from the substrate.¹⁵ The reducing equivalents for the reaction are provided by oxidation of a pair of cysteines in the active site,³⁰⁻³² with a subtype of the class III enzyme which uses formate as the reductant as the sole exception.³³ The class II RNR utilizes adenosylcobalamin as a cofactor³ whereas the class III system uses a stable G• to generate the transient C•.³⁴ These observations raise the issue of why and how Nature evolved a 35 Å oxidation process in the class I RNR⁷ instead of a direct H-atom abstraction process that is used by other classes of RNRs. The turnover number for deoxynucleotide formation (2–10 s⁻¹)³⁵ and the large distance between Y₁₂₂• and C₄₃₉• in the class Ia RNR^{7,36} require intermediates in the oxidation process and raises the question of how the thermodynamic and kinetic landscape of this process has evolved to maintain balanced dNTP pools and avoid self-inactivation. Investigation of this oxidation process has proven challenging primarily due to the rate-limiting conformation change(s) that occurs in the α2β2 complex subsequent to S/E binding and prior to RT.³⁵ Furthermore, the substantial overlap in the EPR spectra of the pathway Y•s has precluded insight into the thermodynamic landscape of the RT pathway.

4.4.1 Thermodynamic landscape of the RT pathway within the β2 subunit. Recently we reported the successful assembly of the diferric-NO₂Y• cofactor (t_{1/2} of 40 s at 25 °C) in β2.¹⁴ Unexpectedly, this β2 mutant could overcome the conformational gating typically seen in wt RNR (2–10 s⁻¹),³⁵ and gave us the first opportunity to observe pathway Y• intermediates; the reaction of Y₁₂₂NO₂Y-β2, α2, CDP and ATP rapidly accumulated Y₃₅₆• (100–300 s⁻¹). Surprisingly, generation of Y₃₅₆• was accompanied by reduction of NO₂Y• to the phenolate (NO₂Y⁻). This is in

contrast to our observations with wt RNR, where electron transfer (ET) from Y_{356} to Y_{122}^{\bullet} is accompanied by PT from a water molecule on the diferric cluster (Fe1-H₂O) to Y_{122}^{\bullet} to generate the Y_{122} phenol.²⁶ In the case of $Y_{122}NO_2Y$ - $\beta 2$, subsequent to one turnover and re-oxidation of Y_{356} , the inability of Y_{356}^{\bullet} to re-oxidize NO_2Y^- prevented completion of the catalytic cycle and any subsequent dCDP production. This observation provides the first insight into the relative potentials of Y_{122} and Y_{356} . Our studies with NO_2Y and F_nY ($n = 2, 3$ or 4) incorporated in place of residues Y_{356} , Y_{731} and Y_{730} have shown that turnover is completely abolished when the ΔE° between any of the pathway residues is varied by >200 mV.^{13,37,38} These observations are in excellent agreement with studies conducted on model PCET systems such as azurin, which have demonstrated that uphill ET reactions are feasible, but highly inefficient if the reaction is > 200 mV uphill.³⁹ (and references therein) These results together provide a constraint for ΔE° between the NO_2Y^{\bullet}/NO_2Y^- and $Y_{356}^{\bullet}/Y_{356}$ couples; we predict that this number is ≥ 200 mV.

In addition to providing insight into the thermodynamic landscape within $\beta 2$, the inability of Y_{356}^{\bullet} to re-oxidize NO_2Y^- afforded the first opportunity to investigate equilibration of Y_{356}^{\bullet} with Y_{731}^{\bullet} and Y_{730}^{\bullet} in $\alpha 2$.¹² Due to the substantial overlap in the EPR spectra of the pathway Y^{\bullet} s, two constructs were designed that have provided evidence for equilibration. In one experiment F_2Y was inserted at Y_{731} or Y_{730} and the reaction was probed for the presence of the F_2Y^{\bullet} EPR spectroscopic signature (i.e features in the low- and high-field regions of the spectrum). These experiments showed the presence of 10–15% $F_2Y_{731}^{\bullet}$ (or $F_2Y_{730}^{\bullet}$). Previous pH titration experiments performed with NO_2Y_{731} (or NO_2Y_{730}) have established a pK_a perturbation of ~ 1 unit at these positions compared to the solution pK_a of NO_2Y .¹³ This observation in conjunction with differential pulse voltammetry (DPV) studies performed on the *N*-acetyl 3,5-difluoro-*L*-tyrosinamide²⁹ provides an estimate of 85–95 mV for the reduction potential difference between

$Y_{731}\bullet$ (or $Y_{730}\bullet$) and $Y_{356}\bullet$. This calculation is in excellent agreement with a second experiment where $Y_{122}NO_2Y\bullet\text{-}\beta 2$ was reacted with $[\beta\text{-}^2H_2]Y\text{-}\alpha 2$ and probed for variations in the EPR spectrum. Temperature dependent studies calculated a ΔE° ($[\beta\text{-}^2H_2]Y\bullet\text{-}Y_{356}\bullet$) of ~ 100 mV (Figure 4.1). Taken together these studies show that the RNR protein environment perturbs F_2Y and Y in a similar fashion and that F_2Y is a good probe for the reduction potential of both Y_{731} and Y_{730} .

In Chapter 3, we reported the detailed kinetic analysis of the $Y_{122}(2,3,5)F_3Y\text{-}\beta 2/\alpha 2/CDP/ATP$ reaction.¹⁹ F_3Y is predicted to increase the driving force for RT by 10 mV⁹ based on the solution DPV data,²⁹ and the pK_a perturbation of + 3 units measured for position 122 using NO_2Y .¹³ This calculation assumes that $F_3Y\bullet$ is reduced by PCET, generating the F_3Y phenol; we will return to this assumption subsequently. The reaction of $Y_{122}(2,3,5)F_3Y\text{-}\beta 2/\alpha 2/CDP/ATP$ generates a kinetically and chemically competent $Y_{356}\bullet$ ($20\text{-}30\text{ s}^{-1}$) that in contrast to $Y_{356}\bullet$ generated by $Y_{122}NO_2Y\text{-}\beta 2$ is capable of re-oxidizing F_3Y . In fact, this re-oxidation process is slow and rate-limiting for subsequent dCDP formation. To achieve equilibration of $F_3Y\bullet$ and $Y_{356}\bullet$, we blocked the RT pathway with $Y_{731}F\text{-}\alpha 2$. A single experiment performed with $Y_{730}F$ provided almost identical results to $Y_{731}F\text{-}\alpha 2$ suggesting that removal of a putative H-bonding interaction at the subunit interface does not dramatically perturb the reduction potential of $Y_{356}\bullet$. In fact, previous studies performed with 2,3-difluorotyrosine ($2,3\text{-}F_2Y$) at Y_{356} have shown that even complete removal of the $2,3\text{-}F_2Y_{356}$ proton does not affect turnover,⁴⁰ due to a change in RNR mechanism from PCET to ET at pH values greater than the pK_a of $2,3\text{-}F_2Y$. Our study with $Y_{730}F\text{-}\alpha 2$ taken together with this earlier work on $2,3\text{-}F_2Y$ support that PT is not crucial to PCET at Y_{356} . Herein, we have varied either the temperature or pH to demonstrate equilibration of $F_3Y\bullet$ and $Y_{356}\bullet$. Each of these studies provides unique insight into different aspects of RNR catalysis. The temperature dependent studies provide information about the thermodynamic landscape within the

$\beta 2$ subunit whereas, the pH experiments determine the fate of the Y_{356} proton during PCET across the β/α interface. Each of these results are discussed in turn.

To quantitate the reduction potential increase that occurs upon replacement of Y_{122} with F_3Y , it is important to determine the state of F_3Y (i.e F_3Y phenol or F_3Y^- phenolate) during RT. As shown in Scheme 4.1, we favor the model where F_3Y^- is generated upon RT. In support of this proposal is the observation of NO_2Y^- in the $Y_{122}NO_2Y$ - $\beta 2$ system.¹⁴ The solution pK_a of NO_2Y is 7.1⁴¹ and the visualization of NO_2Y^- can be rationalized if Fe1-H₂O has a pK_a between 8.0 and 10.0. Although ferric iron typically reduces the pK_a of bound water,⁴² diiron clusters have been known to move this value into the physiological pH range ($> \text{pH } 7.0$)⁴³ in a manner highly dependent on protein environment. The diferric cluster environment in the class Ia RNR is unique and has been previously shown to perturb the pK_a of Y_{122} by >3 units.¹³ If the pK_a of Fe1-H₂O is perturbed to >8.0 , initiation of the reaction with F_3Y^\bullet would primarily result in the generation of F_3Y^- . The protonation state of F_3Y is currently unknown, but could be examined by Mössbauer spectroscopy studies similar to those performed on wt RNR, which can establish whether Fe1-H₂O is converted to Fe1-OH during RT in $Y_{122}(2,3,5)F_3Y$ - $\beta 2$.²⁶

The potential difference of ~ 16 mV calculated between F_3Y^\bullet and Y_{356}^\bullet (Figure 4.3) make generation of F_3Y^- an appealing model. We predicted that $\Delta E^\circ (NO_2Y^\bullet/NO_2Y^- - Y_{356}^\bullet/Y_{356})$ is ≥ 200 mV. Taking these two values we can estimate $\Delta E^\circ (NO_2Y^\bullet/NO_2Y^- - F_3Y^\bullet/F_3Y^-)$ as $\geq \sim 184$ mV. This number directly agrees with the predicted potential difference between these two analogs based on the solution DPV data collected on the protected amino acids (~ 180 mV).^{29,41} However, we note that we cannot at present directly extrapolate the potential difference calculated between NO_2Y^\bullet/NO_2Y^- (or F_3Y^\bullet/F_3Y^-) and Y_{356}^\bullet/Y_{356} to Y_{122}^\bullet/Y_{122} . This is primarily due to the unique nature of this position compared to the other pathway Ys. The Y_{122} site is not in equilibrium with

solvent over the time course of our experiments (< 20 s), and its reduction potential is pH independent and directly determined by the dielectric constant of the protein environment. Due to this issue, we turned to an alternate way to monitor equilibration of $Y_{122}\bullet$ and $Y_{356}\bullet$ where the native $Y_{122}\bullet$ remains intact but Y_{356} is replaced with F_2Y .

Our observations with $Y_{122}NO_2Y\text{-}\beta 2$ ¹² and the pH dependent studies reported herein support that $\Delta E^\circ (Y_{122}\bullet/Y_{122}\text{-}Y_{356}\bullet/Y_{356})$ can be easily extrapolated from $\Delta E^\circ (Y_{122}\bullet/Y_{122}\text{-}F_2Y_{356}\bullet/F_2Y_{356}^-)$. The proton from Y_{356} is in rapid exchange with solvent (Figure 4.5) allowing us to predict the exact perturbation of the reduction potential when Y_{356} is replaced with F_2Y . As observed with positions 731 and 730 in the $Y_{122}NO_2Y\text{-}\beta 2$ system,¹² we predict that F_2Y_{356} is a good approximation of Y_{356} and experiences the same reduction potential perturbation as Y_{356} within the RNR environment. The reaction of $Y_{356}(3,5)F_2Y\text{-}\beta 2/Y_{731}F\text{-}\alpha 2/CDP/ATP$ allowed quantitation of $\sim 3\%$ $F_2Y\bullet$ and let us estimate a ΔE° of ~ 70 mV between $F_2Y_{356}\bullet/F_2Y_{356}^-$ and $Y_{122}\bullet/Y_{122}$. At the experimental pH 8.2, the reduction potentials of the $F_2Y_{356}\bullet/F_2Y_{356}^-$ and $Y_{356}\bullet/Y_{356}$ couples are roughly the same.²⁹ At pH 7.6, the standard assay conditions for RNR, the reduction potential of $Y_{356}\bullet$ is expected to increase by ~ 30 mV,²⁹ providing a $\Delta E^\circ (Y_{356}\bullet\text{-}Y_{122}\bullet)$ of ~ 100 mV (Figure 4.8). Recently, Tommos and coworkers have obtained reversible voltammograms for $Y\bullet$ in a three alpha helix protein system (α_3Y), which contains a single redox active Y in a hydrophobic pocket.⁴⁴ Interestingly, square wave voltammetry experiments on α_3Y show that Y is ~ 150 mV more oxidizing in this hydrophobic environment compared to our solution DPV data,²⁹ an observation we have also recently extended to α_3F_2Y (Chapter 2).²⁸ Within the RT pathway in RNR, the polar environment of Y_{356} likely results in a reduction potential similar to that calculated from the solution DPV studies.²⁹ Similar to α_3Y , $Y_{122}\bullet$ in RNR is located in a hydrophobic protein environment. However, in contrast to α_3Y , our calculations support that Y_{122}

is ~100 mV less oxidizing than Y_{356} . These observations suggest the possibility that the diferric cluster could influence the reduction potential of Y_{122} by as much as ~250 mV. Finally, we note that our data taken together propose that at 25 °C and pH 7.6, F_3Y_{122} is ~116 mV more oxidizing than Y_{122} within the RNR protein environment. This difference is 10-fold greater than we had originally predicted.⁹

4.4.2 Relationship between the thermodynamic landscape and kinetics. It is important to note that the equilibration studies described in this work were performed under non-turnover conditions (with $Y_{731}F-\alpha 2$). Thus, a key issue to address is whether the protein environment can alter the thermodynamic landscape to lower ΔE° ($Y_{356}^\bullet - Y_{122}^\bullet$) and facilitate turnover. Although this is a likely possibility, we argue that oxidation of Y_{356} by Y_{122}^\bullet must be uphill even under turnover conditions. Evidence for this conclusion is provided by our combined studies with wt RNR,³⁵ $Y_{122}(2,3,5)F_3Y-\beta 2$ ¹⁹ and $Y_{122}NO_2Y-\beta 2$.¹⁴

In the case of wt RNR, investigation of RT has been hindered by the inability to monitor Y_{122}^\bullet disappearance and reappearance during turnover.³⁵ To account for this observation, we have previously modeled that the reverse RT process in wt RNR by which Y_{356}^\bullet re-oxidizes Y_{122} must be downhill and rapid (10^3 s^{-1}).³⁵ In the case of $Y_{122}(2,3,5)F_3Y-\beta 2$ we have monitored formation of Y_{356}^\bullet and demonstrated that re-oxidation of F_3Y by Y_{356}^\bullet is slow (0.4 s^{-1}) and rate-limiting for multiple turnovers.¹⁹ Finally, in the $Y_{122}NO_2Y-\beta 2$ system, Y_{356}^\bullet accumulates due to the inability of this pathway radical to re-oxidize NO_2Y^- subsequent to the first turnover.¹⁴ Taken together these studies suggest that Y_{356}^\bullet can be observed during turnover only when reverse RT is slowed down ($Y_{122}(2,3,5)F_3Y-\beta 2$) or completely inhibited ($Y_{122}NO_2Y-\beta 2$) and as a direct result of the potential difference between Y_{122} and Y_{356} . DPV studies have estimated that reduction potential increases in the order $Y < F_3Y < NO_2Y$ ^{29,41} supporting that the reduction potential at Y_{122} must be increased

in order to accumulate Y_{356}^{\bullet} and reinforcing our model that oxidation of Y_{356} by Y_{122}^{\bullet} is uphill. We have previously proposed that the conformational change that triggers RT targets the initial PT step from Fe1-H₂O to Y_{122}^{\bullet} .²⁶ Uncoupled PT and ET in $Y_{122}NO_2Y-\beta 2$ and potentially, $Y_{122}(2,3,5)F_3Y-\beta 2$ suggest that we may have at least partially overcome this conformational gating and obtained direct insight into the thermodynamic effect of replacing Y_{122} with these unnatural analogs. Further support for this model is obtained when the forward RT rate constants in $Y_{122}NO_2Y-\beta 2$ and $Y_{122}(2,3,5)F_3Y-\beta 2$ are analyzed using the Moser-Dutton equation⁴⁵ (Eq. 4.3) for dependence of k_{ET} on distance (R) and driving force (ΔG).

$$\log k_{ET} = 15 - 0.6R - 3.1(\Delta G + \lambda)^2/\lambda \quad (4.3)$$

Assuming identical distances and reorganizational energies (λ) for ET in $Y_{122}NO_2Y-\beta 2$ and $Y_{122}(2,3,5)F_3Y-\beta 2$, the individual expressions for $\log k_{ET}$ can be combined to assess the effect of the driving force differences (ΔG , 200 mV vs 16 mV, Figure 4.3) on k_{ET} . The net equation requires estimation of λ ; by varying the reorganizational energy from 0.7 to 1.4 eV,⁴⁶ k_{ET} in $Y_{122}NO_2Y-\beta 2$ was calculated as 9–11-fold faster than k_{ET} in $Y_{122}(2,3,5)F_3Y-\beta 2$. This approximation is in direct agreement with our experimental data (5–15-fold) supporting that the driving force dictates the kinetics in these mutant RNRs and that both NO_2Y^{\bullet} and F_3Y^{\bullet} are reduced to the corresponding phenolates during RT.

Based on our static thermodynamic picture constructed from the studies with $Y_{122}NO_2Y-\beta 2$ and those reported herein, we propose that the landscape from Y_{122} to Y_{730} is ~200 mV uphill (at 25 °C and pH 7.6, Figure 4.8). Electrochemical measurements on glutathione and Y have revealed that C and Y have similar midpoint potentials at pH 7.0⁴⁷ estimating formation of ~0.04% C_{439}^{\bullet} in the $\alpha 2\beta 2$ complex. Given the predicted rate constant for H₂O loss from the 2' position (10^6-10^8 s^{-1})¹⁶⁻¹⁸ of the nucleotide, the rate of this reaction in the presence of 0.04% C_{439}^{\bullet} would

be $\sim 10^2$ – 10^4 -fold faster than conformationally gated nucleotide reduction (2 – 10 s $^{-1}$).³⁵ The calculation shown here is based on a scenario where the reaction landscape is isoenergetic subsequent to generation of Y₇₃₁•. However, DFT calculations performed on the individual crystal structure of $\alpha 2$ and on model systems have provided an estimate of ~ 120 mV for ΔE° (C₄₃₉•–Y₇₃₀•)^{48,49} and ~ 90 – 260 mV for 3' H-atom abstraction by C₄₃₉•.^{5, 50-52} If the measured ΔE° (Y₇₃₀•–Y₁₂₂•) of 200 mV is reflective of the thermodynamic landscape under turnover conditions, then we estimate that the combined steps of C₄₃₉ oxidation and 3' H-atom abstraction must be < 200 mV uphill to maintain a turnover number of > 10 s $^{-1}$. This is in accordance with previous calculations by Dutton, which suggested that the reaction landscape can be up to 450 mV uphill and still support turnover.⁵³ The DFT calculations performed on RNR primarily use the crystal structure of $\alpha 2$ due to the lack of structural information for the $\alpha 2\beta 2$ complex. It is possible that the RT pathway and the active site of $\alpha 2$ will be conformationally altered in the complex. Furthermore, Dutton has demonstrated that uphill reactions can be partially compensated for by decreasing the ET distance.⁴⁶ The distances between Y₁₂₂, Y₃₅₆ and Y₇₃₁ remain unknown as the C-terminal tail of $\beta 2$, which contains Y₃₅₆, is structurally disordered in all crystal structures. A structure of the active complex is thus, crucial to completing the overall landscape of the reaction and assessing the contribution of each PCET step to overall turnover of the enzyme. Nonetheless, it is apparent from the combined studies discussed herein that the overall reaction (Y₁₂₂• to abstraction of the H-atom) is uphill but driven forward by rapid, irreversible loss of H₂O from the 2' position of the substrate (10^6 – 10^8 s $^{-1}$, Figure 4.8).¹⁶⁻¹⁸

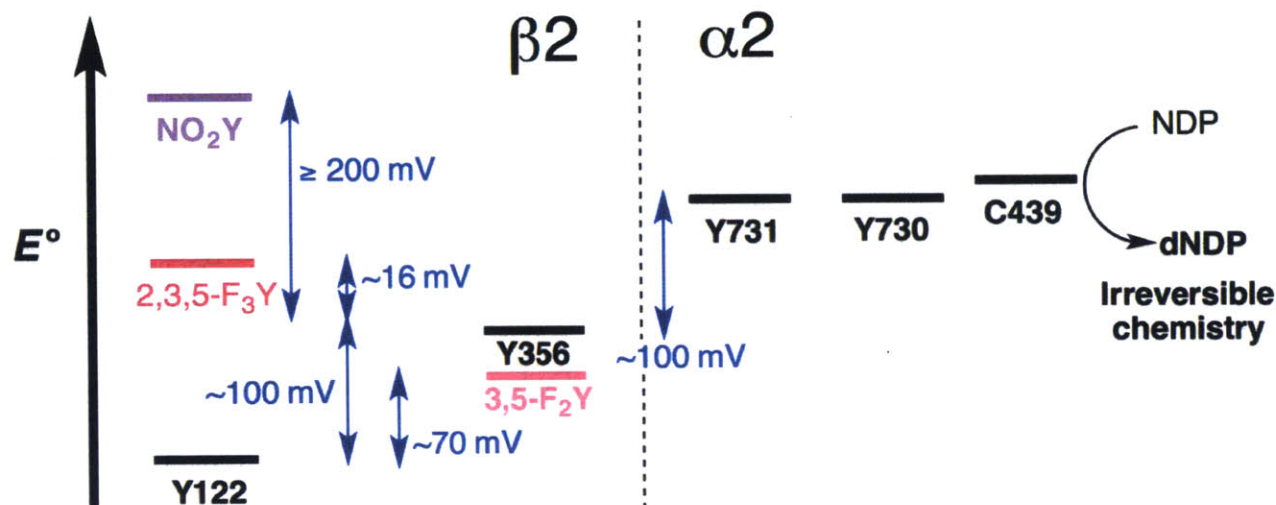


Figure 4.8 Current thermodynamic landscape of the RT pathway at 25 °C and pH 7.6. Studies performed on Y₁₂₂(2,3,5)F₃Y-β2 and Y₃₅₆(3,5)F₂Y-β2 described in this work provided an estimate of the relative reduction potentials of Y₁₂₂ and Y₃₅₆. W₄₈ has been removed from the landscape for the sake of clarity.

4.4.3 *Equilibration of F₃Y• and Y₃₅₆• as a function of pH: PCET across the β/α interface involves fast proton exchange between Y₃₅₆ and solvent.* Thus far, we have discussed the equilibration of Y₁₂₂• and Y₃₅₆• as a function of temperature and provided insight into thermodynamics of the RT pathway. Alternatively, the equilibrium between F₃Y₁₂₂• and Y₃₅₆• can be perturbed by pH affording information about the fate of the Y₃₅₆ proton upon oxidation of this pathway Y. The log([Y₃₅₆•]/[F₃Y•]) data reported in Figure 4.5 are directly proportional to the pH of the reaction mixture with a slope of 1. These data can be interpreted to report on rapid exchange of the Y₃₅₆ proton with solvent, with either an amino acid residue or water functioning as the initial proton acceptor. Below, we outline current evidence that provides insight into the identity of this proton acceptor.

Whereas we do not have any structural information for the β/α interface, the number of conserved amino acid residues in the class Ia RNRs are few and are typically limited to the cluster site, the nucleotide reduction site and the RT pathway.^{8,54} This lack of sequence consensus in the class Ia RNRs leaves very few residues that can function as a proton acceptor for Y₃₅₆. The

proposed candidate has been E₃₅₀, located on the flexible C-terminal tail of β 2 and conserved in all class Ia sequences. The observation that mutation of this residue to A abolishes RNR activity²⁷ led Climent et al to propose that this residue participates in PT during radical propagation.²⁷ More recently, we have utilized our ability to incorporate unnatural Y analogs to RNR to show that E₃₅₀ may not be the proton acceptor for Y₃₅₆, but that the essentiality of this residue to RNR stems from its involvement in the protein conformational gate and subunit interaction (Chapter 5).²³ Thus far, no other amino acid candidate is readily apparent, which can function as a proton acceptor for Y₃₅₆.

To assess the environment of Y•s on pathway and identify putative proton acceptors, we have recently performed electron-nuclear double resonance (ENDOR) spectroscopy on mutant RNRs containing the radical trap, 3-aminotyrosine (NH₂Y) in place of either Y₃₅₆ or Y₇₃₁, leading to accumulation of NH₂Y₃₅₆• or NH₂Y₇₃₁•.^{20,55} These studies revealed that the electrostatic environment of NH₂Y₃₅₆• is perturbed more than NH₂Y₇₃₁•, although no strong or moderate hydrogen bonding interactions were detected.⁵⁵ We proposed that the altered electrostatic environment of NH₂Y₃₅₆• could be explained by the presence of water clusters at the interface.⁵⁵

The simulated EPR spectrum of F₂Y₃₅₆• (Figure 4.7A) provides further insight into the environment of Y₃₅₆. We have resolved the 3,5-¹⁹F couplings at this position, providing a complete picture of the average A_{zz} values for F₂Y• at all positions on pathway (Y₁₂₂,¹¹ Y₃₅₆, Y₇₃₁¹² and Y₇₃₀¹²) for the first time (Table 4.3). The ¹⁹F hyperfine interaction provides a useful probe of the electron spin density distribution, and is especially important information to obtain for Y₃₅₆ for which no crystallographic structural information is available. Compared with the other pathway F₂Y•s, the 3,5-¹⁹F splitting for Y₃₅₆ is somewhat weaker (Table 4.3), trending towards the situation for F₂Y• in solvent (~70 MHz).²⁹ This observation supports our finding that the Y₃₅₆ proton is in rapid exchange with the solvent, as well as our inability to resolve any defined hydrogen bonds

with $\text{NH}_2\text{Y}_{356}\bullet$ using high-frequency ENDOR spectroscopy.⁵⁵ The results as a whole suggest a weaker/more dynamic hydrogen bond network for $\text{Y}_{356}\bullet$ compared with the other pathway $\text{Y}\bullet$ s, possibly as a result of greater solvent accessibility. The experiments presented herein, the E_{350} studies described in Chapter 5,²³ and the ENDOR results⁵⁵ together make fast proton exchange between Y_{356} and solvent via water an appealing model for PCET across the interface although, we currently cannot rule out an amino acid residue as the initial proton acceptor.

4.4.4 Conclusions. Efforts to detect equilibration of the pathway $\text{Y}\bullet$ s in wt RNR have proven unsuccessful.¹⁰ These results can be reconciled by the large potential difference between $\text{Y}_{122}\bullet$ and $\text{Y}_{356}\bullet$ (~ 100 mV) or $\text{Y}_{731}\bullet/\text{Y}_{730}\bullet$ (~ 200 mV), which would result in accumulation of $< 2\%$ of $\text{Y}_{356}\bullet$ and $< 0.04\%$ of $\text{Y}_{731}\bullet$ or $\text{Y}_{730}\bullet$. The spectral overlap of $\text{Y}\bullet$ s prevents detection of these low amounts in wt RNR by standard EPR methods. We have shown for the first time, equilibration of $\text{Y}_{122}\bullet$ and $\text{Y}_{356}\bullet$ with the use of F_3Y in place of Y_{122} or F_2Y in place of Y_{356} . These studies confirm that Y_{122} is solvent inaccessible and is the thermodynamic minimum on the RT pathway. We have additionally utilized this equilibration to provide insight into the environment of $\text{Y}_{356}\bullet$ and showed that the Y_{356} proton is transferred to solvent upon oxidation of this pathway Y . These studies also highlight the utility of $\text{F}_n\text{Y}\bullet$ s in detecting small quantities of a $\text{Y}\bullet$ in reaction mixtures containing multiple radical species.

4.5 REFERENCES

1. Thelander, L. Physicochemical characterization of ribonucleoside diphosphate reductase from *Escherichia coli*, *J. Biol. Chem.* **1973**, *248*, 4591-4601.
2. Brown, N. C.; Reichard, P. Ribonucleoside diphosphate reductase: Formation of active and inactive complexes of proteins B1 and B2, *J. Mol. Biol.* **1969**, *46*, 25-38.
3. Licht, S.; Gerfen, G. J.; Stubbe, J. Thiyl radicals in ribonucleotide reductases, *Science* **1996**, *271*, 477-481.
4. Jordan, A.; Reichard, P. Ribonucleotide reductases, *Annu. Rev. Biochem.* **1998**, *67*, 71-98.
5. Stubbe, J.; van der Donk, W. A. Protein radicals in enzyme catalysis, *Chem. Rev.* **1998**, *98*, 705-762.
6. Nordlund, P.; Reichard, P. Ribonucleotide reductases, *Annu. Rev. Biochem.* **2006**, *75*, 681-706.
7. Uhlin, U.; Eklund, H. Structure of ribonucleotide reductase protein R1, *Nature* **1994**, *370*, 533-539.
8. Stubbe, J.; Nocera, D. G.; Yee, C. S.; Chang, M. C. Y. Radical initiation in the class I ribonucleotide reductase: long-range proton-coupled electron transfer?, *Chem. Rev.* **2003**, *103*, 2167-2201.
9. Minnihan, E. C.; Nocera, D. G.; Stubbe, J. Reversible, long-range radical transfer in *E. coli* class Ia ribonucleotide reductase, *Acc. Chem. Res.* **2013**, *46*, 2524-2535.
10. Ekberg, M.; Sahlin, M.; Eriksson, M.; Sjöberg, B. M. Two conserved tyrosine residues in protein R1 participate in an intermolecular electron transfer in ribonucleotide reductase, *J. Biol. Chem.* **1996**, *271*, 20655-20659.
11. Minnihan, E. C.; Young, D. D.; Schultz, P. G.; Stubbe, J. Incorporation of fluorotyrosines into ribonucleotide reductase using an evolved, polyspecific aminoacyl-tRNA synthetase, *J. Am. Chem. Soc.* **2011**, *133*, 15942-15945.
12. Yokoyama, K.; Smith, A. A.; Corzilius, B.; Griffin, R. G.; Stubbe, J. Equilibration of tyrosyl radicals (Y₃₅₆[•], Y₇₃₁[•], Y₇₃₀[•]) in the radical propagation pathway of the *Escherichia coli* class Ia ribonucleotide reductase, *J. Am. Chem. Soc.* **2011**, *133*, 18420-18432.
13. Yokoyama, K.; Uhlin, U.; Stubbe, J. Site-specific incorporation of 3-nitrotyrosine as a probe of pK_a perturbation of redox-active tyrosines in ribonucleotide reductase, *J. Am. Chem. Soc.* **2010**, *132*, 8385-8397.
14. Yokoyama, K.; Uhlin, U.; Stubbe, J. A hot oxidant, 3-NO₂Y₁₂₂ radical, unmasks conformational gating in ribonucleotide reductase, *J. Am. Chem. Soc.* **2010**, *132*, 15368-15379.
15. Licht, S.; Stubbe, J. Mechanistic investigations of ribonucleotide reductases, *Compr. Nat. Prod. Chem.* **1999**, *5*, 163-203.
16. Steenken, S.; Davies, M. J.; Gilbert, B. C. Pulse radiolysis and electron spin resonance studies of the dehydration of radicals from 1,2-diols and related compounds, *J Chem Soc Perkin Trans.* **1986**, *2*, 1003-1010.

17. Bansal, K. M.; Gratzel, M.; Henglein, A.; Janata, E. Polarographic and optical absorption studies of radicals produced in the pulse radiolysis of aqueous solutions of ethylene glycol, *J. Phys. Chem.* **1973**, *77*, 16-19.
18. Lenz, R.; Giese, B. Studies on the mechanism of ribonucleotide reductases, *J. Am. Chem. Soc.* **1997**, *119*, 2784-2794.
19. Ravichandran, K. R.; Minnihhan, E. C.; Wei, Y.; Nocera, D. G.; Stubbe, J. Reverse electron transfer completes the catalytic cycle in a 2,3,5-trifluorotyrosine-substituted ribonucleotide reductase, *J. Am. Chem. Soc.* **2015**, *137*, 14387-14395.
20. Minnihhan, E. C.; Seyedsayamdost, M. R.; Uhlin, U.; Stubbe, J. Kinetics of radical intermediate formation and deoxynucleotide production in 3-aminotyrosine-substituted *Escherichia coli* ribonucleotide reductases, *J. Am. Chem. Soc.* **2011**, *133*, 9430-9440.
21. Chen, H.; Gollnick, P.; Phillips, R. S. Site-directed mutagenesis of His343-->Ala in *Citrobacter freundii* tyrosine phenol-lyase. Effects on the kinetic mechanism and rate-determining step, *Eur. J. Biochem.* **1995**, *229*, 540-549.
22. Seyedsayamdost, M. R.; Yee, C. S.; Stubbe, J. Site-specific incorporation of fluorotyrosines into the R2 subunit of *E. coli* ribonucleotide reductase by expressed protein ligation, *Nat. Protoc.* **2007**, *2*, 1225-1235.
23. Minnihhan, E. C. Mechanistic studies of proton-coupled electron transfer in aminotyrosine- and fluorotyrosine-substituted class Ia ribonucleotide reductase. Ph.D. Thesis, Massachusetts Institute of Technology, **2012**.
24. Orme-Johnson, W. H.; Beinert, H.; Blakley, R. L. Cobamides and ribonucleotide reduction. XII. The electron paramagnetic resonance spectrum of "active coenzyme B12", *J. Biol. Chem.* **1974**, *249*, 2338-2343.
25. von Döbeln, U.; Reichard, P. Binding of substrates to *Escherichia coli* ribonucleotide reductase, *J. Biol. Chem.* **1976**, *251*, 3616-3622.
26. Wörsdorfer, B.; Conner, D. A.; Yokoyama, K.; Livada, J.; Seyedsayamdost, M. R.; Jiang, W.; Silakov, A.; Stubbe, J.; Bollinger, J. M., Jr.; Krebs, C. Function of the diiron cluster of *Escherichia coli* class Ia ribonucleotide reductase in proton-coupled electron transfer, *J. Am. Chem. Soc.* **2013**, *135*, 8585-8593.
27. Climent, I.; Sjöberg, B. M.; Huang, C. Y. Site-directed mutagenesis and deletion of the carboxyl terminus of *Escherichia coli* ribonucleotide reductase protein R2 - effects on catalytic activity and subunit interaction, *Biochemistry* **1992**, *31*, 4801-4807.
28. Ravichandran, K. R.; Liang, L.; Stubbe, J.; Tommos, C. Formal reduction potential of 3,5-difluorotyrosine in a structured protein: insight into multistep radical transfer, *Biochemistry* **2013**, *52*, 8907-8915.
29. Seyedsayamdost, M. R.; Reece, S. Y.; Nocera, D. G.; Stubbe, J. Mono-, di-, tri-, and tetra-substituted fluorotyrosines: new probes for enzymes that use tyrosyl radicals in catalysis, *J. Am. Chem. Soc.* **2006**, *128*, 1569-1579.
30. Mao, S. S.; Holler, T. P.; Yu, G. X.; Bollinger, J. M., Jr.; Booker, S.; Johnston, M. I.; Stubbe, J. A model for the role of multiple cysteine residues involved in ribonucleotide reduction: amazing and still confusing, *Biochemistry* **1992**, *31*, 9733-9743.

31. Booker, S.; Licht, S.; Broderick, J.; Stubbe, J. Coenzyme B12-dependent ribonucleotide reductase: evidence for the participation of five cysteine residues in ribonucleotide reduction, *Biochemistry* **1994**, *33*, 12676-12685.
32. Wei, Y.; Funk, M. A.; Rosado, L. A.; Baek, J.; Drennan, C. L.; Stubbe, J. The class III ribonucleotide reductase from *Neisseria bacilliformis* can utilize thioredoxin as a reductant, *Proc. Natl. Acad. Sci. U. S. A.* **2014**, *111*, E3756-3765.
33. Wei, Y.; Mathies, G.; Yokoyama, K.; Chen, J.; Griffin, R. G.; Stubbe, J. A chemically competent thiosulfuranyl radical on the *Escherichia coli* class III ribonucleotide reductase, *J. Am. Chem. Soc.* **2014**, *136*, 9001-9013.
34. Mulliez, E.; Fontecave, M.; Gaillard, J.; Reichard, P. An iron-sulfur center and a free radical in the active anaerobic ribonucleotide reductase of *Escherichia coli*, *J. Biol. Chem.* **1993**, *268*, 2296-2299.
35. Ge, J.; Yu, G.; Ator, M. A.; Stubbe, J. Pre-steady-state and steady-state kinetic analysis of *E. coli* class I ribonucleotide reductase, *Biochemistry* **2003**, *42*, 10071-10083.
36. Bennati, M.; Robblee, J. H.; Mugnaini, V.; Stubbe, J.; Freed, J. H.; Borbat, P. EPR distance measurements support a model for long-range radical initiation in *E. coli* ribonucleotide reductase, *J. Am. Chem. Soc.* **2005**, *127*, 15014-15015.
37. Seyedsayamdost, M. R.; Stubbe, J. Site-specific replacement of Y₃₅₆ with 3,4-dihydroxyphenylalanine in the β 2 subunit of *E. coli* ribonucleotide reductase, *J. Am. Chem. Soc.* **2006**, *128*, 2522-2523.
38. Seyedsayamdost, M. R.; Yee, C. S.; Reece, S. Y.; Nocera, D. G.; Stubbe, J. pH rate profiles of F_nY₃₅₆-R2s (n = 2, 3, 4) in *Escherichia coli* ribonucleotide reductase: evidence that Y₃₅₆ is a redox-active amino acid along the radical propagation pathway, *J. Am. Chem. Soc.* **2006**, *128*, 1562-1568.
39. Warren, J. J.; Ener, M. E.; Vicek, A.; Winkler, J. R.; Gray, H. B. Electron hopping through proteins, *Coord. Chem. Rev.* **2012**, *256*, 2478-2487.
40. Yee, C. S.; Chang, M. C. Y.; Ge, J.; Nocera, D. G.; Stubbe, J. 2,3-difluorotyrosine at position 356 of ribonucleotide reductase R2: A probe of long-range proton-coupled electron transfer, *J. Am. Chem. Soc.* **2003**, *125*, 10506-10507.
41. Yee, C. S.; Seyedsayamdost, M. R.; Chang, M. C. Y.; Nocera, D. G.; Stubbe, J. Generation of the R2 subunit of ribonucleotide reductase by intein chemistry: insertion of 3-nitrotyrosine at residue 356 as a probe of the radical initiation process, *Biochemistry* **2003**, *42*, 14541-14552.
42. Holm, R. H.; Kennepohl, P.; Solomon, E. I. Structural and functional aspects of metal sites in biology, *Chem. Rev.* **1996**, *96*, 2239-2314.
43. Tinberg, C. E.; Lippard, S. J. Revising the mechanism of dioxygen activation in soluble methane monooxygenase from *M. capsulatus* (Bath): Evidence for a multi-step proton-dependent reaction pathway, *Biochemistry* **2009**, *48*, 12145-12158.
44. Berry, B. W.; Martínez-Rivera, M. C.; Tommos, C. Reversible voltammograms and a Pourbaix diagram for a protein tyrosine radical, *Proc. Natl. Acad. Sci. U. S. A.* **2012**, *109*, 9739-9743.

45. Moser, C. C.; Dutton, P. L. Engineering protein structure for electron transfer function in photosynthetic reaction centers, *Biochim. Biophys. Acta.* **1992**, *1101*, 171-176.
46. Moser, C. C.; Anderson, J. L. R.; Dutton, P. L. Guidelines for tunneling in enzymes, *Biochim. Biophys. Acta.* **2010**, *1797*, 1573-1586.
47. Madej, E.; Wardman, P. The oxidizing power of the glutathione thiyl radical as measured by its electrode potential at physiological pH, *Arch. Biochem. Biophys.* **2007**, *462*, 94-102.
48. Siegbahn, P. E.; Eriksson, L. A.; Himo, F.; Pavlov, M. Hydrogen atom transfer in ribonucleotide reductase (RNR), *J. Phys. Chem. B.* **1998**, *102*, 10622-10629.
49. Argirević, T.; Riplinger, C.; Stubbe, J.; Neese, F.; Bennati, M. ENDOR spectroscopy and DFT calculations: evidence for the hydrogen-bond network within $\alpha 2$ in the PCET of *E. coli* ribonucleotide reductase, *J. Am. Chem. Soc.* **2012**, *134*, 17661-17670.
50. Zipse, H. The influence of hydrogen bonding interactions on the C-H bond activation step in class I ribonucleotide reductase, *Org. Biomol. Chem.* **2003**, *1*, 692-699.
51. Pelmeshnikov, V.; Cho, K.; Siegbahn, P. E. Class I ribonucleotide reductase revisited: The effect of removing a proton on Glu441, *J. Comput. Chem.* **2003**, *25*, 311-321.
52. Bennati, M.; Lenzian, F. M. S.; Zipse, H. Spectroscopic and theoretical approaches for studying radical reactions in class I ribonucleotide reductase, *Biol. Chem.* **2005**, *386*, 1007-1022.
53. Page, C. C.; Moser, C. C.; Chen, X.; Dutton, P. L. Natural engineering principles of electron tunnelling in biological oxidation-reduction, *Nature* **1999**, *402*, 47-52.
54. Nilsson, O.; Lundqvist, T.; Hahne, S.; Sjöberg, B. M. Structure-function studies of the large subunit of ribonucleotide reductase from *Escherichia coli*, *Biochem. Soc. Trans.* **1988**, *16*, 91-94.
55. Nick, T.; Lee, W.; Kossmann, S.; Neese, F.; Stubbe, J.; Bennati, M. Hydrogen bond network between amino acid radical intermediates on the proton-coupled electron transfer pathway of *E. coli* $\alpha 2$ ribonucleotide reductase, *J. Am. Chem. Soc.* **2015**, *137*, 289-298.

Chapter 5

A structural role for E₃₅₀ in RNR function

5.1 INTRODUCTION

RNR utilizes one stable and three transient Y•s to convert all four nucleotides into their corresponding 2'-deoxynucleotides as dictated by the allosteric effectors.^{1,2} Oxidation of each Y on pathway requires the concerted loss of a proton and an electron, a process referred to as proton-coupled electron transfer (PCET). In Chapter 4, we showed that PCET across the β/α interface involves rapid proton exchange between Y₃₅₆ and solvent (Figure 4.5, section 4.3.2). However, we could not confirm if the initial proton acceptor during Y₃₅₆ oxidation is an amino acid residue in RNR or water. Similarly, the identity of the proton acceptor during oxidation of Y₇₃₁ has not yet been identified. In this Chapter, we describe our efforts to determine whether E₃₅₀, a conserved residue on the C-terminal tail of $\beta 2$, can function as the proton acceptor for either Y₃₅₆ or Y₇₃₁ during oxidation of these pathway Ys.

Whereas the individual subunits of the *E. coli* class Ia RNR ($\alpha 2$ and $\beta 2$) have been crystallized,^{3,4} no structural information is currently available for the subunit interface. In all $\beta 2$ structures to date, only residues 1–340 are well defined, whereas residues 341–375 are structurally disordered.⁴⁻⁶ Potential insight about the location of residues 360–375 has been provided by crystallization of $\alpha 2$ with a peptide corresponding to these residues of $\beta 2$.³ Subunit affinity is largely governed by the C-terminal tail of $\beta 2$,⁷ and these crystallization conditions allowed observation of the interaction between residues 360–375 and $\alpha 2$. However, structural information is still missing for residues 340–360 of $\beta 2$, the region in which Y₃₅₆ is located.

To look for potential candidates that can function as a proton acceptor, we and others have performed sequence alignments of NrdA ($\alpha 2$) and NrdB ($\beta 2$) from different class Ia RNRs. In the case of $\alpha 2$, the conserved residues are limited to the $\alpha 2$ active site, the pathway Ys and the C-terminal cysteines that are involved in re-reduction. Although not conserved in sequence, an E or

a D is always present in a flexible loop region (residues 321–331, *E. coli* numbering) that is located close to the β/α interface. It is possible that this residue participates in proton transfer (PT), but there is not yet evidence of its importance to RNR function.

In the case of $\beta 2$, the conserved residues are mostly limited to the diferric cluster site and Y₁₂₂, W₄₈ and Y₃₅₆. Focusing on the C-terminal tail of $\beta 2$, Y₃₅₆ and E₃₅₀ are the only absolutely conserved amino acids within this disordered region. Thus, early studies by Sjöberg and coworkers addressed the role of E₃₅₀ by site-directed mutagenesis of this residue to A.⁸ Standard RNR assays showed that E₃₅₀A- $\beta 2$ maintained only 0.5% of wt RNR activity, an amount that can be ascribed to low levels of contaminating endogenous RNR that co-purifies with all mutants of this enzyme^{vi,9}. The authors of this initial work also showed that E₃₅₀A- $\beta 2$ was capable of assembling the diferric-Y• cofactor and had a subunit dissociation constant of 0.5 μ M compared to 0.2 μ M for wt- $\beta 2$. More recently, E₃₅₀X- $\beta 2$ (X = A, D, Q) have been prepared and characterized in our lab to assess their effects on cofactor assembly and enzyme activity.¹⁰ The results of these experiments are summarized in Table 5.1. All three constructs can self-assemble the diferric-Y• cofactor (0.7–1.1 Y•/ $\beta 2$ compared to 1.2 Y•/ $\beta 2$ for wt¹¹) but possess only 0.1–0.3% of the wt activity. These site-directed mutagenesis studies affirm the essentiality of E₃₅₀ for RNR function and support the original proposal of Sjöberg and coworkers that this residue participates in the radical propagation pathway. Based on these results, it was suggested that E₃₅₀ might function as the proton acceptor for Y₃₅₆ during its oxidation.^{1,8}

^{vi} Sjöberg and coworkers performed an additional experiment where E₃₅₀A- $\beta 2$ was reacted with the inhibitor, N₃CDP. In the case of wt RNR, this reaction results in loss of Y₁₂₂• concomitant with formation of an active site radical (N•) within 1 min. In the case of E₃₅₀A- $\beta 2$, no N• was observed but slow loss of Y₁₂₂• was observed over 6 h. This led the authors to conclude that E₃₅₀A- $\beta 2$ is active. We are currently reproducing these studies in our lab to assess if E₃₅₀A- $\beta 2$ is active or if the results report on instability of Y₁₂₂• in this mutant RNR.

Table 5.1 Specific activities of E₃₅₀X-β2 as determined by the radioactive assay for RNR.

Sample	Specific activity ^a (nmol/min/mg)	Y•/β2	Specific activity scaled (nmol/min/mg)	% wild type activity
wt-β2	7000	1.2	na	na
E ₃₅₀ A-β2	3	0.7	5	0.07
E ₃₅₀ D-β2	18	1.1	20	0.29
E ₃₅₀ Q-β2	6	1.1	7	0.1

^aSpecific activities were measured by Ellen C. Minnihhan.¹⁰

Whereas site-directed mutagenesis could establish the importance of E₃₅₀ to the *E. coli* class Ia RNR, it could not implicate PT as the affected step during turnover. Our ability to site-specifically incorporate unnatural Y analogs into RNR^{10,12-14} afforded us the opportunity to ascertain the role of E₃₅₀ in RNR function. In one set of experiments, 3-aminotyrosine (NH₂Y) was inserted in the place of Y₃₅₆ and the reaction of the double mutant E₃₅₀A/Y₃₅₆NH₂Y-β2 with α₂, CDP and ATP was investigated by SF vis and EPR spectroscopic methods (Minnihan, Stubbe unpublished results). NH₂Y lowers the reduction potential of Y while minimally perturbing its pK_a.¹⁵ This analog acts as a radical trap and previous studies with the single mutant Y₃₅₆NH₂Y-β2 have shown accumulation of 30–40% NH₂Y₃₅₆• (biphasic kinetics, 30 s⁻¹ and 2 s⁻¹ for the two phases, respectively) when this enzyme is reacted with α₂, CDP and ATP.¹² Thus, it was hypothesized that if E₃₅₀ functions as the proton acceptor for Y₃₅₆, then mutation of this residue should result in failure to generate NH₂Y₃₅₆•. Figure 5.1A shows analysis of this reaction by EPR spectroscopy. For comparison, EPR analysis of the Y₃₅₆NH₂Y-β2/α₂/CDP/ATP reaction is shown in Figure 5.1B. The EPR spectrum of the E₃₅₀A/Y₃₅₆NH₂Y-β2 reaction looks almost identical to the spectrum of Y₁₂₂•; subtraction of Y₁₂₂• (blue, Figure 5.1A) from the spectrum of a reaction mixture quenched at 30 s (pink, Figure 5.1A) shows no features characteristic of NH₂Y₃₅₆• (Figure 5.1B, black).¹² SF analysis of the E₃₅₀A/Y₃₅₆NH₂Y-β2/α₂/CDP/ATP reaction showed no loss of Y₁₂₂• (410 nm, blue, Figure 5.1C) and no formation of NH₂Y₃₅₆• (324 nm, pink, Figure 5.1C).

These results support the importance of E₃₅₀ in NH₂Y₃₅₆ oxidation. However, similar to the mutagenesis experiments, these studies could not confirm if E₃₅₀ is the proton acceptor for Y₃₅₆. Experiments with E₃₅₀D/Y₃₅₆NH₂Y-β2 and E₃₅₀Q/Y₃₅₆NH₂Y-β2 have not been examined.

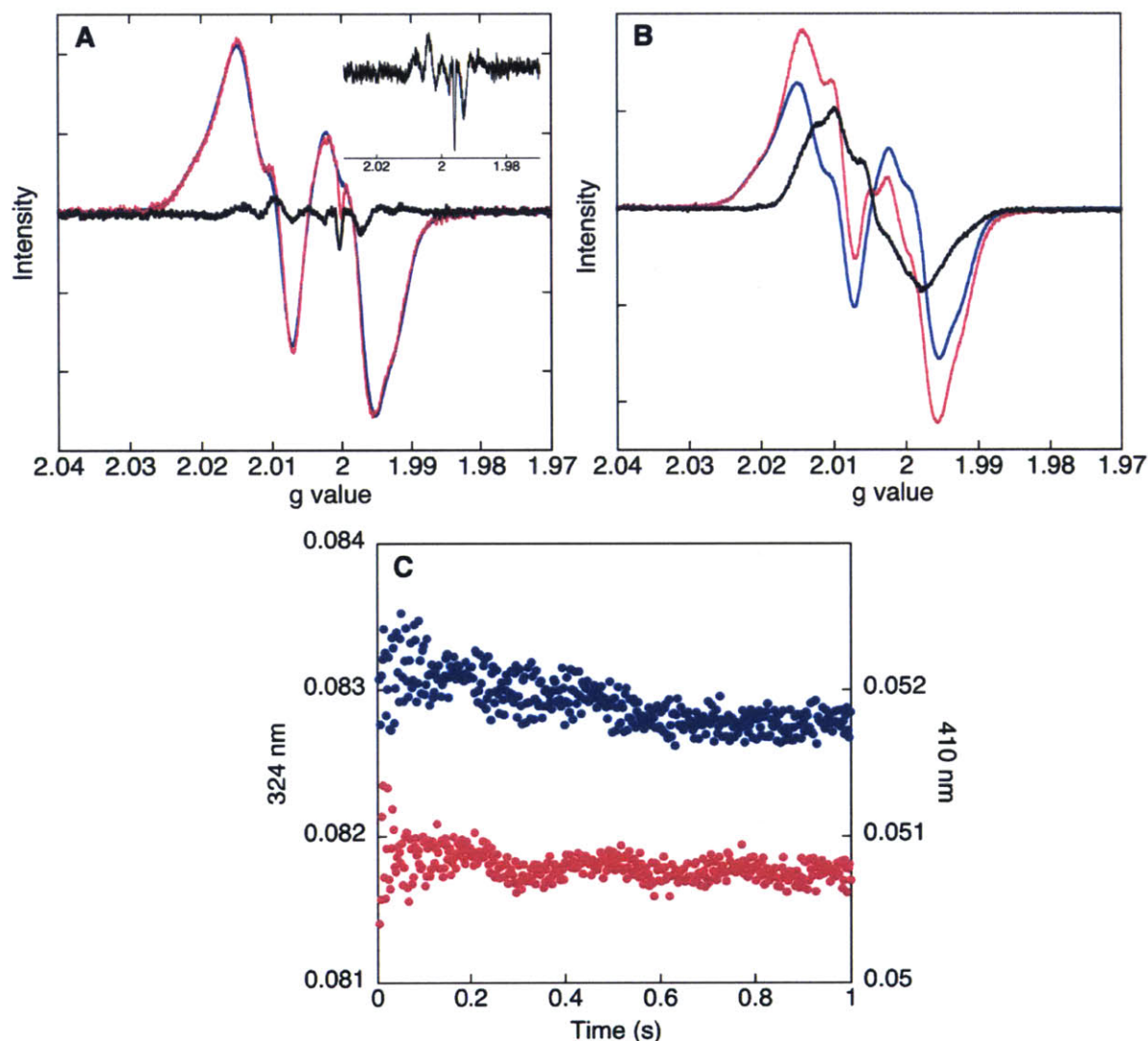


Figure 5.1 A. EPR analysis of the reaction of E₃₅₀A/Y₃₅₆NH₂Y-β2, α2, CDP and ATP. The Y₁₂₂• spectrum (blue) was subtracted from the reaction spectrum (pink) to reveal spectral noise (black, inset). The sharp feature seen at g =2 in the reaction spectrum is due to a glitch in the finger dewar. B. EPR analysis of the reaction of Y₃₅₆NH₂Y-β2, α2, CDP and ATP. The Y₁₂₂• spectrum (blue) was subtracted from the reaction spectrum (pink) to reveal the spectrum of NH₂Y₃₅₆•. Data collection and analysis were performed by Wankyue Lee. C. SF UV-vis analysis of the reaction of E₃₅₀A/Y₃₅₆NH₂Y-β2, wt-α2, CDP and ATP. The reaction was monitored at 410 nm for Y₁₂₂• (blue) and 324 nm for NH₂Y₇₃₁• (pink). Data were collected by Ellen C. Minnihan.¹⁰

To directly investigate the role of E₃₅₀ in PT, we took advantage of our ability to site-specifically replace the pathway Ys with F_nYs (n = 2,3. The lowered pK_as (6.4–7.8) of these analogs compared to Y (10.0)^{16,17,18} allow accessibility of the protonated and deprotonated states of F_nY over the pH regime where RNR is active (pH 6.0–9.0). These unnatural Y analogs can thus function as probes of PT. We have previously utilized F_nYs to show that orthogonal PCET is operative through Y₃₅₆.¹⁷ In these experiments, Y₃₅₆ was replaced with 2,3-F₂Y (pK_a 7.8)¹⁸ using EPL and its pH rate profile with α₂, CDP and ATP was collected. No correlation was observed between enzyme activity and the protonation state of 2,3-F₂Y. The data were interpreted to report on a change in mechanism from orthogonal PCET to ET upon deprotonation of 2,3-F₂Y. This conclusion has since been supported by the pH rate profiles of Y₃₅₆F_nY-β₂ generated by EPL or the nonsense codon suppression method.^{10,19} A schematic of the experimental design is shown in Figure 5.2A (X = F, Z = H). To investigate if E₃₅₀ functions as the obligate proton acceptor for Y₃₅₆, we utilized the nonsense codon suppression method to isolate and characterize E₃₅₀X/Y₃₅₆(3,5)F₂Y-β₂ (X = A or D). Accounting for the pK_a perturbation of +0.4 units at position 356,²⁰ 3,5-F₂Y₃₅₆ has a pK_a of 7.6 compared to 10.0 for Y₃₅₆ and minimally perturbs its reduction potential (≤ 30 mV as dictated by the pH).^{18,21} We posited that if E₃₅₀ is the proton acceptor during Y₃₅₆ oxidation, then the double mutant E₃₅₀X/Y₃₅₆F_nY-β₂ (X = A or D) would possess no activity when F_nY is protonated. Furthermore, increasing amounts of activity would be observed with increasing pH, correlated with deprotonation of the fluorophenol and a change in mechanism from PCET to ET.

The pH rate profiles of E₃₅₀X/Y₃₅₆(3,5)F₂Y-β₂ (X = A, green; D, blue) are shown in Figure 5.3 and reveal low levels of activity (0.2–0.5%) compared to wt-β₂ (purple, Figure 5.3A) or the single mutant Y₃₅₆(3,5)F₂Y-β₂ (pink, Figure 5.3A) over the entire pH regime (Minnihan, Stubbe

unpublished results). This activity is within the range typically reported for contaminating endogenous RNR⁹ and suggests that E₃₅₀X/Y₃₅₆(3,5)F₂Y-β₂ does not catalyze nucleotide reduction at any pH. These studies indicate that the role of E₃₅₀ in RT is more complicated than previously proposed.^{1,8} We speculated that E₃₅₀ might play a role in other major aspects of RNR catalysis, namely, subunit interaction and/or the protein conformational change that triggers RT.

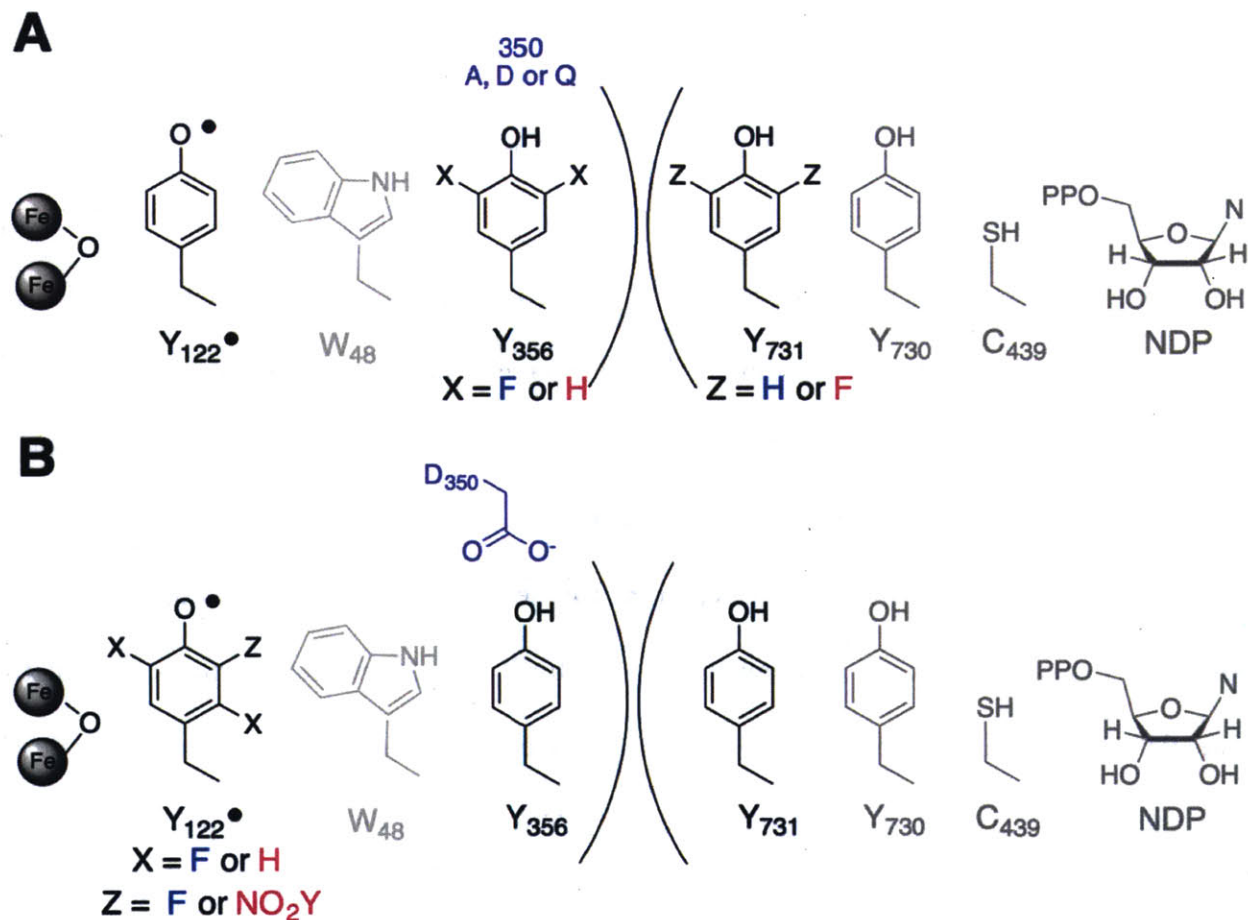


Figure 5.2 Probes for investigating the role of E₃₅₀ in RNR function. A. 3,5-F₂Y as a probe for PT. E₃₅₀ is mutated to A, D or Q in all experiments. To test if E₃₅₀ acts as a proton acceptor at the interface, 3,5-F₂Y is incorporated at Y₃₅₆ (X = F, Z = H) or at Y₇₃₁ (X = H, Z = F) or at both positions (X = F, Z = F). The activities of these mutant enzymes are tested as a function of pH. B. Y₁₂₂(2,3,5)F₃Y-β₂ (X = F, Z = F) and Y₁₂₂NO₂Y-β₂ (X = H, Z = NO₂Y) as probes for E₃₅₀'s role in the conformational change(s). E₃₅₀ is mutated to D in these experiments, and the reaction is monitored by RFQ-EPR spectroscopy to look for formation of Y₃₅₆• or W⁺.

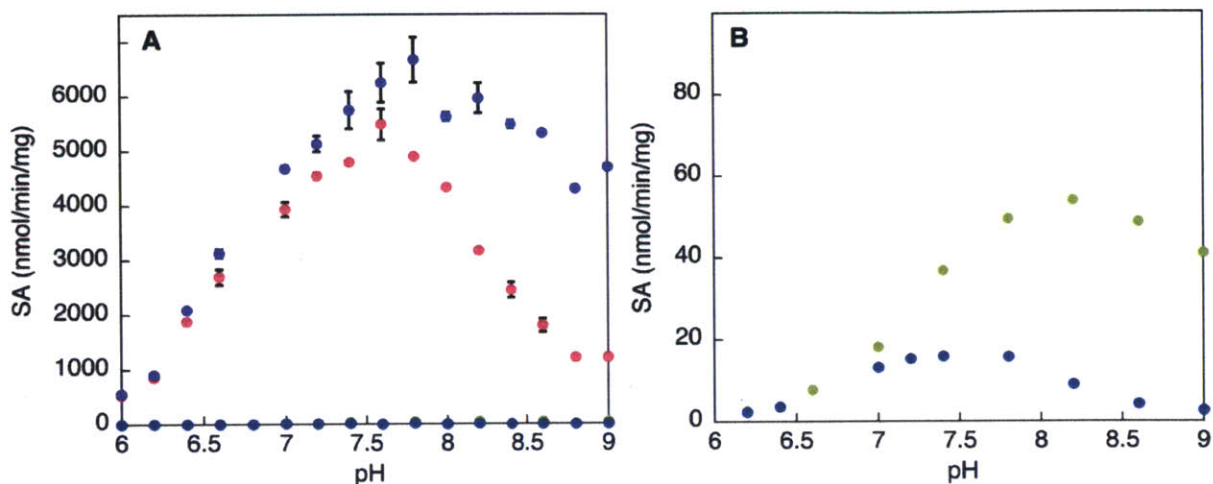


Figure 5.3 The pH rate profiles of E₃₅₀X/Y₃₅₆(3,5)F₂Y-β₂ as determined by the radioactive assay for RNR. A. Wt-β₂ (purple), Y₃₅₆(3,5)F₂Y-β₂ (pink), E₃₅₀X/Y₃₅₆(3,5)F₂Y-β₂ (X = A (green), D (blue)) B. Expanded view of the pH rate profile of E₃₅₀A/Y₃₅₆(3,5)F₂Y-β₂ (green) and E₃₅₀D/Y₃₅₆(3,5)F₂Y-β₂ (blue). Data were collected by Ellen C. Minnihan.¹⁰

In this chapter we report a number of additional experiments undertaken to understand E₃₅₀'s role in the *E. coli* class Ia RNR. These experiments were designed to test E₃₅₀'s involvement in three aspects of RNR catalysis: subunit interaction, PT and the conformational change(s) that precedes RT. First, we describe competitive inhibition spectrophotometric assays performed on the single mutants, E₃₅₀D-β₂ or E₃₅₀Q-β₂, to determine the effect of these mutations on the affinity between the two subunits.⁷ These studies show that the K_d increases by ~10-fold for both mutants, suggesting the importance of E₃₅₀ for subunit interaction. In a second set of experiments, 3,5-F₂Y was utilized as a PT probe to address if E₃₅₀ facilitates PT during oxidation of Y₃₅₆ (Figure 5.2A, X = F, Z = H), Y₇₃₁ (Figure 5.2A, X = H, Z = F) or during oxidation of both Ys (Figure 5.2A, X = F, Z = F). No activity was observed in any of the experiments regardless of the protonation state of 3,5-F₂Y. The third set of experiments employed Y₁₂₂(2,3,5)F₃Y-β₂¹⁴ and Y₁₂₂NO₂Y-β₂¹³ (Figure 5.2B) as probes to address E₃₅₀'s role in the slow protein conformational change(s)²² that precedes RT. In the case of Y₁₂₂(2,3,5)F₃Y-β₂, the rate-limiting conformational gate is partially

lifted ($20\text{--}30\text{ s}^{-1}$), providing the ability to visualize a kinetically and chemically competent $Y_{356}\bullet$ (Chapter 3). This conformational gate is further lifted in $Y_{122}NO_2Y\text{-}\beta 2$ ($100\text{--}300\text{ s}^{-1}$), and the reaction of $Y_{122}NO_2Y\text{-}\beta 2$ with $\alpha 2$, CDP and ATP accumulates $Y_{356}\bullet$ after one turnover due to the inability of this radical to re-oxidize NO_2Y^- .¹³ Furthermore, incubation of the double mutant $Y_{122}NO_2Y/Y_{356}F\text{-}\beta 2$ with $\alpha 2$, CDP and ATP generates several W^+ s (Yokoyama, Stubbe unpublished results). Using these two probes we show that mutation of E_{350} to D abolishes formation of $Y_{356}\bullet$ or W^+ . Taken together, the results presented in this Chapter suggest that E_{350} plays an important role in subunit interaction and in the conformational change(s) that initiates RT. E_{350} 's role in PT cannot currently be examined due to the inability to initiate RT when this residue is mutated. A function for E_{350} at the subunit interface is proposed and discussed.

5.2 MATERIALS AND METHODS

5.2.1 Materials. Wt- β 2 (7000 nmol/min/mg), E₃₅₀D- β 2, E₃₅₀Q- β 2 and E₃₅₀Q/Y₃₅₆(3,5)F₂Y- β 2 were isolated as previously reported.^{10,20} Wt- α 2 (2500 nmol/min/mg) was purified following the published protocol¹² and Y₇₃₁(3,5)F₂Y- α 2 (1300 nmol/min/mg) was expressed and purified by Ellen C. Minnihan.¹⁰ The substrate analog, 2'-azido-2'-deoxyuridine 5'-diphosphate (N₃UDP) was available from a previous study.²³ Thioredoxin (TR, 40 U/mg) and thioredoxin reductase (TRR, 1400 U/mg) were purified following the standard protocols.^{24, 25} Glycerol minimal medium with leucine (GMMML) contains final concentrations of 1% (v/v) glycerol, 0.05% (w/v) NaCl, 1 mM MgSO₄, 0.1 mM CaCl₂ and 0.3 mM L-leucine. 5'-[³H] CDP was purchased from ViTrax (Placentia, CA). Roche provided the calf alkaline phosphatase (20 U/ μ L). ATP, CDP, TTP, deoxycytidine (dC) and NADPH were obtained from Sigma Aldrich. Assay buffer consists of 50 mM HEPES pH 7.6, 15 mM MgSO₄, 1 mM EDTA unless otherwise specified. Temperature was controlled at 25 °C for all experiments using a Lauda circulating water bath. All specific activities are reported with respect to the subunit that is limiting in concentration.

5.2.2 K_d for α 2/E₃₅₀X- β 2 (X = D or Q) interaction. Subunit affinity was determined using the competitive inhibition assay.⁷ Reaction mixtures contained in a total volume of 300 μ L, 0.15 μ M wt- α 2, 0.3 μ M wt- β 2, 1 mM CDP, 1.6 mM ATP, 50 μ M TR, 1 μ M TRR, 0.2 mM NADPH and increasing concentrations of E₃₅₀X- β 2 (0.1–20 μ M) in assay buffer. The reaction was monitored continuously for 1 min at 340 nm for the consumption of NADPH (6200 M⁻¹cm⁻¹). The data were fit to Eq. 5.1:

$$[E_{350}X - \beta 2]_{bound} = \frac{[E_{350}X - \beta 2]_{max} \times [E_{350}X - \beta 2]_{free}}{K_d + [E_{350}X - \beta 2]_{free}} \quad (5.1)$$

where $[E_{350}X-\beta 2]_{\text{bound}}$ is the amount of wt- $\alpha 2/E_{350}X-\beta 2$ complex, $[E_{350}X-\beta 2]_{\text{max}}$ is the concentration of the wt- $\alpha 2/E_{350}X-\beta 2$ complex at maximum amounts of $[E_{350}X-\beta 2]_{\text{free}}$ and K_d is the dissociation constant for the interaction of wt- $\alpha 2$ and $E_{350}X-\beta 2$. Equation 5.1 assumes that the amount of wt $\alpha 2\beta 2$ complex at different concentrations of the inhibitor scales with the activity of $\alpha 2$.

5.2.3 Reaction of $E_{350}X-\beta 2$ ($X = D, Q$), wt- $\alpha 2$, $N_3\text{UDP}$ and TTP monitored by EPR spectroscopy. Reaction mixtures (245 μL) containing $E_{350}X-\beta 2$ ($X = D$ or Q , 1.2 $\text{Y}\cdot/\beta 2$, 80 μM), wt- $\alpha 2$ (80 μM), $N_3\text{UDP}$ (2 mM) and TTP (0.5 mM) in assay buffer were incubated in a 25 °C water bath and quenched in liquid isopentane (-140 °C) for analysis by EPR spectroscopy at 2, 5 and 10 min. From each composite spectrum, the previously reported spectrum of $\text{N}\cdot^{26}$ was subtracted to quantitate the percentage of $\text{Y}_{122}\cdot$.

5.2.4 Specific activity of $E_{350}Q/Y_{356}(3,5)F_2Y-\beta 2$ at pH 6.7 and pH 8.0. $E_{350}Q/Y_{356}(3,5)F_2Y-\beta 2$ (0.7 $\text{Y}\cdot/\beta 2$, 0.8 μM), wt- $\alpha 2$ (4 μM), CDP (1 mM), ATP (3 mM), TR (30 μM), TRR (0.5 μM) and NADPH (0.2 mM) were combined in 50 mM MES (pH 6.7) or 50 mM HEPES (pH 8.0), 15 mM MgSO_4 , 1 mM EDTA. The reaction was monitored for 1 min at 340 nm for the consumption of NADPH.

5.2.5 The pH rate profile of $E_{350}D-\beta 2/Y_{731}(3,5)F_2Y-\alpha 2$. The pH rate profile was determined using the radioactive assay for RNR as previously described.¹⁹ Assays were performed in 50 mM MES (pH 6.0–7.0), HEPES (pH 7.0–8.0) or TAPS (pH 8.0–9.0), 15 mM MgSO_4 and 1 mM EDTA. The reaction contained in a total volume of 200 μL , 0.8 μM $\text{Y}_{731}(3,5)F_2Y-\alpha 2$, 4 μM $E_{350}D-\beta 2$ (1.2 $\text{Y}\cdot/\beta 2$), 0.5 mM 5'-[³H] CDP (8000 cpm/nmol), 3 mM ATP, 30 μM TR, 0.5 μM TRR and 1 mM NADPH. The reaction was initiated by the addition of $\text{Y}_{731}(3,5)F_2Y-\alpha 2$ and NADPH. Aliquots (40

μL) were quenched in 25 μL of 2% HClO_4 and neutralized by the addition of 20 μL of 0.5 M KOH. Samples were centrifuged (20,000 \times g, 4 $^\circ\text{C}$ for 20 min) to remove KClO_4 and precipitated protein, and the resulting supernatant was dephosphorylated by the addition of 20 U calf alkaline phosphatase, 120 nmol carrier dC in 175 mM Tris pH 8.5, 1.5 mM EDTA. Cytidine and dC were separated as described by Steeper and Steuart.²⁷

5.2.6 Specific activity of the triple mutant $E_{350}\text{Q}/Y_{356}(3,5)\text{F}_2\text{Y}-\beta 2$ and $Y_{731}(3,5)\text{F}_2\text{Y}-\alpha 2$ at pH 6.8 and pH 8.4. Standard spectrophotometric assays were performed to assess the activity of the triple mutant $E_{350}\text{Q}/Y_{356}(3,5)\text{F}_2\text{Y}-\beta 2$ and $Y_{731}(3,5)\text{F}_2\text{Y}-\alpha 2$. In a total volume of 300 μL , $E_{350}\text{Q}/Y_{356}(3,5)\text{F}_2\text{Y}-\beta 2$ (0.7 μM), $Y_{731}(3,5)\text{F}_2\text{Y}-\alpha 2$ (4 μM), CDP (1 mM), ATP (3 mM), TR (30 μM), TRR (0.5 μM) and NADPH (0.2 mM) were combined in 50 mM MES (pH 6.8) or TAPS (pH 8.4), 15 mM MgSO_4 and 1 mM EDTA. The reaction was monitored for 1 min at 340 nm.

5.2.7 Construction of $p\text{BAD}-nr\text{dB}_{122}\text{TAG}-E_{350}\text{D}$. Site-directed mutagenesis to replace E_{350} with D was performed using $p\text{BAD}-nr\text{dB}_{122}\text{TAG}$ as the template,²⁸ forward primer 5'-G GTT GCT CCG CAG GAT GTG GAA GTC AGT TC-3' and reverse primer 5'-GA ACT GAC TTC CAC ATC CTG CGG AGC AAC C-3'. The mutagenesis was performed using the Stratagene QuikChange kit and confirmed by DNA sequencing at the MIT Biopolymers Laboratory.

5.2.8 Expression, purification and reconstitution of $Y_{122}(2,3,5)\text{F}_3\text{Y}/E_{350}\text{D}-\beta 2$. The $p\text{BAD}-Y_{122}\text{TAG}-E_{350}\text{D}$ and $p\text{EVOL}-F_n\text{Y}-\text{RS}$ ²⁸ plasmids were co-transformed into *E. coli* Top10 chemically competent cells. Apo $Y_{122}(2,3,5)\text{F}_3\text{Y}/E_{350}\text{D}-\beta 2$ was expressed, purified and reconstituted as described for $Y_{122}(2,3,5)\text{F}_3\text{Y}-\beta 2$ in Chapter 3. A total of 10 mg pure apo protein was obtained per g of wet cell paste. An average yield of 0.5 $\text{F}_3\text{Y}\cdot/\beta 2$ was obtained from two separate reconstitution attempts and no efforts were made to improve the radical yield.

5.2.9 Reaction of $Y_{122}(2,3,5)F_3Y/E_{350}D-\beta_2$, $wt-\alpha_2$, CDP and ATP monitored by RFQ-EPR spectroscopy. Rapid freeze quench (RFQ) experiments were performed on an Update Instruments 1019 syringe ram unit and a model 715 Syringe Ram controller. $Wt-\alpha_2$ (80 μ M) and ATP (6 mM) in assay buffer were mixed with $Y_{122}(2,3,5)F_3Y/E_{350}D-\beta_2$ (0.5 $F_3Y\bullet/\beta_2$, 80 μ M) and CDP (2 mM) in assay buffer and aged for varying times (16–535 ms) based on the previously reported kinetics for $Y_{356}\bullet$ formation (Chapter 3).¹⁴ The reaction mixture was then sprayed at a drive ram velocity of 1.25–1.6 cm/s into liquid isopentane (-140 °C). The crystals were packed into X-band EPR tubes and the data were acquired and analyzed as described in Chapter 3.

5.2.10 Expression and purification of $Y_{122}NO_2Y/E_{350}D-\beta_2$. The pBAD- $Y_{122}TAG-E_{350}D$ and pEVOL- F_nY-RS ²⁸ plasmids were co-transformed into *E. coli* Top10 chemically competent cells. A single colony was used to inoculate 5 mL of LB containing ampicillin (Amp, 100 μ g/mL) and chloramphenicol (Cm, 35 μ g/mL). The starter culture was grown until saturation (~ 16 h, 37 °C) and diluted 200-fold into 200 mL of LB containing the antibiotics. After 12 h at 37 °C, this culture was diluted 100-fold into 5 x 2 L of GMMML medium containing Amp, Cm, 0.05% (w/v) D-glucose, 0.25% (w/v) Asp, 0.1% (w/v) L-arabinose, 0.2 g/L of all amino acids except Tyr, Cys and Phe and a 1X heavy metal solution. The 1000X heavy metal stock solution contained the following per liter: 500 mg of $Na_2MoO_4\cdot 2H_2O$, 250 mg of $CoCl_2$, 175 mg of $CuSO_4\cdot 5H_2O$, 1 g of $MnSO_4\cdot H_2O$, 8.75 g of $MgSO_4\cdot 7H_2O$, 1.25 g of $ZnSO_4\cdot 7H_2O$, 1.25 g of $FeCl_2\cdot 4H_2O$, 2.5 g of $CaCl_2\cdot 2H_2O$ and 1 g of H_3BO_3 dissolved in 1M HCl.²⁰ NO_2Y (2 mM) was included from the start of growth and the cultures were incubated for 18 h at 37 °C with shaking. Cells were harvested by centrifugation (4000 x g, 15 min, 4 °C). $Y_{122}NO_2Y/E_{350}D-\beta_2$ was purified using anion exchange chromatography methods as previously reported.^{13,20} A total yield of 30 mg pure protein containing 1.8 diferric clusters/ β_2 was obtained per g wet cell paste.

5.2.11 *Chelation of iron from Y₁₂₂NO₂Y/E₃₅₀D-β2*. As-isolated Y₁₂₂NO₂Y/E₃₅₀D-β2 (3 mL, 570 μM) was dialyzed against 2 L of 50 mM 8-hydroxyquinoline-5-sulfonic acid pH 7.0, 1 M imidazole and 30 mM NH₂OH in a Slide-a-lyzer cassette for 3 h. The protein mixture was desalted using a G-25 Sephadex column pre-equilibrated in 50 mM HEPES pH 7.6, 5% glycerol. The recovery yield was 75%.

5.2.12 *Reaction of Y₁₂₂NO₂Y/E₃₅₀D-β2, wt-α2, CDP and ATP monitored by RFQ-EPR spectroscopy*. Apo Y₁₂₂NO₂Y/E₃₅₀D-β2 (450 μL, 500 μM) was deoxygenated on a Schlenk line and taken into the anaerobic chamber maintained at 4 °C. The protein was treated with 5 equiv. of Fe^{II}(NH₄)₂(SO₄)₂, diluted to 90 μM in anaerobic 50 mM HEPES pH 7.6, 5% glycerol and loaded into an RFQ syringe. The syringe was sealed, taken out of the anaerobic chamber and attached to the RFQ instrument. Fe²⁺-Y₁₂₂NO₂Y/E₃₅₀D-β2 was mixed with O₂ saturated 50 mM HEPES pH 7.6, 5% glycerol containing 3 mM CDP. The mixture was aged for 0.5 s and then mixed with 90 μM wt-α2 and 9 mM ATP contained in a third syringe. Samples were aged for 16–131 ms and quenched in liquid isopentane (-140 °C) for analysis by X-band EPR spectroscopy. The different aging times were determined based on the previously reported kinetics for diferric-NO₂Y• formation¹³ and Y₃₅₆•¹³/W⁺ formation (Yokoyama, Stubbe unpublished results).

5.3 RESULTS

5.3.1 K_d for $\alpha 2/E_{350}X-\beta 2$ ($X = D$ or Q) interaction. Previous studies of Sjöberg and coworkers have shown that the K_d for $\alpha 2/E_{350}A-\beta 2$ interaction is 3-fold higher than wt.⁸ To determine the affinity of $E_{350}X-\beta 2$ ($X = D$ or Q) for $\alpha 2$, we followed the same protocol in which RNR activity is determined by spectrophotometric assays.²⁹ In these assays, $E_{350}X-\beta 2$ is added as a competitive inhibitor of nucleotide reduction by the wt $\alpha 2\beta 2$ complex.⁷ The loss in activity is measured as a function of $E_{350}X-\beta 2$ concentration (0.1–20 μM) to quantitate the amount of bound and free $E_{350}X-\beta 2$. The results of these assays are shown in Figure 5.4. The data were analyzed using Eq. 5.1 and the resulting K_d values are shown in Table 5.2. Due to the weak interaction between wt- $\alpha 2$ and wt- $\beta 2$ (0.18 μM ,⁷ Table 5.2), RNR activity assays are typically performed with a limiting concentration of one subunit and a 5-fold excess of the second subunit. As reported in Table 5.2, mutation of E_{350} increases the K_d for subunit interaction by 9–12-fold (1.7–2.2 μM compared to 0.18 μM for wt). Therefore, the concentrations of the E_{350} mutants and $\alpha 2$ in all subsequent experiments have been adjusted to ensure 60–100% complex formation.

Table 5.2 K_d values for $E_{350}X-\beta 2/\alpha 2$ as determined by the competitive inhibition assay.

$\beta 2$	K_d (μM)
wt	0.18 ^a
$E_{350}A$	0.5 ^a
$E_{350}D$	1.7 \pm 0.1
$E_{350}Q$	2.2 \pm 0.3

^a Previously reported by Climent et al.⁷

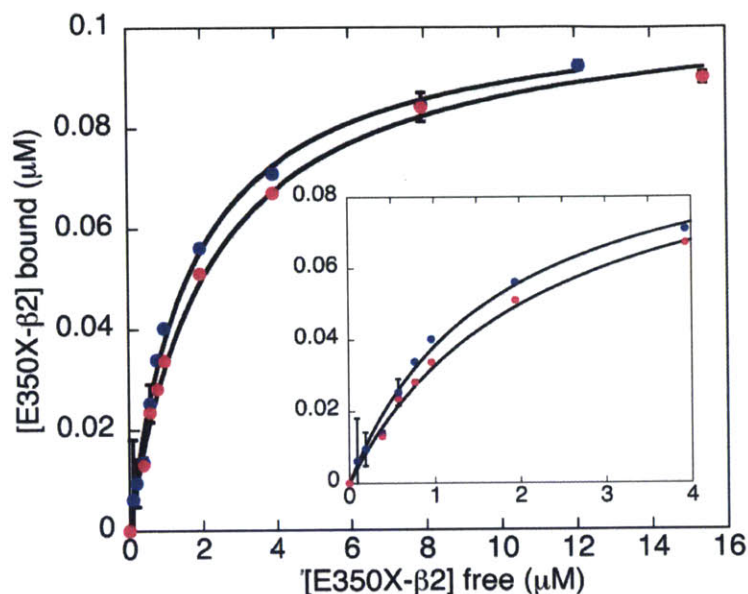


Figure 5.4 K_d for $\alpha 2/E_{350}X-\beta 2$ ($X = D$ or Q) interaction. The K_d for subunit interaction was determined using $E_{350}X-\beta 2$ ($X = D$, blue; Q , pink) as a competitive inhibitor of nucleotide reduction.⁷ Each data point represents the average of two trials. The data were fit to Eq. 5.1 and provided the K_d values listed in Table 5.2.

5.3.2 Amount of $N\bullet$ generated in the reaction of $E_{350}X-\beta 2/\alpha 2/N_3UDP/TTP$ is consistent with contaminating wt RNR. As reported in Table 5.1, $E_{350}X-\beta 2$ ($X = A, D, Q$) activities are 0.1–0.3% that of wt- $\beta 2$, amounts that cannot be distinguished from contaminating endogenous RNR.⁹ To determine if $E_{350}X-\beta 2$ can catalyze nucleotide reduction, we incubated this mutant enzyme with $\alpha 2$, effector TTP and the mechanism-based inhibitor N_3UDP . This analog has been shown to be a stoichiometric inhibitor of RNR.^{30,31} $C_{439}\bullet$ in the $\alpha 2\beta 2$ complex initiates the reaction with N_3UDP by abstraction of the 3' H-atom; subsequently, the enzyme is inactivated by the generation of a nitrogen-centered ($N\bullet$) radical that is covalently bound to the active site of $\alpha 2$. At maximum, $N\bullet$ constitutes 50% of the total radical content in the wt RNR reaction.³² If $E_{350}X-\beta 2$ ($X = A, D, Q$) is capable of turnover, we anticipated that the same percentage of $N\bullet$ would be visualized (50%),

albeit at a slower rate constant^{vii} than wt- β 2. In the wt case, 50% of N• is observed after 3 min at 25 °C and has a half-life of ~12 min.²⁶ We considered the possibility that N• formation with E₃₅₀X- β 2 could be slower than with wt, but N• half-life could remain the same. In this case, N• may not be visualized in the E₃₅₀X- β 2 (X= A, D, Q) reaction. However, we reasoned that formation of N• requires reduction of Y₁₂₂•, and expected that Y₁₂₂• loss would still be monitored in this scenario. E₃₅₀X- β 2 (X = D or Q) was reacted with α 2, N₃UDP and TTP, and samples were quenched at 2, 5 and 10 min and assessed for variations in spectral features or total radical amounts.

Figure 5.5A shows EPR spectra of the E₃₅₀D- β 2/ α 2/N₃UDP/TTP reaction recorded at 2 min (pink), 5 min (blue) and 10 min (green). No changes in total radical content were observed (1.2–1.4 Y•/ β 2, Table 5.3) and no variations in spectral features were seen between the different samples. To quantitate the percentage of the active site radical, a previously recorded spectrum of N• (pink, Figure 5.5B) was subtracted from each of the composite spectra (Figure 5.5B shows the 10 min spectrum as an example). The spectrum of N• shows a broad feature at $g = \sim 1.985$ that is unique to this radical. Thus, the subtractions were performed using this feature as a handle and the intensity of N• was varied until the net spectrum (blue) revealed a smooth baseline. Quantitation of N• was performed for all three time points using this protocol and the results are summarized in Table 5.3. These low amounts of N• (5% within 10 min) can be rationalized by the presence of 10% contaminating wt- β 2. However, we note that these amounts of N• cannot be accurately quantitated despite the presence of a unique spectroscopic handle ($g = \sim 1.985$). In fact, the intensity

^{vii} We cannot accurately predict how long it would take to form 50% N• with E₃₅₀X- β 2. In wt RNR, there is no correlation between steady-state activity and the kinetics of N• formation. Turnover occurs at 2–10 s⁻¹ but complete N• formation with N₃UDP requires 3 min.

of N• was varied 2–3-fold below the quantitated amounts (5%, Table 5.3) with minimal effects on the net spectrum.

Identical experiments were also performed with E₃₅₀Q-β₂/α₂/N₃UDP/TTP by EPR spectroscopy and are described in Figure 5.6. Similar to the E₃₅₀D-β₂ reaction, no variations were recorded in total radical concentration (1.1–1.3 Y•/β₂, Table 5.3) and no changes were observed in spectral features with time (Figure 5.6A). The N• spectrum (pink, Figure 5.6B) was subtracted from the composite spectra; Figure 5.6B shows the 10 min sample as an example. The observed amounts of N• (4.5%, Table 5.3) are consistent with 9% contaminating wt-β₂. We conclude from these studies that E₃₅₀X-β₂ (X = D or Q) cannot catalyze nucleotide reduction.

Table 5.3 Percentage of N• generated in the reaction of E₃₅₀X-β₂/α₂/N₃UDP/TTP.

β ₂	Incubation time (min)	Total spin/β ₂	% N• of total spin
wt ^a	3	1.2	50
E ₃₅₀ D	2	1.4	5
E ₃₅₀ D	5	1.2	5
E ₃₅₀ D	10	1.2	5
E ₃₅₀ Q	2	1.3	4.5
E ₃₅₀ Q	5	1.2	4.5
E ₃₅₀ Q	10	1.1	4.5

^a Previously reported data taken from Ref. 26.

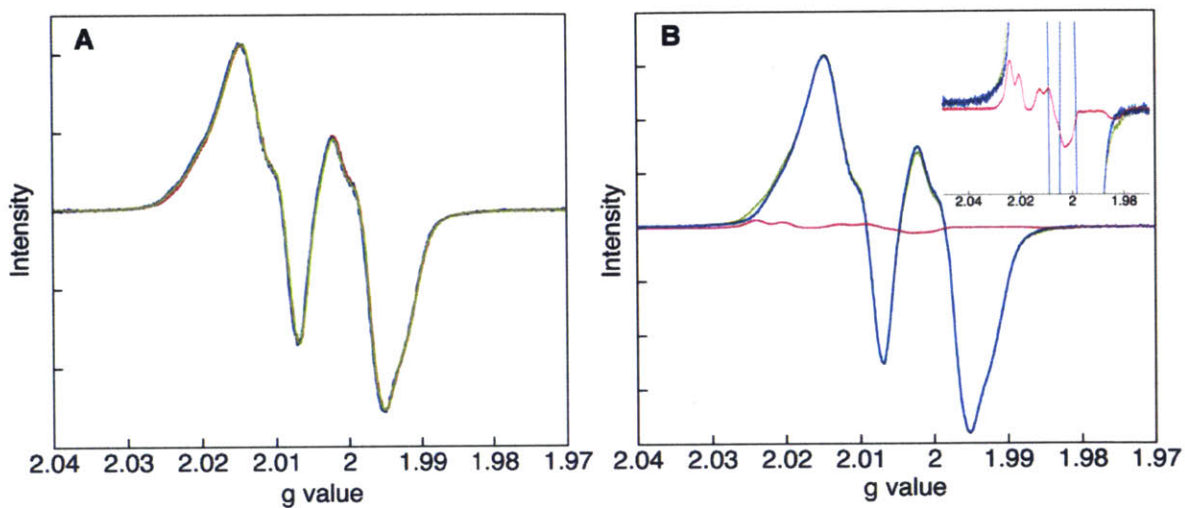


Figure 5.5 Reaction of E₃₅₀D-β₂, wt-α₂, N₃UDP and TTP monitored by EPR spectroscopy. A. Overlay of the composite spectra at 2 (pink), 5 (blue) and 10 min (green) shows no changes in the reaction spectrum with time. B. Subtraction of the N• spectrum (pink) from the composite spectrum at 10 min (green) gives the spectrum in blue. The inset shows an expanded view of the spectrum of N• observed in the wt RNR reaction.

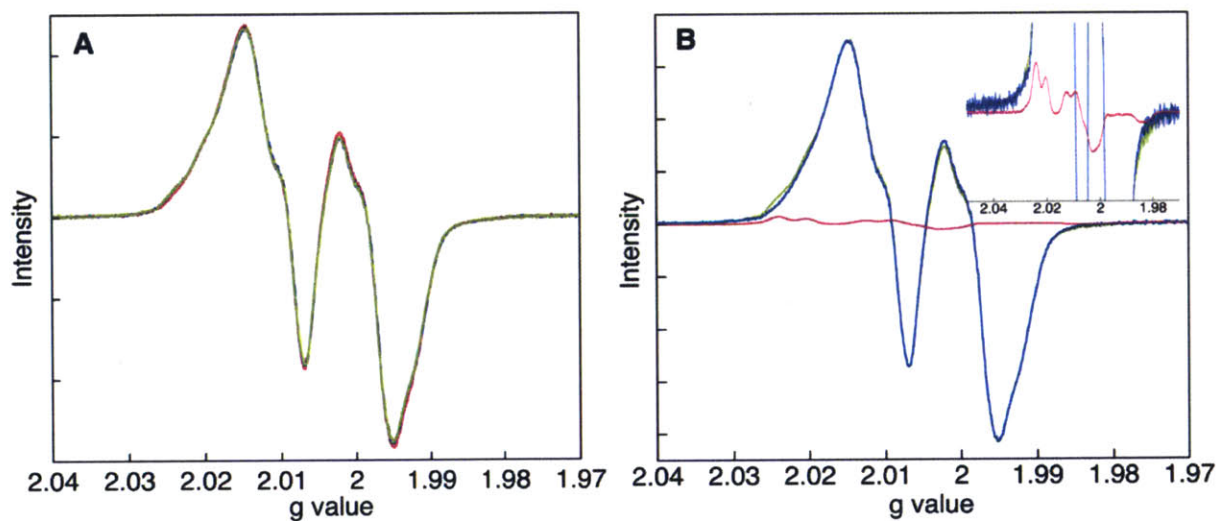


Figure 5.6 Reaction of E₃₅₀Q-β₂, wt-α₂, N₃UDP and TTP monitored by EPR spectroscopy. A. Overlay of the composite spectra at 2 (pink), 5 (blue) and 10 min (green) shows minimal changes in the EPR spectrum with time. B. Subtraction of the N• spectrum (pink) from the composite spectrum at 10 min (green) gives the spectrum in blue. The inset shows an expanded view of the spectrum of N• observed in the wt reaction.

5.3.3 $E_{350}Q/Y_{356}(3,5)F_2Y-\beta 2$ is not active for nucleotide reduction at pH 6.7 or pH 8.0. We have previously shown that $E_{350}X/Y_{356}(3,5)F_2Y-\beta 2$ ($X = A$ or D) cannot catalyze nucleotide reduction at any pH (0.2–0.5% of wt activity from pH 6.0–9.0, Figure 5.3).¹⁰ $E_{350}Q/Y_{356}(3,5)F_2Y-\beta 2$ was expressed and purified as previously reported¹⁰ to assess the effect of this structurally analogous mutation at position 350.

The activity of $E_{350}Q/Y_{356}(3,5)F_2Y-\beta 2$ was monitored at two different pH values, 6.7 and 8.0. Titration experiments performed on $Y_{356}NO_2Y-\beta 2$ ²⁰ have shown that the pK_a of NO_2Y_{356} is 0.4 units higher than the solution pK_a of NO_2Y . Taking this perturbation into account, we anticipated that 89% of 3,5- F_2Y will be protonated at pH 6.7 and 72% will be deprotonated at pH 8.0. At these pH values, 3,5- F_2Y minimally perturbs the reduction potential of Y . Previous studies on the single mutant $Y_{356}(3,5)F_2Y-\beta 2$ have shown that this construct maintains activity at both pH 6.7 and pH 8.0 (Ref. 10. and reproduced here in Table 5.4). Compared to $Y_{356}(3,5)F_2Y-\beta 2$, $E_{350}Q/Y_{356}(3,5)F_2Y-\beta 2$ shows 0% and 0.07% activity at the two pH values, respectively (Table 5.4). Although a complete pH rate profile has not been constructed for $E_{350}Q/Y_{356}(3,5)F_2Y-\beta 2$, these data suggest that $E_{350}Q/Y_{356}(3,5)F_2Y-\beta 2$ is inactive over the entire pH regime (6.0–9.0), similar to our previous observations with $E_{350}A/Y_{356}(3,5)F_2Y-\beta 2$ and $E_{350}D/Y_{356}(3,5)F_2Y-\beta 2$.

Table 5.4 Specific activity of $E_{350}Q/Y_{356}(3,5)F_2Y-\beta 2$ as determined by the spectrophotometric assay for RNR.

$\beta 2$	$\alpha 2$	pH	Specific activity (nmol/min/mg)
$Y_{356}(3,5)F_2Y$	wt	6.6	2690 ± 142^a
$Y_{356}(3,5)F_2Y$	wt	8.0	4320 ± 10^a
$E_{350}Q/Y_{356}(3,5)F_2Y$	wt	6.7	$-^b$
$E_{350}Q/Y_{356}(3,5)F_2Y$	wt	8.0	3 ± 2

The specific activities reported represent the averages of two trials each.

^a These data were previously reported by Ellen C. Minnihan.¹⁰

^b The measured slopes were similar to the background slope observed in the absence of $\beta 2$.

5.3.4 $E_{350}D\text{-}\beta 2/Y_{731}(3,5)F_2Y\text{-}\alpha 2$ is not active for nucleotide reduction at any pH. As with Y_{356} , the proton acceptor for Y_{731} has not been identified. Due to the negative results observed with $E_{350}X/Y_{356}(3,5)F_2Y\text{-}\beta 2$, we speculated that E_{350} could function as a proton acceptor for Y_{731} . This explanation could account for the loss of activity observed with $E_{350}X/Y_{356}(3,5)F_2Y\text{-}\beta 2$; mutation of E_{350} would result in inability to oxidize Y_{731} . Thus, steady-state activity assays were conducted with $E_{350}D\text{-}\beta 2$ and $Y_{731}(3,5)F_2Y\text{-}\alpha 2$ as a function of pH (6.0–9.0). The pK_a of 3,5- F_2Y at position 731 is predicted to be 0.9 units higher than the solution pK_a (7.2).²⁰ Therefore, it was anticipated that if E_{350} participates in PT with Y_{731} , low activities would be measured at $pH < 8.1$, but activity would increase as a function of pH consistent with deprotonation of 3,5- F_2Y at $pH > 8.1$.

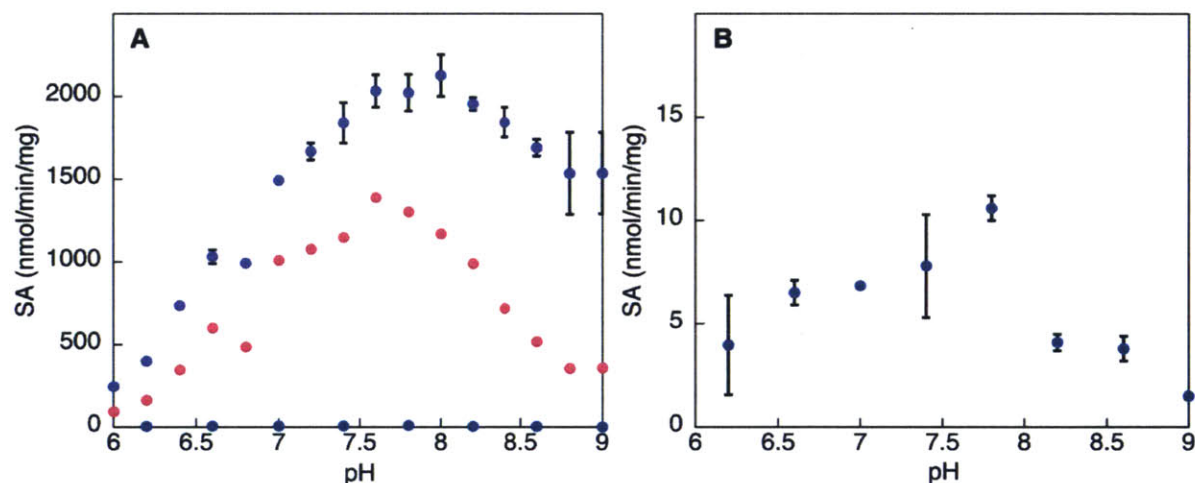


Figure 5.7 The pH rate profile of $E_{350}D\text{-}\beta 2/Y_{731}(3,5)F_2Y\text{-}\alpha 2$ as determined by the radioactive assay for RNR. A. The pH rate profile of wt- $\beta 2$ /wt- $\alpha 2$ (purple), wt- $\beta 2/Y_{731}(3,5)F_2Y\text{-}\alpha 2$ (pink) and $E_{350}D\text{-}\beta 2/Y_{731}(3,5)F_2Y\text{-}\alpha 2$ (blue). B. Expanded view of the pH rate profile of $E_{350}D\text{-}\beta 2/Y_{731}(3,5)F_2Y\text{-}\alpha 2$. Data points represent either a single trial (A, pink) or the average of two independent trials (purple, blue). The pH rate profile of wt- $\beta 2$ /wt- $\alpha 2$ and wt- $\beta 2/Y_{731}(3,5)F_2Y\text{-}\alpha 2$ were previously reported by Ellen C. Minnihan.¹⁰

The pH rate profile of the single mutant $Y_{731}(3,5)F_2Y\text{-}\alpha 2$ has been previously reported and is shown here in Figure 5.7A (pink).¹⁰ Although this mutant does not maintain the same pH rate

profile as wt- $\alpha 2$ (purple),¹⁰ it can catalyze multiple turnovers in the entire pH regime where RNR activity is typically monitored. By comparison, $E_{350}D\text{-}\beta 2/Y_{731}(3,5)F_2Y\text{-}\alpha 2$ shows 0.3–0.7% activity at all pH values (Figure 5.7B), consistent with contaminating endogenous RNR. These results suggest that E_{350} may not function as the proton acceptor for Y_{731} .

5.3.5 $E_{350}Q/Y_{356}(3,5)F_2Y\text{-}\beta 2$ cannot catalyze nucleotide reduction with $Y_{731}(3,5)F_2Y\text{-}\alpha 2$ at any pH. From the experiments discussed in sections 5.3.3 and 5.3.4, E_{350} does not appear to function solely as the proton acceptor for Y_{356} or Y_{731} . One possible explanation for these results is that E_{350} functions as the proton acceptor for both Y_{356} and Y_{731} . This hypothesis is supported by the experiments described in Chapter 4 that demonstrate that the Y_{356} proton is in rapid exchange with solvent. E_{350} could shuttle the Y_{356} proton to solvent and subsequently do the same for Y_{731} . This role for E_{350} could explain why the individual mutants, $E_{350}X/Y_{356}(3,5)F_2Y\text{-}\beta 2$ ($X = A, D$ or Q) or $E_{350}D\text{-}\beta 2/Y_{731}(3,5)F_2Y\text{-}\alpha 2$, are inactive; activity could require the presence of a deprotonated amino acid at both positions on pathway. To address if E_{350} performs in this capacity, we monitored the activity of $E_{350}Q/Y_{356}(3,5)F_2Y\text{-}\beta 2$ with $Y_{731}(3,5)F_2Y\text{-}\alpha 2$ at either pH 6.8 or 8.4. At pH 6.8, we anticipate the amounts of protonated 3,5- F_2Y to be 86% and 95% at positions 356 and 731, respectively. The amount of deprotonated 3,5- F_2Y at pH 8.4 was calculated as 86% and 66% at position 356 and 731, respectively. Thus, activity assays at these two pH values are sufficient to confirm whether E_{350} is responsible for deprotonation of both Y_{356} and Y_{731} . We have previously measured the activities of $Y_{356}(3,5)F_2Y\text{-}\beta 2$ and $Y_{731}(3,5)F_2Y\text{-}\alpha 2$ (Figures 5.3 and 5.7).¹⁰ The activity of the double mutant $Y_{356}(3,5)F_2Y\text{-}\beta 2/Y_{731}(3,5)F_2Y\text{-}\alpha 2$ was determined in the presence of an intact E_{350} at pH 6.8 and 8.4 to confirm that RNR can function in the presence of two protonated or deprotonated 3,5- F_2Y s on pathway.

Table 5.5 Specific activity of E₃₅₀Q/Y₃₅₆(3,5)F₂Y-β2 with Y₇₃₁(3,5)F₂Y-α2 as determined by the spectrophotometric assay.

β2	α2	pH	Specific activity (nmol/min/mg)
wt	Y ₇₃₁ (3,5)F ₂ Y	6.8	490 ^a
wt	Y ₇₃₁ (3,5)F ₂ Y	8.4	720 ^a
Y ₃₅₆ (3,5)F ₂ Y	wt	6.8	3300 ^a
Y ₃₅₆ (3,5)F ₂ Y	wt	8.4	2400 ± 140 ^a
Y ₃₅₆ (3,5)F ₂ Y	Y ₇₃₁ (3,5)F ₂ Y	6.8	810 ± 30
Y ₃₅₆ (3,5)F ₂ Y	Y ₇₃₁ (3,5)F ₂ Y	8.4	1660 ± 30
E ₃₅₀ Q/Y ₃₅₆ (3,5)F ₂ Y	Y ₇₃₁ (3,5)F ₂ Y	6.8	- ^b
E ₃₅₀ Q/Y ₃₅₆ (3,5)F ₂ Y	Y ₇₃₁ (3,5)F ₂ Y	8.4	- ^b

^a Previously reported by Ellen C. Minnihan.¹⁰

^b The measured slope was similar to the background slope observed in the absence of β2.

As summarized in Table 5.5, Y₃₅₆(3,5)F₂Y-β2, Y₇₃₁(3,5)F₂Y-α2 and the double mutant containing 3,5-F₂Y at positions 356 and 731 maintain activity at pH 6.8 and 8.4. The differences in activities observed between the constructs are primarily related to our assay method. Due to the weak affinity between α2 and β2 ($K_d = 0.2 \mu\text{M}$ for wt),⁷ we typically assay one subunit with a 5-fold excess of the second subunit. The calculated specific activity of α2 is always lower than that of β2, primarily due to the differences in the molecular weights between the two subunits (172 kDa and 87 kDa for α2 and β2, respectively) but also due to the ability of β2 to act catalytically (Chapter 3). We have previously shown the rate-limiting step during wt RNR turnover can switch from the protein conformational changes to re-reduction of α2 by TR based on the assay conditions.²² Under conditions of limiting α2, subsequent turnover is only possible upon re-reduction by TR. However, when β2 is limiting, a single β2 can rapidly dissociate and re-associate with a second reduced α2 molecule without re-reduction. Consistent with this proposal, the activities measured with Y₃₅₆(3,5)F₂Y-β2 are higher than those observed with Y₇₃₁(3,5)F₂Y-α2 (Table 5.5). For the double mutant, Y₃₅₆(3,5)F₂Y-β2/Y₇₃₁(3,5)F₂Y-α2, we chose to perform the assay under conditions in which the β2 concentration is limiting, thus improving our lower limit

of detection. The activity of this double mutant is ~30–70% of that measured for the single mutant $Y_{356}(3,5)F_2Y-\beta_2$, suggesting that the presence of two 3,5- F_2Y s on pathway attenuates turnover. In contrast to the double mutant, no activity can be detected at either pH value for the triple mutant containing $E_{350}Q$. Taken together, the results of sections 5.3.3, 5.3.4 and 5.3.5 confirm that E_{350} plays a role in RNR function that is not related to PT through Y_{356} , Y_{731} or through both pathway Y s.

5.3.6 Reaction of $Y_{122}(2,3,5)F_3Y/E_{350}D-\beta_2$, wt- α_2 , CDP and ATP does not accumulate Y_{356}^\bullet . The absence of activity under the different experimental conditions described above suggests that E_{350} is essential to catalysis in all mutant RNRs in a manner that is not related to PT. One possible explanation for the data is that E_{350} plays a role in the protein conformational change that initiates RT in the class Ia RNR.²² This conformational change occurs upon substrate/effector (S/E) binding to α_2 and is proposed to be related to the initial PT step from $Fe1-H_2O$ to Y_{122}^\bullet that occurs concomitant with ET from Y_{356} to Y_{122}^\bullet .³³ In Chapter 4, we proposed that PT and ET are uncoupled in the $Y_{122}(2,3,5)F_3Y-\beta_2$ system, resulting in the formation of 2,3,5- F_3Y^\bullet during RT. This uncoupling allows $Y_{122}(2,3,5)F_3Y-\beta_2$ to partially overcome conformational gating; Y_{356}^\bullet and dCDP are generated at rate constants of 20–30 s^{-1} ,¹⁴ whereas, turnover in the wt system occurs at 2–10 s^{-1} .²² We speculated that partial removal of conformational gating with this probe might facilitate observation of Y_{356}^\bullet in the reaction of $Y_{122}(2,3,5)F_3Y/E_{350}D-\beta_2$, α_2 , CDP and ATP.

$Y_{122}(2,3,5)F_3Y/E_{350}D-\beta_2$ was expressed, purified and reconstituted as described in Chapter 3. The reaction of $Y_{122}(2,3,5)F_3Y/E_{350}D-\beta_2$, wt- α_2 , CDP and ATP was monitored by RFQ-EPR spectroscopy and the EPR spectra at different time points are shown in Figure 5.8A. No changes were observed in the total amount of radical (0.5 F_3Y^\bullet/β_2) and no variations were seen in spectral features between 16 ms and 535 ms. Subtraction of 2,3,5- F_3Y^\bullet from any of the composite spectra

(Figure 5.8B) revealed the spectrum in black (inset), which does not resemble that of Y_{356}^{\bullet} ^{13,14,28} (shown in Figure 5.8C for comparison). These results contrast with our observations for the single mutant, $Y_{122}(2,3,5)F_3Y$ - $\beta 2$, where 50% Y_{356}^{\bullet} accumulates within 100 ms (Figure 3.3, Chapter 3). The data support that $2,3,5-F_3Y^{\bullet}$ cannot oxidize Y_{356} when E_{350} is mutated.

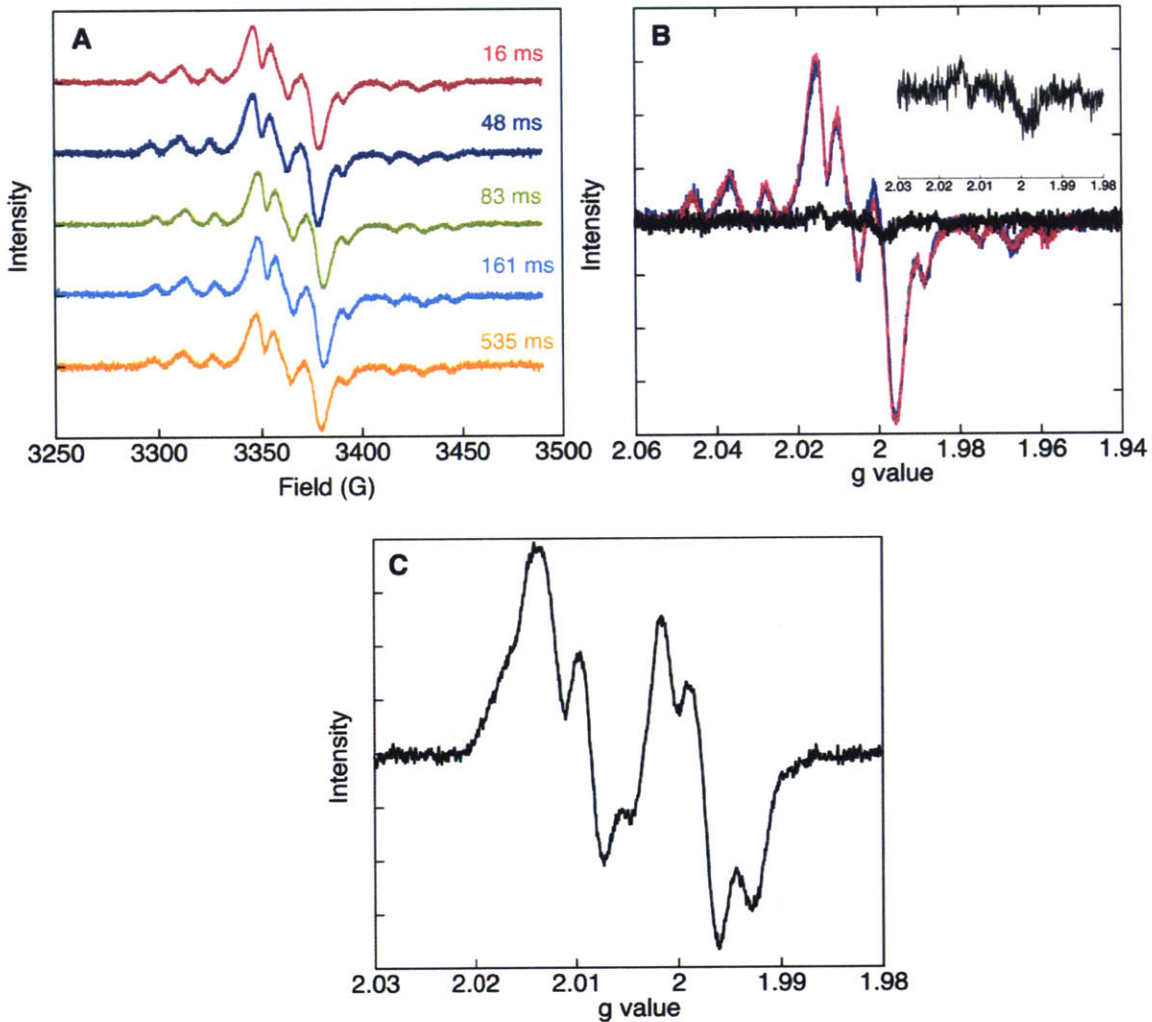


Figure 5.8 Reaction of $Y_{122}(2,3,5)F_3Y/E_{350}D$ - $\beta 2$, wt- $\alpha 2$, CDP and ATP monitored by RFQ-EPR spectroscopy. A. The composite EPR spectra recorded at the indicated time points. B. Subtraction of $2,3,5-F_3Y^{\bullet}$ (blue) from the composite spectrum at 16 ms (pink) reveals the spectrum in black (inset). C. Spectrum of Y_{356}^{\bullet} observed in the reaction of $Y_{122}(2,3,5)F_3Y$ - $\beta 2$, $\alpha 2$, CDP and ATP (Chapter 3).¹⁴

5.3.7 Reaction of $Y_{122}NO_2Y/E_{350}D-\beta 2$, wt- $\alpha 2$, CDP and ATP does not accumulate $Y_{356}\bullet$ or $W^{+\bullet}$. Similarly to the $Y_{122}(2,3,5)F_3Y-\beta 2$ system, $Y_{122}NO_2Y-\beta 2$ is a RT driving force modulator that accumulates $Y_{356}\bullet$ when reacted with $\alpha 2$, CDP and ATP.¹³ Upon binding of S/E to $\alpha 2$, uncoupled PT and ET in this system results in generation of NO_2Y^- concomitant with oxidation of Y_{356} . Rate constants of 100–300 s⁻¹ are measured for dCDP and $Y_{356}\bullet$ formation, and in Chapter 4 we proposed that these rate constants directly report on the thermodynamic effect of replacing Y_{122} with NO_2Y . The negative results observed with $Y_{122}(2,3,5)F_3Y/E_{350}D-\beta 2$ suggest that radical initiation does not occur when E_{350} is mutated. We investigated the reaction of $Y_{122}NO_2Y/E_{350}D-\beta 2$, $\alpha 2$, CDP and ATP with the following expectations; (i) If E_{350} is involved only in the conformational change that targets PT from Fe1-H₂O and not in PT at Y_{356} , $Y_{356}\bullet$ should accumulate in the reaction. We have previously shown that the reaction of the double mutant $Y_{122}NO_2Y/Y_{356}F-\beta 2$ with $\alpha 2$, CDP and ATP generates multiple $W^{+\bullet}$ s as a result of off-pathway oxidation (Yokoyama, Stubbe unpublished results); (ii) If E_{350} is involved in the conformational change that targets PT from Fe1-H₂O and in PT at Y_{356} , then $Y_{122}NO_2Y/E_{350}D-\beta 2$ should behave in an identical fashion to $Y_{122}NO_2Y/Y_{356}F-\beta 2$, i.e $W^{+\bullet}$ formation should be observed. As stated earlier, RT in the $Y_{122}NO_2Y-\beta 2$ system is triggered by S/E binding to $\alpha 2$; (iii) As a third outcome we anticipated that if E_{350} is involved in this communication between the two subunits that initiates RT, then no radicals will be visualized in the reaction of $Y_{122}NO_2Y/E_{350}D-\beta 2$ with $\alpha 2$, CDP and ATP.

The reaction of $Y_{122}NO_2Y/E_{350}D-\beta 2$, $\alpha 2$, CDP and ATP was performed using a three-syringe mixing protocol as described in section 5.2.12. Figure 5.9A shows the EPR spectra of the reaction mixtures quenched at the time points indicated in the panel. No changes were observed in the total amount of radical (1.1–1.2 $NO_2Y\bullet/\beta 2$) and no variations were seen in spectral features

between 16 ms and 131 ms. The EPR spectrum of $\text{NO}_2\text{Y}\cdot$ (blue, Figure 5.9B) was subtracted from each of the composite spectra. As an example, Figure 5.9B shows the subtraction analysis on the 16 ms sample (pink). The net spectrum (black) does not resemble $\text{Y}_{356}\cdot$ (Figure 5.8C) or W^{++} (Figure 5.9C). These results confirm the requirement of E_{350} in initiation of RT.

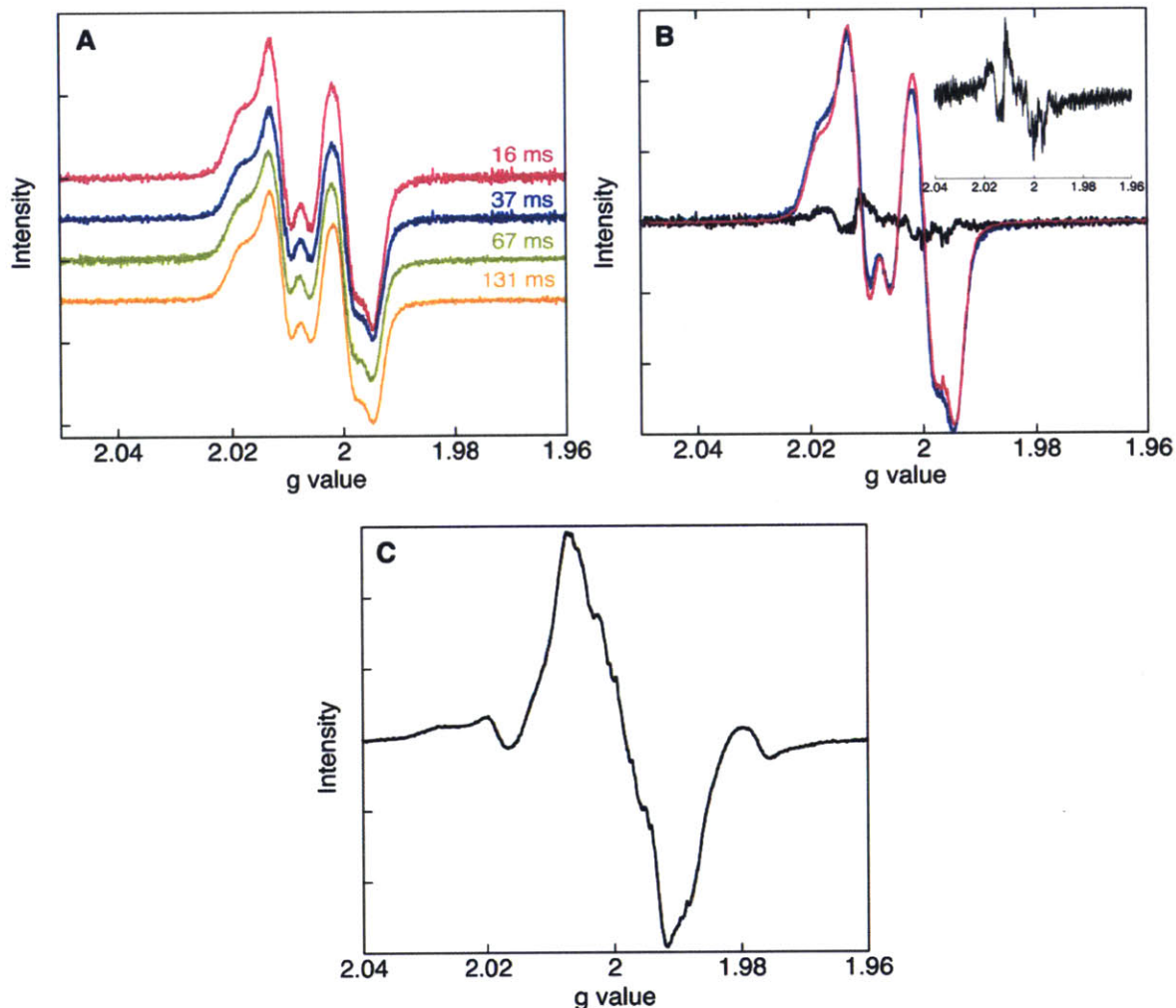


Figure 5.9 Reaction of $\text{Y}_{122}\text{NO}_2\text{Y}/\text{E}_{350}\text{D-}\beta 2$, $\text{wt-}\alpha 2$, CDP and ATP monitored by RFQ-EPR spectroscopy. A. The composite EPR spectra collected at the indicated time points. B. Subtraction of $\text{NO}_2\text{Y}\cdot$ (blue) from the composite spectrum at 16 ms (pink) produces the spectrum in black (inset). C. Spectrum of W^{++} recorded in the reaction of $\text{Y}_{122}\text{NO}_2\text{Y}/\text{Y}_{356}\text{F-}\beta 2$, $\text{wt-}\alpha 2$, CDP and ATP (Yokoyama, Stubbe unpublished results). The spectrum of $\text{Y}_{356}\cdot$ generated by the single mutant ($\text{Y}_{122}\text{NO}_2\text{Y-}\beta 2$) is identical to that shown in Figure 5.8C.

5.4 DISCUSSION

Generation of $Y\bullet$ at physiological pH involves the loss of a proton and an electron.³⁴ Recent studies have identified that a water molecule on the diferric cluster functions as the PT partner for Y_{122} ,³³ whereas Y_{731} functions in this role for Y_{730} .³⁵ However, the identities of the proton acceptors for Y_{356} and Y_{731} at the β/α interface have remained a mystery. Others and we have hypothesized that E_{350} could function as the proton acceptor for Y_{356} ,^{1,8} a hypothesis largely driven by its conservation in sequences of all class Ia RNRs. Initial site-directed mutagenesis studies supported the importance of this residue to RNR function, but absence of activity precluded mechanistic conclusions about the involvement of E_{350} in PT.⁸

Our ability to uncover details of radical propagation using non-canonical amino acids^{12-14,28} provided several alternate ways to investigate the role of E_{350} in the *E. coli* enzyme. With the experiments described in this Chapter, we showed that E_{350} plays at least two major roles during catalysis; it is involved in subunit interaction and in a conformational change that triggers RT. These two functions of E_{350} could be related; structural information about the β/α interface is critical to assess how changes in this region affect radical initiation at $Y_{122}\bullet$. Recent work in the lab suggests that E_{350} 's role at the subunit interface could be electrostatic in nature. Mutation of this residue increases the K_d for subunit interaction by ~10-fold. Similarly, our lab has shown that mutation of a residue in $\alpha 2$ close to the subunit interface, R_{411} , to A also increases the K_d for subunit interaction by 10-fold.³⁶ Taken together, these studies suggest that electrostatics may play a role at the interface, although subunit interaction is largely governed by the hydrophobic C-terminal tail of $\beta 2$ (residues 360–375).⁷ We also note that a purely electrostatic role for E_{350} cannot explain why mutation of this residue to D affects subunit affinity. Following the observations made

for E₃₅₀ and R₄₁₁, we have begun identifying other conserved charged residues that affect subunit interaction and turnover (Lin, Shao unpublished results).

The structural role that E₃₅₀ plays in triggering RT remains less understood. A conformational change associated with PT to Y₁₂₂• from Fe1-H₂O has been identified as one of the changes that initiates RT.³³ In the case of Y₁₂₂(2,3,5)F₃Y-β2 and Y₁₂₂NO₂Y-β2, we postulate that conformational gating can be overcome by uncoupling PT from ET and generating F₃Y⁻ or NO₂Y⁻; this phenomenon allows us to directly monitor the effect of reduction potential on RT kinetics (Chapter 4). However, it should be noted that only one of the conformational changes that triggers RT has been removed in these systems; at least in the case of Y₁₂₂NO₂Y-β2, we have shown that chemistry can only occur upon CDP binding to α2.¹³ This observation suggests the presence at least one additional conformational change that allows communication between α2 and β2 and dictates initiation of RT. This conclusion is supported by previous studies performed on DOPA-³⁷ and NH₂Y-RNRs¹² that have shown that S is directly responsible for triggering RT, whereas E can modulate the efficiency of the process. It is currently unknown how the conformational change in α2 is translated to the diferric cluster site in β2, but is likely that this mechanism involves communication via the β/α interface where E₃₅₀ is located. The observation that a single glutamate can control conformational dynamics over a long distance is not unique to RNR and has been previously noted in EmrE, an *E. coli* drug efflux pump that couples extrusion of lethal compounds to the influx of protons.³⁸ EmrE toggles between two major conformational states during efflux, and it has been shown that the protonation state of an active site glutamate (E₁₄) controls the interconversion between the two states.³⁹ In fact, the conformational changes that occur upon changing the protonation state of E₁₄ are translated as far as 25 Å from the active site, demonstrating long-range allosteric control by the residue.³⁹ Furthermore, mutation of E₁₄

(pK_a 6.8–8.5) to D lowers the pK_a of this residue by ~ 2 units,⁴⁰ attenuates the conformational change³⁹ and ultimately results in lowered efflux activity. It is possible that E₃₅₀ plays a similar role in RNR, where its protonation state controls the conformational dynamics that are required for RT. This model could also explain why mutation of E₃₅₀ to D abolishes nucleotide reduction activity.

The involvement of E₃₅₀ in subunit interaction and in protein conformational changes precludes assessment of its importance to PT during PCET across the β/α interface. The Nocera and Stubbe labs have recently developed a photochemical RNR in which a [Re^I] photooxidant at position 355 in $\beta 2$ can directly oxidize Y₃₅₆ and inject into the RT pathway in $\alpha 2$.^{41,42} The ability of photo RNR to bypass the protein conformational gate that triggers RT in native RNR could afford the opportunity to disentangle E₃₅₀'s involvement in PT from its structural role in RNR function.

5.5 REFERENCES

1. Stubbe, J.; Nocera, D. G.; Yee, C. S.; Chang, M. C. Y. Radical initiation in the class I ribonucleotide reductase: long-range proton-coupled electron transfer?, *Chem. Rev.* **2003**, *103*, 2167-2201.
2. Minnihhan, E. C.; Nocera, D. G.; Stubbe, J. Reversible, long-range radical transfer in *E. coli* class Ia ribonucleotide reductase, *Acc. Chem. Res.* **2013**, *46*, 2524-2535.
3. Uhlin, U.; Eklund, H. Structure of ribonucleotide reductase protein R1, *Nature* **1994**, *370*, 533-539.
4. Nordlund, P.; Sjöberg, B. M.; Eklund, H. Three-dimensional structure of the free radical protein of ribonucleotide reductase, *Nature* **1990**, *345*, 593-598.
5. Högbom, M.; Galander, M.; Andersson, M.; Kolberg, M.; Hofbauer, W.; Lassmann, G.; Nordlund, P.; Lendzian, F. Displacement of the tyrosyl radical cofactor in ribonucleotide reductase obtained by single-crystal high-field EPR and 1.4 Å X-ray data, *Proc. Natl. Acad. Sci. U. S. A.* **2003**, *100*, 3209-3214.
6. Logan, D. T.; Su, X. D.; Aberg, A.; Regnström, K.; Hajdu, J.; Eklund, H.; Nordlund, P. Crystal structure of reduced protein R2 of ribonucleotide reductase: the structural basis for oxygen activation at a dinuclear iron site, *Structure* **1996**, *4*, 1053-1064.
7. Climent, I.; Sjöberg, B. M.; Huang, C. Y. Carboxyl-terminal peptides as probes for *Escherichia coli* ribonucleotide reductase subunit interaction: kinetic analysis of inhibition studies, *Biochemistry* **1991**, *30*, 5164-5171.
8. Climent, I.; Sjöberg, B. M.; Huang, C. Y. Site-directed mutagenesis and deletion of the carboxyl terminus of *Escherichia coli* ribonucleotide reductase protein R2 - effects on catalytic activity and subunit interaction, *Biochemistry* **1992**, *31*, 4801-4807.
9. Aberg, A.; Hahne, S.; Karlsson, M.; Larsson, A.; Ormö, M.; Ahgren, A.; Sjöberg, B. M. Evidence for two different classes of redox-active cysteines in ribonucleotide reductase of *Escherichia coli*, *J. Biol. Chem.* **1989**, *264*, 12249-12252.
10. Minnihhan, E. C. Mechanistic studies of proton-coupled electron transfer in aminotyrosine- and fluorotyrosine-substituted class Ia ribonucleotide reductase. Ph.D. Thesis, Massachusetts Institute of Technology, **2012**.
11. Tong, W. H.; Chen, S.; Lloyd, S. G.; Edmondson, D. E.; Huynh, B. H.; Stubbe, J. Mechanism of assembly of the diferric cluster-tyrosyl radical cofactor of *Escherichia coli* ribonucleotide reductase from the diferrous form of the R2 subunit, *J. Am. Chem. Soc.* **1996**, *118*, 2107-2108.
12. Minnihhan, E. C.; Seyedsayamdost, M. R.; Uhlin, U.; Stubbe, J. Kinetics of radical intermediate formation and deoxynucleotide production in 3-aminotyrosine-substituted *Escherichia coli* ribonucleotide reductases, *J. Am. Chem. Soc.* **2011**, *133*, 9430-9440.
13. Yokoyama, K.; Uhlin, U.; Stubbe, J. A hot oxidant, 3-NO₂Y₁₂₂ radical, unmasks conformational gating in ribonucleotide reductase, *J. Am. Chem. Soc.* **2010**, *132*, 15368-15379.

14. Ravichandran, K. R.; Minnihan, E. C.; Wei, Y.; Nocera, D. G.; Stubbe, J. Reverse electron transfer completes the catalytic cycle in a 2,3,5-trifluorotyrosine-substituted ribonucleotide reductase, *J. Am. Chem. Soc.* **2015**, *137*, 14387-14395.
15. Seyedsayamdost, M. R.; Xie, J.; Chan, C. T.; Schultz, P. G.; Stubbe, J. Site-specific insertion of 3-aminotyrosine into subunit $\alpha 2$ of *E. coli* ribonucleotide reductase: direct evidence for involvement of Y₇₃₀ and Y₇₃₁ in radical propagation, *J. Am. Chem. Soc.* **2007**, *129*, 15060-15071.
16. Kim, K.; Cole, P. A. Kinetic analysis of a protein tyrosine kinase reaction transition state in the forward and reverse directions, *J. Am. Chem. Soc.* **1998**, *120*, 6851-6858.
17. Yee, C. S.; Chang, M. C. Y.; Ge, J.; Nocera, D. G.; Stubbe, J. 2,3-difluorotyrosine at position 356 of ribonucleotide reductase R2: A probe of long-range proton-coupled electron transfer, *J. Am. Chem. Soc.* **2003**, *125*, 10506-10507.
18. Seyedsayamdost, M. R.; Reece, S. Y.; Nocera, D. G.; Stubbe, J. Mono-, di-, tri-, and tetra-substituted fluorotyrosines: new probes for enzymes that use tyrosyl radicals in catalysis, *J. Am. Chem. Soc.* **2006**, *128*, 1569-1579.
19. Seyedsayamdost, M. R.; Yee, C. S.; Reece, S. Y.; Nocera, D. G.; Stubbe, J. pH rate profiles of F_nY₃₅₆-R2s (n = 2, 3, 4) in *Escherichia coli* ribonucleotide reductase: evidence that Y₃₅₆ is a redox-active amino acid along the radical propagation pathway, *J. Am. Chem. Soc.* **2006**, *128*, 1562-1568.
20. Yokoyama, K.; Uhlin, U.; Stubbe, J. Site-specific incorporation of 3-nitrotyrosine as a probe of pK_a perturbation of redox-active tyrosines in ribonucleotide reductase, *J. Am. Chem. Soc.* **2010**, *132*, 8385-8397.
21. Ravichandran, K. R.; Liang, L.; Stubbe, J.; Tommos, C. Formal reduction potential of 3,5-difluorotyrosine in a structured protein: insight into multistep radical transfer, *Biochemistry* **2013**, *52*, 8907-8915.
22. Ge, J.; Yu, G.; Ator, M. A.; Stubbe, J. Pre-steady-state and steady-state kinetic analysis of *E. coli* class I ribonucleotide reductase, *Biochemistry* **2003**, *42*, 10071-10083.
23. Olshansky, L. Kinetics and dynamics controlling proton-coupled electron transfer in ribonucleotide reductase. Ph.D. Thesis, Massachusetts Institute of Technology, **2015**.
24. Chivers, P. T.; Prehoda, K. E.; Volkman, B. F.; Kim, B. M.; Markley, J. L.; Raines, R. T. Microscopic pK_a values of *Escherichia coli* thioredoxin, *Biochemistry* **1997**, *36*, 14985-14991.
25. Russel, M.; Model, P. Direct cloning of the *trxB* gene that encodes thioredoxin reductase, *J. Bacteriol.* **1985**, *163*, 238-242.
26. Artin, E. Mechanistic studies of the class I ribonucleotide reductase from *Escherichia coli*. Ph.D. Thesis, Massachusetts Instituted of Technology, **2006**.
27. Steeper, J. R.; Steuart, C. D. A rapid assay for CDP reductase activity in mammalian cell extracts, *Anal. Biochem.* **1970**, *34*, 123-130.

28. Minnihhan, E. C.; Young, D. D.; Schultz, P. G.; Stubbe, J. Incorporation of fluorotyrosines into ribonucleotide reductase using an evolved, polyspecific aminoacyl-tRNA synthetase, *J. Am. Chem. Soc.* **2011**, *133*, 15942-15945.
29. Thelander, L.; Sjöberg, B. M.; Eriksson, S. Ribonucleoside diphosphate reductase (*Escherichia coli*), *Methods. Enzymol.* **1978**, *51*, 227-237.
30. Salowe, S. P.; Ator, M. A.; Stubbe, J. Products of the inactivation of ribonucleoside diphosphate reductase from *Escherichia coli* with 2'-azido-2'-deoxyuridine 5'-diphosphate, *Biochemistry* **1987**, *26*, 3408-3416.
31. Salowe, S.; Bollinger, J. M., Jr.; Ator, M.; Stubbe, J.; McCracken, J.; Peisach, J.; Samano, M. C.; Robins, M. J. Alternative model for mechanism-based inhibition of *Escherichia coli* ribonucleotide reductase by 2'-azido-2'-deoxyuridine 5'-diphosphate, *Biochemistry* **1993**, *32*, 12749-12760.
32. Fritscher, J.; Artin, E.; Wnuk, S.; Bar, G.; Robblee, J. H.; Kacprzak, S.; Kaupp, M.; Griffin, R. G.; Bennati, M.; Stubbe, J. Structure of the nitrogen-centered radical formed during inactivation of *E. coli* ribonucleotide reductase by 2'-azido-2'-deoxyuridine-5'-diphosphate: trapping of the 3'-ketonucleotide, *J. Am. Chem. Soc.* **2005**, *127*, 7729-7738.
33. Wörsdorfer, B.; Conner, D. A.; Yokoyama, K.; Livada, J.; Seyedsayamdost, M.; Jiang, W.; Silakov, A.; Stubbe, J.; Bollinger, J. M., Jr.; Krebs, C. Function of the diiron cluster of *Escherichia coli* class Ia ribonucleotide reductase in proton-coupled electron transfer, *J. Am. Chem. Soc.* **2013**, *135*, 8585-8593.
34. Reece, S. Y.; Hodgkiss, J. M.; Stubbe, J.; Nocera, D. G. Proton-coupled electron transfer: the mechanistic underpinning for radical transport and catalysis in biology, *Philos. Trans. R. Soc. Lond. B Biol. Sci.* **2006**, *361*, 1351-1364.
35. Nick, T.; Lee, W.; Kossmann, S.; Neese, F.; Stubbe, J.; Bennati, M. Hydrogen bond network between amino acid radical intermediates on the proton-coupled electron transfer pathway of *E. coli* $\alpha 2$ ribonucleotide reductase, *J Am Chem Soc* **2015**, *137*, 289-298.
36. Kasanmascheff, M.; Lee, W.; Nick, T.; Stubbe, J.; Bennati, M. Radical transfer in *E. coli* ribonucleotide reductase: a NH₂Y₇₃₁/R₄₁₁- α mutant unmasks a new conformation of the pathway residue 731, *Chem. Sci.* **2016**, *7*, 2170-2178.
37. Seyedsayamdost, M. R.; Stubbe, J. Site-specific replacement of Y₃₅₆ with 3,4-dihydroxyphenylalanine in the $\beta 2$ subunit of *E. coli* ribonucleotide reductase, *J. Am. Chem. Soc.* **2006**, *128*, 2522-2523.
38. Grinius, L. L.; Goldberg, E. B. Bacterial multidrug resistance is due to a single membrane protein which functions as a drug pump, *J. Biol. Chem.* **1994**, *269*, 29998-30004.
39. Gayen, A.; Leninger, M.; Traaseth, N. J. Protonation of a glutamate residue modulates the dynamics of the drug transporter EmrE, *Nat. Chem. Biol.* **2015**, *12*, 141-145.
40. Muth, T. R.; Schuldiner, S. A membrane-embedded glutamate is required for ligand binding to the multidrug transporter EmnR, *EMBO J.* **2000**, *19*, 234-240.
41. Pizano, A. A.; Olshansky, L.; Holder, P. G.; Stubbe, J.; Nocera, D. G. Modulation of Y356 photooxidation in *E. coli* class Ia ribonucleotide reductase by Y731 across the $\alpha 2$: $\beta 2$ interface, *J Am Chem Soc.* **2013**, *135*, 13250-13253.

42. Olshansky, L.; Pizano, A. A.; Wei, Y.; Stubbe, J.; Nocera, D. G. Kinetics of hydrogen atom abstraction from substrate by an active site thiyl radical in ribonucleotide reductase, *J. Am. Chem. Soc.* **2014**, *136*, 16210-16216.

Chapter 6

Chemical steps required to generate a stable $\alpha_2\beta_2$ complex

6.1 INTRODUCTION

RNR synthesizes all four dNDPs from their corresponding NDPs and controls both the absolute numbers and relative ratios of dNDPs inside the cell.^{1,2} The active form of the *E. coli* class Ia RNR is generally accepted to be an $\alpha_2\beta_2$ complex.³⁻⁶ However, the interaction between the two subunits is relatively weak ($K_d = 0.2 \mu\text{M}$),^{3,7} precluding crystallization of the active complex. The highest resolution structure of the complex that is currently available is a docking model created by Uhlin and Eklund based on the individual crystal structures of α_2 and β_2 .⁴ Unfortunately, this model contains no structural information for residues 340–360 of the β_2 C-terminal tail within which Y₃₅₆, a key player in mediating PCET across the β/α interface, is located (Chapters 3 and 4). Recently, we showed that subunit affinity increases ($K_d = 7 \text{ nM}$) when an unnatural 3-aminotyrosyl radical ($\text{NH}_2\text{Y}\bullet$) is trapped at position 730 in α_2 .⁶ In this Chapter, we aim to understand which chemical steps are responsible for stabilizing the $\alpha_2\beta_2$ complex with the ultimate goal of obtaining a high resolution structure of the active complex that can provide insight into PCET across the β/α interface.

Seminal analytical ultracentrifugation (AUC) experiments performed by Reichard and coworkers³ and later on by Thelander⁸ provided the first evidence for an active 1:1 complex of the form $\alpha_2\beta_2$ in the *E. coli* class Ia RNR. These studies together with crystallographic information for α_2 and β_2 , led Uhlin and Eklund to propose the docking model for $\alpha_2\beta_2$.⁴ Although a structure of the active complex remains elusive, extensive evidence for formation of $\alpha_2\beta_2$ has been obtained using a variety of biophysical approaches. In one set of experiments, small-angle X-ray scattering (SAXS)⁹ studies demonstrate that the *E. coli* enzyme can exist in three interconverting states in solution: $\alpha_2 + \beta_2 \rightleftharpoons \alpha_2\beta_2 \rightleftharpoons \alpha_4\beta_4$, the relative populations of which are dependent on protein concentration, and the nature and concentration of the nucleotide. DeoxyATP binding to the

activity site induces formation of an inactive $\alpha 4\beta 4$ ring that has been well characterized structurally.^{9,10} It has been suggested that high protein concentrations ($> 10 \mu\text{M}$) can also convert the active $\alpha 2\beta 2$ into the inactive $\alpha 4\beta 4$ state.⁹ Most importantly, however, SAXS curves obtained at low protein concentrations and in the presence of CDP suggest that the major species under these conditions is $\alpha 2\beta 2$.

Strong support for formation of an $\alpha 2\beta 2$ complex has also been provided by pulsed electron electron double resonance (PELDOR) spectroscopy experiments^{5,11,12} that utilize our ability to trap radicals at different positions on pathway. As described in Chapter 3, radical distribution in $\beta 2$ is proposed to follow a two or none model where active $\beta 2$ contains a $\text{Y}\cdot$ in each monomer. Additionally, half-sites reactivity of $\beta 2$ dictates that only one of the two $\text{Y}\cdot$ s reacts at a time. The reaction of $\beta 2$ and $\alpha 2$ with a mechanism-based inhibitor, 2'-azido-2'-deoxycytidine-5'-diphosphate (N_3CDP), generates a covalent $\alpha 2$ active site radical abbreviated as $\text{N}\cdot$.¹³ PELDOR spectroscopy measured a distance of 48 Å between $\text{N}\cdot$ in one α/β pair and the unreacted $\text{Y}_{122}\cdot$ in the second α/β pair,⁵ consistent with the distance predicted by the docking model. Similar PELDOR studies performed on $\text{DOPA}\cdot$ or $\text{NH}_2\text{Y}\cdot$ ^{14,15} trapped at different positions on pathway have provided distance measurements for Y_{356} , Y_{731} and Y_{730} .¹¹ The distances recorded for Y_{731} and Y_{730} (38–39 Å) further affirmed formation of an $\alpha 2\beta 2$ complex, whereas that for Y_{356} set the first structural constraint on its location in the active complex.

More recently, we took advantage of the ability to trap a kinetically competent $\text{NH}_2\text{Y}\cdot$ at position Y_{730} ^{15,16} to show generation of a kinetically stable $\alpha 2\beta 2$ complex upon $\text{NH}_2\text{Y}\cdot$ formation.⁶ Competitive inhibition spectrophotometric assays⁷ demonstrated that the K_d for the $\text{Y}_{730}\text{NH}_2\text{Y}\cdot$ - $\alpha 2/\beta 2$ interaction (7–17 nM)⁶ is 10–30-fold lower than wt $\alpha 2/\beta 2$ (0.2 μM).⁷ SF and steady-state fluorescence experiments supported formation of a tight $\text{Y}_{730}\text{NH}_2\text{Y}\cdot$ - $\alpha 2/\beta 2$ complex, and the k_{off}

for the complex was measured to be $\sim 10^4$ slower than wt $\alpha 2/\beta 2$.⁶ Lastly, generation of this tight $\alpha 2\beta 2$ complex allowed its first observation by negative stain electron microscopy (EM). The EM images demonstrated a compact $\alpha 2\beta 2$ that resembled the docking model put forth by Uhlin and Eklund from the individual crystal structures of $\alpha 2$ and $\beta 2$.^{4,17} Taken together, the data supported formation of a kinetically stable $\alpha 2\beta 2$ complex that is dependent on the generation of $\text{NH}_2\text{Y}\cdot$. These initial studies laid the foundation for the work described herein, which is aimed at understanding the chemical basis for the generation of the tight complex.

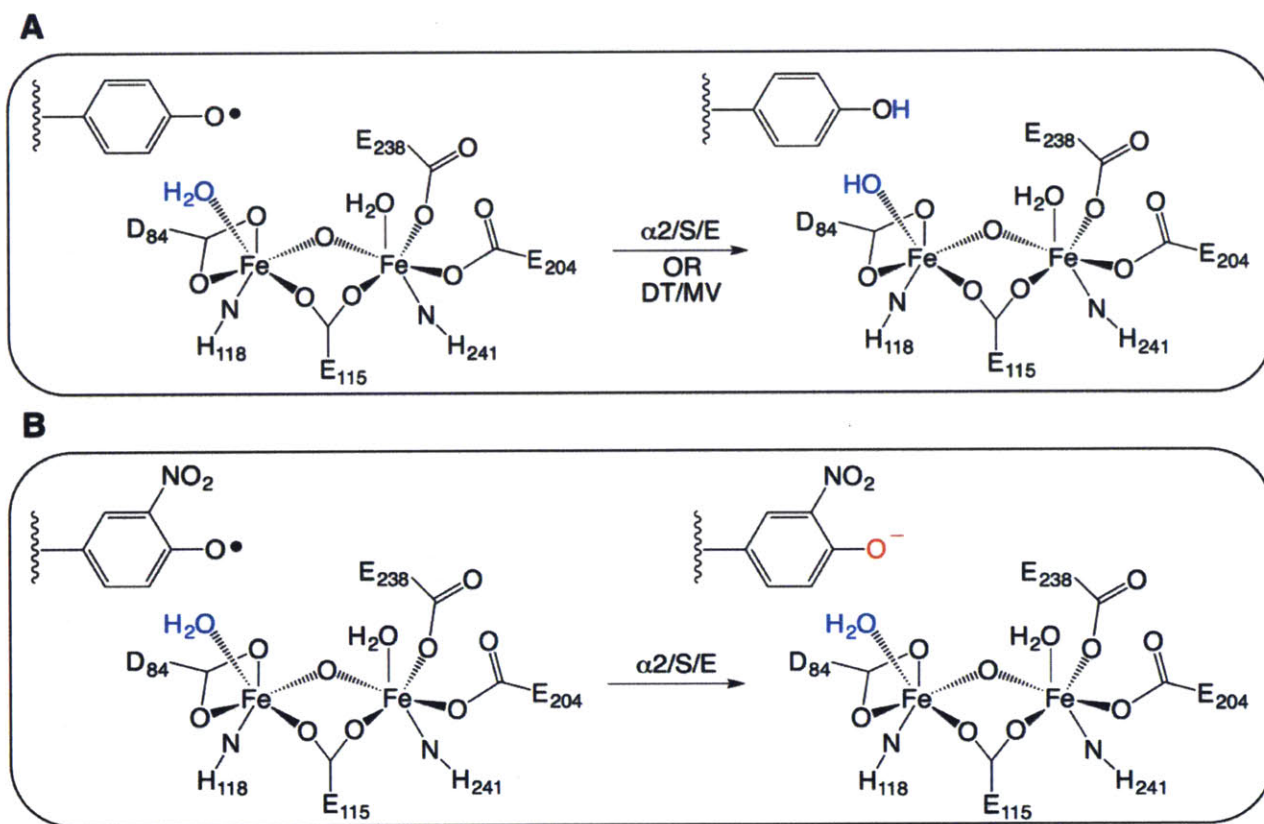


Figure 6.1 Conditions under which a stable $\alpha 2\beta 2$ complex can be generated. A. Alteration of the diferric cluster charge by one unit upon RT (in the presence of $\alpha 2$, substrate (S) and effector (E)) or by reduction of the cluster with dithionite (DT) and methyl viologen (MV). B. Alteration of the Y₁₂₂ charge by one unit upon initiation of RT with $\text{NO}_2\text{Y}\cdot$. The cluster remains neutral.

Two primary questions are addressed in this chapter. First, we originally hypothesized⁶ that formation of a tight complex is a phenomenon common to any condition under which a pathway

radical intermediate accumulates. In the current work, this hypothesis is tested in the reaction of $\alpha 2/Y_{122}NO_2Y-\beta 2$, which generates a kinetically competent $Y_{356}\bullet^{18}$ and in the reaction of wt $\alpha 2/\beta 2$ with $N_3CDP^{13,19}$ which generates $N\bullet$. In both cases, nickel-nitrilotriacetic acid (Ni-NTA) pull-down assays show formation of a stable $\alpha 2\beta 2$ complex compared to the wt $\alpha 2/\beta 2/CDP/ATP$ control reaction. These preliminary studies suggest that our original hypothesis holds true and that a stable $\alpha 2\beta 2$ complex can be generated under any conditions where a pathway radical intermediate accumulates.

The second question that we aimed to address is the identity of the chemical steps that need to occur to generate a tight $\alpha 2\beta 2$ complex. In the case of $Y_{730}NH_2Y-\alpha 2$, catalysis includes the protein conformational change(s) that precedes radical transport (RT), the PCET steps that transport the oxidant from Y_{122} to C_{439} , nucleotide reduction in the active site of $\alpha 2$ and reverse RT that regenerates $Y_{122}\bullet$.¹⁶ To investigate which of these transformations are required to form a stable $\alpha 2\beta 2$ complex, we systematically block each step in catalysis and probe for tight complex formation using Ni-NTA pull-down assays. The results together provide a model where introduction of a negative charge into the neutral diferric- $Y\bullet$ site is the only step required to form a stable $\alpha 2\beta 2$ complex (Figure 6.1). This negative charge can be generated in one of two ways. Conversion of the neutral $Fe1-H_2O$ cluster state to the $Fe1-OH$ state (Figure 6.1A) forms a tight complex; this transformation typically occurs upon RT but can also be artificially produced by reduction of the diferric- $Y\bullet$ cofactor with an electron from DT.²⁰ Alternatively, initiation of RT with the unnatural $NO_2Y\bullet$ that generates NO_2Y^- can also make a stable $\alpha 2\beta 2$ complex (Figure 6.1B). The results described in this work provide a model where electrostatics at the diferric- $Y\bullet$ site partially control subunit affinity. This model makes several predictions that are outlined in this

Chapter and can be readily tested. The proposal for tight complex formation in the *E. coli* class Ia RNR may function as a general strategy for capturing the active complexes of other class I systems.

6.2 MATERIALS AND METHODS

6.2.1 Materials. Wt- $\beta 2^{21}$ (1.2 Y•/ $\beta 2$, 7000 nmol/min/mg), His₆- $\alpha 2^{16}$ and His₆-Y₇₃₁F- $\alpha 2^{16}$ were isolated as previously reported. Apo Y₁₂₂NO₂Y- $\beta 2^{18}$ and met- $\beta 2^{22}$ were prepared by Kenichi Yokoyama. N₃CDP was available from an earlier study.¹⁶ Ni-NTA agarose was purchased from Qiagen. DT, MV, CDP, ATP and imidazole were obtained from Sigma Aldrich. Assay buffer consists of 50 mM HEPES pH 7.6 and 15 mM MgSO₄. All pull-down assays were performed at 4 °C with buffers that were maintained on ice. Each experiment was conducted a single time with the exception of the DT/MV pull-down assay (section 6.2.5) which was performed in duplicate (see Appendix 7 for the results of the second trial).

6.2.2 Pull-down assay of Y₁₂₂NO₂Y- $\beta 2$ by His₆- $\alpha 2$. Apo Y₁₂₂NO₂Y- $\beta 2$ (100 μ L of 100 μ M) was deoxygenated and taken into the anaerobic chamber maintained at 4 °C. The protein was treated with 5 equiv. of Fe^{II}(NH₄)₂(SO₄)₂ and incubated for 15 min. Fe²⁺-Y₁₂₂NO₂Y- $\beta 2$ was brought out of the chamber sealed and reacted with 3.5 equiv. of O₂ in the form of O₂-saturated 50 mM HEPES pH 7.6, 5% glycerol to assemble the diferric-NO₂Y• cofactor. The reconstituted protein was immediately diluted to a final concentration of 5 μ M in a reaction mixture containing 5 μ M His₆- $\alpha 2$, 1 mM CDP and 3 mM ATP in assay buffer. The reaction mixture (300 μ L) was combined with a 200 μ L suspension of Ni-NTA resin that had been pre-equilibrated in assay buffer. The suspension was inverted 3–4 times and centrifuged (100 x g, 30 s). The supernatant was collected and the resin was washed twice with 600 μ L of assay buffer containing 300 mM NaCl and 15 mM imidazole (wash buffer). The wash fractions were collected by centrifugation (100 x g, 30 s) and the bound protein was eluted with 600 μ L of assay buffer containing 300 mM NaCl and 250 mM imidazole (elution buffer). The total time between initiation of the reaction and elution of the protein was 3.5 min. As a control reaction, the pull-down of $\beta 2$ (1.2 Y•/ $\beta 2$) by His₆-

$\alpha 2$ was assessed in an identical manner. The elution fractions from both reactions were concentrated 5-fold and analyzed by SDS-PAGE.

Quantitation of the relative amounts of $\alpha 2$ and $\beta 2$ in each reaction was performed by densitometry analysis. The elution fractions from each of the assays were loaded on a SDS-PAGE gel along with different amounts of His₆- $\alpha 2$ and $\beta 2$ (1–6 pmol of each) to prepare standard curves. After staining with Coomassie, protein bands were analyzed by densitometry (Quantity One version 4.4.0, Bio-Rad) using a background-subtracted pixel count for each band on the gel. Briefly, a rectangle was drawn around each protein band and the pixel density in each band was multiplied by the volume of the rectangle. This rectangle was copied and dragged to the nearest blank area of the gel, i.e. an area around that protein band where no staining occurred. The density of the background rectangle was quantitated similarly and subtracted from the pixel count determined for the protein band. Standard curves were constructed from the different amounts of His₆- $\alpha 2$ and $\beta 2$, and the elution samples for the pull-downs were compared to the standard curves to assess protein concentration. Three different volumes of each elution sample were loaded on the gel to assess the error associated with this quantitation method.

6.2.3 Pull-down assay of wt- $\beta 2$ by His₆- $\alpha 2$ in the presence of N₃CDP. The reaction mixture contained in a total volume of 120 μ L, 5 μ M each of His₆- $\alpha 2$ and wt- $\beta 2$, 250 μ M N₃CDP and 3 mM ATP in assay buffer. The reaction was initiated by the addition of His₆- $\alpha 2$, incubated on ice for 1 min and loaded onto a 70 μ L suspension of Ni-NTA resin in assay buffer. The pull down assay was performed as detailed in section 6.2.2 with minor variations. The resin was washed twice with 240 μ L of the wash buffer and the bound protein was eluted with 240 μ L of the elution buffer.

6.2.4 Pull-down assay of Y₁₂₂NO₂Y- $\beta 2$ by His₆-Y₇₃₁F- $\alpha 2$. The assay was performed as detailed in section 6.2.2 with a single exception: His₆- $\alpha 2$ was replaced with His₆-Y₇₃₁F- $\alpha 2$.

6.2.5 *Pull-down assay of DT/MV- β 2 by His₆-Y₇₃₁F- α 2.* Lyophilized 4X assay buffer (200 mM HEPES pH 7.6, 60 mM MgSO₄), a lyophilized solution of CDP/ATP (6 mM and 18 mM respectively), solid DT (16 mg) and solid MV (5 mg) were taken into the 4 °C anaerobic chamber where water or 50 mM HEPES pH 7.6 5% glycerol was added to dissolve each sample. A solution containing 50 μ M each of wt- β 2 (1.2 Y•/ β 2) and His₆-Y₇₃₁F- α 2 was deoxygenated and taken into the anaerobic chamber. In a total volume of 300 μ L, wt- β 2 (5 μ M), His₆-Y₇₃₁F- α 2 (5 μ M), CDP (1 mM), ATP (3 mM), DT (20 μ M) and MV (20 μ M) were combined. The solution was immediately brought out of the chamber and loaded onto a 200 μ L Ni-NTA suspension pre-equilibrated in assay buffer. The pull down assay was performed as described in section 6.2.2. As control experiments, either DT was omitted from the reaction mixture or met- β 2 (prepared by reduction of β 2 with hydroxyurea)²² was utilized instead of wt- β 2. The pull down assay was also repeated in the absence of CDP/ATP to assess the effect of S/E on subunit interaction.

6.3 RESULTS

6.3.1 Multiple turnovers are not required for generation of a stable $\alpha_2\beta_2$ complex. In the absence of an external reducing system, wt RNR is capable of generating a theoretical maximum of 4 dCDP/ α_2 , although only 3 dCDP/ α_2 are routinely observed due to partial oxidation of α_2 (Chapter 3).²³ In the case of $Y_{730}NH_2Y-\alpha_2$, we have previously shown that only 0.7 dCDP/ α_2 are formed in the absence of a reducing system.¹⁶ Standard RNR assays are typically performed with 1:1 $\alpha_2:\beta_2$ (1.2 $Y\cdot/\beta_2$). Owing to the “two or none” radical distribution model (Figure 3.2, Chapter 3) and half-sites reactivity in RNR,^{14,18,24} a single turnover by an α/β generates 0.5 dCDP/ $Y\cdot$ (or 0.6 dCDP/ α_2). The amount of product observed with $Y_{730}NH_2Y-\alpha_2$ (0.7 dCDP/ α_2) is close to that predicted for a single turnover (0.6 dCDP/ α_2), suggesting that $Y_{730}NH_2Y-\alpha_2$ may not be catalytically active for multiple turnovers. However, this result contradicts steady-state activity assays that have measured activities of 3–12% for the NH_2Y -RNRs compared to wt RNR.¹⁶ These numbers are higher than those predicted for contaminating wt RNR²⁵ and support the ability of this mutant enzyme to perform multiple turnovers. The basis for sub-stoichiometric product generation by $Y_{730}NH_2Y-\alpha_2$ in the absence of a reducing system is not understood. To avoid any ambiguity regarding the chemical steps required for generation of the tight complex, we turned to the $Y_{122}NO_2Y-\beta_2$ system. In this case, we have shown formation of a kinetically and chemically competent $Y_{356}\cdot$ that accumulates after a single turnover due to the inability of $Y_{356}\cdot$ to re-oxidize NO_2Y^- .¹⁸ With this system, we aimed to address if a single turnover is sufficient to generate a tight complex, but also if accumulation of a pathway radical at Y_{356} instead of at Y_{730} ($Y_{730}NH_2Y-\alpha_2$)¹⁵ can stabilize $\alpha_2\beta_2$.

The experimental design is similar to that previously reported.⁶ His₆-α2, Y₁₂₂NO₂Y-β2 (untagged), CDP and ATP were reacted in the absence of a reducing system to generate Y₃₅₆•. The reaction mixture was immediately loaded onto Ni-NTA agarose, quickly washed with buffer containing low concentrations of imidazole and the bound protein was eluted with a high concentration of imidazole to quantitate the amount of Y₁₂₂NO₂Y-β2 that co-elutes with His₆-α2. Due to the instability of NO₂Y• (t_{1/2} of 40 s at 25 °C)¹⁸ the pull-down reaction was performed immediately after reconstitution of the diferric-NO₂Y• cofactor as described in section 6.2.2. Formation of Y₃₅₆• by NO₂Y• is rapid (100–300 s⁻¹);¹⁸ thus, no incubation time was provided for the reaction mixture prior to loading onto the Ni-NTA resin. The total time between initiation of the reaction and elution of the protein was ~3.5 min. It is currently unknown how this time relates to the half-life of Y₃₅₆•. An identical reaction was also performed with wt-β2 (untagged) to examine the relative amount of wt-β2 that co-elutes with His₆-α2 under these conditions.

Figure 6.2A shows the SDS-PAGE analysis of different samples from the pull-down assays. A majority of His₆-α2 and β2 are lost in the flow-through (FT) and wash (W1) samples likely due to the brief incubation time of the proteins with the resin (<30 s) prior to centrifugation. However, a comparison of lane 4 (elution (E) for the control reaction) and lane 8 (E, Y₁₂₂NO₂Y-β2 reaction), reveals that more Y₁₂₂NO₂Y-β2 co-elutes with (His)₆-α2 than wt-β2. This variation between Y₁₂₂NO₂Y-β2 and wt-β2 is readily apparent when the E samples are concentrated 5-fold and re-analyzed by SDS-PAGE (Figure 6.2B).

To quantitate the amounts of α2 and β2 in each pull-down, standard curves were prepared from His₆-α2 and β2 (1–6 pmol each) and loaded onto a gel containing different amounts of the E samples (Figure 6.3). The concentration of α2 and β2 in each lane was quantitated by densitometry analysis (section 6.2.2), providing the ratios shown in Table 6.1. Under the experimental

conditions utilized for the pull-down (1:1 $\alpha_2:\beta_2$ with 1.2 $\text{NO}_2\text{Y}\cdot/\beta_2^{\text{viii}}$), the anticipated ratio of $\alpha_2:\beta_2$ is ~ 1.7 due to the presence of only 60% active β_2 (Chapter 3).²⁴ The ratio of $\alpha_2:\beta_2$ in the control reaction is ~ 8 . The residual wt- β_2 that co-elutes with His₆- α_2 is likely related to insufficient washing of the resin prior to elution of bound His₆- α_2 . In contrast to the control reaction, the ratio of $\alpha_2:\text{Y}_{122}\text{NO}_2\text{Y}\text{-}\beta_2$ was quantitated as 1.3 ± 0.1 , similar to the theoretical yield (1.7). These pull-down assays confirm that generation of a tight complex is not unique to $\text{NH}_2\text{Y}_{730}\cdot$, that a single turnover is sufficient to form a stable complex and that completion of the catalytic cycle is not a requirement for tight complex formation.

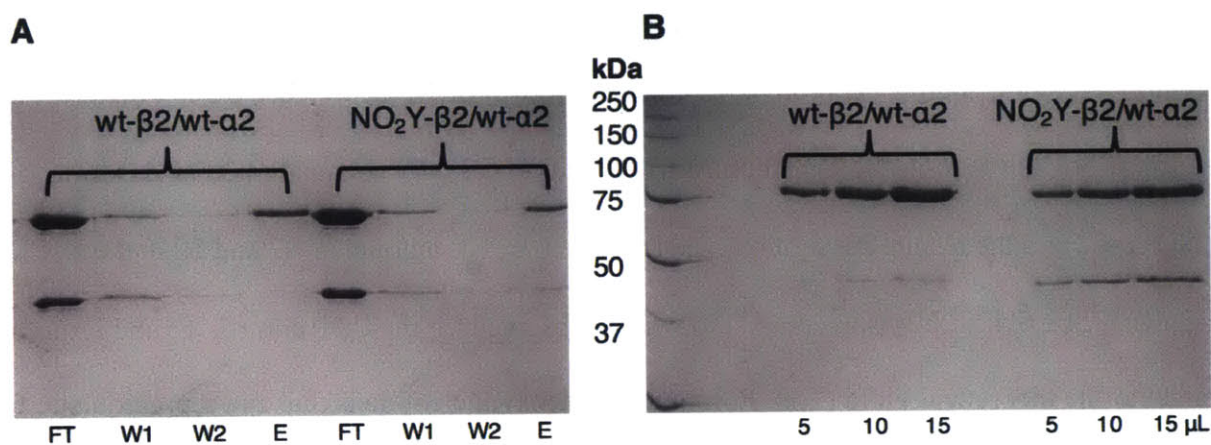


Figure 6.2 Pull-down assay of wt- β_2 or $\text{Y}_{122}\text{NO}_2\text{Y}\text{-}\beta_2$ by His₆- α_2 analyzed by SDS-PAGE. The α and β monomers are represented by the bands at ~ 75 kDa and ~ 43 kDa. A. The individual steps are as indicated: flow-through (FT), first wash (W1), second wash (W2), elution (E) for wt- β_2 (left) and $\text{Y}_{122}\text{NO}_2\text{Y}\text{-}\beta_2$ (right). B. Elution fractions from panel A were concentrated 5-fold and loaded in different amounts (5, 10 and 15 μL).

6.3.2 *CDP reduction is not required for formation of a stable $\alpha_2\beta_2$ complex.* We next sought to monitor the effect of abolishing nucleotide reduction activity on the formation of a stable $\alpha_2\beta_2$ complex. We turned to the substrate analog N_3CDP ,^{13,26} which acts as a mechanism-based

^{viii} This is the maximum amount of $\text{NO}_2\text{Y}\cdot$ that can be generated based on previous studies by Kenichi Yokoyama. The exact amount of $\text{NO}_2\text{Y}\cdot$ that is formed under the pull-down conditions is unknown but presumed to be the same.

inhibitor of RNR.^{27,28} C₄₃₉• initiates nucleotide reduction by abstraction of the 3' H-atom from N₃CDP and subsequently the enzyme is inactivated by generation of a substrate-based radical (N•). To assess if formation of N• in the active site of $\alpha 2$ can generate a tight $\alpha 2\beta 2$ complex, we performed pull-down assays similar to those described for Y₁₂₂NO₂Y- $\beta 2$. His₆- $\alpha 2$, wt- $\beta 2$, N₃CDP and ATP were reacted on ice for 1 min to maximize the generation of N•.²⁹ Subsequent work up of the reaction mixture took a total of ~3.5 min. Based on previously reported kinetics, no loss of N• is expected to occur over this time frame (Figure A7.1, Appendix 7).²⁹ As a control reaction, His₆- $\alpha 2$, wt- $\beta 2$, CDP and ATP were reacted and worked up following the same protocol.

SDS-PAGE analysis of the pull-down reaction is shown in Figure 6.4. As indicated by the concentrated elution samples (Figure 6.4B), the pull-down of wt- $\beta 2$ by His₆- $\alpha 2$ is greater in the presence of N₃CDP than in the CDP control. The ratio of $\alpha 2:\beta 2$ was quantitated as described for Y₁₂₂NO₂Y- $\beta 2$ and the results are summarized in Table 6.1. The amount of $\alpha 2$ and $\beta 2$ in the N₃CDP pull-down ($1.8 \pm 0.4 \alpha 2:\beta 2$) is in contrast to what is observed for the CDP control (8) and is almost identical to the theoretical yield (1.7). Formation of deoxynucleotide is thus not a prerequisite for tight complex generation.

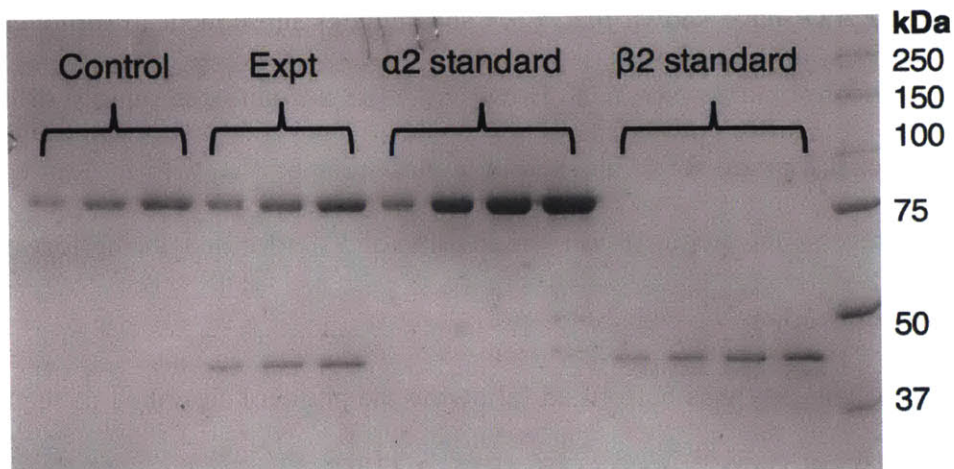


Figure 6.3 SDS-PAGE quantitation of the $\alpha 2$: $\beta 2$ ratio in the pull-down assays. The concentrated elution fractions from each pull-down are typically loaded (1, 2 and 4 μ L) onto a gel containing different amounts of wt- $\alpha 2$ and $\beta 2$ (1–6 pmol). The intensity of each band is then quantitated by densitometry analysis, as described in the text. Quantitation of the pull-down assay from Figure 6.2 is shown here as an example.

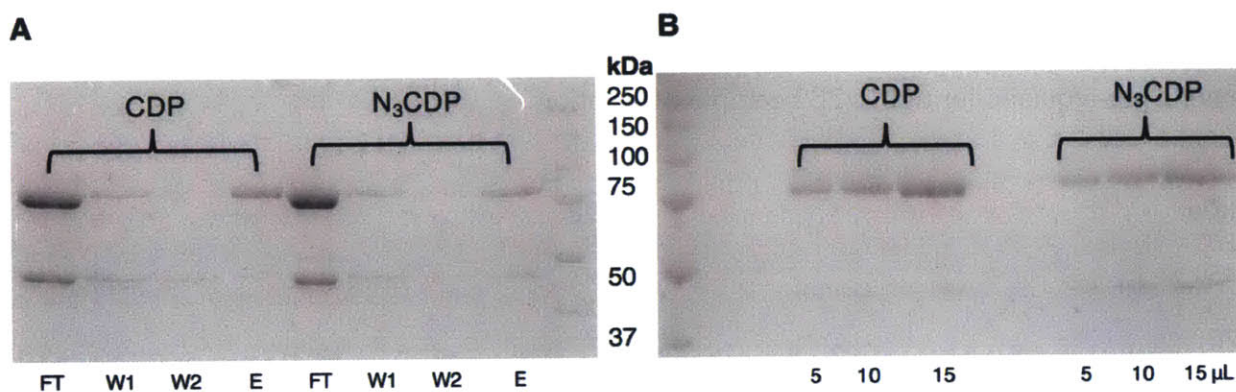


Figure 6.4 Pull-down assay of wt- $\beta 2$ by His₆- $\alpha 2$ in the presence of CDP or N₃CDP analyzed by SDS-PAGE. A. The individual steps are as indicated: flow-through (FT), first wash (W1), second wash (W2), elution (E) for CDP (left) and N₃CDP (right). B. Elution fractions from panel A were concentrated 5-fold and loaded in different amounts (5, 10 and 15 μ L).

6.3.3 Radical injection into $\alpha 2$ is not required for generation of a stable $\alpha 2\beta 2$ complex.

The next question we sought to tackle is whether PCET across the β/α interface is a necessity for tight complex formation. To address this problem, we turned back to our knowledge of Y₁₂₂NO₂Y- $\beta 2$ chemistry. Detailed rapid freeze-quench (RFQ)-EPR studies on the reaction of Y₁₂₂NO₂Y- $\beta 2$

with $\alpha 2$, CDP and ATP have shown that Y_{356}^{\bullet} accumulates subsequent to turnover, due to the inability of Y_{356}^{\bullet} to re-oxidize NO_2Y^- .¹⁸ However, Y_{356}^{\bullet} accumulates rapidly (100 s^{-1}) in the absence of turnover if forward RT is blocked by replacement of Y_{731} with F.¹² As with the Y_{356}^{\bullet} generated during reverse RT (with wt- $\alpha 2$), the lifetime of Y_{356}^{\bullet} formed during forward RT (with $Y_{731}F-\alpha 2$) remains unknown.

The pull-down assay was performed following the protocol described in section 6.2.2 for $\alpha 2/Y_{122}NO_2Y-\beta 2$. Similarly to our observations for the single mutant, a significant pull-down of $Y_{122}NO_2Y-\beta 2$ is observed with His₆- $Y_{731}F-\alpha 2$ compared to pull-down of wt- $\beta 2$ (Figure 6.5B). The ratio of $Y_{731}F-\alpha 2:Y_{122}NO_2Y-\beta 2$ in the elution sample was quantitated as 1.3 ± 0.1 (Table 6.1). The pull-down of wt- $\beta 2$ by His₆- $Y_{731}F-\alpha 2$ in the control reaction was below the detection limit of the $\beta 2$ standard curve ($<10:1\ \alpha 2:\beta 2$, Table 6.1). We conclude that radical injection into the $\alpha 2$ subunit is not a pre-requisite for tight $\alpha 2\beta 2$ complex formation.

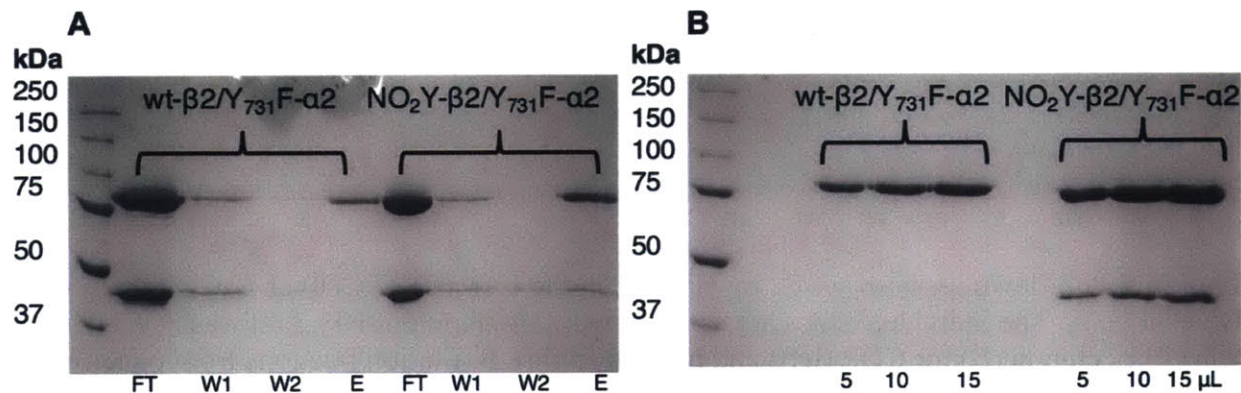


Figure 6.5 Pull-down assay of wt- $\beta 2$ or $Y_{122}NO_2Y-\beta 2$ by His₆- $Y_{731}F-\alpha 2$ analyzed by SDS-PAGE. A. The individual steps are as indicated: flow-through (FT), first wash (W1), second wash (W2), elution (E) for wt- $\beta 2$ (left) and $Y_{122}NO_2Y-\beta 2$ (right). B. Elution fractions from panel A were concentrated 5-fold and loaded in different amounts (5, 10 and 15 μL).

Table 6.1 Quantitation of the $\alpha 2:\beta 2$ ratio in the pull-down assays.

Assay	Experiment ($\alpha 2:\beta 2$)	Control ($\alpha 2:\beta 2$)
$Y_{122}NO_2Y-\beta 2/His_6-\alpha 2$	1.3 ± 0.1	7.8
wt- $\beta 2/His_6-\alpha 2/N_3CDP$	1.8 ± 0.4	8 ± 3
$Y_{122}NO_2Y-\beta 2/His_6-Y_{731}F-\alpha 2$	1.3 ± 0.1	- ^a
DT/MV- $\beta 2/ His_6-Y_{731}F-\alpha 2$	1.9 ± 0.2	- ^a

An example quantitation gel is shown in Figure 6.2. All pull-down assays were performed a single time, except for the DT/MV- $\beta 2$ assay which was performed in duplicate (Figure A7.2 shows the second trial).

^a The amounts of $\beta 2$ in the control reactions were below the detection limit of the $\beta 2$ standard curve (<10:1 $\alpha 2:\beta 2$).

6.3.4 Injection of a single electron into the diferric cluster of wt- $\beta 2$ is sufficient to form a stable $\alpha 2\beta 2$ complex. With the pull-down assays described thus far, we confirmed that neither turnover nor PCET across the β/α interface is required for the generation of a tight $\alpha 2\beta 2$ complex. We speculated that formation of a stable $\alpha 2\beta 2$ complex might be governed by the initiating step in RT that controls the environment of the diferric- Y^\bullet cluster in $\beta 2$. In all pull-down assays presented previously⁶ and described herein ($Y_{730}NH_2Y-\alpha 2$, $Y_{122}NO_2Y-\beta 2$ and N_3CDP), the first step in RT involves transfer of an electron from Y_{356} to Y_{122}^\bullet (or $NO_2Y_{122}^\bullet$). The three cases simply differ by the absence or presence of simultaneous PT that would generate the Y_{122} phenol. With $Y_{730}NH_2Y-\alpha 2$ or N_3CDP , a proton is transferred from a water molecule on the diferric cluster upon ET from Y_{356} .³⁰ In contrast to these systems, ET from Y_{356} to $NO_2Y_{122}^\bullet$ is not accompanied by PT and hence NO_2Y^- is generated instead of the anticipated phenol. However, in common to all these reactions is the fact that an electron is injected into the system, changing the charge of the diferric- Y^\bullet cofactor by one unit. In the case of $Y_{730}NH_2Y-\alpha 2$ or N_3CDP , the neutrally charged resting state cluster¹⁷ acquires a negative charge upon PT to Y_{122}^\bullet . With $Y_{122}NO_2Y-\beta 2$, while the cluster remains neutral, NO_2Y^- is generated upon RT. We hypothesized that alteration of the electrostatics

in the cluster region by injection of a single electron into the diferric-Y• site is sufficient to generate a stable $\alpha 2\beta 2$ complex and sought for alternate ways to test this model.

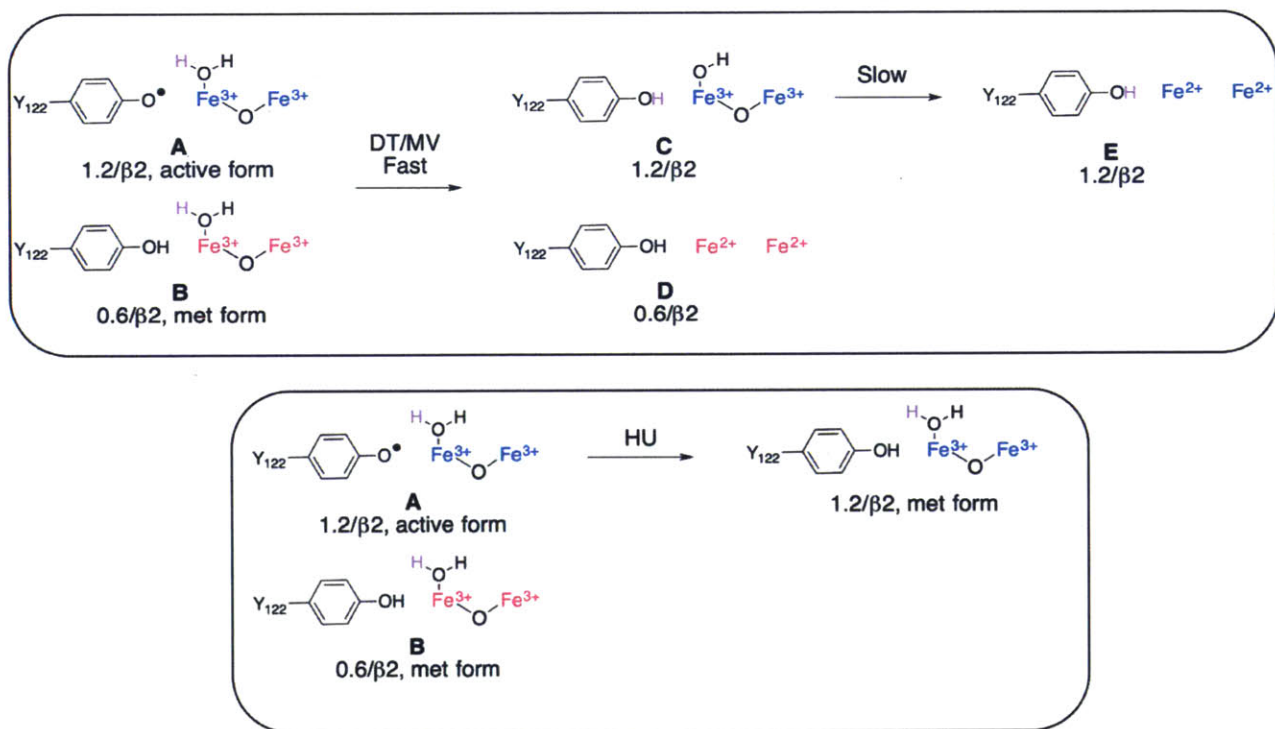


Figure 6.6 Reduction of the diferric-Y• cofactor by DT/MV (top panel) or HU (bottom panel). As-isolated $\beta 2$ contains 1.2 Y•/β2. Our current radical distribution model proposes that this material contains 60% of $\beta 2$ with 2 Y•s (A, active form) and 40% of $\beta 2$ with no Y• (B, met form). Although not shown, all preparations of $\beta 2$ contain 10% apo protein.

A search of the RNR literature revealed a study conducted by Stankovich and coworkers²⁰ that monitored the effect of DT on the diferric-Y• cofactor. Different preparations of the $\beta 2$ subunit typically contain 3.6 Fe³⁺/β2 (or 1.8 diferric centers) and 1.2 Y•/β2, indicating that only two-thirds of the diferric cluster (1.2/1.8) are associated with a Y• (Figure 6.6, A). The remaining one-third of the diiron sites is radical free and referred to as met-β2 (Figure 6.6, B). The diferric-Y• cofactor in the two-thirds active $\beta 2$ can be reduced either by treatment of $\beta 2$ with hydroxyurea (HU)^{22,31} or

by exposing $\beta 2$ to DT in the presence of a mediator (MV).²⁰ In the former case, HU reduces the cluster by a proton and an electron, converting the two-thirds active state protein (**A**, Figure 6.6, bottom panel) into met- $\beta 2$ that is identical to the one-third met protein already present in as-isolated $\beta 2$ (**B**).³⁰ Evidence for the structure of met- $\beta 2$ was provided by Mössbauer spectroscopy on the ⁵⁷Fe-labeled protein.³⁰ We have proposed that, in the first step of RT in wt RNR ($\beta 2/\alpha 2$ /CDP/ATP), $Y_{122}\bullet$ is reduced by ET from $Y_{356}\bullet$ concomitant with PT from a water molecule on the diferric cluster (Fe1-H₂O). Mössbauer spectroscopy in combination with DFT calculations distinguished the Fe1-H₂O resting state of the enzyme from the Fe1-OH “radical-translocated” state and provided evidence for orthogonal PCET at Y_{122} . As a control experiment, we performed a similar study with met- $\beta 2$ and found that the Mössbauer spectrum is consistent with Fe1-H₂O and not Fe1-OH.³⁰ These studies provided the model for HU reduction shown in Figure 6.6. In contrast to the met- $\beta 2$ generated by HU, treatment of as-isolated $\beta 2$ with DT/MV does not result in conversion of **A** to **B**. Stankovich and coworkers²⁰ performed this reaction anaerobically and observed rapid loss of $Y\bullet$ (within 15 s) concomitant with reduction of only one-third of the diferric sites to Fe²⁺ generating states **C** and **D** (Figure 6.6, top panel). Subsequently, the remaining two-thirds of the diiron cluster were reduced on a much slower time scale (~3 h) resulting in **E**. These experiments suggested the presence of two distinct types of diferric clusters in $\beta 2$; the one-third met- $\beta 2$ (**B**) cluster is reduced first and is distinct from the two-thirds diferric cluster that is associated with $Y\bullet$ (**A**).

Reduction of $Y\bullet$ at physiological pH requires simultaneous delivery of a proton and an electron.³² Thus, injection of an electron via DT/MV must be accompanied by PT to $Y\bullet$ to generate state **C**. The most likely candidate that can function as the proton donor is the water molecule on Fe1 of the diferric cluster. This model proposes that reduction of $\beta 2$ by DT/MV is identical to the

radical-translocated state with the exception of the electron source. Mössbauer studies similar to those described above should confirm if state C (Figure 6.6) is the same as the radical-translocated state.³⁰ If so, the cluster develops an overall negative charge immediately upon treatment of $\beta 2$ with DT/MV, similarly to RT with $Y_{730}NH_2Y-\alpha 2$ or N_3CDP . Eventually, however, the entire cluster is reduced to the Fe^{2+} state, and Stankovich and coworkers²⁰ have demonstrated that addition of O_2 to this state (E) results in re-assembly of $1.2 Y\cdot/\beta 2$.

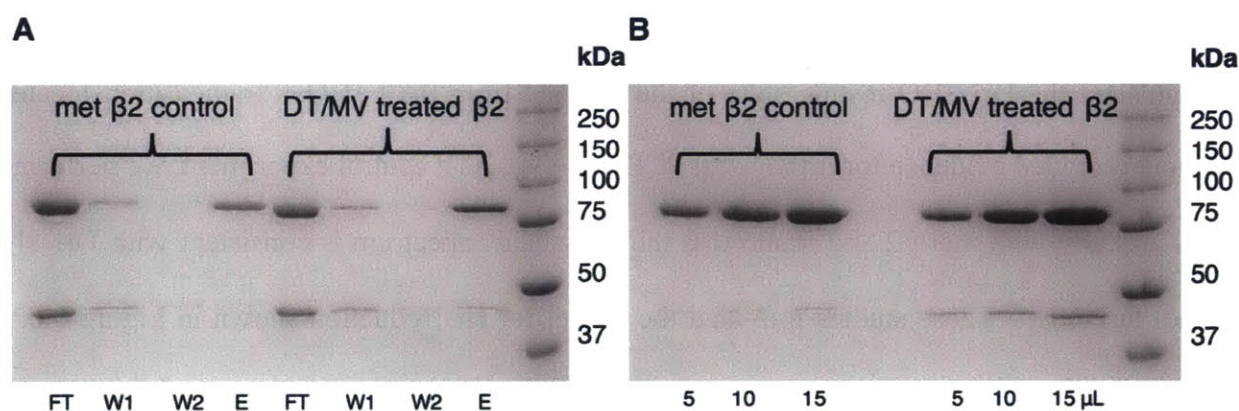


Figure 6.7 Pull-down assay of met- $\beta 2$ or DT/MV treated- $\beta 2$ by $His_6-Y_{731}F-\alpha 2$ analyzed by SDS-PAGE. A. The individual steps are indicated: flow-through (FT), first wash (W1), second wash (W2), elution (E) for met- $\beta 2$ (left) and DT/MV treated $\beta 2$ (right). B. Elution fractions from panel A were concentrated 5-fold and loaded in different amounts (5, 10 and 15 μL).

Based on the results of the reduction studies described above, we predicted that state C (Figure 6.6) would be capable of forming a stable $\alpha 2\beta 2$ complex. To test this hypothesis, a mixture of as-isolated wt- $\beta 2$ and $His_6-Y_{731}F-\alpha 2$ was taken into an anaerobic chamber maintained at 4 °C. $His_6-Y_{731}F-\alpha 2$, and not wt- $\alpha 2$, was utilized in this study to avoid any turnover that could occur as a result of incomplete reduction by DT/MV. The protein mixture was mixed with a solution of CDP/ATP, treated with DT/MV and immediately taken out of the anaerobic chamber to perform the pull-down assay. Based on the studies of Stankovich and coworkers, complete loss of $Y\cdot$ and one-third of the diferric cluster is expected between the time the mixture was taken out of the box

and the time it was loaded onto the Ni-NTA resin (<1 min). Minimal loss of the two-thirds diferric cluster (<5%) is anticipated over the time course of the pull-down assay (~3.5 min).

Figure 6.7 shows the SDS-PAGE analysis of the pull-down assay, comparing the pull-down of DT/MV-treated $\beta 2$ by His₆-Y₇₃₁F- $\alpha 2$ to the pull-down of met- $\beta 2$ by His₆-Y₇₃₁F- $\alpha 2$. Met- $\beta 2$ was generated by the treatment of $\beta 2$ with HU,^{22,31} which results in complete conversion of the active diferric-Y• state to state **B** (Figure 6.6).³⁰ As seen by the concentrated E samples (Figure 6.7B), the pull-down of DT/MV-treated $\beta 2$ is greater than that seen with met- $\beta 2$. Quantitation of His₆-Y₇₃₁F- $\alpha 2$ and DT/MV-treated $\beta 2$ in the elution sample provides an $\alpha 2$: $\beta 2$ ratio of 1.9 ± 0.2 (Table 6.1). This amount is similar to the anticipated ratio if two-thirds of the diferric cluster were in state **C** (1.7^{ix}, Figure 6.6). In contrast to these observations, the pull-down of met- $\beta 2$ by His₆-Y₇₃₁F- $\alpha 2$ was below the detection limit set by the $\beta 2$ standard curve (<10:1 $\alpha 2$:met- $\beta 2$, Table 6.1). These results support that generation of a stable $\alpha 2\beta 2$ complex is a direct result of changing the electrostatics at the diferric cluster site; met- $\beta 2$ with a neutral cluster does not form a stable complex, whereas DT/MV-treated $\beta 2$ with two-thirds of a negatively charged cluster (state **C**, Figure 6.6) generates a tight $\alpha 2\beta 2$ complex. Control experiments performed in the absence of DT establish that the tight complex is a direct result of reduction of $\beta 2$ with DT/MV (Figure A7.2, Appendix 7). Interestingly, a single control experiment performed in the absence of CDP/ATP showed no pull-down of DT/MV-treated $\beta 2$ with His₆-Y₇₃₁F- $\alpha 2$ (Figure A7.3). These results suggest that in addition to the conformational change that occurs upon generation of state **C** (Figure

^{ix} As-isolated $\beta 2$ only contains 1.8 diferric clusters/ $\beta 2$ (anticipated amount is 2/ $\beta 2$). This suggests the presence of 10% apo $\beta 2$ in all preparations of the enzyme. Two-thirds of the total cluster amount is in the form of state **C**. This is equivalent to 3/5 of the total $\beta 2$ protein.

6.6), a conformational change associated with CDP/ATP binding is required for formation of the stable $\alpha_2\beta_2$ complex.

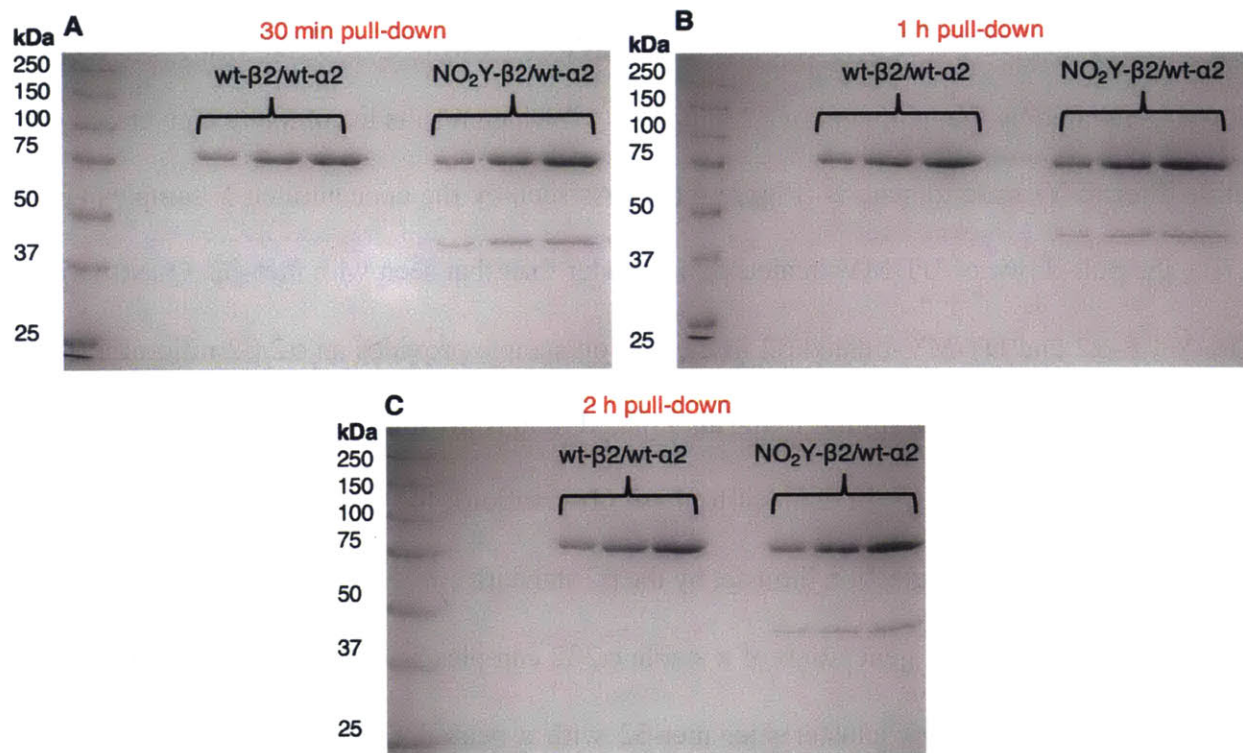


Figure 6.8 Pull-down assay of $Y_{122}NO_2Y$ - β_2 or wt- β_2 by His₆- α_2 analyzed by SDS-PAGE. The reaction mixture (β_2 , α_2 , CDP and ATP) was incubated for 30 min (A), 1 h (B) or 2 h (C) at 4 °C prior to the pull-down assay (see section 6.2.2 for protocol). The gels show only the elution fractions from each pull-down, loaded in different amounts (5, 10 and 15 μ L).

6.4 DISCUSSION

Whereas the individual crystal structures of $\alpha 2$ and $\beta 2$ have been solved,^{4,17} a structure of an active class I RNR complex remains elusive. Recently, we have utilized a variety of biochemical and biophysical methods to show that the reaction of $Y_{730}NH_2Y-\alpha 2$, wt- $\beta 2$, CDP and ATP generates a kinetically stable $\alpha 2\beta 2$ complex that is dependent on the formation of $NH_2Y\bullet$.⁶ These initial studies raised important questions that we sought to tackle regarding which radical and chemical transformations are required to stabilize subunit interactions. The combined pull-down assays described in this Chapter suggest that electrostatic changes at the diferric- $Y\bullet$ cofactor site partially control subunit affinity. A stable complex is generated either by changing the cluster charge by one unit ($Fe1-H_2O \rightarrow Fe1-OH$, during RT or treatment with DT/MV) or by generation of NO_2Y^- in the cluster site. Most importantly, the results presented in this Chapter suggest that a stable complex can only be trapped when turnover is prevented. This observation contrasts with our original model, which suggested that the stable $Y_{730}NH_2Y-\alpha 2/\beta 2$ complex is catalytically active.⁶

When NH_2Y was first chosen for incorporation into RNR, we had predicted that this Y analog would function as a radical sink; the lowered reduction potential of NH_2Y (> 190 mV,³³ Lee, Stubbe unpublished results) would prevent oxidation of the next pathway Y by $NH_2Y\bullet$. Surprisingly, activity assays performed in the absence and presence of a reducing system, and assays monitoring $N\bullet$ formation, suggest that $Y_{730}NH_2Y-\alpha 2$ is catalytically active.¹⁶ We have previously utilized SF vis spectroscopy to show that $NH_2Y\bullet$ formation is biphasic in all NH_2Y -RNRs (NH_2Y_{356} , NH_2Y_{731} or NH_2Y_{730}).^{15,16} These experiments suggested the presence of two different populations of $NH_2Y\bullet$ and extensive kinetic studies by Ellen C. Minnihan allowed construction of a model in which the rate-limiting step in NH_2Y -RNR catalysis is the

interconversion between the two $\text{NH}_2\text{Y}\cdot$ states.³⁴ We propose that our model for stable complex generation is consistent with these observations with $\text{NH}_2\text{Y}\cdot$; one conformer of $\text{NH}_2\text{Y}\cdot$ is active in nucleotide reduction and the second is inactive and responsible for generation of the stable complex. This conclusion is further supported by the k_{off} measured for the stable $\text{Y}_{730}\text{NH}_2\text{Y}-\alpha 2/\beta 2$. The experimental details are discussed below, but the $\text{Y}_{730}\text{NH}_2\text{Y}-\alpha 2/\beta 2$ complex dissociation (0.001 s^{-1})⁶ is not kinetically competent for turnover. The steady-state turnover of $\text{Y}_{730}\text{NH}_2\text{Y}-\alpha 2$ is $0.2\text{--}0.6\text{ s}^{-1}$ ^{15,16} and the data are consistent with a model in which the inactive $\text{NH}_2\text{Y}\cdot$ generates the tight complex.

One of the most interesting questions to address is whether the lifetimes of the $\alpha 2\beta 2$ complexes that are observed in the pull-down experiments are identical to those of the pathway radical intermediates. Kinetic information regarding the stability of the $\alpha 2\beta 2$ complex is currently only available in one instance; for the $\text{NH}_2\text{Y}\cdot$ -induced stable complex, two lines of evidence support a longer half-life for the complex than for $\text{NH}_2\text{Y}\cdot$. First, k_{off} for $\text{Y}_{730}\text{NH}_2\text{Y}-\alpha 2/\beta 2$ has been measured by steady-state fluorescence experiments.⁶ In these studies, the stable $\text{Y}_{730}\text{NH}_2\text{Y}-\alpha 2/\beta 2$ complex was mixed with an excess of $\beta 2$ modified with an environmentally sensitive fluorophore, dansyl at position 365 on the C-terminal tail ($\text{V}_{365}\text{C-DAN}-\beta 2$).³⁵ A slow increase in fluorescence intensity was monitored over 40 min, reporting on the movement of the fluorophore into a more hydrophobic environment upon binding of $\text{DAN}-\beta 2$ to $\text{Y}_{730}\text{NH}_2\text{Y}-\alpha 2$ subsequent to dissociation of $\beta 2$.^{6,35,36} These studies measured a k_{off} of 0.001 s^{-1} ($t_{1/2} = \sim 12\text{ min}$) for the $\text{Y}_{730}\text{NH}_2\text{Y}-\alpha 2/\beta 2$ complex, although we note that data analysis was complicated by a drop in fluorescence intensity of unknown origin (during the first 8 min of the reaction) that occurred prior to the increase (8–40 min). Nonetheless, these studies showed extremely slow dissociation of the $\text{Y}_{730}\text{NH}_2\text{Y}-\alpha 2/\beta 2$ complex compared to the lifetime of $\text{NH}_2\text{Y}_{730}\cdot$ in the $\text{Y}_{730}\text{NH}_2\text{Y}-\alpha 2/\beta 2$ complex (0.004 s^{-1} or $t_{1/2}$

of ~ 2.8 min).³⁷ This preliminary study provides the first evidence for a complex that is longer-lived than the pathway radical. Additional support for this model was provided by SAXS studies that characterized the structure of the $Y_{730}NH_2Y\text{-}\alpha 2/\beta 2/CDP/ATP$ reaction. The wt *E. coli* class Ia RNR (wt- $\alpha 2$, met- $\beta 2$, CDP and ATP) can exist in three interconverting states in solution: $\alpha 2 + \beta 2 \rightleftharpoons \alpha 2\beta 2 \rightleftharpoons \alpha 4\beta 4$.⁹ It has been suggested that high protein concentrations can shift the equilibrium toward $\alpha 4\beta 4$.⁹ However, shifting of the solution equilibrium toward $\alpha 4\beta 4$ has been experimentally confirmed only in the presence of the negative allosteric effector dATP.⁹ Due to the enhanced stability of the $Y_{730}NH_2Y\text{-}\alpha 2/\beta 2$ complex, we were interested in monitoring its resistance to dATP-induced $\alpha 4\beta 4$ formation. Time dependent SAXS studies showed extremely slow and incomplete conversion of $Y_{730}NH_2Y\text{-}\alpha 2/\beta 2$ to $Y_{730}NH_2Y\text{-}\alpha 4/\beta 4$; only $\sim 20\%$ of the initial $Y_{730}NH_2Y\text{-}\alpha 2/\beta 2$ was converted to $Y_{730}NH_2Y\text{-}\alpha 4/\beta 4$ over 22 min (Figure A7.4).³⁴ EPR experiments have shown that $NH_2Y_{730}\bullet$ is almost completely lost within 10 min ($k_{obs} = 0.004\text{ s}^{-1}$),³⁷ providing further support that $Y_{730}NH_2Y\text{-}\alpha 2/\beta 2$ has a longer lifetime than $NH_2Y_{730}\bullet$.

Whereas kinetic information is currently unavailable for the stable $\alpha 2\beta 2$ complexes reported herein, preliminary pull-down assays performed with $Y_{122}NO_2Y\text{-}\beta 2$ suggest that our observations with $Y_{730}NH_2Y\text{-}\alpha 2$ (above) could be extended to the $Y_{356}\bullet$ -induced $Y_{122}NO_2Y\text{-}\beta 2/\alpha 2$ complex. The location of Y_{356} at the subunit interface along with our observations that the Y_{356} proton is in rapid exchange with solvent (Chapter 4) make it unlikely that $Y_{356}\bullet$ would be long-lived; at least in the case of $Y_{122}(2,3,5)F_3Y\text{-}\beta 2$ the lifetime of $Y_{356}\bullet$ when turnover is blocked is on the order of minutes (Chapter 4). However, pull-down assays performed with $Y_{122}NO_2Y\text{-}\beta 2$, $\alpha 2$, CDP and ATP show a stable $Y_{122}NO_2Y\text{-}\beta 2/\alpha 2$ complex even after 2 h at 4 °C (Figure 6.8). The

ratio of $\alpha 2:Y_{122}NO_2Y-\beta 2$ in the 2 h pull-down assay was quantitated as 1.9 ± 0.5 (anticipated ratio is 1.7), suggesting that almost no dissociation of the stable complex has occurred relative to the 3.5 min pull-down. The combined results from the $Y_{730}NH_2Y-\alpha 2$ and $Y_{122}NO_2Y-\beta 2$ studies can be reconciled by our model for tight complex formation. If electrostatics at the diferric- Y^\bullet site control subunit affinity, then the lifetimes of the stable complexes would be independent of the lifetimes of the pathway radical intermediates. Rather, we propose that complex dissociation is dictated by how fast the charge of the diferric- Y^\bullet site is reset; in the case of the $Y_{730}NH_2Y-\alpha 2$ (or N_3CDP) experiments, complex dissociation would occur with re-protonation of $Fe1-OH$, whereas in the case of $Y_{122}NO_2Y-\beta 2$, protonation of NO_2Y^- could once again lower the affinity between the two subunits. Due to the buried nature of the diferric- Y^\bullet cofactor, both of these events are proposed to be slow.

In this Chapter, we reported several strategies for generating a stable $\alpha 2\beta 2$ complex, which led to the proposed model where electrostatics at the diferric- Y^\bullet site control subunit affinity. This model makes several predictions that can be readily tested. First, steady-state fluorescence and EPR studies should be performed to assess the stabilities of all complexes and pathway radicals described herein; we anticipate $\alpha 2\beta 2$ complex lifetimes to be similar between the different systems but independent of the pathway radical lifetimes. Fortunately, formation of pathway radicals is not limited to the systems described in this work. Studies performed by the Stubbe and Sjöberg labs have shown that the reaction of a mutant $\alpha 2$, $E_{441}Q-\alpha 2$, with $\beta 2$, CDP and ATP accumulates a disulfide radical anion in the active site.^{38,39} Preliminary studies suggest that a stable $\alpha 2\beta 2$ complex can be observed by pull-down assay of the reaction mixture (data not shown), although the ratio of $\alpha 2:\beta 2$ in this assay remains undetermined. Investigation of the $E_{441}Q-\alpha 2/\beta 2$ complex stability and comparison of its lifetime to that of the disulfide radical anion would establish if our

electrostatics model is accurate. As a negative control, we also propose testing tight complex formation in the $Y_{122}(2,3,5)F_3Y-\beta_2$ system. We had previously hypothesized that the tight complex is capable of turnover.⁶ However, our current model requires that the charge at the cluster site remains perturbed by one unit for the duration in which the subunits are locked together. This model predicts that constant addition and removal of a charge at the cluster site could result in association and dissociation of the active complex, precluding the pull-down of a stable $\alpha_2\beta_2$ complex. In Chapter 3, we showed that Y_{356} is the thermodynamic minimum on the RT pathway in $Y_{122}(2,3,5)F_3Y-\beta_2$ and that once formed, Y_{356}^\bullet disappearance cannot be monitored under steady-state turnover conditions (+ TR/TRR/NADPH). However, we have proposed that, during this reaction, 2,3,5- F_3Y is repeatedly oxidized (2,3,5- F_3Y^\bullet , neutral cluster site) and reduced (2,3,5- F_3Y^- , charged cluster site, Chapter 4). Pull-down of this reaction mixture could provide further support for the electrostatic model presented in this Chapter, although we note that slow rate-limiting re-oxidation of 2,3,5- F_3Y^- by Y_{356}^\bullet ²⁴ (Chapter 3) could still result in observation of a stable complex.

With the combined studies proposed in this Chapter, we aim to confirm if the stable complex is longer-lived than any of the pathway radical intermediates. If true, this exciting observation opens up the possibility of identifying ways to maintain perturbed electrostatics at the cluster site. For example, increasing the pH of the reaction could slow down complex dissociation by slowing down protonation of Fe1-OH (or NO_2Y^-). Some of the methods reported herein, such as the reaction with N_3CDP , may serve as a general strategy for targeting other class I RNR complexes. The active complex of human RNR is still a question of debate but is thought to be either $\alpha_2\beta_2$ or $\alpha_6\beta_2$.⁴⁰⁻⁴² Pull-down assays similar to those described in this work are currently ongoing with human RNR (Julia Page).

6.5 REFERENCES

1. Jordan, A.; Reichard, P. Ribonucleotide reductases, *Annu. Rev. Biochem.* **1998**, *67*, 71-98.
2. Stubbe, J.; van der Donk, W. A. Protein radicals in enzyme catalysis, *Chem. Rev.* **1998**, *98*, 705-762.
3. Brown, N. C.; Reichard, P. Ribonucleoside diphosphate reductase: Formation of active and inactive complexes of proteins B1 and B2, *J. Mol. Biol.* **1969**, *46*, 25-38.
4. Uhlin, U.; Eklund, H. Structure of ribonucleotide reductase protein R1, *Nature* **1994**, *370*, 533-539.
5. Bennati, M.; Robblee, J. H.; Mugnaini, V.; Stubbe, J.; Freed, J. H.; Borbat, P. EPR distance measurements support a model for long-range radical initiation in *E. coli* ribonucleotide reductase, *J. Am. Chem. Soc.* **2005**, *127*, 15014-15015.
6. Minnihan, E. C.; Ando, N.; Brignole, E. J.; Olshansky, L.; Chittuluru, J.; Asturias, F. J.; Drennan, C. L.; Nocera, D. G.; Stubbe, J. Generation of a stable, aminotyrosyl radical-induced $\alpha 2\beta 2$ complex of *Escherichia coli* class Ia ribonucleotide reductase, *Proc Natl. Acad. Sci. U. S. A.* **2013**, *110*, 3835-3840.
7. Climent, I.; Sjöberg, B. M.; Huang, C. Y. Carboxyl-terminal peptides as probes for *Escherichia coli* ribonucleotide reductase subunit interaction: kinetic analysis of inhibition studies, *Biochemistry* **1991** *30*, 5164-5171.
8. Thelander, L. Physicochemical characterization of ribonucleoside diphosphate reductase from *Escherichia coli*, *J. Biol. Chem.* **1973**, *248*, 4591-4601.
9. Ando, N.; Brignole, E. J.; Zimanyi, C. M.; Funk, M. A.; Yokoyama, K.; Asturias, F. J.; Stubbe, J.; Drennan, C. L. Structural interconversions modulate activity of *Escherichia coli* ribonucleotide reductase, *Proc. Natl. Acad. Sci. U. S. A* **2011**, *108*, 21046-21051.
10. Zimanyi, C. M.; Ando, N.; Brignole, E. J.; Asturias, F. J.; Stubbe, J.; Drennan, C. L. Tangled Up in Knots: Structures of inactivated forms of *E. coli* class Ia ribonucleotide reductase, *Structure.* **2012**, *20*, 1374-1383.
11. Seyedsayamdost, M. R.; Chan, C. T.; Mugnaini, V.; Stubbe, J.; Bennati, M. PELDOR spectroscopy with DOPA- $\beta 2$ and NH₂Y- $\alpha 2$ s: distance measurements between residues involved in the radical propagation pathway of *E. coli* ribonucleotide reductase, *J. Am. Chem. Soc.* **2007**, *129*, 15748-15749.
12. Yokoyama, K.; Smith, A. A.; Corzilius, B.; Griffin, R. G.; Stubbe, J. Equilibration of tyrosyl radicals (Y₃₅₆[•], Y₇₃₁[•], Y₇₃₀[•]) in the radical propagation pathway of the *Escherichia coli* class Ia ribonucleotide reductase, *J. Am. Chem. Soc.* **2011**, *133*, 18420-18432.
13. Sjöberg, B. M.; Gräslund, A.; Eckstein, F. A substrate radical intermediate in the reaction between ribonucleotide reductase from *escherichia coli* and 2'-azido-2'-deoxynucleoside diphosphates, *J. Biol. Chem.* **1983**, *258*, 8060-8067.
14. Seyedsayamdost, M. R.; Stubbe, J. Site-specific replacement of Y₃₅₆ with 3,4-dihydroxyphenylalanine in the $\beta 2$ subunit of *E. coli* ribonucleotide reductase, *J. Am. Chem. Soc.* **2006**, *128*, 2522-2523.

15. Seyedsayamdost, M. R.; Xie, J.; Chan, C. T.; Schultz, P. G.; Stubbe, J. Site-specific insertion of 3-aminotyrosine into subunit $\alpha 2$ of *E. coli* ribonucleotide reductase: direct evidence for involvement of Y₇₃₀ and Y₇₃₁ in radical propagation, *J. Am. Chem. Soc.* **2007**, *129*, 15060-15071.
16. Minnihan, E. C.; Seyedsayamdost, M. R.; Uhlin, U.; Stubbe, J. Kinetics of radical intermediate formation and deoxynucleotide production in 3-aminotyrosine-substituted *Escherichia coli* ribonucleotide reductases, *J. Am. Chem. Soc.* **2011**, *133*, 9430-9440.
17. Nordlund, P.; Sjöberg, B. M.; Eklund, H. Three-dimensional structure of the free radical protein of ribonucleotide reductase, *Nature* **1990**, *345*, 593-598.
18. Yokoyama, K.; Uhlin, U.; Stubbe, J. A hot oxidant, 3-NO₂Y₁₂₂ radical, unmasks conformational gating in ribonucleotide reductase, *J. Am. Chem. Soc.* **2010**, *132*, 15368-15379.
19. Fritscher, J.; Artin, E.; Wnuk, S.; Bar, G.; Robblee, J. H.; Kacprzak, S.; Kaupp, M.; Griffin, R. G.; Bennati, M.; Stubbe, J. Structure of the nitrogen-centered radical formed during inactivation of *E. coli* ribonucleotide reductase by 2'-azido-2'-deoxyuridine-5'-diphosphate: trapping of the 3'-ketonucleotide, *J. Am. Chem. Soc.* **2005**, *127*, 7729-7738.
20. Miller, M. A.; Gobena, F. T.; Kauffmann, K.; Munck, E.; Que, L.; Stankovich, M. T. Differing roles for the diiron clusters of ribonucleotide reductase from aerobically grown *Escherichia coli* in the generation of the Y₁₂₂ radical, *J. Am. Chem. Soc.* **1999**, *121*, 1096-1097.
21. Yokoyama, K.; Uhlin, U.; Stubbe, J. Site-specific incorporation of 3-nitrotyrosine as a probe of pK_a perturbation of redox-active tyrosines in ribonucleotide reductase, *J. Am. Chem. Soc.* **2010**, *132*, 8385-8397.
22. Brown, N. C.; Eliasson, R.; Reichard, P.; Thelander, L. Spectrum and iron content of protein B2 from ribonucleoside diphosphate reductase, *Eur. J. Biochem.* **1969**, *9*, 512-518.
23. Ge, J.; Yu, G.; Ator, M. A.; Stubbe, J. Pre-steady-state and steady-state kinetic analysis of *E. coli* class I ribonucleotide reductase, *Biochemistry* **2003**, *42*, 10071-10083.
24. Ravichandran, K. R.; Minnihan, E. C.; Wei, Y.; Nocera, D. G.; Stubbe, J. Reverse electron transfer completes the catalytic cycle in a 2,3,5-trifluorotyrosine-substituted ribonucleotide reductase, *J. Am. Chem. Soc.* **2015**, *137*, 14387-14395.
25. Aberg, A.; Hahne, S.; Karlsson, M.; Larsson, A.; Ormö, M.; Ahgren, A.; Sjöberg, B. M. Evidence for two different classes of redox-active cysteines in ribonucleotide reductase of *Escherichia coli*, *J. Biol. Chem.* **1989**, *264*, 12249-12252.
26. Thelander, L.; Larsson, B. Active site of ribonucleoside diphosphate reductase from *Escherichia coli*. Inactivation of the enzyme by 2'-substituted ribonucleoside diphosphates, *J. Biol. Chem.* **1976**, *251*, 1398-1405.
27. Salowe, S. P.; Ator, M. A.; Stubbe, J. Products of the inactivation of ribonucleoside diphosphate reductase from *Escherichia coli* with 2'-azido-2'-deoxyuridine 5'-diphosphate, *Biochemistry* **1987**, *26*, 3408-3416.
28. Salowe, S.; Bollinger, J. M., Jr.; Ator, M.; Stubbe, J.; McCracken, J.; Peisach, J.; Samano, M. C.; Robins, M. J. Alternative model for mechanism-based inhibition of *Escherichia coli*

- ribonucleotide reductase by 2'-azido-2'-deoxyuridine 5'-diphosphate, *Biochemistry* **1993**, *32*, 12749-12760.
29. Artin, E. Mechanistic studies of the class I ribonucleotide reductase from *Escherichia coli*. Ph.D. Thesis, Massachusetts Institute of Technology, **2006**.
 30. Wörsdorfer, B.; Conner, D. A.; Yokoyama, K.; Livada, J.; Seyedsayamdost, M. R.; Jiang, W.; Silakov, A.; Stubbe, J.; Bollinger, J. M., Jr.; Krebs, C. Function of the diiron cluster of *Escherichia coli* class Ia ribonucleotide reductase in proton-coupled electron transfer, *J. Am. Chem. Soc.* **2013**, *135*, 8585-8593.
 31. Karlsson, M.; Sahlin, M.; Sjöberg, B. M. *Escherichia coli* ribonucleotide reductase. Radical susceptibility to hydroxyurea is dependent on the regulatory state of the enzyme, *J. Biol. Chem.* **1992**, *267*, 12622-12626.
 32. Reece, S. Y.; Hodgkiss, J. M.; Stubbe, J.; Nocera, D. G. Proton-coupled electron transfer: the mechanistic underpinning for radical transport and catalysis in biology, *Philos. Trans. R. Soc. Lond. B Biol. Sci.* **2006**, *361*, 1351-1364.
 33. DeFilippis, M. R.; Murthy, C. P.; Broitman, F.; Weinraub, D.; Faraggi, M.; Klapper, M. H. Electrochemical properties of tyrosine phenoxy and tryptophan in indolyl radicals in peptides and amino acid analogs, *J. Phys. Chem.* **1991**, *95*, 3416-3419.
 34. Minnihan, E. C. Mechanistic studies of proton-coupled electron transfer in aminotyrosine- and fluorotyrosine-substituted class Ia ribonucleotide reductase. Ph.D. Thesis, Massachusetts Institute of Technology, **2012**.
 35. Hassan, A. Q.; Wang, Y.; Plate, L.; Stubbe, J. Methodology to probe subunit interactions in ribonucleotide reductases, *Biochemistry* **2008**, *47*, 13046-13055.
 36. Olshansky, L. Kinetics and dynamics controlling proton-coupled electron transfer in ribonucleotide reductase. Ph.D. Thesis, Massachusetts Institute of Technology, **2015**.
 37. Seyedsayamdost, M. R. Investigation of the mechanism of radical propagation in *E. coli* ribonucleotide reductase by site-specific incorporation of unnatural amino acids. Ph.D. Thesis, Massachusetts Institute of Technology, **2007**.
 38. Lawrence, C. C.; Bennati, M.; Obias, H. V.; Bar, G.; Griffin, R. G.; Stubbe, J. High-field EPR detection of a disulfide radical anion in the reduction of cytidine 5'-diphosphate by the E₄₄₁Q-R1 mutant of *Escherichia coli* ribonucleotide reductase, *Proc. Natl. Acad. Sci. U. S. A* **1999**, *96*, 8979-8984.
 39. Persson, A. L.; Eriksson, M.; Katterle, B.; Pötsch, S.; Sahlin, M.; Sjöberg, B. M. A new mechanism-based radical intermediate in a mutant R1 protein affecting the catalytically essential Glu441 in *Escherichia coli* ribonucleotide reductase, *J. Biol. Chem.* **1997**, *272*, 31533-31541.
 40. Fairman, J. W.; Wijerathna, S. R.; Ahmad, M. F.; Xu, H.; Nakano, R.; Jha, S.; Prendergast, J.; Welin, R. M.; Flodin, S.; Roos, A.; Nordlund, P.; Li, Z.; Walz, T.; Dealwis, C. G. Structural basis for allosteric regulation of human ribonucleotide reductase by nucleotide-induced oligomerization, *Nat. Struct. Mol. Biol.* **2011**, *18*, 316-322.
 41. Rofougaran, R.; Vodnala, M.; Hofer, A. Enzymatically active mammalian ribonucleotide reductase exists primarily as an $\alpha_6\beta_2$ octamer, *J. Biol. Chem.* **2006**, *281*, 27705-27711.

42. Ando, N.; Li, H.; Brignole, E. J.; Thompson, S.; McLaughlin, M. I.; Page, J. E.; Asturias, F.; Stubbe, J.; Drennan, C. L. Allosteric inhibition of human ribonucleotide reductase by dATP entails the stabilization of a hexamer, *Biochemistry* **2016**, *55*, 373-381.

Appendix 1

Supporting Information for Chapter 1

Table A1.1 PELDOR distance measurements in the *E. coli* class Ia RNR.

$\beta 2$	$\alpha 2$	S/E	Diagonal pair	PELDOR (Å)	Docking model (Å)	Ref.
wt	-	-	$Y_{122}^{\bullet}-Y_{122}^{\bullet}$	33.1 ± 0.2	33	1
wt	wt	N_3 UDP/TTP	$Y_{122}^{\bullet}-Y_{122}^{\bullet}$	33 ± 1	33	2
wt	wt	N_3 UDP/TTP	$Y_{122}^{\bullet}-N^{\bullet}$	48 ± 1	47	2
wt	$Y_{731}NH_2Y$	GDP/TTP	$Y_{122}^{\bullet}-Y_{122}^{\bullet}$	33.2	33	3
wt	$Y_{731}NH_2Y$	GDP/TTP	$Y_{122}^{\bullet}-NH_2Y_{731}^{\bullet}$	38.7 ± 1.8	40	3
wt	$Y_{730}NH_2Y$	GDP/TTP	$Y_{122}^{\bullet}-Y_{122}^{\bullet}$	32.7	33	3
wt	$Y_{730}NH_2Y$	GDP/TTP	$Y_{122}^{\bullet}-NH_2Y_{730}^{\bullet}$	38.1 ± 1.2	39	3
$Y_{356}DOPA$	wt	GDP/TTP	$Y_{122}^{\bullet}-DOPA_{356}^{\bullet}$	30.6 ± 0.5	-	3
$Y_{356}DOPA-\beta\beta'$	wt	GDP/TTP	$Y_{122}^{\bullet}-DOPA_{356}^{\bullet}$	30.6 ± 0.5	-	4
$Y_{356}NH_2Y$	wt	CDP/ATP	$Y_{122}^{\bullet}-Y_{122}^{\bullet}$	32.6 ± 0.5	33	5
$Y_{356}NH_2Y$	wt	CDP/ATP	$Y_{122}^{\bullet}-NH_2Y_{356}^{\bullet}$	30.2 ± 1.6	-	5
$Y_{122}NO_2Y$	wt	CDP/ATP	$NO_2Y_{122}^{\bullet}-NO_2Y_{122}^{\bullet}$	33.1 ± 0.4	33	6
$Y_{122}NO_2Y$	wt	CDP/ATP	$NO_2Y_{122}^{\bullet}-Y_{356}^{\bullet}$	30.0 ± 0.4	-	6
$Y_{122}NO_2Y$	wt	CDP/ATP	$NO_2Y_{122}^{\bullet}-Y_{731}^{\bullet}$ (or Y_{730}^{\bullet})	38.1 ± 0.5	39-40	6
$Y_{122}NO_2Y$	$Y_{731}F$	CDP/ATP	$NO_2Y_{122}^{\bullet}-NO_2Y_{122}^{\bullet}$	32.7 ± 0.3	33	6
$Y_{122}NO_2Y$	$Y_{731}F$	CDP/ATP	$NO_2Y_{122}^{\bullet}-Y_{356}^{\bullet}$	30.1 ± 0.4	-	6
$Y_{122}(2,3,5)F_3Y$	wt	CDP/ATP	$F_3Y_{122}^{\bullet}-Y_{356}^{\bullet}$	30 ± 1	-	7
$Y_{122}(2,3,5)F_3Y$	$Y_{731}F$	CDP/ATP	$F_3Y_{122}^{\bullet}-Y_{356}^{\bullet}$	30.4 ± 0.6	-	7

Table A1.2 Radical content and specific activities of all UAA-substituted β 2s.

β 2	Y•/ β 2	Specific activity (nmol/min/mg) at pH 7.6	Ref.
wt- β 2	1.2	6000–8000	
EPL-Y	0.34	450	8
EPL-3,5-F ₂ Y	0.31	450	8
EPL-2,3,5-F ₃ Y	0.42	365	8
EPL-2,3-F ₂ Y	0.33	370	8
EPL-2,3,6-F ₃ Y	0.41	95	8
EPL-F ₄ Y	0.42	30	8
Y ₃₅₆ DOPA	0.3	-	9
Y ₃₅₆ NH ₂ Y	0.5	305 ± 38	10
Y ₃₅₆ (3,5)F ₂ Y	0.9	5480 ± 290	5
Y ₃₅₆ (2,3,5)F ₃ Y	0.8	680 ± 3	5
Y ₃₅₆ (2,3)F ₂ Y	0.74	2880 ± 30	5
Y ₁₂₂ (3,5)F ₂ Y	1.0	5780 ± 230	11
Y ₁₂₂ (2,3,5)F ₃ Y	0.9	1300 ± 100	11
Y ₁₂₂ (2,3)F ₂ Y	0.8	450 ± 20	11
Y ₁₂₂ (2,3,6)F ₃ Y	1.2	350 ± 10	11
Y ₁₂₂ NO ₂ Y	1.2	- ^a	12

^a Y₁₂₂NO₂Y- β 2 performs only a single turnover (0.5 dCDP/NO₂Y•, 100 s⁻¹) prior to inactivation.

REFERENCES

1. Bennati, M.; Weber, A.; Antonic, J.; Perlstein, D. L.; Robblee, J.; Stubbe, J. Pulsed ELDOR spectroscopy measures the distance between the two tyrosyl radicals in the R2 subunit of the *E. coli* ribonucleotide reductase, *J. Am. Chem. Soc.* **2003**, *125*, 14988-14989.
2. Bennati, M.; Robblee, J. H.; Mugnaini, V.; Stubbe, J.; Freed, J. H.; Borbat, P. EPR distance measurements support a model for long-range radical initiation in *E. coli* ribonucleotide reductase, *J. Am. Chem. Soc.* **2005**, *127*, 15014-15015.
3. Seyedsayamdost, M. R.; Chan, C. T.; Mugnaini, V.; Stubbe, J.; Bennati, M. PELDOR spectroscopy with DOPA- β 2 and NH₂Y- α 2s: distance measurements between residues involved in the radical propagation pathway of *E. coli* ribonucleotide reductase, *J. Am. Chem. Soc.* **2007**, *129*, 15748-15749.
4. Seyedsayamdost, M. R. Investigation of the mechanism of radical propagation in *E. coli* ribonucleotide reductase by site-specific incorporation of unnatural amino acids. Ph.D. Thesis, Massachusetts Institute of Technology, **2007**.
5. Minnihan, E. C. Mechanistic studies of proton-coupled electron transfer in aminotyrosine- and fluorotyrosine-substituted class Ia ribonucleotide reductase. Ph.D. Thesis, Massachusetts Institute of Technology, **2012**.
6. Yokoyama, K.; Smith A. A.; Corzilius, B.; Griffin, R.G.; Stubbe, J. Equilibration of tyrosyl radicals (Y₃₅₆•, Y₇₃₁• and Y₇₃₀•) in the radical propagation pathway of the *Escherichia coli* class Ia ribonucleotide reductase, *J. Am. Chem. Soc.* **2011**, *133*, 18420-18432.
7. Nick, T. U. Hydrogen bonds and electrostatic environment of radical intermediates in ribonucleotide reductase class Ia. Ph.D. Thesis, University of Göttingen, **2015**.
8. Seyedsayamdost, M. R.; Yee, C. S.; Reece, S. Y.; Nocera, D. G.; Stubbe, J. pH rate profiles of F_nY₃₅₆-R2s (n = 2, 3, 4) in *Escherichia coli* ribonucleotide reductase: evidence that Y₃₅₆ is a redox-active amino acid along the radical propagation pathway, *J. Am. Chem. Soc.* **2006**, *128*, 1562-1568.
9. Seyedsayamdost, M. R.; Stubbe, J. Site-specific replacement of Y₃₅₆ with 3,4-dihydroxyphenylalanine in the β 2 subunit of *E. coli* ribonucleotide reductase, *J. Am. Chem. Soc.* **2006**, *128*, 2522-2523.
10. Minnihan, E. C.; Seyedsayamdost, M. R.; Uhlin, U.; Stubbe, J. Kinetics of radical intermediate formation and deoxynucleotide production in 3-aminotyrosine-substituted *Escherichia coli* ribonucleotide reductases, *J. Am. Chem. Soc.* **2011**, *133*, 9430-9440.
11. Oyala, P. H.; Ravichandran, K. R.; Funk, M. A.; Stucky, P. A.; Stich, T. A.; Drennan, C. L.; Britt, R. D.; Stubbe, J. Biophysical characterization of fluorotyrosine probes site-specifically incorporated into enzymes: *E. coli* ribonucleotide reductase as an example, *J. Am. Chem. Soc.* **2016**, *submitted*.
12. Yokoyama, K.; Uhlin, U.; Stubbe, J. A hot oxidant, 3-NO₂Y₁₂₂ radical, unmasks conformational gating in ribonucleotide reductase, *J. Am. Chem. Soc.* **2010**, *132*, 15368-15379.

Appendix 2

Expression and purification of α_3F_nY s ($n = 2, 3$)

A2.1 INTRODUCTION

To investigate the mechanism of long-range RT in the *E. coli* class Ia RNR we have utilized a range of unnatural Y analogs that perturb the pK_a and the reduction potentials of the different Ys on pathway.¹⁻⁶ Extrapolation of the observations made on these unnatural systems to wt RNR requires exact knowledge of the perturbation to the pK_a and ΔE° upon replacing Y with these analogs. Focusing on the F_nY analogs, solution pK_a measurements have been made on the *N*-acetyl fluoro-L-tyrosinamides⁷. These studies in conjunction with pH titration experiments performed with NO_2Y at the different pathway positions⁸ have provided a good estimate of the pK_a of the F_nY s at Y_{122} , Y_{356} , Y_{731} and Y_{730} . To assess the perturbation to ΔE° upon incorporation of F_nY at the different positions, we have previously collected DPV data on the protected analogs.⁷ However, rapid chemical reactions that occur upon formation of $F_nY\cdot$ in solution result in irreversible voltammograms that can only provide peak potentials for F_nY , and not formal reduction potentials. Recently, a three alpha helix bundle (α_3) was designed containing a single buried redox active amino acid.⁹ Using this system, Tommos and coworkers were able to obtain the formal reduction potential of Y as a function of pH.¹⁰ In Chapter 2, we successfully showed the incorporation of 3,5- F_2Y into the alpha helix bundle ($\alpha_3(3,5)F_2Y$) and measured the formal potential for the 3,5- $F_2Y\cdot/3,5-F_2Y$ couple in α_3 using square wave voltammetry (SWV). Herein we describe the expression and purification of the other α_3F_nY s as Smt3 tagged proteins. These proteins have been utilized by the Tommos lab to obtain the formal reduction potentials of the entire F_nY series.

A2.1 MATERIALS AND METHODS

A2.2.1 Materials. Tyrosine phenol lyase (TPL) was purified as previously reported.¹¹ F_nY_s ($n = 2, 3$) were enzymatically synthesized from the corresponding phenol using TPL as the catalyst.¹² SUMO protease was expressed from pTB145-*ulp1* as a His₆-tagged construct as previously reported.¹³ Kanamycin (Kan), chloramphenicol (Cm), 2XYT, L-arabinose and isopropyl- β -D-thiogalactoside (IPTG) were purchased from Sigma Aldrich.

A2.2.2 Construction of pESUMO- α_3TAG_{32} . α_3TAG_{32} was amplified from the previously described pET32b- α_3TAG_{32} ¹⁴ using the forward primer 5'-ccgcaacagattggaggtGGATCCCGTGTG-3' and reverse primer 5'-cgaattcggatcctctagcatTTACAGTTTTTTAATTTCTTC-3'. The nucleotides in lower case overlap with the pE-SUMO vector and the nucleotides in upper case overlap with α_3TAG_{32} . The gene was inserted into the pE-SUMO vector using the Gibson isothermal assembly kit (NEB) following the manufacturer's protocol.¹⁵ The construct was confirmed by sequencing at the MIT Biopolymers Laboratory.

A2.2.3 Expression of α_3F_nY as a His₆-Smt3 fusion protein. The pESUMO- α_3TAG_{32} plasmid was co-transformed with a plasmid (pEVOL- F_nY -RS-E3)⁵ harboring the fluorotyrosine tRNA synthetase (F_nY -RS) into BL21(DE3) chemically competent cells and grown overnight (37 °C) on LB plates supplemented with Kan (50 μ g/mL) and Cm (35 μ g/mL). Unnatural amino acid incorporation and protein expression were optimized on a small scale for each α_3F_nY resulting in the following protocol. A 5 mL culture containing Kan and Cm was started from a single colony and grown for ~12 h at 37 °C. This culture was used to inoculate (100-fold dilution) 4 x 2 L of 2XYT medium containing the antibiotics and 1–1.5 mM F_nY (500 mM stock solution prepared in water, NH₄OH solubilized). At an OD₆₀₀ of 0.1–0.2, 0.05% (w/v) L-arabinose was added to induce F_nY -RS. IPTG (0.5 mM) was added at an OD₆₀₀ of 0.9 to induce the expression of His₆-Smt3-

α_3F_nY . Cells were harvested after an additional 5 h of growth at 37 °C. A typical yield of 2.5 g cell paste/L culture was obtained.

A2.2.4 Purification of α_3F_nY . Cell paste (10–20 g) was re-suspended (5 mL/g cell paste) in buffer A (20 mM Tris pH 7.9, 500 mM NaCl, 1 mM PMSF) and lysed via a single passage through the French pressure cell (14,000 psi). Cell debris was removed by centrifugation (20,000 g, 15 min, 4 °C) and the supernatant was loaded onto 30 mL of Ni-NTA agarose (Qiagen) equilibrated with buffer A. The column was washed with 20 column volumes (CVs) of buffer A containing 20 mM imidazole and bound His₆-Smt3- α_3F_nY was eluted with buffer A containing 250 mM imidazole. Protein containing fractions were identified by the Bradford assay, exchanged into buffer A and concentrated to ~5 mg/mL. The His₆-Smt3 tag was removed by incubating the fusion protein with SUMO protease (1:500 protease:Smt3- α_3F_nY) and 5 mM DTT for 1 h at 25 °C. The digestion mixture was passed through a nickel column (30 mL of Ni-NTA agarose) to remove the SUMO protease, His₆-Smt3 and any undigested material. The column was washed with 2–3 CVs of buffer A (with 20 mM imidazole). The α_3F_nY containing fractions were identified by SDS-PAGE and sent to the Tommos lab for further purification by reversed-phase HPLC.

A2.3 RESULTS

A2.3.1 Optimized expression conditions for α_3F_nYs . In Chapter 2, we described the isolation of $\alpha_3(3,5)F_2Y$ as a thioredoxin fusion protein expressed from pET32b- α_3TAG_{32} .¹⁴ With the expression protocol utilized for thioredoxin- $\alpha_3(3,5)F_2Y$ (2 mM 3,5- F_2Y , 0.05% L-arabinose at OD₆₀₀ of 0.2 and 1 mM IPTG at OD₆₀₀ of 0.5), a total of 3 mg full-length $\alpha_3(3,5)F_2Y$ was obtained per L culture. This represents a suppression efficiency of only ~10% compared to 20–100% that we have successfully observed in RNR.^{16,17} It was previously noted that F_nY incorporation to RNR is dependent on the expression vectors; the ratio of full-length to truncated material and the resulting suppression efficiency can change with different vectors.¹⁶ The α_3TAG_{32} gene was cloned into the pE-SUMO vector to assess if the suppression efficiency could be improved with this construct. The pE-SUMO vector appends Smt3, a ~14 kDa ubiquitin-like protein from *S. cerevisiae*, to the N-terminus of α_3F_nY (7.5 kDa), offering several advantages for purification of α_3 . The SUMO protease cleaves the Smt3 tag leaving behind native α_3F_nY with no extra amino acids added between the cleavage site and α_3F_nY . Furthermore, the protease can be easily purified¹³ in large quantities and digestion of the Smt3 tag requires minimal amounts of the protease (1:500 protease:protein) and minimal incubation times (1 h, 25 °C in the case of α_3F_nY).

In a series of small-scale test expressions (100 mL cultures each), the following variables were tested for their effects on the expression of His₆-Smt3- α_3F_nY : F_nY concentration, L-arabinose and IPTG concentrations and induction time. These studies showed that the required concentration of amino acid is dependent on the F_nY ; expression of $\alpha_3(3,5)F_2Y$ and $\alpha_3(2,3,5)F_3Y$ were optimal with 1 mM F_nY , whereas the concentration of 2,3- F_2Y and 2,3,6- F_3Y were increased to 1.5 mM for expression of $\alpha_3(2,3)F_2Y$ and $\alpha_3(2,3,6)F_3Y$ respectively. Expression of His₆-Smt3- α_3F_nY was not affected by variations in the concentration of L-arabinose (0.05–0.1%) or IPTG (0.5–1 mM).

Thus, concentrations of 0.05% (w/v) and 0.5 mM were used for L-arabinose and IPTG respectively. Finally, expression of His₆-Smt3- α_3 F_nY was most sensitive to the timing of L-arabinose and IPTG addition. Optimized expression of His₆-Smt3- α_3 F_nYs required early addition of L-arabinose (OD₆₀₀ of 0.1–0.2) and late addition of IPTG (OD₆₀₀ of 0.9) to the growth medium. Figure A2.1 shows the SDS-PAGE expression gel for each His₆-Smt3- α_3 F_nY under these optimized conditions.

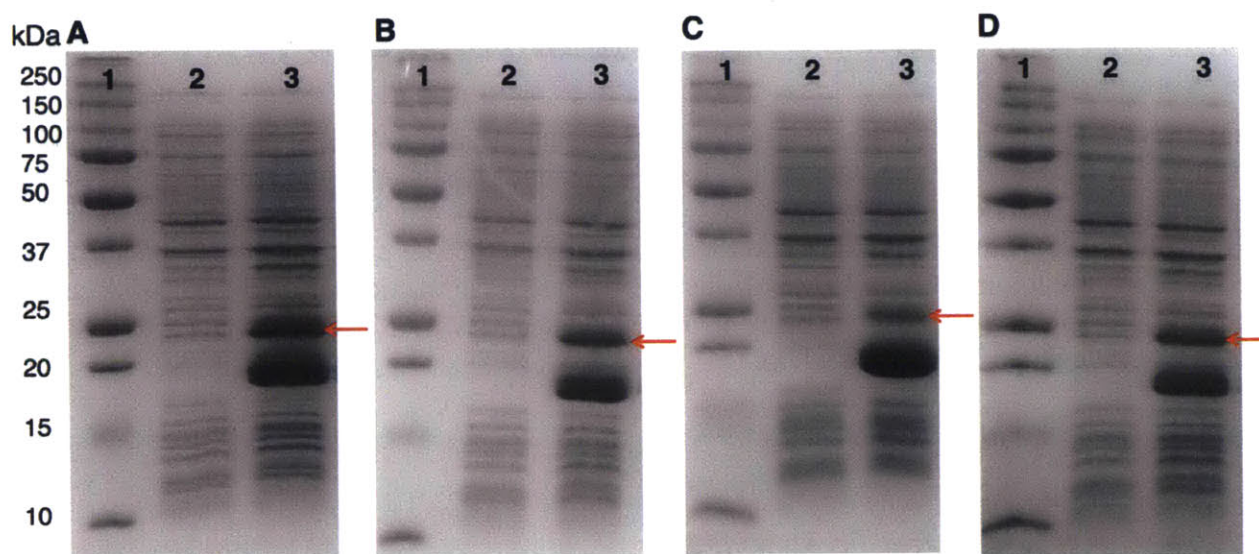


Figure A2.1 SDS-PAGE analysis of α_3 F_nY expression. The SDS-PAGE gels (15%) display in lane (1) molecular weight markers, lane (2) pre-induction sample and in lane (3) expression of α_3 F_nY in the presence of 3,5-F₂Y (panel A), 2,3,5-F₃Y (panel B), 2,3-F₂Y (panel C) and 2,3,6-F₃Y (panel D). α_3 F_nY is expressed as a His₆-Smt3 fusion protein. The calculated molecular weight of truncated His₆-Smt3- α_3 (residues 1–31) is 15971 Da. The calculated molecular weights of full-length His₆-Smt3- α_3 F_nY are 19949 Da (F₂Y at position 32) and 19967 Da (F₃Y at position 32) respectively. Full-length His₆-Smt3- α_3 F_nY is indicated by the red arrow in each panel.

A2.3.2 Purification of α_3 F_nY. Purification of all α_3 F_nYs were straightforward and performed as described in section A2.2.4. Figure A2.2 shows the SDS-PAGE analysis of fractions from the two Ni-NTA columns for $\alpha_3(2,3,5)$ F₃Y as an example. Fractions 5–11 from the second Ni-NTA column (Figure A2.2B) of this particular purification trial were sent to Cecilia Tommos for further purification by HPLC. Fractions containing full-length and truncated $\alpha_3(2,3)$ F₂Y and $\alpha_3(2,3,6)$ F₃Y were collected in a similar fashion.

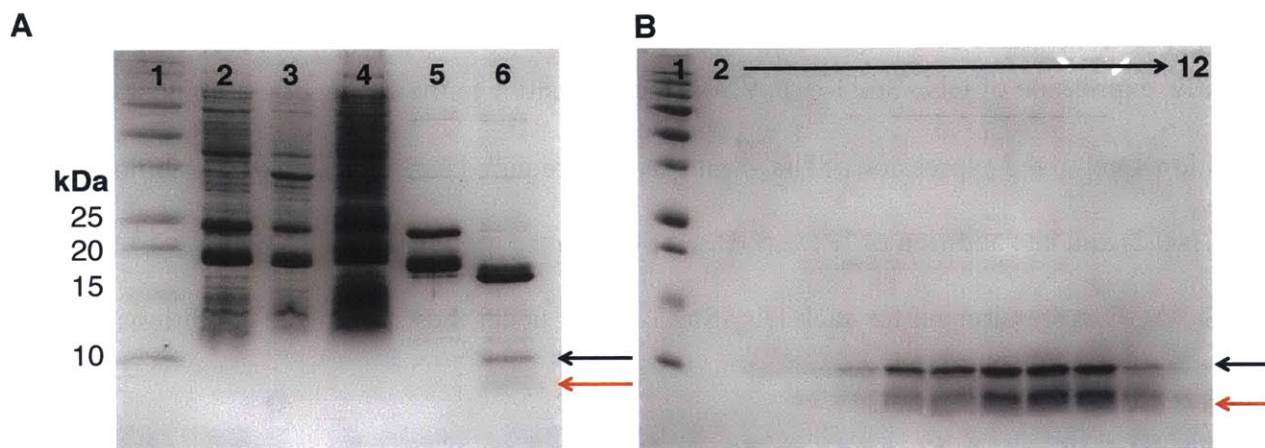


Figure A2.2 Typical purification gels for α_3F_nY . A. Samples from the first Ni-NTA column. The lanes are as follows: (1) MW ladder, (2) lysate containing full-length and truncated His₆-Smt3- $\alpha_3(2,3,5)F_3Y$, (3) cell debris, (4) flow-through from the Ni-NTA column, (5) elution from the Ni-NTA column, (6) sample subsequent to digestion with the SUMO protease. B. Samples from the second Ni-NTA column. Lane (1) MW ladder, (2–12) are wash fractions from the Ni-NTA column showing full-length $\alpha_3(2,3,5)F_3Y$ (black arrow, calculated MW is 7575 Da) and α_3 (residues 1–31, red arrow, calculated MW is 3579 Da).

A2.4 CONCLUSIONS

All α_3F_nY s were successfully expressed and purified. The full-length and truncated α_3F_nY s were separated by reversed-phase HPLC and the formal reduction potentials of all $F_nY\bullet/F_nY$ couples were obtained by SWV (Cecilia Tommos). Calculation of the suppression efficiency for α_3F_nY expressed from pE-SUMO is ongoing.

A2.5 REFERENCES

1. Seyedsayamdost, M. R.; Stubbe, J. Site-specific replacement of Y₃₅₆ with 3,4-dihydroxyphenylalanine in the β 2 subunit of *E. coli* ribonucleotide reductase, *J. Am. Chem. Soc.* **2006**, *128*, 2522-2523.
2. Seyedsayamdost, M. R. ; Stubbe, J. Replacement of Y₇₃₀ and Y₇₃₁ in the α 2 subunit of *Escherichia coli* ribonucleotide reductase with 3-aminotyrosine using an evolved suppressor tRNA/tRNA-synthetase pair, *Methods Enzymol.* **2009**, *462*, 45-76.
3. Minnihan, E. C.; Seyedsayamdost, M. R.; Uhlin, U.; Stubbe, J. Kinetics of radical intermediate formation and deoxynucleotide production in 3-aminotyrosine-substituted *Escherichia coli* ribonucleotide reductases, *J. Am. Chem. Soc.* **2011**, *133*, 9430-9440.
4. Yokoyama, K.; Uhlin, U.; Stubbe, J. A hot oxidant, 3-NO₂Y₁₂₂ radical, unmasks conformational gating in ribonucleotide reductase, *J. Am. Chem. Soc.* **2010**, *132*, 15368-15379.
5. Minnihan, E. C.; Young, D. D.; Schultz, P. G.; Stubbe, J. Incorporation of fluorotyrosines into ribonucleotide reductase using an evolved, polyspecific aminoacyl-tRNA synthetase, *J. Am. Chem. Soc.* **2011**, *133*, 15942-15945.
6. Ravichandran, K. R.; Minnihan, E. C.; Wei, Y.; Nocera, D. G.; Stubbe, J. Reverse electron transfer completes the catalytic cycle in a 2,3,5-trifluorotyrosine-substituted ribonucleotide reductase, *J. Am. Chem. Soc.* **2015**, *137*, 14387-14395.
7. Seyedsayamdost, M. R.; Reece, S. Y.; Nocera, D. G.; Stubbe, J. Mono-, di-, tri-, and tetra-substituted fluorotyrosines: new probes for enzymes that use tyrosyl radicals in catalysis, *J. Am. Chem. Soc.* **2006**, *128*, 1569-1579.
8. Yokoyama, K.; Uhlin, U.; Stubbe, J. Site-specific incorporation of 3-nitrotyrosine as a probe of pK_a perturbation of redox-active tyrosines in ribonucleotide reductase, *J. Am. Chem. Soc.* **2010**, *132*, 8385-8397.
9. Martínez-Rivera, M. C.; Berry, B. W.; Valentine, K. G.; Westerlund, K.; Hay, S.; Tommos, C. Electrochemical and structural properties of a protein system designed to generate tyrosine Pourbaix diagrams, *J. Am. Chem. Soc.* **2011**, *133*, 17786-17795.
10. Berry, B. W.; Martínez-Rivera, M. C.; Tommos, C. Reversible voltammograms and a Pourbaix diagram for a protein tyrosine radical, *Proc. Natl. Acad. Sci. U. S. A.* **2012**, *109*, 9739-9743.
11. Chen, H.; Gollnick, P.; Phillips, R. S. Site-directed mutagenesis of His343-->Ala in *Citrobacter freundii* tyrosine phenol-lyase. Effects on the kinetic mechanism and rate-determining step, *Eur. J. Biochem.* **1995**, *229*, 540-549.
12. Seyedsayamdost, M. R.; Yee, C. S.; Stubbe, J. Site-specific incorporation of fluorotyrosines into the R2 subunit of *E. coli* ribonucleotide reductase by expressed protein ligation, *Nat. Protoc.* **2007**, *2*, 1225-1235.
13. Bendezú, F. O.; Hale, C. A.; Bernhardt, T. G.; de Boer, P. A. RodZ (YfgA) is required for proper assembly of the MreB actin cytoskeleton and cell shape in *E. coli*, *EMBO J.* **2009**, *28*, 193-204.

14. Ravichandran, K. R.; Liang, L.; Stubbe, J.; Tommos, C. Formal reduction potential of 3,5-difluorotyrosine in a structured protein: insight into multistep radical transfer, *Biochemistry* **2013**, *52*, 8907-9015.
15. Gibson, D. G.; Young, L.; Chuang, R. Y.; Venter, J. C.; Hutchison, C. A., 3rd, and Smith, H. O. Enzymatic assembly of DNA molecules up to several hundred kilobases, *Nat. Methods*. **2009**, *6*, 343-345.
16. Minnihan, E. C. Mechanistic studies of proton-coupled electron transfer in aminotyrosine- and fluorotyrosine-substituted class Ia ribonucleotide reductase. Ph.D. Thesis, Massachusetts Institute of Technology, **2012**.
17. Minnihan, E. C.; Nocera, D. G.; Stubbe, J. Reversible, long-range radical transfer in *E. coli* class Ia ribonucleotide reductase, *Acc. Chem. Res.* **2013**, *46*, 2524-2535.

Appendix 3

Kinetics of cofactor assembly in $Y_{122}F_nY\text{-}\beta 2$

Adapted in part from Oyala, P. H.; Ravichandran, K. R.; Funk, M. A.; Stucky, P. A.; Drennan, C. L.; Britt, R. D.; Stubbe, J. J. Am. Chem. Soc. Submitted. 2016.

A3.1 INTRODUCTION

The diferric- $Y\bullet$ cofactor in the class Ia RNR can be self-assembled *in vitro* by the addition of Fe^{2+} and O_2 to the apo protein.¹ The diferrous form of $\beta 2$ reacts with O_2 to form a μ -peroxodiferric intermediate² which is subsequently reduced by W_{48} to generate X, an Fe(IV)Fe(III) intermediate and W_{48}^{++} .^{1,3,4} In the presence of an external reductant, W_{48}^{++} is rapidly reduced to W_{48} , and intermediate X is directly responsible for oxidation of Y_{122} to $Y\bullet$. In the case of wt- $\beta 2$, $Y\bullet$ formation is slow (1 s^{-1} at $5\text{ }^\circ\text{C}$)¹ compared to intermediate X (60 s^{-1} at $5\text{ }^\circ\text{C}$).² It is currently unclear which step (ET, PT or PCET) is rate-limiting for $Y\bullet$ generation.

Table A3.1 Properties of F_nY s.

	λ_{\max} (nm)	pK_a^a	ΔE_p (vs $Y\bullet/Y$) ^a (mV)
Y	410	9.9	0
3,5- F_2Y	396	7.2	-30
2,3,5- F_3Y	404	6.4	10
2,3- F_2Y	410	7.8	45
2,3,6- F_3Y	420	7.0	100

^a Measured by pH titration experiments and differential pulse voltammetry (DPV) studies performed on the *N*-acetylated tyrosinamide derivatives.⁵

Herein we describe the kinetics of cofactor assembly in $Y_{122}F_nY\text{-}\beta 2$ with the goal of understanding the reason for slow $Y\bullet$ formation in the wt system. Previous pH titration experiments performed with $Y_{122}NO_2Y\text{-}\beta 2$ show that position 122 experiences a pK_a perturbation of > 3 units.⁶ Thus, all F_nY s are anticipated to be in the protonated state in the apo protein. We speculated that if PT from Y_{122} is rate-limiting during $Y\bullet$ formation, then $F_nY\bullet$ formation kinetics might directly

correlate with the pK_a of the F_nY analogs (Table A3.1); $F_nY\cdot$ formation could be faster at lower pK_a s. The kinetics of $F_nY\cdot$ formation were monitored by SF UV-vis spectroscopy studies performed at 25 °C. As predicted, the $F_nY\cdot$ s are generated at 10–90 s^{-1} , rate constants that are 2–20-fold faster than observed with $Y\cdot$ ($\sim 4 s^{-1}$ at 25 °C). However, radical formation does not directly correlate with the pK_a of the fluorophenol. A model for our kinetic observations is not readily apparent. However, a few possibilities are discussed.

A3.2 MATERIALS AND METHODS

*A3.2.1 Expression and purification of $Y_{122}F_nY-\beta_2$. *E. coli* TOP10 chemically competent cells were transformed with pBAD-*nrdB*_{122TAG} and pEVOL-*F_nYRS-E3*⁷ and grown at 37 °C on LB-agar plates containing 100 µg/mL ampicillin (Amp) and 35 µg/mL chloramphenicol (Cm). A single colony was used to inoculate a starter culture (5 mL) that was grown until saturation (37 °C, 12–16 h). This culture was diluted 100-fold into fresh 2XYT medium supplemented with Amp and Cm. After 16 h at 37 °C, the culture was diluted 100-fold into 4 x 2 L of 2XYT containing the antibiotics and variable concentrations of F_nY (0.5 mM 3,5- F_2Y , 0.7 mM 2,3,5- F_3Y , 1.5 mM 2,3- F_2Y or 1.5 mM 2,3,6- F_3Y). *F_nYRS* and *nrdB* were both induced at an OD₆₀₀ of 0.6 with 0.05% (w/v) L-arabinose. In case of $Y_{122}(2,3,5)F_3Y-\beta_2$ and $Y_{122}(2,3,6)F_3Y-\beta_2$, 100 µM *o*-phenanthroline was added to chelate the iron 30 min prior to induction with L-arabinose. In all cases, growth was continued for an additional 5 h and the cells were harvested by centrifugation (3500 x g, 15 min). Apo $Y_{122}(2,3,5)F_3Y-\beta_2$ and $Y_{122}(2,3,6)F_3Y-\beta_2$ and holo $Y_{122}(3,5)F_2Y-\beta_2$ and $Y_{122}(2,3)F_2Y-\beta_2$ constructs were isolated by anion-exchange chromatography as previously described.⁶ Typical yields were 30 mg ($Y_{122}(3,5)F_2Y-\beta_2$), 10–15 mg ($Y_{122}(2,3,5)F_3Y-\beta_2$), 5–7 mg ($Y_{122}(2,3)F_2Y-\beta_2$) and 7–12 mg ($Y_{122}(2,3,6)F_3Y-\beta_2$) per g wet cell paste.*

A3.2.2 Chelation of iron from holo $Y_{122}(3,5)F_2Y-\beta_2$ and $Y_{122}(2,3)F_2Y-\beta_2$. As-isolated $Y_{122}F_2Y-\beta_2$ was dialyzed against 2 L of 50 mM 8-hydroxyquinoline-5-sulfonic acid pH 7.0, 1 M imidazole and 30 mM NH₂OH in a Slide-a-lyzer cassette for 3 h. The protein mixture was desalted using a G-25 Sephadex column pre-equilibrated in 50 mM HEPES pH 7.6, 5% glycerol. The total recovery of both proteins was ~70%.

A3.2.3 Reconstitution of the diferric- $F_nY\bullet$ cofactors monitored by SF UV-vis spectroscopy. Temperature was controlled with an external circulating water bath set at 25 °C. Prior to the

experiment, the lines were washed with 10 mL of 300 mM dithionite, 10 mL anaerobic water and 10 mL anaerobic 50 mM HEPES pH 7.6, 5% glycerol. The lines were purged with nitrogen throughout the experiment. Apo $Y_{122}F_nY\text{-}\beta 2$ (40 μM) containing 5 equiv. of Fe^{2+} was mixed with an equal volume of O_2 saturated 50 mM HEPES pH 7.6, 5% glycerol. The reaction was monitored at 324 nm and 364 nm for the diferric cluster and at the λ_{max} for each $F_nY\bullet$. The amounts of diferric cluster were calculated using previously reported extinction coefficients.¹ The extinction coefficient of $F_nY\bullet$ was assumed to be identical to $Y\bullet$ ($3700 \text{ M}^{-1}\text{cm}^{-1}$).¹ In the case of $Y_{122}(2,3,5)F_3Y\text{-}\beta 2$ and $Y_{122}(2,3,6)F_3Y\text{-}\beta 2$, kinetic traces were acquired every 10 nm between 310 nm and 450 nm for point-by-point reconstruction of the reactions.

A3.2.4 Reconstitution of the diferric-2,3,6- $F_3Y\bullet$ monitored by RFQ-EPR spectroscopy.

Temperature was controlled at 25 °C using a circulating water bath. Apo $Y_{122}(2,3,6)F_3Y\text{-}\beta 2$ (80 μM) containing 5 equiv. Fe^{2+} in anaerobic 50 mM HEPES pH 7.6, 5% glycerol was loaded into one syringe and mixed with an equal volume of O_2 saturated 50 mM HEPES pH 7.6, 5% glycerol contained in the second syringe. The reaction mixture was aged for varying times (23 ms–60 s), sprayed into liquid isopentane (140 °C) and the crystals were packed into EPR tubes for analysis by X-band EPR spectroscopy. The EPR parameters are reported in Chapter 3. The spectrum of 2,3,6- $F_3Y\bullet$ at 0.8 s was subtracted from the composite spectrum at each of the early time points (23 ms, 83 ms and 256 ms). Intermediate X was quantitated by double integration of the net spectrum.

A3.2.5 Reconstitution of the diferric-3,5- $F_2Y\bullet$ monitored by RFQ-EPR spectroscopy.

RFQ experiments were performed as described above with minor variations. Temperature was controlled with an external circulating water bath set at 5 °C and the reconstitution of $Y_{122}(3,5)F_2Y\text{-}\beta 2$ was only monitored at two time points: 11 ms and 16 ms.

A3.3 RESULTS

A3.3.1 SF analysis of cofactor assembly in $Y_{122}F_nY-\beta 2$ shows rapid generation of $F_nY\bullet$ compared to $Y\bullet$. When the diferric- $Y\bullet$ cofactor is assembled *in vitro* in the presence of excess Fe^{2+} (5 equiv.), a highly oxidizing Fe(IV)Fe(III) intermediate (X, λ_{max} of ~ 360 nm) is generated that is directly responsible for oxidation of Y_{122} to $Y_{122}\bullet$.^{1,2} The sharp absorbance feature of $Y_{122}\bullet$ at 410 nm facilitates accurate quantitation of this radical using the dropline correction method;¹ when A_{410} is corrected to the line defined by A_{405} and A_{415} , the contribution of $Y_{122}\bullet$ can be isolated. This corrected absorbance is directly proportional to the concentration of $Y_{122}\bullet$. In the case of wt- $\beta 2$, this correction protocol facilitates de-convolution of the visible spectrum at 410 nm; the reaction monitored at 360 nm provides the rate constant for X formation ($60\text{--}80\text{ s}^{-1}$ at $5\text{ }^\circ\text{C}$),² whereas the dropline corrected spectrum at 410 nm provides the rate constant for $Y_{122}\bullet$ ($\sim 1\text{ s}^{-1}$ at $5\text{ }^\circ\text{C}$). The slow rate of formation of $Y_{122}\bullet$ compared to intermediate X results in a lag phase ($60\text{--}80\text{ s}^{-1}$) in A_{410} (dropline corrected) prior to the rise phase for $Y_{122}\bullet$ formation. In contrast to $Y_{122}\bullet$, the visible spectra of $F_nY\bullet$ s are broad,⁵ precluding quantitation of $F_nY\bullet$ amounts by the dropline correction method. As a result, we cannot de-convolute the visible spectra at the λ_{max} for $F_nY\bullet$ s. However, we hypothesized that replacement of Y_{122} with F_nY might affect the rate constant for radical formation but not the rate constant for intermediate X formation. We performed the reconstitution reactions at $25\text{ }^\circ\text{C}$ where intermediate X formation is anticipated to occur at $\sim 200\text{--}300\text{ s}^{-1}$. This rate constant would result in complete formation of X within the first few ms of the reaction ($<5\text{ ms}$), providing the opportunity to isolate $F_nY\bullet$ formation kinetics. If X is directly responsible for generation of $F_nY\bullet$, then we expected that $F_nY\bullet$ formation would either be on par or slower than X formation.

Figures A3.1A and B show the kinetic traces acquired at 396 nm ($3,5\text{-F}_2\text{Y}\cdot$) and 410 nm ($2,3\text{-F}_2\text{Y}\cdot$). The maximum yield of $\text{F}_2\text{Y}\cdot$ is similar to that observed in wt RNR (Table A3.2, $1.0\text{--}1.3 \text{F}_2\text{Y}\cdot/\beta 2$ compared to $1.2 \text{Y}\cdot/\beta 2$ for wt). Additionally, $\text{F}_2\text{Y}\cdot$ formation is biphasic in both cases with rate constants of $\sim 80 \text{ s}^{-1}$ and $\sim 10 \text{ s}^{-1}$ for the two phases, respectively (Table A3.3). However, the two reactions vary in the relative amplitudes of the two phases. For $3,5\text{-F}_2\text{Y}\cdot$, 88% of the radical is generated in the fast phase, whereas this number drops to 17% for $2,3\text{-F}_2\text{Y}\cdot$. Despite our inability to apply the dropline correction method, it is apparent that $\text{F}_2\text{Y}\cdot$ is formed faster than $\text{Y}\cdot$.

Single wavelength kinetics monitoring the $\text{Y}_{122}\text{F}_3\text{Y}\text{-}\beta 2$ reconstitution reactions at 404 nm ($2,3,5\text{-F}_3\text{Y}\cdot$) and 420 nm ($2,3,6\text{-F}_3\text{Y}\cdot$) are shown in Figures A3.2A and A3.3A, respectively. At maximum, yields of 1.3 and $0.8 \text{F}_3\text{Y}\cdot/\beta 2$ are observed for $2,3,5\text{-F}_3\text{Y}\cdot$ and $2,3,6\text{-F}_3\text{Y}\cdot$, respectively (Table A3.2). Similar to our observations for $\text{F}_2\text{Y}\cdot$, $\text{F}_3\text{Y}\cdot$ kinetics are biphasic with rate constants of $60\text{--}70 \text{ s}^{-1}$ and 10 s^{-1} for the two phases (Table A3.3). When the $\text{F}_3\text{Y}\cdot$ s are compared to each other, 90% of $2,3,5\text{-F}_3\text{Y}\cdot$ is generated in the fast phase; however, only 30% of $2,3,6\text{-F}_3\text{Y}\cdot$ is formed in this phase. The kinetics of cofactor assembly in $\text{Y}_{122}\text{F}_3\text{Y}\text{-}\beta 2$ were additionally monitored from 300–450 nm (or 500 nm) to perform point-by-point reconstructions of the reaction spectra (Figures A3.2B and A3.3B). As seen in these reconstructions, the diferric- $\text{F}_3\text{Y}\cdot$ is visible even at 10 ms supporting fast formation of $\text{F}_3\text{Y}\cdot$. The data together support that all $\text{F}_n\text{Y}\cdot$ s are produced rapidly with biphasic kinetics ($60\text{--}90 \text{ s}^{-1}$ and $\sim 10 \text{ s}^{-1}$) that do not correlate with the $\text{p}K_a$ of the fluorophenol (6.4–7.8, Table A3.1).

Finally, although only the first 0.2 s (Figures A3.1A and A3.2A) to 0.4 s (Figures A3.1B, A3.3A) of each reconstitution is shown reaction, all reactions were monitored for ~ 100 s. No loss of $\text{F}_n\text{Y}\cdot$ was recorded in any case except $\text{Y}_{122}(2,3,6)\text{F}_3\text{Y}\text{-}\beta 2$ where $\sim 30\%$ of $2,3,6\text{-F}_3\text{Y}\cdot$ was lost

with a rate constant of 0.05 s^{-1} (Figure A3.4). The instability of $2,3,6\text{-F}_3\text{Y}\cdot$ is supported by the RFQ studies discussed subsequently.

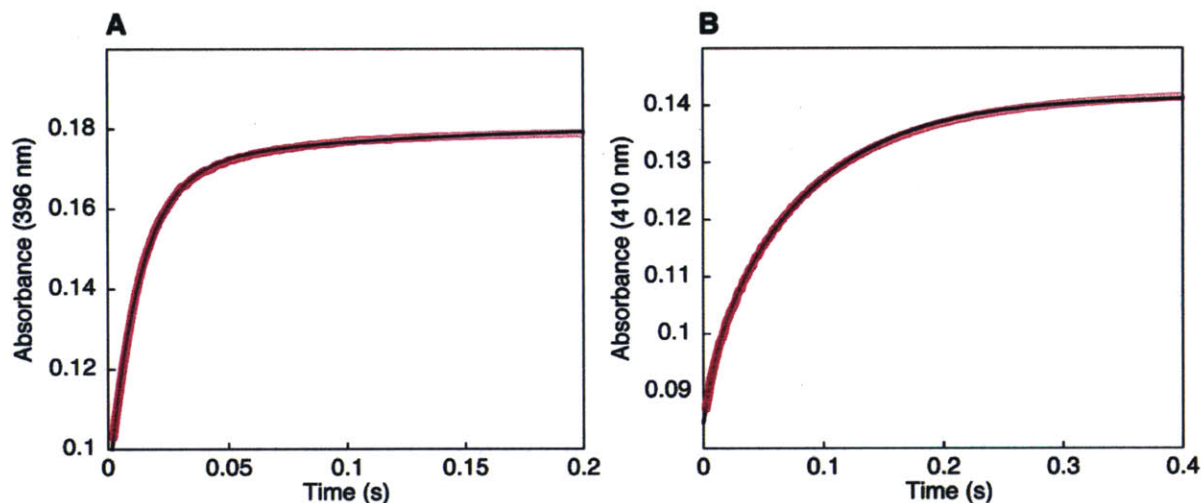


Figure A3.1 Reconstitution of the diferric-3,5- $\text{F}_2\text{Y}\cdot$ (A) and the diferric-2,3- $\text{F}_2\text{Y}\cdot$ (B) cofactors monitored by SF vis spectroscopy conducted at 25°C . Single wavelength kinetics were monitored at either 396 nm (3,5- $\text{F}_2\text{Y}\cdot$) or 410 nm (2,3- $\text{F}_2\text{Y}\cdot$). Each kinetic trace represents the average of 7–10 shots. The black lines represent bi-exponential fits to the data with the rate constants shown in Table A3.3.

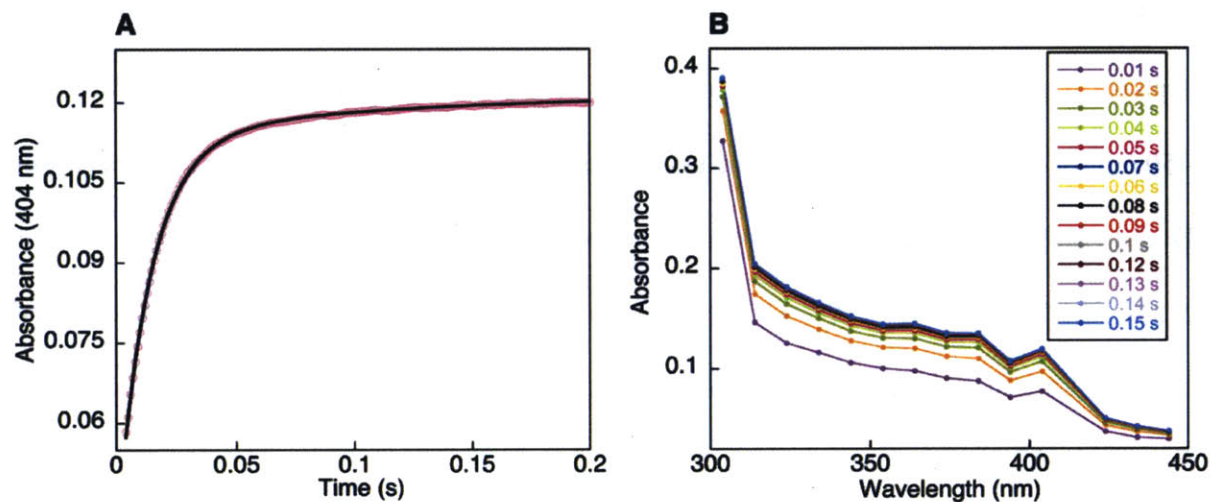


Figure A3.2 Reconstitution of the diferric-2,3,5- $\text{F}_3\text{Y}\cdot$ cofactor monitored by SF vis spectroscopy performed at 25°C . A. Single wavelength kinetics monitoring the reaction at 404 nm (2,3,5- $\text{F}_3\text{Y}\cdot$). Each kinetic trace represents the average of 4–5 shots. The data were fit to a bi-exponential equation providing the rate constants shown in Table A3.3. B. Point-by-point reconstruction of the reaction from kinetic traces acquired every 10 nm between 310 nm and 450 nm. One shot per wavelength is shown but each trace was acquired 2–3 times.

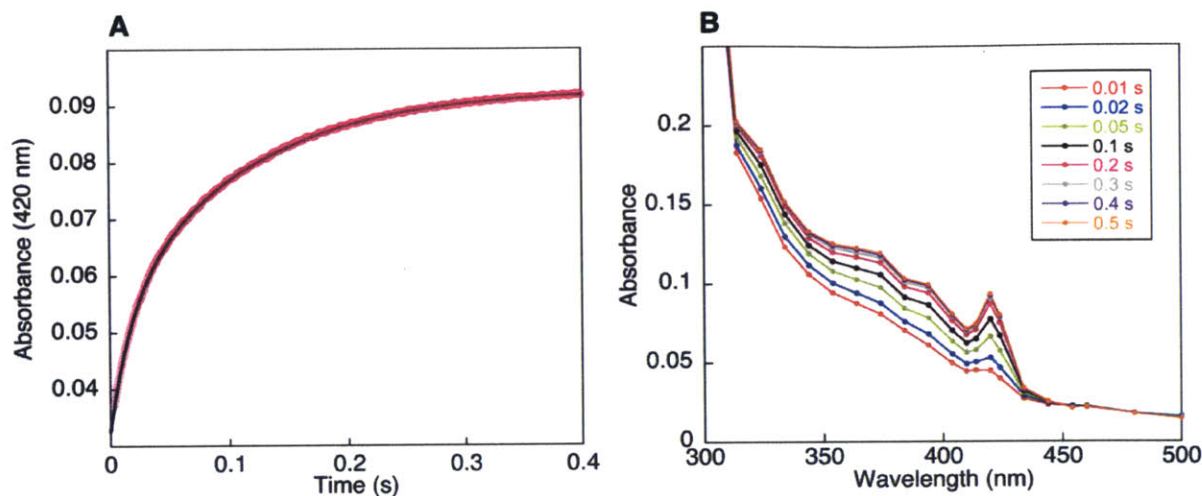


Figure A3.3 Reconstitution of the diferric-2,3,6- F_3Y^\bullet cofactor monitored by SF vis spectroscopy performed at 25 °C. A. Single wavelength kinetics monitoring the reaction at 420 nm (2,3,6- F_3Y^\bullet). Each kinetic trace represents the average of 5–7 shots. The data were fit to a bi-exponential equation providing the rate constants shown in Table A3.3. Point-by-point reconstruction of the reaction from kinetic traces acquired every 10 nm between 310 nm and 500 nm. One shot per wavelength is shown but each trace was acquired 2–3 times.

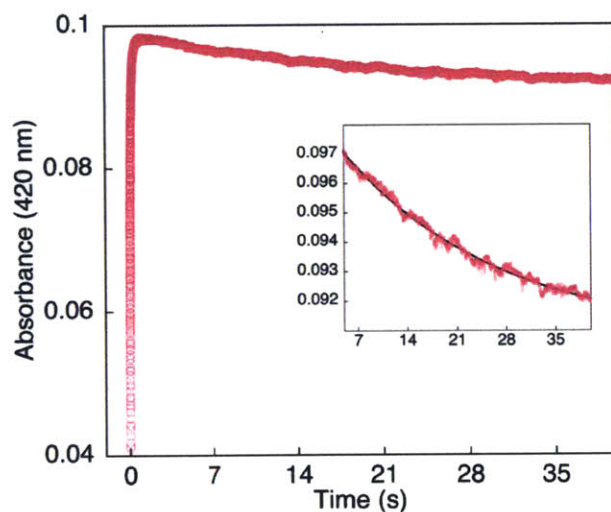


Figure A3.4 Loss of 2,3,6- F_3Y^\bullet with time as observed by SF vis spectroscopy. Single wavelength kinetics monitoring the reaction at 420 nm show loss of 30% 2,3,6- F_3Y^\bullet within 40 s after reconstitution. An expanded view of reaction from 3 ms–0.4 s is shown in Figure A3.3. The inset shows an expanded view of the reaction between 5 s and 40 s. The black trace represents a mono-exponential fit to a rate constant of 0.05 s^{-1} .

Table A3.2 Maximum amounts of intermediate X, diferric cluster and $F_nY\cdot$ observed by SF and RFQ assembly of the diferric- $F_nY\cdot$ cofactors.

$\beta 2$	SF		RFQ	
	Cluster/ $\beta 2^a$	$F_nY\cdot/\beta 2^a$	X/ $\beta 2$	$F_nY\cdot/\beta 2$
3,5- F_2Y	1.5	1.3	nd	nd
2,3,5- F_3Y	1.5	1	nd	nd
2,3- F_2Y	1.6	1.3	nd	nd
2,3,6- F_3Y	1	0.8	1.2	1.2

nd = not determined.

^aThese amounts were calculated from the absorbance values at 324 nm and 364 nm (diferric cluster) and ~410 nm ($F_nY\cdot$) at the time point where maximum amounts of $F_nY\cdot$ are observed. The extinction coefficients of the diferric cluster and $Y\cdot$ have been reported previously.¹ The extinction coefficient of $Y\cdot$ was utilized for $F_nY\cdot$.

Table A3.3 $F_nY\cdot$ formation kinetics at 396 nm (3,5- $F_2Y\cdot$), 404 nm (2,3,5- $F_3Y\cdot$), 410 nm (2,3- $F_2Y\cdot$) and 420 nm (2,3,6- $F_3Y\cdot$).

	SF ^a				RFQ ^b	
	First phase		Second phase		k (s^{-1})	A (%)
	k_1 (s^{-1})	A (%)	k_2 (s^{-1})	A (%)		
3,5- F_2Y	78	88	10	12	nd	nd
2,3,5- F_3Y	72	90	10	10	nd	nd
2,3- F_2Y	86	17	12	83	nd	nd
2,3,6- F_3Y^c	58	30	10	69	7.5	100

^aThe SF trace at the λ_{max} for each $F_nY\cdot$ (~410 nm) was fit to a bi-exponential equation providing the rate constants and amplitudes.

^bThe RFQ-EPR data were fit to a single exponential phase. Formation of 2,3,6- $F_3Y\cdot$ was accompanied by simultaneous loss of intermediate X at $10 s^{-1}$. Data represent a single trial. nd = not determined.

^cSubsequent to generation of maximum amounts of 2,3,6- $F_3Y\cdot$, loss of 30% (SF) to 40% (RFQ) of the radical is observed at $0.05 s^{-1}$ (SF rate constant).

A3.3.2 RFQ assembly of the diferric-2,3,6-F₃Y• and diferric-3,5-F₂Y• cofactors. All SF reconstitution reactions were monitored at 324 nm and 364 nm (data not shown) in addition to the λ_{max} for F_nY• (Figures 3.1–3.4). These wavelengths report on formation of the μ -oxo diferric cluster (324 and 364 nm) and on intermediate X (364 nm). In the case of wt RNR, fast formation of intermediate X (60–80 s⁻¹ at 5 °C)² but slow generation of Y• (~1 s⁻¹ at 5 °C) results in accumulation of intermediate X prior to generation of the μ -oxo diferric cluster. Thus, at early time points in the reconstitution reaction (< 0.2 s), a broad feature can be observed only at ~360 nm (intermediate X) with no visible feature at 320 nm (i.e no diferric cluster).⁸ In the case of the F_nY•s, the entire spectrum (300–500 nm) was only monitored in two of the reconstitution reactions: 2,3,5-F₃Y• and 2,3,6-F₃Y• (Figures A3.2B and A3.3B). However, in both cases the diferric-F_nY• could be visualized even at the earliest time points (<10 ms) suggesting either the absence of X, or the inability to isolate intermediate X from the diferric cluster. Furthermore, the kinetics at 324 and 364 nm were identical to those at the λ_{max} for F_nY• (Table A3.3) suggesting that these kinetics directly report on formation of the μ -oxo diferric cluster that accompanies F_nY oxidation with little or no contribution from intermediate X. These data support that intermediate X formation is fast in Y₁₂₂F_nY- β 2. To assess if any intermediate X can be visualized during F_nY• formation and to determine if intermediate X is directly responsible for generation of F_nY•, we decided to monitor the kinetics of diferric-F_nY• formation in more detail by RFQ-EPR spectroscopy. The assembly of 2,3,6-F₃Y• and 3,5-F₂Y• are described below. The reconstitution kinetics of 2,3-F₂Y• and 2,3,5-F₃Y• by RFQ-EPR spectroscopy have not yet been measured.

The time course for the assembly of the diferric-2,3,6-F₃Y• is shown in Figure A3.5. The spectra between 23 and 256 ms (Figure A3.5A-C, blue) are distinct from that of 2,3,6-F₃Y• alone (Figure A3.5D, orange) and indicate the presence of another EPR active species. The spectrum of

2,3,6-F₃Y• observed at 0.8 s was subtracted from each of the reaction spectra between 23 and 256 ms revealing the presence of a broad singlet (Figures A3.5A-C, red) that is characteristic of intermediate X. Quantitation of intermediate X and 2,3,6-F₃Y• in each of the samples showed that 0.7 X/ β 2 and 0.4 F₃Y•/ β 2 were present at 23 ms. In the case of wt- β 2, a maximum of 1.2 X/ β 2 is observed that is directly responsible for oxidation of 1.2 Y/ β 2. Assuming that a similar amount of X is generated in the 2,3,6-F₃Y reaction, ~40% of this intermediate has already produced F₃Y• within 23 ms. These results suggest rapid formation of both intermediate X and 2,3,6-F₃Y• and support the SF kinetics reported in Table A3.3. With time, loss of X was monitored (10 s⁻¹) concomitant with complete formation of 2,3,6-F₃Y• within 256 ms (1.2 F₃Y•/ β 2, 7.5 s⁻¹, Table A3.3). This rate constant is very similar to the second phase for 2,3,6-F₃Y• formation measured by SF-vis spectroscopy (10 s⁻¹, Table A3.2). Unfortunately, we do not have enough RFQ data points at present to comment on the first fast phase that is observed by SF (58 s⁻¹, Table A3.3).

The 2,3,6-F₃Y• reconstitution reaction was additionally monitored from 256 ms–60 s. Identical to the SF observations, the total amount of radical decayed to 0.7 F₃Y•/ β 2 over 60 s and then remained unchanged (Figure A3.5D). Our current model to explain this observation is that 2,3,6-F₃Y• exists in at least two distinct conformations generated during β 2 folding. One gives rise to a rapidly decaying radical, while the other results in a radical that is substantially stabilized.

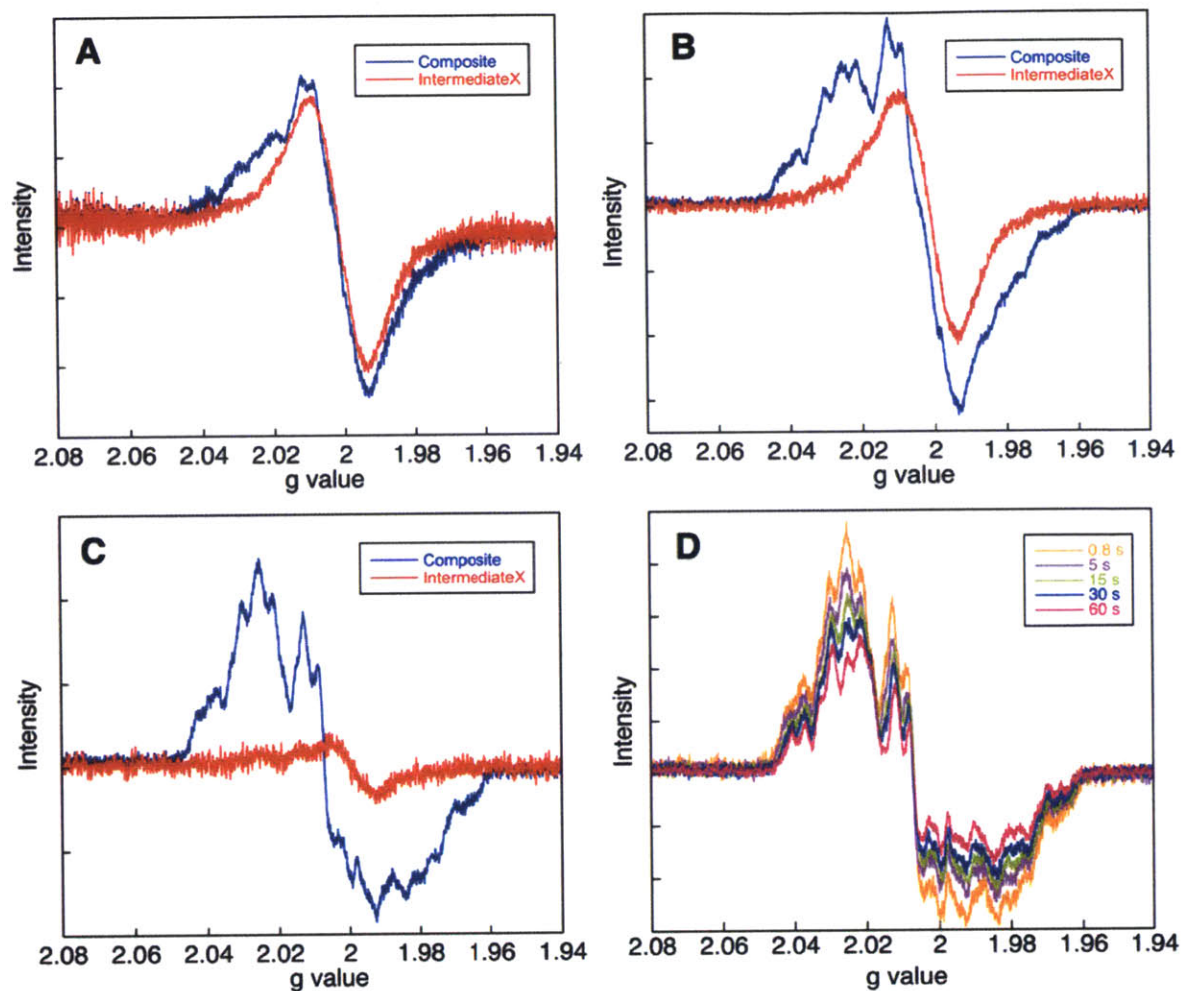


Figure A3.5 Reconstitution of the diferric-2,3,6-F₃Y• cofactor monitored by RFQ-EPR spectroscopy performed at 25 °C. Subtraction of the EPR spectrum of the 0.8 s sample (D, orange) from the composite spectrum at 23 ms (A), 83 ms (B) and 256 ms (C) revealed intermediate X (A, B and C, red). D. Changes can be visualized in the spectrum of 2,3,6-F₃Y• with time. These changes are accompanied by a spin loss of ~ 40% between the 0.8 s and 60 s samples. Data represent a single trial.

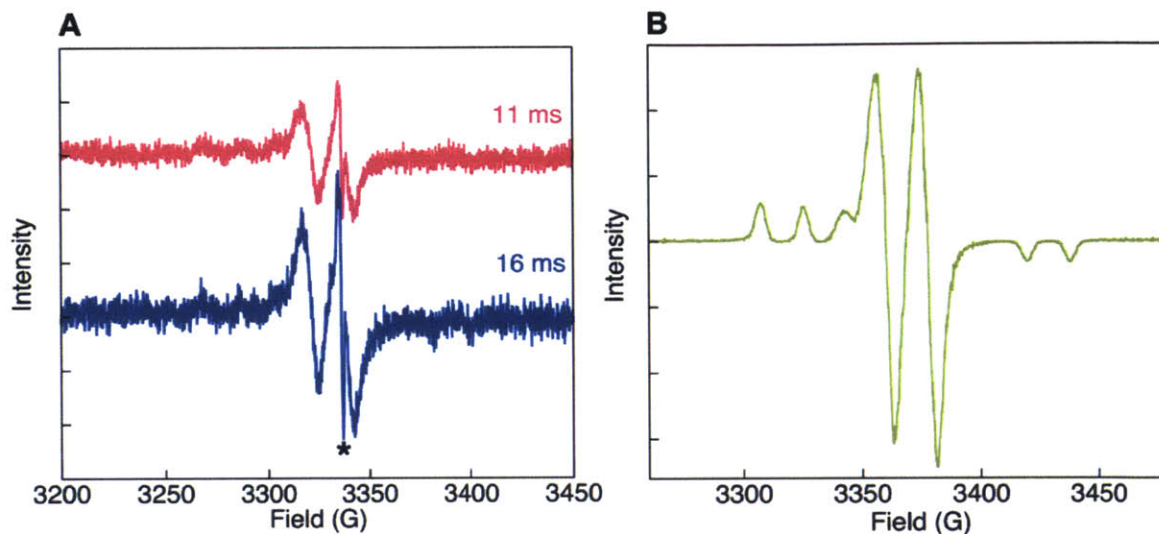


Figure A3.6 A. Reconstitution of the diferric-3,5-F₂Y• cofactor monitored by RFQ-EPR spectroscopy performed at 5 °C. The traces represent the composite EPR spectra at the indicated time points. The asterisk (*) indicates an artifact arising from the finger dewar. B. Reference spectrum of 3,5-F₂Y•. The variations in Field (G) between the two panels arise from differences in the microwave frequency (9.34 GHz, A; 9.45 GHz, B).

The RFQ reconstitution reaction described above shows that intermediate X accumulates during 2,3,6-F₃Y• assembly but also that X is directly responsible for oxidation of 2,3,6-F₃Y at a rate constant of 7.5–10 s⁻¹. However, the fast rate constant of F₃Y• formation precludes isolation of intermediate X from F₃Y• even at the earliest time points. As seen in Table A3.3, ~90% of 2,3,5-F₃Y• and 3,5-F₂Y• are generated at 70–80 s⁻¹. Thus, we predicted that intermediate X may not accumulate during reconstitution of these radical cofactors. Since radical formation in these cases is extremely fast, we decided to lower the temperature to 5 °C and maximize our chances of observing any intermediates. The reconstitution of 3,5-F₂Y• was performed at 5 °C and the EPR spectra of the reaction at two time points (11 ms and 16 ms) are shown in Figure A3.6A. Even at the earlier time point (11 ms), no evidence of intermediate X could be obtained and the spectrum of the reaction is almost identical to that of 3,5-F₂Y• alone (Figure A3.6B). The total radical amount increased from 0.29 F₂Y•/β₂ at 11 ms to 0.36 F₂Y•/β₂ at 16 ms, demonstrating formation

of $F_2Y\bullet$ with time. Additional time points were not collected and therefore, the rate constant for 3,5- $F_2Y\bullet$ formation by RFQ-EPR is currently unavailable. However, as predicted, the data support that intermediate X does not accumulate in the assembly of 3,5- $F_2Y\bullet$.

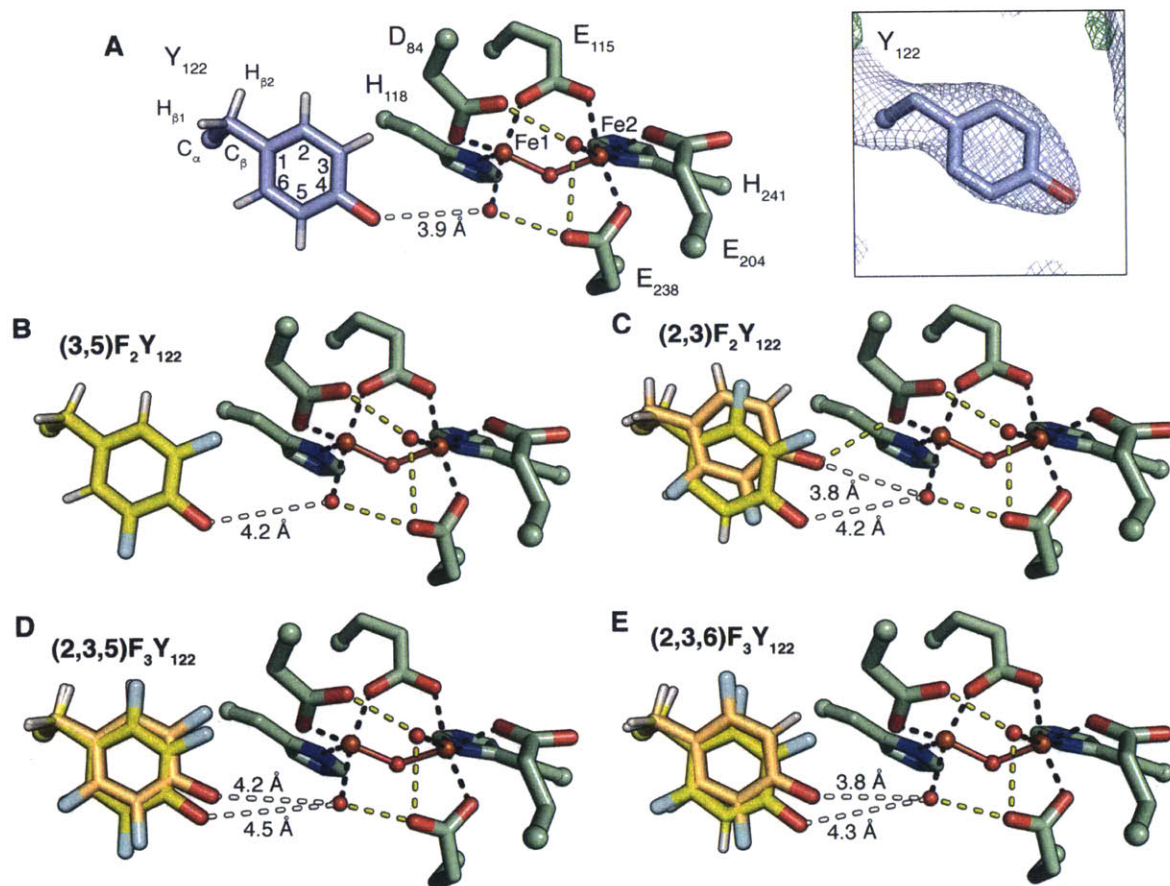


Figure A3.7 Cofactor arrangement in $Y_{122}F_nY\text{-}\beta 2$. (A) The structure of wt met- $\beta 2$ contains a diferric cluster (Fe1 and Fe2, ball and stick) that coordinates two water molecules (red spheres). Iron ligation by protein residues (green) or water is represented by black dashes. Putative hydrogen bonds are shown as yellow dashes. Y_{122} (light blue) is positioned adjacent to Fe1, but not within hydrogen bonding distance (white dash). The electron density for Y_{122} is shown inset ($2F_o - F_c$ at 1σ ; green: $F_o - F_c$ at 3σ ; red: $F_o - F_c$ at -3σ). (B-E) Each $F_nY\text{-}\beta 2$ is shown as in (A). For 2,3- F_2Y , 2,3,5- F_3Y , and 2,3,6- F_3Y two conformations are present. The IN conformation (yellow) in each structure places the fluorine atoms on carbon 2 and 3 adjacent to D_{84} . The OUT conformation (orange) is flipped 180° . Analysis of the occupancy of these conformations suggests the IN conformation is typically dominant. Figure reproduced from Ref. 9.

A3.4 CONCLUSIONS

The kinetics of cofactor assembly in $Y_{122}F_nY-\beta 2$ were investigated with the goal of assessing the effect of pK_a on the kinetics of F_nY_{122} oxidation. If PT is rate-limiting for Y oxidation, we predicted that the rate constant for $F_nY\bullet$ formation would directly correlate with the pK_a of the fluorophenol. SF vis and RFQ-EPR spectroscopic methods show rapid formation of all $F_nY\bullet$ s but with no apparent correlation between pK_a and F_nY oxidation kinetics. The pK_a increases in the order $2,3,5-F_3Y < 2,3,6-F_3Y < 3,5-F_2Y < 2,3-F_2Y$ (Table 3.1); however, the kinetics of cofactor assembly are biphasic in all cases, with rate constants of $60-90\text{ s}^{-1}$ and 10 s^{-1} for the two phases.

Based on the SF data reported in Table A3.3, we hypothesized that the bi-phasic nature of $F_nY\bullet$ formation could reflect formation of two conformationally distinct $F_nY\bullet$; support for this hypothesis is provided by the SF and RFQ assembly studies performed with $2,3,6-F_3Y\bullet$ that show rapid loss of $\sim 40\%$ of the total $2,3,6-F_3Y\bullet$ within ~ 1 min (Figures A3.4 and A3.5D). In collaboration with the Drennan and Britt labs, we recently undertook the task of identifying the conformational changes that occur in $\beta 2$ upon replacement of Y with F_nY . Crystallography studies on $Y_{122}F_nY-\beta 2$ and high field EPR and ENDOR studies on $F_nY\bullet$ both suggest multiple conformations of the reduced F_nY and the oxidized $F_nY\bullet$ within $\beta 2$.⁹ For all asymmetric F_nY s, the X-ray data point to a situation where the two conformations place the position 2 and 3 fluorines either toward D_{84} (IN), one of the ligands to Fe1 of the diferric cluster or have the fluorines flipped 180° (OUT, Figure A3.7). A very rough estimate of the two populations suggests that the IN conformer is the predominant form in all asymmetric F_nY s ($>50\%$). The EPR experiments performed on $F_nY\bullet$ suggest only a single conformation for the asymmetric $2,3-F_2Y\bullet$, which is assigned as the IN conformer. For both $2,3,5-F_3Y\bullet$ and $2,3,6-F_3Y\bullet$, different populations of the IN and OUT conformers are observed by EPR spectroscopy. A majority of $2,3,5-F_3Y\bullet$ exists in the

IN conformation (80%), whereas a majority of 2,3,6-F₃Y• exists in the OUT conformation (75%). The observation of multiple conformers of 2,3,6-F₃Y• was surprising, given that the EPR studies were only performed on the second, more stable 2,3,6-F₃Y•. These results indicate the possibility of additional conformers of F_nY• that are not IN or OUT (Figure A3.7). Comparing 2,3,5-F₃Y and 2,3-F₂Y, the crystallography and EPR data agree that the IN conformer is dominant. However, this contrasts with our kinetic observations where the majority of 2,3,5-F₃Y• (90%) is formed at $\sim 70 \text{ s}^{-1}$, whereas the majority of 2,3-F₂Y• (83%) is formed at $\sim 10 \text{ s}^{-1}$ (Table A3.3). These data suggest that the bi-phasic nature of F_nY• formation does not report on the oxidation of the IN and OUT conformers of F_nY.

In conclusion, we do not currently understand the basis for the observed F_nY• formation kinetics. The SF data reported herein are challenging to deconvolute due to the spectral overlap between intermediate X and F_nY•. Detailed RFQ-EPR studies on the remaining F_nY•s could provide some insight into cluster assembly in Y₁₂₂F_nY-β2 that can be related back to wt-β2.

A3.5 REFERENCES

1. Bollinger, J. M., Jr.; Edmondson, D. E.; Huynh, B. H.; Filley, J.; Norton, J. R.; Stubbe, J. Mechanism of assembly of the tyrosyl radical-dinuclear iron cluster cofactor of ribonucleotide reductase, *Science* **1991**, *253*, 292-298.
2. Tong, W. H.; Chen, S.; Lloyd, S. G.; Edmondson, D. E.; Huynh, B. H.; Stubbe, J. Mechanism of assembly of the diferric cluster-tyrosyl radical cofactor of *Escherichia coli* ribonucleotide reductase from the diferrous form of the R2 subunit, *J. Am. Chem. Soc.* **1996**, *118*, 2107-2108.
3. Bollinger, J. M., Jr; Tong, W. H.; Ravi, N.; Huynh, B. H.; Edmondson, D. E.; Stubbe, J. Mechanism of assembly of the tyrosyl radical-diiron(II) cofactor of *Escherichia coli* ribonucleotide reductase 3. Kinetics of the limiting Fe²⁺ Reaction by optical, EPR, and Mössbauer spectroscopies, *J. Am. Chem. Soc.* **1994**, *116*, 8024-8032.
4. Ravi, N.; Bollinger, J. M., Jr.; Huynh, B. H.; Edmondson, D. E.; Stubbe, J. Mechanism of assembly of the tyrosyl radical-diiron (III) cofactor of *E. coli* ribonucleotide reductase. 1. Mossbauer characterization of the diferric radical precursor, *J. Am. Chem. Soc.* **1994**, *116*, 8007-8014.
5. Seyedsayamdost, M. R.; Reece, S. Y.; Nocera, D. G.; Stubbe, J. Mono-, di-, tri-, and tetra-substituted fluorotyrosines: new probes for enzymes that use tyrosyl radicals in catalysis, *J. Am. Chem. Soc.* **2006**, *128*, 1569-1579.
6. Yokoyama, K.; Uhlin, U.; Stubbe, J. Site-specific incorporation of 3-nitrotyrosine as a probe of pK_a perturbation of redox-active tyrosines in ribonucleotide reductase, *J. Am. Chem. Soc.* **2010**, *132*, 8385-8397.
7. Minnihan, E. C.; Young, D. D.; Schultz, P. G.; Stubbe, J. Incorporation of fluorotyrosines into ribonucleotide reductase using an evolved, polyspecific aminoacyl-tRNA synthetase, *J. Am. Chem. Soc.* **2011**, *133*, 15942-15945.
8. Bollinger, J. M., Jr. On the chemical mechanism of assembly of the tyrosyl radical-dinuclear iron cluster cofactor of *E. coli* ribonucleotide reductase, Ph.D. Thesis, Massachusetts Institute of Technology, **1993**.
9. Oyala, P. H.; Ravichandran, K. R.; Funk, M. A.; Stucky, P.; Stich, T. A.; Drennan, C. L.; Britt, R. D.; Stubbe, J. Biophysical characterization of fluorotyrosine probes site-specifically incorporated into enzymes: *E. coli* ribonucleotide reductase as an example, *J. Am. Chem. Soc. submitted*. **2016**.

Appendix 4

Investigating the role of W₄₈ in long-range radical transport in RNR

A4.1 INTRODUCTION

The participation of W₄₈ in long-range RT was originally suggested by Nordlund and Sjöberg¹ and later by Uhlin and Eklund² based on the individual crystal structures of $\alpha 2$ and $\beta 2$, and the absolute sequence conservation of this residue in all class I RNRs. Evidence for generation of a W₄₈^{•+} has been obtained during *in vitro* assembly of the diferric-Y• cofactor.³ During cluster formation, an extra electron is required to generate the Fe(IV)/Fe(III) intermediate, X, which subsequently oxidizes Y₁₂₂ to Y₁₂₂•. Under conditions of limiting iron (2.0–2.4 Fe²⁺/β2) and in the absence of any exogenous reductant, this extra electron is provided by W₄₈ generating W₄₈^{•+}.³ Replacement of W₄₈ with a redox inert F abolishes formation of this radical; however, it does not eliminate Y₁₂₂• generation and a mixture of intermediate X and Y₁₂₂• is observed by EPR and Mössbauer spectroscopic methods.⁴ Unfortunately, the W₄₈F-β2 variant could not be tested for its activity in nucleotide reduction due to rapid decay of Y₁₂₂• upon subsequent reaction with intermediate X.⁴ The importance of W₄₈ to dCDP formation has been established in the mouse enzyme.⁵ The W₄₈ equivalent, W₁₀₃, was mutated to either Y or F and these variants were tested for their ability to assemble the diferric-Y• cofactor, maintain subunit interaction and catalyze nucleotide reduction. Interestingly, W₁₀₃Y could assemble wt levels of Y• (0.6 Y•/β for each) whereas, W₁₀₃F contained only ~0.03 Y•/β. Both constructs maintained the ability to bind $\alpha 2$ (K_d of ~0.15 μ M for wt and mutant βs), but were inactive as determined by a single time point assay monitoring CDP to dCDP conversion after 30 min at 37 °C.⁵

More recently, we utilized our ability to accumulate radical intermediates on pathway by the site-specific incorporation of UAAs, to investigate the role of W_{48} in RT. Specifically, the double mutant $Y_{122}NO_2Y/Y_{356}F-\beta 2$ was reacted with $\alpha 2$, CDP and ATP and monitored for the presence of $W\cdot$ (or $W^{+\cdot}$)^x (Yokoyama, Stubbe unpublished results). NO_2Y at position 122 is postulated to raise the driving force for RT by ~ 200 mV.⁶ Use of this strong oxidant to initiate RT with $\alpha 2$ results in rapid accumulation of $Y_{356}\cdot$ ($100\text{--}300\text{ s}^{-1}$),⁷ offering an alternate way to test the involvement of W_{48} in the RT pathway. With the double mutant $Y_{122}NO_2Y/Y_{356}F-\beta 2$, cluster assembly is unaffected as the native W_{48} is intact, but $Y_{356}\cdot$ cannot be generated due to its replacement with the redox inert F (Figure A4.1). This experimental design allows us to address if $W\cdot$ (+) could accumulate in the reaction of $Y_{122}NO_2Y/Y_{356}F-\beta 2$ with $\alpha 2$. However, it is important to note that this study can establish if $W\cdot$ (+) is generated in a kinetically competent manner, but it cannot demonstrate chemical competence due to presence of $Y_{356}F$. The reaction of $Y_{122}NO_2Y/Y_{356}F-\beta 2$, $\alpha 2$, CDP and ATP was investigated in detail using a variety of spectroscopic methods (SF vis, RFQ-EPR and PELDOR). These studies demonstrated rapid formation of $W^{+\cdot}$ ^{xi} ($100\text{--}300\text{ s}^{-1}$); however, multiple $W^{+\cdot}$ s located at positions throughout $\beta 2$ were detected by PELDOR spectroscopy including $W_{48}^{+\cdot}$ (Yokoyama, Stubbe unpublished results). These results precluded assessment of W_{48} 's involvement RT and suggested that the strong oxidant, $NO_2Y\cdot$ is capable of off-pathway oxidation when Y_{356} is blocked.

Given the results obtained with $Y_{122}NO_2Y/Y_{356}F-\beta 2$, we sought to modulate the driving force of RT to a lesser extent. With this goal in mind, $Y_{122}F_nY/Y_{356}F-\beta 2$ s were investigated for

^x $W\cdot$ (or $W^{+\cdot}$) will be abbreviated as $W\cdot$ (+) through out this work.

^{xi} The assignment of the radical as $W^{+\cdot}$ and not $W\cdot$ is based on the observation of an absorption peak centered around 560 nm by SF vis spectroscopy.

their ability to generate $W_{48}^{\bullet (+)}$. These Y analogs span the ΔE regime between Y and NO_2Y (Figure A4.1). In contrast to $Y_{122}NO_2Y-\beta 2$, the single mutants $Y_{122}(2,3,5)F_3Y-\beta 2$ and $Y_{122}(2,3)F_2Y-\beta 2$, can catalyze multiple turnovers while maintaining the ability to accumulate Y_{356}^{\bullet} .^{8,9} The reaction of $Y_{122}(2,3,5)F_3Y/Y_{356}F-\beta 2$ (or $Y_{122}(2,3)F_2Y/Y_{356}F-\beta 2$) with $\alpha 2$, CDP and ATP was investigated by hand-quench EPR and SF vis spectroscopic methods (Minnihan, Stubbe unpublished results). These studies showed no loss of F_nY^{\bullet} or formation of $W_{48}^{\bullet (+)}$.

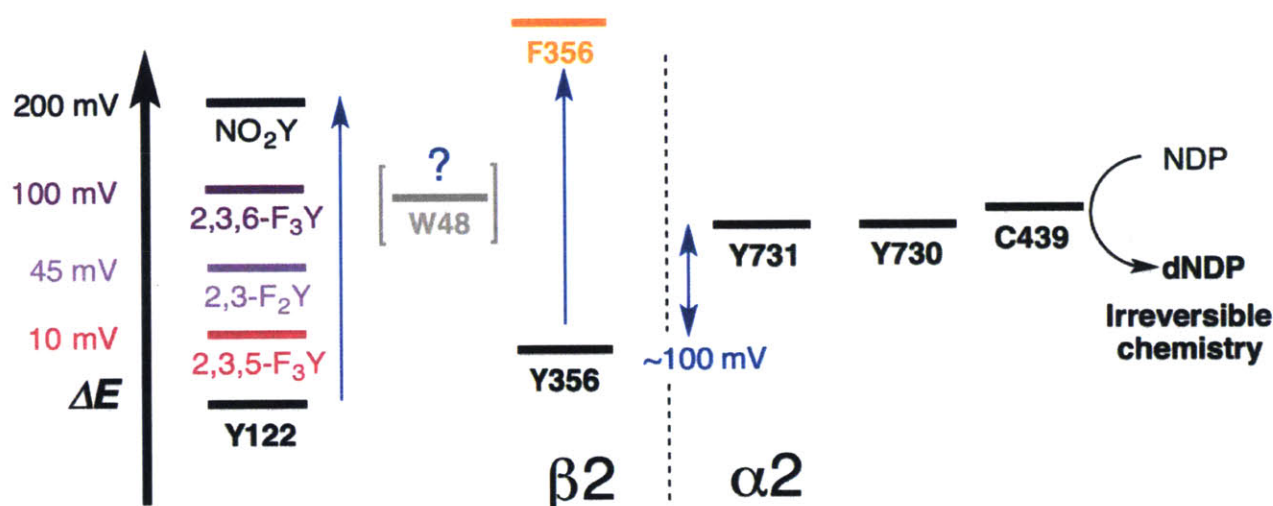


Figure A4.1 Experimental design to test the role of W_{48} in RT. Y_{122} is replaced with unnatural Y analogs that raise the driving force for radical propagation. ΔE was calculated from previously reported solution peak potentials^{xii, 10} Y_{356} is replaced with a redox inert F.

Herein we describe further efforts to detect $W_{48}^{\bullet (+)}$ in the $Y_{122}F_nY/Y_{356}F-\beta 2$ systems. The reaction of $Y_{122}(2,3,5)F_3Y/Y_{356}F-\beta 2$ (or $Y_{122}(2,3)F_2Y/Y_{356}F-\beta 2$) with $\alpha 2$, CDP and ATP was investigated by RFQ-EPR spectroscopy and show no evidence for $W_{48}^{\bullet (+)}$ formation, supporting the earlier SF UV-vis spectroscopy studies. We additionally describe the site-specific insertion of

^{xii} The potential differences were calculated from the DPV data on the *N*-acetylated tyrosinamide derivatives. The exact perturbation to the reduction potential of Y_{122} remains unknown. At least in the case of $Y_{122}(2,3,5)F_3Y-\beta 2$, the driving force was shown to increase by ~ 116 mV instead of the anticipated 10 mV (Chapter 4). Although we do not know the exact ΔE , the order shown in the Figure is predicted to hold true.

2,3,6-F₃Y at position 122, and monitor the reaction of the single mutant, Y₁₂₂(2,3,6)F₃Y-β₂, or the double mutant, Y₁₂₂(2,3,6)F₃Y/Y₃₅₆F-β₂, with α₂, CDP and ATP. The 2,3,6-F₃Y analog is proposed to be more oxidizing than 2,3-F₂Y but less oxidizing than NO₂Y.^{10,11} In agreement with our observations for Y₁₂₂(2,3,5)F₃Y-β₂, Y₁₂₂(2,3)F₂Y-β₂ and Y₁₂₂NO₂Y-β₂, EPR spectroscopy demonstrates that the single mutant, Y₁₂₂(2,3,6)F₃Y-β₂, accumulates Y₃₅₆• (50% of total spin) when reacted with α₂, CDP and ATP. SF UV-vis spectroscopy of the reaction of the double mutant, Y₁₂₂(2,3,6)F₃Y/Y₃₅₆F-β₂, with α₂, CDP and ATP shows biphasic generation of a W• (+) (40–100 s⁻¹ and 5–10 s⁻¹ for the two phases) that together constitute 30–40% of the total radical content in the reaction. RFQ-EPR spectroscopy of the reaction supports the SF studies and shows rapid formation of 30% W• (+) within 60 ms. The data taken together suggest that W• (+) cannot be observed until the driving force for RT is significantly perturbed; ΔE_p between the 2,3,6-F₃Y•/2,3,6-F₃Y and Y•/Y couples is predicted to be ~100 mV.¹⁰ Further experimental studies including PELDOR spectroscopy on the Y₁₂₂(2,3,6)F₃Y/Y₃₅₆F-β₂/α₂/CDP/ATP reaction are required to confirm the location of the W• (+) observed in this system and determine its implications to RT.

A4.2 MATERIALS AND METHODS

A4.2.1 Materials. $Y_{122}(2,3,5)F_3Y/Y_{356}F-\beta 2$ (0.9 $F_3Y\bullet/\beta 2$) and $Y_{122}(2,3)F_2Y/Y_{356}F-\beta 2$ (0.6 $F_2Y\bullet/\beta 2$) were expressed, purified and reconstituted by Ellen C. Minnihan.^{8,12} Expression of apo $Y_{122}(2,3,6)F_3Y-\beta 2$ (or $Y_{122}(2,3,6)F_3Y/Y_{356}F-\beta 2$) was performed in the presence of 1.5 mM 2,3,6- F_3Y following the protocol described in Appendix 3. Typical yields of 10–15 mg pure protein were obtained per g wet cell paste for each construct. The wt- $\alpha 2$ (2500 nmol/min/mg) was purified as previously described.¹³ CDP and ATP were purchased from Sigma Aldrich. Assay buffer consists of 50 mM HEPES pH 7.6, 15 mM $MgSO_4$ and 1 mM EDTA. Temperature was controlled at 25 °C using an external Lauda RM6 circulating water bath unless otherwise specified.

A4.2.2 Reaction of $Y_{122}(2,3,5)F_3Y/Y_{356}F-\beta 2$, $\alpha 2$, CDP and ATP monitored by RFQ-EPR spectroscopy. RFQ experiments were performed on an Update Instruments 1019 syringe ram unit and a model 715 Syringe Ram controller (ram speed 1.25–1.6 cm/s). $Y_{122}(2,3,5)F_3Y/Y_{356}F-\beta 2$ (0.9 $F_3Y\bullet/\beta 2$, 80 μM) and CDP (2 mM) in assay buffer was rapidly (16–161 ms) mixed with an equal volume of wt- $\alpha 2$ (80 μM) and ATP (6 mM). The time points for the reaction were chosen based on the kinetics of $Y_{356}\bullet$ formation measured with the single mutant $Y_{122}(2,3,5)F_3Y-\beta 2$ (Chapter 3). The reaction mixtures were sprayed into liquid isopentane (-140 °C) and packed into X-band EPR tubes for analysis by EPR spectroscopy. The EPR parameters were previously described (Chapter 3).

A4.2.3 Reaction of $Y_{122}(2,3)F_2Y/Y_{356}F-\beta 2$, $\alpha 2$, CDP and ATP monitored by RFQ-EPR spectroscopy. The reaction was performed identical to that described above except $Y_{122}(2,3,5)F_3Y/Y_{356}F-\beta 2$ was replaced with $Y_{122}(2,3)F_2Y/Y_{356}F-\beta 2$ (0.6 $F_2Y\bullet/\beta 2$, 80 μM). The reaction was quenched at either 16 ms or 48 ms and analyzed by X-band EPR spectroscopy using

the parameters described in Chapter 3. Residual 2,3-F₂Y• was subtracted from each reaction mixture by aligning the distinct features of this radical on the high- and low-field sides of the spectrum as previously demonstrated.¹²

A4.2.4 Reaction of Y₁₂₂(2,3,6)F₃Y-β2 (or Y₁₂₂(2,3,6)F₃Y/Y₃₅₆F-β2), α2, CDP and ATP monitored by EPR spectroscopy. Apo Y₁₂₂(2,3,6)F₃Y-β2 or Y₁₂₂(2,3,6)F₃Y/Y₃₅₆F-β2 (300 μL of 200 μM) was deoxygenated and taken into the anaerobic chamber (4 °C). Fe^{II}(NH₄)₂(SO₄)₂ (5 equiv.) was incubated with the protein for 15 min. The iron-loaded protein was split into two aliquots, each contained in a sealed eppendorf tube, taken out of the chamber and mixed one at a time with 3.5 equiv. of O₂ in the form of O₂-saturated 50 mM HEPES pH 7.6, 5% glycerol (4 °C). One aliquot of the protein (240 μL) was frozen 30 s after the addition of O₂ in liquid N₂ to record the EPR spectrum of 2,3,6-F₃Y• and quantitate the total amount of radical. The second aliquot was diluted immediately after the addition of O₂ to a final concentration of 30 μM in assay buffer containing 30 μM wt-α2, 1 mM CDP and 3 mM ATP maintained on ice. The reaction mixture was transferred to an X-band EPR tube and frozen in liquid nitrogen at 30 s. The EPR spectra were recorded at 77K using the parameters described in Chapter 3. The spectrum of 2,3,6-F₃Y• at 30 s was subtracted from that of the reaction mixture at 30 s by aligning the distinct features of the radical on the high- and low-field sides of the spectrum.

A4.2.5 Reaction of Y₁₂₂(2,3,6)F₃Y/Y₃₅₆F-β2, α2, CDP and ATP monitored by SF vis spectroscopy. SF experiments were performed on an Applied Photophysics DX 17MV instrument with a Pro-Data upgrade. Prior to the experiment the lines were washed with 10 mL of 300 mM dithionite, 10 mL of anaerobic water and 10 mL of anaerobic 50 mM HEPES pH 7.6, 5% glycerol. The connections of the stopped flow syringes were purged with nitrogen throughout the experiment. Y₁₂₂(2,3,6)F₃Y/Y₃₅₆F-β2 (80 μM containing 5 equiv. Fe²⁺) in assay buffer was mixed

with O₂-saturated 50 mM HEPES pH 7.6, 5% glycerol containing 4 mM CDP. The reconstituted protein was aged for 1 s to allow complete formation of 2,3,6-F₃Y• (Appendix 3) and then mixed with an equal volume of α 2 (40 μ M) and ATP (6 mM) in 2X assay buffer. The reaction was monitored continuously for 10 s at 420 nm (F₃Y•, 3700 M⁻¹cm⁻¹), 510 nm (W•, ~2200 M⁻¹cm⁻¹) and 560 nm (W⁺, ~3000 M⁻¹cm⁻¹).

A4.2.6 Reaction of Y₁₂₂(2,3,6)F₃Y/Y₃₅₆F- β 2, α 2, CDP and ATP monitored by RFQ-EPR spectroscopy. RFQ experiments were performed following a three-syringe mixing protocol. Apo Y₁₂₂(2,3,6)F₃Y/Y₃₅₆F- β 2 was loaded with 5 equiv. of Fe^{II}(NH₄)₂(SO₄)₂ in the anaerobic chamber. The iron-loaded protein was diluted to 90 μ M in 50 mM HEPES pH 7.6, 5% glycerol and loaded into an RFQ syringe. The sealed syringe was brought out of the chamber and attached to the RFQ instrument. Fe²⁺-Y₁₂₂(2,3,6)F₃Y/Y₃₅₆F- β 2 was mixed with an equal volume of O₂-saturated 50 mM HEPES pH 7.6, 5% glycerol containing 3 mM CDP. The reaction was aged for 1 s (see Appendix 3) and then mixed with an equal volume of α 2 (90 μ M) and ATP (9 mM). The mixture was incubated for 23–131 ms and then sprayed into liquid isopentane (-140 °C). Samples were analyzed by EPR spectroscopy using previously described parameters (Chapter 3).

A4.2.7 Reaction of Y₁₂₂(2,3,6)F₃Y/Y₃₅₆F- β 2, α 2, CDP and ATP monitored by SF vis spectroscopy equipped with a diode array detection system. Experiments were performed on a Hi-Tech Scientific SF61 DX2 double mixing SF system equipped with a KinetaScan CCD detector for monitoring the reaction spectrum (350–800 nm) with time. The connections of the stopped flow syringes were purged with nitrogen throughout the experiment. Iron-loaded Y₁₂₂(2,3,6)F₃Y/Y₃₅₆F- β 2 (70 μ M containing 5 equiv. Fe^{II}) in anaerobic 50 mM HEPES pH 7.6, 5% glycerol was mixed with an equal volume of O₂-saturated 50 mM HEPES pH 7.6, 5% glycerol containing 4 mM CDP. The reaction was aged for 1 s (see Appendix 3) and then mixed with α 2

(35 μM) and ATP (6 mM) in 2X assay buffer. The reaction was monitored at all wavelengths (350–800 nm) for 0.5 s. As a control experiment, CDP was omitted from the reaction.

A4.3 RESULTS

A4.3.1 No evidence of $W_{48}^{\bullet (+)}$ in the reaction of $Y_{122}(2,3,5)F_3Y/Y_{356}F-\beta 2$, $\alpha 2$, CDP and ATP. The reaction of $Y_{122}(2,3,5)F_3Y/Y_{356}F-\beta 2$ with $\alpha 2$, CDP and ATP has been previously monitored by hand-quench EPR and SF vis spectroscopic methods.¹² In both cases, no evidence was obtained for loss of the stable F_3Y^{\bullet} or formation of W_{48}^{\bullet} (or $W_{48}^{\bullet (+)}$). To corroborate these studies, we monitored the reaction of $Y_{122}(2,3,5)F_3Y/Y_{356}F-\beta 2$ with $\alpha 2$, CDP and ATP by RFQ-EPR spectroscopy. Figure A4.2A shows the RFQ time course of the reaction at the indicated time points. No variations in the total radical amount ($0.9 F_3Y^{\bullet}/\beta 2$) were observed and no changes in the spectral features were recorded. At each time point, the EPR spectrum of 2,3,5- F_3Y^{\bullet} was subtracted from the composite spectrum by utilizing the distinct features of the radical on the low- and high-field regions of the spectrum. Figure A4.2B shows the subtraction analysis on the 16 ms sample as an example. The net spectrum (black) is not consistent with $W^{\bullet (+)}$. These results support our previous conclusions that $W_{48}^{\bullet (+)}$ is not generated in the reaction of $Y_{122}(2,3,5)F_3Y/Y_{356}F-\beta 2$ with $\alpha 2$, CDP and ATP.

A4.3.2 No evidence of $W_{48}^{\bullet (+)}$ in the reaction of $Y_{122}(2,3)F_2Y/Y_{356}F-\beta 2$, $\alpha 2$, CDP and ATP. Similar to our observations with $Y_{122}(2,3,5)F_3Y/Y_{356}F-\beta 2$, hand-quench EPR and SF vis spectroscopic methods show no evidence for $W_{48}^{\bullet (+)}$ formation in the reaction of $Y_{122}(2,3)F_2Y/Y_{356}F-\beta 2$ with $\alpha 2$, CDP and ATP.¹² To validate these observations, $Y_{122}(2,3)F_2Y/Y_{356}F-\beta 2$ and CDP were rapidly mixed with $\alpha 2$ and ATP and the reaction was monitored by RFQ-EPR spectroscopy. Figure A4.3A shows the EPR spectra of reaction mixtures quenched at 16 ms and 48 ms. No changes in spectral features were observed between the two samples and no loss in radical content ($0.6 F_2Y^{\bullet}/\beta 2$) was recorded. Subtraction of the stable 2,3- F_2Y^{\bullet} spectrum (blue, Figure A4.3B) from the reaction mixture at 16 ms (pink) reveals spectral

noise (black). Subtraction of 2,3-F₂Y• from the reaction mixture at 48 ms provided identical observations. The data agree with our previous conclusions and we conclude that W₄₈• (+) is not generated in the reaction of Y₁₂₂(2,3)F₂Y/Y₃₅₆F-β2 with α2, CDP and ATP.

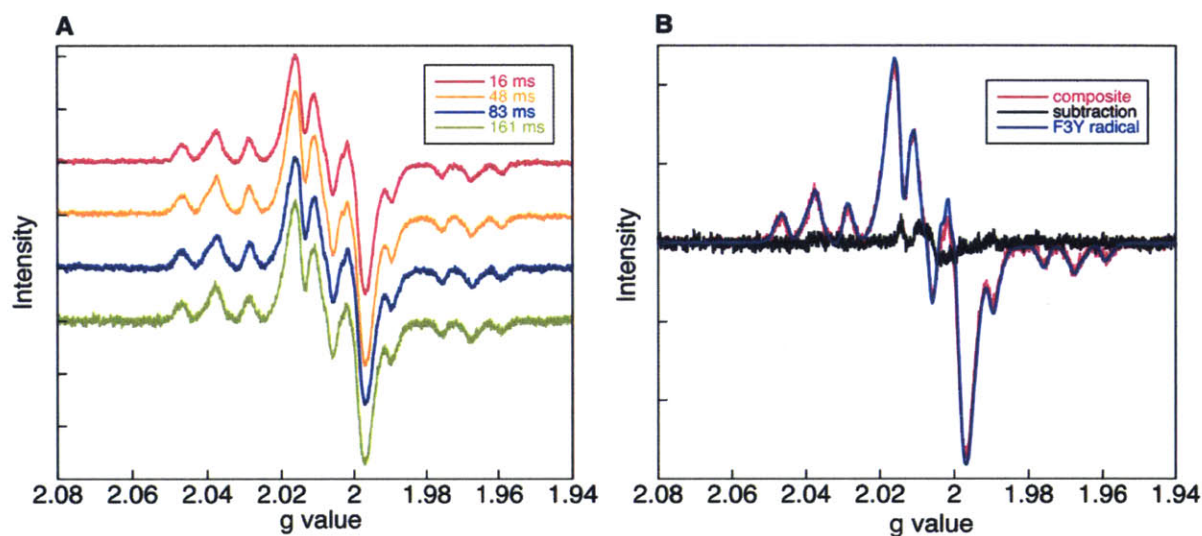


Figure A4.2 Reaction of Y₁₂₂(2,3,5)F₃Y/Y₃₅₆F-β2, α2, CDP and ATP monitored by RFQ-EPR spectroscopy. A. The composite EPR spectra recorded at the time points indicated. B. Subtraction of 2,3,5-F₃Y• (blue) from a composite spectrum (16 ms, pink) reveals spectral noise (black).

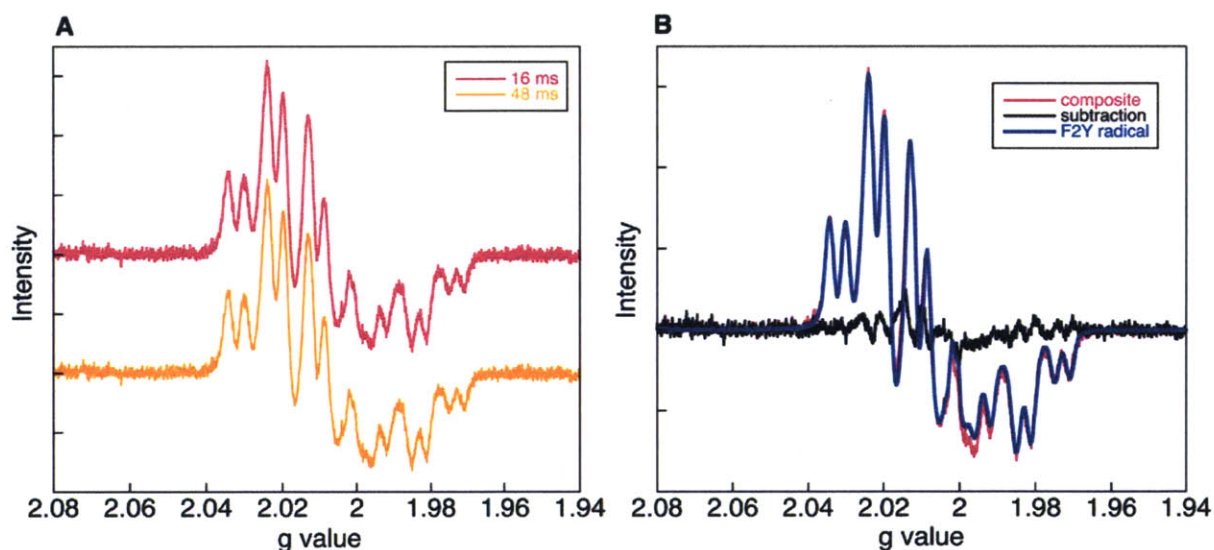


Figure A4.3 Reaction of Y₁₂₂(2,3)F₂Y/Y₃₅₆F-β2, α2, CDP and ATP monitored by RFQ-EPR spectroscopy. A. The composite EPR spectra recorded at the time points indicated. B. Subtraction of 2,3-F₂Y• (blue) from a composite spectrum (16 ms, pink) reveals spectral noise (black).

A4.3.3 $Y_{356}\bullet$ is generated in the reaction of $Y_{122}(2,3,6)F_3Y\text{-}\beta 2$ with $\alpha 2$, CDP and ATP. Upon confirming that $W\bullet (+)$ is not generated by $Y_{122}(2,3,5)F_3Y/Y_{356}F\text{-}\beta 2$ or $Y_{122}(2,3)F_2Y/Y_{356}F\text{-}\beta 2$, we turned to 2,3,6- F_3Y as a driving force modulator. This analog is predicted to be ~ 100 mV harder to oxidize than Y compared to 10 mV and 45 mV for 2,3,5- F_3Y and 2,3- F_2Y respectively.^{10,11} Prior to investigating the reaction of the double mutant $Y_{122}(2,3,6)F_3Y/Y_{356}F\text{-}\beta 2$ with $\alpha 2$, we wanted to confirm that the single mutant $Y_{122}(2,3,6)F_3Y\text{-}\beta 2$ maintained the ability to accumulate $Y_{356}\bullet$.

Similar to wt- $\beta 2$ and the other $Y_{122}F_nY\text{-}\beta 2$ s, the diferric-2,3,6- $F_3Y\bullet$ can be self-assembled *in vitro* by the addition of Fe^{2+} and O_2 to the apo protein. The detailed kinetic analysis of the cluster assembly process in $Y_{122}(2,3,6)F_3Y\text{-}\beta 2$ is presented in Appendix 3. SF UV-vis and RFQ-EPR spectroscopic methods show that 0.8–1.2 $F_3Y\bullet/\beta 2$ can be self-assembled rapidly (biphasic kinetics; 50–60 s^{-1} and 10 s^{-1} respectively). However, $\sim 40\%$ of the total radical content is lost within 2 min, leaving behind $\sim 60\%$ 2,3,6- $F_3Y\bullet$ that is stable on the order of at least half an hour. Furthermore, subtle changes in spectral features are observed during the initial loss of the radical (Figure A3.5D, Appendix 3). We have interpreted these data as reporting on the presence of multiple conformations of 2,3,6- $F_3Y\bullet$ within $\beta 2$. Due to these complications, all subsequent reactions with $Y_{122}(2,3,6)F_3Y\text{-}\beta 2$ are performed either immediately after reconstitution of the cluster (for hand-quench experiments), or via a double-mixing protocol (for SF and RFQ studies). This experimental plan ensures that all conformations of 2,3,6- $F_3Y\bullet$ are tested for their ability to generate pathway radicals. However, a caveat of this design is the deconvolution of the kinetics. Different conformations of 2,3,6- $F_3Y\bullet$ could react with different rate constants.

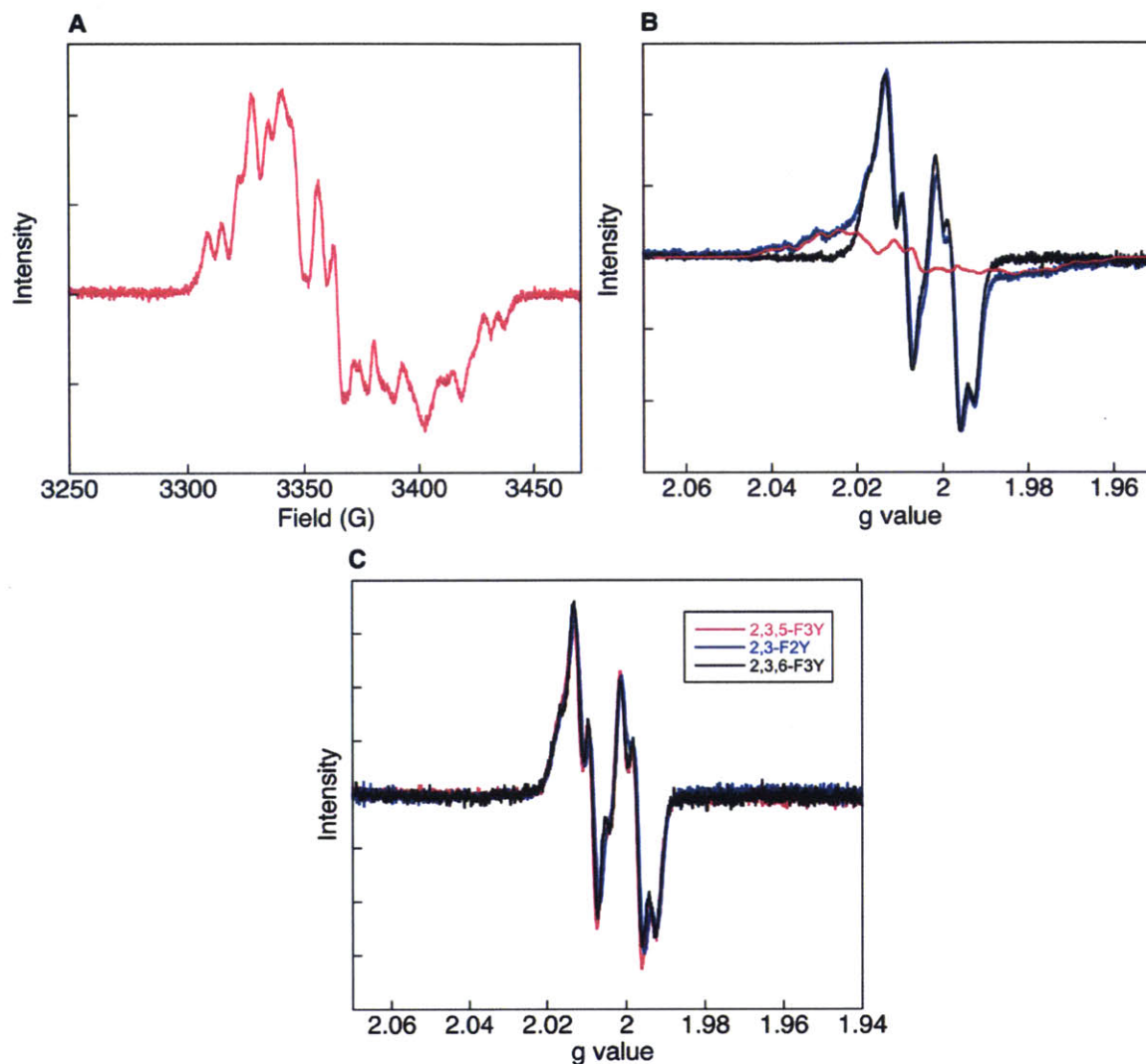


Figure A4.4 A. X-band EPR spectrum of the stable 2,3,6-F₃Y• recorded at 30 s. Detailed analysis of the reconstitution process including the spectrum of the unstable radical are presented in Appendix 3. B. Reaction of Y₁₂₂(2,3,6)F₃Y-β₂, wt-α₂, CDP and ATP monitored by HQ-EPR spectroscopy. The reaction was performed on ice. Subtraction of 2,3,6-F₃Y• (A, B, pink) from the composite spectrum (blue) reveals a new Y• (black). C. Spectral overlay of the pathway radical from B (black) with the radicals observed in the Y₁₂₂(2,3,5)F₃Y-β₂ and Y₁₂₂(2,3)F₂Y-β₂ systems (pink and blue respectively) supports that the new Y• is located at Y₃₅₆.

Apo Y₁₂₂(2,3,6)F₃Y-β₂ was reconstituted by the addition of 5 equiv. of Fe²⁺ and 3.5 equiv. of O₂ and frozen for EPR analysis at 30 s. The X-band EPR spectrum of the resulting 2,3,6-F₃Y• (0.7 F₃Y•/β₂) is shown in Figure A4.4A. A second aliquot of Fe²⁺-Y₁₂₂(2,3,6)F₃Y-β₂ was exposed to O₂-saturated buffer, mixed with α₂, CDP and ATP and frozen in liquid N₂ within 30 s. The EPR

spectrum of 2,3,6-F₃Y• shows subtle variations with time (Figure A3.5D, Appendix 3); thus, we wanted to compare the spectrum of the reaction mixture at the same time point as reconstituted Y₁₂₂(2,3,6)F₃Y-β2 (Figure A4.4A). Figure A4.4B shows the EPR spectrum of the 30 s reaction mixture (blue). The total amount of radical did not vary from that observed with reconstituted Y₁₂₂(2,3,6)F₃Y-β2 alone (0.7 F₃Y•/β2). From this composite spectrum, residual 2,3,6-F₃Y• (pink, Figure A4.4A and B) was subtracted to reveal the spectrum in black. The net spectrum strongly resembles the Y• seen in the reaction of Y₁₂₂(2,3,5)F₃Y-β2 or Y₁₂₂(2,3)F₂Y-β2 with α2 (Figure A4.4C). These results support that the radical observed in the reaction of Y₁₂₂(2,3,6)F₃Y-β2 with α2 is also Y₃₅₆•.

A4.3.4 No evidence for W₄₈• (+) in the reaction of Y₁₂₂(2,3,6)F₃Y-β2 with α2, CDP and ATP monitored by HQ-EPR spectroscopy. After establishing that the single mutant Y₁₂₂(2,3,6)F₃Y-β2 could accumulate Y₃₅₆• when reacted with α2, we performed an identical experiment with the double mutant Y₁₂₂(2,3,6)F₃Y/Y₃₅₆F-β2. The spectrum of the reaction mixture quenched at 30 s is shown in Figure A4.5 (pink). Subtraction of 2,3,6-F₃Y• (blue) from the reaction mixture revealed only spectral noise (black). However, a spin loss of ~14% was recorded between reconstituted Y₁₂₂(2,3,6)F₃Y/Y₃₅₆F-β2 at 30 s and the reaction mixture at 30 s. These results suggested the possibility of rapid formation of W₄₈• (+) that subsequently decayed. To test this hypothesis, we performed the SF and RFQ-EPR experiments outlined in further sections.

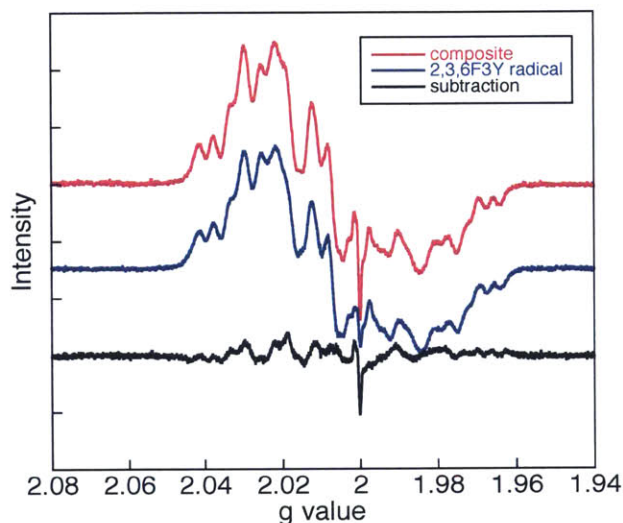


Figure A4.5 Reaction of $Y_{122}(2,3,6)F_3Y/Y_{356}F-\beta 2$, $\alpha 2$, CDP and ATP monitored by HQ-EPR spectroscopy. The reaction was performed on ice. Subtraction of the stable 2,3,6- $F_3Y\bullet$ spectrum (blue) from the composite spectrum (pink) reveals spectral noise (black). The glitch at $g=2$ is associated with the finger dewar.

A4.3.5 SF UV-vis spectroscopy reveals formation of a species with absorbance at 510 and 550 nm in the reaction of $Y_{122}(2,3,6)F_3Y/Y_{356}F-\beta 2$, $\alpha 2$, CDP and ATP. Due to the spin loss observed in the HQ-EPR reaction of $Y_{122}(2,3,6)F_3Y/Y_{356}F-\beta 2$ with $\alpha 2$, CDP and ATP, we turned to SF UV-vis spectroscopy to monitor the kinetics of the reaction on a ms time scale. The experiment was performed using a four-syringe mixing protocol, where 2,3,6- $F_3Y\bullet$ was generated and immediately mixed with $\alpha 2$, CDP and ATP. Single wavelength kinetics of the reaction were monitored at 420 nm (2,3,6- $F_3Y\bullet$), 510 nm ($W\bullet$) and 550 nm (W^{++}) and the results are shown in Figure A4.6. Unexpectedly, increases in absorbances were measured at all three wavelengths. The data were fit to a bi-exponential equation using the rate constants shown in Table A4.1.

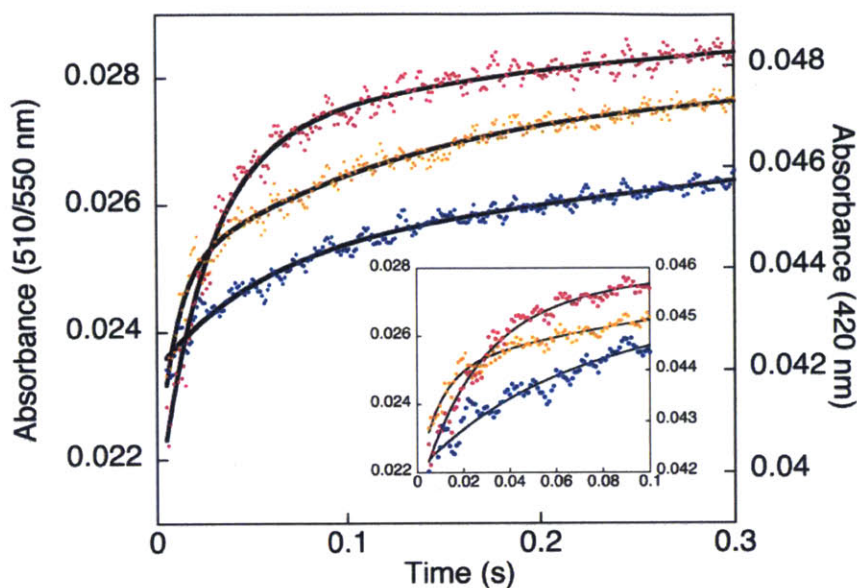


Figure A4.6 SF vis analysis of the reaction of $Y_{122}(2,3,6)F_3Y/Y_{356}F-\beta_2$ with α_2 , CDP and ATP. Single wavelength kinetics were monitored at 420 nm ($2,3,6-F_3Y\cdot$, blue), 510 nm ($W\cdot$ anticipated, pink), and 550 nm (W^{++} anticipated, orange). The black traces represent bi-exponential fits using the rate constants shown in Table A4.1. The inset shows the first 0.1 s of the reaction.

At both 510 nm and 550 nm, a fast phase ($40\text{--}110\text{ s}^{-1}$) and a slow phase ($4\text{--}7\text{ s}^{-1}$) are recorded for formation of the absorbing species (Table A4.1). Whereas the amplitudes of the two phases are equivalent at 550 nm, 73% of the amplitude change is recorded in the fast phase at 510 nm. The total absorbance changes at the two wavelengths correspond to 45% (510 nm) and 25% (550 nm) of the total radical amount in the reaction. These differences in the kinetics at 510 nm and 550 nm could report on the formation of multiple $W\cdot (+)$ species. However, the changes observed at 510 and 550 nm do not appear to correlate with loss of $2,3,6-F_3Y\cdot$. In fact, an increase in absorbance is also recorded at 420 nm, equivalent to $\sim 10\%$ of the total radical amount in the reaction. The kinetics at this wavelength are also biphasic and fit to rate constants of 12 s^{-1} and 2 s^{-1} , each corresponding to an amplitude of $\sim 50\%$ (or 5% of the total radical amount).

The SF vis analysis of the reaction can be interpreted as reporting on the generation of either a single species with a broad absorbance profile (510–550 nm) or a mixture of $W\cdot (+)$ spread

throughout $\beta 2$. The visible spectrum of 2,3,6- F_3Y^\bullet are broad compared to Y^\bullet .¹⁰ The lack of kinetic correlation between 420, 510 and 550 nm suggests the possibility of additional species in the $Y_{122}(2,3,6)F_3Y/Y_{356}F-\beta 2$ experiment that spectrally overlap with 2,3,6- F_3Y^\bullet . There are a total of 16 Y residues in a single β monomer (including Y_{122} and Y_{356}). It is possible that the reaction of $Y_{122}(2,3,6)F_3Y/Y_{356}F-\beta 2$, $\alpha 2$, CDP and ATP accumulates Y^\bullet ($\lambda_{max}=410$ nm) in addition to W^\bullet (+). Loss of 2,3,6- F_3Y^\bullet concomitant with formation of Y^\bullet could produce the observed kinetics. Lastly, we note that the maximum amount of 2,3,6- F_3Y^\bullet that is generated from apo $Y_{122}(2,3,6)F_3Y/Y_{356}F-\beta 2$ is only 0.5 $F_3Y^\bullet/\beta 2$. This amount contrasts with our observations for the single mutant $Y_{122}(2,3,6)F_3Y-\beta 2$ where 1.2 $F_3Y^\bullet/\beta 2$ can be obtained (Appendix 3). The lowered radical yield for the double mutant is reproducible (sections A4.3.6 and A4.3.7), but its source remains unknown.

Table A4.1 SF vis analysis of the reaction of $Y_{122}(2,3,6)F_3Y/Y_{356}F-\beta 2$ with $\alpha 2$, CDP and ATP.

Wavelength (nm)	First phase		Second phase		% Total radical change ^b
	k_{obs} (s ⁻¹)	A ^a (%)	k_{obs} (s ⁻¹)	A ^a (%)	
420	12	57	2	43	10
510	40	73	4	27	45
550	110	50	7	50	25

^a A represents the amplitude of the reaction and was calculated as a percentage of the total radical change observed at that wavelength (^b).

A4.3.6 RFQ-EPR analysis shows formation of a putative W^\bullet (+) in the reaction of $Y_{122}(2,3,6)F_3Y/Y_{356}F-\beta 2$, $\alpha 2$, CDP and ATP. The SF studies described in the previous section suggest formation of one or multiple species with absorbances at 510 and 550 nm. To determine if W^\bullet (+) is generated in the reaction of $Y_{122}(2,3,6)F_3Y/Y_{356}F-\beta 2$ with $\alpha 2$, CDP and ATP, we monitored the reaction by RFQ-EPR spectroscopy. We anticipated that if the 510 and 550 nm absorbance features are associated with W^\bullet (+), its EPR spectrum might be akin to that of $W^{+\bullet}$ observed in the $Y_{122}NO_2Y/Y_{356}F-\beta 2$ system (Yokoyama, Stubbe unpublished results).

The reaction of $Y_{122}(2,3,6)F_3Y/Y_{356}F-\beta 2$ with $\alpha 2$, CDP and ATP was performed using a three-syringe mixing protocol. Figure A4.7A shows the RFQ time course of the reaction. No spin loss was observed between the different samples (0.5 total spin/ $\beta 2$). Although noisy, the spectra of the reaction mixtures are distinct from that of $2,3,6-F_3Y\bullet$ alone (Figure A4.4A) and suggest the presence of at least one other EPR-active species. From each composite spectrum, $2,3,6-F_3Y\bullet$ was subtracted to quantitate the percentage of the new radical(s). The subtraction protocol performed on the 37 ms sample is shown in Figure A4.7B and the overlay of the net spectra generated from each subtraction is shown in Figure A4.7C. There is significant error associated with the subtraction procedure. Due to the noise in the EPR spectra, the features of $2,3,6-F_3Y\bullet$ on the high- and low-field sides (Figure A4.7B, pink, $g = \sim 2.04$ and $g = \sim 1.97$) of the spectra could not be accurately aligned with the reference sample (Figure A4.7B, blue). The subtracted spectra shown in Figure A4.7C represent our best efforts to obtain baseline in these regions where $2,3,6-F_3Y\bullet$ contributes.

Figure A4.7 shows an overlay between the net spectrum in the $Y_{122}(2,3,6)F_3Y/Y_{356}F-\beta 2$ reaction to that observed in the $Y_{122}NO_2Y/Y_{356}F-\beta 2$ reaction. The similarity between the two EPR spectra suggests the presence of a putative $W\bullet (+)$ in the reaction of $Y_{122}(2,3,6)F_3Y/Y_{356}F-\beta 2$ with $\alpha 2$, CDP and ATP. Quantitation of the new radical at each time point reveals that maximum amounts (30%) are generated by 67 ms (Figure A4.8). This number agrees well with our observations by SF vis spectroscopy (Table A4.1). Unfortunately, detailed kinetic analysis of the $Y_{122}(2,3,6)F_3Y/Y_{356}F-\beta 2$ reaction by RFQ-EPR is challenging due to the issues associated with the subtraction protocol. Subtraction of this radical from a reaction mixture containing multiple species is limited by the protein concentrations and EPR scan times that are currently utilized. $Y_{122}(2,3,6)F_3Y/Y_{356}F-\beta 2$ also assembles only 0.5 $F_3Y\bullet/\beta 2$ in contrast to the single mutant

$Y_{122}(2,3,6)F_3Y-\beta_2$ (1.2 $F_3Y\bullet/\beta_2$, Appendix 3). The extensive hyperfine features of $2,3,6-F_3Y\bullet$ (Figure A4.4A), the lowered radical yield, and half-sites reactivity in the *E. coli* class Ia RNR^{7,9,14,15} greatly affect the signal to noise in our experiments and the ability to obtain high quality spectra. Unfortunately, the protein concentrations in these experiments cannot be increased. The quaternary structure of the *E. coli* class Ia RNR as a function of protein concentration remains to be investigated, but likely involves higher order oligomeric states based on the preliminary results of Ando *et al.*¹⁶

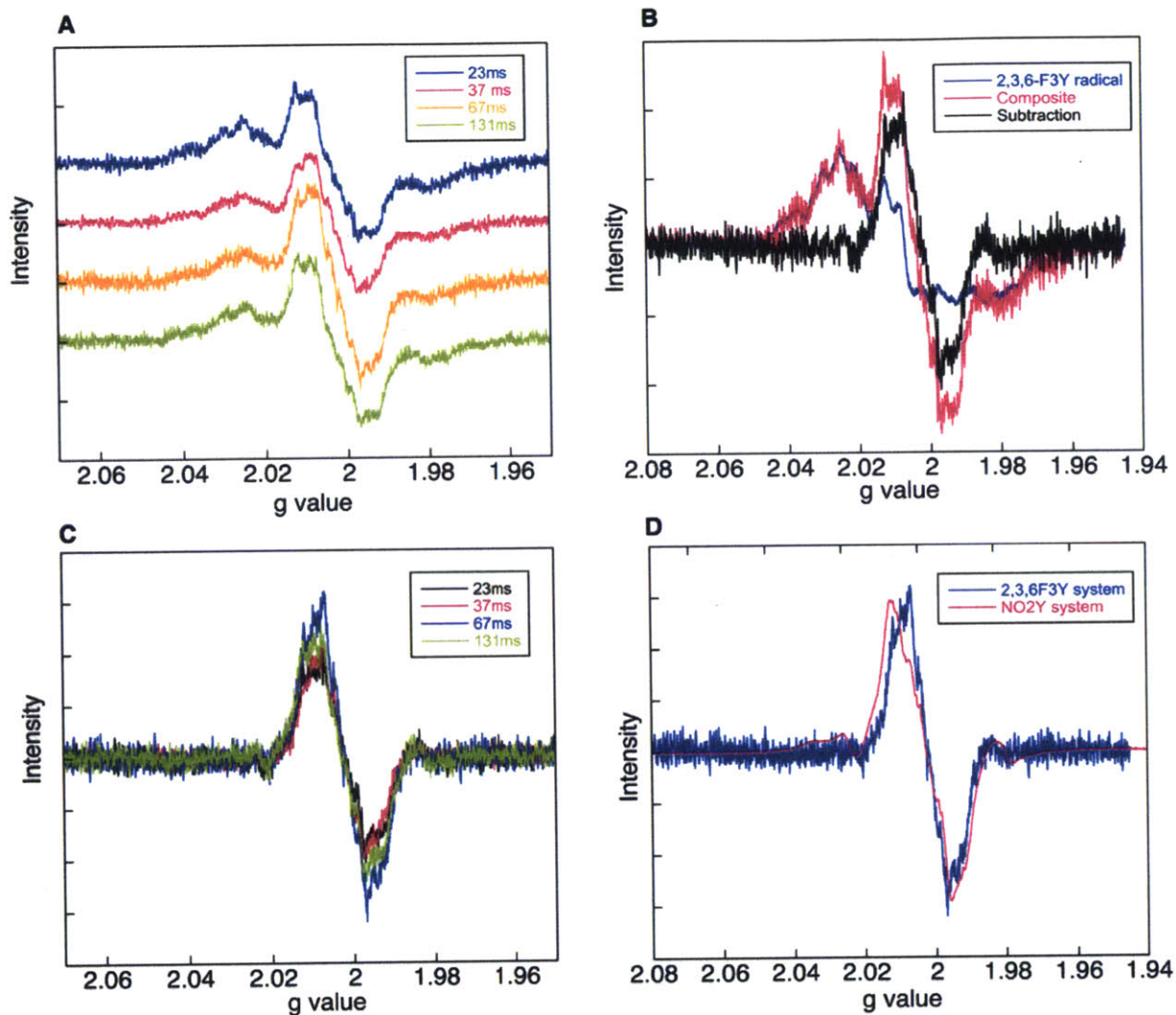


Figure A4.7 RFQ-EPR analysis of the reaction of Y₁₂₂(2,3,6)F₃Y/Y₃₅₆F-β₂ with α₂, CDP and ATP. The reaction was conducted by three-syringe sequential mixing, as described in the text. A. The composite EPR spectra recorded at the indicated time points. B. An example of the subtraction protocol. The spectrum of 2,3,6-F₃Y• was subtracted from each composite spectrum (37 ms shown as an example) to reveal the spectrum in black. C. Overlay of the net spectra at the indicated time points. D. Overlay of the net spectrum with that of W^{+•} generated in the Y₁₂₂NO₂Y-β₂ system.

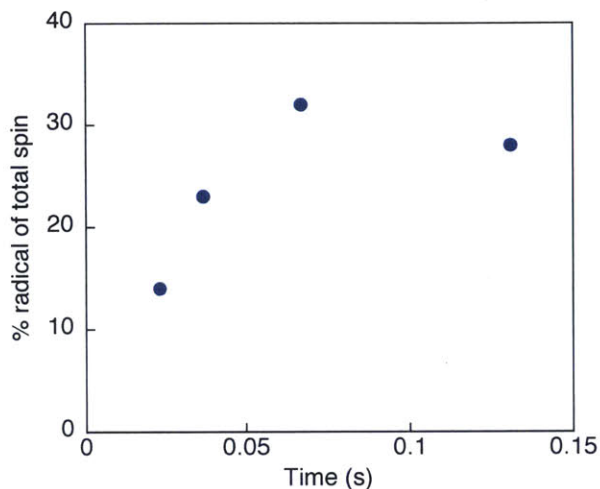


Figure A4.8 Percentage of the new radical generated in the reaction of $Y_{122}(2,3,6)F_3Y/Y_{356}F-\beta 2$ with $\alpha 2$, CDP and ATP.

A4.3.7 SF vis spectroscopy equipped with a diode array system shows formation of multiple species in the reaction of $Y_{122}(2,3,6)F_3Y/Y_{356}F-\beta 2$, $\alpha 2$, CDP and ATP. Due to the challenges associated with obtained high quality RFQ-EPR data, we switched back to SF vis spectroscopy to understand the $Y_{122}(2,3,6)F_3Y/Y_{356}F-\beta 2$ reaction. However, this time we monitored the reaction using a diode array detection system to obtain information about the entire spectrum with time (350–800 nm, 0.001–0.5 s). Figure A4.9A shows the reaction spectra collected from 1 ms–0.5 s in a control experiment performed in the absence of CDP. A total of ~100 spectra were recorded between the two time points; however, only ~20 spectra are shown for the sake of clarity. Unexpectedly, increases in absorbance values were observed at all wavelengths monitored (350–700 nm). These increases appear to be associated with two broad peaks, one centered at ~450 nm and a second at ~560 nm. Inclusion of CDP in the reaction (Figure A4.9B) results in no visible changes compared to the control. However, the absorbance increases occur within 0.1 s compared to the 0.5 s observed for the control reaction. The control spectra at selected time points (1 ms, 8

ms, 15 ms, 23 ms, 30 ms, 40 ms, 50 ms and 100 ms) were subtracted from the reaction spectra collected at the same time points. These subtracted spectra are shown in Figure A4.9C and demonstrate growth of the 450 nm and 560 nm features with time. We ascribe the 560 nm feature to either one or multiple W^{+} s, as previously noted in $Y_{122}NO_2Y/Y_{356}F-\beta 2$ (Yokoyama, Stubbe unpublished results). We currently do not have a candidate for the 450 nm feature. This SF study represents only a single trial; the experiment should be repeated to confirm our findings.

Table A4.2 SF UV-vis analysis of the $Y_{122}(2,3,6)F_3Y/Y_{356}F-\beta 2$, $\alpha 2$, CDP and ATP reaction monitored using a diode array detection system.

Wavelength (nm)	Control (- CDP)		Reaction (+ CDP)	
	A (% of total radical)	k_{obs} (s^{-1})	A (% of total radical)	k_{obs} (s^{-1})
450	- ^a	9	- ^a	22
510	40	9.6	40	40
560	30	9.6	40	52

^aThe amplitude (A) remains undetermined as the identity and extinction coefficient of this species is unknown.

The individual wavelength data at 510 and 550 nm in the control (-CDP) and the reaction (+CDP) are shown in Figure A4.9D. The data were fit to a mono-exponential equation providing the rate constants shown in Table A4.2. The amplitude changes at 510 and 550 nm were calculated as a percentage of the total radical in the reaction using extinction co-efficients of $2200 M^{-1}cm^{-1}$ and $3000 M^{-1}cm^{-1}$, respectively. In both the control (-CDP) and in the reaction (+CDP), ~40% of W^{+} is generated, similar to the amounts observed by single wavelength SF spectroscopy (section A4.3.5) and RFQ-EPR spectroscopy (section A4.3.6). The rate constant for W^{+} formation in the reaction (+CDP, 40–52 s^{-1}) is also similar to that measured by single wavelength SF spectroscopy (40–100 s^{-1} , section A4.3.5). This rate constant is 4–5-fold faster than in the control (-CDP, ~10 s^{-1}), demonstrating rate acceleration upon inclusion of substrate in the reaction. Rate enhancement for the unknown feature at 450 nm is less than that observed for W^{+} ; the rate constant for formation of this feature is ~2-fold faster in the reaction (+CDP) than in the control (-CDP).

However, it should be noted that the diode array system is not reliable for accurate kinetic measurements. The reaction should be investigated by single wavelength SF spectroscopy to confirm the 450 nm kinetics.

The data reported in this section support that W^{+} formation in the reaction of $Y_{122}(2,3,6)F_3Y/Y_{356}F-\beta 2$ with $\alpha 2$ is a result of off-pathway oxidation by the strong oxidant, 2,3,6- $F_3Y\bullet$. Although a rate acceleration is observed in the presence of CDP, the reaction can occur in the absence of substrate. This observation contrasts with previous studies on DOPA- and NH_2Y -substituted RNRs, which show that substrate is directly responsible for triggering RT.

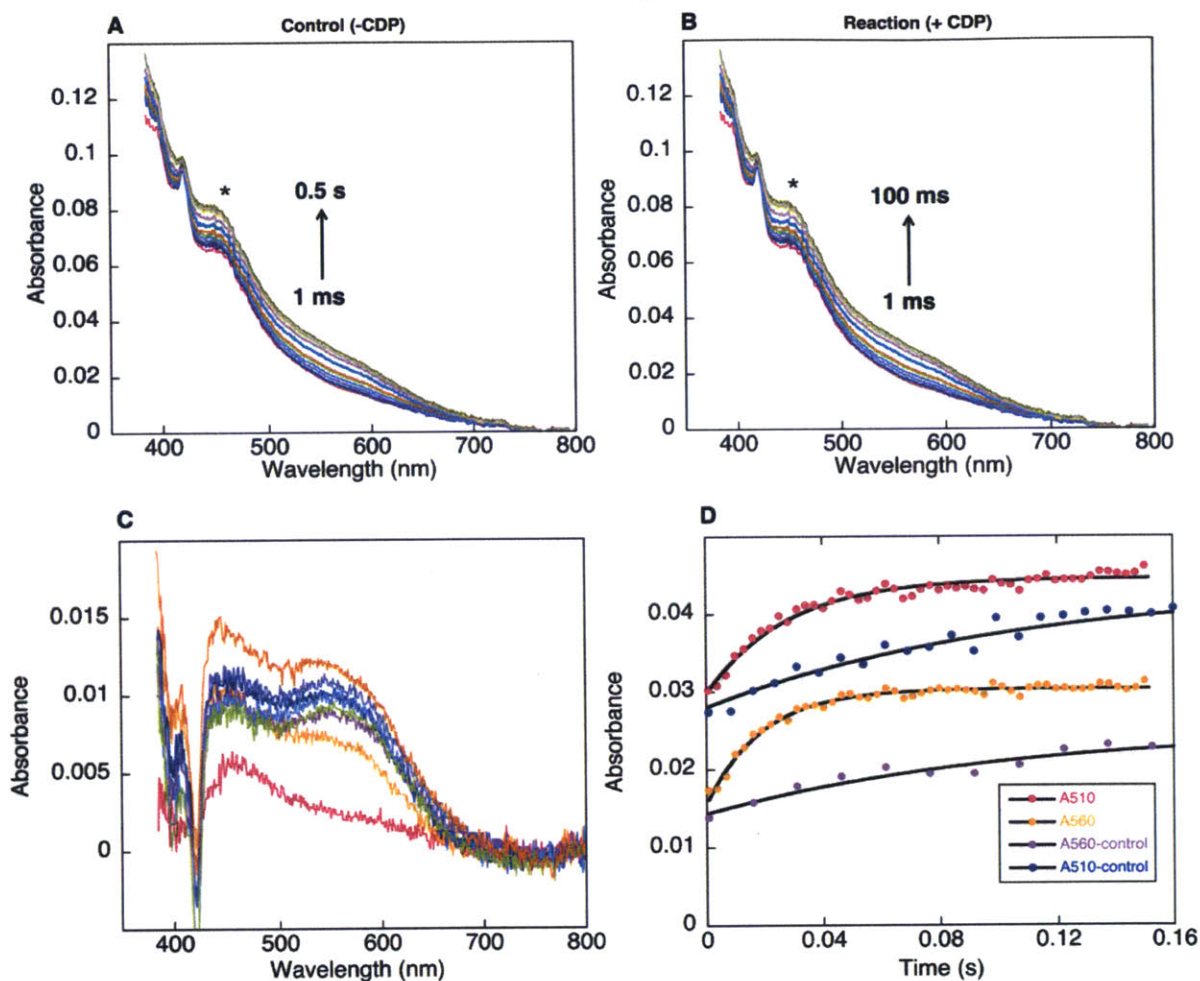


Figure A4.9 Reaction of $Y_{122}(2,3,6)F_3Y/Y_{356}F-\beta_2$ with α_2 , CDP and ATP monitored by SF vis spectroscopy equipped with a diode array detection system. The reaction was performed at 25 °C using a three-syringe sequential mixing protocol, as described in the text. A. Spectra between 1 ms and 0.5 s for the control reaction performed in the absence of CDP. B. Spectra between 1 ms and 0.1 s for the reaction performed in the presence of CDP. The sharp peak at 420 nm in A and B represent $2,3,6-F_3Y^\bullet$. The asterisk indicates an unidentified species in the reaction. C. A few net spectra between 1 ms (pink) and 0.1 s (dark orange), generated by subtraction of the control spectra (A) from the reaction spectra (B). D. Single wavelength data points recorded at 510 nm (W^\bullet , anticipated) and 550 nm (W^{++} , anticipated) in the absence (blue and purple) and presence (pink and orange) of CDP. The black traces represent single exponential fits to the data using the rate constants shown in Table A4.2.

A4.4 CONCLUSIONS

In this work, we attempted to address if W_{48} participates in long-range RT as was originally proposed based on sequence conservation and the individual crystal structures of $\alpha 2$ and $\beta 2$.^{1,2} W_{48}^{+} has been observed during cluster assembly,³ but mutation of W_{48} affects cofactor assembly precluding investigation of its role in RT. Efforts in our lab to replace W_{48} with unnatural W analogs have been unsuccessful (Lee, Stubbe unpublished results) with poor suppression efficiencies and low cofactor yields as the primary sources of failure. Our ability to systematically modulate the driving force of RT with $F_n Y$ s (all except 3,5- $F_2 Y$) and $NO_2 Y$ provided an alternate way to address the role of W_{48} in turnover. These analogs alter the driving force by a predicted +10–200 mV^{10,11} and accumulate Y_{356}^{\bullet} when reacted with $\alpha 2$, CDP and ATP. At least in the case of $Y_{122}NO_2 Y-\beta 2$ and $Y_{122}(2,3,5)F_3 Y-\beta 2$, it was previously shown that Y_{356}^{\bullet} is kinetically and chemically competent for nucleotide reduction.^{7,9} By reacting the double mutants (either $Y_{122}F_n Y/Y_{356}F-\beta 2$ or $Y_{122}NO_2 Y/Y_{356}F-\beta 2$) with $\alpha 2$, CDP and ATP, we sought to establish if W_{48} participates in long-range RT. The experiments presented herein along with those previously reported¹² (Yokoyama, Stubbe unpublished results) support that $W^{\bullet (+)}$ formation does not occur until the driving force is substantially increased; SF vis and RFQ-EPR spectroscopic methods could detect $W^{\bullet (+)}$ only in $Y_{122}(2,3,6)F_3 Y/Y_{356}F-\beta 2$ (+100 mV)¹⁰ and $Y_{122}NO_2 Y/Y_{356}F-\beta 2$ (+200 mV)⁶ but not in $Y_{122}(2,3,5)F_3 Y/Y_{356}F-\beta 2$ (10 mV) or $Y_{122}(2,3)F_2 Y/Y_{356}F-\beta 2$ (45 mV). These data suggest that $W^{\bullet (+)}$ formation is a result of off-pathway oxidation by these powerful oxidants when the native pathway is blocked.

Evidence for the absence of a discrete radical intermediate at W_{48} is further supported by our studies on the single mutant $Y_{122}(2,3,5)F_3 Y-\beta 2$ (Chapter 3).⁹ In this system we have shown kinetically and chemically competent oxidation of Y_{356} by 2,3,5- $F_3 Y^{\bullet}$ and re-oxidation of 2,3,5-

F₃Y (or 2,3,5-F₃Y⁻) by Y₃₅₆•. No evidence was obtained for the formation of W₄₈• (+) during forward or reverse RT, an observation that can be interpreted in two ways: either W₄₈ does not participate as radical intermediate during RT or W₄₈ formation and disappearance are fast enough to preclude observation of this intermediate.

Recently, the Bollinger and Krebs labs have used a strategy similar to ours in the class Ic RNR from *Chlamydia trachomatis*.¹⁷ This enzyme uses a Mn(IV)Fe(III) cofactor to initiate RT; similar to the class Ia RNR, a slow protein conformational change prior to RT prevents the observation of chemically competent radical intermediates. During cofactor assembly, the class Ic RNR accesses a super-oxidized Mn(IV)Fe(IV) state similar to intermediate X in class Ia. The reaction of this super-oxidized enzyme with α₂, CDP and ATP accumulates Y₃₃₈• (equivalent to Y₃₅₆ in *E. coli* class Ia).¹⁷ Mutation of Y₃₃₈ to F failed to reveal any W₅₁• (+) (equivalent to W₄₈ in *E. coli* class Ia), consistent with our observations for Y₁₂₂(2,3,5)F₃Y/Y₃₅₆F-β₂ and Y₁₂₂(2,3)F₂Y/Y₃₅₆F-β₂.

Taken together, the data support that W₄₈ does not participate as a discrete radical intermediate during RT in the class Ia RNR. Removal of W₄₈ from the RT pathway, increases the distance over which the oxidant must traverse. Placement of Y₃₅₆ roughly halfway between Y₁₂₂ and Y₇₃₁, which are separated by ~33 Å,² could support conformationally gated turnover (2–10 s⁻¹).¹⁸ We have previously shown that orthogonal PCET is operative at Y₃₅₆.¹⁹ This model would require that orthogonal PCET is also functional during oxidation of Y₇₃₁. Alternatively, it is possible that the C-terminal tail of β₂ that contains Y₃₅₆ is conformationally flexible during RT, bringing Y₃₅₆ closer to either Y₁₂₂ or Y₇₃₁.

A4.5 REFERENCES

1. Nordlund, P.; Sjöberg, B. M.; Eklund, H. Three-dimensional structure of the free radical protein of ribonucleotide reductase, *Nature* **1990**, *345*, 593-598.
2. Uhlin, U.; Eklund, H. Structure of ribonucleotide reductase protein R1, *Nature* **1994**, *370*, 533-539.
3. Bollinger, J. M., Jr.; Tong, W. H.; Ravi, N.; Huynh, B. H.; Edmondson, D. E.; Stubbe, J. Mechanism of assembly of the tyrosyl radical-diiron(II) cofactor of *Escherichia coli* ribonucleotide reductase 3. Kinetics of the limiting Fe²⁺ Reaction by optical, EPR, and Mössbauer spectroscopies, *J. Am. Chem. Soc.* **1994**, *116*, 8024-8032.
4. Krebs, C.; Chen, S.; Baldwin, J.; Ley, B. A.; Patel, U.; Edmondson, D. E.; Huynh, B. H., Bollinger, J. M., Jr. Mechanism of rapid electron transfer during oxygen activation in the R2 subunit of *Escherichia coli* ribonucleotide reductase. 2. Evidence for and consequences of blocked electron transfer in the W48F variant, *J. Am. Chem. Soc.* **2000**, *122*, 12207-12219.
5. Rova, U.; Goodtzova, K.; Ingemarson, R.; Behravan, G.; Gräslund, A.; Thelander, L. Evidence by site-directed mutagenesis supports long-range electron transfer in mouse ribonucleotide reductase, *Biochemistry* **1995**, *34*, 4267-4275.
6. Yee, C. S.; Seyedsayamdost, M. R.; Chang, M. C. Y.; Nocera, D. G.; Stubbe, J. Generation of the R2 subunit of ribonucleotide reductase by intein chemistry: insertion of 3-nitrotyrosine at residue 356 as a probe of the radical initiation process, *Biochemistry* **2003**, *42*, 14541-14552.
7. Yokoyama, K.; Uhlin, U.; Stubbe, J. A hot oxidant, 3-NO₂Y₁₂₂ radical, unmasks conformational gating in ribonucleotide reductase, *J. Am. Chem. Soc.* **2010**, *132*, 15368-15379.
8. Minnihan, E. C.; Young, D. D.; Schultz, P. G.; Stubbe, J. Incorporation of fluorotyrosines into ribonucleotide reductase using an evolved, polyspecific aminoacyl-tRNA synthetase, *J. Am. Chem. Soc.* **2011**, *133*, 15942-15945.
9. Ravichandran, K. R.; Minnihan, E. C.; Wei, Y.; Nocera, D. G.; Stubbe, J. Reverse electron transfer completes the catalytic cycle in a 2,3,5-trifluorotyrosine-substituted ribonucleotide reductase, *J. Am. Chem. Soc.* **2015**, *137*, 14387-14395.
10. Seyedsayamdost, M. R.; Reece, S. Y.; Nocera, D. G.; Stubbe, J. Mono-, di-, tri-, and tetra-substituted fluorotyrosines: new probes for enzymes that use tyrosyl radicals in catalysis, *J. Am. Chem. Soc.* **2006**, *128*, 1569-1579.
11. Minnihan, E. C.; Nocera, D. G.; Stubbe, J. Reversible, long-range radical transfer in *E. coli* class Ia ribonucleotide reductase, *Acc. Chem. Res.* **2013**, *46*, 2524-2535.
12. Minnihan, E. C. Mechanistic studies of proton-coupled electron transfer in aminotyrosine- and fluorotyrosine-substituted class Ia ribonucleotide reductase. Ph.D. Thesis, Massachusetts Institute of Technology, **2012**.

13. Minnihan, E. C.; Seyedsayamdost, M. R.; Uhlin, U.; Stubbe, J. Kinetics of radical intermediate formation and deoxynucleotide production in 3-aminotyrosine-substituted *Escherichia coli* ribonucleotide reductases, *J. Am. Chem. Soc.* **2011**, *133*, 9430-9440.
14. Fritscher, J.; Artin, E.; Wnuk, S.; Bar, G.; Robblee, J. H.; Kacprzak, S.; Kaupp, M.; Griffin, R. G.; Bennati, M.; Stubbe, J. Structure of the nitrogen-centered radical formed during inactivation of *E. coli* ribonucleotide reductase by 2'-azido-2'-deoxyuridine-5'-diphosphate: trapping of the 3'-ketonucleotide, *J. Am. Chem. Soc.* **2005**, *127*, 7729-7738.
15. Seyedsayamdost, M. R.; Stubbe, J. Site-specific replacement of Y₃₅₆ with 3,4-dihydroxyphenylalanine in the β 2 subunit of *E. coli* ribonucleotide reductase, *J. Am. Chem. Soc.* **2006**, *128*, 2522-2523.
16. Ando, N.; Brignole, E. J.; Zimanyi, C. M.; Funk, M. A.; Yokoyama, K.; Asturias, F. J.; Stubbe, J.; Drennan, C.L. Structural interconversions modulate activity of *Escherichia coli* ribonucleotide reductase, *Proc. Natl. Acad. Sci. U. S. A.* **2011**, *108*, 21046-21051.
17. Dassama, L. M.; Jiang, W.; Varano, P. T.; Pandelia, M. E.; Conner, D. A.; Xie, J.; Bollinger, J. M., Jr.; Krebs, C. Radical-translocation intermediates and hurdling of pathway defects in "super-oxidized" (Mn(IV)Fe(IV)) chlamydia trachomatis ribonucleotide reductase, *J. Am. Chem. Soc.* **2012**, *134*, 20498-20506.
18. Ge, J.; Yu, G.; Ator, M. A.; Stubbe, J. Pre-steady-state and steady-state kinetic analysis of *E. coli* class I ribonucleotide reductase, *Biochemistry* **2003**, *42*, 10071-10083.
19. Yee, C. S.; Chang, M. C. Y.; Ge, J.; Nocera, D. G.; Stubbe, J. 2,3-difluorotyrosine at position 356 of ribonucleotide reductase R2: A probe of long-range proton-coupled electron transfer, *J. Am. Chem. Soc.* **2003**, *125*, 10506-10507.

Appendix 5

Supporting Figures for Chapter 3

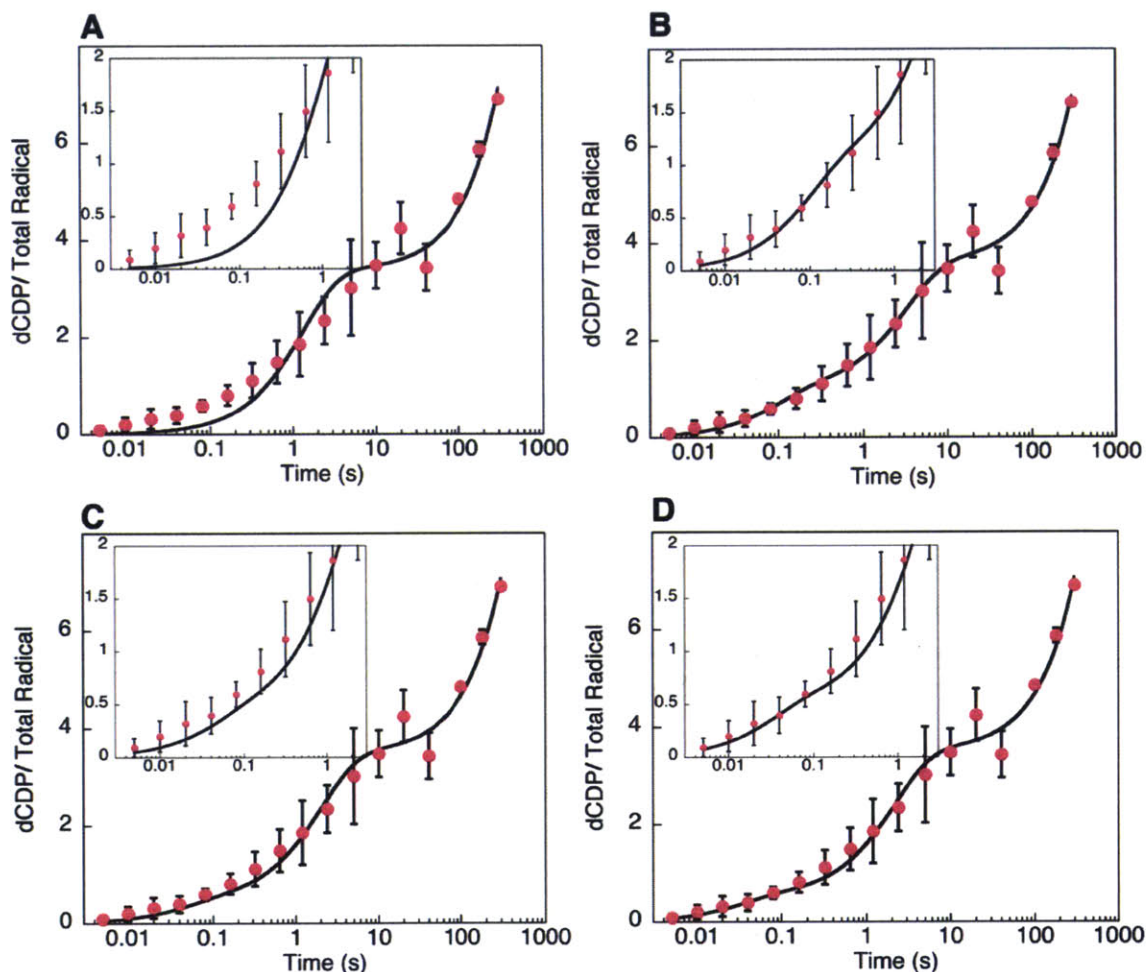


Figure A5.1 Alternative fits to dCDP kinetics in the reaction of $Y_{122}(2,3,5)F_3Y$ - $\beta 2$, wt- $\alpha 2$, CDP and ATP at 25 °C. A. The data were initially fit to a single exponential phase for dCDP formation (k_1) followed by a linear phase for steady-state cytosine production (k_2) providing k_1 of $0.5 \pm 0.1 \text{ s}^{-1}$ (3.1 ± 0.2 equiv.) and k_2 of $0.012 \pm 0.001 \text{ s}^{-1}$. An expanded view of the first few ms of the reaction shows very poor correlation between the data points and the fit suggesting an initial fast phase for product formation. B. The data were next fit to two exponential phases followed by a linear phase. This provided k_1 of $11 \pm 6 \text{ s}^{-1}$ (1.0 ± 0.3 equiv.), k_2 of $0.3 \pm 0.1 \text{ s}^{-1}$ (2.6 ± 0.3 equiv.) and k_3 of $0.011 \pm 0.001 \text{ s}^{-1}$. We rule out this fit to the data based on results collected in the presence of a reducing system (Table 3.2). If dCDP formation were slower than Y_{356}^{\bullet} generation (30 s^{-1} , Table 3.2), no burst phase would be visualized in the presence of TR/TRR/NADPH. However, our experimental observations (Figure 3.6) show a burst of dCDP prior to steady-state turnover supporting that dCDP formation on the first turnover occurs on par or faster than Y_{356}^{\bullet} formation. C. We next attempted to fit the data with a fixed first phase identical in kinetics to the first phase

observed in the presence of a reducing system (0.4 equiv. at 22 s^{-1} , Figure 3.6, Table 3.2). This analysis provided rate constants of $0.5 \pm 0.1\text{ s}^{-1}$ (k_2 , 3.0 ± 0.1 equiv.) and $0.012 \pm 0.001\text{ s}^{-1}$ (k_3). An expanded view of the first few ms shows that the fit is consistently below all data points suggesting a larger amplitude for the first phase. D. The data were finally fit to a fixed first phase of amplitude 0.5 equiv. and rate constant 30 s^{-1} , identical in kinetics to Y_{356}^\bullet formation at this temperature. D provided the best fit and the resulting kinetic information is presented in Table 3.2. To further corroborate our data analysis we performed the experiment described in Figure A5.2.

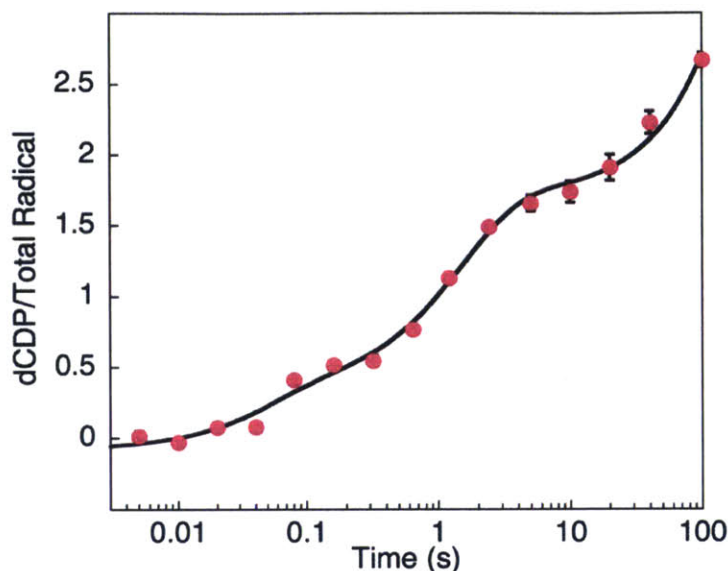


Figure A5.2 Reaction of $Y_{122}(2,3,5)F_3Y\text{-}\beta 2$, wt- $\alpha 2$, CDP and ATP monitored by the RCQ method at 25 °C. One of the issues with fitting the first phase in Figure 3.6 is its relatively small amplitude (< 7 % of total amplitude). We predicted that the amplitude of this phase would remain constant (0.4–0.5 dCDP/ $F_3Y\bullet$) with different radical amounts as it reports on the very first turnover by an α/β pair. Increasing the radical amount in the reaction mixture should thus maintain the same amplitude for the first phase, but decrease the overall amplitude since each radical now does fewer turnovers. The reaction was repeated with final concentrations of 30 μM $Y_{122}(2,3,5)F_3Y\text{-}\beta 2$ (0.4 $F_3Y\bullet/\beta 2$), 10 μM wt- $\alpha 2$, 1 mM CDP and 3 mM ATP. As predicted, the overall amplitude decreases by ~60 %. The data now fit to three phases with the following rate constants: $k_1 = 19 \text{ s}^{-1}$ ($A = 0.43$ equiv.), $k_2 = 0.7 \text{ s}^{-1}$ ($A = 1.4$ equiv.) and $k_3 = 0.01 \text{ s}^{-1}$. Note: when analyzed with respect to $\alpha 2$ only 2 dCDP/ $\alpha 2$ are made in the first two phases (expected – 3 dCDP/ $\alpha 2$) owing to partial oxidation of this particular batch of $\alpha 2$.

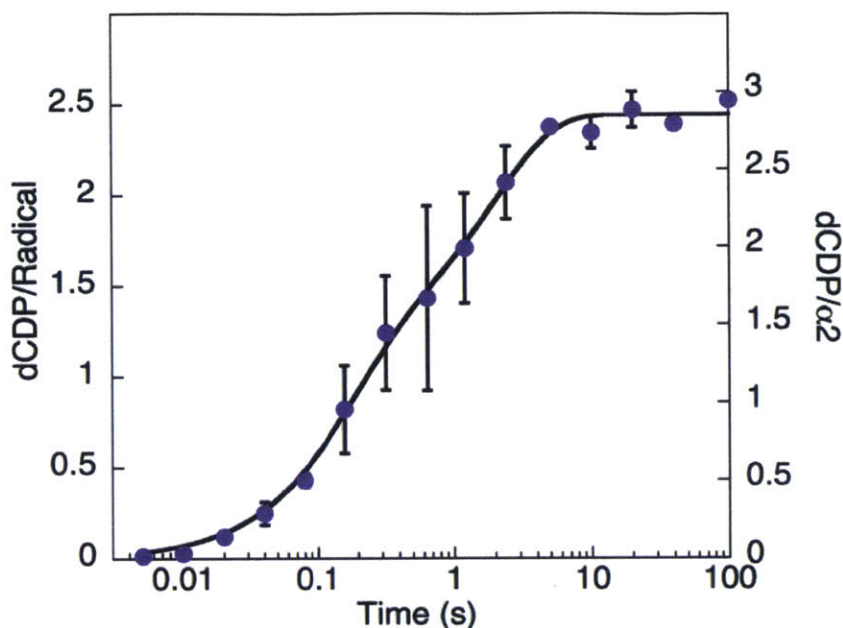


Figure A5.3 Kinetics of dCDP formation in wt RNR in the absence of TR/TRR/NADPH. The reaction mixture contained wt- $\beta 2$ ($1.2 Y\cdot/\beta 2$, $10 \mu M$), wt- $\alpha 2$ ($10 \mu M$), [3H] CDP (0.5 mM) and ATP (3 mM). Two phases are measured for dCDP production, an initial fast phase ($6 \pm 1 \text{ s}^{-1}$, $1.3 \pm 0.2 \text{ dCDP}/\alpha 2$) that we have previously interpreted to report on the generation of the first two dCDPs by each α monomer and a slower phase ($0.5 \pm 0.1 \text{ s}^{-1}$, $1.6 \pm 0.2 \text{ dCDP}/\alpha 2$) that reflects re-reduction of $\alpha 2$ for the generation of two more dCDPs.¹ The ability of $\beta 2$ to associate with multiple $\alpha 2$ s is reflected by the observation of $1.1 \pm 0.1 \text{ dCDP}/Y\cdot$ and $1.3 \pm 0.1 \text{ dCDP}/Y\cdot$ in each kinetic phase. Given our two or none model, 2.2 and 2.6 dCDP/active $\beta 2$ are generated in each phase, greater than the amount of product made by a single $\alpha 2$ during the same time. This observation supports multiple turnovers by $\beta 2$ in each kinetic phase such that all $\alpha 2$ s are oxidized.

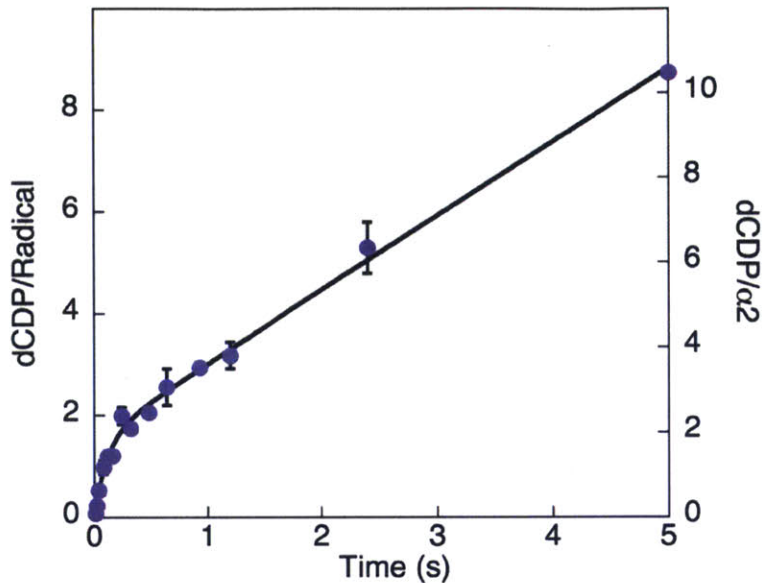


Figure A5.4 Kinetics of dCDP formation in wt RNR in the presence of TR/TRR/NADPH. The reaction mixture contained $\alpha 2$ (10 μM), $\beta 2$ (1.2 $\text{Y}\cdot/\beta 2$, 10 μM), [^3H] CDP (1 mM), ATP (3 mM), TR (40 μM), TRR (0.8 μM) and NADPH (1 mM). A burst phase of 1.9 ± 0.1 dCDP/ $\alpha 2$ (or 1.5 dCDP/ $\text{Y}\cdot$) is observed at a rate constant of 9 ± 2 s^{-1} . The linear phase fits to a rate constant of 1.85 ± 0.05 s^{-1} relative to $\alpha 2$ or 1.45 ± 0.04 s^{-1} relative to $\text{Y}\cdot$. The rate-limiting step for dCDP formation in wt RNR is the conformational change(s) prior to PCET. However, during steady-state turnover in the presence of TR/TRR/NADPH, the rate-limiting step can change depending on the assay conditions. We have previously shown that the turnover number of the wt enzyme decreases with increasing concentration of $\alpha 2$ or $\beta 2^1$ and we proposed that at higher, non-physiological concentrations of the subunits, the rate-limiting step shifts from the conformational change(s) to re-reduction of oxidized $\alpha 2$ by the TR system. Evidence for this proposal is seen in the data presented here. The data support a model where 2 dCDPs are generated by all $\alpha 2$ s during the burst phase prior to re-reduction of the enzyme. Since the reaction mixture only contains 60% active $\beta 2$ (two or none model), the burst phase in wt RNR does not represent a single turnover. This is reflected in the observation of 1.5 dCDP/ $\text{Y}\cdot$ in the burst phase.

REFERENCES

1. Ge, J.; Yu, G.; Ator, M. A.; Stubbe, J. Pre-steady-state and steady-state kinetic analysis of *E. coli* class I ribonucleotide reductase, *Biochemistry* **2003**, *42*, 10071-10083.

Appendix 6

Supporting Figures for Chapter 4

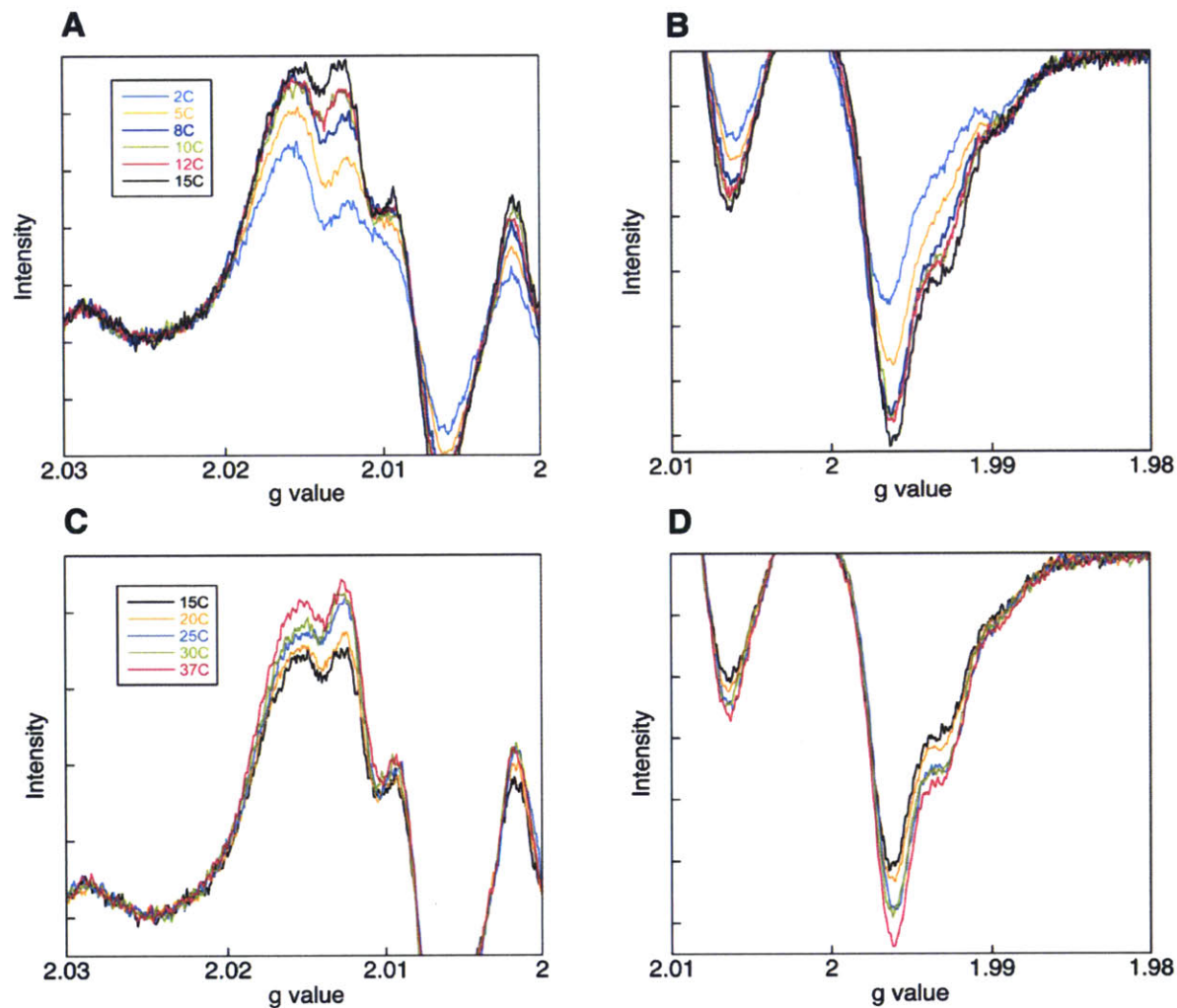


Figure A6.1 Temperature dependence (2–37 °C) of $Y_{356}\bullet$ formation monitored by HQ-EPR spectroscopy. All spectra were collected on three independently prepared samples. Spectra from one trial are shown in Chapter 4 (Figures 4.2B-E). A and B. Expanded views of the low- and high-field regions of the spectra (2 °C to 15 °C) from the second trial. The color code is shown in panel A. C and D. Expanded views of the low- and high-field regions of the spectra (15 °C to 37 °C) from the second trial. The color code is indicated in panel C.

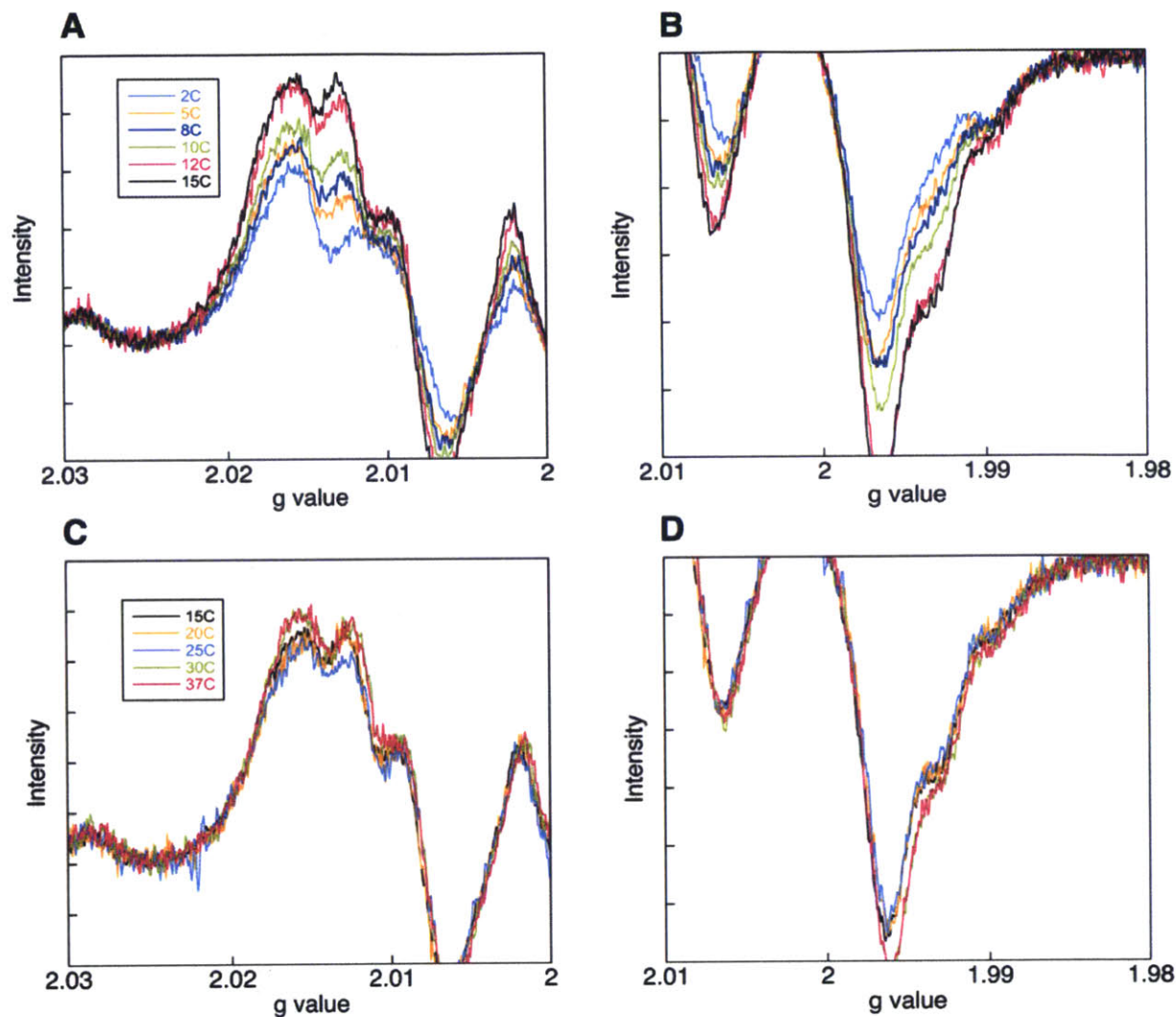


Figure A6.2 Temperature dependence (2–37 °C) of Y_{356}^{\bullet} formation monitored by HQ-EPR spectroscopy. All spectra were collected on three independently prepared samples. Spectra from one trial are shown in Chapter 4 (Figures 4.2B-E). A and B. Expanded views of the low- and high-field regions of the spectra (2 °C to 15 °C) from the third trial. The color code is shown in panel A. C and D. Expanded views of the low- and high-field regions of the spectra (15 °C to 37 °C) from the third trial. The color code is indicated in panel C.

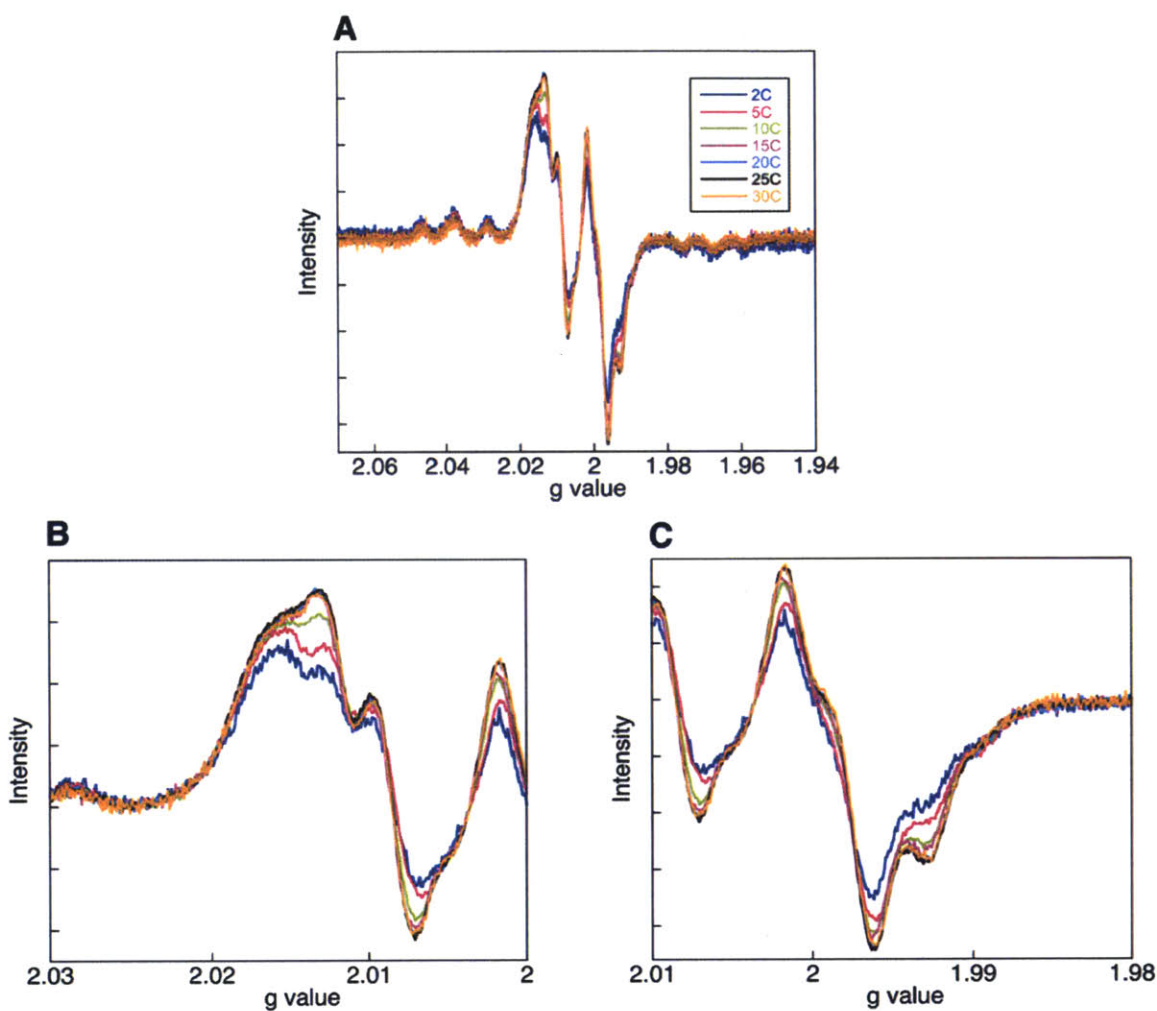


Figure A6.3 Temperature dependence of $Y_{356}\bullet$ formation monitored by RFQ-EPR spectroscopy. The composite EPR spectra recorded upon reacting $Y_{122}(2,3,5)F_3Y\text{-}\beta 2$ (0.8 $F_3Y\bullet/\beta 2$, final concentration $35\ \mu\text{M}$), $Y_{731}F\text{-}\alpha 2$ ($35\ \mu\text{M}$), CDP (1 mM) and ATP (3 mM) are shown in A. B and C. Expanded views of the low- and high-field regions of the spectra respectively. The color code is described in panel A.

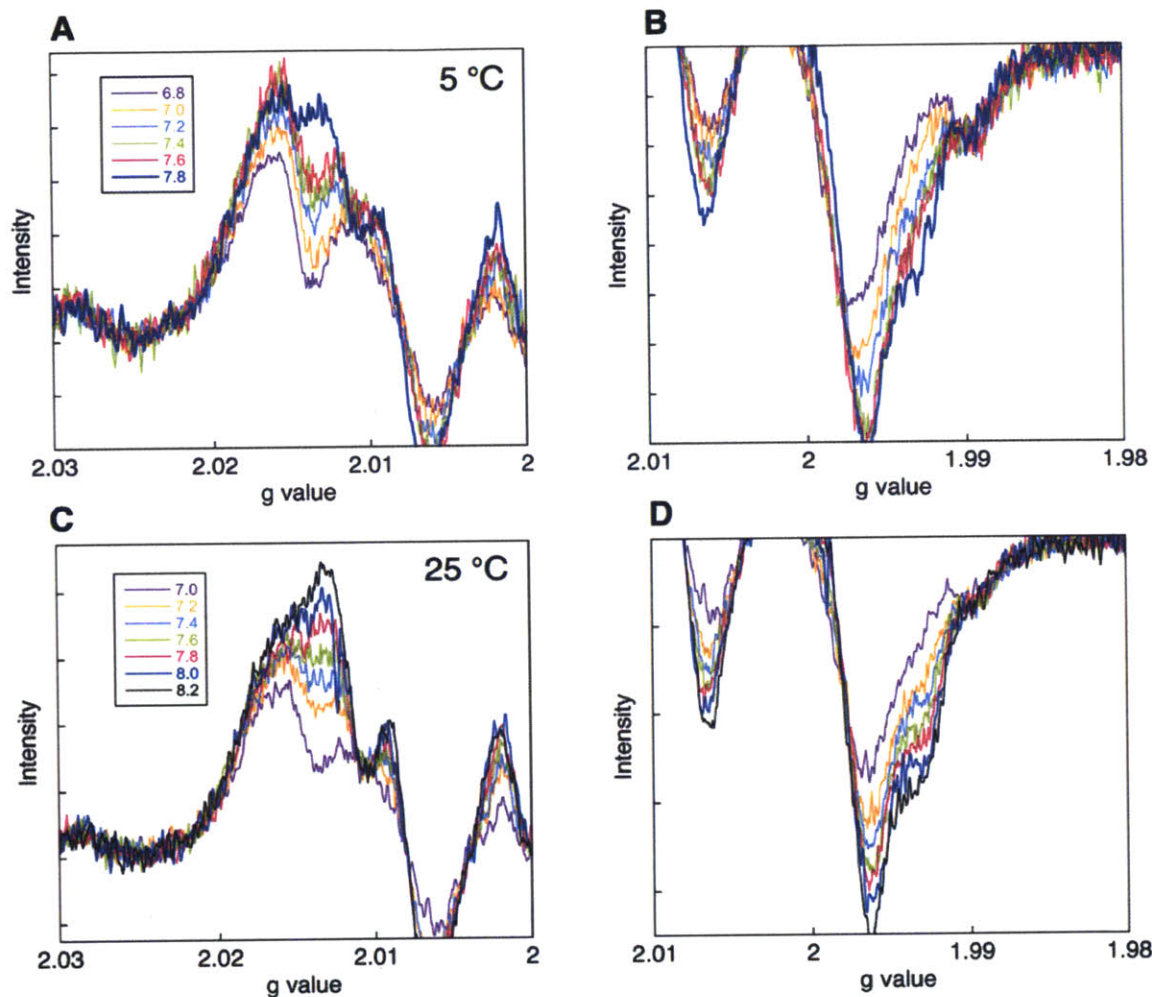


Figure A6.4 Composite EPR spectra of the $Y_{122}(2,3,5)F_3Y-\beta_2/Y_{731}F-\alpha_2/CDP/ATP$ reaction as a function of pH. All spectra were collected on two independently prepared samples. The spectra from the first trial are shown in Chapter 4 (Figure 4.2). A and B. Expanded views of the low- and high-field regions of the spectra from the second trial conducted at 5 °C. The color code is shown in panel A. C and D. Expanded views of the low- and high-field regions of the spectra from the second trial conducted at 25 °C. The color code is shown in panel C.

Appendix 7

Supporting Figures for Chapter 6

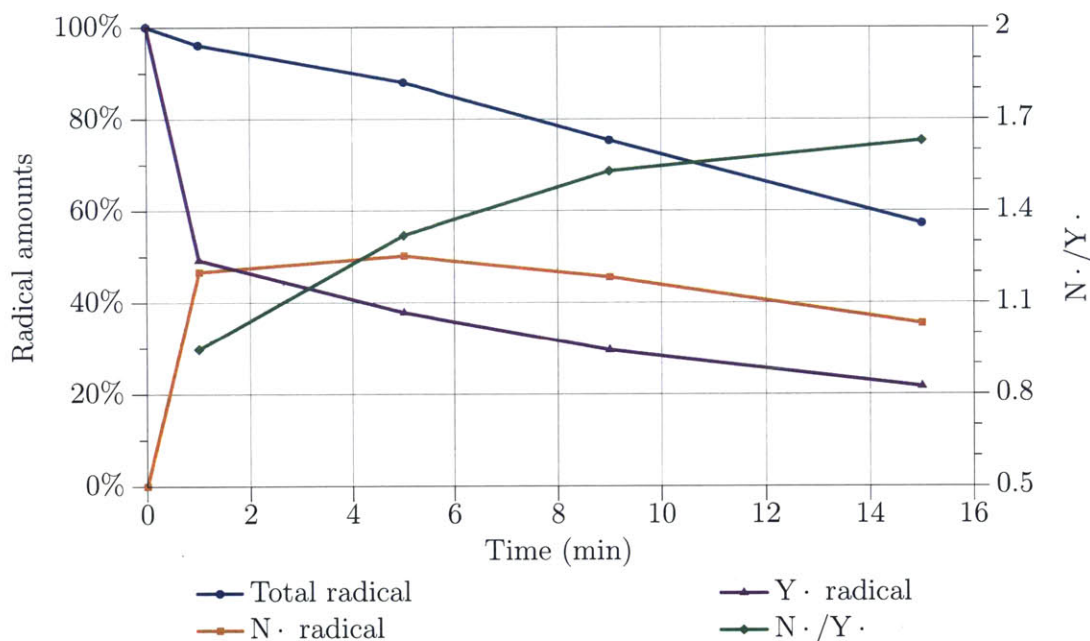


Figure A7.1 Decay curves for radical species in the reaction of wt- $\alpha 2$ (120 μM), wt- $\beta 2$ (1.2 Y•/ $\beta 2$, 100 μM), N₃CDP (1 mM) and TTP (0.5 mM). The reaction components were mixed, incubated in a 25 °C water bath for the desired amount of time and quenched in liquid nitrogen. Figure reproduced from Ref. 1.

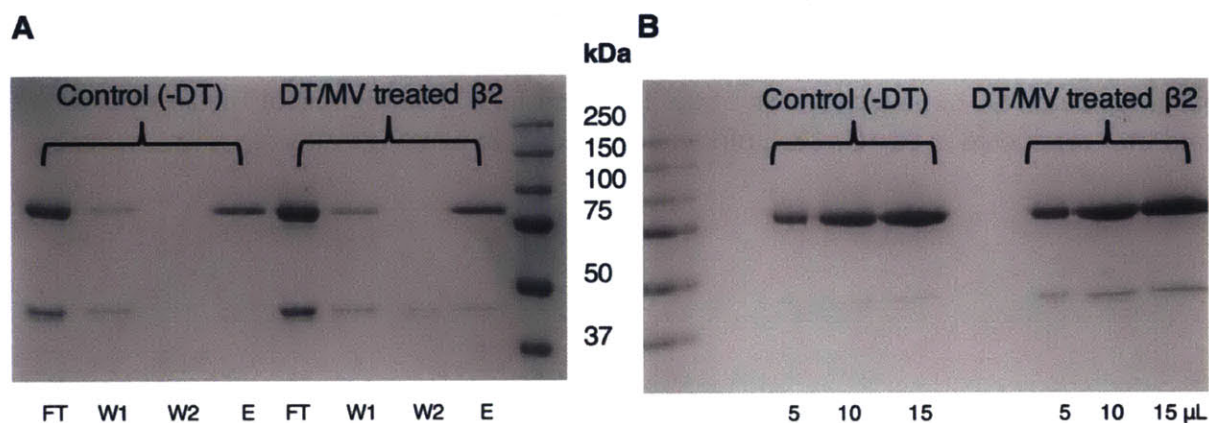


Figure A7.2 Pull-down assay of met- $\beta 2$ or DT/MV treated- $\beta 2$ by His₆-Y₇₃₁F- $\alpha 2$ analyzed by SDS-PAGE: Trial 2. A. The individual steps are indicated: flow-through (FT), first wash (W1), second wash (W2), elution (E) for the control experiment in which no DT was added (left) and DT/MV

treated $\beta 2$ (right). B. Elution fractions from panel A were concentrated 5-fold and loaded in different amounts (5, 10 and 15 μL).

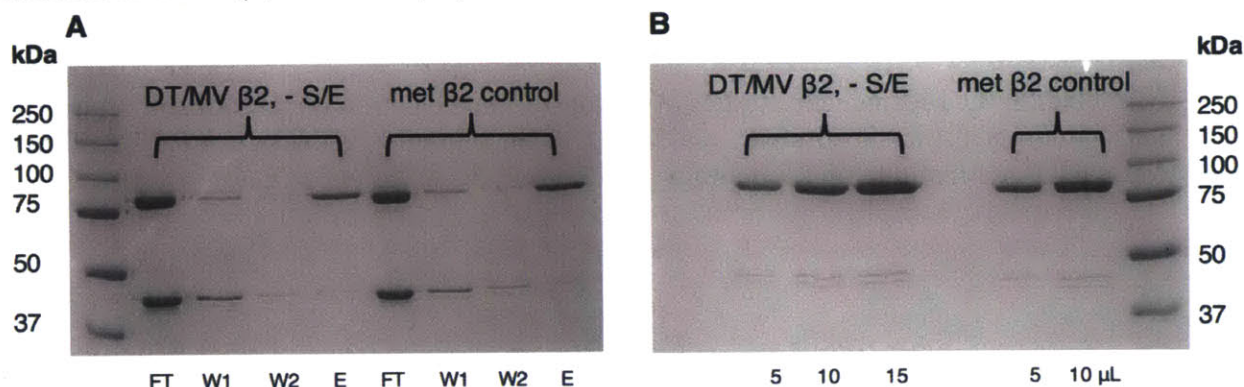


Figure A7.3 Pull-down assay of met- $\beta 2$ or DT/MV treated- $\beta 2$ by His₆-Y₇₃₁F- $\alpha 2$ in the absence of CDP/ATP (S/E) analyzed by SDS-PAGE. A. The individual steps are indicated: flow-through (FT), first wash (W1), second wash (W2), elution (E) for met- $\beta 2$ (right) and DT/MV treated $\beta 2$ (left). B. Elution fractions from panel A were concentrated 5-fold and loaded in different amounts (5, 10 and 15 μL).

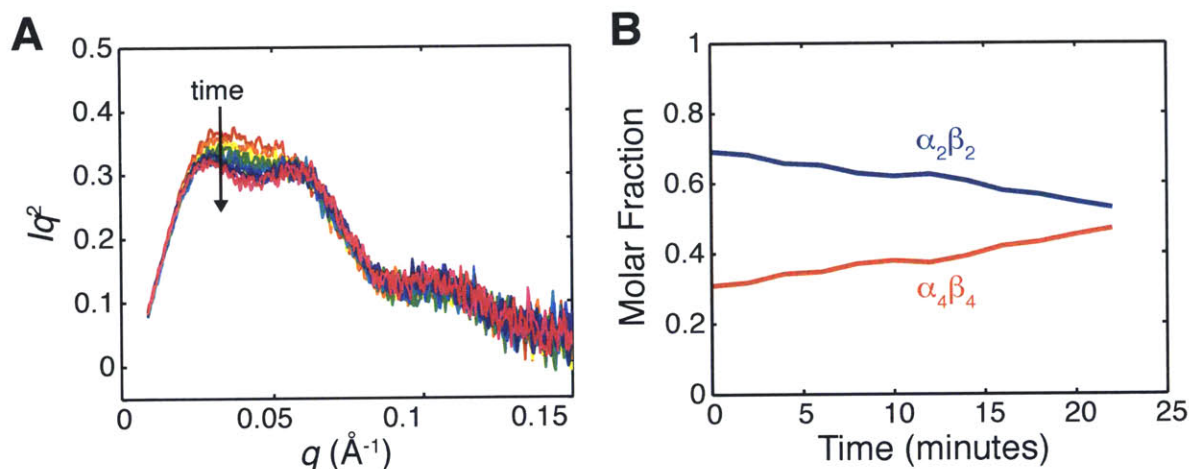


Figure A7.4 Resistance of the Y₇₃₀NH₂Y- $\alpha 2$ / $\beta 2$ complex to dATP-induced $\alpha 4\beta 4$ formation. The reaction conditions were 30 μM each of Y₇₃₀NH₂Y- $\alpha 2$ and wt- $\beta 2$, 1 mM CDP and 175 μM dATP. A. A kratky plot of the SAXS profile indicates no major shift in the solution species over 22 min. B. Fitting the data with linear combinations of the theoretical scattering from the docking model and experimental scattering of $\alpha 4\beta 4$ provides molar fraction of each species. Figure reproduced from Ref. 2.

REFERENCES

1. Artin, E. J. Mechanistic studies of the class I ribonucleotide reductase from *Escherichia coli*. Ph.D. Thesis. Massachusetts Institute of Technology, **2006**.
2. Minnihan, E. C. Mechanistic studies of proton-coupled electron transfer in aminotyrosine- and fluorotyrosine-substituted class Ia ribonucleotide reductase. Ph.D. Thesis. Massachusetts Institute of Technology, **2012**.